Transport and dynamical properties of electron-phonon coupled systems

David Jansen

Dissertation
for the award of the degree
"Doctor rerum naturalium" (Dr.rer.nat.)
of the Georg-August-Universität Göttingen

within the doctoral program
of the Georg-August University School of Science (GAUSS)

submitted by
David Jansen
from Oslo

Göttingen, 25.10.2022

Thesis Committee:

Prof. Dr. Fabian Heidrich-Meisner
Institut für Theoretische Physik, Georg-August-Universität Göttingen

Prof. Dr. Christian Jooss
Institut für Material Physik, Georg-August-Universität Göttingen

Prof. Dr. Peter Sollich
Institut für Theoretische Physik, Georg-August-Universität Göttingen

Members of the Examination Board:

Reviewer: Prof. Dr. Fabian Heidrich-Meisner
Institut für Theoretische Physik, Georg-August-Universität Göttingen

Second Reviewer: Prof. Dr. Stefan Kehrein
Institut für Theoretische Physik, Georg-August-Universität Göttingen

Further members of the Examination Board:

Prof. Dr. Christian Jooss
Institut für Material Physik, Georg-August-Universität Göttingen

Prof. Dr. Peter Sollich
Institut für Theoretische Physik, Georg-August-Universität Göttingen

Prof. Dr. Thomas Weitz
I. Physikalisches Institut, Georg-August-Universität Göttingen

Prof. Dr. Claus Ropers
IV. Physikalisches Institut, Georg-August-Universität Göttingen and Max Planck Institute for Multidisciplinary Sciences

Date of the oral examination: 06.12.2022

Contents

Additional publication

During this Ph.D., I also contributed to the following publication:
Eigenstate thermalization hypothesis through the lens of autocorrelation functions
Christoph Schönle, David Jansen, Fabian Heidrich-Meisner, and Lev Vidmar
Phys. Rev. B 103, 235137 (2021)
https://journals.aps.org/prb/abstract/10.1103/PhysRevB.103.235137

Chapter 1

Introduction

How is charge transported in solids? What role do the vibrations of the atoms play? Why are some materials insulating and others conducting? These are just some of the questions that have fascinated solid-state physicists for more than a century, and already in the year 1900, Drude published his seminal work on transport in metals [1, 2].

The Drude model describes the metal as a composition of positively charged heavy ions and negatively charged light electrons (a thorough discussion can be found in Ref. [3]). In the model, the valence electrons move around and scatter on the immobile ions, and their motion can be described by kinetic gas theory. Even though the model captures some phenomena, like the classical Hall effect, it makes some important assumptions. For example, it does not directly account for electron-electron interactions or electron-ion interactions between collisions, and it does not incorporate quantum mechanics and band structures [3]. The latter two are essential for a qualitative description of metals.

Even when one moves away from the Drude model and treats the electrons quantum mechanically, the question still remains: how to account for the effect the electrons have on the ions in the crystal and vice versa? An electron will interact with the ions and bring them out of their equilibrium position, which leads to vibrations [this is illustrated in Fig. 1.1(a)]. However, any Hamiltonian containing all possible interactions is too complicated to solve, and further approximations are needed. One approach is the Born-Oppenheimer approximation [4, 5] (also known as the adiabatic approximation), and it is based on the assumption that the electrons move with velocities much greater than those of the ions. The electronic problem can then be solved for a given nuclei configuration. One can also describe the lattice in terms of classical harmonic oscillators, which, for example, recovers the correct high-temperature heat capacity (Dulong–Petit law). However, one needs a proper quantum-mechanical treatment of the nuclei to get the correct low-temperature behavior [3].

In a quantum mechanical theory, the (now quantized) lattice vibrations can be described by phonons, and the electron-phonon interaction is responsible for a range of interesting physical phenomena such as the polaron [6] and charge-density-wave (CDW) [7] formation, conventional (Bardeen–Cooper–Schrieffer (BCS)-type) superconductivity [8], and changes in material properties like resistivity [6, 9] and the optical absorption spectra [10].

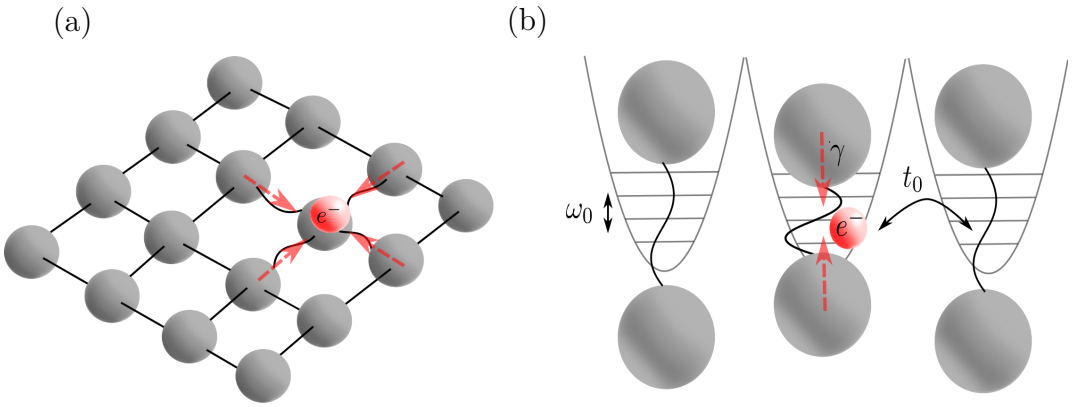

Figure 1.1: (a) Illustration of an electron (red) in a (two dimensional) lattice. The electron interacts with the ions in its vicinity, bringing them out of their equilibrium position. (b) Illustration of the one-dimensional Holstein model. The electron propagates in a crystal and interacts with diatomic molecules. The electron can tunnel from one molecule to another with a tunneling amplitude t_0 and it couples locally to the displacement of the molecules with an interaction strength γ. The molecular vibrations are modeled by quantum harmonic oscillators with frequency ω_0.

The goal of this thesis is to better understand the interplay between the electrons and the lattice vibrations from the perspective of minimal theoretical models that contain CDW and polaron formation. I will do that using numerical algorithms which treat the systems fully quantum mechanically, and in particular, I will focus on the effects of temperature.

One of the aforementioned consequences of electron-phonon interaction is the formation of a quasi-particle called a polaron. In nature, polarons appear in many forms, and a comprehensive review can be found in Ref. [6]. Some types of polarons are large polarons (delocalized over many lattice sites) [11], small polarons (localized on one or a few lattice sites) [12], bipolarons (emerging when the attraction induced by the lattice potential is stronger than the Coulomb repulsion) [13, 14], Jahn-Teller polarons (when the electron energy level degeneracy is broken by lattice distortions) [15, 16], and magnetic polarons (emerging from the interaction between electrons and localized spins) [17, 18], all with different features.

This makes understanding polarons essential for describing the different properties of many materials like TiO_2 [11, 19, 20], halide perovskites [21, 22], manganites [23–31], and organic semiconductors [32, 33]. For example, the low-temperature dependence of the resistivity differs in systems with large and small polarons. As explained in Ref. [6], a large polaron has properties similar to a free charge carrier but with an effective mass. When the temperature is increased, the polaron will scatter more often with other phonons and the resistivity will increase. Materials with small polarons display the opposite behavior. There, the charge carriers need to be thermally activated, and the resistivity decreases when the temperature is increased.

Electron-phonon physics does not only impact the resistivity in some materials but

can also influence properties such as thermal and optical conductivity and charge carrier relaxation. Since this plays an important role in many technological applications, there is a profound interest in better understanding the exact role of polarons, see e.g., Refs. [21,22, 34,35]. There are also many studies on the importance of the quasi-particle in the widely investigated TiO_2 [11,19,20,36], and on its influence on properties of manganites, such as charge ordering, colossal magnetoresistance, and on the absorption spectrum [9,23–31]. In the context of engineering quantum materials with desirable properties [37], Zhang et al. recently demonstrated that one can have high-temperature superconductivity in a simple bipolaron model [38].

In this work, the other electron-phonon-induced phenomenon I focus on is the formation of CDW states [7]. These states are insulating and can emerge from a Peierls transition, meaning that a band gap opens as a consequence of the electron-phonon interaction. By now, they have been the subject of comprehensive studies, for example on the photon-induced melting of CDW states [39,40] and collective excitations [41,42].

From a theoretical perspective, simple models with electron-phonon interaction have been able to describe many of the emerging physical phenomena, and two prominent examples are the Holstein [43,44] and the Fröhlich [45,46] Hamiltonians. Whereas the Fröhlich model approximates the crystal as a continuum and has long-range electron-phonon interactions, the Holstein model contains local interactions in a discrete lattice and will be the focus of this work.

The Holstein model, sketched in Fig. 1.1(b), aims to describe electrons propagating in a lattice with a hopping amplitude t_0 and interacting with diatomic molecules. The electron density couples locally to the displacement of the molecules with an interaction strength γ, and the induced molecular vibrations (the phonons) are modeled by quantum harmonic oscillators with a frequency ω_0. The model displays many of the features induced by electron-phonon interaction, such as small-polaron physics [44], and a transition from a metallic to a CDW phase at half filling (seen, e.g., Refs. [47,48] for phase diagrams). For this reason, the model has already been extensively studied. For example, the polaron problem (one electron in a lattice) has been studied in Refs. [10,49–70], and the model with different electron densities in Refs. [47,48,71–77]. The model has also been a testing ground for new numerical methods for electron-phonon systems, see, e.g., Refs. [68,69,78]. The Holstein model also serves as a basis for more complex models. For example, by allowing for electron-electron interaction, the Holstein model becomes the widely studied Holstein-Hubbard model [79–90]. Recent work has also pointed out that if one includes phonon hopping in the Holstein model (giving the phonons a finite bandwidth), interesting physics emerges, such as changes in spectral functions, effective mass, and CDW formation [67,91–93].

The progress in the theoretical modeling of electron-phonon systems has been accompanied and motivated by advances in experimental techniques. They have allowed for clear connections between theoretical work and experimental results. Most notably in the context of this thesis is the progress in angle-resolved photoemission spectroscopy (ARPES), see Refs. [94–96], optical spectroscopy, and methods to measure thermal properties [97–99].

ARPES experiments enable the study of ultrafast dynamics in materials. This can be used, for example, to access electron energies and momenta by shining a narrow light beam

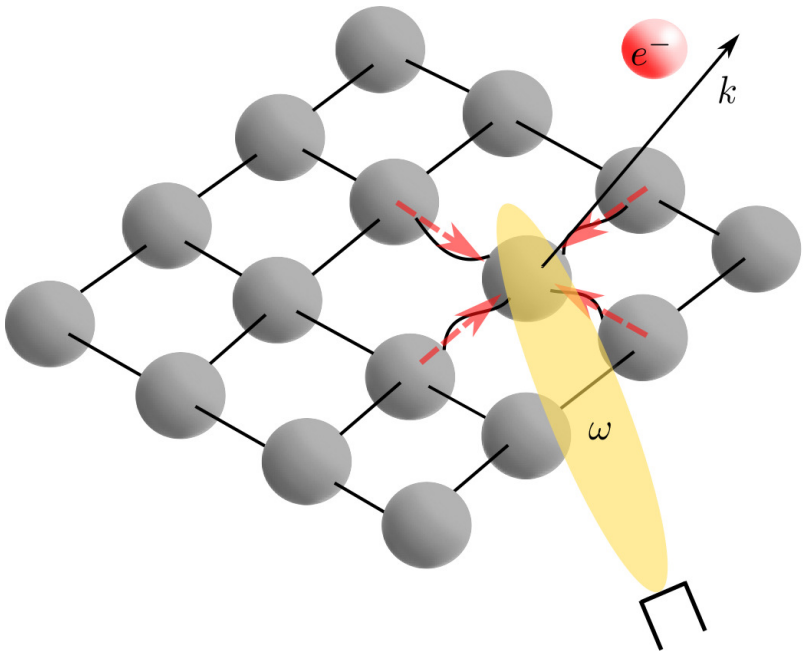

Figure 1.2: Simplified sketch of an ARPES experiment. The electron has absorbed a photon with frequency ω and is excited out of the lattice with momentum k.

with frequency ω on the sample. By varying the beam frequency, one can detect when the photons have sufficient energy to excite an electron with momentum k out of the lattice. I have illustrated the idea in Fig. 1.2. ARPES has allowed for the detection of the polaron spectral function, see, e.g., Refs. [100,101], and the detection of CDWs, see, e.g., Ref. [102]. In optical spectroscopy experiments, on the other hand, one can, for example, detect how much light is reflected by the material. This can be used to determine the polaron optical conductivity [25, 28, 31], the polaron reduced mass [103, 104], and to study the formation of CDW gaps [105].

This fusion of experiment and theory would not be possible without the development of powerful numerical techniques. Prominent examples are density functional theory (DFT) [106, 107], density-matrix renormalization group methods (DMRG) [108–111], dynamic mean field theory (DMFT) [112], quantum Monte Carlo algorithms [113–116], Lanczos methods [117–119], and trajectory-based methods like multiconfigurational Ehrenfest (MCE) [120, 121], multitrajectory Ehernfest (MTE) [122, 123] and surface hopping [124–126].

In general, for a complete understanding of theoretical models, one needs several numerical and analytical methods with complementary strengths and weaknesses. DMRG-based methods, for example, are well-established tools for one-dimensional systems (extensions to higher dimensions are also an active research field [127–131]). Even though DMRG was originally developed to find ground states, it has now been extended to time-evolution [132–137] and finite-temperature calculations [138–144]. These methods are numerically exact, and the error made is well controlled and understood [111,145]. They work

for strongly correlated systems (where it can be difficult to approximate the exchange-correlation energy in DFT methods [146]) and away from regimes that are suitable for perturbation theory. The methods are also very flexible, meaning that a variety of systems and initial states can be studied with only minor modifications to existing codes. However, there are some drawbacks to DMRG algorithms. For example, quantum states are often represented by matrix-product states (see Ref. [111] and Ch. 3 for details). In this way, many of the states relevant for practical applications (such as ground states and product states [111]) can be truncated efficiently with negligible error. However, when doing non-trivial time evolution (for example after a quench [147, 148]), the error (or the computational cost) increase. This means that one can not do time evolution to arbitrary long times, and for this purpose, one has to use Lanczos or exact methods (which again are very restricted in possible system sizes).

For higher dimensions, DMRG-based methods can also have limitations due to the enhanced difficulty of representing the state efficiently (a discussion of why can be found in Ch. 3). In this situation, one is better off with QMC methods in systems that are not plagued by the sign problem or problems without analytic continuation [149, 150]. Alternatively, one can use DMFT, however, this method might have challenges in one and two dimensions. There, the key approximations, namely the absence of vertex corrections in current-current correlation functions (needed for transport studies) and the locality of the self energy, might not be valid [52, 58, 112]. One example can be found in Ref. [58], where the authors compare optical conductivity data for the one-dimensional Holstein polaron calculated with DMFT and exact diagonalization and found a thermally activated resonance not present in the DMFT data. The authors attributed this to the fact that the local DMFT treatment could not capture the required transitions between polaron states with different spatial structures.

In this thesis, the aim is to study electron-phonon systems, described by the Holstein model, in one-dimensional chains. I will study CDW melting and compute finite-temperature correlation functions for polarons, bipolarons, and at finite filling. The goal is to use and develop algorithms that can be applied to these problems and are flexible enough to handle modifications in the corresponding Hamiltonians. Such modifications include introducing a finite phonon bandwidth and electron-electron interactions, and in the future, they might be used to study electron-phonon-spin systems and include different local electron-phonon interaction terms. Another goal is to provide reliable data for many physical relevant quantities as a benchmark for other methods. For these reasons, I mainly use DMRG based methods in this thesis.

As previously stated, DMRG algorithms can efficiently treat one-dimensional systems. However, they can have difficulties dealing with systems with large local Hilbert spaces. This is particularly important for models like the Holstein model. To simulate that model with DMRG, one must introduce a local cutoff in the number of harmonic oscillator states M, and depending on the model parameters, M might have to be very large to capture the correct physics, see, e.g., Refs. [56, 76, 78]. For example, for the polaron in the strong coupling limit, the phonon number expectation value in the ground state is $\approx (\gamma/\omega_0)^2$ (where γ is the coupling parameter and ω_0 is the phonon frequency). To treat the Holstein

model efficiently, I use a technique called local basis optimization (LBO) [151]. The idea of LBO is to find a basis by diagonalizing reduced density matrices in which the state can be truncated with negligible error. There are other promising approaches [152–155], but LBO has proven itself as an effective method for time evolution [63, 76, 156] and ground-state calculations [76, 157].

In this thesis, I will present results from a series of publications. In the first publication [158], we combine LBO with purification [138] (a DMRG scheme to do finite temperature calculations) and use this method to calculate different spectral functions for the Holstein polaron model. Purification is a well-established tool [141, 159–163] for finite-temperature matrix-product-state calculations where the infinite-temperature density matrix is imaginary-time evolved to the required temperature. We first demonstrate that even though the infinite-temperature density matrix is ill-defined for the Holstein model (since M must be ∞), this is still an effective method to treat electron-phonon systems accurately at low temperatures. We further show that this method is sped up at low temperatures when combined with LBO, which allows us to efficiently calculate the polaron spectral function, the electron emission function, and the phonon spectral function.

For the polaron spectral function, we test our method by comparing it to data in the literature calculated with the Lanczos method [65]. This verifies that our approach works and that we can calculate larger systems and include more phonons. We detect the known polaron features in the intermediate electron-phonon coupling regime, such as peaks separated by the phonon frequency and that spectral weight appears below the quasiparticle peak when the temperature is increased [65]. For the electron emission function, we report the emergence of a new thermally activated polaron band and demonstrate the shift in electron density to larger quasi-momenta states at higher temperatures. For the phonon spectral function, we recover the flat free-phonon line and the polaron band seen in Ref. [57] for the ground state but observe a thermally activated phonon line and polaron band at negative frequencies.

In the second publication, Ref. [164], the goal is to extract the optical conductivity for the Holstein polaron and bipolaron by computing the Fourier transformation of real-time current-current correlation functions. In Ref. [156], it was already explained how LBO can be used for time-evolving matrix-product states with the time-evolution block decimation (TEBD) algorithm [132]. However, recent results indicate that the time-dependent variational principle (TDVP) algorithms [135, 136] often perform better and allow for a longer time evolution [137]. For this reason, we combine LBO with TDVP. Using a parallel implementation [165, 166] and a serial single-site implementation (without LBO) of the TDVP algorithm, we are now able to calculate the correlation functions for times long enough for a good resolution in frequency space. We do this for different parameters, at finite temperatures, and with a finite phonon bandwidth. For weak and intermediate electron-phonon coupling, we compare our ground-state results to data obtained with the Lanczos method and find quantitative agreement. Whereas the ground-state spectral function and optical conductivity was studied in Ref. [67], we study the effects of a finite phonon bandwidth at finite temperatures for the polaron and bipolaron in different parameter regimes.

Our finite-temperature results show that for weak and intermediate electron-phonon

coupling strengths, the prominent one-phonon emission peak is moved to lower frequencies when the temperature is increased. For the intermediate electron-phonon coupling strength, the peak structure induced by a downward phonon dispersion relation remains at the accessible temperatures. Furthermore, we demonstrate that in the strong electron-phonon coupling regime, the results can be well understood by analyzing the Born-Oppenheimer Hamiltonian. We recover the known result of an asymmetric Gaussian function [10, 58, 167] for both the polaron and bipolaron but see how the center of the spectra gets shifted to higher or lower frequencies. The shift depends on the shape of the phonon dispersion relation, consistent with the change in energy differences between the Born-Oppenheimer surfaces.

I will then demonstrate that the analysis based on the Born-Oppenheimer surfaces holds, even for bipolarons (two electrons with different spins in a Holsten lattice) with electron-electron repulsion (weak enough to still have a bound bipolaron). In the DMRG data, one can clearly see a thermally activated resonance at frequency $\approx 2t_0$, and that the spectra is shifted to lower frequencies when the electron-electron repulsion is increased.

In the last part of the chapter, I use the same numerical methods to calculate optical conductivities and energy transport coefficients at finite frequencies at filling $n = 1/3$ and $n \approx 1/2$. For strong electron-phonon coupling in the adiabatic regime, I find that the optical conductivity for $n = 1/3$ resembles the conductivity for a single electron in a Holstein lattice, indicating that the spectra is dominated by polaron physics. Additionally, I find that the same features appear in the energy transport coefficient. For an intermediate electron-phonon coupling strength and phonon frequency, the optical conductivity has a broader spectra for $n = 1/3$ than the single polaron. Additionally, the energy transport coefficient exhibits a plateau at frequencies where the optical conductivity has decayed to zero. These features also remain when the filling is increased to $n \approx 1/2$.

After that, the focus will shift to CDW dynamics in the Holstein model and the Holstein model coupled to tight-binding leads (a Holstein heterostructure). The latter is known as the Anderson-Holstein model [168–170] for a single Holstein site. In our publication, Ref. [171], we interpolate a voltage linearly through the Holstein model and heterostructure (with nine Holstein sites), and analyze how the CDWs break down (similar studies have been done on the breakdown of Mott insulating states coupled to tight-binding leads [172, 173]). We find that the order parameters remain unchanged when the inter-site voltage difference is much smaller than the polaron binding energy. However, as the two become comparable in magnitude, the electrons start tunneling out of the phonon-induced potential and the order parameter decays. For the Holstein heterostructure in the metallic parameter regime, we compute the current-voltage diagram (done for the Anderson-Holstein model in Ref. [174]) and show how the current flowing through the system decreases when the electron-phonon coupling is increased.

In the last part of this thesis, I will present a study, Ref. [175], where we investigate typical solid-state physics questions such as how do electrons spread in a lattice [66, 176], how does a CDW melt [75–77, 177, 178], and how is energy transferred between electronic and phononic degrees of freedom [62, 63, 76]. The emphasis, however, is on determining whether a full quantum treatment of the phonons is required or if numerically cheaper

trajectory-based methods, where the phonons propagate according to classical equations of motion, can be used. We compare numerically exact results to calculations done with the trajectory-based methods multitrajectory Ehrenfest (MTE) [122, 123], surface hopping [124–126], and multiconfigurational Ehrenfest (MCE) [120, 121]. First, we study how a localized electron (bare and dressed with phonons) spreads in a lattice, similar to the studies done in, e.g., Refs. [66, 179, 180]. Here, we find that all methods capture the initial spread of the electron density well, but at later times deviate from the numerically exact results (computed with DMRG with LBO). We also look at the phonon number expectation value and find that all the methods capture the time dependence qualitatively, except for MTE, which predicts much smaller values.

We then compare the MTE algorithm to DMRG with LBO for dressed and bare CDW initial states. Whereas the dynamics of these states were addressed with DMRG in Ref. [76], we focus on understanding if and how well MTE works. We find that in the adiabatic parameter regime, the electron kinetic energy and order parameter are computed very accurately with MTE for the dressed CDW. For the bare CDW, the order parameter is still captured accurately, but the kinetic energy shows significant deviations. In both cases, the phonon number deviates from the DMRG values. In the anti-adiabatic regime (which is expected to be difficult for MTE), all the observables differ from the DMRG results.

This thesis is structured as follows: In Ch. 2, I introduce the Holstein model. Chapter 3 reviews the key ideas of the numerical methods I use. I particularly focus on how to incorporate LBO into matrix-product-state algorithms. In Ch. 4, I show the results for the Holstein-polaron spectral functions computed with DMRG and LBO. The formalism is then extended to TDVP, finite filling, and the bipolaron in Ch. 5. There, results for the energy transport coefficient and optical conductivity are presented. CDW melting in the Holstein model and Holstein heterostructures is studied in Ch. 6, and in Ch. 7, our analysis of the trajectory-based approaches are presented. Finally, I conclude in Ch. 8.

Chapter 2

The Holstein model

Holstein introduced a model in Ref. [43] to describe electrons moving around in a molecular crystal and interacting with diatomic molecules. Known as the Holstein model, it is an economical model, but captures a lot of the fundamental physics that emerges due to electron-phonon interaction. In the Holstein model, the molecules can only oscillate with one frequency and are modeled by local harmonic oscillators. This makes the model well suited to capture phenomena that occur due to the interaction between electrons and optical (so-called Einstein) phonons, such as polaron formation [44] and phonon-induced phase transitions [47, 48, 181, 182]. The Hamiltonian of an L site one dimensional lattice with open boundary conditions has the following form

$$\hat{H} = -t_0 \sum_{j=1,s=\uparrow,\downarrow}^{L-1} \left(\hat{c}^\dagger_{j,s} \hat{c}_{j+1,s} + \hat{c}^\dagger_{j+1,s} \hat{c}_{j,s} \right) + \omega_0 \sum_{j=1}^{L} \hat{b}^\dagger_j \hat{b}_j + \gamma \sum_{j=1}^{L} \hat{n}_j \hat{X}_j \,. \tag{2.1}$$

In Eq. (2.1), $\hbar = 1$, t_0 is the hopping amplitude of the electrons, ω_0 is the phonon frequency, and γ determines the electron-phonon interaction strength. The operators $\hat{c}^\dagger_{j,s}$ ($\hat{c}_{j,s}$) are the electron creation (annihilation) operators which create (annihilate) an electron at site j with spin $s \in \{\uparrow, \downarrow\}$. The phonon operators $\hat{b}^\dagger_j$ ($\hat{b}_j$) correspondingly create (annihilate) a phonon on site j. The last term in the Hamiltonian is the coupling between the local electron occupation number, $\hat{n}_j = \hat{n}_{j,\downarrow} + \hat{n}_{j,\uparrow} = \hat{c}^\dagger_{j,\downarrow} \hat{c}_{j,\downarrow} + \hat{c}^\dagger_{j,\uparrow} \hat{c}_{j,\uparrow}$, and the local oscillator displacement, $\hat{X}_j = \hat{b}^\dagger_j + \hat{b}_j$. A common basis choice for the Hamitonian in Eq. (2.1) is the number-occupation basis $|n_1\rangle_{el} |m_1\rangle_{ph} |n_2\rangle_{el} |m_2\rangle_{ph} \ldots |n_L\rangle_{el} |m_L\rangle_{ph}$, where n_j (m_j) is the electron (phonon) number on site j. The model is sketched in Fig. 2.1.

One can generate a finite phonon bandwidth by introducing a phonon hopping term

$$\hat{H}_{\text{ph-hopping}} = t_{\text{ph}} \sum_{j=1}^{L-1} \left(\hat{b}^\dagger_j \hat{b}_{j+1} + \hat{b}^\dagger_{j+1} \hat{b}_j \right) \,. \tag{2.2}$$

t_{ph} is the phonon hopping amplitude and one should chose $|t_{\text{ph}}| \ll \omega_0$ to model realistic optical phonons. In this work, I will only look at the effect of a finite phonon bandwidth when discussing transport coefficients in Ch. 5.

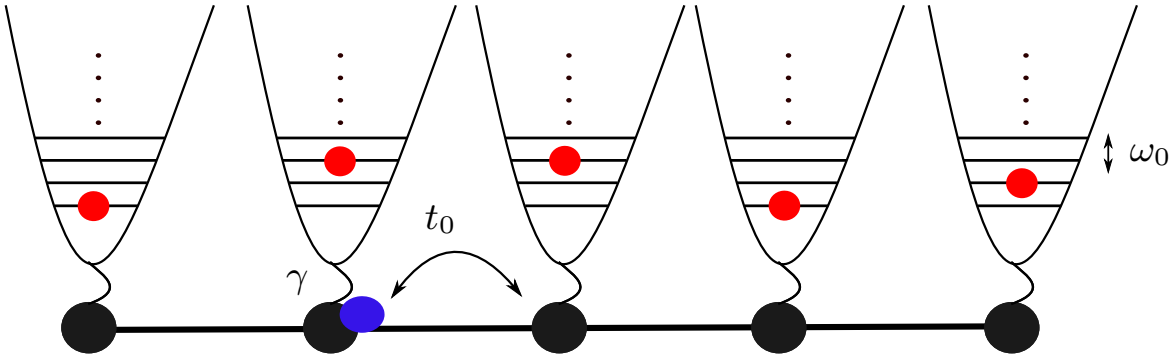

Figure 2.1: Sketch of the Holstein model. The fermion (blue circle) can tunnel between sites with a tunneling amplitude t_0. On each site, there is a local harmonic oscillator with frequency ω_0, and the fermion couples to the oscillator with a coupling strength γ. The red circles illustrate the occupied harmonic oscillator states.

By including electron-electron interaction of the form

$$\hat{H}_{\text{el-el}} = U \sum_{j=1}^{L} \hat{n}_{j,\downarrow} \hat{n}_{j,\uparrow} \,, \tag{2.3}$$

the Holstein model turns into the Holstein-Hubbard model. This is an interesting extension of the Holstein model with an additional layer of complexity due to the competition between electron-electron and electron-phonon interactions, and its phase transition has been extensively studied, e.g., in Refs. [79–82]. For only two electrons with different spins, the introduction of electron-electron repulsion allows for the formation of both bound and unbound bipolarons, see e.g., Refs. [83–90]. In Ch. 5, I will demonstrate how the optical conductivity of these bipolarons can be understood based on the Born-Oppenheimer surfaces, which I will introduce in Sec 2.3.

2.1 Holstein polarons

By only allowing for one or two electrons in the Holstein model, one can study polaron physics [44]. The polarons have a variety of physical properties depending on the model parameters, and a phase diagram can be found in Ref. [59]. To guide the discussion, I will introduce the adiabatic parameter

$$\alpha = \omega_0 / t_0 \,, \tag{2.4}$$

which characterizes the adiabatic ($\alpha \ll 1$), fast electron motion compared to the lattice vibrations, and the anti-adiabatic ($\alpha \gg 1$) regime. Furthermore, I define

$$\lambda = \frac{\gamma^2}{2 t_0 \omega_0} \,. \tag{2.5}$$

λ is the ratio of the ground-state energies in the polaron (taking $t_0 \to 0$ gives $E_{GS,\text{pol}} = -E_P = -\gamma^2/\omega_0$) and the free electron limit ($E_{GS,\text{free } el} = -2t_0$). The parameter characterizes the transition from a small polaron with $\lambda \gg 1$ to a large polaron with $\lambda \ll 1$. In the limit of $t_0 \to 0$, the Holstein Hamiltonian can be diagonalized with a Lang-Firsov transformation [183], $\hat{\tilde{H}} = e^{\hat{S}} \hat{H} e^{-\hat{S}}$, with $\hat{S} = \frac{\gamma}{\omega_0} \sum_j \hat{n}_j (\hat{b}_j^\dagger - \hat{b}_j)$. By transforming the phonon operators, one gets

$$\hat{\tilde{b}}_j^\dagger = \hat{b}_j^\dagger - \frac{\gamma}{\omega_0}, \; \hat{\tilde{b}}_j = \hat{b}_j - \frac{\gamma}{\omega_0} \,. \tag{2.6}$$

Now, the Hamiltonian can be written as a sum of one-site terms $\hat{\tilde{H}} = \sum_j \hat{\tilde{h}}_j$, with

$$\begin{aligned} \hat{\tilde{h}}_j &= e^{\hat{S}} \hat{h}_j e^{-\hat{S}} = \omega_0 \hat{\tilde{b}}_j^\dagger \hat{\tilde{b}}_j + \gamma(\tilde{b}_j^\dagger + \tilde{b}_j) = \omega_0 (\hat{b}_j^\dagger - \frac{\gamma}{\omega_0})(\hat{b}_j - \frac{\gamma}{\omega_0}) + \gamma(b_j^\dagger + b_j - 2\frac{\gamma}{\omega_0}) \\ &= \omega_0 \hat{b}_j^\dagger \hat{b}_j - \frac{\gamma^2}{\omega_0} = \omega_0 \hat{b}_j^\dagger \hat{b}_j - E_P \,, \end{aligned} \tag{2.7}$$

and $E_P = \frac{\gamma^2}{\omega_0}$. The ground state, with respect to a certain site j, can be written as $\langle GS_j | \hat{h}_j | GS_j \rangle = \langle GS_j | e^{-\hat{S}} e^{\hat{S}} \hat{h}_j e^{-\hat{S}} e^{\hat{S}} | GS_j \rangle = \langle GS_j | e^{-\hat{S}} \hat{\tilde{h}}_j e^{\hat{S}} | GS_j \rangle$. From Eq. (2.7), one sees that $e^{\hat{S}} |GS_j\rangle = |0\rangle_{ph} \hat{c}_j^\dagger |0\rangle_{el}$. This is the coherent state,

$$\begin{aligned} |GS\rangle_j &= e^{-\hat{S}} |0\rangle_{ph} \hat{c}_j^\dagger |0\rangle_{el} = e^{-\frac{\gamma}{\omega_0}(\hat{b}_j^\dagger - \hat{b}_j)} |0\rangle_{ph} \hat{c}_j^\dagger |0\rangle_{el} = e^{-\frac{\gamma}{\omega_0}\hat{b}_j^\dagger} e^{\frac{\gamma}{\omega_0}\hat{b}_j} e^{\frac{\gamma^2}{2\omega_0^2}[\hat{b}_j^\dagger, \hat{b}_j]} |0\rangle_{ph} \hat{c}_j^\dagger |0\rangle_{el} \\ &= e^{-\frac{\gamma^2}{2\omega_0^2}} e^{-\frac{\gamma}{\omega_0}\hat{b}_j^\dagger} |0\rangle_{ph} \hat{c}_j^\dagger |0\rangle_{el} \,, \end{aligned} \tag{2.8}$$

with energy $-E_P$. If one now does perturbation theory in t_0 with the term

$$\hat{H}_{\text{kin}} = -t_0 \sum_{j=1, s=\uparrow,\downarrow}^{L-1} \left(\hat{c}_{j,s}^\dagger \hat{c}_{j+1,s} + \hat{c}_{j+1,s}^\dagger \hat{c}_{j,s} \right) \tag{2.9}$$

to first order, one gets a contribution between the degenerate ground state with the electron of neighboring sites ${}_{j+1}\langle GS | \hat{H}_{\text{kin}} | GS \rangle_j = t_0 e^{-\frac{\gamma^2}{\omega_0^2}} = \tilde{t}_0$. $\tilde{t}_0$ is now referred to as the renormalized hopping amplitude. In this thesis, I will refer to the Holstein polaron as the Holstein model with one electron in the lattice, and a bipolaron as the Holstein model with two electrons with different spins.

2.2 Half filling

At half filling, the one dimensional Holstein model exhibits a phase transition from a Tomonaga-Luttinger liquid (TLL) to a charge density wave (CDW), and the phase diagram has been calculated using (Quantum) Monte Carlo and DMRG methods [47, 48, 181, 182].

The CDW formation can be understood in several parameter limits, and the following results are derived in Ref. [181]. In the adiabatic limit, $\alpha \to 0$, one is left with a staggered potential induced by the displaced harmonic oscillators and this leads to gap opening. Interestingly, there is, however, no CDW gap emerging in the limit $\alpha \to \infty$, where the phonons react instantaneously to the electronic motion. For spinless electrons, which we will consider later, one recovers the free electron model. Another interesting limit is the strong electron-phonon coupling limit. There, the spinless Holstein model can be mapped to spinless fermions with repulsive interaction (or an antiferromagnetic XXZ-Hamiltonian) using second-order perturbation theory. Since the CDW states emerges due to phonon-induced dimerization, the transition is also referred to as a Peierls transition.

In Ch. 6 and Ch. 7, the focus will be on CDWs in the spinless Holstein model and the spinless Holstein model coupled to two tight-binding leads. To determine if the system is in a CDW state, following, e.g., Ref. [76], I introduce an order parameter in the electron sector

$$\mathcal{O}_n = \frac{1}{N_{el}} \sum_{i=1}^{L} (-1)^{i-1} \langle \hat{n}_i \rangle \ , \tag{2.10}$$

where N_{el} is the number of electrons. In the phonon sector, I use

$$\mathcal{O}_X = \frac{-1}{N_{el}} \sum_{i=1}^{L} (-1)^{i-1} \langle \hat{X}_i \rangle \ . \tag{2.11}$$

The -1 in Eq. (2.11) is only to ensure a positive value for $\mathcal{O}_X$ in the CDW phase with our convention of the sign of γ. In Ch. 6, I will use odd L and $N_{el} = (L+1)/2$. In this case, both $\mathcal{O}_n$ and $\mathcal{O}_X$ go to zero when $L \to \infty$ in the TLL phase. On the other hand, in the strong coupling limit, $\mathcal{O}_X \to 2\frac{\gamma}{\omega_0}$ and $\mathcal{O}_n \to 1$ for $L \to \infty$. There will also be a discussion of CDWs in Ch. 7, but with a slightly different convention than what I introduced here. That convention will be explained in the publication in Ch. 7.

2.3 The Born-Oppenheimer Hamiltonian

In some situations, it is convenient to rewrite the Holstein Hamiltonian in terms of the nuclei momentum and position operators $\hat{p}_i$ and $\hat{x}_i$. The Hamiltonian then becomes

$$\hat{H} = \hat{H}_{\text{ekin}} + \sum_{i=1}^{L} \left(\gamma \sqrt{2m\omega_0} \hat{n}_i \hat{x}_i + \frac{m\omega_0^2}{2} \hat{x}_i^2 + \frac{\hat{p}_i^2}{2m} - \frac{m\omega_0}{2} \right), \tag{2.12}$$

and a derivation can be found in Appendix C.2. The Hamiltonian in Eq. (2.12) can now be divided into two terms: the nuclear kinetic energy $\hat{T}^{\text{nuc}} = \sum_{i=1}^{L} \frac{\hat{p}_i^2}{2m}$ and the Born-Oppenheimer Hamiltonian $\hat{H}_{\text{BO}}(\hat{R})$ [4,5]. $\hat{H}_{\text{BO}}(\hat{R})$ depends on the nuclear configuration $\hat{R}$, and for a fixed R, $\langle R | \hat{H}_{\text{BO}}(\hat{R}) | R \rangle = \hat{H}_{\text{BO}}(R)$ is an electronic operator. This is particularly useful in the adiabatic regime (slow phonons), where the change in phonon coordinates

($\hat{T}^{\text{nuc}}$) often can be neglected. In many cases, the eigenstates of the Born-Oppenheimer Hamiltonian serve as a convenient electronic basis [5], with

$$\hat{H}_{\text{BO}}(R)\phi_a(R) = E_a^{\text{BO}}\phi_a(R)\,. \tag{2.13}$$

For the Holstein dimer ($L = 2$), one can gain more insight into the model by defining the relative coordinate $\hat{q} = \frac{1}{\sqrt{2}}(\hat{x}_1 - \hat{x}_2)$ and the center of mass coordinate $\hat{Q} = \frac{1}{\sqrt{2}}(\hat{x}_1 + \hat{x}_2)$. By letting $\hat{q} \to q$, neglecting the Q terms, which are just independent oscillators, and defining $\bar{q} = q\sqrt{\frac{1}{m\omega_0}}$, one obtains

$$\hat{H}_{\text{BO}} = \hat{H}_{\text{kin}} + \gamma[\bar{q}(\hat{n}_1 - \hat{n}_2)] + \frac{1}{2}\bar{q}^2\omega_0\,. \tag{2.14}$$

Written as a matrix, one has

$$\hat{H}_{\text{BO}} = \begin{pmatrix} \frac{\bar{q}^2}{2}\omega_0 + \gamma\bar{q} & -t_0 \\ -t_0 & \frac{\bar{q}^2}{2}\omega_0 - \gamma\bar{q} \end{pmatrix}, \tag{2.15}$$

with the energies are $E_{\pm}^{\text{BO}} = \frac{1}{2}\left(\bar{q}^2\omega_0 \pm 2\sqrt{(\gamma\bar{q})^2 + t_0^2}\right)$. This formalism can be extended to the Holstein-Hubbard bipolaron, but one has a 4×4 matrix

$$\hat{H}_{\text{BO}} = \begin{pmatrix} \frac{\bar{q}^2}{2}\omega_0 + 2\gamma\bar{q} + U & -t_0 & -t_0 & 0 \\ -t_0 & \frac{\bar{q}^2}{2}\omega_0 & 0 & -t_0 \\ -t_0 & 0 & \frac{\bar{q}^2}{2}\omega_0 & -t_0 \\ 0 & -t_0 & -t_0 & \frac{\bar{q}^2}{2}\omega_0 - 2\gamma\bar{q} + U \end{pmatrix}, \tag{2.16}$$

which now can be diagoanlized numerically. Note that we have chosen the electron basis $|{\uparrow\downarrow}, 0\rangle, |{\uparrow}, {\downarrow}\rangle, |{\downarrow}, {\uparrow}\rangle, |0, {\uparrow\downarrow}\rangle$. In Ch. 5, I will demonstrate that many of the properties of the small polaron and bipolaron transport coefficients can be understood in terms of the Born-Oppenheimer Hamiltonians.

2.4 Spectral functions

One of the main goals of modern numerical methods is to be able to efficiently calculate Green's functions and transport coefficients. The importance of these quantities has made them standard textbook material, e.g., in Refs. [167, 184, 185]. One key result of this work is the calculation of these quantities for different polaron systems with the matrix-product state-based methods (see Ch. 3).

I will first define the greater and lesser Greens function for spinless fermions in equilibrium as

$$G_T^{>}(t,k) = -i\,\langle \hat{c}_k(t)\hat{c}_k^{\dagger}(0)\rangle_T\,,\; G_T^{<}(t,k) = i\,\langle \hat{c}_k^{\dagger}(0)\hat{c}_k(t)\rangle_T\,, \tag{2.17}$$

where $\langle\hat{A}\rangle_T = Tr[\frac{1}{Z}e^{-\beta\hat{H}}\hat{A}]$ is the thermal expectation value at temperature $T = 1/\beta$, Z is the partition function and $Tr[\ldots]$ is the trace. $\hat{c}_k(t)$ is the fermionic annihilation

operator defined in quasi-momentum space in the Heisenberg picture. In Eq. (2.17), one can, for example, interpret $G^<(\omega, k)$ as the probability amplitude of inserting an electron with quasi-momentum k and removing an electron with quasi-momentum k at a later time t.

One can now do the Fourier transformation into frequency space and write $G^>(\omega, k)$ [similar for $G^<(\omega, k)$] in the Lehmann representation

$$\begin{aligned} G^>_T(\omega, k) &= \frac{-i}{Z}\int_{-\infty}^{\infty} dt e^{-\omega i t}\sum_{n,m} e^{-E_n\beta}\,\langle n|c_k(t)|m\rangle\,\langle m|c_k^\dagger|n\rangle \\ &= -2\pi\frac{i}{Z}\sum_{n,m} e^{-E_n\beta}\,\langle n|c_k|m\rangle\,\langle m|c_k^\dagger|n\rangle\,\delta(\omega - E_n + E_m)\,. \end{aligned} \tag{2.18}$$

The steps are textbook material, see e.g. Refs. [184], and can be found in Appendix A. As an example, I will consider a non-interacting tight-binding chain [just the electron kinetic energy from Eq. (2.1)], and focus on the vacuum state ($|0\rangle$) contribution. One then gets

$$G^>_{T,0}(k,\omega) = -2\pi i\sum_m \langle 0|c_k|m\rangle\,\langle m|c_k^\dagger|0\rangle\,\delta(\omega - \epsilon_m)\,, \tag{2.19}$$

where the ϵ_m are the eigenenergies $\epsilon_m = -2t_0\cos(k_m)$, and k_m is the m-th quasi-momentum. I then define the (later polaron) spectral function to be

$$A(k,\omega) = -\frac{1}{2\pi}\mathrm{Im}\{G^>_{T,0}(k,\omega)\}\,. \tag{2.20}$$

For the free electron, $A(k,\omega)$ just recovers the fermion cosine shaped band. Note that I introduced the sub-index $T, 0$ to indicate that the trace is calculated in the zero-electron sector at temperature T. When calculating Eq. (2.18) for the Holstein polaron, $|n\rangle = |\vec{n}\rangle_{ph}\,|0\rangle_e$, where $|\vec{n}\rangle_{ph} = |n_1\rangle_{ph}\,|n_2\rangle_{ph}\ldots|n_L\rangle_{ph}$ is the phonon configuration on all sites, and E_n the corresponding energy. $|m\rangle$ and E_m become the eigenstates and energies for the polaron problem. For $T \to 0$, there are no phonons in the system and we just recover the polaron band with an incoherent part.

I further define the electron emission function, where an electron is removed from the polaron system, as

$$A^+(k,\omega) = \frac{1}{2\pi}\mathrm{Im}\{G^<_{T,1}(k,\omega)\}\,. \tag{2.21}$$

Lastly, I define the phonon spectral function

$$B(k,\omega) = \frac{-1}{2\pi}\mathrm{Im}\{D^>_{T,1}(k,\omega)\}\,, \tag{2.22}$$

where $D^>_{T,1}(k,\omega)$ is

$$D^>_{T,1}(k,t) = -i\,\langle \hat{X}_k(t)\hat{X}_k(0)\rangle_T\,. \tag{2.23}$$

The spectral functions can be solved analytically for the single-site problem, and the results will be presented in Ch. 4. A thorough derivation of the single site emission function and the phonon spectral function is given in Appendix B.1. The single-site polaron spectral function was derived in Ref. [65].

2.5 Transport coefficients

A powerful tool to get insights into microscopic systems is linear response theory, see, e.g., the textbooks [184, 185]. This formalism allows us to account for a perturbative field $F(t)$ to linear order by evaluating expectation values with the unperturbed Hamiltonian. In the following, I will introduce the transport coefficients calculated in this work. This discussion follows Ref. [176], which reviews recent progress on transport in one-dimensional lattice models at finite temperatures. To calculate transport coefficients, I consider a conserved quantity $\hat{Q} = \sum_j \hat{q}_j$, with $[\hat{H}, \hat{Q}] = 0$. For later reference, I will give the energy, $\hat{Q} = \hat{H}$, the label $Q = E$ and the charge, $\hat{Q} = \sum_i \hat{n}_i$, the label $Q = C$. I now consider a perturbative field $F_Q(\omega)$ which couples to a polarization $\hat{A}_Q = \sum_j j\hat{q}_j$. The conductivity $\mathcal{L}_{Q,Q}$ is defined as the Fourier space proportionality between an extensive current and the perturbing field $F_Q(\omega)$ via

$$\langle J^Q \rangle (\omega) = \mathcal{L}_{Q,Q}(\omega) F_Q(\omega) \,. \tag{2.24}$$

The conductivity can be split up into a real an imaginary part

$$\mathcal{L}_{Q,Q}(\omega) = \mathcal{L}'_{Q,Q}(\omega) + i\mathcal{L}''_{Q,Q}(\omega) \,, \tag{2.25}$$

which are related through the Kramers-Kronig relation [186]. Through the Kubo formula [187], one gets

$$\mathcal{L}'_{Q,Q}(\omega) = \frac{1 - e^{-\beta\omega}}{\omega} \int_0^\infty dt \lim_{L\to\infty} \frac{\mathrm{Re}\{e^{i\omega t} \left\langle J^Q(t) J^Q(0) \right\rangle_T\}}{L} \,. \tag{2.26}$$

In the derivation, one uses the fact that the derivative of the polarization with respect to time, $\dot{A}_Q$, is related to the current operator through the continuity equation. Locally, this becomes $\dot{q}_j = j^Q_{i+1} - j^Q_i$, with the local currents j^Q_i and $J^Q = \sum_j j^Q_i$. The integral over the transport coefficients can be related to $\hat{A}_Q$ via the f-sum rule:

$$\int_0^\infty d\omega \mathcal{L}'_{Q,Q}(\omega) = \frac{\pi}{2i} \frac{\langle [\hat{A}^Q, \hat{J}^Q] \rangle_T}{L} \,, \tag{2.27}$$

which can often serve as consistency and accuracy check for numerical calculations. In practice, I will introduce

$$C^Q_T(\omega) = \int_{-\infty}^\infty e^{i\omega t} f(t) C^Q_T(t) dt = \int_{-\infty}^\infty e^{i\omega t} f(t) \left\langle J^Q(t) J^Q(0) \right\rangle_T dt \,, \tag{2.28}$$

with a window function $f(t)$ which will be $e^{-\eta|t|}$ (Lorenzian) or $e^{-\eta t^2}$ (Gaussian). For the Holstein model, the charge-current operator is

$$\hat{J}^C = it_0 \sum_{i=1}^{L-1} (\hat{c}^\dagger_j \hat{c}_{j+1} - \hat{c}^\dagger_{j+1} \hat{c}_j) \,, \tag{2.29}$$

and the energy-current operator, without a phonon hopping term [see Eq. (2.2)], becomes

$$\hat{J}^E = i\Big(t_0^2 \sum_{j=2}^{L-1} (\hat{c}_{j-1}^\dagger \hat{c}_{j+1} - \hat{c}_{j+1}^\dagger \hat{c}_{j-1}) - t_0 \gamma \sum_{j=2}^{L} (\hat{c}_{j-1}^\dagger \hat{c}_j - \hat{c}_j^\dagger \hat{c}_{j-1})(\hat{b}_j + \hat{b}_j^\dagger)\Big)\,. \tag{2.30}$$

Finally, the real part of the optical conductivity for a finite system becomes:

$$\sigma'(\omega) = \frac{1 - e^{-\omega/T}}{2\omega L} C_T^C(\omega)\,. \tag{2.31}$$

For not having $\sigma'(\omega) \to 0$ for $L \to \infty$ for the polaron and bipolaron, I will omit the factor $1/L$ in those cases. The derivation of an energy transport coefficient is more subtle since the inverse temperature gradient is not a microscopic potential. However, on can find a similar expression as in Eq. (2.26), see Refs. [176, 185, 188, 189]. In this work, I define in the energy transport coefficient in a system at finite filling to be

$$\kappa'(\omega) = \frac{1 - e^{-\omega/T}}{2T\omega L} C_T^E(\omega)\,. \tag{2.32}$$

Note that in general, the thermal conductivity can be calculated from a heat current [3,167] $\hat{J}^{Th} = \hat{J}^E - \mu \hat{J}^C$, which introduces an extra term to the energy transport coefficient proportional to $\langle \hat{J}^C(t) \hat{J}^E(0) \rangle$.

In this work, the Holstein polaron and bipolaron optical conductivity, the optical conductivity and energy transport coefficient for the Holstein model at finite filling, and the Holstein-Hubbard bipolaron optical conductivity will be analyzed in Ch. 5.

Chapter 3

Numerical methods

Great insights into quantum systems, such as their ground states and optical absorption spectra, can be gained from analytic calculations, see e.g., Refs. [10, 49, 183, 190, 191]. However, it is also desirable to investigate systems in parameter regimes where no analytical approaches are available. To do that, one has to do numerical simulations.

One approach is to treat the quantum systems exactly by diagonalizing their Hamiltonians. This has has helped our understanding of many systems, e.g., regarding their transport and thermalization properties [56, 72, 192, 193]. However, one problem with exact diagonalization is that the Hilbert space dimension often scales exponentially with the system size, and one is thus limited to small systems. This can be countered by utilizing all symmetries of the Hamiltonian, see, e.g., Ref. [194], but still, the exact simulations will at one point become unfeasible on any classical hardware. For example, to treat the Holstein model exactly (see Ch. 2), one first has to invoke an artificial cutoff of the harmonic oscillator states, which I will denote with M. Then, for the polaron problem, one must diagonalize the Hamiltonian of dimension $L(M+1)^L$. If one either increases M or L or includes more electrons, the Hilbert space dimension will soon become unmanageable. For example, in Ref. [64], we did a full diagonalization study of the Holstein polaron model and were limited to $L = 8$ sites and maximum $M = 3$ phonons per site, and in Ref. [195] we used $L = 16$ sites but with hard-core bosons. In Ref. [56], Schubert et al. were able to calculate the optical conductivity for $L = 6$ sites with a total of 45 phonons, and Zhang et al. studied different electon configurations in the Holstein model with $L = 6$ sites using local basis optimization in Ref. [72]. To counter the problems of exact diagonalization, several numerical methods have been developed. They include density-matrix renormalization group methods (DMRG) [108–111], Lanczos methods [117–119, 196, 197], dynamic mean field theory [112], quantum Monte Carlo methods [113, 116], and trajectory-based methods like multiconfigurational Ehrenfest (MCE) [120, 121], mulitrajectory Ehernfest (MTE) [122, 123, 198], and surface hopping [124–126].

In the first part of this chapter, I will introduce matrix-product states and briefly explain how they can be used to do ground-state search, time-evolution, and finite temperature calculations. My emphasis will be on explaining how the time-evolution algorithms can be accelerated for electron-phonon systems by incorporating local basis transformations.

I will then explain the key ideas of the trajectory-based methods MTE, surface hopping, and MCE before I discuss some other promising new methods in the field.

3.1 Matrix-product states

In this section, I will do a brief review of matrix-product states. For a more detailed discussion, I refer to several good reviews, e.g., Refs. [111,129]. This section follows Ref. [111].

The density-matrix renormalization group (DMRG) papers by Steven White [108,109] and the connections drawn to matrix-product state (MPS) [199], gave theorists a new tool to study one-dimensional quantum systems. Though the original work was intended to find ground states, the formalism has now found its way into a broad range of applications such as time-evolution, see, e.g., Refs. [132–137], and finite-temperature calculations, see, e.g., Refs. [138–144]. There are even promising extensions to higher dimensions [127–131], but in this work, I will focus on one-dimensional systems.

One can get great insights with a simple example into why the MPS representation of a state can be useful. Namely, how can one approximate a matrix? Assume there is a matrix M of rank l, and you want to approximate this matrix optimally by another matrix M' with respect to the Frobenius norm ($\|M\|_F^2 = \sum_{i,j} |M_{i,j}|^2$). The only restriction is that M' is truncated, meaning that it has rank $l' < l$. To do this, one must carry out a singular value decomposition, $M = USV^\dagger$, where S is a diagonal matrix with the s_i singular values as its elements. I will always order the singular values such that $s_1 \geq s_2 \geq \ldots \geq s_l \geq 0$. Furthermore, $V^\dagger V = \mathbb{1}$ and $U^\dagger U = \mathbb{1}$. Now, M' is obtained by only keeping the $l' < l$ largest singular values of S (I will denote that diagonal matrix as S'), and by computing $M' = US'V^\dagger$.

By a similar line of thought, one can look at a pure state $|\psi\rangle$ partitioned into subsystems A and B on site n,

$$|\psi\rangle = \sum_{\vec{\sigma}_i, \vec{\sigma}_j} \psi_{\vec{\sigma}_i \vec{\sigma}_j} |\vec{\sigma}_i\rangle_A |\vec{\sigma}_j\rangle_B . \tag{3.1}$$

I use the notation $|\vec{\sigma}\rangle_A = |\sigma_1, \sigma_2, \ldots, \sigma_n\rangle$, where $|\sigma_i\rangle$ is the state on site i, and $|\vec{\sigma}\rangle_B = |\sigma_{n+1}, \sigma_{n+2} \ldots, \sigma_L\rangle$. For example, for a spin chain $|\sigma_i\rangle \in \{|\uparrow\rangle, |\downarrow\rangle\}$. By carrying out such a SVD on $\psi_{\vec{\sigma}_i \vec{\sigma}_j} := \boldsymbol{\psi} = USV^\dagger$, the wave function takes the form

$$|\psi\rangle = \sum_{a=1}^{l} s_a |a\rangle_A |a\rangle_B , \tag{3.2}$$

where I used that $|a\rangle_A = \sum_{\vec{\sigma}_i} U_{a\vec{\sigma}_i} |\vec{\sigma}_i\rangle_A$, $|a\rangle_B = \sum_{\vec{\sigma}_j} V^\dagger_{a\vec{\sigma}_j} |\vec{\sigma}_j\rangle_B$, and s_a are the singular values of the matrix $\boldsymbol{\psi}$. Note that Eq. (3.2) is a Schmidt decomposition of $|\psi\rangle$. For a density matrix $\hat{\rho} = |\psi\rangle\langle\psi|$, one can obtain the reduced density matrix $\hat{\rho}_A$ by tracing out subsystem B from $\hat{\rho}$, $\hat{\rho}_A = Tr_B[|\psi\rangle\langle\psi|]$. In a similar fashion, one can obtain $\hat{\rho}_B$. By doing this on the reduced density matrix belonging to the state in Eq. (3.2), one gets

$$\hat{\rho}_A = \sum_{a=1}^{l} s_a^2 |a\rangle_A \, {}_A\langle a| , \tag{3.3}$$

and the von Neuman entropy is

$$S_{A,B}(|\psi\rangle) = -Tr[\hat{\rho}_A \log \hat{\rho}_A] = -Tr[\hat{\rho}_B \log \hat{\rho}_B] = -\sum_{a=1}^{l} s_a^2 \log s_a^2 \,. \tag{3.4}$$

The important observation is that the wave function can be approximated by the state $|\psi'\rangle$ with respect to the 2-norm, by only keeping the l' largest singular values of $|\psi\rangle$ with $l' < l$. The truncated state reads

$$|\psi'\rangle = \sum_{a=1}^{l'} s_a \, |a\rangle_A \, |a\rangle_B \ . \tag{3.5}$$

Note that if one wants $|\psi'\rangle$ to be normalized, the singular values must be renormalized. One can now see that the faster the values s_a decay, the better is the approximation for a small l'. It turns out that there are many interesting situations where only a small l' (not exponential in the system size) is needed to capture the correct physics. This is rooted in the so-called area law of entanglement entropy [111,200,201]. The area law states that for a Hamiltonian with short-range interactions and an excitation gap, the entanglement of the ground state does not scale with the volume $L^{\tilde{D}}$ ($\tilde{D}$ is the spatial dimension), but rather with the surface $L^{\tilde{D}-1}$. This means that $S_{A,B} \sim$ const for a one-dimensional system (if L is larger than the correlation length associated with the smallest gap). For gapless systems, one has $S_{A,B} \sim$ const + const $\cdot \log L$ [202, 203], which still leads to great computational advantages. This is the core of why DMRG is so powerful in one dimension.

A cornerstone of modern DMRG-based algorithms is the matrix-product-state representation of quantum states. A general state

$$|\psi\rangle = \sum_{\sigma_1,\sigma_2,\ldots,\sigma_L} \psi_{\sigma_1\sigma_2\ldots\sigma_L} \, |\sigma_1, \sigma_2, \ldots, \sigma_L\rangle \ , \tag{3.6}$$

this can be written as a matrix-product state by a series of SVDs so that [111]

$$\begin{aligned} |\psi\rangle &= \sum_{a_1,a_2,\ldots,a_L} \sum_{\sigma_1,\sigma_2,\ldots,\sigma_L} A^{\sigma_1}_{a_1} A^{\sigma_2}_{a_1 a_2} \ldots A^{\sigma_L}_{a_L} \, |\sigma_1, \sigma_2, \ldots, \sigma_L\rangle \\ &= \sum_{\sigma_1,\sigma_2,\ldots,\sigma_L} A^{\sigma_1} A^{\sigma_2} \ldots A^{\sigma_L} \, |\sigma_1, \sigma_2, \ldots, \sigma_L\rangle \ . \end{aligned} \tag{3.7}$$

In the second line, the summation over the so-called bond indices a_i is implied. I will do that for a clearer notation unless the bond indices are specifically needed. Furthermore, the A^{σ_j} matrices are left-normalized, $\sum_{\sigma_j} A^{\sigma_j\,\dagger} A^{\sigma_j} = \mathbb{1}$. The representation of the state in Eq. (3.6) as Eq. (3.7) is exact if no truncation is performed, and the truncation of $|\psi\rangle$ is done on the dimension of the bond indices. I will denote the maximum bond dimension of the matrix-product state with D.

In many situations, it can be convenient to use tensor diagrams to describe different algorithms. In this convention, a circle with three lines is the tensor $A^{\sigma_i}_{a_{i-1}a_i}$. This is shown in Fig. 3.1(a). The line pointing upwards is the physical index, and the lines pointing to

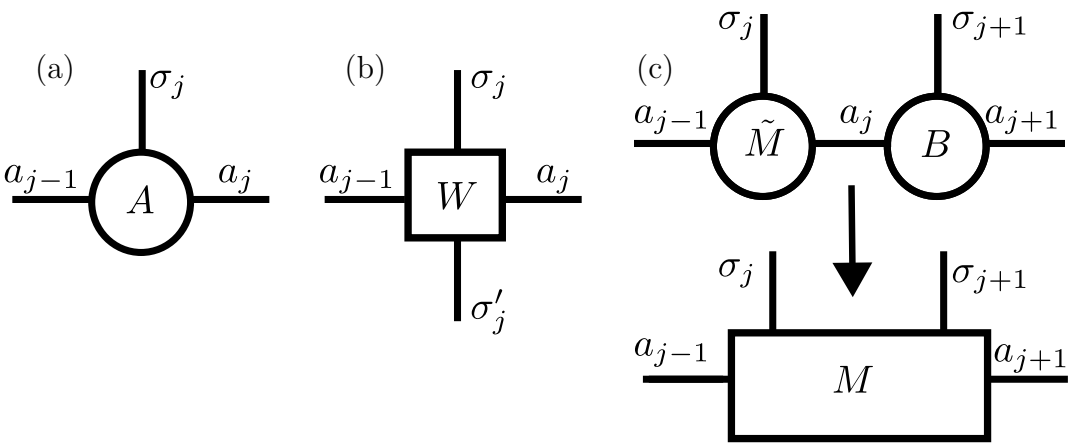

Figure 3.1: (a) Tensor $A^{\sigma_j}_{a_{j-1}a_j}$. (b) Tensor $W^{\sigma_j\sigma'_j}_{a_{j-1}a_j}$. (c) Contracting over the bond index a_j gives $M^{\sigma_j\sigma_{j+1}}_{a_{j-1}a_{j+1}} = \sum_{a_j} \tilde{M}^{\sigma_j}_{a_{j-1}a_j} B^{\sigma_{j+1}}_{a_j a_{j+1}}$

the left and to the right correspond to the bond indices. I sometimes use upper indices for readability. Figure 3.1(b) shows the building blocks of matrix-product operators $W^{\sigma_i\sigma'_i}_{a_{i-1}a_i}$, which I will introduce later. In the pictorial representation, lines connecting two tensors are summed over. This is demonstrated in Fig. 3.1(c). A thorough description of this convention can be found in, e.g., Refs. [111, 129].

Matrix-product states possess gauge freedom, meaning that the tensors are not uniquely defined. This allows the states to be expressed in many forms. In this work, I will use different matrix-product state representations. One is the so-called site canonical form

$$|\psi\rangle = \sum_{\sigma_1,\sigma_2,\ldots,\sigma_L} A^{\sigma_1} \ldots A^{\sigma_{j-1}} \tilde{M}^{\sigma_j} B^{\sigma_{j+1}} \ldots B^{\sigma_L} |\sigma_1, \sigma_2, \ldots, \sigma_L\rangle \,, \tag{3.8}$$

where the A matrices are left normalized, $\sum_{\sigma_j} A^{\sigma_j\,\dagger} A^{\sigma_j} = \mathbb{1}$, and the B matrices are right normalized, $\sum_{\sigma_j} B^{\sigma_j} B^{\sigma_j\,\dagger} = \mathbb{1}$. A diagrammatic representation of Eq. (3.8) can be seen in Fig. 3.2(a). $\langle\psi|$ becomes

$$\langle\psi| = \sum_{\sigma_1,\sigma_2,\ldots,\sigma_L} \langle\sigma_1, \sigma_2, \ldots, \sigma_L| \, B^{\sigma_L\dagger} \ldots B^{\sigma_{j+1}\dagger} \ldots \tilde{M}^{\sigma_j\dagger} A^{\sigma_{j-1}\dagger} \ldots A^{\sigma_1\dagger} \,, \tag{3.9}$$

and is shown in Fig. 3.2(b). I will further use a two-site canonical form

$$|\psi\rangle = \sum_{\sigma_1,\sigma_2,\ldots,\sigma_L} A^{\sigma_1} \ldots A^{\sigma_{j-1}} M^{\sigma_j\sigma_{j+1}} B^{\sigma_{j+2}} \ldots B^{\sigma_L} |\sigma_1, \sigma_2, \ldots, \sigma_L\rangle \,, \tag{3.10}$$

where $M^{\sigma_j\sigma_{j+1}} = \tilde{M}^{\sigma_j} B^{\sigma_{j+1}}$, and the bond canonical form

$$|\psi\rangle = \sum_{\sigma_1,\sigma_2,\ldots,\sigma_L} A^{\sigma_1} \ldots A^{\sigma_{j-1}} \Lambda B^{\sigma_j} \ldots B^{\sigma_L} |\sigma_1, \sigma_2, \ldots, \sigma_L\rangle \,. \tag{3.11}$$

In the parallel time-dependent variational principle algorithm [166] used in Ch. 5, I will also need the inverse canonical form introduced in Ref. [165]

$$|\psi\rangle = \sum_{\sigma_1,\sigma_2,\ldots,\sigma_L} \psi^{\sigma_1} V^1 \psi^{\sigma_2} V^2 \ldots V^{L-1} \psi^{\sigma_L} |\sigma_1, \sigma_2, \ldots, \sigma_L\rangle \,, \tag{3.12}$$

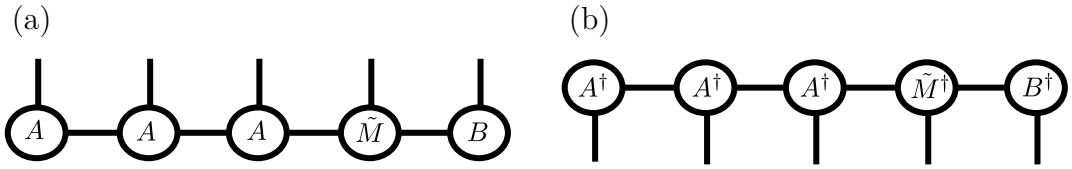

Figure 3.2: (a) $|\psi\rangle$ as a matrix-product state in the site-canonical form from Eq. (3.8), depicted with tensor diagrams. (b) $\langle\psi|$ as a matrix-product state.

which is related to the canonical form [132, 204]

$$|\psi\rangle = \sum_{\sigma_1,\sigma_2,\ldots,\sigma_L} \Gamma^{\sigma_1}\tilde{\Lambda}^1\Gamma^{\sigma_2}\tilde{\Lambda}^2\ldots\tilde{\Lambda}^{L-1}\Gamma^{\sigma_L}\,|\sigma_1,\sigma_2,\ldots,\sigma_L\rangle\ , \tag{3.13}$$

via inserting $V^j\tilde{\Lambda}^j = \mathbb{1}$ and defining $\psi^{\sigma_j} = \tilde{\Lambda}^{j-1}\Gamma^{\sigma_j}\tilde{\Lambda}^j$.

A similar representation can be found for operators. The operator

$$\hat{O} = \sum_{\substack{\sigma_1',\sigma_2',\ldots,\sigma_L',\\ \sigma_1,\sigma_2,\ldots,\sigma_L}} O^{\sigma_1'\sigma_2'\ldots\sigma_L'}_{\sigma_1\sigma_2\ldots\sigma_L}\,|\sigma_1,\sigma_2,\ldots,\sigma_L\rangle\langle\sigma_1',\sigma_2',\ldots,\sigma_L'|\ , \tag{3.14}$$

becomes a matrix-product operator (MPO) [111]

$$\hat{O} = \sum_{\substack{\sigma_1',\sigma_2',\ldots,\sigma_L',\\ \sigma_1,\sigma_2,\ldots,\sigma_L}} W^{\sigma_1\sigma_1'}W^{\sigma_2\sigma_2'}\ldots W^{\sigma_L\sigma_L'}\,|\sigma_1,\sigma_2,\ldots,\sigma_L\rangle\langle\sigma_1',\sigma_2',\ldots,\sigma_L'|\ . \tag{3.15}$$

In Fig. 3.1(b), I show $W^{\sigma_j\sigma_j'}$, and Fig. 3.3 depicts a complete MPO drawn with tensor diagrams.

Several operations become simple in the matrix-product state representation and can be nicely illustrated with tensor diagrams. For example, computing the norm of the matrix-product state $|\psi\rangle$ in the site-canonical form becomes

$$\begin{aligned}\langle\psi|\psi\rangle &= \sum_{\sigma_1,\sigma_2,\ldots,\sigma_L} B^{\sigma_L\dagger}\ldots B^{\sigma_{j+1}\dagger}\ldots\tilde{M}^{\sigma_j\dagger}A^{\sigma_{j-1}\dagger}\ldots A^{\sigma_1\dagger}A^{\sigma_1}\ldots A^{\sigma_{j-1}}M^{\sigma_j\sigma_{j+1}}B^{\sigma_{j+2}}\ldots B^{\sigma_L}\\ &= \sum_{\sigma_j} Tr[\tilde{M}^{\sigma_j\dagger}\tilde{M}^{\sigma_j}]\,,\end{aligned} \tag{3.16}$$

where I used the properties of the left and right normalized matrices. This process is illustrated with diagrams in Figs. 3.4(a) and (b). Figure 3.4(c) demonstrates how to compute the expectation value $\langle\psi|\hat{O}|\psi\rangle$. For a local operator only acting on a single site, the picture simplifies even more using the left and right normalization and is shown in Fig. 3.4(d). I refer to Ref. [111] for a detailed description of how to do these calculations efficiently in practice. I also note that all matrix-product-state calculations presented here are done with the ITensor Software Library [205].

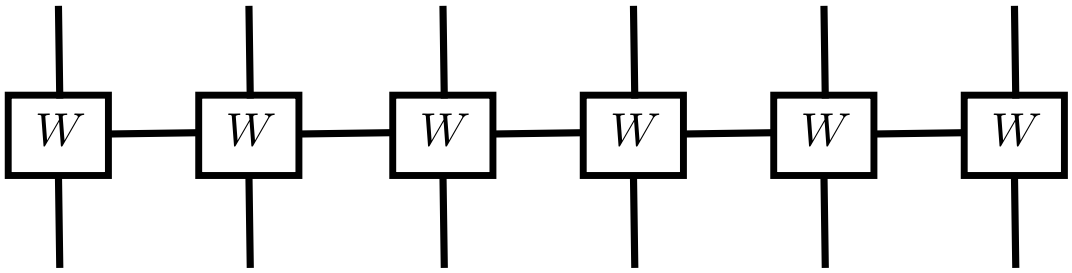

Figure 3.3: Matrix-product operator from Eq. (3.15), illustrated with tensor diagrams.

3.1.1 Single-site DMRG

Even though this work primarily focuses on time-evolution algorithms, I will briefly sketch the key ideas of the ground state single-site DMRG algorithm since this motivates some of the objects I will need later. The idea is to extremizie the equation $\langle\psi|\hat{H}|\psi\rangle - \lambda\langle\psi|\psi\rangle$, where λ is a Lagrange multiplier [111]. To do this, one starts in the site-canonical representation from Eq. (3.8) and iterates through the system by changing the position of the tensor $\tilde{M}^{\sigma_i}$. At each site i, one computes

$$\frac{\partial}{\partial \tilde{M}^{\sigma_i\,\dagger}}[\,\langle\psi|\hat{H}|\psi\rangle - \lambda\,\langle\psi|\psi\rangle] = 0\,. \tag{3.17}$$

This is illustrated in Fig. 3.5. One is then left with solving the eigenvalue equation

$$\sum_{\sigma_i',a_{i-1}',a_i'} H^{eff\,\sigma_i\sigma_i'}_{a_{i-1}a_i a_{i-1}' a_i'} \tilde{M}^{\sigma_i'}_{a_{i-1}'a_i'} = \lambda \tilde{M}^{\sigma_i}_{a_{i-1}a_i}\,, \tag{3.18}$$

where $H^{eff\,\sigma_i\sigma_i'}_{a_{i-1}a_i a_{i-1}' a_i'}$ is called the effective Hamiltonian and is illustrated in Fig. 3.6(a). Since one is trying to find the ground state, Eq. (3.18) can be solved using a Krylov solver. Once the new tensor $\tilde{M}^{\sigma_i}_{a_{i-1}a_i}$ is found, one moves the center of the site-canonical matrix-product state to the right (if one currently is sweeping from left to right). Now, one minimizes with respect to the tensor on the new site. To obtain the ground state, one sweeps back and forth until convergence. For more details on how to implement the algorithm efficiently and a discussion of its problems, as well as of the two-site version, I refer to Ref. [111].

For of the time-dependent variational principle algorithm, I also need the bond-canonical version of $H^{eff\,\sigma_i\sigma_i'}_{a_{i-1}a_i a_{i-1}' a_i'}$, which I will refer to as $K_{lml'm'}$. A tensor diagram of $K_{lml'm'}$ can be seen in Fig. 3.6(b).

3.1.2 Finite-temperature calculations

Matrix-product states can only represent pure states. Still, their representative power can be utilized for finite temperature calculations with minimally entangled typical thermal states (METTS) [140, 142] or purification [138, 139, 141, 143, 162]. In Ref. [144], Binder and Barthel compared the METTS and purification algorithms for different models and

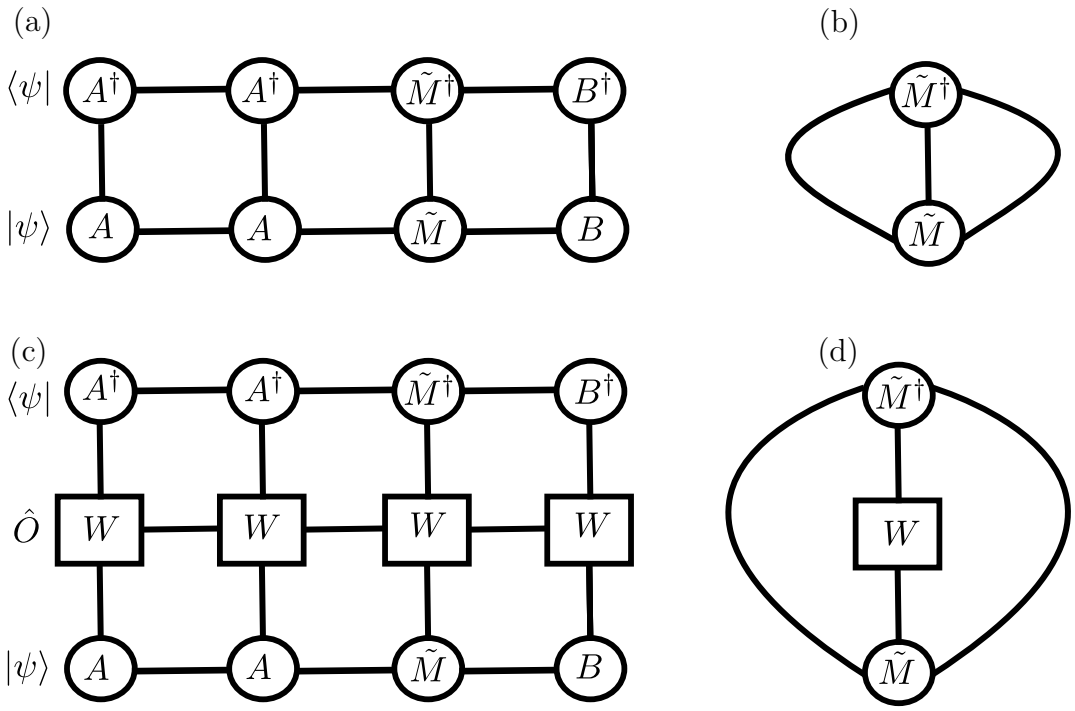

Figure 3.4: (a) Calculating $\langle\psi|\psi\rangle$ depicted with tensor diagrams. (b) Calculating $\langle\psi|\psi\rangle$ and utilizing left and right normalization of the MPS. (c) Calculating the expectation value $\langle\psi|\hat{O}|\psi\rangle$ depicted with tensor diagrams. (d) Utilizing left and right normalization to calculate the expectation value of $\langle\psi|\hat{O}|\psi\rangle$ if $\hat{O}$ only acts on one site.

found purification to be more accurate for all but very low temperatures at the same computational cost, which is the reason why I use that method in this work.

In this section, I will outline the idea of purification and, again, I will follow Ref. [111]. Whereas the density matrix of a mixed state can not be represented by a pure state in the physical Hilbert space $\mathcal{H}_P$, it can be represented by a pure state $|\psi\rangle$ in $\mathcal{H}_P$ and an auxiliary Hilbert space $\mathcal{H}_A$, so that $|\psi\rangle \in \mathcal{H}_P \otimes \mathcal{H}_A$. The scheme is drawn in Fig. 3.7. To obtain the mixed-state density matrix, one must first write $|\psi\rangle$ as Schmidt decomposition, see Eq. (3.2), over $\mathcal{H}_P$ and $\mathcal{H}_A$:

$$|\psi\rangle = \sum_{a=1}^{l} s_a \, |a\rangle_P \, |a\rangle_A \, . \tag{3.19}$$

Then, one can obtain the density matrix by tracing out the auxiliary degrees of freedom

$$\hat{\rho}_P = \sum_{a=1}^{l} s_a^2 |a\rangle_P \, {}_P\langle a| = Tr_A[\, |\psi\rangle\langle\psi|\,] \, . \tag{3.20}$$

With this ansatz, one can now calculate the thermal density operator $\hat{\rho}_\beta$ at a temperature $T = 1/\beta$. Assuming one knows how to write $\hat{\rho}_0$ in terms of purified state, so that $\hat{\rho}_0 =$

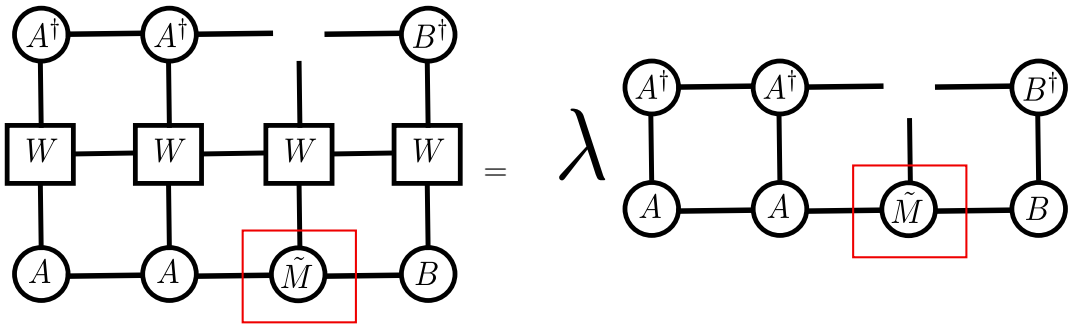

Figure 3.5: Illustration of the single-site DMRG equation after having taken the derivative with respect to $\tilde{M}^{\sigma_i\dagger}$, see Eq. (3.17). The tensor that will be optimized is marked with red.

$Tr_A[\,|\psi_0\rangle\langle\psi_0|]$. One then computes

$$\hat{\rho}_\beta = Z(\beta)^{-1}e^{-\beta\hat{H}} = \frac{Z(0)}{Z(\beta)}e^{-\beta\hat{H}/2}\hat{\rho}_0 e^{-\beta\hat{H}/2} = \frac{Z(0)}{Z(\beta)}Tr_A[e^{-\beta\hat{H}/2}\,|\psi_0\rangle\langle\psi_0|\,e^{-\beta\hat{H}/2}]\,, \tag{3.21}$$

where I used that the identity $\hat{\mathbb{1}} = \hat{\rho}_0 Z(0)$ and $Z(\beta) = Tr_P[e^{-\beta\hat{H}}]$. This means that if one has $\hat{\rho}_0$, one can get the thermal density matrix by imaginary-time evolution:

$$|\psi_\beta\rangle = e^{-\beta\hat{H}/2}\,|\psi_0\rangle\ . \tag{3.22}$$

The expectation value of an operator $\hat{O}$ in a thermal ensemble at temperature $T = 1/\beta$, $\langle\hat{O}\rangle_T$, can be computed as

$$\langle\hat{O}\rangle_T = \frac{\langle\psi_\beta|\hat{O}|\psi_\beta\rangle}{\langle\psi_\beta|\psi_\beta\rangle}\,, \tag{3.23}$$

where I used that $Z(\beta)/Z(0) = \langle\psi_\beta|\psi_\beta\rangle$. Now, the remaining task is to find $\hat{\rho}_0$. This can, in many cases, be done analytically or by a ground state search with respect to an appropriate Hamiltonian [162, 206].

For the Holstein and Holstein-Hubbard models introduced in Ch. 2, I will first illustrate how to compute $\hat{\rho}_0$ in the phonon sector, denoted as $\hat{\rho}_{ph,0}$. If one truncates the local phonon Hilbert space at M and has L sites in the physical system, the phonon Hilbert space dimension is $(M+1)^L$. For $\hat{\rho}_{ph,0}$, one has

$$\hat{\rho}_{ph,0} = \frac{\mathbb{1}}{(M+1)^L} = \left(\frac{\mathbb{1}}{M+1}\right)^{\otimes L}\,. \tag{3.24}$$

$\hat{\rho}_{ph,0}$ can in fact be written as a product state with maximally entangled physical and auxiliary sites $|\psi_{0,ph}\rangle = |\psi^1_{ph}\rangle\,|\psi^2_{ph}\rangle\ldots|\psi^L_{ph}\rangle$, with

$$|\psi^i_{ph}\rangle = \sum_{n_{ph}=0}^{M}\frac{1}{\sqrt{M+1}}\,|n_{ph}\rangle_P\,|n_{ph}\rangle_A\ . \tag{3.25}$$

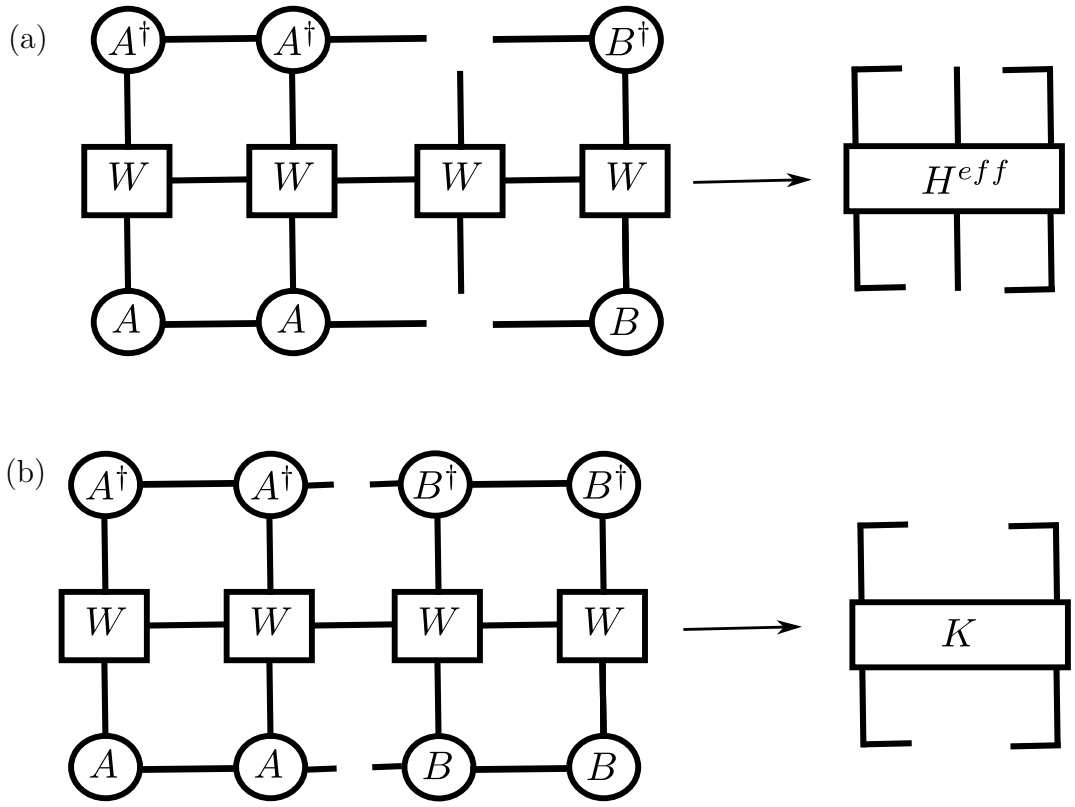

Figure 3.6: (a) Diagram representation of the the effective Hamiltonian $H^{eff\,\sigma_i\sigma_i'}_{a_{i-1}a_i a_{i-1}' a_i'}$. (b) Diagram representation of the bond-canonical effective Hamiltonian $K_{lml'm'}$.

For each site i, one obtains

$$\begin{aligned}\frac{1}{M+1}\hat{\mathbb{1}} &= \frac{1}{M+1}\sum_{n_{ph}=0}^{M} |n_{ph}\rangle_P\, {}_P\langle n_{ph}| \\ &= Tr_A\left[\left(\sum_{n_{ph}=0}^{M}\frac{1}{\sqrt{M+1}}|n_{ph}\rangle_P|n_{ph}\rangle_A\right)\left(\sum_{n_{ph}=0}^{M}\frac{1}{\sqrt{M+1}}\,{}_P\langle n_{ph}|\,{}_A\langle n_{ph}|\right)\right].\end{aligned} \tag{3.26}$$

If one wants to conserve the number of fermions in the system, generating $|\psi_{0,el}\rangle$ is a little more complicated. Following Ref. [162], one writes

$$|\psi_{0,el}\rangle \propto \frac{1}{N_{el}!}\left(\sum_{i=1}^{L}\hat{c}^\dagger_{i,P}\otimes\hat{c}^\dagger_{i,A}\right)^{N_{el}}|0_{el}\rangle_P\,|0_{el}\rangle_A\ . \tag{3.27}$$

The state used to generate the infinite temperature density matrix for the total system is then given by $|\psi_0\rangle = |\psi_{0,el}\rangle\otimes|\psi_{0,ph}\rangle$.

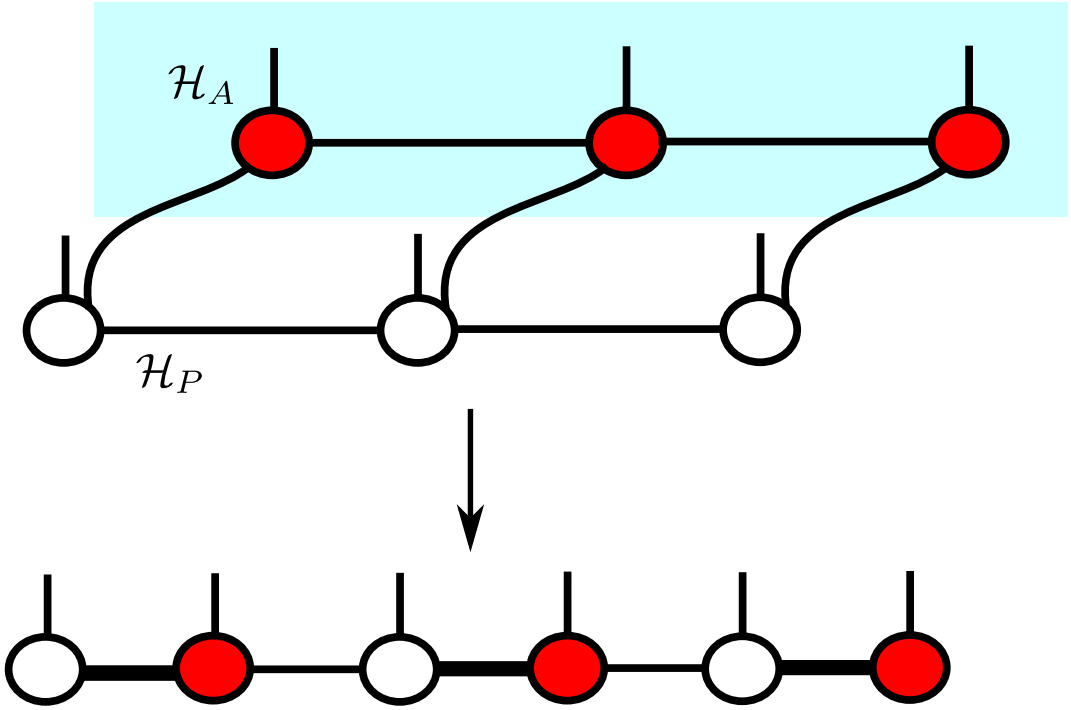

Figure 3.7: Illustration of purification. One makes a copy of $|\psi\rangle$, which lives auxiliary Hilbert space $\mathcal{H}_A$. The site in $\mathcal{H}_A$ is then maximally entangled with the corresponding site in the physical Hilbert space $\mathcal{H}_P$. Finally, the states are merged together to one MPS. The thick black lines illustrate the maximally entangled bonds.

3.1.3 Time-evolution with matrix-product states

An important aspect of matrix-product states and DMRG algorithms is that they can efficiently be extended to do time-evolution of quantum states [132–137]. There are many situations where this is important, such as in quantum quench setups, e.g., in Refs. [147,148], when studying relaxation mechanisms in electron-phonon lattice models [62, 76], or when computing time-dependent correlation functions at equilibrium of the form $\langle \hat{A}(t)\hat{B}(0)\rangle_T$ (see Ch. 2). For the latter, one has to do an imaginary-time evolution to obtain the thermal state, see Sec. 3.1.2, followed by a real-time evolution.

The importance of time-dependent problems has led to the development of many efficient time-evolution algorithms, see Ref. [137] for a review. They include the time-evolving block decimation TEBD and time-dependent DMRG (tDMRG) algorithms [132–134], the $W^{I,II}$ method [207], and time-dependent variational principle (TDVP) algorithms [135, 136].

Even with the variety of algorithms available, one remaining problem is that many matrix-product state-based methods (not only those for time evolution) have an unfavorable scaling with the local Hilbert space dimension. For many systems, such as Fermi-Hubbard and spin-1/2 models, this can be neglected. However, it can become problematic

for the electron-phonon models studied in this work (I truncate the number of local harmonic oscillator states to M, and M must often be large to capture the correct physics).

To tackle this problem, different schemes have been developed. They include pseudosite (PS) DMRG [152], local basis optimization (LBO) [151], and projected purification (PP) [153]. The idea of PS-DMRG is to substitute the large local Hilbert spaces with hard-core boson pseudosites which incorporate the binary representation of the phonon states. The LBO method finds a so-called "optimal basis" based on the reduced density matrix, in which the state can be efficiently truncated. This is the method used in this work and will be discussed in more detail in Sec. 3.1.4. The PP algorithm uses the fact that incorporating symmetries can speed up matrix-product state calculations, and one enforces $U(1)$ symmetry in the phonon sector by introducing a bath. The two last ideas were successfully combined with time-evolution algorithms [154, 156].

In Ref. [78], Stolpp et al. benchmarked the aforementioned algorithms for the Holstein-model ground-state problem. They found that with their implementations, all methods could characterize the different phases of the model. However, PS-DMRG has the problem that it introduces long-range interactions, which leads to a larger bond dimension. For PP-DMRG, the authors found that it requires a larger bond dimension but with the computational benefit of having a $U(1)$ symmetry. In their calculations, the LBO algorithm needed the smallest bond dimension for a certain accuracy. Their results do not necessarily translate to time evolution algorithms, and a separate benchmark would have to be conducted.

In the following sections, I briefly review the time-evolution algorithms tDMRG and TDVP and focus on how they can be combined with LBO. First, however, I will discuss the main difficulty of time-evolving a matrix-product states and introduce some practical tricks for calculating correlation functions.

The main issue with time-evolving matrix-product states is that while the state $|\psi(0)\rangle$ can be expressed with a small bond dimension D, this is not always true for the time-evolved state $|\psi(t)\rangle$ [145]. In fact, for a quench and a fixed D, the error made in the state representation will grow exponentially [208]. Even for local perturbations, the error will eventually dominate. One way to counter this is to fix the truncation error and allow D to grow. However, this will eventually lead to the simulations being too costly and restrict the accessible times.

When conducting the real-time evolution to compute $\langle \hat{A}(t)\hat{B}(0)\rangle_T$, it has been shown that time-evolving the auxiliary space backwards in time can lead to a significantly smaller bond dimension for a fixed truncation [159–161, 209]. Though this is not an optimal procedure [210], it can easily be incorporated into existing time-evolution methods. I will denote $\hat{U}^A(t) = e^{i\hat{H}^A t}$ as the time-evolution operator acting on the state in the auxiliary space and $\hat{U}^P(t) = e^{-i\hat{H}^P t}$ as the time-evolution operator acting on the state in the physical space. Following Ref. [161] and using the fact that $|\psi_\beta\rangle$ is an eigenstate [163] of $\hat{H}^P - \hat{H}^A$, I write

$$\begin{aligned}\langle \hat{A}(t)\hat{B}(0)\rangle_T &= \langle \hat{A}(t/2)\hat{B}(-t/2)\rangle_T = \langle \hat{A}\hat{U}^A(t/2)U^P(t/2)U^A(t/2)U^P(t/2)\hat{B}\rangle_T \\ &= \langle \phi_L|\phi_R\rangle \ ,\end{aligned} \tag{3.28}$$

where $|\phi_R\rangle = U^A(t/2)U^P(t/2)\hat{B}e^{-\beta\hat{H}/2}|\psi_0\rangle$ and $\langle\phi_L| = \langle\psi_0|e^{-\beta\hat{H}/2}\hat{A}\hat{U}^A(t/2)U^P(t/2)$. The argument why this leads to computational improvements is presented by Kennes and Karrasch in Ref. [163]. The first advantage is that one only has to time evolve two states up to $t/2$. The second advantage is that the time-evolution of $|\phi_R\rangle$ (for example) previously was plagued by entanglement building up between the physical and auxiliary Hilbert space. This happens even if $\hat{B} = \mathbb{1}$. Now, one would just evolve an eigenstate without increasing the entanglement. Even for $\hat{B} \neq \mathbb{1}$, one only has entanglement buildup in the spatial support of $e^{i\hat{H}t}\hat{B}e^{-i\hat{H}t}$ [160, 209].

3.1.4 Time-dependent DMRG with local basis optimization

The first algorithm I will introduce is called time-dependent DMRG (tDMRG) [111, 133]. This algorithm is mathematically equivalent to the TEBD algorithm and is based on a Trotter-Suzuki decomposition [211] of the time-evolution operator. For a Hamiltonian containing at maximum next nearest-neighbor interactions, one can write $\hat{H} = \sum_j \hat{h}_{j,j+1}$. Now, the interaction between the sites j and $j+1$ is contained in the operator $\hat{h}_{j,j+1}$. The next step is to split $\hat{H}$ up into even and odd terms: $\hat{H}_{\text{even}} = \sum_{j:\text{even}} \hat{h}_{j,j+1}$ and $\hat{H}_{\text{odd}} = \sum_{j:\text{odd}} \hat{h}_{j,j+1}$. Note that the individual terms in $\hat{H}_{\text{odd (even)}}$ commute. Using the second order Trotter-Suzuki decomposition [211], one can express the time-evolution operator $\hat{U}(dt)$ as

$$\hat{U}(dt) = e^{-idt\hat{H}_{\text{odd}}/2}e^{-idt\hat{H}_{\text{even}}}e^{-idt\hat{H}_{\text{odd}}/2} + \mathcal{O}(dt^3), \tag{3.29}$$

where the error per time step is of order $\mathcal{O}(dt^3)$. Now, one takes advantage of the fact that the individual exponents factorize and writes

$$\hat{U}^{\text{even}}(dt) = \prod_{i:\text{even}} e^{-idt\hat{h}_{i,i+1}} = \prod_{i:\text{even}} \hat{U}_{i,i+1}\,. \tag{3.30}$$

$\hat{U}_{i,i+1}$ has the components $U_{\sigma_i\sigma_{i+1}\sigma'_i\sigma'_{i+1}}$, and is drawn in Fig. 3.8(a). In the algorithm, one iterates through the matrix-product state by bringing it into a two-site canonical form, see Eq. (3.10), applying the corresponding time-evolution gate, doing a SVD, and going to the next site. Note that an optimal procedure would be to first apply all gates and then truncate variationally [111], but this would require storing larger matrix-product states. An illustration of how one can apply $\hat{U}(dt)$ is shown with tensor diagrams in Fig. 3.8(b), and more details can be found in Ref. [137]. When doing the SVDs, the number of singular values I discard is set by ϵ_{bond}, so that

$$\sum_{\text{discarded }\eta} s_\eta^2/(\sum_{\text{all }\eta} s_\eta^2) < \epsilon_{\text{bond}}\,. \tag{3.31}$$

The cost of the SVD is of order $\mathcal{O}(D^3d^3)$, where d is the local Hilbert space and D the bond dimension of the matrix-product state. This part of the algorithm, in particular, benefits from the local basis optimization (LBO) [151].

LBO is based on the idea that by diagonalizing the reduced density matrix, one can find a basis in which the state can be accurately represented with a smaller physical dimension.

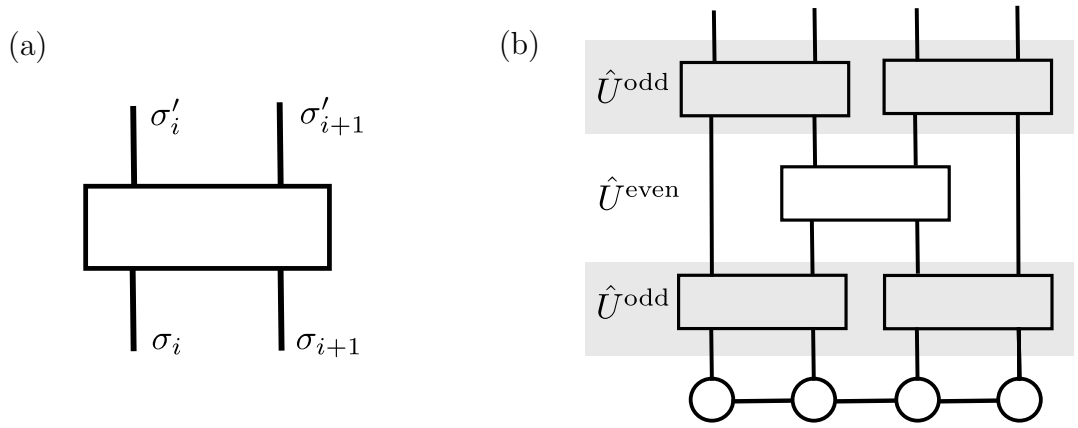

Figure 3.8: (a) Local time-evolution gate $\hat{U}_{i,i+1}$ acting on site i and $i+1$ as a tensor diagram. (b) Application of the complete time-evolution operator on a matrix-product state.

This can be motivated by the strong-coupling regime for the Holstein polaron, see Ch. 2, where one can either write the ground state effectively in terms of one coherent state or as a superposition of many bare phonon modes. So far, LBO has been combined with different numerical methods [72] and proven useful in a variety of matrix-product state based applications such as ground-state search [76, 157], real-time evolution [63, 76, 156], and for finite-temperature calculations (see Ch. 4 and Ch. 5).

To explain how to incorporate LBO into the tDMRG algorithm, I will first consider a state in the optimal basis, which I will denote with $\tilde{\sigma}_i$ on site i. Then, I write the components of the time evolution gate acting on site i and $i+1$ as $U_{\sigma_i\sigma_{i+1}\tilde{\sigma}_i\tilde{\sigma}_{i+1}}$. Here, two of the indices are now in the optimal basis. If the state is in the two-site canonical form from Eq. (3.10), I can compute

$$\Phi_{\sigma'_i\sigma'_{i+1}a_ja_{j+2}} = \sum_{\tilde{\sigma}_i,\tilde{\sigma}_{i+1}} U_{\sigma'_i\sigma'_{i+1}\tilde{\sigma}_i\tilde{\sigma}_{i+1}} M^{\tilde{\sigma}_i\tilde{\sigma}_{i+1}}_{a_ja_{j+2}} \,. \tag{3.32}$$

Now, I generate the local density matrix

$$\rho_{\sigma'_i\sigma_i} = \sum_{\sigma_{i+1},a_{j+2},a_j} \Phi_{\sigma'_i\sigma_{i+1}a_ja_{j+2}} \Phi^\dagger_{a_{j+2}a_j\sigma_{i+1}\sigma_i} \,. \tag{3.33}$$

The next step is to diagonalize $\rho = R^\dagger W R$, where W is a diagonal matrix with entries w_α, and R is the transformation matrix which takes an index on site i from the physical to the new optimal basis. The truncation is done based on the magnitude of the eigenvalues w_α. The same procedure is done for site $i+1$. I now make the transformation

$$\Phi_{\tilde{\sigma}_i\tilde{\sigma}_{i+1}a_ja_{j+2}} = \sum_{\sigma_i,\sigma_{i+1}} \Phi_{\sigma_i\sigma_{i+1}a_ja_{j+2}} R_{\sigma_i\tilde{\sigma}_i} R_{\sigma_{i+1}\tilde{\sigma}_{i+1}} \,, \tag{3.34}$$

before the following SVD. The scheme is illustrated in Fig. 3.9. When diagonalizing ρ from Eq. (3.33), I will disregard the states belonging to the smallest eigenvalues w_α based on a

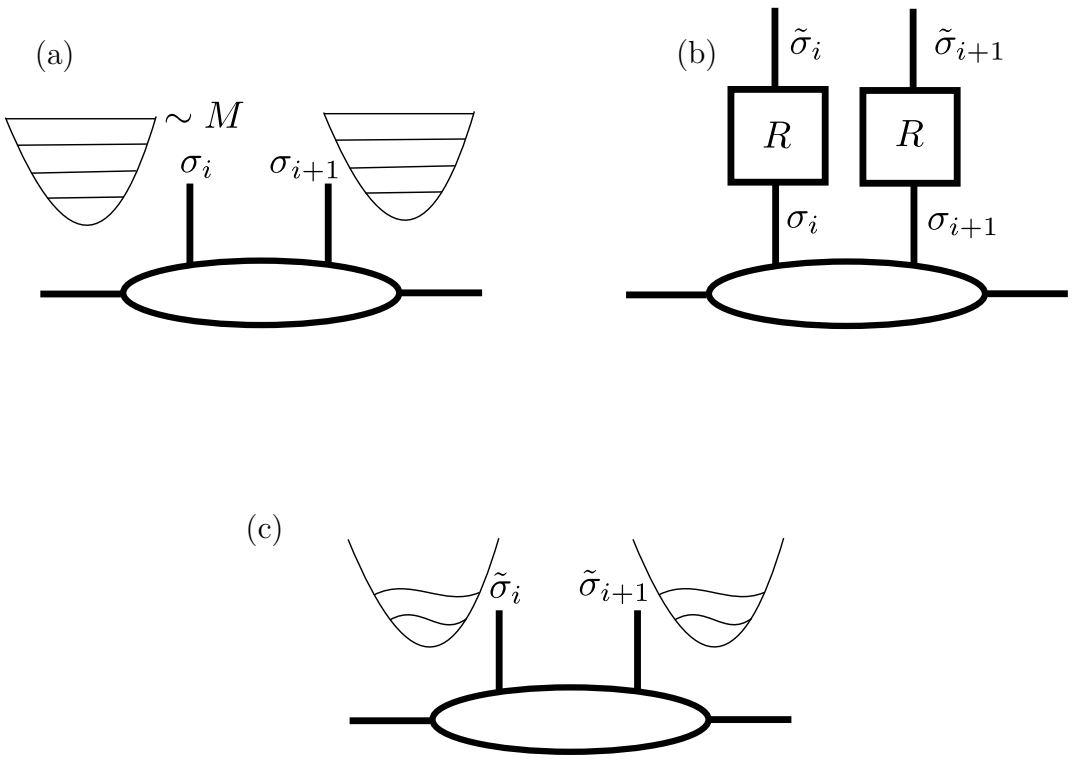

Figure 3.9: (a) Pictorial representation of a two site tensor in the occupation basis. The number of local states is dictated by the phonon cut-off M. (b) Applying the transformation matrices R obtained from the local reduced density matrix. R transforms the local site from the occupation basis σ_i to the optimal basis $\tilde{\sigma}_i$. (c) Pictorial representation of a two site tensor in the optimal basis.

cut-off ϵ_{LBO} so that

$$\sum_{\text{discarded } \eta} w_\eta / (\sum_{\text{all } \eta} w_\eta) < \epsilon_{\mathrm{LBO}} \,. \tag{3.35}$$

I will denote the truncated optimal basis dimension with d_{LBO}. The SVD now has the cost of order $\mathcal{O}(D^3 d_{\mathrm{LBO}}^3)$, and the transformation is only beneficial if $d_{\mathrm{LBO}} \ll d$. If this is not the case, the algorithm actually becomes more expensive since the cost of building ρ in Eq. (3.33) is of order $\mathcal{O}(D^2 d^3)$, the cost of diagonalizing it is of order $\mathcal{O}(d^3)$, and the cost of transformation itself is of order $\mathcal{O}(D^2 d_{\mathrm{LBO}} d^2)$. However, $d_{\mathrm{LBO}} \ll d$ can often be realized since the eigenvalues w_α often decay exponentially. This is for example demonstrated in Ref. [62] and Ch. 6 for different setups. In Chapter 6, I also present a situation where the LBO basis can not be significantly truncated.

3.1.5 Time-dependent variational principle with local basis optimization

I will now discuss a different set of time-evolution methods, namely time-dependent variational principle (TDVP) algorithms [135, 136]. In recent years, these algorithms have been used extensively with and without improvements, see e.g., Refs. [66, 166, 212–215]. In Reference [137], the efficiency and accuracy of several matrix-product state time-evolution algorithms were compared, and the results were in large part favorable for the two-site TDVP algorithm.

In Ch. 5, I will present results we obtained with single-site TDVP (1TDVP), two-site TDVP with LBO (2TDVP-LBO), and parallel two-site TDVP with LBO (p2TDVP-LBO). For self-consistency, I will briefly introduce the basic ideas of 1TDVP since these ideas also provide the basis of the other algorithms, but I will then focus on how I incorporate LBO into 2TDVP. In this section, I will follow Ref. [137].

TDVP considers a manifold of matrix-product states set by their bond dimension. When applying a matrix-product operator, this normally takes us out of that manifold, but the idea in TDVP is to now project the matrix-product state back onto the manifold's tangent space $\mathcal{T}_{|\psi\rangle}$. This is done by defining the projection operator $\hat{P}_{\mathcal{T}_{|\psi\rangle}}$, so that the effective Schrödinger equation becomes

$$\frac{\partial}{\partial t}|\psi\rangle = -i\hat{P}_{\mathcal{T}_{|\psi\rangle}}\hat{H}|\psi\rangle \ . \tag{3.36}$$

The tangent space projector takes the form

$$\hat{P}_{\mathcal{T}_{|\psi\rangle}} = \sum_{i=1}^{L} \hat{P}_{j-1}^{L,|\psi\rangle} \otimes \mathbb{1} \otimes \hat{P}_{j+1}^{R,|\psi\rangle} - \sum_{i=1}^{L-1} \hat{P}_{j}^{L,|\psi\rangle} \otimes \hat{P}_{j+1}^{R,|\psi\rangle} \ , \tag{3.37}$$

where

$$\hat{P}_{j}^{L,|\psi\rangle} = \sum_{\substack{\sigma_1',\ldots,\sigma_j' \\ \sigma_1,\ldots,\sigma_j}} A^{\sigma_1}\ldots A^{\sigma_j}A^{\sigma_j'\dagger}\ldots A^{\sigma_1'\dagger}|\sigma_1,\sigma_2,\ldots,\sigma_j\rangle\langle\sigma_1',\sigma_2',\ldots,\sigma_j'| \otimes \hat{\mathbb{1}}_{j+1}^{R} \ , \tag{3.38}$$

and

$$\hat{P}_{j}^{R,|\psi\rangle} = \hat{\mathbb{1}}_{j-1}^{L} \otimes \sum_{\substack{\sigma_j',\ldots,\sigma_L' \\ \sigma_j,\ldots,\sigma_L,}} B^{\sigma_L'\dagger}\ldots B^{\sigma_j'\dagger}B^{\sigma_j}\ldots B^{\sigma_L}|\sigma_j,\ldots,\sigma_L\rangle\langle\sigma_L',\ldots,\sigma_j'| \ . \tag{3.39}$$

The next step is to approximate the solution of Eq. (3.36). This can be done by sequentially solving the forward in time [first term to the right-hand side in Eq. (3.36)] and backward in time [second term on the right-hand side of Eq. (3.36)] differential equations. In the end, one is left with solving the local equations

$$\frac{\partial}{\partial t}M_{a_{i-1}a_i}^{\sigma_i}(t) = -i\sum_{\sigma_i',a_{i-1}',a_i'} H_{a_{i-1}a_i a_{i-1}' a_i'}^{eff\,\sigma_i\sigma_i'} M_{a_{i-1}'a_i'}^{\sigma_i'}(t) \ , \tag{3.40}$$

where $H^{eff\sigma_i\sigma'_i}_{a_{i-1}a_i a'_{i-1}}$ is drawn in Fig 3.6(a), and

$$\frac{\partial}{\partial t}\Lambda_{lm}(t) = +i \sum_{l',m'} K_{lml'm'}\Lambda_{l'm'}(t)\,, \tag{3.41}$$

where $K_{lml'm'}$ is drawn in Fig 3.6(b). In general, these equations are solved with a Krylov solver. As is the case for the DMRG algorithm introduced in Sec. 3.1.1, one solves these equations for all sites and bonds sequentially by sweeping through the system. One can reduce the error by sweeping through the matrix-product state from left to right and back again, each with a halved time step. The advantage of 1TDVP is that the norm and energy are conserved. However, the projection might induce an error if the bond dimension of the initial state is too small [137].

Alternatively, one can use the two-site version 2TDVP. In this algorithm, one evolves a two-site tensor forward in time. The tensor is then split up, and a one-site tensor is evolved backward in time. The equations one has to solve are

$$\frac{\partial}{\partial t}M^{\sigma_i\sigma_{i+1}}_{a_{i-1}a_{i+1}}(t) = -i \sum_{\substack{\sigma'_i,\sigma'_{i+1},\\ a'_{i-1},a'_{i+1}}} H^{eff\sigma_i\sigma_{i+1}\sigma'_i\sigma'_{i+1}}_{a_{i-1}a_{i+1}a'_{i-1}a'_{i+1}} M^{\sigma'_i\sigma'_{i+1}}_{a'_{i-1}a'_{i+1}}(t)\,, \tag{3.42}$$

where $H^{eff\sigma_i\sigma_{i+1}\sigma'_i\sigma'_{i+1}}_{a_{i-1}a_{i+1}a'_{i-1}a'_{i+1}}$ is the two-site version of Fig 3.6(a), and (if sweeping from left to right),

$$\frac{\partial}{\partial t}\tilde{M}^{\sigma_{i+1}}_{a_i a_{i+1}}(t) = +i \sum_{\substack{\sigma'_{i+1},\\ a'_i,a'_{i+1}}} H^{eff\sigma_{i+1}\sigma'_{i+1}}_{a_i a_{i+1}a'_i a'_{i+1}} \tilde{M}^{\sigma'_{i+1}}_{a'_i a'_{i+1}}(t)\,. \tag{3.43}$$

Equation (3.42) (and the other TDVP equations) are solved by

$$M^{\sigma_i\sigma_{i+1}}_{a_{i-1}a_{i+1}}(t+\frac{dt}{2}) = \sum_{\substack{\sigma'_i,\sigma'_{i+1},\\ a'_{i-1},a'_{i+1}}} e^{-i\frac{dt}{2}tH^{eff\sigma_i\sigma_{i+1}\sigma'_i\sigma'_{i+1}}_{a_{i-1}a_{i+1}a'_{i-1}a'_{i+1}}} M^{\sigma'_i\sigma'_{i+1}}_{a'_{i-1}a'_{i+1}}(t)\,, \tag{3.44}$$

which is followed by an SVD of $M^{\sigma_i\sigma_{i+1}}_{a_{i-1}a_{i+1}}(t+\frac{dt}{2})$.

The advantage of 2TDVP is that the bond dimension can be increased and that it can time-evolve a Hamiltonian with nearest-neighbor interaction without a projection error. The disadvantage is that the algorithm no longer conserves the norm and energy due to the truncation. For finite temperature calculations, the initial state has a low bond dimension and the Hamiltonian has next-nearest neighbor interactions (due to the purification introduced in Sec. 3.1.2). How I control convergence will be discussed in more detail when I present the corresponding results.

There are two situations in the 2TDVP algorithm where one can think of applying LBO. The first is before the SVD of $M^{\sigma_i\sigma_{i+1}}_{a_{i-1}a_{i+1}}(t+\frac{dt}{2})$. The procedure is similar to what I discussed for tDMRG and is simple and (in many cases) efficient. Note that due to the similarity

between the TDVP and ground-state DMRG algorithms, this can also be included in the latter. The second situation is when solving Eq. (3.44), since contracting the effective Hamiltonian with the two-site tensor is a costly procedure. Normally, as previously stated, the equation is solved with a Krylov method. In the work presented in Ch. 5, however, we propose using a fourth-order Runge-Kutta, which we combined with LBO (RK4-LBO). In the following discussion, I will denote all "left" indices with $\alpha = (\sigma_i, a_{i-1})$ and all "right" indices with $\beta = (\sigma_{i+1}, a_{i+1})$. The RK4 algorithm is then

$$M_{\alpha\beta}(t + \frac{dt}{2}) = M_{\alpha\beta}(t) + \frac{-idt}{6}\frac{1}{2}(k^1_{\alpha\beta} + 2k^2_{\alpha\beta} + 2k^3_{\alpha\beta} + k^4_{\alpha\beta})\,. \tag{3.45}$$

To incorporate LBO, one first obtains the optimal basis $\tilde{\sigma}_i$ and $\tilde{\sigma}_{i+1}$ from $M_{\alpha\beta}(t)$, as I explained in Sec 3.1.4. One then transforms $M_{\alpha\beta}(t) \to M_{\tilde{\alpha}\tilde{\beta}}(t)$. Now, $\tilde{\alpha} = (\tilde{\sigma}_i, a_{i-1})$ and $\tilde{\beta} = (\tilde{\sigma}_{i+1}, a_{i+1})$. One then computes

$$k^1_{\alpha\beta} = \sum_{\tilde{\alpha}',\tilde{\beta}'} H^{eff}_{\alpha\beta\tilde{\alpha}'\tilde{\beta}'} M_{\tilde{\alpha}'\tilde{\beta}'}(t)\,. \tag{3.46}$$

Next, one obtains the optimal basis of $(M(t) + \frac{-idt}{2}\frac{1}{2}k^1)_{\alpha'\beta'}$, and computes

$$k^2_{\alpha\beta} = \sum_{\tilde{\alpha}',\tilde{\beta}'} H^{eff}_{\alpha\beta\tilde{\alpha}'\tilde{\beta}'}(M(t) + \frac{-idt}{2}\frac{1}{2}k^1)_{\tilde{\alpha}'\tilde{\beta}'}\,, \tag{3.47}$$

and so on. Note that, as with all LBO applications, this procedure does not guarantee a speedup, but better performance is observed in many practical applications. This will also be demonstrated in Ch. 5. There, the algorithm is more thoroughly discussed and benchmarked, and I will also illustrate and discuss why this algorithm scales favorably compared to using LBO with a Krylov solver.

In Fig. 3.10(a), I compare the current-current correlation functions for the Holstein model at finite temperature computed with tDMRG-LBO and p2TDVP-LBO. There, one sees that the data matches but that the p2TDVP-LBO algorithm reaches longer times. This can be understood by comparing the maximum bond dimension of the matrix-product states [inset in Fig. 3.10(a)]. In that figure, one can observe that the p2TDVP algorithm uses a smaller bond dimension for a fixed truncation $\epsilon_{\text{bond}} = 10^{-9}$, which allows a longer time evolution (consistent with other benchmarks [137]). The importance of this is demonstrated in Fig. 3.10(b), where I show the optical conductivity obtained by Fourier-transforming the two data sets. The p2TDVP algorithm gives a significantly better resolution. In Ch. 5, I will also demonstrate that the required local optimal basis dimensions are roughly the same for the two methods. There, a physical interpretation of the data is also presented. I also want to note that increasing the frequency resolution is an active research field, either by extrapolating from real-time data [141,216,217] or analytic continuation of the Green's function [218].

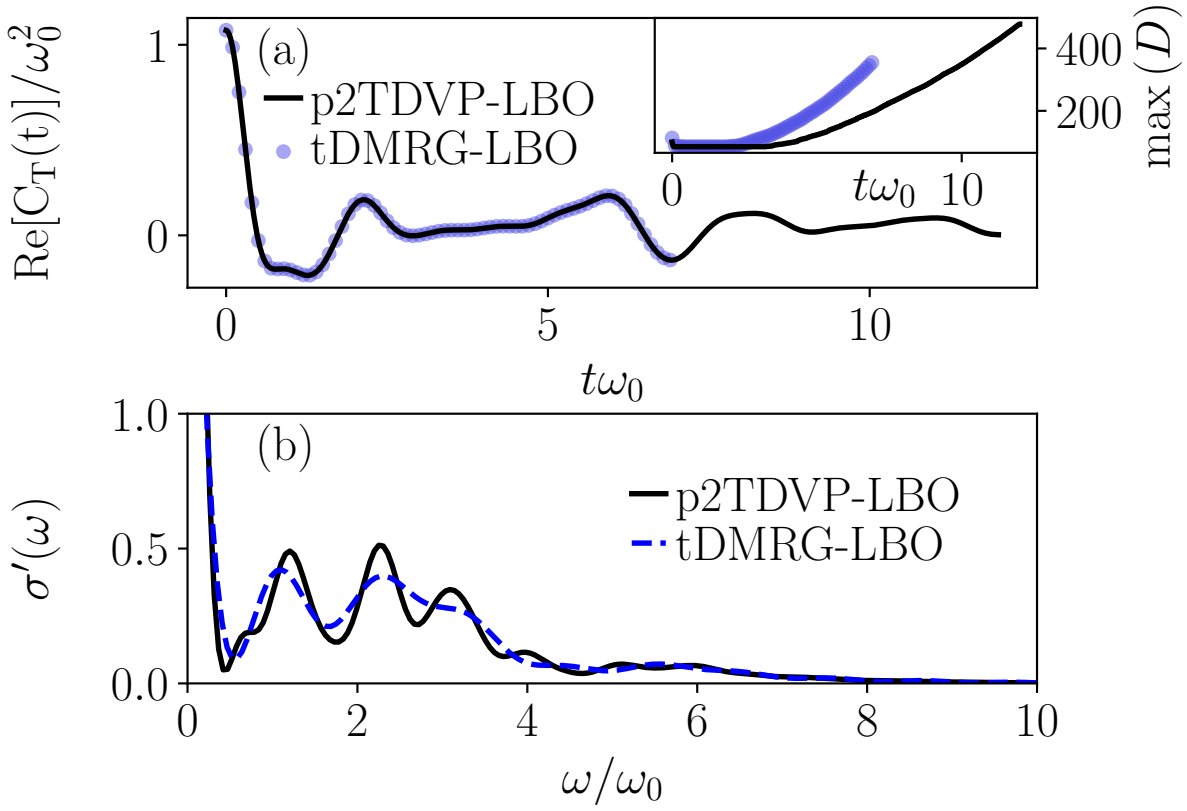

Figure 3.10: Comparing p2TDVP-LBO to tDMRG-LBO. (a) Comparing the current-current correlation function for the Holstein polaron model at temperature $T/\omega_0 = 0.1$, $\gamma/\omega_0 = \sqrt{2}$, $t_0/\omega_0 = 1.0$, and $M = 20$. For both methods I use $\epsilon_{\mathrm{bond}} = \epsilon_{\mathrm{LBO}} = 10^{-9}$. Inset of (a): Maximum bond dimension D of the matrix-product states as a function of time. (b) Real part of the optical conductivity obtained from the data in (a), see Ch. 2 and Ch. 5 for details.

3.2 Trajectory-based approaches

As explained so far, there have been different algorithms trying to efficiently treat the large phonon Hilbert spaces in electron-phonon models. In this section, I will briefly introduce some other approaches, but note that a more in-depth-discussion is contained in the publication in Ch. 7. The methods are called trajectory-based methods, and the idea is to describe the phonons with trajectories following Hamiltonian equations of motion and the electrons quantum mechanically. This leads an immense numerical simplifications, and the validity of the ansatz will also be explored in Ch. 7. I will first introduce the Wigner (or Weyl) transformation [219–223] to map the operator $\hat{A}$ to a function of the phase space coordinates $A(R, P)$. Here, I will consider a one-dimensional system, but the procedure can be extended to higher dimensions. For a system composed of electronic and vibrational degrees of freedom, one writes the wave function in terms of nuclei coordinates $|R\rangle$ and a

nuclei-coordinate dependent electron basis $|\phi_l(R)\rangle$,

$$|\psi\rangle = \int dR \sum_l |R, \phi_l(R)\rangle \, \psi_l(R) \, . \tag{3.48}$$

The next step, is to do a Wigner transformation on the nuclear coordinates only, see Refs. [224, 225], so that

$$A_{k,l,W}(R,P) = \int dZ e^{iPZ} \left[\left\langle R - \frac{Z}{2}, \phi_k(R - \frac{Z}{2}) \right| \hat{A} \left| R + \frac{Z}{2}, \phi_l(R + \frac{Z}{2}) \right\rangle \right] . \tag{3.49}$$

This is also known as a partial Wigner transformation. Now, by partially Wigner transforming the density matrix $\hat{\rho}$, the calculation of expectation values turns in to a computation in phase space

$$\langle \hat{A} \rangle = \sum_{k,l} \int dR \int dP A_{k,l,W}(R,P) \frac{\rho_{k,l,W}(R,P)}{2\pi} . \tag{3.50}$$

Note that I will define $W_{k,l}(R,P) := \frac{\rho_{k,l,W}(R,P)}{2\pi}$, but that this is not a probability distribution in phase space, since it can have negative values. Written out, the partially transformed density matrix becomes

$$W_{k,l}(R,P) = \int dZ \frac{e^{iPZ}}{2\pi} \psi_k(R - \frac{Z}{2}) \psi_l^*(R + \frac{Z}{2}) \, . \tag{3.51}$$

The first set out algorithms I will introduced is called independent trajectory methods, and they try to approximate $\hat{W}(R,P,t)$ from Eq. (3.51) with a set of N_t independent classical nuclear trajectories (which I index with α) attached to the electronic density matrix $\hat{\rho}_{el}^{\alpha}$. With each of these trajectories, one associates a coordinate $R^{\alpha}(t)$ and a momentum $P^{\alpha}(t)$ and assigns them a point in phase space $(R^{\alpha}(t), P^{\alpha}(t))$. The next step is to approximate

$$\hat{W}(R,P,t) \approx \frac{1}{N_t} \sum_{\alpha=1}^{N_t} w^{\alpha} \delta(R - R^{\alpha}(t)) \delta(P - P^{\alpha}(t)) \hat{\rho}_{el}^{\alpha}(t) \, , \tag{3.52}$$

where w^{α} is a weighting factor and $\rho_{el}^{\alpha}(t)$ is the electron density matrix. The expectation values can now be calculated with Eq. (3.50). For one trajectory, $N_t = 1$ and $w^1 = 1$, one gets

$$\begin{aligned} \langle \hat{A} \rangle &= \sum_{k,l} \int dR \int dP A_{k,l,W}(R,P) \delta(R - R^1(t)) \delta(P - P^1(t)) \rho_{k,l,el}^1(t) \\ &= \sum_{k,l} A_{k,l,W}(R^1(t), P^1(t)) \rho_{k,l,el}^1(t) \, . \end{aligned} \tag{3.53}$$

As a simple example, I will consider the observable $\hat{R} = \int dR \, |R\rangle \, R \, \langle R|$ at time $t = 0$.

Inserting this into Eq. (3.53) gives

$$\begin{aligned}
\langle \hat{R} \rangle &= \sum_{k,l} \int dZ \int dR' e^{iP^1 Z} \left[\langle R^1 - \frac{Z}{2} | R' \rangle \, R' \, \langle R' | R^1 + \frac{Z}{2} \rangle \right] \langle \phi_k(R^1 - \frac{Z}{2}) | \phi_l(R^1 + \frac{Z}{2}) \rangle \, \rho^1_{k,l,el} \\
&= \sum_{k,l} \int dR' \int dZ e^{iP^1 Z} R' \delta(R^1 - \frac{Z}{2} - R') \delta(R' - R^1 - \frac{Z}{2}) \\
&\times \langle \phi_k(R^1 - \frac{Z}{2}) | \phi_l(R^1 + \frac{Z}{2}) \rangle \, \rho^1_{k,l,el} \\
&= \sum_{k,l} \int dZ e^{iP^1 Z} (R^1 - \frac{Z}{2}) \delta\Big((R^1 - \frac{Z}{2}) - R^1 - \frac{Z}{2} \Big) \langle \phi_k(R^1 - \frac{Z}{2}) | \phi_l(R^1 + \frac{Z}{2}) \rangle \, \rho^1_{k,l,el} \\
&= \sum_{k,l} \int dZ e^{iP^1 Z} (R^1 - \frac{Z}{2}) \delta(-Z) \, \langle \phi_k(R^1 - \frac{Z}{2}) | \phi_l(R^1 + \frac{Z}{2}) \rangle \, \rho^1_{k,l,el} \\
&= \sum_{k,l} R^1 \, \langle \phi_k(R^1) | \phi_l(R^1) \rangle \, \rho^1_{k,l,el} = \sum_{k,l} R^1 \delta_{k,l} \rho^1_{k,l,el} = R^1 \, .
\end{aligned} \tag{3.54}$$

The time evolution is now calculated by propagating each trajectory independently. The nuclei propagate according to classical mechanics

$$\frac{\partial R^\alpha}{\partial t} = \frac{\partial H^{nuc,\alpha}}{\partial P^\alpha} \, , \frac{\partial P^\alpha}{\partial t} = - \frac{\partial H^{nuc,\alpha}}{\partial R^\alpha} \, , \tag{3.55}$$

where $H^{nuc,\alpha}$ the classical Hamiltonian of the nuclei. The electronic density matrix is evolved with respect to the nuclear positions. This is also where the approaches presented here differ. The question is how to compute $H^{nuc,\alpha}$?

In this work, I will present results obtained with two independent trajectory methods: Multitrajectory Ehrenfest (MTE) [122,123,198] and fewest-switching surface hopping (FSSH) [124–126].

The MTE algorithm uses a mean field approximation for the nuclei Hamiltonian, $H^{nuc,\alpha}$, which is used to propagate the nuclear coordinates. First, one splits the nuclear Hamiltonian into a kinetic term and "the rest". One then calculates the trace of the electron density matrix ρ^α_{el} and the Born-Oppenheimer Hamiltonian (see Ch 2), so that

$$H^{nuc,\alpha} = T^{\text{nuc},\alpha}(P^\alpha) + Tr[\hat{H}^{BO}(R^\alpha) \hat{\rho}^\alpha_{el}] \, . \tag{3.56}$$

Note that $\hat{H}^{BO}(R^\alpha)$ is an electronic operator. One now uses $\hat{H}^{BO}\Big(R^\alpha(t)\Big)$ to propagate $\hat{\rho}^\alpha_{el}(t)$ via

$$\frac{d\hat{\rho}^\alpha_{el}}{dt} = -i[\hat{H}^{BO}\Big(R^\alpha(t)\Big), \hat{\rho}^\alpha_{el}(t)] \, . \tag{3.57}$$

In Ch. 7, we will see that MTE can have difficulties if the electron wave function has contributions on two Born-Oppenheimer surfaces after crossing through a region with strong-adiabatic coupling. Far away from this region, the contributions should evolve independently again, but the nuclear coordinates will depend on both contributions [126,226,227] due to the trace with the electron density matrix.

The other algorithm, FSSH [124–126], tries to avoid the problems of MTE. Instead of a mean-field approach, FSSH considers the force from a single surface only, but allows for stochastic hopping between the surfaces. For the following discussion, I write the electron-wave function in the Born-Oppenheimer basis, see Ch. 2, as

$$|\psi_{el}^{\alpha}(t)\rangle = \sum_a \psi_{el,a}^{\alpha}(t)\,|\phi_a^{\mathrm{BO}}(R^{\alpha}(t))\rangle\ . \tag{3.58}$$

The probability of the electron to be on one Born-Oppenheimer surface $E_a^{\alpha}(R^{\alpha}) = \langle\phi_a^{\mathrm{BO}}|\hat{H}^{\mathrm{BO}}(R^{\alpha})|\phi_a^{\mathrm{BO}}\rangle$ is given by $|\psi_{el,a}^{\alpha}(t)|^2$. Instead of a mean-field approach, the nuclei Hamiltonian $H^{nuc,\alpha}$ now contains the forces from the currently active energy surface $E_{\lambda^{\alpha}}(R^{\alpha})$ and becomes

$$H^{nuc,\alpha} = T^{\mathrm{nuc},\alpha}(P^{\alpha}) + E_{\lambda^{\alpha}}(R^{\alpha})\,, \tag{3.59}$$

where λ^{α} indicates the activate surface. The algorithm aims to reproduce the populations $|\psi_{el,a}^{\alpha}(t)|^2$ on the different trajectories and the changing probabilities with the fewest number hops between surfaces possible. There are also many improvements to FSSH, which will be addressed in Ch. 7.

The final algorithm I will discuss is the multiconfigurational Ehrenfest (MCE) method [120, 121]. MCE does quantum simulations using an incomplete basis (configurations) for the phonons, and can in principle become exact. The key is to identify a small but relevant part of the Hilbert space where the calculations are greatly simplified. MCE comes in two versions, MCEv1 [120]and MCEv2 [121], and both rely on sampling coherent states in the phononic subsystem, from which the wave functions are constructed. This work only contains results obtained with MCEv1. For the configuration α, one writes the product state of coherent oscillators as

$$|\vec{z^{\alpha}}\rangle = e^{\sum_{j=1}^{L}(z_j^{\alpha}\hat{b}_j^{\dagger} - \bar{z}_j^{\alpha}\hat{b}_j - \mathrm{Im}\{z_j^{\alpha}\}\mathrm{Re}\{z_j^{\alpha}\})}\,|0\rangle_{ph}\ , \tag{3.60}$$

with $\hat{b}_j\,|\vec{z^{\alpha}}\rangle = z_j^{\alpha}\,|\vec{z^{\alpha}}\rangle$. The ansatz for the total wave function is

$$|\psi\rangle = \sum_{\alpha=1}^{N_c}|\psi^{\alpha}\rangle = \sum_{\alpha=1}^{N_c}|\phi^{\alpha}\rangle\otimes\,|\vec{z^{\alpha}}\rangle = \sum_{\alpha=1}^{N_c}\sum_{i=1}^{L} a_i^{\alpha}(t)\hat{c}_i^{\dagger}\,|0\rangle_{el}\otimes\,|\vec{z^{\alpha}}\rangle\ , \tag{3.61}$$

where I used that $|\phi^{\alpha}\rangle = \sum_{i=1}^{L} a_i^{\alpha}(t)\hat{c}_i^{\dagger}\,|0\rangle_{el}$, and N_c is the number of configurations. The key to a good and efficient MCE algorithm is too cleverly choose $\{z^{\alpha}\}_{\alpha=1\ldots N_c}$. The electron coefficients a_i^{α} are time-evolved using the Dirac-Frenkel time-dependent variational principle with the Lagrangian $\mathcal{L} = \langle\psi|i\frac{\partial}{\partial t} - \hat{H}|\psi\rangle$, such that $\frac{\partial\mathcal{L}}{\partial a_i^{\alpha *}} = \frac{d}{dt}\frac{\partial\mathcal{L}}{\partial \dot{a}_i^{\alpha *}}$. For the nuclei coordinates, the time-evolution is done with the Ehrenfest equations of motion with $H^{nuc,\alpha} = \langle\psi^{\alpha}|H^{nuc,\alpha}|\psi^{\alpha}\rangle\,/\,\langle\psi^{\alpha}|\psi^{\alpha}\rangle$, leading to

$$i\dot{z}_i^{\alpha} = \frac{\partial H^{nuc,\alpha}}{\partial \dot{z}_i^{\alpha *}} = \omega_0 z_i^{\alpha} - \gamma\frac{|a_i^{\alpha}|^2}{\sum_j |a_j^{\alpha}|^2} \tag{3.62}$$

for the Holstein model. Note that all algorithms, their sampling procedure, and convergence are discussed in greater detail in Ch. 7.

The MCE calculations presented in this work were done by Stefan Gräber in [228] and the FSSH calculations by Michael ten Brink in Ref. [229]. Both contributed to the MTE results.

3.3 Other methods

In this last section, I want to briefly mention some of the many new developments in numerical methods that aim to efficiently treat electron-phonon systems. As is often the case, a rich set of methods with different strengths and weaknesses is needed for a comprehensive understanding of such models.

The newly developed projected purification (PP) method [153] mentioned in Sec. 3.1.3, for example, shows encouraging results for time-evolution [154, 155] and the ground-state search [78] with matrix-product states (MPSs). Some of the method's advantages is it's flexibility and that it can easily be implemented into existing MPS codes that already take advantage of $U(1)$ symmetries. Still, the pros ($U(1)$ symmetry) and cons (next nearest neighbor interaction) of introducing the phonon bath in time-evolution algorithms still need to be thoroughly investigated, and a benchmark with LBO would be desirable. For finite temperature calculations and for a finite phonon bandwidth, the effects of PP have yet to be explored. It is plausible that LBO and PP will complement each other in the future.

Quantum Monte Carlo (QMC) methods are another tool that has been used to successfully study the Holstein model. For example, Hohenadler studied the time-dependent spin and charge correlation functions of the Holstein model (with spins) using a continuous-time QMC [116] method in Ref. [230]. He considered a quench from a Peierls insulating state to a non-interacting Hamiltonian (setting $\gamma = 0$) and obtained exact results for the correlation functions. Furthermore, Hohenadler and Batrouni used a version of the continuous-time QMC algorithm to investigate the phase diagram of the half-filled Holstein model on a square lattice in Ref. [231]. There, the authors examined the presence of charge density wave and superconducting order at temperatures $T/t_0 \geq 0.1$. A further example is given in Ref. [232], where the authors calculated the specific heat, compressibility, and electron and phonon spectral functions for the one-dimensional Holstein model at half-filling using another QMC method [233]. Despite their success, QMC methods can have some drawbacks. Algorithms relying on integrating out the phononic degrees of freedom, for example, will have difficulties including phonon interaction terms [234]. Additionally, they can suffer from the sign problem [149].

The electron spectral functions of the Holstein polaron model have also recently been calculated with momentum space hierarchical equations of motion (HEOM) by Janković et al. in Ref. [70], and in Ref. [68], Mitrić et al. calculated the spectral function in one dimension with dynamic mean field theory (DMFT). In the latter, they demonstrated that DMFT can give very accurate results in one dimension for the spectral functions for most

parameters. These findings are very encouraging, though the paper shows that the method gives inaccurate results for large quasi-momenta in the polaron crossover regime (which is a regime where DMRG works very well). Note that the authors in Ref. [68] benchmark some data with results presented in this work. The HEOM method can also compute accurate electron spectral functions, but as stated in Ref. [70], it will be more difficult to compute quantities like the phonon spectral function.

Another approach to compute the polaron spectral function was newly published by Robinson et al. in Refs. [69, 235], namely using cumulant expansion (CE) methods. The method approximates the Green's functions in real time by evaluating the exponential of the sum of the cumulants. The perturbative CE method presented in Ref. [69] works very well at small but struggles at large quasi-momenta. The results for large quasi-momenta were significantly improved by a self-consistent CE in Ref. [235], and there the authors could also include dispersive phonons. However, self-consistent CE can also introduce some nonphysical features at small quasi-momenta such as negative spectral weight (not present for perturbative CE).

For dynamical quantities, one can also use the Lanczos method [119, 196, 197]. The method with a variational Hilbert space [236, 237] was used to benchmark many of the DMRG results presented in this work. Recently, the Lanczos method has been used to calculate finite-temperature spectral functions for the Holstein polaron [65], Holstein polaron ground-state spectral functions and optical conductivity with dispersive phonons [67], and the spectral functions of a polaron coupled to hard-core bosons [238]. In the first two cases, the authors also used a variational Hilbert space.

The Lanczos method with a variational Hilbert space is an efficient and reliable method to calculate spectral functions and transport coefficients directly in frequency space. The method's drawback is that it allows for fewer phonons and smaller system sizes than matrix-product-state based methods. In Ref. [67], for example, Bonča et al. used 28 phonons on the center site but fewer on the sites further away. Furthermore, the variational Hilbert space method cannot be utilized at finite filling, and thus the possible system sizes will be limited. All the Lanczos results in this thesis were computed by Prof. Janez Bonča.

A very different approach is to move away from a complete quantum-mechanical treatment of the phonons. In Sec. 3.2, I introduced a set of trajectory-based methods, which can severely simplify the computational cost for electron-phonon systems. This has already been utilized in combination with different numerical techniques. For example in Ref. [177], Weber and Freericks used time dependent Monte Carlo and Green's function methods to analyze electron-phonon systems with static phonons. In Ref. [178], Petrović et al. extended the formalism to phonons following Ehrenfest equations of motion which allowed them to study the long-time evolution of a charge density wave brought out of equilibrium. The method show promising results, but will struggle at very low temperatures, away from adiabatic parameter regime, and it might have problems incorporating electron-electron interaction.

In Ref. [239], Picano et al. studied the equilibrium properties of the Holstein-Anderson model (see Ch. 6) with a semi-classical approach that incorporates electron fluctuations into the phonon dynamics, leading to stochastic phonon equations. Their motivation was

to propose this scheme to solve the DMFT electron-phonon impurity problem. The authors compared the phonon distribution calculated with various techniques, including an (up to error bars) exact QMC method. For small values of the phonon frequency, they found their method to give good results for all but very low temperatures. However, they could still report good agreement for the electron Green's function at all temperatures, signaling that it only depends qualitatively on the phonon distribution. As expected, their method also shows strong deviations for large phonon frequencies.

Chapter 4

Thermodynamics and finite-temperature spectral functions

In this chapter, I will start presenting the results for the Holstein model introduced in Ch. 2. Such theoretical models can be related to experimental results through the computation of quantities like spectral functions and transport coefficients. In Ch. 3, I introduced different numerical techniques which one can use to, in principle, do these computations. Here, I will present publication where we have utilized these tools to calculate several different spectral functions for the Holstein polaron.

Experimental techniques like angle-resolved photoemission spectroscopy (ARPES) and time-resolved ARPES (see, e.g., Refs. [94–96] for reviews) have helped our understanding of quantum materials, see e.g., Refs. [100, 101, 240–243]. These experiments give us access to the quasi-momentum resolved single-particle spectral function, which provides us with information about the materials' internal structures. Recently, for example, Kang et al. used ARPES to measure the spectral functions of a surface-doped layered semiconductor MoS_2 [100]. They observed a renormalized band and sub-bands separated by the phonon frequency, which are distinct features of the Holstein polaron. Furthermore, by using ARPES on molybdenum blue bronze, which is a quasi-one-dimensional material with a charge-density-wave low-temperature state, the authors in Ref. [101] were able to identify Holstein-polaron formation with decreasing temperature.

Sine detailed knowledge of the polaron spectral functions is required to interpret such experimental results, the Holstein polaron spectral functions have been studied in a series of works, e.g., in Refs. [72, 74, 244–253]. However, due to the difficulty of finite-temperature calculations, the temperature dependence of the polaron spectral function was only recently analyzed by Bonča et al. in Ref. [65] with the finite-temperature Lanczos method (FTLM) [119]. That work was then followed up by an analysis of the hard-core bosons version [238].

On the contrary, the phonon spectral function for the Holstein polaron has gained less attention [55, 57, 60]. In Ref. [57], it was studied by Loos et al. in the ground state with a cluster approach and analytic calculations, and they identified distinct features such as the flat phonon band and a renormalized polaron band.

With these results in mind, it would be desirable to have an efficient numerical method that can be used to reliably compute time-dependent correlation functions for electron-phonon systems at finite temperatures and that can, in principle, be extended to finite densities. The method must also be effective in intermediate parameter regimes, which is the most difficult regime as it can not be treated with perturbation theory. In this chapter, I present a publication where we take steps in that direction by combining the purification scheme introduced in Ch. 3 and the time-dependent density-matrix renormalization group (tDMRG) with local basis optimization (LBO) (also see Ch. 3). We use this to conduct both the imaginary and real-time evolution needed to compute different time-dependent Green's functions at finite temperatures for the polaron (one electron) problem. By Fourier transforming the results, we then extract the polaron spectral function, the electron emission function, and the phonon spectral function.

As I explained in Ch. 3, purification requires an imaginary time evolution from a $T = \infty$ state. For the Holstein model, this state naturally depends on the local harmonic oscillator cutoff M. It is also unclear if LBO can give a computational advantage at all since all states are equally important at high temperatures. We first demonstrate that if M is chosen large enough, this method allows us to enter a low-temperature regime where we can describe the physics correctly. We further show that LBO becomes computationally beneficial in this regime.

For the polaron spectral function, we verify that our results are consistent with the FTLM method from Bonča et al. in Ref. [65]. Additionally, we demonstrate that we can access the full quasi-momentum dependence and do calculations for system sizes up to $L = 101$ with $M = 20$. For the electron emission function, we show how the momentum occupation changes with temperature and report the emergence of a polaron band when T is increased. For the phonon spectral function, we recover the polaron band and the free phonon line. Additionally, a previously thermally suppressed polaron band and free phonon line appear at negative frequencies.

The work presented here introduces an efficient scheme to treat electron-phonon systems at finite temperatures and calculate their spectral functions. As we will see in Ch. 5, the formalism can also be combined with other time-evolution methods and extended to other quantities, such as current-current correlation functions. There, we will also study bipolaron physics and systems at finite filling. Alternatively, one could focus on polaron physics in more complicated models, see, e.g., Ref. [254] for a review on the theory of manganites. However, each application must be tested individually to see which quantities are numerically accessible.

4.1 Publication: Finite-temperature density-matrix renormalization group method for electron-phonon systems: Thermodynamics and Holstein-polaron spectral functions

Reprinted article with permission from
David Jansen, Janez Bonča, and Fabian Heidrich-Meisner
Phys. Rev. B 102, 165155 (2020)
https://doi.org/10.1103/PhysRevB.102.165155

Author contributions: D. J. wrote the manuscript, implemented the algorithm, produced the data, and derived the analytical results. F. H.-M. took the initiative to study the finite-temperature properties of the model with methods using local basis optimization. J. B. provided the Lanczos data and suggested looking at the electron emission and phonon spectral functions. F. H.-M. and J. B. both revised the manuscript. All authors contributed to interpreting the results and discussed the data.

Editors' Suggestion

Finite-temperature density-matrix renormalization group method for electron-phonon systems: Thermodynamics and Holstein-polaron spectral functions

David Jansen,[1] Janez Bonča,[2,3] and Fabian Heidrich-Meisner[1]
[1]*Institut für Theoretische Physik, Georg-August-Universität Göttingen, D-37077 Göttingen, Germany*
[2]*J. Stefan Institute, 1000 Ljubljana, Slovenia*
[3]*Faculty of Mathematics and Physics, University of Ljubljana, 1000 Ljubljana, Slovenia*

(Received 30 July 2020; revised 1 October 2020; accepted 2 October 2020; published 29 October 2020)

We investigate the thermodynamics and finite-temperature spectral functions of the Holstein polaron using a density-matrix renormalization group method. Our method combines purification and local basis optimization (LBO) as an efficient treatment of phonon modes. LBO is a scheme which relies on finding the optimal local basis by diagonalizing the local reduced density matrix. By transforming the state into this basis, one can truncate the local Hilbert space with a negligible loss of accuracy for a wide range of parameters. In this work, we focus on the crossover regime between large and small polarons of the Holstein model. Here, no analytical solution exists and we show that the thermal expectation values at low temperatures are independent of the phonon Hilbert space truncation provided the basis is chosen large enough. We then demonstrate that we can extract the electron spectral function and establish consistency with results from a finite-temperature Lanczos method. We additionally calculate the electron emission spectrum and the phonon spectral function and show that all the computations are significantly simplified by the local basis optimization. We observe that the electron emission spectrum shifts spectral weight to both lower frequencies and larger momenta as the temperature is increased. The phonon spectral function experiences a large broadening and the polaron peak at large momenta gets significantly flattened and merges almost completely into the free-phonon peak.

DOI: 10.1103/PhysRevB.102.165155

I. INTRODUCTION

Developments in experimental methods with ultrafast dynamics (see, e.g., Refs. [1–5] and Refs. [6,7] for a review) have reinforced the interest in the theoretical modeling of electron-phonon interactions. Despite the complexity of real materials, qualitative insights can be gained from model systems such as the Holstein model [8–37], Hubbard-Holstein model [38–47], hard-core boson-phonon models [48,49], the t-J model augmented with phonons [50,51], and spin-boson models [52–55]. It is believed that many experimental results can be interpreted by studying such toy Hamiltonians that contain important key features. A paradigmatic example is the Holstein-polaron model [8] which consists of one electron interacting with local bosons. Since the electron-boson interaction is the only means of thermalization in the system (see, e.g., Ref. [56]), the model allows us to study this particular relaxation channel, which plays an important role in real materials, in a controlled way.

The Holstein polaron at zero temperature has been the subject of intense research [13,18,27,57–61]. Recent developments in the field of thermalization in isolated quantum systems and quench dynamics have fueled the demand for additional research on the model at a finite temperature [56,62–71]. In particular, the momentum dependence of the spectral function and the self-energy have recently been computed using a finite-temperature Lanczos method by Bonča *et al.* in Ref. [72], followed by a comparison between spectral properties of the Holstein polaron and an electron coupled to hard-core bosons [73].

In this paper, we introduce an alternative numerical approach. We demonstrate that a density-matrix renormalization group (DMRG) method [74–76] can efficiently reproduce the spectral function. We also compute the electron emission spectrum, which can be accessed in angle-resolved photoemission spectroscopy (ARPES) experiments [77–82] and the phonon spectral function. The method further allows us to compute thermodynamic observables for very large system sizes compared to other wave-function based methods.

We combine finite-temperature DMRG with purification [83–86], time-dependent DMRG (tDMRG) [76,87–90], and local basis optimization (LBO) [91] to obtain an efficient scheme to both generate the finite-temperature matrix-product state (MPS) and to compute different Green's functions. LBO, originally introduced by Zhang *et al.* in Ref. [91], has already been used for the real-time evolution [35,37,92,93] and ground-state algorithms [37,52,94–100]. The DMRG method with purification requires an infinite-temperature state as its starting point which is artificial and strongly dependent on the truncation of the phonon Hilbert space. Our results, however, become independent of that truncation in the polaron-crossover regime at low temperatures, which is physically most relevant. This allows for the efficient computation of static and dynamic properties of the Holstein model at finite temperatures.

In particular, using finite-temperature states we compute the electron addition spectral function. This quantity has already been analyzed thoroughly at finite temperatures by Bonča *et al.* in Ref. [72] for a system with periodic boundary

conditions. We show that we can resolve the same peaks as the finite-temperature Lanczos method and observe an excellent quantitative agreement. We additionally compute the electron emission spectrum and the phonon spectral function. The electron emission spectrum was computed in Ref. [62] for a two-site and two-electron system. Here, we focus on one electron and go up to twenty one sites. We further show that the LBO scheme proposed in Ref. [92] becomes computationally beneficial at low temperatures and significantly simplifies the computations of these spectral functions.

This paper is structured as follows. In Sec. II, we introduce the Holstein-polaron model, the observables, and the spectral functions. We proceed in Sec. III with a description of the methods used. We introduce DMRG with purification in Sec. III A, the time-evolution algorithm in Sec. III B, and the finite-temperature Lanczos method in Sec. III C. In Sec. III D and Sec. III E, we show the spectral functions for the single-site Holstein model. We present the results for the thermodynamic expectation values in Sec. IV and the results for the spectral functions in Sec. V. In Sec. VI, we summarize the paper and provide an outlook.

II. MODEL

A. The Holstein polaron

To study finite-temperature polaron properties we consider the single-electron Holstein model [8]. The Hamiltonian is defined as

$$\hat{H} = \hat{H}_{\text{kin}} + \hat{H}_{\text{ph}} + \hat{H}_{\text{e-ph}} . \tag{1}$$

The model has L sites and we use open boundary conditions, unless stated otherwise. We set $\hbar = 1$ throughout this paper. The first term, the kinetic energy of the electron, then becomes

$$\hat{H}_{\text{kin}} = -t_0 \sum_{j=1}^{L-1} (\hat{c}_j^\dagger \hat{c}_{j+1} + \hat{c}_{j+1}^\dagger \hat{c}_j) , \tag{2}$$

with $\hat{c}_j^\dagger(\hat{c}_j)$ being the electron creation (annihilation) operator on site j and t_0 the hopping amplitude. The second term is the phonon energy

$$\hat{H}_{\text{ph}} = \omega_0 \sum_{j=1}^{L} \hat{b}_j^\dagger \hat{b}_j , \tag{3}$$

where $\hat{b}_j^\dagger(\hat{b}_j)$ is the creation (annihilation) operator of an optical phonon on site j with the constant frequency ω_0. The last term is the electron-phonon coupling

$$\hat{H}_{\text{e-ph}} = \gamma \sum_{j=1}^{L} \hat{n}_j (\hat{b}_j^\dagger + \hat{b}_j) , \tag{4}$$

with $\hat{n}_j = \hat{c}_j^\dagger \hat{c}_j$. We furthermore define the dimensionless coupling parameter

$$\lambda = \frac{\gamma^2}{2 t_0 \omega_0} , \tag{5}$$

which characterizes the crossover from a large ($\lambda < 1$) to a small ($\lambda > 1$) polaron. In this work, we focus on the intermediate regime and set $\lambda = 1$. For a discussion of other parameter regimes, see Appendix A.

B. Thermodynamics

We first want to study the thermodynamics of the model. The thermal expectation value of an observable $\hat{O}$ in the canonical ensemble at temperature T is defined as

$$\langle \hat{O} \rangle_T = \text{Tr}[\hat{\rho}(T)\hat{O}] , \tag{6}$$

where $\hat{\rho}(T)$ is the thermal density matrix at temperature T. In the canonical ensemble,

$$\hat{\rho}(T) = \frac{1}{Z} e^{-\beta \hat{H}} , \tag{7}$$

where we have set $k_{\text{B}} = 1$ such that $\beta = 1/T$ and Z is the partition function. We will focus on four observables: the total energy $E(T) = \langle \hat{H} \rangle_T$, the kinetic energy $E_{\text{kin}}(T) = \langle \hat{H}_{\text{kin}} \rangle_T$, the coupling energy $E_{\text{e-ph}}(T) = \langle \hat{H}_{\text{e-ph}} \rangle_T$, and the phonon energy $E_{\text{ph}}(T) = \langle \hat{H}_{\text{ph}} \rangle_T$.

C. Spectral functions

We are also interested in dynamical quantities by investigating Green's functions of operators acting on sites m and n. We define the greater Green's function

$$G^{>}_{T,0}(m, n, t) = -i \langle \hat{c}_m(t) \hat{c}_n^\dagger(0) \rangle_{T,0} , \tag{8}$$

where the subindices $T, 0$ indicate that the thermal expectation value is calculated in the zero-electron sector. Since we use open boundary conditions, we construct the Fourier transform into quasimomentum space (see, e.g., Refs. [101,102]) as

$$\hat{c}_k = \sqrt{\frac{2}{L+1}} \sum_{j=1}^{L} \sin(kj) \hat{c}_j , \tag{9}$$

where $k = \pi m_k/(L+1)$ and $1 \leqslant m_k \leqslant L$. The greater Green's function in k and ω space then becomes

$$G^{>}_{T,0}(k, \omega) = -i \int_{-\infty}^{\infty} dt e^{i\omega t - |t|\eta} G_{T,0}(k, t) , \tag{10}$$

where $\eta = 0^+$ is an artificial broadening. From the greater Green's function, we extract the electron spectral function

$$A(k, \omega) = -\frac{1}{2\pi} \text{Im}[G^{>}_{T,0}(k, \omega)] . \tag{11}$$

Since we are in the zero-electron sector, Eq. (11) contains all the information about the spectrum.

Here, we extend previous studies [62,72] of the finite-temperature Holstein polaron by also computing the lesser Green's function in the one-electron sector

$$G^{<}_{T,1}(m, n, t) = i \langle \hat{c}_m^\dagger(0) \hat{c}_n(t) \rangle_{T,1} , \tag{12}$$

which we use to obtain the electron emission spectrum

$$A^+(k, \omega) = -\frac{1}{2\pi} \text{Im}[-G^{<}_{T,1}(k, \omega)] . \tag{13}$$

We are further interested in the greater Green's function in the phonon sector

$$D^{>}_{T,1}(m, n, t) = -i \langle \hat{X}_m(t) \hat{X}_n(0) \rangle_{T,1} , \tag{14}$$

where $\hat{X}_n = \hat{b}_n + \hat{b}_n^\dagger$ is the phonon displacement. We use Eq. (14) to calculate the phonon spectral function

$$B(k,\omega) = -\frac{1}{2\pi}\mathrm{Im}[D^{>}_{T,1}(k,\omega)]\,. \tag{15}$$

III. METHODS

In this section, we first describe our main numerical method, DMRG using purification and local basis optimization. We next briefly review the finite-temperature Lanczos method used in Ref. [72]. In order to guide the discussion of the numerical results, we compute the three spectral functions in the single-site limit.

A. Density-matrix renormalization group with purification

While the density-matrix renormalization group and matrix-product states were originally developed to find ground states [74–76], they have proven to be extremely useful tools for calculating spectral functions [103–108], carrying out the time evolution [76,87–90], and finite-temperature calculations [83–85,109–116] as well. There are several ways to utilize matrix-product states at finite temperatures. These include, among others, minimally entangled typical thermal state algorithms [117–119], purification algorithms [84–86,120], or a mixture of both [121,122].

In this paper, we use the purification method [83] which doubles the system by adding an auxiliary space to the physical Hilbert space $\mathscr{H}_\mathrm{P} \to \mathscr{H}_\mathrm{P} \otimes \mathscr{H}_\mathrm{A}$. One can write down a state in this doubled Hilbert space $|\psi\rangle \in \mathscr{H}_\mathrm{P} \otimes \mathscr{H}_\mathrm{A}$. If one now traces out the auxiliary space, one can simulate a mixed state in the physical Hilbert space with the density matrix

$$\hat{\rho}_\mathrm{P} = \mathrm{Tr}_\mathrm{A}[|\psi\rangle\langle\psi|]\,. \tag{16}$$

Since we are working with a fixed number of electrons, we will use the notation where $|\psi^n_\beta\rangle$ represents a state at temperature T with n electrons in the physical system. For example, the state $|\psi^1_{\beta=0}\rangle \in \mathscr{H}_P \otimes \mathscr{H}_A$ can be expressed analytically. This state can then be used to simulate the density matrix from Eq. (7) for one electron at $\beta = 0$. The density matrix for $\beta \neq 0$ is generated by the evolution in imaginary time of $|\psi^n_{\beta=0}\rangle$ as $|\psi^n_\beta\rangle = e^{-\hat{H}\beta/2}|\psi^n_{\beta=0}\rangle$. The thermal expectation value of an observable $\hat{O}$ can then be calculated as

$$\langle\hat{O}\rangle_{T,n} = \frac{\langle\psi^n_\beta|\hat{O}|\psi^n_\beta\rangle}{\langle\psi^n_\beta|\psi^n_\beta\rangle}\,. \tag{17}$$

Since we use thermal states with both one and zero electrons we briefly illustrate how to generate both of them at $\beta = 0$. Since the Holstein model contains infinitely many local phonon degrees of freedom, we first introduce a local cutoff M which represents the maximal number of phonons on each site. We furthermore define a local basis state $|\sigma_i\rangle = |n_i^\mathrm{e}, n_i^\mathrm{ph}\rangle$ with electron occupation $n_i^\mathrm{e} \in \{0,1\}$ and phonon occupation $n_i^\mathrm{ph} \in \{0,\ldots M\}$. This determines the local dimension $d = 2(M+1)$. We further write $|\vec{\sigma}\rangle = |\sigma_1,\sigma_2,\ldots,\sigma_L\rangle$. The zero-electron state $|\psi^0_{\beta=0}\rangle$ becomes

$$\left|\psi^0_{\beta=0}\right\rangle = \sum_{\vec{\sigma}^\mathrm{P},\vec{\sigma}^\mathrm{A}} A_1^{\sigma_1^\mathrm{P},\sigma_1^\mathrm{A}} A_2^{\sigma_2^\mathrm{P},\sigma_2^\mathrm{A}} \ldots A_L^{\sigma_L^\mathrm{P},\sigma_L^\mathrm{A}} |\vec{\sigma}^\mathrm{P},\vec{\sigma}^\mathrm{A}\rangle\,, \tag{18}$$

where each $A_i^{\sigma_i^\mathrm{P},\sigma_i^\mathrm{A}} = \delta_{n_i^{e,\mathrm{A}},0}\delta_{n_i^{e,P},0}\delta_{n_i^{\mathrm{ph,P}},n_i^{\mathrm{ph,A}}}$ is the local tensor corresponding to maximum entanglement between the physical site σ_i^P and the auxiliary site σ_i^A. To generate the one-electron state $|\psi^1_{\beta=0}\rangle$, we proceed in a similar fashion as in Ref. [123]. We first write down the maximum entangled one-electron tensor $\tilde{A}_j^{\sigma_j^\mathrm{P},\sigma_j^\mathrm{A}} = \delta_{n_j^{e,\mathrm{A}},1}\delta_{n_j^{e,\mathrm{P}},1}\delta_{n_j^{\mathrm{ph,A}},n_j^{\mathrm{ph,P}}}$. We then define our wave function as the superposition of terms which all have the one-electron tensor $\tilde{A}_j^{\sigma_j^\mathrm{P},\sigma_j^\mathrm{A}}$ at a different site j. On the sites $i \neq j$, we just place the zero-electron tensors $A_i^{\sigma_i^\mathrm{P},\sigma_i^\mathrm{A}}$ from Eq. (18). The total wave function becomes

$$\left|\psi^1_{\beta=0}\right\rangle = \sum_{j=1}^{L}\sum_{\vec{\sigma}^\mathrm{P},\vec{\sigma}^\mathrm{A}} A_1^{\sigma_1,\sigma_1'}\ldots\tilde{A}_j^{\sigma_j,\sigma_j'}\ldots A_L^{\sigma_L,\sigma_L'}|\vec{\sigma}^\mathrm{P},\vec{\sigma}^\mathrm{A}\rangle\,. \tag{19}$$

After constructing $|\psi^n_{\beta=0}\rangle$, one then generates the desired $|\psi^n_\beta\rangle$ by imaginary-time evolution.

B. Time evolution with local basis optimization

Since we are interested in thermodynamics and spectral functions at finite temperatures, we need to carry out both imaginary and real-time evolution. This subsection explains the procedure and its application to electron-phonon systems. To calculate the time evolution we use tDMRG [87,88] combined with local basis optimization (LBO) [91]. The idea of the local basis optimization is to find a numerically efficient representation of the phonon Hilbert space, thus reducing the computational cost. This has already been combined with exact diagonalization to study zero-temperature dynamical properties of the Holstein model, e.g., by Zhang *et al.* in Ref. [14], and with matrix-product states to calculate the real-time evolution of pure states, e.g., by Brockt *et al.* [92] for the polaron problem, by Stolpp *et al.* [37] for a charge density wave, as well as in Refs. [35,93]. In this paper, we demonstrate that the local basis optimization is computationally beneficial for computing thermodynamics and real-time evolution at finite temperature for the Holstein polaron.

For the tDMRG method, we first write our Hamiltonian as a sum of terms $\hat{h}_l$ which act on the two neighboring sites l and $l+1$. For a time step dt ($-id\tau$ for imaginary-time evolution) one can then carry out a second-order Trotter-Suzuki decomposition into even and odd terms

$$e^{-idt\hat{H}} = e^{-idt\hat{H}_\mathrm{even}/2}e^{-idt\hat{H}_\mathrm{odd}}e^{-idt\hat{H}_\mathrm{even}/2} + O(dt^3)\,. \tag{20}$$

One can further write each exponential as the product of local elements $e^{-idt\hat{H}_\mathrm{even}/2} = \prod_{l:\mathrm{even}} e^{-idt\hat{h}_l/2}$. Since each physical site is connected to an auxiliary site, one must first apply a fermionic swap gate [118,124] to swap site σ_l^P and σ_l^A. One then acts with the time evolution gate $e^{-idt\hat{h}_l/2}$ followed by another gate which swaps σ_l^P and σ_l^A back.

To illustrate how the local basis optimization works, we assume that our MPS is already in an optimal local basis $|\tilde{\sigma}^\mathrm{P}\rangle$ and that the local transformation matrices $R^{\tilde{\sigma}_i^\mathrm{P}}_{\sigma_i^\mathrm{P}}$ transform the physical index from the bare into the optimal basis. We then first transform two of the legs from our time-evolution gate

$U^{\sigma_i'^{\mathrm{P}},\sigma_{i+1}'^{\mathrm{P}}}_{\sigma_i^{\mathrm{P}},\sigma_{i+1}^{\mathrm{P}}}$ to

$$U^{\sigma_i'^{\mathrm{P}},\sigma_{i+1}'^{\mathrm{P}}}_{\tilde{\sigma}_i^{\mathrm{P}},\tilde{\sigma}_{i+1}^{\mathrm{P}}} = R^{\sigma_i^{\mathrm{P}}}_{\tilde{\sigma}_i^{\mathrm{P}}} R^{\sigma_{i+1}^{\mathrm{P}}}_{\tilde{\sigma}_{i+1}^{\mathrm{P}}} U^{\sigma_i'^{\mathrm{P}},\sigma_{i+1}'^{\mathrm{P}}}_{\sigma_i^{\mathrm{P}},\sigma_{i+1}^{\mathrm{P}}} . \tag{21}$$

We then apply this gate to the two-site tensor $M^{\tilde{\sigma}_i^{\mathrm{P}},\tilde{\sigma}_{i+1}^{\mathrm{P}}} = A^{\tilde{\sigma}_i^{\mathrm{P}}} A^{\tilde{\sigma}_{i+1}^{\mathrm{P}}}$ and get

$$\phi^{\sigma_i'^{\mathrm{P}},\sigma_{i+1}'^{\mathrm{P}}} = U^{\sigma_i'^{\mathrm{P}},\sigma_{i+1}'^{\mathrm{P}}}_{\tilde{\sigma}_i^{\mathrm{P}},\tilde{\sigma}_{i+1}^{\mathrm{P}}} M^{\tilde{\sigma}_i^{\mathrm{P}},\tilde{\sigma}_{i+1}^{\mathrm{P}}} . \tag{22}$$

We then generate the local reduced density matrix

$$\rho^{\sigma_i'^{\mathrm{P}}}_{\sigma_i^{\mathrm{P}}} = \phi^{\dagger}_{\sigma_i^{\mathrm{P}},\sigma_{i+1}^{\mathrm{P}}} \phi^{\sigma_i'^{\mathrm{P}},\sigma_{i+1}^{\mathrm{P}}} , \tag{23}$$

which we diagonalize such that

$$\rho^{\sigma_i'^{\mathrm{P}}}_{\sigma_i^{\mathrm{P}}} = R^{\tilde{\sigma}_i^{\mathrm{P}}}_{\sigma_i^{\mathrm{P}}} D^{\tilde{\sigma}_i'^{\mathrm{P}}}_{\tilde{\sigma}_i^{\mathrm{P}}} R^{\dagger\sigma_i'^{\mathrm{P}}}_{\tilde{\sigma}_i'^{\mathrm{P}}} . \tag{24}$$

The matrix $R^{\tilde{\sigma}_i^{\mathrm{P}}}_{\sigma_i^{\mathrm{P}}}$ is now the updated transformation matrix which rotates the site i into the adapted optimal basis. The transformation matrices can then be applied to $\phi^{\sigma_i',\sigma_{i+1}'}$ from Eq. (22) before the following singular value decomposition. If the optimal basis has dimension d_{LBO} and the MPS has a bond dimension χ, the cost of the SVD has then changed from $O(d^3\chi^3)$ to $O(d_{\mathrm{LBO}}^3\chi^3)$ [92]. The transformation is only beneficial if we can truncate the optimal basis such that $d_{\mathrm{LBO}} \ll d$, since the transformation itself has a cost of $O(d^3\chi^2)$ for building the reduced-density matrix, $O(d^3)$ for the diagonalization thereof, and $O(d^2 d_{\mathrm{LBO}}\chi^2)$ for the basis transformation [92]. To control the truncation, we discard the smallest eigenvalues w_α such that the truncation error is below a threshold: $\sum_{\alpha\in\mathrm{discarded}} w_\alpha/(\sum_{\mathrm{all}\,\alpha} w_\alpha) < \rho_{\mathrm{LBO}}$. When carrying out a regular singular-value decomposition in the tDMRG algorithm, we discard all singular values such that $\sum_{\alpha\in\mathrm{discarded}} s_\alpha^2/(\sum_{\mathrm{all}\,\alpha} s_\alpha^2) < \rho_{\mathrm{bond}}$.

To calculate a general correlation function $C_{T,n}(\omega, k)$, such as the Green's functions in Eqs. (8), (12), and (14), we first obtain the desired state $|\psi_\beta^n\rangle$ through imaginary-time evolution. In that process, we apply the LBO only to the physical sites such that only these are in their optimal basis. Before we start the real-time evolution, we first iterate through the MPS and obtain the optimal basis for both the physical and the auxiliary sites by creating the matrix $M^{\sigma_i^{\mathrm{P}},\sigma_i^{\mathrm{A}}}$ and getting the transformation matrices $R^{\tilde{\sigma}_i^{\mathrm{P}}}_{\sigma_i^{\mathrm{P}}}$ and $R^{\tilde{\sigma}_i^{\mathrm{A}}}_{\sigma_i^{\mathrm{A}}}$. We then follow Ref. [85] and compute the desired correlation functions

$$C_{T,n}(m,l,t) = \left\langle \psi_\beta^n \middle| \hat{A}_m(t/2)\hat{B}_l(-t/2) \middle| \psi_\beta^n \right\rangle , \tag{25}$$

where $\hat{A}$, $\hat{B}$ are general operators and

$$\hat{A}_m(t) = \hat{U}^{\mathrm{P}\dagger}(t/2)\hat{U}^{\mathrm{A}\dagger}(t/2)\hat{A}_m\hat{U}^{\mathrm{P}}(t/2)U^{\mathrm{A}}(t/2) . \tag{26}$$

In Eq. (26), $\hat{U}^{\mathrm{P}}(t/2) = e^{-i\hat{H}^{\mathrm{P}}t/2}$ acts on the part of the state in the physical Hilbert space and $\hat{U}^{\mathrm{A}}(t/2) = e^{i\hat{H}^{\mathrm{A}}t/2}$ correspondingly time evolves the part of the state in the auxiliary space in the opposite direction. This is done to keep the entanglement entropy low during the real-time evolution [111–115]. Even though this procedure is not optimal [116], it provides a natural extension of the local basis optimization to the auxiliary sites and allows us to keep them in an optimal basis during the time evolution. We then obtain $C_{T,n}(k,\omega)$ from $C_{T,n}(m,l,t)$ by Fourier transformations in space and time.

We further use linear prediction [85,125,126] to access larger times. Since we do the real-time evolution on states $|\phi_\beta^n\rangle = \hat{A}_l|\psi_\beta^n\rangle$, which are not normalized, e.g., $\langle\phi_\beta^n|\phi_\beta^n\rangle \neq 1$, we do not renormalize the state after applying the time-evolution gate. We observe that the norm of $|\phi_\beta^n\rangle$ is still of $O(1)$, so that we can apply the same truncation criteria as if we worked with normalized states. For all imaginary-time evolutions, we use $d\tau\omega_0 = 0.1$ and for the real-time evolution, we use $dt\omega_0 = 0.01$. The real-time evolution is done up to a maximum time $t_{\max}\omega_0$. The accessible $t_{\max}\omega_0$ depends on the observable and model parameters and is determined by the computational resources available. All DMRG calculations are carried out using Ref. [127].

C. Finite-temperature Lanczos method

We now proceed by introducing alternative methods used as benchmarks. The thermodynamic quantities will be compared to exact diagonalization (ED) and the spectral function from Eq. (11) will be compared to the finite-temperature Lanczos method [128,129] (FTLM).

The finite-temperature Lanczos method data used here is obtained from Ref. [72]. The electron spectral function is expressed as

$$A(k,\omega) = Z^{-1}\sum_{r=1}^{R}\sum_{j=1}^{M}\sum_{n=1}^{N} e^{-\beta\epsilon_n^0}\,\langle r^0|\phi_n^0\rangle\langle\phi_n^0|\hat{c}_k|\psi_j\rangle \times \langle\psi_j|\hat{c}_k^\dagger|r^0\rangle\delta\left(\omega-\epsilon_j+\epsilon_n^0\right), \tag{27}$$

where Z is the partition function, $|r^0\rangle$ are random states in the zero-electron basis, $|\phi_n^0\rangle$ are the zero-electron eigenstates, and $|\psi_j\rangle$ are the Lanczos vectors from the one-electron subspace with the corresponding energy ϵ_j. The variational Hilbert space [13,18] is used together with twisted boundary conditions [130–132] to limit finite-size effects.

D. Single-site spectral function and emission spectrum

In order to gain a better understanding of the emission spectrum at low temperatures, we derive an analytical expression for the single-site system. This is done for the spectral function in Ref. [133] and a detailed derivation is presented in Ref. [72]. This section is a simple extension of that work but is included for self consistency and to guide the discussion. The single-site Hamiltonian is

$$\hat{H}_{\mathrm{s}} = \gamma\hat{n}(\hat{b}^\dagger+\hat{b}) + \omega_0\hat{b}^\dagger\hat{b}. \tag{28}$$

The solution for the case of a single electron is given by the well-known coherent states

$$|0_s\rangle = e^{-\tilde{g}^2/2}\sum_{m=0}^{\infty}\frac{(-\tilde{g})^m}{\sqrt{m!}}|m\rangle , \tag{29}$$

where $\tilde{g} = \gamma/\omega_0$ and $|m\rangle$ are bare phonon modes. The ground state $|0\rangle_s$ has the energy $E_{0,s} = -\omega_0\tilde{g}^2$. The excited states $|m\rangle_s$ have an energy $E_{m,s} = -\omega_0\tilde{g}^2 + m\omega_0$ and are given by

$$|m_s\rangle = \frac{(b^\dagger+\tilde{g})^m}{\sqrt{m!}}|0_s\rangle . \tag{30}$$

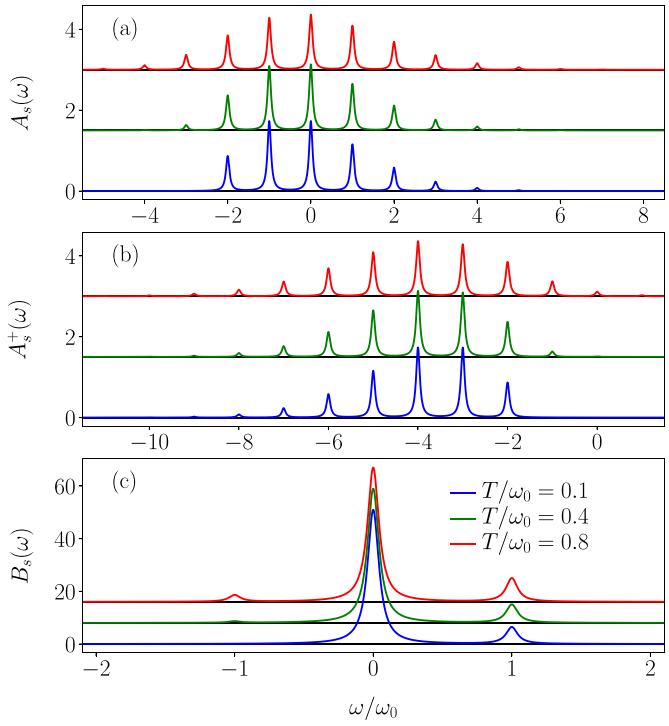

FIG. 1. (a) Single-site spectral function $A_s(\omega)$ from Eq. (31). (b) Single-site emission spectrum $A_s^+(\omega)$ from Eq. (32). (c) Single-site phonon spectral function $B_s^+(\omega)$ from Eq. (36). We set $\gamma/\omega_0 = \sqrt{2}$ and use a Lorentzian for the delta function with half width at half maximum (HWHM) $\eta = 0.05$.

The single-site spectral function $A_s(\omega)$, derived in Ref. [72], is

$$A_s(\omega) = \frac{1}{Z}\sum_{n,m=0}^{\infty} e^{-\beta\omega_0 n}|\langle m_s|n\rangle|^2\delta(\omega + E_n - E_{m,s}), \quad (31)$$

where $|n\rangle$ are the bare phonon modes and E_n the corresponding energies. We show $A_s(\omega)$ in Fig. 1(a) for $\lambda = 1$.

The electron emission spectrum is

$$A_s^+(\omega) = \frac{1}{Z}\sum_{n,m=0}^{\infty} e^{-\beta E_{m,s}}|\langle n|m_s\rangle|^2\delta(\omega + E_n - E_{m,s}). \quad (32)$$

The overlap between the coherent state and the normal mode is given by

$$\langle n|m_s\rangle = e^{-\tilde{g}^2/2}\sum_{l=0}^{\min\{m,n\}}(-1)^{n-l}\tilde{g}^{n+m-2l}\frac{\sqrt{m!n!}}{l!(m-l)!(n-l)!}. \quad (33)$$

If we send $T/\omega_0 \to 0$, only the $m = 0$ term contributes in Eq. (32). This gives

$$\langle n|0_s\rangle = e^{-\tilde{g}^2/2}(-1)^n\tilde{g}^n\frac{\sqrt{n!}}{n!}. \quad (34)$$

The emission spectrum then takes the form

$$A_s^+(\omega) = \sum_{n=0}^{\infty} e^{-\tilde{g}^2}\tilde{g}^{2n}\frac{1}{n!}\delta(\omega + n\omega_0 + \omega_0\tilde{g}^2), \quad (35)$$

which has a polaron peak for $n = 0$ at $\omega_{\rm pol}/\omega_0 = -\omega_0\tilde{g}^2$. The spectrum further has peaks at negative ω, which are separated by ω_0. It is also clear that at larger temperatures, peaks at $\omega > -\omega_0\tilde{g}^2$ will appear.

In Fig 1(b), we show the single-site emission spectrum $A_s^+(\omega)$. There, the peaks at $\omega < \omega_0\tilde{g}$ are visible. One can also observe the peaks at $\omega > \omega_0\tilde{g}$ appearing for larger temperatures.

E. Single-site phonon spectral function

The single-site phonon spectral function is

$$B_s(\omega) = \frac{1}{Z}\sum_{n,m=0}^{\infty} e^{-\beta E_{m,s}}|\langle n_s|\hat{b} + \hat{b}^\dagger|m_s\rangle|^2 \times \delta(\omega + E_{m,s} - E_{n,s}). \quad (36)$$

We use that

$$\hat{b}\,|0_s\rangle = -\tilde{g}\,|0_s\rangle\,, \quad (37)$$

and

$$\hat{b}\,|m_s\rangle = \sqrt{m}\,|(m-1)_s\rangle - \tilde{g}\,|m_s\rangle\,, \quad (38)$$

to obtain

$$\langle n_s|\hat{b} + \hat{b}^\dagger|m_s\rangle = \sqrt{n}\,\langle(n-1)_s\,|m_s\rangle + \sqrt{m}\,\langle n_s\,|(m-1)_s\rangle - 2\tilde{g}\,\langle n_s\,|m_s\rangle\,. \quad (39)$$

At $T/\omega_0 = 0$, the spectral function becomes

$$B_s(\omega) = 4\tilde{g}^2\delta(\omega) + \delta(\omega - \omega_0). \quad (40)$$

$B_s(\omega)$ is shown for different T/ω_0 in Fig. 1(c). We observe two peaks separated by ω_0 at the lowest temperatures as predicted in Eq. (40). This is the polaron peak and the free-phonon peak. When the temperature is increased, a smaller free-phonon peak starts to appear at $-\omega_0$.

IV. DMRG RESULTS FOR THERMODYNAMICS

In this section, we show the results for the thermodynamic quantities introduced in Sec. II B. Thermodynamics for electron-phonon models has already been studied with Monte Carlo methods, see, e.g., Refs. [134–137] for results for two-dimensional lattices. As explained in Sec. III A, the DMRG purification method starts at $T = \infty$. Finite temperatures are then obtained by imaginary-time evolution. For the Holstein-polaron model with a local phonon cutoff M, we have $\langle\hat{H}\rangle_{T=\infty}/(\omega_0 L) = M/2$, such that depending on the phonon number truncation, the imaginary-time evolution will start at a different energy. Additionally, starting points with a finite M are artificial since they do not represent the true $T = \infty$ limit of the system. For this reason, we first want to investigate whether there is a range of temperatures where we can produce states with expectation values that are independent of M for the polaron in the crossover regime $\lambda = 1$. Since the results become M dependent and unphysical for large T/ω_0, we choose to focus on $0.1 \leqslant T/\omega_0 \lesssim 0.4$. Secondly, we want to investigate how the optimal local basis is affected by the imaginary-time evolution.

We first verify that the purification method reproduces values calculated with ED. In Fig. 2, we compare the results

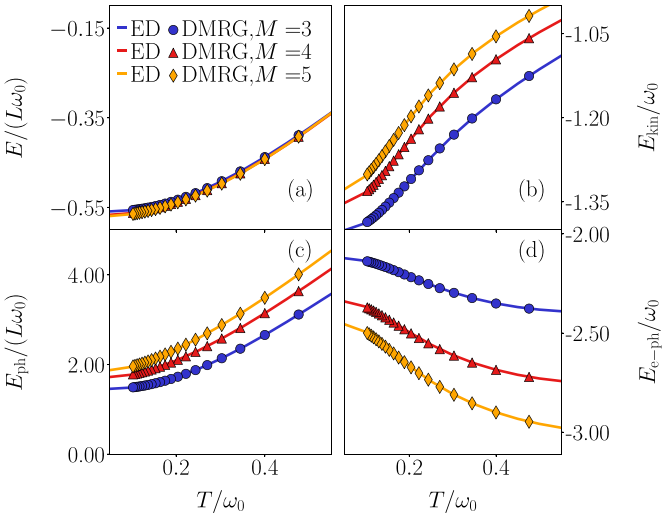

FIG. 2. Expectation values for different observables for $\gamma/\omega_0 = \sqrt{2}, t_0/\omega_0 = 1, L = 5$ and $M = 3, 4, 5$. The solid lines are obtained with ED and the symbols with DMRG. We show (a) the total energy, (b) the electron kinetic energy, (c) the phonon energy, and (d) the coupling energy. Many points overlap almost completely, and therefore, not all lines and points are visible. For clarity, we only show every fourth point of the DMRG data.

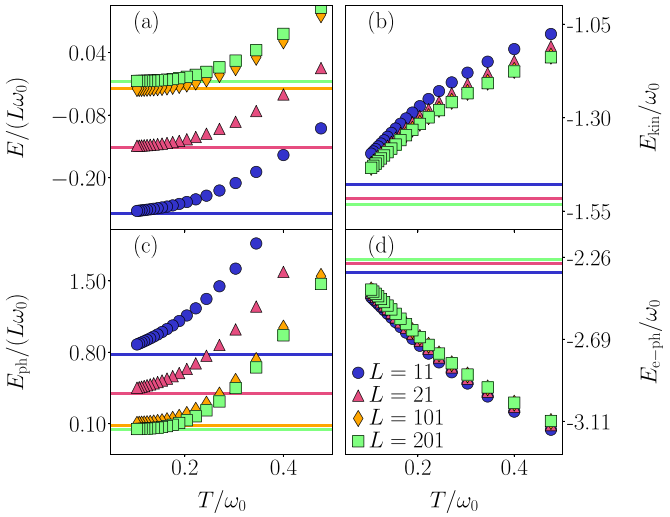

FIG. 3. Expectation values for different observables for $\gamma/\omega_0 = \sqrt{2}, t_0/\omega_0 = 1, M = 20$ and different L. We show (a) the total energy, (b) the electron kinetic energy, (c) the phonon energy, and (d) the coupling energy. The solid lines show the ground-state values calculated with ground-state DMRG. They sometimes overlap, and therefore, some lines are not always visible. For clarity, we only show every fourth data point.

to ED for $L = 5$ and different M. We show the four observables defined in Sec. II B as a function of temperature T/ω_0. One sees that the finite-temperature DMRG method (symbols) reproduces the ED (solid lines) for the corresponding M. The clear dependence of the observables on M suggests that the local Hilbert space is not chosen large enough to yield the correct low-temperature physics for these parameters. Most importantly, the DMRG method reproduces the ED results for the accessible system sizes.

We proceed by comparing the expectation values for different system sizes L. The results are shown in Fig. 3. Notice that the ground-state energy is intensive in the single-electron problem. Therefore, $E/(\omega_0 L)$ should approach zero in the thermodynamic limit. This can be observed in Fig. 3(a). The figure also serves as a consistency check by showing that the imaginary-time evolution approaches the ground-state energy calculated with ground-state DMRG [74–76] (solid lines). Both the total energy E and the phonon energy $E_{\rm ph}$ are extensive at finite temperature, and therefore, we divide both of these expectation values by the system size L to get a quantity that only depends on temperature for sufficiently large L. The observables $E_{\rm kin}$ and $E_{\rm e\text{-}ph}$ [Figs. 3(b) and 3(d)] are automatically intensive since there is only one electron in the system. Figure 3 therefore illustrates that the purification method gives access to thermodynamic quantities in systems with very large local Hilbert spaces.

We next demonstrate that the DMRG method can access values of M large enough to obtain cutoff-independent results in the low-temperature regime. In Fig. 4, we show the same observables as in Fig. 2 with $L = 21$ and $M = 20, 30$ calculated with DMRG. We find that even though the two initial states start at two completely different energies $\langle \hat{H} \rangle_{T=\infty}/(\omega_0 L)$, they still converge to the same expectation value up to an accuracy of $O(10^{-5})$ below $T/\omega_0 \lesssim 0.5$. We thus conclude that we correctly reproduce results for the real phonon limit $M \to \infty$ below a certain temperature if M is chosen large enough. Therefore, the method gives access to thermodynamics at temperatures for system sizes and phonon numbers unavailable to ED and regular Lanczos methods. For the rest of this paper, we choose $M = 20$.

To demonstrate that the imaginary-time evolution results are converged in the low-temperature limit, we vary $\rho_{\rm bond}$ and

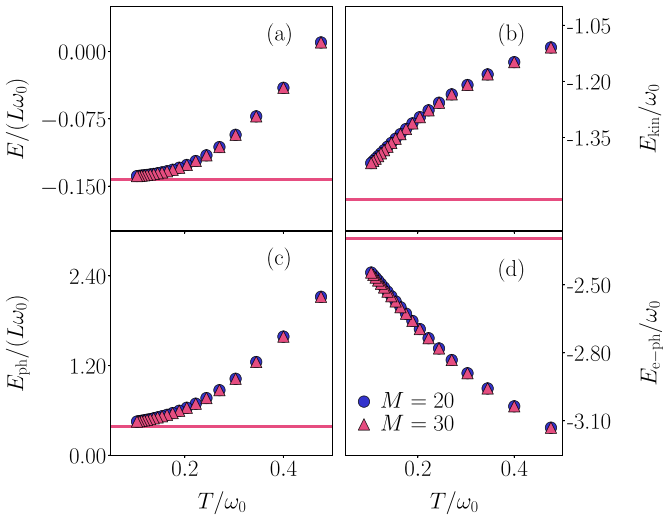

FIG. 4. Expectation values for different observables for $\gamma/\omega_0 = \sqrt{2}, t_0/\omega_0 = 1, L = 21$ and $M = 20, 30$. We show (a) the total energy, (b) the electron kinetic energy, (c) the phonon energy, and (d) the coupling energy. The solid lines show the ground-state values calculated with ground-state DMRG for $M = 20$. The points lie on top of each other such that the $M = 20$ data is not always clearly visible. For clarity, we only show every fourth point of the data.

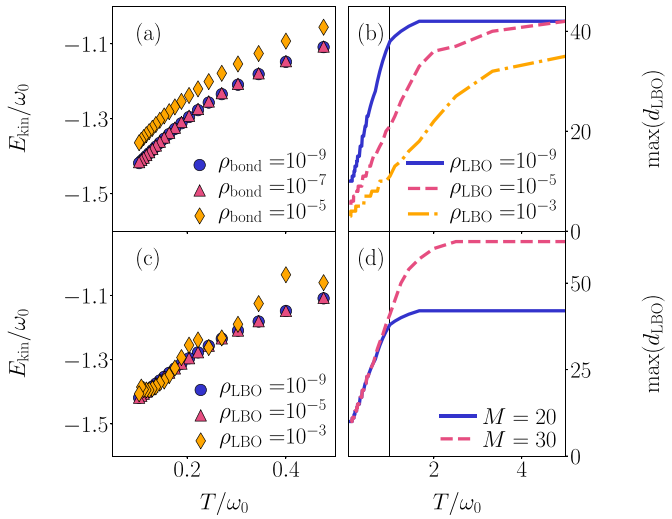

FIG. 5. Electron kinetic energy from Eq. (2) for different $\rho_{\rm bond}$ (a) and $\rho_{\rm LBO}$ (c). We show results for $\gamma/\omega_0=\sqrt{2}, t_0/\omega_0=1, L=21$ and $M=20$. In (a), we set $\rho_{\rm LBO}=10^{-9}$ and in (c), we set $\rho_{\rm bond}=10^{-9}$. (b) The maximum local optimal dimension $\max(d_{\rm LBO})$ of the system for the same parameters as (a). (d) $\max(d_{\rm LBO})$ for the same parameters as in (a), but with $\rho_{\rm bond}=10^{-9}$, $M=20$ and $M=30$. The black solid lines in (b) and (d) show $T/\omega_0=1.0$. For clarity, we only show every fourth point of the data in (a) and (c).

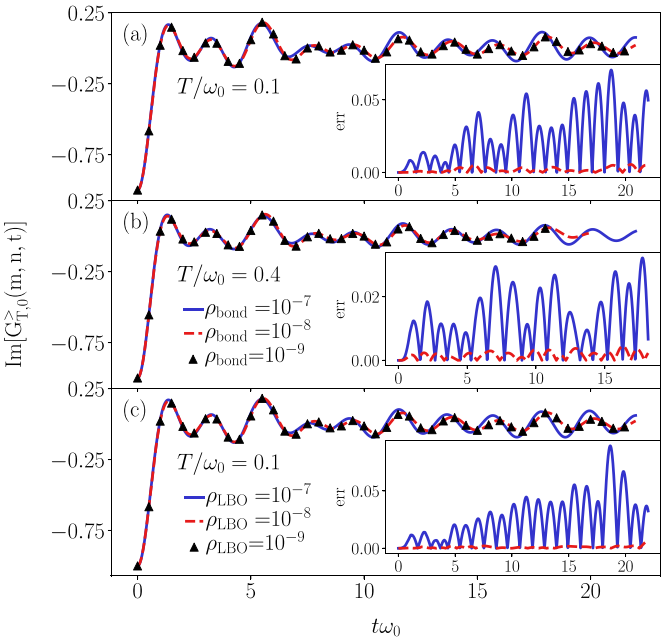

FIG. 6. Imaginary part of $G^{>}_{T,0}(m,n,t)$ in Eq. (8). We set $n=m=11, \gamma/\omega_0=\sqrt{2}, t_0/\omega_0=1$ and $L=21$. (a) $T/\omega_0=0.1$ and fixed $\rho_{\rm LBO}=10^{-8}$ for different $\rho_{\rm bond}$. (b) $T/\omega_0=0.4$ and fixed $\rho_{\rm LBO}=10^{-8}$ for different $\rho_{\rm bond}$. (c) $T/\omega_0=0.1$ and fixed $\rho_{\rm bond}=10^{-8}$ for different $\rho_{\rm LBO}$. For the symbols, we only show every 50th point for clarity. The insets show the absolute error err [see Eq. (41)], defined as the difference between the data with the smallest truncation error 10^{-9} and either 10^{-8} (red) or 10^{-7} (blue).

$\rho_{\rm LBO}$. As explained in Sec. III, the truncation of the bond dimension is controlled by $\rho_{\rm bond}$ whereas $\rho_{\rm LBO}$ controls the truncation of the optimal local basis of the MPS. In Figs. 5(a) and 5(c), we illustrate how $E_{\rm kin}$ is affected by changes in $\rho_{\rm bond}$ and $\rho_{\rm LBO}$. The change is significant if one of the discarded weights is chosen too large. If $\rho_{\rm bond}$ is too large, the expectation values lie above the converged value. In the other case, for $\rho_{\rm LBO}$ too large, we start to get fluctuating expectation values. We do this test for all terms in the Hamiltonian in Eq. (1) and find that they are all converged for $\rho_{\rm bond}=10^{-7}$ and $\rho_{\rm LBO}=10^{-5}$ to an accuracy of $O(10^{-3})$. However, exactly how they behave for a too small cutoff is observable- and system-size dependent. Since the expectation values already have converged for both $\rho_{\rm bond}$ and $\rho_{\rm LBO}=10^{-7}$ [red triangles in Figs. 5(a) and 5(c)], the 10^{-9} markers (blue circles) are barely visible.

In Figs. 5(b) and 5(d), we analyze the maximum dimension $\max(d_{\rm LBO})$ of the optimal basis of the physical Hilbert space. One clearly sees that this becomes equal to the local bare basis dimension $2(M+1)$ for large T/ω_0. This is expected since all the phonon modes become equally probable at $T/\omega_0=\infty$. However, $\max(d_{\rm LBO})$ starts to decrease rapidly below a certain temperature and the rotation into the optimal basis becomes computationally beneficial for a given truncation error. This means that the eigenvalues of the reduced-density matrix first do not decay at all until a certain temperature is reached. After that, they start decreasing rapidly as a function of T/ω_0. Figure 5(d) shows that this trend becomes more pronounced for larger M. Furthermore, it illustrates that as M is increased, the rotation into the optimal basis becomes beneficial at higher T/ω_0.

The accurate evaluation of thermal expectation values also serves as an important test for the spectral function calculations in Sec. V. In Appendix C, we show that the first temperature-dependent moments can be calculated by either integrating the spectral function or by computing thermal expectation values. We verify the accuracy of the spectral function by comparing both methods. For the rest of this work, we set $\rho_{\rm LBO}=\rho_{\rm bond}=10^{-9}$ during the imaginary-time evolution.

V. SPECTRAL FUNCTIONS

A. Real-time evolution

We now proceed by calculating dynamical properties of our model. We first check that the real-time evolution converges with respect to $\rho_{\rm bond}$ and $\rho_{\rm LBO}$. This is illustrated in Fig. 6. There, we show the imaginary part of $G^{>}_{T,0}(m,n,t)$ from Eq. (8) with $m=n=11$. From Figs. 6(a) and 6(b), it becomes apparent that as $\rho_{\rm bond}$ is decreased, the results are indiscernible on the scale of the figure. A similar behavior is also seen with respect to $\rho_{\rm LBO}$ [see Fig. 6(c)]. In the insets of Fig. 6, we show the absolute error

$$\mathrm{err}=|\mathrm{Im}[\mathrm{G}^{>}_{\mathrm{T},0}(\mathrm{m},\mathrm{n},\mathrm{t})]_{\rho_i}-\mathrm{Im}[\mathrm{G}^{>}_{\mathrm{T},0}(\mathrm{m},\mathrm{n},\mathrm{t})]_{\rho_j}|, \quad (41)$$

with $i\neq j$ and ρ_i being set by $\rho_{\rm bond}$ or $\rho_{\rm LBO}$. For the data shown in the inset, we fix $\rho_i=10^{-9}$ and subtract the remaining two datasets. We can also report a large increase in the bond dimension as the temperature is increased (for details, see Appendix A). This is the reason why the time evolution for certain values of $\rho_{\rm bond}$ in Fig. 6(b) is stopped earlier. The reachable time for the smallest truncation also determines

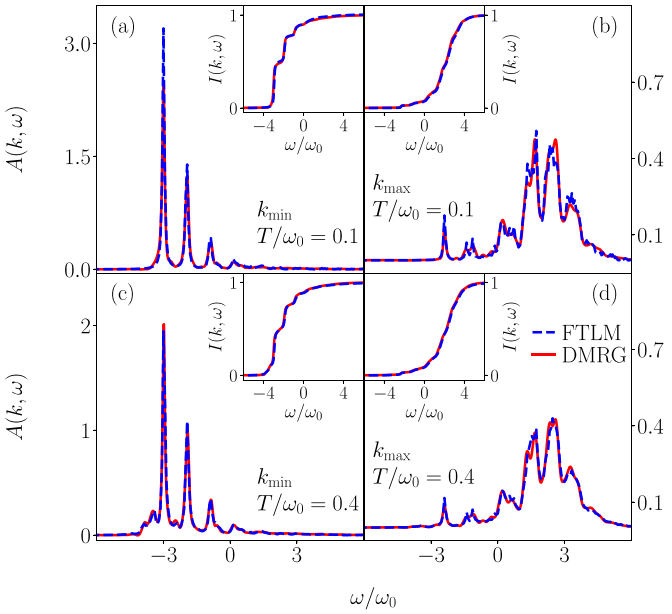

FIG. 7. Electron spectral function $A(k,\omega)$ from Eq. (11) for $\gamma/\omega_0 = \sqrt{2}, t_0/\omega_0 = 1, L = 21, M = 20, \eta = 0.05$ and $t_{\max}\omega_0 = 18.0$. We show $T/\omega_0 = 0.1$ in (a) and (b) and $T/\omega_0 = 0.4$ in (c) and (d). For the DMRG data (red line), we show $k_{\min} = \pi/(L+1)$ and $k_{\max} = \pi L/(L+1)$. For the FTLM data (blue dashed line), $L = 12$ and we show $k_{\min} = 0$ in (a) and (c) and $k_{\max} = \pi$ in (b) and (d). The insets show $I(k,\omega)$ defined in Eq. (42).

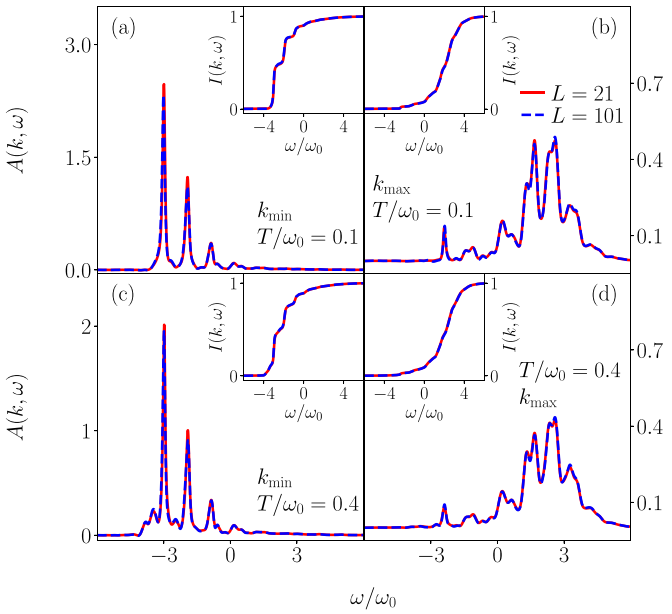

FIG. 8. Electron spectral function $A(k,\omega)$ from Eq. (11) for $\gamma/\omega_0 = \sqrt{2}, t_0/\omega_0 = 1, M = 20, \eta = 0.05$ and $t_{\max}\omega_0 = 18.0$. We show $T/\omega_0 = 0.1$ in (a) and (b) and $T/\omega_0 = 0.4$ in (c) and (d). For $L = 21$, we show $k_{\min} = \pi/(L+1)$ and $k_{\max} = \pi L/(L+1)$. The $L = 101$ data (blue dashed lines) is calculated with the simplified Fourier transform (see the text for details) and $k_{\min} = 0$ and $k_{\max} = \pi$. The insets show $I(k,\omega)$ defined in Eq. (42).

$t_{\max}$, such that the convergence is tested for the whole time interval used for the Fourier transformation. The limitation in accessible times also constrains the energy resolution of the spectral function.

As explained in Sec. III, we additionally apply linear prediction. The spectral functions tend to oscillate around zero away from the peaks as a result of the finite time interval. By applying linear prediction, the oscillation amplitude goes from order 10^{-1} to 10^{-5} without changing the peak position or height in the spectrum. However, the exact decrease of the amplitude is spectral-function and temperature dependent. Due to the oscillations, we always show the absolute values of the spectral functions in the normalized log-scaled plots. The real-time evolution for all the following spectral functions is done with $\rho_{\text{bond}} = \rho_{\text{LBO}} = 10^{-8}$.

To test the accuracy of the method, we also derive the first temperature-dependent moment of the spectral functions and compare the thermal expectation values to our numerical data. The results in Appendix C show good agreement. We further want to emphasize that in the zero-electron sector, it is trivial to obtain the finite-temperature initial state for the real-time evolution since it only contains noninteracting local harmonic oscillators. For this reason, we compare results using both the trivially obtained thermal states and those obtained with the imaginary-time evolution algorithm to verify its correctness.

B. Electron spectral function and comparison to the FTLM

In Fig. 7, we show the electron spectral function $A(k,\omega)$ and compare it to results obtained with FTLM. We show the results for $T/\omega_0 = 0.1$ in Figs. 7(a) and 7(b) and $T/\omega_0 = 0.4$ in Figs. 7(c) and 7(d). Our method can resolve the same peak positions as the FTLM. One can identify the polaron peak at $\omega_{\text{pol}}/\omega_0 \approx -3.0$ and the peaks corresponding to the polaron with additional phonons separated by $n\omega_0$ in the incoherent part of the spectrum. We also observe a significant decrease of the quasiparticle weight for $k_{\min}$ compared to $k_{\max}$. This has already been reported in Ref. [72] and is consistent with other ground-state approaches [16,19,138–140].

In the inset, we show

$$I(k,\omega) = \int_{-\infty}^{\omega} d\omega' A(k,\omega'). \tag{42}$$

There are only small differences between the FTLM and the DMRG data. The amplitude of the polaron peak exhibits small temperature-dependent differences between the two methods. For larger values of k, we also observe some different weight distribution in the incoherent part of the spectrum. The results for $I(k,\omega)$ still almost completely overlap. We want to emphasize that we show results for two different k values for the methods due to the difference in boundary conditions. For the DMRG method, we choose $k_{\min} = \pi/(L+1)$, $k_{\max} = \pi L/(L+1)$ and for the FTLM method, we select $k_{\min} = 0$, $k_{\max} = \pi$. We conclude that despite these differences, the DMRG and FTLM method show a very good quantitative agreement.

Alternatively to computing the complete correlation function, one can calculate $G^{>}_{T,0}(m,n,t)$ for a fixed $n = L/2$ and $m \leqslant n$. This gives access to much larger system sizes, as illustrated in Fig. 8. There, we calculate the spectral function for $L = 101$. We first fix $n = 51$ and set $G^{>}_{T,0}(n+m,n,t) = G^{>}_{T,0}(n-m,n,t)$. We then compute the Fourier transform

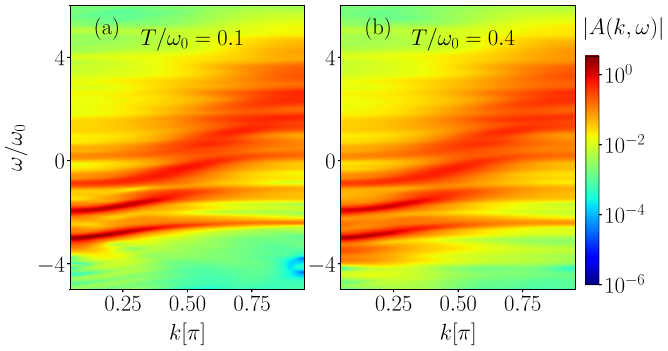

FIG. 9. Electron spectral function $A(k,\omega)$ obtained with DMRG. We set $\gamma/\omega_0 = \sqrt{2}, t_0/\omega_0 = 1, L = 21, M = 20, \eta = 0.05$ and $t_{\max}\omega_0 = 18.0$. (a) $T/\omega_0 = 0.1$ and (b) $T/\omega_0 = 0.4$.

into k space as $G^{>}_{T,0}(k,t) = \frac{1}{L}\sum_{m=1}^{L} e^{i(m-n)k} G^{>}_{T,0}(m,n,t)$. Here, we use periodic boundary-condition quasimomenta with $k = 2\pi m/L$ and $-\frac{L}{2} \leqslant m \leqslant \frac{L}{2}$. This is often done (e.g., in Refs. [86,141]) and the method works well here since the noninteracting harmonic oscillators are homogeneously distributed in the initial state and there is no electron in the system. In Fig. 8, we show comparison between data produced with periodic-boundary condition momenta ($L = 101$) with results for open-boundary momenta ($L = 21$). Only small changes in the largest peaks [see Figs. 8(a) and 8(c)] can be seen even though the $L = 101$ data use $k_{\min} = 0, k_{\max} = \pi$ while the $L = 21$ data use $k_{\min} = \pi/(L+1), k_{\max} = \pi L/(L+1)$. This is, however, not the case for the other spectral functions studied in this work since the one-electron state has an inhomogeneous electron distribution. The previously described approach does, therefore, not fulfill the sum rules in those cases. Moreover, we mention that the calculations with the periodic boundary-condition Fourier transformation is more sensible to the choice of parameters for the linear prediction for our data. For a more quantitative discussion of the error of the methods, see Appendix B.

In Fig. 9, we show $A(k,\omega)$ as a function of ω for all k. Here, the spectral weight at $\omega < \omega_{\text{pol}}$ [see Fig. 7(a)] becomes visible at larger T/ω_0. This has been reported in Ref. [72] and corresponds to the electron absorbing a thermal phonon. One can also see that the polaron band structure is shifted downwards and renormalized compared to the free-fermion case which would have its ground-state energy at $\omega/\omega_0 = -2$ and a bandwidth of $4t_0$. In all cases, we confirm that the sum rule $\int_{-\infty}^{\infty} d\omega A(k,\omega) = 1$ is fulfilled up to 10^{-5}.

C. Electron emission spectrum

We next discuss $A^+(k,\omega)$, defined in Eq. (13). Computationally, this function is the easiest to obtain with our method since the most demanding part of the calculation, namely the real-time evolution, is done without an electron in the physical system. In Fig. 10, we show $A^+(k,\omega)$ for two different temperatures. At low T/ω_0, Fig. 10(b) unveils the presence of several peaks that are separated by ω_0. The peaks can be understood by inspecting the single-site emission spectrum at low temperatures from Eq. (35). There, one clearly sees a peak at $-\gamma^2/\omega_0$. Furthermore, there are several peaks at negative

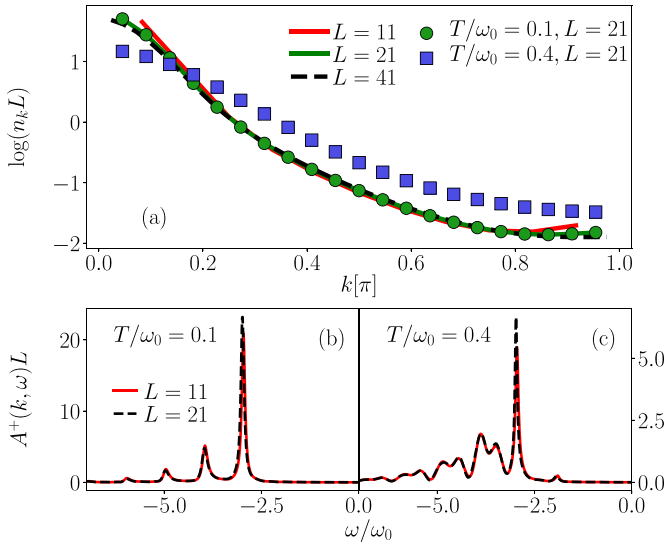

FIG. 10. (a) Momentum distribution n_k calculated with $\gamma/\omega_0 = \sqrt{2}, t_0/\omega_0 = 1, M = 20, t_{\max}\omega_0 = 18.0, \eta = 0.05$ for different system sizes at different temperatures. The symbols show n_k extracted from the Fourier transformed data [see Eq. (43)] and the solid lines were obtained by calculating the expectation value $\langle \hat{n}_k \rangle_T$ at $T/\omega_0 = 0.1$. (b) and (c) show the electron emission spectrum $A^+(k,\omega)$ defined in Eq. (13) for the same parameters as in (a) for $T/\omega_0 = 0.1$, $T/\omega_0 = 0.4$, and $k = \pi/(L+1)$. We show $L = 11$ (red solid line) and $L = 21$ (black dashed line).

ω separated with ω_0. In Fig. 10(b), we have one main peak at the ground-state energy $\omega_{\text{pol}}/\omega_0 \approx -3$. This peak is also robust against an increase in temperature [see Fig. 10(c)]. The peaks at lower ω, however, acquire more structure at elevated T/ω_0. We also observe a peak at $\omega_{\text{pol}}/\omega_0 + 1$ which is completely suppressed at $T/\omega_0 = 0.1$. In Fig. 11, the complete function $A^+(k,\omega)$ is plotted as a function of k and ω. At

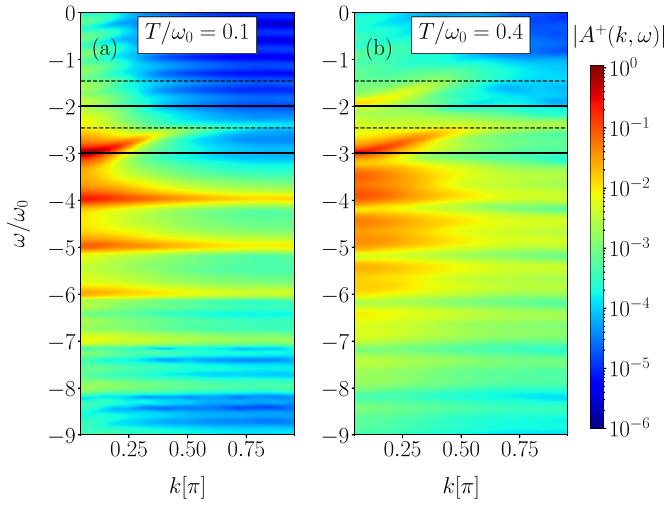

FIG. 11. Electron emission spectrum $A^+(k,\omega)$ defined in Eq. (13) obtained with DMRG. The parameters are $\gamma/\omega_0 = \sqrt{2}, t_0/\omega_0 = 1, L = 21, M = 20, \eta = 0.05$ and $t_{\max}\omega_0 = 18.0$ for (a) $T/\omega_0 = 0.1$ and (b) $T/\omega_0 = 0.4$. The solid lines show $\omega/\omega_0 = -3$ and $\omega/\omega_0 = -2$. The dashed lines show $\omega/\omega_0 = -3 + 4e^{-g^2}$ and $\omega/\omega_0 = -2 + 4e^{-g^2}$.

$T/\omega_0 = 0.4$ [Fig. 11(b)], we see two clear polaron bands starting at $\omega/\omega_0 = -3$ and $\omega/\omega_0 = -2$. Both have a bandwidth of $D \approx e^{-\tilde{g}^2} 4 \approx 0.54$, which is illustrated by the black dashed and solid lines. The peaks at lower frequencies also seem to shift towards higher frequencies and additional peaks appear to emerge at approximately D away from the already existing ones at $\omega/\omega_0 < -3$.

In Fig. 10(a), we show the electron momentum distribution calculated for different system sizes. This quantity can be calculated directly as the thermal expectation value $\langle n_k \rangle_T$ or extracted from the lesser Green's function

$$n_k = \int_{-\infty}^{\infty} d\omega A^+(k,\omega)\,. \tag{43}$$

As a consistency check, we show both. Figure 10(a) illustrates that some finite-size effects exist for small L, but as L is increased, $n_k L$ converges. Note that with increasing L, the number of k points also increases, however, $\sum_k n_k = 1$. This is, of course, different for the spectral function discussed in Sec. V B, where

$$\int_{-\infty}^{\infty} d\omega A(k,\omega) = 1 \tag{44}$$

for all k and L. We thus conclude that already at the low temperatures studied here, n_k starts to flatten out and the difference in amplitude between the polaron peak and the other peaks decrease.

D. Phonon spectral function

We now move on to the phonon spectral function. Its ground-state properties have already been studied thoroughly (see, e.g., Refs. [27,60]). In Ref. [60], Loos *et al.* used analytic and numerical methods to study this spectral function in a variety of parameter regimes. They found that the dominating features of the phonon spectral function are a free-phonon line and a renormalized band dispersion with an additional structure appearing for intermediate electron-phonon coupling. Vidmar *et al.* [27] studied the low-energy spectrum and identified several bound and antibound states in different parameter regimes.

Here, we are interested in this function at finite temperature and in Fig. 12, we display $B(k,\omega)$ for $T/\omega_0 = 0.1$ and 0.4 for different k. At $T/\omega_0 = 0.1$, which is close to the ground state, we clearly recognize two distinct peaks, one at $\omega/\omega_0 = 1$ and another one that gets shifted with k. The peak at $\omega/\omega_0 = 1$ originates from the free phonon, whereas the other peak originates from the phonon being coupled to the electron. When temperature is increased, the phonon spectral function changes dramatically. For $k = L\pi/(L+1)$, the peaks get significantly broader and the polaron and the free-phonon peaks are almost completely merged. We also see structure appearing at $\omega/\omega_0 < 0$ which is suppressed at low temperatures, exactly as is the case for the single-site phonon spectral function in Sec. III E.

In Fig. 13, we show the complete $B(k,\omega)$. Here, the polaron band structure with a width of $D \approx 4e^{-\tilde{g}^2}$ is visible. It also becomes clear that whereas we only observe the appearance of a free-phonon peak at negative frequencies in the single-site case, here, there is a complete reflected polaron

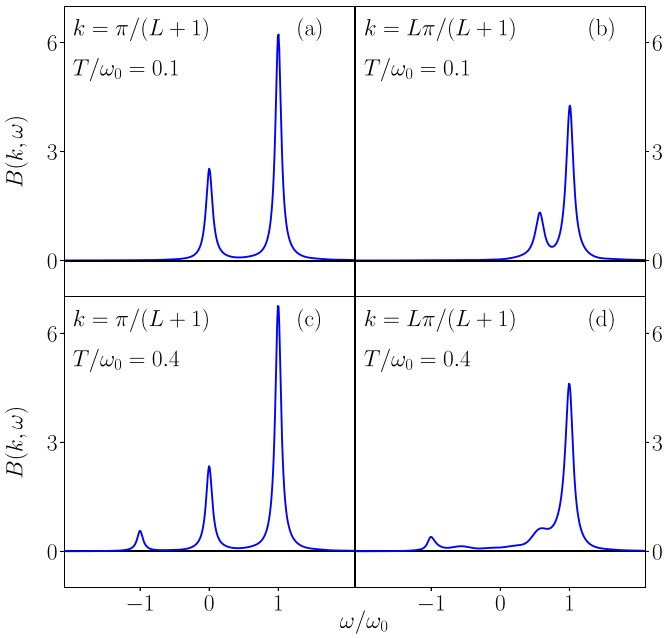

FIG. 12. Phonon spectral function $B(k,\omega)$ from Eq. (15) obtained with DMRG. The parameters are $\gamma/\omega_0 = \sqrt{2}$, $t_0/\omega_0 = 1$, $L = 21$, $M = 20$, $\eta = 0.05$ and $t_{\max}\omega_0 = 15.8$. (a) and (b) show $T/\omega_0 = 0.1$ with $k = \pi/(L+1)$ and $k = L\pi/(L+1)$. (c) and (d) show the same k values for $T/\omega_0 = 0.4$.

band appearing for $T/\omega_0 = 0.4$ at $\omega/\omega_0 < 0$ [see Fig. 13(b)]. This is similar to what we find for the emission spectrum in Fig. 11.

VI. SUMMARY

We have generalized the DMRG method combined with purification and local basis optimization to efficiently compute static as well as dynamic properties of the Holstein polaron in the intermediate coupling regime at finite temperatures. We first showed that the method enabled us to generate thermal states at a finite temperature by performing imaginary-time evolution. We then computed the electron spectral function and showed that our results quantitatively agree with those obtained using the finite-temperature

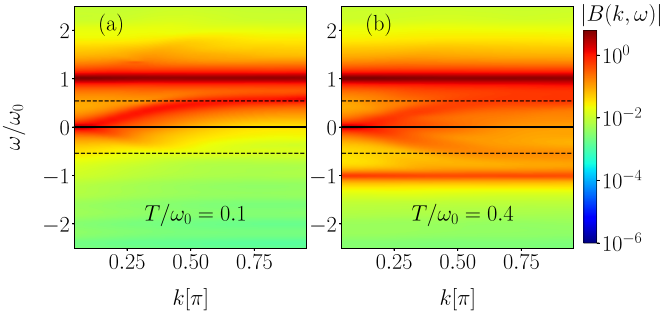

FIG. 13. Phonon spectral function $B(k,\omega)$ from Eq. (15) obtained with DMRG. The parameters are $\gamma/\omega_0 = \sqrt{2}$, $t_0/\omega_0 = 1$, $L = 21$, $M = 20$, $\eta = 0.05$ and $t_{\max}\omega_0 = 15.8$. (a) shows $T/\omega_0 = 0.1$ and (b) shows $T/\omega_0 = 0.4$. The solid lines show $\omega/\omega_0 = 0$ and the dashed lines show $\omega/\omega_0 = \pm 4e^{-\tilde{g}^2}$.

Lanczos method of Ref. [72]. We also analyzed the electron emission spectrum and found that the difference between the amplitude of the polaron peak and the other peaks decreased and that n_k flattened out with increasing temperature. In addition, we observed an additional band appearing at larger ω. Regarding the phonon spectral function, our work unveils that with increasing temperature, the spectrum broadens at larger momentum accompanied by the emergence of a mirrored image at $\omega < 0$.

We propose a number of future applications of the method introduced in this work. A natural extension would be to compare the results presented in this work to similar calculations done with minimally entangled typical thermal state algorithms [117–119,142–144]. Another direction would be to combine the local basis optimization with other time-evolution methods [145–149]. A further possible area of application is to calculate thermal expectation values combined with quench dynamics [35,37,54,92,93,150–153] to test the predictions of the eigenstate thermalization hypothesis [56,64–66,68,70,71,154]. The proposed method can also be generalized to investigate heterojunctions containing vibrational degrees of freedom [137,155–160] and to study the evolution of polaron states in manganites [161–164]. Further challenging continuations could involve the numerical study of time-dependent spectral functions (see, e.g., Refs. [81,141]) relevant to time-dependent ARPES experiments [78,79,165,166] or to compute the optical conductivity at finite temperatures (see, e.g., Refs. [29,167,168]).

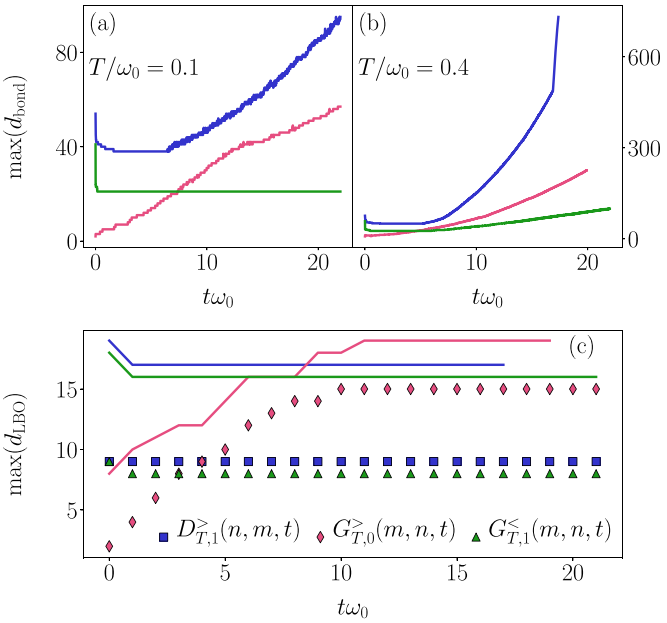

FIG. 14. (a) Maximum bond dimensions used in the MPS representations of $D^{>}_{T,1}(m,n,t)$ (blue), $G^{>}_{T,0}(m,n,t)$ (red), and $G^{<}_{T,1}(m,n,t)$ (green) [see Eqs. (14), (8), (12)] at $T/\omega_0 = 0.1$. The parameters are $\gamma/\omega_0 = \sqrt{2}, t_0/\omega_0 = 1, L = 21, M = 20$ and fixed $m = n = 11$. (b) Same as in (a) but at $T/\omega_0 = 0.4$. (c) Maximum local optimal basis dimension for $T/\omega_0 = 0.1$ (symbols) and $T/\omega_0 = 0.4$ (solid lines). We only show every 100th point for the symbols in (c) for clarity.

ACKNOWLEDGMENTS

We acknowledge useful discussions with A. Feiguin, E. Jeckelmann, C. Karrasch, S. Manmana, C. Meyer, S. Paeckel, and J. Stolpp. D.J. and F.H.-M. were funded by the Deutsche Forschungsgemeinschaft (DFG, German Research Foundation) - 217133147 via SFB 1073 (project B09). J.B. acknowledges the support by the program P1-0044 of the Slovenian Research Agency, support from the Centre for Integrated Nanotechnologies, a U.S. Department of Energy, Office of Basic Energy Sciences user facility, and funding from the Stewart Blusson Quantum Matter Institute.

APPENDIX A: BOND AND LBO DIMENSION IN REAL-TIME EVOLUTION

In Fig. 14, we show the maximum bond dimension [Fig. 14(a) and Fig. 14(b)] and maximum local optimal basis dimension [Fig. 14(c)] as a function of time. The bond dimension is clearly dependent on the temperature and on the specific Greens's function. It increases a lot faster for the $G^{>}_{T,0}(t,m,n)$ (red) and $D^{>}_{T,1}(t,m,n)$ (blue). For these Greens's functions, the real-time evolution is done with an electron in the physical system which causes the large increase in the bond dimension. One also sees that as temperature is increased, the computations become much more costly. This is especially true for the phonon Green's function $D^{>}_{T,1}(t,m,n)$. The drop at $t\omega_0 = 0$ comes from the fact that the imaginary-time evolution is carried out with $\rho_{\text{LBO}} = \rho_{\text{bond}} = 10^{-9}$, whereas the real-time evolution is done with $\rho_{\text{LBO}} = \rho_{\text{bond}} = 10^{-8}$. This leads to some states getting truncated away right at the beginning. This is not the case for the red curve that shows $G^{>}_{T,0}(m,n,t)$. There, the insertion of the electron into the system directly leads to a much larger bond dimension. We also observe that the maximum dimension of the local optimal basis remains approximately constant during the real-time evolution for the Green's functions in the one-electron sector. The dimension clearly increases for larger temperature [$T/\omega_0 = 0.1$ (symbols) and $T/\omega_0 = 0.4$ (solid lines)] but it is, in both cases, clearly beneficial. This does, of course, not imply that the modes in the optimal basis remain the same. When the Green's function is calculated in the zero-electron sector, inserting the electron clearly leads to an increase in $\max(d_{\text{LBO}})$.

We want to explore the performance of our method away from the intermediate coupling regime. The strength and purpose of our DMRG method is to access the crossover regime, whereas perturbation theory [169] can be used to address the small hopping limit. This is illustrated in Fig. 15, where we show the results for different choices of γ and ω_0.

Figure 15(a) shows the electron spectral function [see Eq. (11)] for $t_0/\omega_0 = 0.2$ and $\gamma/\omega_0 = \sqrt{2}$. This is close to the atomic limit and is in good agreement with the single-site spectral function presented in Fig. 1. In Fig. 15(c), the same quantity is shown for $\gamma/\omega_0 = 1$ and $t_0/\omega_0 = 1$.

The limiting factors for the performance are displayed in Figs. 15(b) and 15(d). Figure 15(b) shows the maximum bond dimension of the matrix-product state for different parameters as a function of time. For both a large coupling and small frequencies, the bond dimension grows more rapidly than

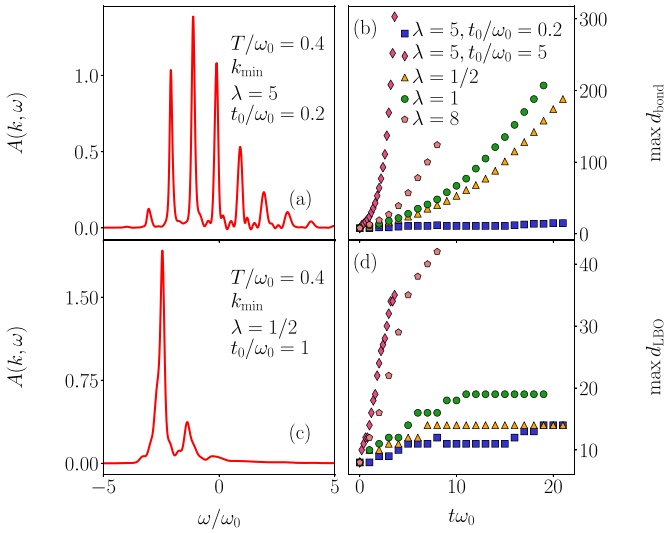

FIG. 15. (a) Electron spectral function [see Eq. (11)], for $\gamma/\omega_0 = \sqrt{2}, t_0/\omega_0 = 0.2, L = 21, M = 20, \eta = 0.05, T/\omega_0 = 0.4$, $k = \pi/(L+1)$ and $t_{\max}\omega_0 = 18.0$. (c) Same as (a) but with $\gamma/\omega_0 = 1, t_0/\omega_0 = 1$. (b) Maximum bond dimension of $G^{>}_{T,0}(m,n,t)$ for different parameters at $T/\omega_0 = 0.4$. (d) Maximum local dimension of $G^{>}_{T,0}(m,n,t)$ for different parameters at $T/\omega_0 = 0.4$. In (b) and (d), we only show every 100th point for clarity.

for the parameters used in the main text. This makes the real-time evolution significantly more difficult. Furthermore, Fig. 15(d) shows the maximum LBO dimension. This quantity also increases more rapidly in both previously mentioned cases, rendering the use of LBO more costly. A sufficient number of bare phonons M is clearly not included in those simulations. To make accurate computations in these parameter regimes, the convergence with increased M would have to be monitored. This can be done adaptively in DMRG-LBO simulations as was demonstrated by Brockt in Ref. [170].

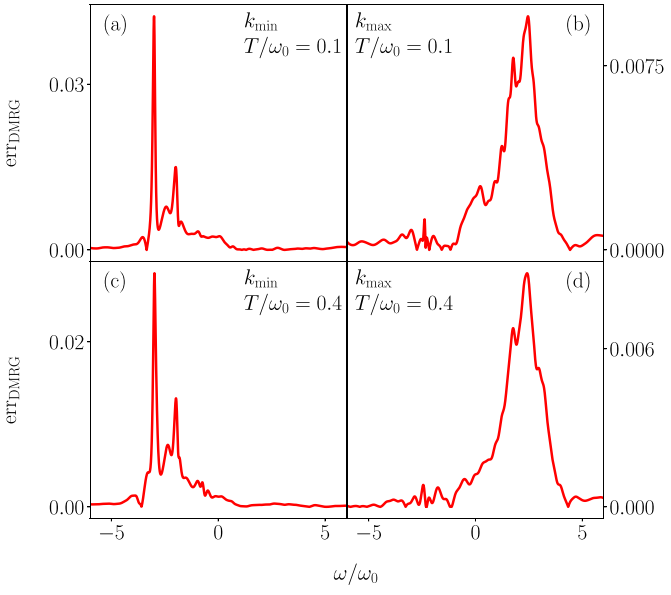

FIG. 16. Difference between DMRG data at different system sizes defined in Eq. (B1). The parameters are the same as in Fig. 8.

Intuitively, one would think that LBO works better in the strong-coupling limit, since in the Lang-Firsov limit, one should be able to describe the system with only two local states at $T/\omega_0 = 0$. As expected, this is the case for $t_0/\omega_0 = 0.2$. In Fig. 15(d), we see that we need $\sim O(10)$ states at later times in this regime. Further, the single-site polaron ground state has a phonon occupation $N_{\text{ph}} = \gamma^2/\omega_0^2$. This would, for example, give $N_{\text{ph}} = 16$ for the $\lambda = 8$ curve in Fig. 15(d), such that the optimal basis for the distribution is out of reach for the $M = 20$ bare-phonon truncation used here.

For the data shown here, we start the time evolution in the trivially obtained zero-electron state. In the process of generating the one-electron state with imaginary time evolution, the particle might jump to the ancilla sites at low temperatures in extreme parameter regimes. This can be overcome with standard solutions, see Refs. [120,123]. One possibility is to generate matrix-product states with particle-number conservation in the physical and ancilla system separately.

APPENDIX B: ERROR OF THE ELECTRON SPECTRAL FUNCTION

In Fig. 16, we show the difference between the integrated [see Eq. (42)] DMRG data with $L = 21$ and $L = 101$

$$\text{err}_{\text{DMRG}} = \frac{|I(k,\omega)_{L=21} - I(k,\omega)_{L=101}|}{\max\{I(k,\omega)_{L=21}\}}. \tag{B1}$$

The data is obtained with different Fourier transformations, see Sec. V B for details.

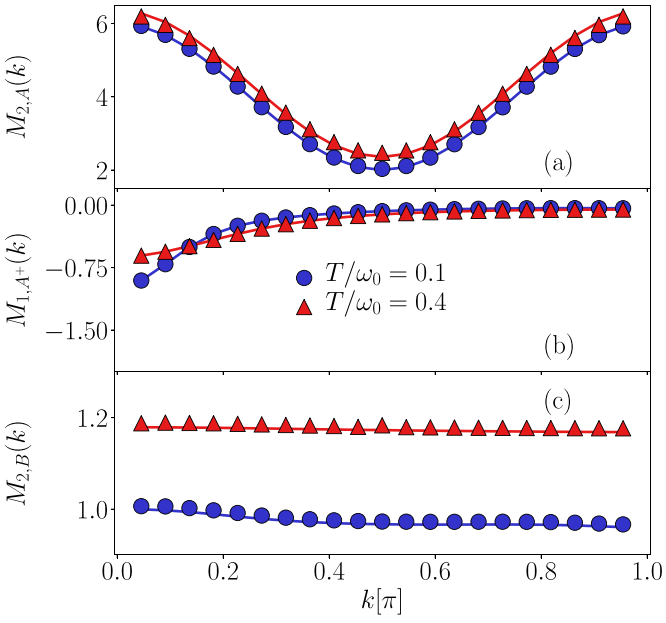

FIG. 17. Temperature dependent moments. The symbols are calculated by numerically integrating the moments as in Eq. (C1) and the solid lines correspond to the thermal expectation values thereof. For all data, we use a Gaussian regularization and $\eta = 0.05/(6\pi)$. (a) Second moment of the electron spectral function for the same parameters as in Fig. 9. (b) First moment of the electron emission spectrum for the same parameters as in Fig. 11. (c) Second moment of the phonon spectral function for the same parameters as in Fig. 13.

APPENDIX C: MOMENTS

To validate that the method captures the correct finite-temperature behavior we compute the first temperature-dependent moment for each spectral function. The moments are defined for the corresponding spectral function [here only shown for $A(k,\omega)$] as

$$M_{m,A}(k) = \int_{-\infty}^{\infty} \omega^m A(k,\omega) d\omega\,. \tag{C1}$$

For $A(k,\omega)$, the first two moments (see Refs. [72,139,171]) become

$$M_{1,A}(k) = \epsilon(k), \tag{C2}$$

$$M_{2,A} = \epsilon^2(k) + \gamma^2(2n_{\mathrm{ph}} + 1), \tag{C3}$$

where $n_{\mathrm{ph}} = 1/(\exp(\omega_0/T) - 1)$, $\epsilon(k) = -2t_0\cos(k)$ with the quasimomenta for open-boundary conditions used in this paper. For $A^+(k,\omega)$, the first moment is already temperature dependent

$$M_{1,A^+}(k) = \frac{2}{L+1}\sum_{i,j}\sin(ki)\sin(kj) \times \langle \hat{c}_j^\dagger \hat{c}_i(\epsilon(k) + \gamma\hat{X}_i)\rangle_T, \tag{C4}$$

and for $B(k,\omega)$ we obtain

$$M_{1,B}(k) = \omega_0, \tag{C5}$$

$$M_{2,B}(k) = \omega_0\frac{2}{L+1}\sum_{i,j}\sin(ik)\sin(jk) \times \langle \omega_0(\hat{X}_i\hat{X}_j) + 2\gamma\hat{n}_i\hat{X}_j\rangle_T. \tag{C6}$$

The results for the temperature-dependent moments are shown in Fig. 17. We see that they can be calculated quite accurately with our method. The mean differences for both temperatures are of the order $O(10^{-5})$ for all the first moments and $O(10^{-2})$ for the second moments. In contrast to the rest of the paper, we here use a Gaussian regularization for the spectral function. The moments show a dependence on the regularization parameter η. One must find a compromise between allowing for unphysical oscillations in the spectral function and the accuracy of the moments. We choose $\eta = 0.05/(6\pi)$. For the second moments, we further limit the integration to $\omega_{\mathrm{min}} \approx -10\omega_0 < \omega < \omega_{\mathrm{max}} \approx 10\omega_0$. We found that the results for the Gaussian regularization are much more robust against changes in ω_{min} and ω_{max} than the Lorentzian regularization.

[1] C. Gadermaier, A. S. Alexandrov, V. V. Kabanov, P. Kusar, T. Mertelj, X. Yao, C. Manzoni, D. Brida, G. Cerullo, and D. Mihailovic, Electron-Phonon Coupling in High-Temperature Cuprate Superconductors Determined from Electron Relaxation Rates, Phys. Rev. Lett. **105**, 257001 (2010).

[2] F. Novelli, G. De Filippis, V. Cataudella, M. Esposito, I. Vergara, F. Cilento, E. Sindici, A. Amaricci, C. Giannetti, D. Prabhakaran, S. Wall, A. Perucchi, S. Dal Conte, G. Cerullo, M. Capone, A. Mishchenko, M. Grüninger, N. Nagaosa, F. Parmigiani, and D. Fausti, Witnessing the formation and relaxation of dressed quasi-particles in a strongly correlated electron system, Nat. Commun. **5**, 5112 (2014).

[3] S. Dal Conte, L. Vidmar, D. Golež, M. Mierzejewski, G. Soavi, S. Peli, F. Banfi, G. Ferrini, R. Comin, B. M. Ludbrook, L. Chauviere, N. D. Zhigadlo, H. Eisaki, M. Greven, S. Lupi, A. Damascelli, D. Brida, M. Capone, J. Bonča, G. Cerullo, and C. Giannetti, Snapshots of the retarded interaction of charge carriers with ultrafast fluctuations in cuprates, Nat. Phys. **11**, 421 (2015).

[4] C. Giannetti, M. Capone, D. Fausti, M. Fabrizio, F. Parmigiani, and D. Mihailovic, Ultrafast optical spectroscopy of strongly correlated materials and high-temperature superconductors: a non-equilibrium approach, Adv. Phys. **65**, 58 (2016).

[5] C. Hwang, W. Zhang, K. Kurashima, R. Kaindl, T. Adachi, Y. Koike, and A. Lanzara, Ultrafast dynamics of electron-phonon coupling in a metal, EPL **126**, 57001 (2019).

[6] D. N. Basov, R. D. Averitt, D. van der Marel, M. Dressel, and K. Haule, Electrodynamics of correlated electron materials, Rev. Mod. Phys. **83**, 471 (2011).

[7] J. Orenstein, Ultrafast spectroscopy of quantum materials, Phys. Today **65**(9), 44 (2012).

[8] T. Holstein, Studies of polaron motion: Part I. The molecular-crystal model, Ann. Phys. (NY) **8**, 325 (1959).

[9] J. E. Hirsch and E. Fradkin, Phase diagram of one-dimensional electron-phonon systems. II. The molecular-crystal model, Phys. Rev. B **27**, 4302 (1983).

[10] G. Wellein, H. Röder, and H. Fehske, Polarons and bipolarons in strongly interacting electron-phonon systems, Phys. Rev. B **53**, 9666 (1996).

[11] G. Wellein and H. Fehske, Polaron band formation in the Holstein model, Phys. Rev. B **56**, 4513 (1997).

[12] G. Wellein and H. Fehske, Self-trapping problem of electrons or excitons in one dimension, Phys. Rev. B **58**, 6208 (1998).

[13] J. Bonča, S. A. Trugman, and I. Batistić, Holstein polaron, Phys. Rev. B **60**, 1633 (1999).

[14] C. Zhang, E. Jeckelmann, and S. R. White, Dynamical properties of the one-dimensional Holstein model, Phys. Rev. B **60**, 14092 (1999).

[15] A. Weiße, H. Fehske, G. Wellein, and A. R. Bishop, Optimized phonon approach for the diagonalization of electron-phonon problems, Phys. Rev. B **62**, R747(R) (2000).

[16] H. Fehske, J. Loos, and G. Wellein, Lattice polaron formation: Effects of nonscreened electron-phonon interaction, Phys. Rev. B **61**, 8016 (2000).

[17] A. Weiße, G. Wellein, and H. Fehske, *Density-Matrix Algorithm for Phonon Hilbert Space Reduction in the Numerical Diagonalization of Quantum Many-Body Systems, in High Performance Computing in Science and Engineering '01* (Springer, Berlin, Heidelberg, 2002), p. 131.

[18] L.-C. Ku, S. A. Trugman, and J. Bonča, Dimensionality effects on the Holstein polaron, Phys. Rev. B **65**, 174306 (2002).

[19] M. Hohenadler, M. Aichhorn, and W. von der Linden, Spectral function of electron-phonon models by cluster perturbation theory, Phys. Rev. B **68**, 184304 (2003).

[20] M. Hohenadler, H. G. Evertz, and W. von der Linden, Quantum Monte Carlo and variational approaches to the Holstein model, Phys. Rev. B **69**, 024301 (2004).
[21] M. Hohenadler, D. Neuber, W. von der Linden, G. Wellein, J. Loos, and H. Fehske, Photoemission spectra of many-polaron systems, Phys. Rev. B **71**, 245111 (2005).
[22] H. Fehske and S. A. Trugman, Numerical solution of the Holstein polaron problem, *Polarons in Advanced Materials*, Vol. 103 of Springer Series in Materials Science (Springer Netherlands, Dordrecht, 2007), pp. 393–461.
[23] L.-C. Ku and S. A. Trugman, Quantum dynamics of polaron formation, Phys. Rev. B **75**, 014307 (2007).
[24] O. S. Barišić and S. Barišić, Phase diagram of the Holstein polaron in one dimension, Eur. Phys. J. B **64**, 1 (2008).
[25] S. Ejima and H. Fehske, Luttinger parameters and momentum distribution function for the half-filled spinless fermion Holstein model: A DMRG approach, EPL **87**, 27001 (2009).
[26] A. Alvermann, H. Fehske, and S. A. Trugman, Polarons and slow quantum phonons, Phys. Rev. B **81**, 165113 (2010).
[27] L. Vidmar, J. Bonča, and S. A. Trugman, Emergence of states in the phonon spectral function of the Holstein polaron below and above the one-phonon continuum, Phys. Rev. B **82**, 104304 (2010).
[28] L. Vidmar, J. Bonča, M. Mierzejewski, P. Prelovšek, and S. A. Trugman, Nonequilibrium dynamics of the Holstein polaron driven by an external electric field, Phys. Rev. B **83**, 134301 (2011).
[29] G. L. Goodvin, A. S. Mishchenko, and M. Berciu, Optical Conductivity of the Holstein Polaron, Phys. Rev. Lett. **107**, 076403 (2011).
[30] G. De Filippis, V. Cataudella, A. S. Mishchenko, and N. Nagaosa, Optical conductivity of polarons: Double phonon cloudconcept verified by diagrammatic Monte Carlo simulations, Phys. Rev. B **85**, 094302 (2012).
[31] S. Sayyad and M. Eckstein, Coexistence of excited polarons and metastable delocalized states in photoinduced metals, Phys. Rev. B **91**, 104301 (2015).
[32] F. Dorfner, L. Vidmar, C. Brockt, E. Jeckelmann, and F. Heidrich-Meisner, Real-time decay of a highly excited charge carrier in the one-dimensional Holstein model, Phys. Rev. B **91**, 104302 (2015).
[33] Z. Huang, L. Wang, C. Wu, L. Chen, F. Grossmann, and Y. Zhao, Polaron dynamics with off-diagonal coupling: beyond the Ehrenfest approximation, Phys. Chem. Chem. Phys. **19**, 1655 (2017).
[34] C. Dutreix and M. I. Katsnelson, Dynamical control of electron-phonon interactions with high-frequency light, Phys. Rev. B **95**, 024306 (2017).
[35] C. Brockt and E. Jeckelmann, Scattering of an electronic wave packet by a one-dimensional electron-phonon-coupled structure, Phys. Rev. B **95**, 064309 (2017).
[36] A. F. Kemper, M. A. Sentef, B. Moritz, T. P. Devereaux, and J. K. Freericks, Review of the theoretical description of time-resolved angle-resolved photoemission spectroscopy in electron-phonon mediated superconductors, Ann. Phys. (Berl.) **529**, 1600235 (2017).
[37] J. Stolpp, J. Herbrych, F. Dorfner, E. Dagotto, and F. Heidrich-Meisner, Charge-density-wave melting in the one-dimensional Holstein model, Phys. Rev. B **101**, 035134 (2020).
[38] H. Fehske, G. Wellein, G. Hager, A. Weiße, and A. R. Bishop, Quantum lattice dynamical effects on single-particle excitations in one-dimensional Mott and Peierls insulators, Phys. Rev. B **69**, 165115 (2004).
[39] P. Werner and A. J. Millis, Efficient Dynamical Mean Field Simulation of the Holstein-Hubbard Model, Phys. Rev. Lett. **99**, 146404 (2007).
[40] H. Fehske, G. Hager, and E. Jeckelmann, Metallicity in the half-filled Holstein-Hubbard model, EPL **84**, 57001 (2008).
[41] D. Golež, J. Bonča, and L. Vidmar, Dissociation of a Hubbard-Holstein bipolaron driven away from equilibrium by a constant electric field, Phys. Rev. B **85**, 144304 (2012).
[42] G. De Filippis, V. Cataudella, E. A. Nowadnick, T. P. Devereaux, A. S. Mishchenko, and N. Nagaosa, Quantum Dynamics of the Hubbard-Holstein Model in Equilibrium and Nonequilibrium: Application to Pump-Probe Phenomena, Phys. Rev. Lett. **109**, 176402 (2012).
[43] P. Werner and M. Eckstein, Phonon-enhanced relaxation and excitation in the Holstein-Hubbard model, Phys. Rev. B **88**, 165108 (2013).
[44] A. Nocera, M. Soltanieh-ha, C. A. Perroni, V. Cataudella, and A. E. Feiguin, Interplay of charge, spin, and lattice degrees of freedom in the spectral properties of the one-dimensional Hubbard-Holstein model, Phys. Rev. B **90**, 195134 (2014).
[45] P. Werner and M. Eckstein, Field-induced polaron formation in the Holstein-Hubbard model, EPL **109**, 37002 (2015).
[46] M. A. Sentef, A. F. Kemper, A. Georges, and C. Kollath, Theory of light-enhanced phonon-mediated superconductivity, Phys. Rev. B **93**, 144506 (2016).
[47] H. Hashimoto and S. Ishihara, Photoinduced charge-order melting dynamics in a one-dimensional interacting Holstein model, Phys. Rev. B **96**, 035154 (2017).
[48] A. Dey, M. Q. Lone, and S. Yarlagadda, Decoherence in models for hard-core bosons coupled to optical phonons, Phys. Rev. B **92**, 094302 (2015).
[49] J. Kogoj, M. Mierzejewski, and J. Bonča, Nature of Bosonic Excitations Revealed by High-Energy Charge Carriers, Phys. Rev. Lett. **117**, 227002 (2016).
[50] L. Vidmar, J. Bonča, S. Maekawa, and T. Tohyama, Bipolaron in the t-J Model Coupled to Longitudinal and Transverse Quantum Lattice Vibrations, Phys. Rev. Lett. **103**, 186401 (2009).
[51] L. Vidmar, J. Bonča, T. Tohyama, and S. Maekawa, Quantum Dynamics of a Driven Correlated System Coupled to Phonons, Phys. Rev. Lett. **107**, 246404 (2011).
[52] C. Guo, A. Weichselbaum, J. von Delft, and M. Vojta, Critical and Strong-Coupling Phases in One- and Two-Bath Spin-Boson Models, Phys. Rev. Lett. **108**, 160401 (2012).
[53] B. Bruognolo, A. Weichselbaum, C. Guo, J. von Delft, I. Schneider, and M. Vojta, Two-bath spin-boson model: Phase diagram and critical properties, Phys. Rev. B **90**, 245130 (2014).
[54] M. L. Wall, A. Safavi-Naini, and A. M. Rey, Simulating generic spin-boson models with matrix product states, Phys. Rev. A **94**, 053637 (2016).
[55] S. A. Sato, A. Kelly, and A. Rubio, Coupled forward-backward trajectory approach for nonequilibrium electron-ion dynamics, Phys. Rev. B **97**, 134308 (2018).

[56] D. Jansen, J. Stolpp, L. Vidmar, and F. Heidrich-Meisner, Eigenstate thermalization and quantum chaos in the Holstein polaron model, Phys. Rev. B **99**, 155130 (2019).

[57] O. S. Barišić, Variational study of the Holstein polaron, Phys. Rev. B **65**, 144301 (2002).

[58] O. S. Barišić, Calculation of excited polaron states in the Holstein model, Phys. Rev. B **69**, 064302 (2004).

[59] O. S. Barišić, Holstein light quantum polarons on the one-dimensional lattice, Phys. Rev. B **73**, 214304 (2006).

[60] J. Loos, M. Hohenadler, A. Alvermann, and H. Fehske, Phonon spectral function of the Holstein polaron, J. Phys. Condens. Matter **18**, 7299 (2006).

[61] J. Loos, M. Hohenadler, and H. Fehske, Spectral functions of the spinless Holstein model, J. Phys. Condens. Matter **18**, 2453 (2006).

[62] E. V. L. de Mello and J. Ranninger, Dynamical properties of small polarons, Phys. Rev. B **55**, 14872 (1997).

[63] S. Paganelli and S. Ciuchi, Tunnelling system coupled to a harmonic oscillator: an analytical treatment, J. Phys.: Condens. Matter **18**, 7669 (2006).

[64] M. Rigol, V. Dunjko, and M. Olshanii, Thermalization and its mechanism for generic isolated quantum systems, Nature (London) **452**, 854 (2008).

[65] M. Rigol and M. Srednicki, Alternatives to Eigenstate Thermalization, Phys. Rev. Lett. **108**, 110601 (2012).

[66] S. Sorg, L. Vidmar, L. Pollet, and F. Heidrich-Meisner, Relaxation and thermalization in the one-dimensional Bose-Hubbard model: A case study for the interaction quantum quench from the atomic limit, Phys. Rev. A **90**, 033606 (2014).

[67] A. S. Mishchenko, N. Nagaosa, G. De Filippis, A. de Candia, and V. Cataudella, Mobility of Holstein Polaron at Finite Temperature: An Unbiased Approach, Phys. Rev. Lett. **114**, 146401 (2015).

[68] L. D'Alessio, Y. Kafri, A. Polkovnikov, and M. Rigol, From quantum chaos and eigenstate thermalization to statistical mechanics and thermodynamics, Adv. Phys. **65**, 239 (2016).

[69] L. Chen and Y. Zhao, Finite temperature dynamics of a Holstein polaron: The thermo-field dynamics approach, J. Chem. Phys. **147**, 214102 (2017).

[70] J. M. Deutsch, Eigenstate thermalization hypothesis, Rep. Prog. Phys. **81**, 082001 (2018).

[71] T. Mori, T. N. Ikeda, E. Kaminishi, and M. Ueda, Thermalization and prethermalization in isolated quantum systems: a theoretical overview, J. Phys. B **51**, 112001 (2018).

[72] J. Bonča, S. A. Trugman, and M. Berciu, Spectral function of the Holstein polaron at finite temperature, Phys. Rev. B **100**, 094307 (2019).

[73] J. Bonča, Spectral function of an electron coupled to hard-core bosons, Phys. Rev. B **102**, 035135 (2020).

[74] S. R. White, Density Matrix Formulation for Quantum Renormalization Groups, Phys. Rev. Lett. **69**, 2863 (1992).

[75] U. Schollwöck, The density-matrix renormalization group, Rev. Mod. Phys. **77**, 259 (2005).

[76] U. Schollwöck, The density-matrix renormalization group in the age of matrix product states, Ann. Phys. (NY) **326**, 96 (2011).

[77] W. Eberhardt and E. W. Plummer, Angle-resolved photoemission determination of the band structure and multielectron excitations in Ni, Phys. Rev. B **21**, 3245 (1980).

[78] A. Damascelli, Z. Hussain, and Z.-X. Shen, Angle-resolved photoemission studies of the cuprate superconductors, Rev. Mod. Phys. **75**, 473 (2003).

[79] A. Damascelli, Probing the electronic structure of complex systems by ARPES, Phys. Scr. **T109**, 61 (2004).

[80] C. Kirkegaard, T. K. Kim, and P. Hofmann, Self-energy determination and electron–phonon coupling on Bi(110), New J. Phys. **7**, 99 (2005).

[81] J. K. Freericks, H. R. Krishnamurthy, and T. Pruschke, Theoretical Description of Time-Resolved Photoemission Spectroscopy: Application to Pump-Probe Experiments, Phys. Rev. Lett. **102**, 136401 (2009).

[82] P. Hofmann, I. Y. Sklyadneva, E. D. L. Rienks, and E. V. Chulkov, Electron–phonon coupling at surfaces and interfaces, New J. Phys. **11**, 125005 (2009).

[83] F. Verstraete, J. J. García-Ripoll, and J. I. Cirac, Matrix Product Density Operators: Simulation of Finite-Temperature and Dissipative Systems, Phys. Rev. Lett. **93**, 207204 (2004).

[84] A. E. Feiguin and S. R. White, Finite-temperature density matrix renormalization using an enlarged Hilbert space, Phys. Rev. B **72**, 220401 (2005).

[85] T. Barthel, U. Schollwöck, and S. R. White, Spectral functions in one-dimensional quantum systems at finite temperature using the density matrix renormalization group, Phys. Rev. B **79**, 245101 (2009).

[86] A. E. Feiguin and G. A. Fiete, Spectral properties of a spin-incoherent Luttinger liquid, Phys. Rev. B **81**, 075108 (2010).

[87] A. J. Daley, C. Kollath, U. Schollwöck, and G. Vidal, Time-dependent density-matrix renormalization-group using adaptive effective Hilbert spaces, J. Stat. Mech.: Theory Exp. (2004) P04005.

[88] S. R. White and A. E. Feiguin, Real-Time Evolution using the Density Matrix Renormalization Group, Phys. Rev. Lett. **93**, 076401 (2004).

[89] G. Vidal, Efficient Simulation of One-Dimensional Quantum Many-Body Systems, Phys. Rev. Lett. **93**, 040502 (2004).

[90] S. Paeckel, T. Köhler, A. Swoboda, S. R. Manmana, U. Schollwöck, and C. Hubig, Time-evolution methods for matrix-product states, Ann. Phys. (NY) **411**, 167998 (2019).

[91] C. Zhang, E. Jeckelmann, and S. R. White, Density Matrix Approach to Local Hilbert Space Reduction, Phys. Rev. Lett. **80**, 2661 (1998).

[92] C. Brockt, F. Dorfner, L. Vidmar, F. Heidrich-Meisner, and E. Jeckelmann, Matrix-product-state method with a dynamical local basis optimization for bosonic systems out of equilibrium, Phys. Rev. B **92**, 241106 (2015).

[93] F. A. Y. N. Schröder and A. W. Chin, Simulating open quantum dynamics with time-dependent variational matrix product states: Towards microscopic correlation of environment dynamics and reduced system evolution, Phys. Rev. B **93**, 075105 (2016).

[94] R. J. Bursill, Density-matrix renormalization-group algorithm for quantum lattice systems with a large number of states per site, Phys. Rev. B **60**, 1643 (1999).

[95] B. Friedman, Optimal phonon approach to the spin Peierls model with nonadiabatic spin-phonon coupling, Phys. Rev. B **61**, 6701 (2000).

[96] W. Barford, R. J. Bursill, and M. Y. Lavrentiev, Breakdown of the adiabatic approximation in trans-polyacetylene, Phys. Rev. B **65**, 075107 (2002).

[97] W. Barford and R. J. Bursill, Effect of quantum lattice fluctuations on the Peierls broken-symmetry ground state, Phys. Rev. B **73**, 045106 (2006).
[98] H. Wong and Z.-D. Chen, Density matrix renormalization group approach to the spin-boson model, Phys. Rev. B **77**, 174305 (2008).
[99] O. R. Tozer and W. Barford, Localization of large polarons in the disordered Holstein model, Phys. Rev. B **89**, 155434 (2014).
[100] F. Dorfner and F. Heidrich-Meisner, Properties of the single-site reduced density matrix in the Bose-Bose resonance model in the ground state and in quantum quenches, Phys. Rev. A **93**, 063624 (2016).
[101] S. Ejima, H. Fehske, and F. Gebhard, Dynamic properties of the one-dimensional Bose-Hubbard model, EPL **93**, 30002 (2011).
[102] H. Benthien, F. Gebhard, and E. Jeckelmann, Spectral Function of the One-Dimensional Hubbard Model Away from Half Filling, Phys. Rev. Lett. **92**, 256401 (2004).
[103] A. C. Tiegel, S. R. Manmana, T. Pruschke, and A. Honecker, Matrix product state formulation of frequency-space dynamics at finite temperatures, Phys. Rev. B **90**, 060406 (2014).
[104] K. A. Hallberg, Density-matrix algorithm for the calculation of dynamical properties of low-dimensional systems, Phys. Rev. B **52**, R9827 (1995).
[105] T. D. Kühner and S. R. White, Dynamical correlation functions using the density matrix renormalization group, Phys. Rev. B **60**, 335 (1999).
[106] E. Jeckelmann, Dynamical density-matrix renormalization-group method, Phys. Rev. B **66**, 045114 (2002).
[107] A. Holzner, A. Weichselbaum, I. P. McCulloch, U. Schollwöck, and J. von Delft, Chebyshev matrix product state approach for spectral functions, Phys. Rev. B **83**, 195115 (2011).
[108] A. Weichselbaum, F. Verstraete, U. Schollwöck, J. I. Cirac, and J. von Delft, Variational matrix-product-state approach to quantum impurity models, Phys. Rev. B **80**, 165117 (2009).
[109] M. Zwolak and G. Vidal, Mixed-State Dynamics in One-Dimensional Quantum Lattice Systems: A Time-Dependent Superoperator Renormalization Algorithm, Phys. Rev. Lett. **93**, 207205 (2004).
[110] J. Sirker and A. Klümper, Real-time dynamics at finite temperature by the density-matrix renormalization group: A path-integral approach, Phys. Rev. B **71**, 241101 (2005).
[111] C. Karrasch, J. H. Bardarson, and J. E. Moore, Finite-Temperature Dynamical Density Matrix Renormalization Group and the Drude Weight of Spin-1/2 Chains, Phys. Rev. Lett. **108**, 227206 (2012).
[112] T. Barthel, U. Schollwöck, and S. Sachdev, Scaling of the thermal spectral function for quantum critical bosons in one dimension, arXiv:1212.3570.
[113] T. Barthel, Precise evaluation of thermal response functions by optimized density matrix renormalization group schemes, New J. Phys. **15**, 073010 (2013).
[114] C. Karrasch, J. H. Bardarson, and J. E. Moore, Reducing the numerical effort of finite-temperature density matrix renormalization group calculations, New J. Phys. **15**, 083031 (2013).
[115] D. Kennes and C. Karrasch, Extending the range of real time density matrix renormalization group simulations, Comput. Phys. Commun. **200**, 37 (2016).
[116] J. Hauschild, E. Leviatan, J. H. Bardarson, E. Altman, M. P. Zaletel, and F. Pollmann, Finding purifications with minimal entanglement, Phys. Rev. B **98**, 235163 (2018).
[117] S. R. White, Minimally Entangled Typical Quantum States at Finite Temperature, Phys. Rev. Lett. **102**, 190601 (2009).
[118] E. M. Stoudenmire and S. R. White, Minimally entangled typical thermal state algorithms, New J. Phys. **12**, 055026 (2010).
[119] B. Bruognolo, Z. Zhenyue, S. R. White, and E. M. Stoudenmire, Matrix product state techniques for two-dimensional systems at finite temperature, arXiv:1705.05578.
[120] A. Nocera and G. Alvarez, Symmetry-conserving purification of quantum states within the density matrix renormalization group, Phys. Rev. B **93**, 045137 (2016).
[121] C.-M. Chung and U. Schollwöck, Minimally entangled typical thermal states with auxiliary matrix-product-state bases, arXiv:1910.03329.
[122] J. Chen and E. M. Stoudenmire, Hybrid purification and sampling approach for thermal quantum systems, Phys. Rev. B **101**, 195119 (2020).
[123] T. Barthel, Matrix product purifications for canonical ensembles and quantum number distributions, Phys. Rev. B **94**, 115157 (2016).
[124] R. Orús, Advances on tensor network theory: symmetries, fermions, entanglement, and holography, Eur. Phys. J. B **87**, 280 (2014).
[125] S. R. White and I. Affleck, Spectral function for the $S = 1$ Heisenberg antiferromagnetic chain, Phys. Rev. B **77**, 134437 (2008).
[126] P. P. Vaidyanathan, *The Theory of Linear Prediction, Synthesis Lectures on Engineering Series* (Morgan & Claypool, Pasadena, 2008).
[127] ITensor Library (version 3.1.0) http://itensor.org.
[128] J. Jaklič and P. Prelovšek, Finite-temperature properties of doped antiferromagnets, Adv. Phys. **49**, 1 (2000).
[129] P. Prelovšek and J. Bonča, *Ground State and Finite Temperature Lanczos Methods, Ground State and Finite Temperature Lanczos Methods* (Springer Berlin Heidelberg, Berlin, Heidelberg, 2013), pp. 1–30.
[130] B. S. Shastry and B. Sutherland, Twisted Boundary Conditions and Effective Mass in Heisenberg-Ising and Hubbard Rings, Phys. Rev. Lett. **65**, 243 (1990).
[131] D. Poilblanc, Twisted boundary conditions in cluster calculations of the optical conductivity in two-dimensional lattice models, Phys. Rev. B **44**, 9562 (1991).
[132] J. Bonča and P. Prelovšek, Thermodynamics of the planar Hubbard model, Phys. Rev. B **67**, 085103 (2003).
[133] S. Ciuchi, F. de Pasquale, S. Fratini, and D. Feinberg, Dynamical mean-field theory of the small polaron, Phys. Rev. B **56**, 4494 (1997).
[134] R. T. Scalettar, N. E. Bickers, and D. J. Scalapino, Competition of pairing and Peierls–charge-density-wave correlations in a two-dimensional electron-phonon model, Phys. Rev. B **40**, 197 (1989).
[135] G. Levine and W. P. Su, Finite-cluster study of superconductivity in the two-dimensional molecular-crystal model, Phys. Rev. B **43**, 10413 (1991).
[136] M. Weber and M. Hohenadler, Two-dimensional Holstein-Hubbard model: Critical temperature, Ising universality, and bipolaron liquid, Phys. Rev. B **98**, 085405 (2018).

[137] Y. Wang, M. Claassen, C. D. Pemmaraju, C. Jia, B. Moritz, and T. P. Devereaux, Theoretical understanding of photon spectroscopies in correlated materials in and out of equilibrium, Nat. Rev. Mater. **3**, 312 (2018).

[138] B. Lau, M. Berciu, and G. A. Sawatzky, Single-polaron properties of the one-dimensional breathing-mode Hamiltonian, Phys. Rev. B **76**, 174305 (2007).

[139] G. L. Goodvin, M. Berciu, and G. A. Sawatzky, Green's function of the Holstein polaron, Phys. Rev. B **74**, 245104 (2006).

[140] M. Berciu and G. L. Goodvin, Systematic improvement of the momentum average approximation for the Green's function of a Holstein polaron, Phys. Rev. B **76**, 165109 (2007).

[141] S. Paeckel, B. Fauseweh, A. Osterkorn, T. Köhler, D. Manske, and S. R. Manmana, Detecting superconductivity out of equilibrium, Phys. Rev. B **101**, 180507 (2020).

[142] M. Binder and T. Barthel, Minimally entangled typical thermal states versus matrix product purifications for the simulation of equilibrium states and time evolution, Phys. Rev. B **92**, 125119 (2015).

[143] S. Goto and I. Danshita, Quasiexact Kondo Dynamics of Fermionic Alkaline-Earth-Like Atoms at Finite Temperatures, Phys. Rev. Lett. **123**, 143002 (2019).

[144] S. Agasti, Simulation of matrix product states for dissipation and thermalization dynamics of open quantum systems, J. Phys. Commun. **4**, 015002 (2020).

[145] J. Haegeman, J. I. Cirac, T. J. Osborne, I. Pižorn, H. Verschelde, and F. Verstraete, Time-Dependent Variational Principle for Quantum Lattices, Phys. Rev. Lett. **107**, 070601 (2011).

[146] J. Haegeman, C. Lubich, I. Oseledets, B. Vandereycken, and F. Verstraete, Unifying time evolution and optimization with matrix product states, Phys. Rev. B **94**, 165116 (2016).

[147] M. Yang and S. R. White, Time-dependent variational principle with ancillary Krylov subspace, Phys. Rev. B **102**, 094315 (2020).

[148] B. Kloss, D. R. Reichman, and R. Tempelaar, Multiset Matrix Product State Calculations Reveal Mobile Franck-Condon Excitations under Strong Holstein-type Coupling, Phys. Rev. Lett. **123**, 126601 (2019).

[149] P. Secular, N. Gourianov, M. Lubasch, S. Dolgov, S. R. Clark, and D. Jaksch, Parallel time-dependent variational principle algorithm for matrix product states, Phys. Rev. B **101**, 235123 (2020).

[150] Y. Murakami, P. Werner, N. Tsuji, and H. Aoki, Interaction quench in the Holstein model: Thermalization crossover from electron- to phonon-dominated relaxation, Phys. Rev. B **91**, 045128 (2015).

[151] N. Das and N. Singh, Hot-electron relaxation in metals within the Götze-Wölfle memory function formalism, Int. J. Mod. Phys. B **30**, 1650071 (2016).

[152] S. Ono, Thermalization in simple metals: Role of electron-phonon and phonon-phonon scattering, Phys. Rev. B **97**, 054310 (2018).

[153] J. R. Mannouch, W. Barford, and S. Al-Assam, Ultra-fast relaxation, decoherence, and localization of photoexcited states in π-conjugated polymers, J. Chem. Phys. **148**, 034901 (2018).

[154] J. Kogoj, L. Vidmar, M. Mierzejewski, S. A. Trugman, and J. Bonča, Thermalization after photoexcitation from the perspective of optical spectroscopy, Phys. Rev. B **94**, 014304 (2016).

[155] M. Galperin, M. A. Ratner, and A. Nitzan, Molecular transport junctions: vibrational effects, J. Phys.: Condens. Matter **19**, 103201 (2007).

[156] E. A. Osorio, T. Bjørnholm, J.-M. Lehn, M. Ruben, and H. S. J. van der Zant, Single-molecule transport in three-terminal devices, J. Phys.: Condens. Matter **20**, 374121 (2008).

[157] T. Koch, J. Loos, A. Alvermann, A. R. Bishop, and H. Fehske, Transport through a vibrating quantum dot: Polaronic effects, J. Phys. Conf. Ser. **220**, 012014 (2010).

[158] N. A. Zimbovskaya and M. R. Pederson, Electron transport through molecular junctions, Phys. Rep. **509**, 1 (2011).

[159] A. Khedri, T. A. Costi, and V. Meden, Nonequilibrium thermoelectric transport through vibrating molecular quantum dots, Phys. Rev. B **98**, 195138 (2018).

[160] A. Dey and S. Yarlagadda, Temperature dependence of long coherence times of oxide charge qubits, Sci. Rep. **8**, 3487 (2018).

[161] W. Westhäuser, S. Schramm, J. Hoffmann, and C. Jooss, Comparative study of magnetic and electric field induced insulator-metal-transitions in $Pr_{1-x}Ca_xMnO_3$ films, Eur. Phys. J. B **53**, 323 (2006).

[162] Y. M. Sheu, S. A. Trugman, L. Yan, J. Qi, Q. X. Jia, A. J. Taylor, and R. P. Prasankumar, Polaronic Transport Induced by Competing Interfacial Magnetic Order in a $La_{0.7}Ca_{0.3}MnO_3/BiFeO_3$ Heterostructure, Phys. Rev. X **4**, 021001 (2014).

[163] D. Raiser, S. Mildner, B. Ifland, M. Sotoudeh, P. Blöchl, S. Techert, and C. Jooss, Evolution of hot polaron states with a nanosecond lifetime in a manganite perovskite, Adv. Energy Mater. **7**, 1602174 (2017).

[164] M. Sotoudeh, S. Rajpurohit, P. Blöchl, D. Mierwaldt, J. Norpoth, V. Roddatis, S. Mildner, B. Kressdorf, B. Ifland, and C. Jooss, Electronic structure of $Pr_{1-x}Ca_xMnO_3$, Phys. Rev. B **95**, 235150 (2017).

[165] M. Eckstein and M. Kollar, Measuring correlated electron dynamics with time-resolved photoemission spectroscopy, Phys. Rev. B **78**, 245113 (2008).

[166] M. Ligges, I. Avigo, D. Golež, H. U. R. Strand, Y. Beyazit, K. Hanff, F. Diekmann, L. Stojchevska, M. Kalläne, P. Zhou, K. Rossnagel, M. Eckstein, P. Werner, and U. Bovensiepen, Ultrafast Doublon Dynamics in Photoexcited $1T$-TaS_2, Phys. Rev. Lett. **120**, 166401 (2018).

[167] J. J. Mendoza-Arenas, D. F. Rojas-Gamboa, M. B. Plenio, and J. Prior, Exciton transport enhancement across quantum Su-Schrieffer-Heeger lattices with quartic nonlinearity, Phys. Rev. B **100**, 104307 (2019).

[168] J. H. Fetherolf, D. Golež, and T. C. Berkelbach, A Unification of the Holstein Polaron and Dynamic Disorder Pictures of Charge Transport in Organic Crystals, Phys. Rev. X **10**, 021062 (2020).

[169] I. G. Lang and Y. A. Firsov, Kinetic theory of semiconductors with low mobility, ZhETF **43**, 1843 (1963) [Sov. Phys. JETP **16**, 1301 (1963)].

[170] C. Brockt, Numerical study of the nonequilibrium dynamics of 1-D electron-phonon systems using a local basis optimization, Ph.D. thesis, Leibniz Universität Hannover, 2018.

[171] P. E. Kornilovitch, Photoemission spectroscopy and sum rules in dilute electron-phonon systems, EPL **59**, 735 (2002).

Chapter 5

Optical conductivity and energy transport coefficients

In the last chapter, I presented results that demonstrate how local basis optimization (LBO) together with time-dependent density-matrix renormalization group (tDMRG) methods can be used to calculate thermodynamics and spectral functions for the Holstein polaron model. In this chapter, I will show that by combining LBO and purification with time-dependent variational principle (TDVP) algorithms, the range of applications can be extended to more complicated systems and observables.

Here, I will study time-dependent charge and energy current-current correlation functions. These quantities contain an additional layer of numerical complexity compared to the Green's functions studied in Ch. 4, since the charge current couples neighboring sites, and the energy current couples next-nearest neighboring sites and phononic to electronic degrees of freedom.

Section 5.1 contains a publication where we extract the real part of the optical conductivity at finite temperatures from charge current-current correlation functions for the Holstein polaron and bipolaron when the phonons have a finite bandwidth. Furthermore, we analyze the spectrum in the strong-coupling electron-phonon interaction regime using the Born-Oppenheimer surfaces introduced in Ch. 2. In Sec. 5.3, I will demonstrate that this formalism can also be used to interpret the spectrum of bound bipolarons when accounting for electron-electron interaction (Holstein-Hubbard model). Finally, in Sec. 5.4, I will present results for the optical conductivity and energy transport coefficients at finite frequencies for the Holstein model at filling $n = 1/3$ and $n \approx 1/2$.

5.1 Finite-temperature optical conductivity

So far, the discussion has been on the spectral functions, but alternatively, one can also study the optical absorption spectra of materials. This can also provide a lot of information about their underlying microscopic structure. In the context of polarons, it allows distinguishing between small and large polarons and identifying the reduced mass of the

quasi-particle [6,103,104]. It has also contributed significantly to our understanding of the role small polarons have in manganites and how they are effected by changes in temperature, see, e.g., Refs. [24,25,28,31,255]. One example is given in Ref. [31]. There, Mildner et al. could detect an absorption spectra characteristic to small polarons in the near infrared region. By using quasi-classical small polaron theory to analyze their results, the authors were able to demonstrate both the power and the limitations of the approach.

There has also been much theoretical work on the optical conductivity of polarons [10,49,51,56,58,67,72,256–258]. These studies have utilized a variety of numerical methods [50,51,56,58,72,256,257] and analytical tools [10,49,58]. Nonetheless, research into the temperature dependence of the spectrum for Holstein polarons has been restricted to analytical calculations in certain limits, exact diagonalization, or dynamic mean field theory [10,49,56,58].

In the results presented here, we extend the previous studies on optical conductivity in the following way: We utilize the matrix-product state purification scheme introduced in Ch. 3 to calculate the optical conductivity of the Holstein polaron and bipolaron at different temperatures in different parameter regimes. Inspired by recent work which has pointed out the interesting effects a finite phonon bandwidth can have on the properties of the Holstein model [67,91,92,235], we also include a phonon hopping term in the Hamiltonian, see Ch. 2.

To achieve this, we combine TDVP [135,136] with LBO [151] for the imaginary time-evolution and use a parallel TDVP-LBO algorithm for the real-time evolution. The parallel implementation is based on Refs. [165, 166]. We also derive a formula for the optical conductivity in the strong coupling regime based on the Born-Oppenheimer Hamiltonian in Ch. 2 (the full derivation is given in Appendix C.2). This formula works for both polarons and bipolarons and takes the effects of the finite phonon bandwidth into account.

For the polaron, we find that a finite phonon bandwidth either makes the different phonon emission peaks in the optical conductivity merge or become more easily distinguishable. The effect, already reported in Ref. [67], depends on whether the phonons have an upwards (cosine with a maximum at large quasi-momenta) or a downwards (cosine with a maximum at small quasi-momenta) dispersion relation. When temperature is increased, the spectral width of the one-phonon emission peak gets enhanced and shifted to smaller frequencies. This effect can be seen for all phonon-emission peaks for intermediate electron-phonon coupling. For intermediate electron-phonon coupling for the bipolaron, we observe that the optical conductivity changes significantly compared to the polaron spectrum and report a thermally activated resonance at a frequency below the phonon frequency ω_0. In the strong coupling regime, we find that a finite phonon bandwidth shifts the center of the spectrum to higher or lower frequencies, depending on the sign of the phonon hopping amplitude. This holds for both the polaron and bipolaron.

In Sec. 5.3, we extend the analysis based on the Born-Oppenheimer surfaces to include electron-electron interation, and in Sec. 5.4, we study both optical conductivity and the energy transport coefficient at finite filling. Other interesting continuations of our work could focus on the experimental distinction between Holstein type and Peierls type bipolarons. The latter was recently addressed as a possible mechanism for high-temperature

super conductivity [38]. Further applications of the methods presented here could be to compute out-of equilibrium quantities [259–262].

5.2 Publication: Finite-temperature optical conductivity with density-matrix renormalization group methods for the Holstein polaron and bipolaron with dispersive phonons

Reprinted article with permission from
David Jansen, Janez Bonča, and Fabian Heidrich-Meisner
Phys. Rev. B 106, 155129 (2022)
https://link.aps.org/doi/10.1103/PhysRevB.106.155129

Author contributions: D. J. wrote the manuscript, implemented the algorithm, produced the data, and derived the analytical results. F. H.-M. had the idea to study the optical conductivity with the previously developed methods. J. B. did the Lanczos calculations, suggested adding phonon dispersion to the model, and suggested to study the bipolaron. J. B. also had the idea to derive the analytical formula with a finite phonon hopping. F. H.-M. and J. B. also revised the manuscript. All authors contributed to interpreting the results and discussed the data.

Finite-temperature optical conductivity with density-matrix renormalization group methods for the Holstein polaron and bipolaron with dispersive phonons

David Jansen,[1] Janez Bonča,[2,3] and Fabian Heidrich-Meisner[1]
[1]*Institut für Theoretische Physik, Georg-August-Universität Göttingen, D-37077 Göttingen, Germany*
[2]*J. Stefan Institute, 1000 Ljubljana, Slovenia*
[3]*Faculty of Mathematics and Physics, University of Ljubljana, 1000 Ljubljana, Slovenia*

(Received 6 June 2022; revised 15 August 2022; accepted 15 August 2022; published 17 October 2022)

A comprehensive picture of polaron and bipolaron physics is essential to understand the optical absorption spectrum in many materials with electron-phonon interactions. In particular, the finite-temperature properties are of interest since they play an important role in many experiments. Here, we combine the parallel two-site time-dependent variational principle algorithm (p2TDVP) with local basis optimization (LBO) and purification to calculate time-dependent current-current correlation functions. From this information, we extract the optical conductivity for the Holstein polaron and bipolaron with dispersive phonons at finite temperatures. For the polaron in the weak and intermediate electron-phonon coupling regimes, we analyze the influence of phonon dispersion relations on the spectra. For strong electron-phonon coupling, the known result of an asymmetric Gaussian is reproduced for a flat phonon band. For a finite phonon bandwidth, the center of the Gaussian is either shifted to larger or smaller frequencies, depending on the sign of the phonon hopping. We illustrate that this can be well understood by considering the Born-Oppenheimer surfaces. Similar behavior is seen for the bipolaron for strong coupling. For the bipolaron with weak and intermediate coupling strengths and a flat phonon band, we obtain two very different spectra. The latter also has a temperature-dependent resonance at a frequency below the phonon frequency.

DOI: 10.1103/PhysRevB.106.155129

I. INTRODUCTION

The interaction of an electron with lattice vibrations leads to the formation of a quasiparticle called a polaron, see, e.g., Ref. [1] for a review. Such a quasiparticle formation is of both theoretical and experimental interest since it is responsible for many material properties, e.g., in manganites [2–5], lead halide, and hybrid perovskites [6–9]. Since one way to experimentally study polaron physics is optical absorption spectroscopy, key insights into such materials can result from a better understanding of the optical excitation spectrum of these quasiparticles. These optical excitations allow for, e.g., the detection of small polarons, see, e.g., Refs. [10–12]. In several cases, theory and experiments were successfully combined to extract information about polarons in manganites, see, e.g., Refs. [10,12–14].

Experiments are inevitably conducted at finite temperatures. This calls for a comprehensive understanding of the temperature dependence of the polaron optical conductivity. For example, in Ref. [15], absorption spectra were used to investigate films of doped manganites by decreasing temperature, with a transition from a paramagnetic into a ferromagnetic phase. This led to the detection of a transition from small to large polarons. Furthermore, recent theoretical work has pointed out the importance of bipolaron formation for high-temperature superconductivity [16] and the experiments conducted in Ref. [17] emphasize the role of bipolarons in the pseudogap formation in the quasi-one-dimensional material $(TaSe_4)2I$.

An prototype microscopic model, capturing the interaction between electrons and optical phonons, is the Holstein model [18]. This model consists of electrons which can move around and interact with local harmonic oscillators. Despite its apparent simplicity, the Holstein model captures essential elements of both single polaron and bipolaron physics. Further, it also exhibits a transition from a charge-density wave (CDW) to a Tomanga-Luttinger liquid (TLL) at half filling in one dimension (see, e.g., Refs. [19,20] for phase diagrams). Due to their importance, the Holstein-polaron model [21–36], the Holstein model at finite filling [19,20,37–43], the Holstein-Hubbard model [44–54], and other similar systems [55–58] have been subject to intense and ongoing theoretical research.

Recent work has pointed out the effects of phonon hopping on CDW formation [59], thermalization properties of a polaron interacting with hard-core bosons [60], the polaron effective mass, the ground-state optical conductivity, and spectral functions [36,61,62]. In this work, we compute the real part of the optical conductivity for the Holstein polaron and bipolaron with dispersive optical phonons at different temperatures. We study weak, intermediate, and strong electron-phonon coupling strengths and work in the intermediate phonon frequency and electron-hopping regime. The combination of different interaction strengths together with a phonon dispersion for the polaron and bipolaron at finite temperatures extends and complements previous studies of the optical conductivity in the Holstein model, e.g., in Refs. [36,38,63–68].

The goal of this work is to characterize how the main features of small and large polarons in a Holstein-type system appear in the optical conductivity. By varying temperature and the phonon bandwidth, we extend the understanding of the basic mechanisms in such theoretical Hamiltonians, which incorporate essential physics induced by electron-phonon interaction. This constitutes an essential step in detecting such features, or lack thereof, in experimental data. Some of our key findings are that a finite phonon bandwidth shifts the center of the optical conductivity to higher or lower frequencies, depending on its shape. This holds for both the polaron and the bound bipolaron. Furthermore, the effect remains even when the temperature is increased enough to significantly alter the spectrum. For small electron-phonon coupling, the polaron-bipolaron spectrum remains similar up to a scaling factor. As the electron-phonon coupling is increased, key distinctions appear, such as a two-phonon emission maximum and a temperature-dependent resonance for the bipolaron, and a stable maximum at the one phonon emission peak for the polaron and only a weak temperature dependence on the spectrum (for the temperatures looked at here).

Computing finite-temperature transport properties of quantum systems can be a challenging task, see Ref. [69] for a review of one-dimensional systems. To compute the optical conductivity, we use a density-matrix renormalization group (DMRG) based method. DMRG [70–72] with matrix-product states (MPS) has already been extensively used to study one-dimensional systems, see, e.g., Refs. [73–81]. One drawback of DMRG is the unfavorable scaling for systems with a large local Hilbert space, as is the case for the Holstein model. For this reason, several schemes to treat these systems more efficiently have been suggested [82–85]. In Ref. [35], we successfully combined the finite-temperature method of purification [73] with tDMRG [74] and local basis optimization (LBO) [82] to compute several spectral functions of the Holstein-polaron model.

Here, we propose a scheme to combine LBO with the two-site time-dependent variational principle algorithm (TDVP) [86–88]. This method is used to conduct the imaginary-time evolution needed to obtain thermal states for weak, intermediate, and strong electron-phonon coupling in the nonadiabatic regime of the Holstein model (the phonon frequency ω_0 is close to the electron tunneling amplitude t_0, $t_0 \approx \omega_0$). We then use parallel two-site TDVP [88] with LBO (p2TDVP-LBO) to compute the real-time evolution of the current-current correlation function in the ground state for all parameters and at low temperatures in the weak and intermediate coupling regimes. For the temperature $T/\omega_0 = 1$ and a strong electron-phonon coupling, p2TDVP becomes computationally too demanding and therefore we use the single-site TDVP algorithm (without LBO) instead. We demonstrate that this combination of methods provides access to the real part of the optical conductivity $\sigma'(\omega)$. We further add phonon hopping with a hopping amplitude t_{ph}. This gives rise to the finite phonon bandwidth shown in Fig. 1. We impose $0 \leqslant |t_{\text{ph}}|/\omega_0 \ll 1$ to model optical phonons. We also compute the real part of the optical conductivity for the bipolaron for weak and intermediate coupling strengths and $t_{\text{ph}} = 0$. Lastly, we analyze the effect of different phonon dispersion relation and a strong electron-phonon coupling on $\sigma'(\omega)$ for the bipolaron.

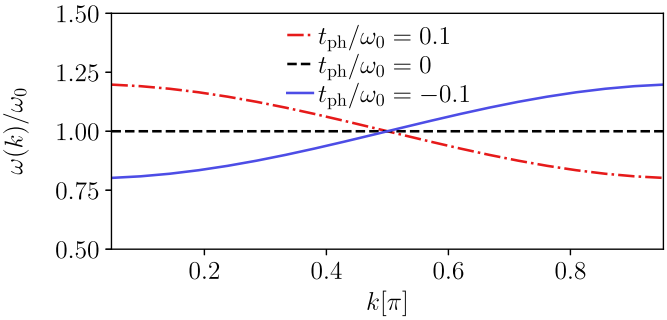

FIG. 1. Phonon dispersion relation $\omega(k)$ for optical phonons with phonon hopping, see Eq. (3). The hopping parameter is t_{ph} and the phonons have a finite bandwidth for $t_{\text{ph}} \neq 0$.

We first test our algorithm by comparing the real part of the optical conductivity with that obtained for the ground state with the Lanczos method [89,90] in the weak and intermediate electron-phonon coupling regime. We find a very good agreement. Further, we derive a formula for the real part of the optical conductivity for the Holstein model with a finite phonon bandwidth based on the Born-Oppenheimer Hamiltonian and the Born-Huang ansatz [91,92]. This formula is consistent with our numerical data for a strong electron-phonon coupling for both the polaron and the bipolaron. In particular, we observe that in this regime, the optical spectrum is similar to that of an asymmetric Gaussian and a downwards phonon dispersion relation (a cosine with a maximum at small momenta, see Fig. 1) shifts the Gaussian to higher frequencies and an upwards phonon dispersion relation (a cosine with a maximum at large momenta, see Fig. 1) shifts it to lower frequencies. Additionally, the upwards phonon dispersion relation leads to less spectral weight at low frequencies for the temperatures studied in this work. These properties hold true for both the polaron and bipolaron.

In the weak and intermediate coupling regime and for the polaron, we see, as previously reported in Ref. [36], that an upwards dispersion relation leads to a continuous spectrum, and a downwards dispersion relation leads to a sequence of distinct peaks for the ground-state optical conductivity. For a weak electron-phonon coupling strength, the maximum of the spectrum shifts to lower frequencies as the temperature is increased and the different peaks merge. In the intermediate coupling regime, we also observe a significant increase of spectral weight for low frequencies, but the peaks remain well separated for the temperatures investigated here. For the bipolaron, we compare the weak and intermediate coupling for dispersionless phonons. We only detect very small changes in the spectrum for a weak electron-phonon coupling compared to twice the single-polaron curve. At intermediate coupling strengths, however, the spectrum differs significantly and an additional large resonance peak is resolved below ω_0.

This work is structured as follows. In Sec. II, we introduce the Holstein model with dispersive phonons and the optical conductivity, and in Sec. III, we derive a formula for the optical conductivity based on the Born-Oppenheimer Hamiltonian. Section IV introduces the p2TDVP-LBO algorithm. In Sec. V, we compare our Holstein-polaron ground-state results to those obtained with the Lanczos method and analytical

calculations. Section VI treats the polaron optical conductivity, and Sec. VII covers the bipolaron, both at finite temperature. Lastly, we conclude in Sec. VIII.

II. MODEL

A. The Holstein polaron and bipolaron

We consider the Holstein model [18] with one (polaron) and two (bipolaron) electrons. The Hamiltonian is defined as

$$\hat{H} = \hat{H}_{\text{kin}} + \hat{H}_{\text{ph}} + \hat{H}_{\text{e-ph}}. \tag{1}$$

The model has L sites and we use open boundary conditions. We set $\hbar = 1$ throughout this paper. The first term, the kinetic energy of the electrons, is

$$\hat{H}_{\text{kin}} = -t_0 \sum_{j=1,s=\uparrow,\downarrow}^{L-1} (\hat{c}^\dagger_{j,s}\hat{c}_{j+1,s} + \hat{c}^\dagger_{j+1,s}\hat{c}_{j,s}), \tag{2}$$

with $\hat{c}^\dagger_{j,s}$ ($\hat{c}_{j,s}$) being the electron creation (annihilation) operator on site j with spin s and the hopping amplitude t_0. The second term is the phonon energy, consisting of the harmonic oscillator energy and phonon kinetic energy:

$$\hat{H}_{\text{ph}} = \omega_0 \sum_{j=1}^{L} \hat{b}^\dagger_j \hat{b}_j + t_{\text{ph}} \sum_{j=1}^{L-1} (\hat{b}^\dagger_j \hat{b}_{j+1} + \hat{b}^\dagger_{j+1}\hat{b}_j), \tag{3}$$

where $\hat{b}^\dagger_j$ ($\hat{b}_j$) creates (annihilates) an optical phonon on site j with frequency ω_0. The phonons have a hopping amplitude t_{ph}. In this work, we always use $t_0/\omega_0 = 1$. The Hamiltonian in Eq. (3) can be diagonalized by going into quasimomentum basis by using the Fourier transformation for open boundary conditions

$$\hat{b}_k = \sqrt{\frac{2}{L+1}} \sum_{j=1}^{L} \sin(kj)\hat{b}_j, \tag{4}$$

where $k = \pi m_k/(L+1)$ and with $1 \leqslant m_k \leqslant L$. Then,

$$\hat{H}_{\text{ph}} = \sum_{k=\pi/(L+1)}^{\pi L/(L+1)} \omega(k)\hat{b}^\dagger_k \hat{b}_k, \tag{5}$$

with $\omega(k) = \omega_0 + 2t_{\text{ph}}\cos(k)$. $\omega(k)$ is the dispersion relation for the optical phonons with a finite bandwidth for $t_{\text{ph}} \neq 0$. In this work, we aim to model optical phonons with zero or small bandwidth and choose $|t_{\text{ph}}| \ll \omega_0$. For $t_{\text{ph}} < 0 (> 0)$, we refer to the phonons as having an upward (downward) dispersion relation. In Fig. 1, we illustrate the phonon dispersion relation for the values of t_{ph}/ω_0 used here.

The final term of the Hamiltonian in Eq. (1) is the electron-phonon coupling

$$\hat{H}_{\text{e-ph}} = \gamma \sum_{j=1}^{L} \hat{n}_j (\hat{b}^\dagger_j + \hat{b}_j), \tag{6}$$

with $\hat{n}_j = \hat{c}^\dagger_{j,\uparrow}\hat{c}_{j,\uparrow} + \hat{c}^\dagger_{j,\downarrow}\hat{c}_{j,\downarrow}$, and the coupling parameter γ. Note that since we do not include electron-electron repulsion in this work, we always deal with a bound bipolaron. Furthermore, we truncate the local phonon-Hilbert space to a finite maximum phonon number M. To characterize the transition between a small and a large polaron, we introduce the dimensionless parameter

$$\lambda = N\frac{\gamma^2}{2t_0\omega_0}, \tag{7}$$

where $N = 1$ for the polaron and $N = 2$ for the bipolaron.

In order to obtain the real part of the optical conductivity, we first define the current-current correlation function as

$$C_T(t) = \langle \hat{J}(t)\hat{J}(0)\rangle_T, \tag{8}$$

where $\langle \ldots \rangle_T$ is the expectation value calculated in the canonical ensemble at temperature T. The current operator $\hat{J}$ is defined as

$$\hat{J} = it_0 \sum_{i=1,s=\uparrow,\downarrow}^{L-1} (\hat{c}^\dagger_{j,s}\hat{c}_{j+1,s} - \hat{c}^\dagger_{j+1,s}\hat{c}_{j,s}). \tag{9}$$

For calculations in the ground state $|GS\rangle$, we write $\lim_{T\to 0} C_T(t) = \lim_{T\to 0}\langle \hat{J}(t)\hat{J}(0)\rangle_T = \langle GS|\hat{J}(t)\hat{J}(0)|GS\rangle = C_{GS}(t)$. We further define its Fourier transformation as

$$C_T(\omega) = \int_{-\infty}^{\infty} e^{i\omega t} f(t) C_T(t) dt, \tag{10}$$

where $f(t)$ is a damping function ensuring a decay which we either choose to be $e^{-\eta|t|}$ or $e^{-\eta t^2}$, leading to a Lorenzian or Gaussian broadening in frequency space, respectively. In general, we obtain a higher accuracy of the moments of the correlation functions, see Appendix B, when using Gaussian broadening. Still, we will show data using Lorenzian broadening in Sec. V since this is used by the benchmark data. Furthermore, presenting results with different broadening functions demonstrates the small differences.

Our goal is to calculate the optical conductivity which can be split into real and imaginary part

$$\sigma(\omega) = \sigma'(\omega) + i\sigma''(\omega). \tag{11}$$

The imaginary part is related to the real part through the Kramers-Kronig relation [93]. The real part of $\sigma(\omega)$ can be extracted from the current-current correlation function via

$$\sigma'(\omega) = \frac{1 - e^{-\omega/T}}{2\omega} C_T(\omega). \tag{12}$$

For the ground state, we have

$$\sigma'_{T\to 0}(\omega) = \frac{1}{2\omega} C_{GS}(\omega). \tag{13}$$

III. OPTICAL CONDUCTIVITY BASED ON THE BORN-OPPENHEIMER HAMILTONIAN

An analytical formula for the optical conductivity for the Holstein polaron has been obtained in several different contexts and for different limiting cases, see, e.g., Refs. [66,94–96]. The theoretical results have been shown to fit both numerical, see, e.g., in Refs. [65,66], and experimental data, see, e.g., Refs. [10,12–14]. In this section, we obtain an expression for the real part of the optical conductivity based on the Born-Oppenheimer (BO) Hamiltonian and the Born-Huang formalism [91,92], which captures the influence of the finite phonon bandwidth for both the polaron and bipolaron. For more details, see Appendix C and Refs. [96–98].

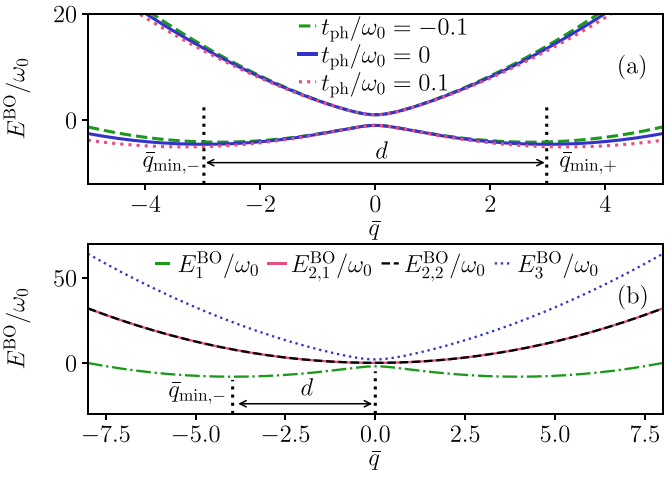

FIG. 2. Born-Oppenheimer surfaces for the polaron and bipolaron in the Holstein dimer. (a) The two polaron Born-Oppenheimer surfaces with different phonon dispersion $t_{\rm ph}/\omega_0$. We use $\gamma/\omega_0 = 3$ and $t_0/\omega_0 = 1$. (b) The four Born-Oppenheimer surfaces for the Holstein-dimer bipolaron with $\gamma/\omega_0 = 2$, $t_{\rm ph}/\omega_0 = 0$, and $t_0/\omega_0 = 1$.

We first rewrite Eq. (1) in terms of the phonon position and momentum operators, using that $\hat{b}_i = \sqrt{\frac{m\omega_0}{2}}(\hat{x}_i + \frac{i}{m\omega_0}\hat{p}_i)$ and $\hat{b}_i^\dagger = \sqrt{\frac{m\omega_0}{2}}(\hat{x}_i - \frac{i}{m\omega_0}\hat{p}_i)$. The total Hamiltonian has the form

$$\hat{H} = \hat{H}_{\rm kin} + \sum_{i=1}^{L}\left(\gamma\sqrt{\frac{m\omega_0}{2}}\hat{n}_i(2\hat{x}_i) + \frac{m\omega_0^2}{2}\left(\hat{x}_i^2 + \frac{1}{m^2\omega_0^2}\hat{p}_i^2 - \frac{1}{m\omega_0}\right)\right) + t_{\rm ph}m\omega_0\sum_{i=1}^{L-1}\left(\hat{x}_i\hat{x}_{i+1} + \frac{1}{m^2\omega_0^2}\hat{p}_i\hat{p}_{i+1}\right). \quad (14)$$

We will now consider the Holstein dimer, i.e., $L = 2$, and go to the relative and center-of-mass coordinates with $\hat{q} = \frac{1}{\sqrt{2}}(\hat{x}_1 - \hat{x}_2)$ and $\hat{Q} = \frac{1}{\sqrt{2}}(\hat{x}_1 + \hat{x}_2)$. Using the fact that the center-of-mass coordinates $\hat{Q}$ are independent of the rest of the system for constant electron density, going in the adiabatic limit of slow phonons (sending all momenta to zero) and sending $\hat{q} \to q$, we can write the Born-Oppenheimer Hamiltonian as

$$\hat{H}_{\rm BO} = \hat{H}_{\rm kin} + \gamma[\bar{q}(n_1 - n_2)] + \tfrac{1}{2}\bar{q}^2(\omega_0 - t_{\rm ph}). \quad (15)$$

Here, we have defined $\bar{q} = q\sqrt{\frac{1}{m\omega_0}}$. $\hat{H}_{\rm BO}$ is now a 2×2 and a 4×4 matrix for the polaron and bipolaron, respectively, see, e.g., Refs. [99,100]. These Hamiltonians can be diagonalized and one obtains two or four Born-Oppenheimer surfaces, where two are degenerate in the latter case. We label the surfaces $E_1^{\rm BO}$ and $E_2^{\rm BO}$ for the polaron and $E_1^{\rm BO}$, $E_{2,1}^{\rm BO} = E_{2,2}^{\rm BO}$, and $E_3^{\rm BO}$ for the bipolaron. The polaron and bipolaron surfaces are shown in Figs. 2(a) and 2(b) for some of the parameters used later in this work. The lowest surface has two minima which differ by a sign. We refer to these as $\bar{q}_{\rm min,\pm}$. The current operator from Eq. (9) can connect the states in the lowest and first excited surface while leaving the phonon configuration

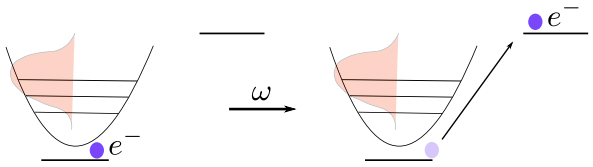

FIG. 3. Illustration of the Franck-Condon excitation, which is the process leading to Eq. (16). The electron is localized on one site in a potential due to the coupling to the phonons (illustrated by the shaded Gauss shape in the harmonic oscillator). Shining light with frequency $\omega = 2E_p$ will lead to the electron escaping the potential generated by the phonons and moving to the next site. During this process, the phonon configuration remains unchanged. This corresponds to a diagonal transition from the lower to the upper Born-Oppenheimer surface in Fig. 2(a).

invariant. This process, also known as a Franck-Condon excitation, is illustrated in Fig. 3 and corresponds to a vertical transition into the next surface at a fixed $\bar{q}$. When $|\bar{q}_{\rm min,\pm}|$ is large, this can be approximated as a transition between two harmonic oscillator potentials separated by a distance d and with an energy shift Δ_E. This leads to

$$\sigma_{SC}(\omega) = N\frac{1-e^{-\omega/T}}{\omega}t_0^2\sqrt{\frac{4\pi}{d^2\coth\left(\frac{\tilde{\omega}_0}{2T}\right)\tilde{\omega}_0^2}} \times e^{-\left(\Delta_E + \frac{d^2\tilde{\omega}_0}{2} - \omega\right)^2 \Big/ \left(d^2\tilde{\omega}_0^2\coth\left(\frac{\tilde{\omega}_0}{2T}\right)\right)}. \quad (16)$$

Here, we set $\tilde{\omega}_0 = \omega_0 - t_{\rm ph}$. For the Holstein polaron, $d = 2\bar{q}_{\rm min}$ and $\Delta_E = 0$. For the Holstein bipolaron, we have $d = \bar{q}_{\rm min}$ and $\Delta_E = E_1^{\rm BO}(\bar{q}_{\rm min})$, as illustrated in Fig. 2. Note that Eq. (16) is an asymmetric Gaussian around $\Delta_E + d^2\tilde{\omega}_0$ which is the energy difference between the lowest and the first excited Born-Oppenheimer surface. For the polaron, everything can be solved analytically and one gets $\bar{q}_{\rm min,\pm} = \pm\frac{\sqrt{\gamma^4 - \tilde{\omega}_0^2 t_0^2}}{\tilde{\omega}_0\gamma}$. For the bipolaron, we obtain the Born-Oppenheimer surfaces numerically. In the case of the polaron, with $T \to 0$, $\gamma \gg t_0$ and $t_{\rm ph} = 0$, we have $\bar{q}_{\rm min,\pm} = \pm\frac{\gamma}{\omega_0}$ and

$$\sigma_{SC}(\omega) = \frac{t_0^2}{\omega}\sqrt{\frac{\pi}{\frac{\gamma^2}{\omega_0}\omega_0}}e^{-\left(2\frac{\gamma^2}{\omega_0} - \omega\right)^2 \Big/ \left(4\frac{\gamma^2}{\omega_0}\omega_0\right)} = \frac{t_0^2}{\omega}\sqrt{\frac{\pi}{E_P\omega_0}}e^{-(2E_P-\omega)^2/(4E_P\omega_0)}, \quad (17)$$

which is the well-known result of an asymmetric Gaussian around twice the polaron binding energy $E_P = \gamma^2/\omega_0$.

IV. METHODS

There have already been many applications utilizing the matrix-product state formalism for finite temperature calculations, see, e.g., Refs. [73,77–80,101,102]. In this work, we use purification [73,77,78,80,103]. In this scheme, one simulates the thermal density matrix of the system by introducing ancillary sites, thus doubling it. The density matrix at the desired temperature T can then be obtained by starting with the infinite-temperature state, imaginary time evolving it to the inverse temperature $1/(2T)$ and then tracing out the ancillary sites. In other words, one obtains the thermal state

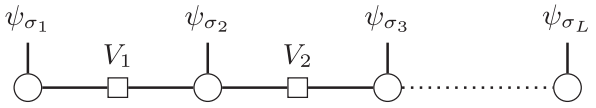

FIG. 4. Matrix-product state in the inverse canonical form.

living in the physical and ancillary Hilbert spaces, H_P and H_A, respectively, i.e., $|\psi_T\rangle \in H_P \otimes H_A$. The thermal expectation value of an observable $\hat{O}$ acting on a state in H_P is given by $\langle\hat{O}\rangle_T = \langle\psi_T|\hat{O}|\psi_T\rangle$. The state $|\psi_\infty\rangle$ can often be obtained either analytically or by finding the ground state of a suitable Hamiltonian [104], and $|\psi_T\rangle$ can be calculated by conducting imaginary time evolution on $|\psi_\infty\rangle$. Note that even though the infinite-temperature state is artificial for our implementation of the Holstein model due to the finite phonon truncation M, this method still captures the correct low-temperature physics, see Ref. [35]. There, a detailed description of how to obtain $|\psi_\infty\rangle$ for the Holstein polaron model is also given.

To obtain the time-dependent correlation functions from Eq. (8), one needs to carry out a real-time evolution after the imaginary-time evolution. The real-time evolution is, however, not carried out on $|\psi_T\rangle$, but rather on the state $|\phi_T\rangle$, which is obtained by acting on the thermal states $|\psi_T\rangle$ with the current operator $\hat{J}$, $|\phi_T\rangle = \hat{J}|\psi_T\rangle$. The real-time evolution of $|\phi_T\rangle$ is the computationally most costly part of our procedure.

There are several ways to time evolve matrix-product states, see Ref. [81] for a review, including the time-evolution block decimation (TEBD) algorithm, see Ref. [76], which also has a parallel implementation [105], and the time-dependent variational principle (TDVP) algorithm, see, e.g., Refs. [86,87,106–109]. In this work, we use the single-site TDVP, the two-site TDVP, and the parallel two-site TDVP (p2TDVP) algorithms introduced in Ref. [88]. We tailor the latter two specifically for electron-phonon systems with local basis optimization (LBO) [82]. Since the single-site and two-site TDVP are standard in the literature [81,86,87], we will, in Sec. IV A, only review the key ideas of parallelization of the two-site TDVP, and focus on how we incorporate LBO into the algorithm. We emphasize that the main idea of the parallelization of TDVP is based on the parallel ground-state DMRG (pDMRG) method introduced by Stoudenmire and White in Ref. [110] and that both the pDMRG and the pTDVP algorithms are described comprehensively in Refs. [110] and [88], respectively.

A. Parallel two-site time-dependent variational principle

For both pDMRG and p2TDVP, the first step is to bring the matrix-product state into the inverse canonical-gauge form

$$|\psi\rangle = \sum_{\vec{\sigma}} \psi_{\sigma_1} V_1 \psi_{\sigma_2} V_2 \dots V_{L-1} \psi_{\sigma_L} |\vec{\sigma}\rangle\,. \tag{18}$$

Here, for a clearer notation, we will not write the bond indices unless they are specifically needed, and $|\vec{\sigma}\rangle = |\sigma_1, \sigma_2, \dots, \sigma_L\rangle$, with σ_l being the physical state on site l. The state is depicted in Fig. 4. For the Holstein polaron model, $|\sigma_l\rangle$ consists of the local electron and phonon state $|\sigma_l\rangle = |n_e, n_{ph}\rangle$, with $n_e = \{0, 1\}$ and $n_{ph} = \{0, \dots, M\}$.

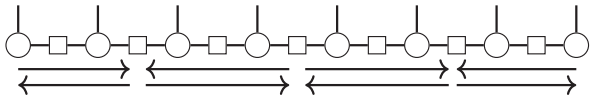

FIG. 5. Sweeping scheme of the pTDVP and pDMRG algorithms. One process starts sweeping either to the left or to the right as indicated by the arrows. At each contact point, the local tensors are shared and one process performs the sweeping step at the boundary. The resulting local tensor is then transported to its corresponding process and the sweeping is then continued in the opposite direction. In this example, the program would run on 4 processes.

Equation (18) can easily be obtained from the state in the canonical gauge [76,111]

$$|\psi\rangle = \sum_{\vec{\sigma}} \Gamma_{\sigma_1} \Lambda_1 \Gamma_{\sigma_2} \Lambda_2 \dots \Lambda_{L-1} \Gamma_{\sigma_L} |\vec{\sigma}\rangle\,, \tag{19}$$

by inserting $V_j \Lambda_j = \mathbb{1}$ and defining $\psi_{\sigma_j} = \Lambda_{j-1} \Gamma_{\sigma_j} \Lambda_j$. The key ingredient of pDMRG is to partition the wave function from Eq. (18) onto several processes which each do their DMRG sweep and only communicate when the respective processes reach their corresponding boundaries. To make this as efficient as possible, one lets two processes start sweeping in different directions and communicate upon return. The scheme is sketched in Fig. 5.

The serial TDVP algorithm can be formulated similarly as DMRG, but by solving local time-dependent equations. For each update, here illustrated for the left-to-right sweep, one proceeds by first computing $\theta_{\alpha\beta} = \psi_{\sigma_i} V_i \psi_{\sigma_{i+1}}$, where the index α (β) contains the local degree of freedom σ_i (σ_{i+1}) and the left (right) bond m_l (m_r), i.e., $\alpha = (\sigma_i, m_l)$ and $\beta = (\sigma_{i+1}, m_r)$. The tensor $\theta_{\alpha\beta}$ is updated by solving the equation

$$\dot{\theta}_{\alpha\beta}(t) = \sum_{\alpha',\beta'} -i\frac{dt}{2} H^{\text{eff}}_{\alpha\beta\alpha'\beta'} \theta_{\alpha'\beta'}(t), \tag{20}$$

where $H^{\text{eff}}_{\alpha\beta\alpha'\beta'}$ is the effective two-site Hamiltonian, calculated by contracting the rest of the matrix-product state with the matrix-product operator Hamiltonian, see e.g., Refs. [72,81,88] for details. Equation (20) has the solution

$$\theta_{\alpha\beta}\left(t + \frac{dt}{2}\right) = \sum_{\alpha',\beta'} e^{-i\frac{dt}{2} H^{\text{eff}}_{\alpha\beta\alpha'\beta'}} \theta_{\alpha'\beta'}(t). \tag{21}$$

Consecutively, a singular value decomposition (SVD) is performed on the updated $\theta_{\alpha\beta} = A_{m_l\sigma_i} \Lambda_i B_{\sigma_{i+1}m_r}$ and $V_i \Lambda_i$ is inserted. We then write $\psi_{\sigma_i} = A_{m_l\sigma_i} \Lambda_i$ and $\psi_{\sigma_{i+1}} = \Lambda_i B_{\sigma_{i+1}m_r}$. For the discussion of the local basis optimization in the algorithm, we refer to solving Eq. (20) as step one and the following SVD as step two. Lastly, the effective one-site Hamiltonian $H^{\text{eff}}_{\gamma\gamma'}$ for site $j+1$ is computed and ψ_γ is evolved backwards in time by solving

$$\psi_\gamma(t) = \sum_{\gamma'} e^{+i\frac{dt}{2} H^{\text{eff}}_{\gamma\gamma'}} \psi_{\gamma'}\left(t + \frac{dt}{2}\right), \tag{22}$$

where we wrote all indices of $\psi_{\sigma_{i+1}}$ as γ for brevity. The same process is then repeated for sites $i+1$ and $i+2$. Similar to pDMRG, one can partition the system for p2TDVP. We illustrate this in Fig. 5. This is done under the assumption that the inverse canonical form is approximately preserved

for small dt. Thereafter, one assigns each partition to an individual process together with the corresponding effective Hamiltonian. For the truncation in the SVDs, we discard all singular values such that

$$\sum_{\text{discarded }\eta} s_\eta^2 / \left(\sum_{\text{all }\eta} s_\eta^2 \right) < \epsilon_{\text{bond}}. \tag{23}$$

B. Local basis optimization

We now discuss how we incorporate the local basis optimization in the 2TDVP algorithm. This procedure is independent of whether the 2TDVP is run serially or in parallel. The idea of LBO [82] is to find a so-called optimal basis in which the state can be represented efficiently and truncated with a negligible error. LBO has already been used in many applications, see, e.g., Refs. [31,35,38,41,43,112,113]. To obtain the transformation matrices into an optimal basis, one first computes the reduced density matrix from, in our algorithm, the two-site tensor

$$\rho_{\sigma_i \sigma_i'} = (\theta \theta^\dagger)_{\sigma_i \sigma_i'}, \tag{24}$$

where all remaining indices have been contracted. $\rho_{\sigma_i \sigma_i'}$ is then diagonalized

$$\rho = R^\dagger W R. \tag{25}$$

The matrix R transforms the site from the physical basis σ_i to the optimal basis $\tilde{\sigma}_i$ and W is a diagonal matrix with the values w_α. The truncation of the optimal basis from the local dimension d into the dimension d_{LBO} is done based on the magnitude of the eigenvalues w_α, which, in many cases, decay exponentially, see, e.g., Refs. [30,43]. When diagonalizing the reduced density matrices in Eq. (24) to obtain the optimal basis, the smallest eigenvalues w_α are discarded such that the truncation error is below a threshold:

$$\sum_{\text{discarded }\eta} w_\eta / \left(\sum_{\text{all }\eta} w_\eta \right) < \epsilon_{\text{LBO}}. \tag{26}$$

There are two costly operations where a transformation of the physical index to an optimal basis can be beneficial. The most costly operation of the algorithm is the contraction of the effective Hamiltonian $H^{\text{eff}}_{\alpha\beta\alpha'\beta'}$ with the local tensor $\theta_{\alpha'\beta'}$ needed to solve Eq. (20) in step one. This has a cost of order $\mathcal{O}(d^3 m^2 D^2 + d^2 m D^3)$, where m is the bond dimension of the Hamiltonian and D the bond dimension of the state. We solve Eq. (20) with a fourth-order Runge-Kutta algorithm (RK4), see, e.g., Ref. [114] for an application of RK in the context of DMRG.

The RK4 algorithm consists of approximating $\theta_{\alpha\beta}(t + \frac{dt}{2})$ as

$$\theta_{\alpha\beta}\left(t + \frac{dt}{2}\right) = \theta_{\alpha\beta}(t) + \frac{-idt}{2} \frac{1}{6} \left(k^1_{\alpha\beta} + 2k^2_{\alpha\beta} + 2k^3_{\alpha\beta} + k^4_{\alpha\beta}\right), \tag{27}$$

where for each k^j, we must contract the effective Hamiltonian with a two-site tensor. To incorporate LBO into the algorithm (RK4-LBO), we first obtain the transformation matrices into the local optimal basis states $\tilde{\sigma}_i$ and $\tilde{\sigma}_{i+1}$ from $\theta_{\alpha\beta}$ as previously explained. We then transform the two sites of the effective Hamiltonian and $\theta_{\alpha\beta}$ into this new basis, $H^{\text{eff}}_{\alpha\beta\tilde{\alpha}\tilde{\beta}}$ and $\theta_{\tilde{\alpha}\tilde{\beta}}$, where $\tilde{\alpha} = (\tilde{\sigma}_i, m_l)$. Then, we compute

$$k^1_{\alpha\beta} = \sum_{\tilde{\alpha}'\tilde{\beta}'} H^{\text{eff}}_{\alpha\beta\tilde{\alpha}'\tilde{\beta}'} \theta_{\tilde{\alpha}'\tilde{\beta}'}(t). \tag{28}$$

We proceed by calculating

$$k^2_{\alpha\beta} = \sum_{\tilde{\alpha}'\tilde{\beta}'} H^{\text{eff}}_{\alpha\beta\tilde{\alpha}'\tilde{\beta}'} \left(\theta(t) + \frac{-idt}{2} \frac{1}{2} k^1 \right)_{\tilde{\alpha}'\tilde{\beta}'}, \tag{29}$$

but now $\tilde{\alpha}$ and $\tilde{\beta}$ are the optimal basis states extracted from the tensor $(\theta(t) + \frac{-idt}{2} \frac{1}{2} k^1)_{\alpha\beta}$. A similar procedure is used to obtain k^3 and k^4. One first adds the needed tensors and then obtains the new optimal basis states before contracting with the environment. Note that it is not ensured that one gains a computational benefit from the algorithm. As mentioned earlier, one must first create the reduced density matrices at a cost of order $\mathcal{O}(D^2 d^3)$, diagonalize them at a cost of order $\mathcal{O}(d^3)$, apply the transformation matrices at a cost of order $\mathcal{O}(D^2 d^2 d_{\text{LBO}})$, and add the tensors at a cost of order $\mathcal{O}(D^2 d^2)$ to get a cost for the contraction of order $\mathcal{O}(d^2 d_{\text{LBO}} m^2 D^2 + d^2 m D^3)$. In practice, however, we find this scheme to lead to a computational speed-up in many situations, compared to only implementing step two. This is also due to the additional benefit of the optimal basis on the many subleading tensor contractions.

A common approach to solve Eq. (20) is to use a Krylov method. While the RK4 algorithm is nonunitary, we also compare some of our data to that obtained using a Krylov solver without LBO and the tDMRG-LBO time-evolution algorithm used in Ref. [35]. The error appears to be negligible in the cases studied here. A comparison and discussion of the different algorithms are contained in Appendix A. Alternatively, one could also apply the local basis transformation when using a Krylov solver, thus needing to find the optimal basis for each Krylov vector. In our tests, this seems to require more optimal basis states than the RK4 scheme. This is addressed in Appendix A as well.

To implement the LBO before the SVD in step two, all one needs to do is to get the local basis of $\theta_{\alpha\beta}(t + \frac{dt}{2})$, then transform the tensor into $\theta_{\tilde{\alpha}\tilde{\beta}}(t + \frac{dt}{2})$, and carry out the singular value decomposition before transforming the tensor back to the bare basis. This step has the cost $\mathcal{O}(d^3 + D^2 d^3)$, but the cost of the SVD becomes of the order $\mathcal{O}(D^3 d^3_{\text{LBO}})$.

In our experience, only implementing step two alone is sufficient to gain a significant computational speed up. This can easily be incorporated into ground-state DMRG algorithms as well. A discussion of the number of local states needed is presented in Appendix A.

For the imaginary-time evolution used to obtain all the thermal states in this work, we only implement step two and use a Krylov solver for the local differential equations in Eq. (20). Our reason is that the imaginary-time evolution is less costly, and RK4 is unstable in our calculations for all but very small imaginary time steps $d\tau$. This computation is also run serially. To ensure that the low bond dimension of the initial states does not lead to a significant projection

error, we compared the states to those obtained using tDMRG for the polaron. For both the polaron and bipolaron, we also compared the states where we imaginary-time evolved using a higher bond dimension through the sub-space expansion introduced in Ref. [108]. If $|\psi_A\rangle$ and $|\psi_B\rangle$ are states obtained with different imaginary time-evolution schemes, we had $|1-\langle\psi_A|\psi_B\rangle|$ of the order of $\mathcal{O}(10^{-6})$ in all cases.

For the real-time evolution, we implement both steps one and two and refer to the algorithm as p2TDVP-LBO. Note that when carrying out the real-time evolution, we simultaneously time-evolve the part of the state in the ancillary space back in time to get a slower increase in the bond dimension [115–119]. While not an optimal procedure, see Ref. [120], this can easily be incorporated into the algorithm. We carry out the real-time evolution until $t_{\max}\omega_0$ and add $4\,t_{\max}\omega_0$ zeros to the signal for better resolution (zero padding) before the Fourier transformation. Alternatively, one can use linear prediction, see, e.g., Refs. [78,121,122], for a higher frequency resolution. We confirmed that both methods give consistent results for our data. Recently, another method for reaching longer times has been proposed [123].

For the real-time evolution, we use a time step $dt/\omega_0 = 0.01$ and for the imaginary-time evolution $d\tau/\omega_0 = 0.1$. When real-time evolving at high temperatures (here $T/\omega_0 = 1$) and in the large-coupling regime, we take advantage of the fact that the thermal states have a relatively large bond dimension (which increases further when we act with $\hat{J}$ on the state) and use a serial single-site TDVP algorithm. This is done since the bond dimension becomes unfeasible for our computational resources otherwise. Furthermore, this approach does not require the implementation of LBO for our applications, since the algorithm scales better with the local Hilbert space dimension. In this case, $\epsilon_{\text{bond},J}$ indicates the cutoff at which we truncate after applying the current operator to the thermal state. Here, convergence is monitored by changing $\epsilon_{\text{bond},J}$, even though the time-evolution scheme itself has a constant bond dimension. To make sure that small bond dimensions on some bonds do not lead to errors, we also compared the results to those obtained with a larger bond dimension by enforcing a minimum bond dimension when applying $\hat{J}$.

To further verify our results, we carefully compare the moments of the time-dependent correlation functions to their finite-temperature expectation values, see Appendix B for details. To test our algorithm, we also compare our ground-state optical conductivity to data obtained with the Lanczos method for weak and intermediate electron-phonon coupling. Furthermore, we check that our finite-temperature polaron data in the weak and intermediate electron-phonon coupling regime is consistent with those obtained with a different time-evolution method whenever possible, namely the tDMRG-LBO method used in Ref. [35]. Additionally, we monitor the f-sum rule in the large electron-phonon coupling regime. This is also contained in Appendix B. All calculations are done with the ITENSOR software library [124].

We now demonstrate how we control the convergence of the p2TDVP-LBO time evolution with respect to ϵ_{bond} and ϵ_{LBO}. This is illustrated in Fig. 6 for the real-time current-current correlation function for $\gamma/\omega_0 = \sqrt{2}$ and $t_{\text{ph}}/\omega_0 = -0.1$. Figure 6(a) shows $\text{Re}[C_T(t)]$ for a fixed ϵ_{LBO} and different ϵ_{bond}. The data illustrate that when ϵ_{bond} is chosen sufficiently small, the correlation functions become independent thereof and the curves are converged for our purposes. In Fig. 6(b), we show a similar plot but for a fixed ϵ_{bond}. As can be seen, both ϵ_{bond} and ϵ_{LBO} must be chosen carefully. We note that during this work, we have observed that, in some cases, one can obtain similar optical conductivities with the same key features even when the correlations functions still depend noticeably on cutoffs. One could control convergence by only monitoring the quality of the optical conductivity. We work with the stricter criteria of monitoring both the correlation functions and the optical conductivity as elaborated on above. Note that in some cases, small deviations could not be avoided with our computational resources.

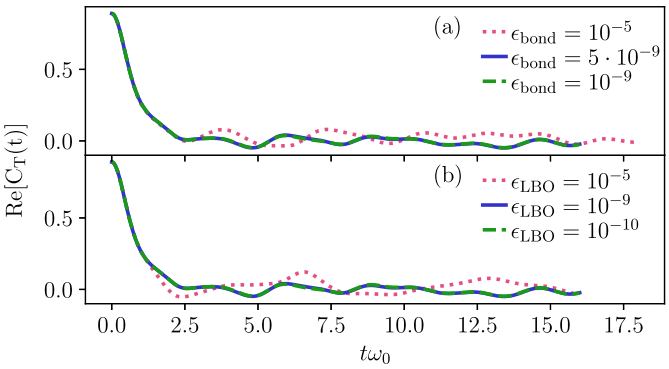

FIG. 6. (a) Real part of the current-current correlation function from Eq. (8) for $L = 20$, $M = 20$, $\gamma/\omega_0 = \sqrt{2}$, and $t_{\text{ph}}/\omega_0 = -0.1$, computed in the ground state ($T/\omega_0 = 0$). We use a fixed $\epsilon_{\text{LBO}} = 10^{-9}$ and different ϵ_{bond}. (b) Same as in (a) but with a fixed $\epsilon_{\text{bond}} = 10^{-9}$ and different ϵ_{LBO}. The calculation is done with p2TDVP-LBO and is distributed onto four processes.

V. GROUND-STATE RESULTS

In this section, we present the results for the real part of the optical conductivity obtained with p2TDVP-LBO for the ground state of the Holstein polaron. The ground state itself is obtained with ground-state DMRG. Our results are compared to calculations with the Lanczos method for weak and intermediate electron-phonon coupling. For strong coupling, we compare to Eq. (16).

A. Ground-state results in the weak- and intermediate-coupling regimes

We first look at the optical conductivity in the ground state for different electron-phonon coupling strengths and different phonon dispersion relations. The effects of the dispersion on the optical conductivity were thoroughly investigated in Ref. [36], however, we also describe the behavior here for self-consistency and to guide the discussion of the results at finite temperature.

We verify the correctness of our results by comparing them to the optical conductivity obtained with the Lanczos method. This method uses a constructed variational Hilbert space and allows for 28 phonons at the initial site of the electron, but fewer and fewer at the sites further away, see Ref. [36] for details. The Lanczos method has the advantage

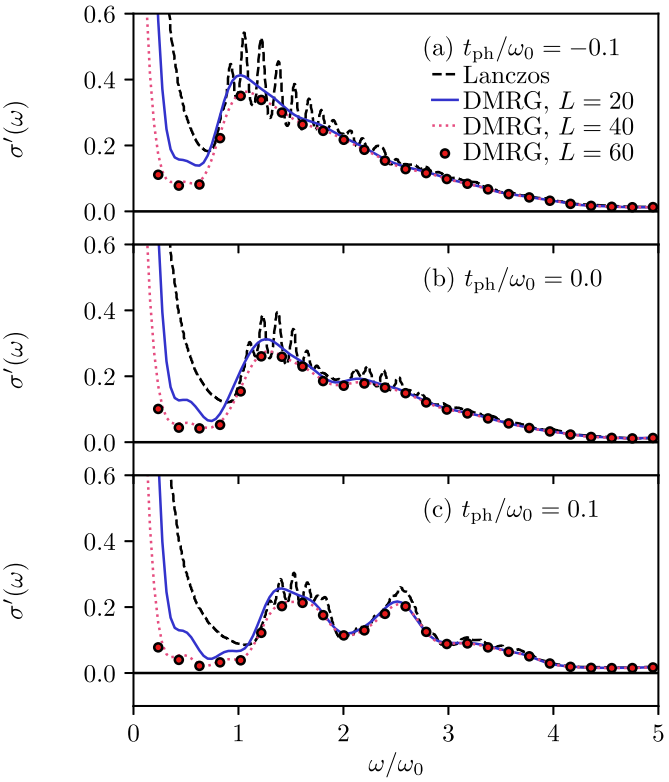

FIG. 7. (a) Real part of the optical conductivity for the Holstein polaron in the ground state for $\lambda = 1/2$, $M = 20$, $\epsilon_{\rm Bond} = \epsilon_{\rm LBO} = 10^{-9}$, and with $t_{\rm ph}/\omega_0 = -0.1$. (b) Same as in (a) but with and $t_{\rm ph}/\omega_0 = 0.0$. (c) Same as in (a) but with $t_{\rm ph}/\omega_0 = 0.1$. We show $L = 60, 40, 20$, and the time evolution is done up to $t_{\rm max}\omega_0 = 16$. We further use a Lorenzian broadening with $\eta = 0.1$. The black dashed line is the reference data computed with the Lanczos method. The DMRG simulations, obtained with p2TDVP-LBO, are distributed onto 12, 8, and 4 processes for $L = 60$, 40, and 20, respectively.

of computing the optical conductivity directly in frequency space and can easily extract the Drude weight. However, it has more difficulties in including many phonons and larger systems than the DMRG method. Lastly, the DMRG has an (in principle) straightforward extension to finite densities. In a setup where the Lanczos method cannot utilize the variational Hilbert space approach, the treatable system sizes will also be limited.

In Fig. 7, we show the real part of the optical conductivity in the Holstein-polaron model in the weak-coupling regime, $\lambda = 1/2$, for different values of the phonon hopping amplitude $t_{\rm ph}$, calculated with the Lanczos method and p2TDVP-LBO for $L = 20$, 40, and 60. The first important result is that the p2TDVP-LBO method reproduces the incoherent part of $\sigma'(\omega)$ from the Lanczos method very accurately. Additionally, we see that we can access system sizes large enough to obtain results approximately independent thereof.

Figure 7(b) shows the real part of the optical conductivity at finite ω and a flat phonon band. The incoherent part is dominated by two peaks starting at approximately $\omega/\omega_0 = 1$ and 2. The appearance of a peak at $\omega/\omega_0 = 1$ is consistent with weak-coupling perturbation theory, see, e.g., Ref. [66], and stems from the one-phonon emission process. The width of the peaks is also given by the possible changes in electron quasimomenta $k_{\rm el}$. This is because the emitted phonon can have any quasimomentum due to the flat dispersion relation and the transition energies are thus dominated by the change in electron energy. Here, the biggest difference between the Lanczos and the p2TDVP-LBO data are visible. The Lanczos data exhibit a peak structure occurring due to the possible electron quasimomenta $k_{\rm el}$, which we cannot resolve with p2TDVP-LBO due to the finite resolution coming from the limited times available and the large number of $k_{\rm el}$.

When a small upward dispersion relation, $t_{\rm ph}/\omega_0 = -0.1$, is introduced, see Fig. 7(a), the distinction between the different phonon emission peaks disappears and the weight of the incoherent spectra gets slightly shifted to lower frequencies. The latter can be explained by the fact that the emitted phonon has an additional energy contribution of $\sim 2t_{\rm ph}$ due to the finite phonon bandwidth. As a result, the peak shifts to $\sim\omega_0 + 2t_{\rm ph}$. The transfer to higher quasimomentum states still remains rather unaffected since $|t_0/t_{\rm ph}| \gg 1$. Similar behavior of the second phonon peak leads to the monotonic decay of the incoherent spectra after the first maximum.

For $t_{\rm ph}/\omega_0 = 0.1$ in Fig. 7(c), we see the opposite effect. The one- and two-phonon emission peaks become more easily separable and their maxima get shifted to larger frequencies. This is consistent with the fact that every transition energy introduces the term $2t_{\rm ph}\cos(k)$. For small k, the energy differences correspond to larger frequencies whereas the opposite happens for larger k with $2t_{\rm ph}\cos(k) > 0$. In total, this leads to a shift of the peaks to higher frequencies and a suppression of their width.

We now turn to the intermediate coupling regime with $\lambda = 1$. The ground-state results are presented in Fig. 8. We show $t_{\rm ph}/\omega_0 = -0.1$ in Fig. 8(a), $t_{\rm ph}/\omega_0 = 0$ in Fig. 8(b), and $t_{\rm ph}/\omega_0 = 0.1$ in Fig. 8(c). Again, essentially the same incoherent structure is produced by both the Lanczos and p2TDVP-LBO method with small differences in some peak heights. In this regime, a small but finite phonon bandwidth has a significant impact on the optical conductivity. In general, the spectra broaden, signaling that the two and three phonon-emission processes play a more important role when the coupling is increased. Note that due to the small values for the dispersion, we do not observe the multi-phonon structure at $\omega < \omega_0$ for $t_{\rm ph} > 0$, as reported in Ref. [36]. Still, the same physical effects as in the weak-coupling case can be observed, although significantly enhanced. For example, the one- and two-phonon peak for $t_{\rm ph}/\omega_0 = 0.1$ in Fig. 8(c) are almost completely distinguishable. In conclusion, we see that the p2TDVP-LBO method can reproduce all the features from the Lanczos method very well in the incoherent part of the spectrum for both $\lambda = 1$ and $\lambda = 1/2$. Note that we observe some oscillations for low frequencies which we attribute to artifacts of the Fourier transformation. This was verified by comparing the DMRG data to only the regular part of the Lanczos data.

B. Ground state in the strong-coupling regime

We now turn to the ground-state optical conductivity in the strong-coupling regime with $\gamma/\omega_0 = 3$. As can be seen from Eq. (16) and by analyzing the Born-Oppenheimer surfaces

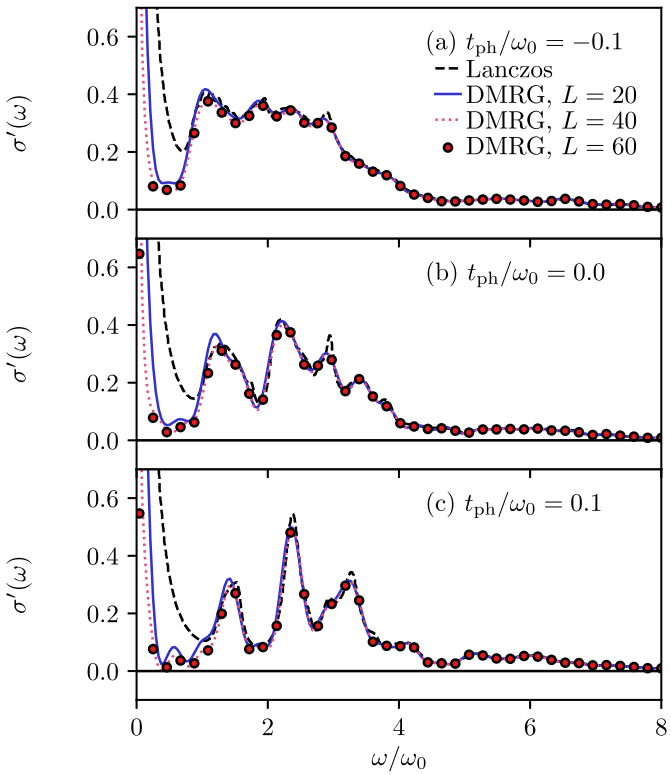

FIG. 8. (a) Real part of the optical conductivity for the Holstein polaron in the ground state for $\lambda = 1, M = 20, \epsilon_{\mathrm{Bond}} = \epsilon_{\mathrm{LBO}} = 10^{-9}$, and with $t_{\mathrm{ph}}/\omega_0 = -0.1$. (b) Same as in (a) but with and $t_{\mathrm{ph}}/\omega_0 = 0.0$. (c) Same as in (a) but with $t_{\mathrm{ph}}/\omega_0 = 0.1$. We show $L = 60$, 40, 20, and the time evolution is done up to $t_{\mathrm{max}}\omega_0 = 15$. We further use a Lorenzian broadening with $\eta = 0.08$. The black dashed line is the reference data computed with the Lanczos method. The DMRG simulations, calculated using p2TDVP-LBO, are distributed onto 12, 8 and 4 processes for $L = 60$, 40, and 20, respectively.

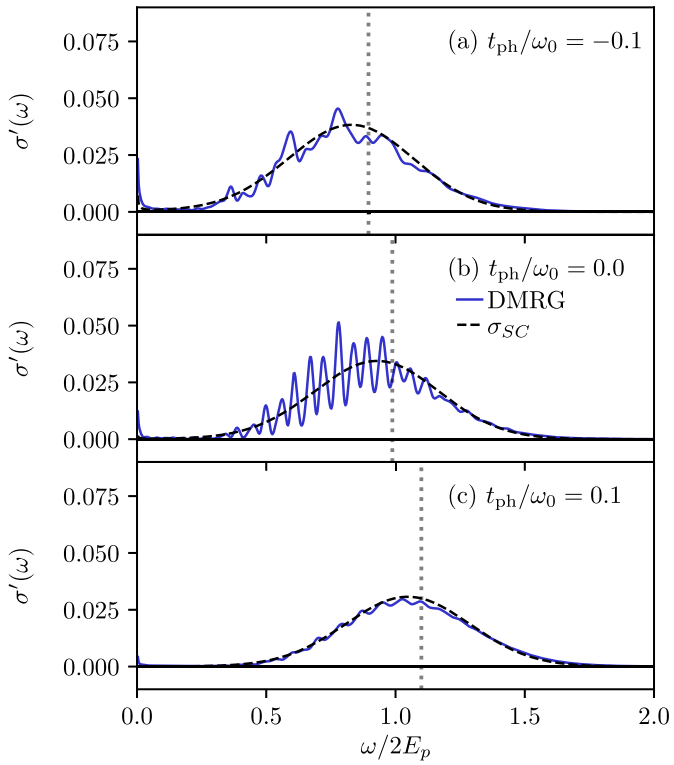

FIG. 9. (a) Real part of the optical conductivity for the Holstein polaron in the ground state for $\lambda = 4.5$. We further set $M = 35$, $\epsilon_{\mathrm{Bond}} = \epsilon_{\mathrm{LBO}} = 10^{-7}$, $L = 20$, and $t_{\mathrm{ph}}/\omega_0 = -0.1$. (b) Same as in (a) but with $t_{\mathrm{ph}}/\omega_0 = 0$. (c) Same as in (a) but with $t_{\mathrm{ph}}/\omega_0 = 0.1$. The blue solid line is the DMRG data and the dashed solid line is the analytical formula from Eq. (16). The vertical gray dashed lines show the respective energy differences between the Born-Oppenheimer surfaces at $\bar{q}_{\mathrm{min},-}$. The time-evolution is done up to $t_{\mathrm{max}}\omega_0 = 11$ and we use a Lorenzian broadening with $\eta = 0.1$. The simulation is distributed onto four processes for the DMRG calculations using p2TDVP-LBO.

in Fig. 2, the expectation is a shifted Gaussian around twice the polaron binding energy E_P for a flat phonon dispersion relation. With a finite phonon bandwidth, one expects the Gaussian to be shifted to either larger or smaller frequencies depending on the sign of t_{ph}. This central peak can be understood in terms of the Franck-Condon transition in the extreme adiabatic limit. There, the motion of the electron is so fast compared to that of the phonons that the electron is excited without changing the phonon configuration with an energy difference of $2E_P$. This process is sketched in Fig. 3. In Fig. 9, the results of the p2TDVP-LBO ground-state calculation for different phonon dispersion is plotted. We show the expression from Eq. (16) and the p2TDVP-LBO data for $t_{\mathrm{ph}}/\omega_0 = -0.1$ in Fig. 9(a), $t_{\mathrm{ph}}/\omega_0 = 0$ in Fig. 9(b), and $t_{\mathrm{ph}}/\omega_0 = 0.1$ in Fig. 9(c). Our numerical results are very well approximated by the analytic formula. Comparing Figs. 9(a)–9(c), it becomes clear that even a small but finite phonon bandwidth significantly alters the position of the maximum of the spectrum. A downwards phonon dispersion relation shifts the absorption spectrum to higher frequencies and an upwards phonon dispersion relation shifts it to lower frequencies. This is expected from inspecting the Born-Oppenheimer surfaces in Sec III. The vertical gray dashed lines in Fig. 9 indicate the energy differences between the two Born-Oppenheimer surfaces at the minimum of the lowest surface.

We conclude that our method also works well for a large electron-phonon coupling in the ground state, but we note that many local modes are needed in the local basis optimization. For example, the calculations in Figs. 7–9, required roughly 10, 15, and 30 local optimal basis states in both steps one and two of the algorithm. We also emphasize that, despite being calculated far from the adiabatic limit ($t_0/\omega_0 = 1$), our results agree well with the analytic predictions. Note that in Fig. 9, there is still a resilient M dependence in the amplitude of some peaks, most notably so in Fig. 9(b). This is further discussed in Appendix B.

VI. FINITE-TEMPERATURE RESULTS

A. Finite-temperature results in the weak and intermediate coupling regimes

We proceed by investigating how the real part of the optical conductivity changes when going from zero to finite temperatures. Figure 10 shows $\sigma'(\omega)$ for the Holstein polaron for $\lambda = 1/2$ at different temperatures and with different values of

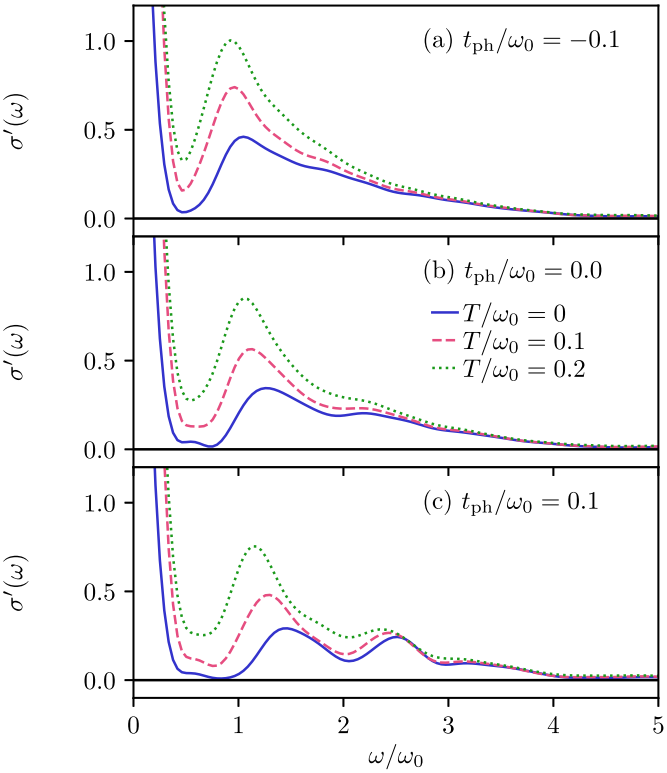

FIG. 10. (a) Real part of the optical conductivity at finite temperatures for $\lambda = 1/2$ and with $t_{\rm ph}/\omega_0 = -0.1$. (b) Same as in (a) but with $t_{\rm ph}/\omega_0 = 0$. (c) Same as in (a) but with $t_{\rm ph}/\omega_0 = 0.1$. We further set $M = 20$, $L = 20$, and $\epsilon_{\rm Bond} = \epsilon_{\rm LBO} = 10^{-9}$. The time evolution is done up to $t_{\rm max}\omega_0 = 15$ and we use a Gaussian broadening with $\eta = 0.1/(4\pi)$. The simulations are carried out with p2TDVP-LBO and distributed onto four processes for the ground-state calculations and onto eight processes at finite temperature.

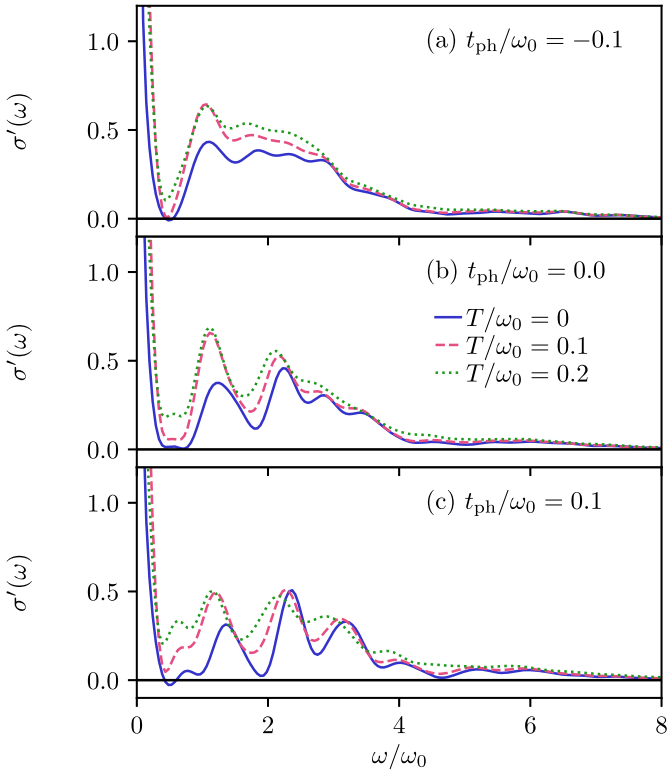

FIG. 11. (a) Real part of the optical conductivity at finite temperatures for $\lambda = 1$ and with $t_{\rm ph}/\omega_0 = -0.1$. (b) Same as in (a) but with $t_{\rm ph}/\omega_0 = 0$. (c) Same as in (a) but with $t_{\rm ph}/\omega_0 = 0.1$. We further set $M = 20$, $L = 20$, and $\epsilon_{\rm Bond} = \epsilon_{\rm LBO} = 10^{-9}$ for $T/\omega_0 = 0$ and $\epsilon_{\rm Bond} = 5 \times 10^{-9}$, $\epsilon_{\rm LBO} = 10^{-9}$ for $T/\omega_0 = 0.1,\ 0.2$. The time evolution is done up to $t_{\rm max}\omega_0 = 13$ and we use a Gaussian broadening with $\eta = 0.1/(4\pi)$. The simulations are carried out with p2TDVP-LBO and distributed onto four processes for the ground-state calculations and onto eight processes at finite temperature.

the phonon hopping amplitude $t_{\rm ph}$. One can observe a similar influence of the finite temperature for the upwards dispersion relation [$t_{\rm ph}/\omega_0 = -0.1$ in Fig. 10(a)], a flat dispersion relation [$t_{\rm ph}/\omega_0 = 0$ in Fig. 10(b)], and downwards dispersion relation [$t_{\rm ph}/\omega_0 = 0.1$ in Fig. 10(c)]. Namely, there is a clear increase in spectral weight at low frequencies. This is consistent with other calculations in the weak-coupling regime [66] (although there in the adiabatic regime). This is due to the contribution of states previously thermally suppressed with a smaller energy difference than ω_0. We further see an increase in the one-phonon emission-peak amplitude. This is due to the enhanced population of higher quasimomentum states at a higher temperature, which now all contribute through one-phonon emission processes. The maximum one-phonon peak also shifts to lower frequencies, and the effect seems more apparent for $t_{\rm ph}/\omega_0 = 0.1$ than for $t_{\rm ph}/\omega_0 = -0.1$. We attribute this to the fact that the sign of the curvature in the polaron and phonon bands differ in the first case and is the same in the latter.

In the intermediate regime, $\lambda = 1$ in Fig. 11, there is a different influence of the finite temperature on the spectrum. Whereas higher T/ω_0 almost washes out the separate peak structure for $t_{\rm ph}/\omega_0 = 0,\ 0.1$, and $\lambda = 1/2$, the peaks remain fairly well separated for all temperatures studied here when $\lambda = 1$. This is valid for $t_{\rm ph}/\omega_0 = 0$ and $t_{\rm ph}/\omega_0 = 0.1$ in Figs. 11(b) and 11(c), respectively. Furthermore, when $t_{\rm ph}/\omega_0 = -0.1$, the spectrum remains largely unaffected by temperature other than enhanced weight at lower frequencies. By decreasing η, we can observe small temperature dependent resonances at low frequencies for $\lambda = 1/2,\ 1$, and $t_{\rm ph}/\omega_0 = 0,\ 0.1$ [this can still be seen in Fig. 11(c)], but from our available data, we cannot conclusively determine if they are physical or an artifact of the Fourier transformation. In this case, a higher frequency resolution would be necessary.

B. Finite-temperature results in the strong-coupling regime

We now analyze how the optical conductivity changes with temperature in the strong-coupling regime, i.e., $\lambda = 4.5$. The results can be seen in Figs. 12(a)–12(c) for the phonon dispersion $t_{\rm ph}/\omega_0 = -0.1,\ 0$, and 0.1, respectively. The analytic formula for the optical conductivity, see Eq. (16), remains a good approximation in all cases in Fig. 12, even as the temperature is increased to $T/\omega_0 = 1$. Still, our data have less spectral weight at low frequencies. The reason is not obvious, but some deviations are to be expected since we are far away from the adiabatic limit. Further, we observe that the phonon dispersion relation affects the finite-temperature behavior. The upwards dispersion relation, see Fig. 12(a), leads to a larger

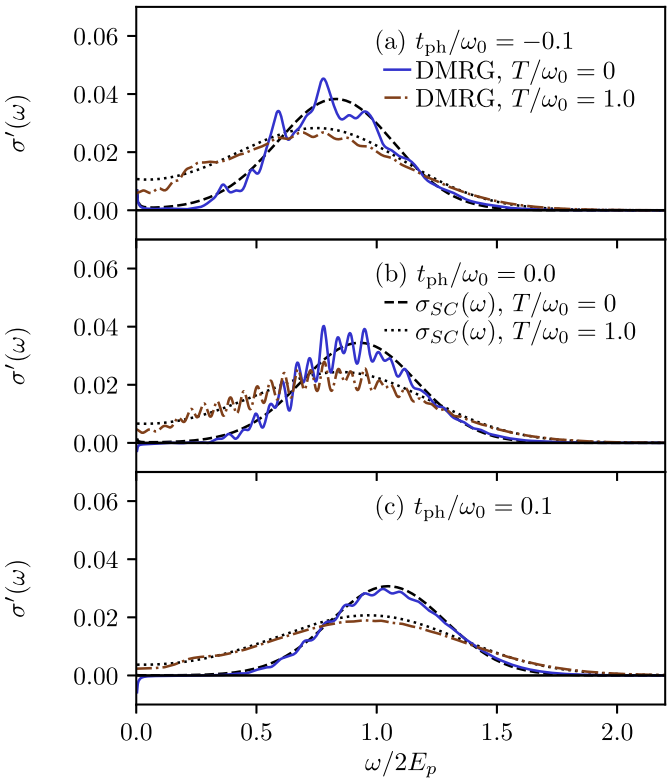

FIG. 12. (a) Real part of the optical conductivity at different temperatures for $\lambda = 4.5$ and with $t_{\rm ph}/\omega_0 = -0.1$. (b) Same as in (a) but with $t_{\rm ph}/\omega_0 = 0$. (c) Same as in (a) but with $t_{\rm ph}/\omega_0 = 0.1$. We further set $M = 35$, $L = 20$, and $\epsilon_{\rm Bond} = \epsilon_{\rm LBO} = 10^{-7}$ for the ground-state calculations. For the real-time evolution for $T/\omega_0 = 1.0$, we use single-site TDVP with $\epsilon_{{\rm bond},J} = 10^{-8}$ for $t_{\rm ph}/\omega_0 = -0.1$, 0.1 and $\epsilon_{{\rm bond},J} = 10^{-9}$ for $t_{\rm ph}/\omega_0 = 0$ (see Sec. IV for details). The time evolution is done up to $t_{\rm max}\omega_0 = 11$ and we use a Gaussian broadening with $\eta = 0.5/(4\pi)$. The black dashed and dotted lines are the analytical formula from Eq. (16). The ground-state DMRG results are distributed onto 4 processes and are calculated with p2TDVP-LBO.

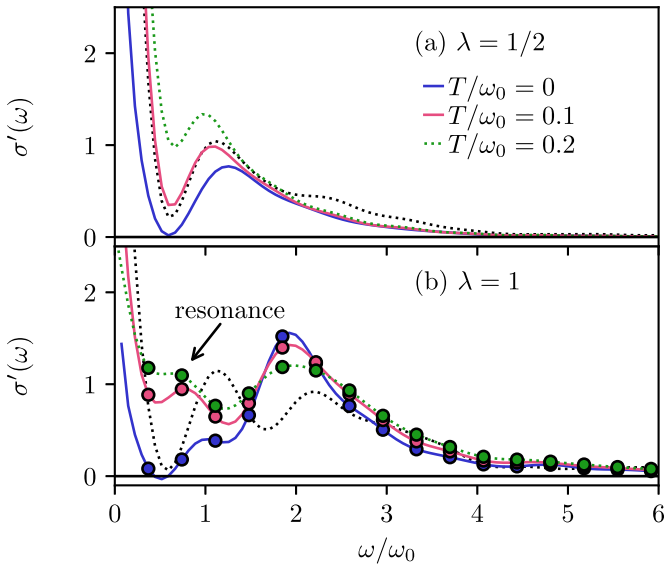

FIG. 13. (a) Optical conductivity for the Holstein bipolaron for $\lambda = 1/2$, $L = 20$, $M = 20$ and $t_{\rm ph}/\omega_0 = 0$. The black dotted line is the polaron curve with $\lambda = 1/2$, $T = 0.1$, $\epsilon_{\rm bond} = \epsilon_{\rm LBO} = 10^{-9}$ and scaled with a factor of two. (b) Same as (a) but with $\lambda = 1$. We use $\epsilon_{\rm bond} = 5 \times 10^{-9}$, $\epsilon_{\rm LBO} = 10^{-9}$ for the ground-state data and $\epsilon_{\rm bond} = 5 \times 10^{-9}$, $\epsilon_{\rm LBO} = 10^{-8}$ for the finite-temperature data. The symbols show the data points without zero padding. We time evolve to $t_{\rm max}\omega_0 = 8.5$ and use a Gaussian broadening with $\eta = 0.2/(4\pi)$. The black dotted line in (b) is the polaron curve with $\lambda = 1$, $T = 0.1$, $\epsilon_{\rm bond} = 5 \times 10^{-9}$, $\epsilon_{\rm LBO} = 10^{-9}$ and scaled with a factor of two. The simulations are done with p2TDVP-LBO and are distributed onto four processes for the ground-state calculations and onto (ten) eight processes for the (bi)polaron finite-temperature calculations.

contribution at low frequencies than the downward dispersion relation in Fig. 12(c). Looking at the $\omega \to 0$ values, it appears that the thermally activated hopping plays a lesser role when there is a downwards than an upwards phonon dispersion relation. This is consistent with the depth of the lower Born-Oppenheimer surfaces increasing, as can be seen in Fig. 2. Furthermore, since the low quasimomenta phonons have higher energy for the downwards dispersion relation, the nondiagonal transition with a small change in electron quasimomenta is suppressed compared to the upwards dispersion relation case. Note that the resonance at $\omega = 2t_0$ seen in Ref. [65] for a small ω_0/t_0 can be qualitatively reproduced by our method (not shown here). We further mention that small finite-size effects can be seen in some of the oscillation amplitudes in the data shown in Fig. 12. This is illustrated in Appendix B.

VII. BIPOLARON RESULTS

We now proceed to study the real part of the optical conductivity of the Holstein bipolaron at finite temperature. In Fig. 13, we plot $\sigma'(\omega)$ for weak and intermediate electron-phonon coupling, $\lambda = 1/2$, 1, with $t_{\rm ph}/\omega_0 = 0$. We observe substantial differences in the spectrum between both the two different electron-phonon coupling parameters, as well as between the polaron and bipolaron for $\lambda = 1$. For $\lambda = 1/2$, see Fig. 13(a), the bipolaron spectrum is almost identical to the single-polaron spectrum weighted by a factor of two. When $\lambda = 1$, we obtain quite a different picture. Whereas the $\omega/\omega_0 = 1$, 2 peaks have a similar amplitude for the polaron when $t_{\rm ph}/\omega_0 = 0$, see Fig. 11(b), the bipolaron has a clear maximum around $\omega/\omega_0 = 2$. This indicates that the two-phonon emission process plays a much more dominant role than for the polaron. As T/ω_0 is increased, a resonance appears that can be distinguished from the rest of the spectrum [indicated by the arrow in Fig. 13(b)]. We believe that this stems from the enhanced importance of the one phonon emission peak, which shifts to lower frequencies, similar to what can be seen in Fig. 13(a). When the temperature is increased, the two electrons act more like separate polarons, and the one-phonon emission process becomes more important (for very high temperatures, the bipolaron will dissolve).

We want to emphasize that we focus on the single-bipolaron limit to properly understand the behavior in a dilute system. This is also motivated by the recent results on bipolaron high-temperature superconductivity reported in Ref. [16]. Going to a finite bipolaron density will add scattering, whose effects are beyond the scope of our study. We also observe that when we increase the density to two spinless

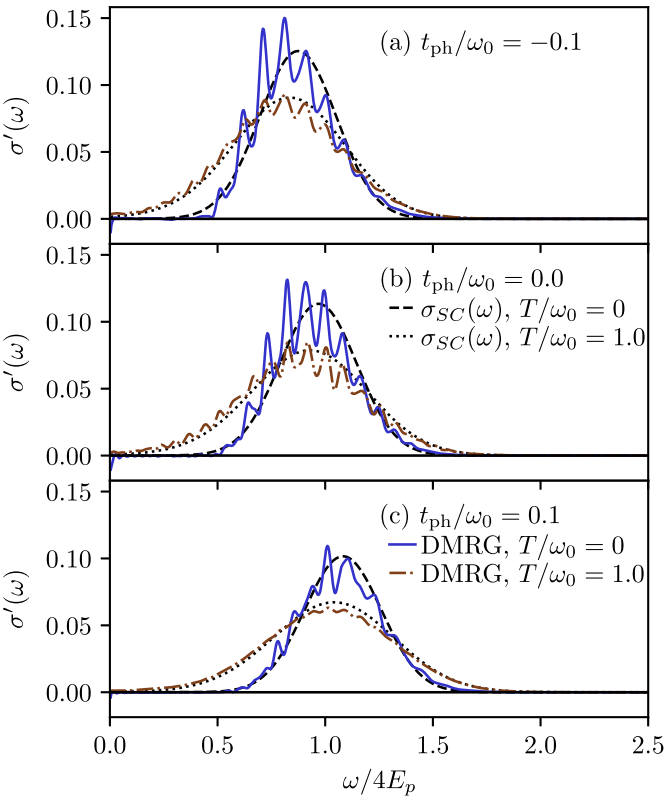

FIG. 14. (a) Optical conductivity for the Holstein bipolaron with $\lambda = 4$ and $t_{\rm ph}/\omega_0 = -0.1$. (b) Same as in (a) but with $t_{\rm ph}/\omega_0 = 0$. (c) Same as in (a) but with $t_{\rm ph}/\omega_0 = 0.1$. We further set $M = 35$, $L = 20$, and $\epsilon_{\rm Bond} = \epsilon_{\rm LBO} = 10^{-7}$ for the ground-state calculations. For the time evolution for $T/\omega_0 = 1.0$, we use single-site TDVP with $\epsilon_{{\rm bond},J} = 10^{-7}$ for $t_{\rm ph}/\omega_0 = -0.1, 0.1$ and $\epsilon_{{\rm bond},J} = 10^{-8}$ for $t_{\rm ph}/\omega_0 = 0$ (see Sec. IV for details). The time-evolution is done up to $t_{\rm max}\omega_0 = 11$ and we use a Gaussian broadening with $\eta = 0.2/(4\pi)$. The dashed and dotted black lines are the analytical formula from Eq. (16). The ground-state simulations are done with p2TDVP-LBO and distributed onto four processes.

electrons, the spectrum does practically not change compared to the single electron case (except for a rescaling with a factor of two). This indicates that the change in the spectrum in Fig. 13(b) can be attributed to the formation of a bound bipolaron and not to the change in density. In Fig. 13(b), we also show the data points without zero padding to illustrate that the resonance is not an artifact of the Fourier transformation. While not shown here, we additionally confirmed that the ground-state data in Fig. 13 and data obtained with the Lanczos method agree, as we illustrate for the polaron in Sec. V.

In Fig. 14, we display the real part of the optical conductivity in the strong-coupling regime ($\lambda = 4$). The first key observation is that the analytical formula in Eq. (16) is qualitatively consistent with the DMRG data. An asymmetric Gaussian with a dispersion-dependent maximum (around $4E_P$ for $t_{\rm ph}/\omega_0 = 0$) is seen in both cases. For $T/\omega_0 = 1$, the maximum is shifted to smaller frequencies and substantial spectral weight can be observed at small ω. This is similar to what occurred for the polaron, see Fig. 12, although a clear dispersion dependence on the low-frequency weight can not be identified for the parameters chosen here. Still, we conclude that Eq. (16) also describes the real part of the optical conductivity for the bound bipolaron quantitatively well. We note that we can still detect small finite-size effects in some of the oscillation amplitudes in Fig. 14. This is further discussed in Appendix B.

VIII. CONCLUSION

In this work, we tackled the challenging task of accurately computing finite-temperature transport properties in polaron systems. We used single-site TDVP and two-site serial and parallel TDVP combined with local basis optimizations to calculate the real part of the optical conductivity for the Holstein polaron and bipolaron models with dispersive phonons at finite temperatures. We first explained how we incorporate LBO into two-site TDVP and reviewed the key ideas of the parallel implementation. The implementation of p2TDVP gives us the possibility to distribute the system onto different processes, thus allowing for an efficient time evolution while taking advantage of modern computer architectures. This, combined with LBO, allows us to compute time-dependent correlation functions for electron-phonon (bi)polaron systems with a variety of electron-phonon interaction strengths.

We first verified that the results obtained with p2TDVP are consistent with those calculated with the Lanczos method for the ground state of the Holstein polaron. We observed that even a small but finite phonon bandwidth has a significant impact on the optical conductivity for weak and intermediate electron-phonon coupling, consistent with previously reported results [36]. Most importantly, our method can accurately reproduce the Lanczos method data. For strong electron-phonon coupling, the known result of an asymmetric Gaussian is reproduced for $t_{\rm ph}/\omega_0 = 0$. However, a finite bandwidth shifts the center of the Gaussian to higher or lower frequencies depending on the sign of the phonon hopping amplitude $t_{\rm ph}$. This can be understood by inspecting the Born-Oppenheimer surfaces of the Holstein dimer as we saw in Sec. III.

Going to finite temperatures significantly alters the optical conductivity. For weak electron-phonon coupling, an increase of spectral weight around $\omega/\omega_0 = 1$ appears. Furthermore, the previously clearly distinguishable peaks almost completely merge at $t_{\rm ph}/\omega_0 = 0.1$.

For intermediate electron-phonon coupling, the separated peaks remain distinguishable for $t_{\rm ph}/\omega_0 = 0, 0.1$, whereas the finite temperatures analyzed here do not alter the spectrum much for $t_{\rm ph}/\omega_0 = -0.1$. In the large coupling case, our data verify the validity for Eq. (16) in the nonadiabatic regime. For $T/\omega_0 = 1$, the maximum of the Gaussian-shaped curve, compared to the $T/\omega_0 = 0$ case, shifts to smaller frequencies, and significant spectral weight is seen at lower frequencies. This is more prominent for an upwards than for a downwards phonon dispersion relation.

Lastly, we presented results for the bound bipolaron. There, we compared weak and intermediate electron-phonon coupling data for dispersionless phonons. While the real part of the optical conductivity for the first parameter set resembles that of the single polaron, a quite different behavior is seen when $\lambda = 1$. There, the maximum of the spectrum is shifted to $\omega/\omega_0 = 2$, signaling the importance of two-phonon emission

processes. These parameters also give rise to a large distinguishable peak at small frequencies. Our strong-coupling bipolaron data reproduce the analytic predictions drawn from the analysis of the Born-Oppenheimer surfaces very well. We reported a dispersion-dependent shift of the maximum of the spectrum and a significant decrease in the amplitude for $T/\omega_0 = 1$, in comparison to the zero-T results. Furthermore, there is enhanced spectral weight for low frequencies.

These results characterize how the main features of small and large polarons in a Holstein-type system change under phonon dispersion and at finite temperatures. Understanding the basic mechanisms in such theoretical Hamiltonians constitutes an essential step in detecting such features, or lack thereof, in experimental data.

There are many interesting extensions to this work. For one, our numerical method can suffer from low-frequency resolution due to the limitations in reachable times. This could lead to small distinct features of the optical conductivity not being detected. Furthermore, despite the benefits of using LBO, there will always be a limit set by phonon truncation. For this reason, one goal of this work is to provide reliable data in the regimes where DMRG is the most powerful (intermediate electron-phonon interaction) which is out of reach of perturbative methods, see, e.g., Ref. [125]. These can then be used to reliably benchmark results obtained with other methods, see, e.g., Refs. [126–135], which might have their strong suit in complementary parameter regimes.

Additionally, including electron-electron interactions in the Born-Oppenheimer formalism can lead to new insights into the transition from bound to unbound bipolarons [44–48,51,53,54]. As this can involve additional numerical complexity, it can also serve as an interesting future application for the methods presented here.

Furthermore, one could try to compare the computations with other finite-temperature matrix-product state methods such as minimally entangled typical thermal state algorithms (METTS), see, e.g., Refs. [79,101,102].

Lastly, an interesting application for our method would be to calculate properties for more complicated Hamiltonians, such as those inspired by manganite physics, see, e.g., Ref. [136] for a theoretical review.

ACKNOWLEDGMENTS

We acknowledge useful discussions with P. Blöchl, C. Jooss, J. Lötfering, S. Manmana, C. Meyer, S. Paeckel, and M. ten Brink. D.J. and F.H.-M. were funded by the Deutsche Forschungsgemeinschaft (DFG, German Research Foundation) 217133147 via SFB 1073 (Project No. B09). J.B. acknowledges the support by the program P1-0044 of the Slovenian Research Agency, support from the Centre for Integrated Nanotechnologies, a U.S. Department of Energy, Office of Basic Energy Sciences user facility, and funding from the Stewart Blusson Quantum Matter Institute.

APPENDIX A: BOND AND LOCAL BASIS DIMENSIONS

We here discuss the numerical details of the p2TDVP-LBO algorithm. In Fig. 15, we compare how the computation of the current-current correlation functions scales compared to the

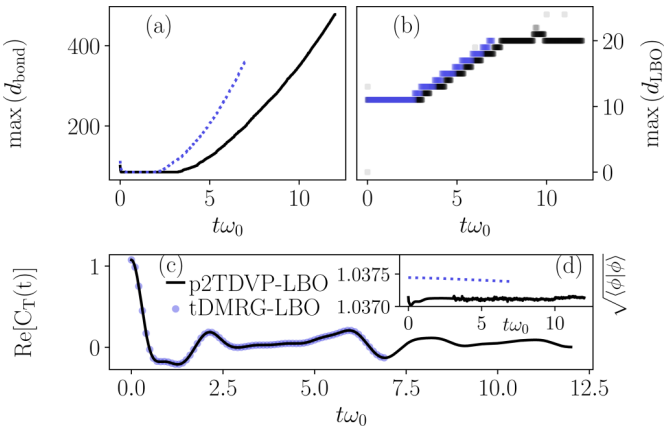

FIG. 15. (a) Maximum bond dimension of the matrix-product state at finite temperature after applying the current operator during the real-time evolution. We use with $\gamma/\omega_0 = \sqrt{2}$, $t_{\text{ph}}/\omega_0 = 0.1$, $M = 20$, $L = 20$, and $\epsilon_{\text{Bond}} = \epsilon_{\text{LBO}} = 10^{-9}$. The time-evolution methods are tDMRG-LBO and p2TDVP-LBO, see Appendix A for details. (b) Maximum local optimal basis dimension after the SVD in the time evolution algorithms (step two for p2TDVP-LBO and see Ref. [35] for details for the tDMRG-LBO algorithm). (c) Real part of the current-current correlation function. (d) Norm of the initial state. (b)–(d) have the same parameters as (a).

tDMRG-LBO algorithm applied in Ref. [35]. Note that we use tDMRG-LBO to obtain the thermal state with imaginary-time evolution and to do the real-time evolution shown in Fig. 15. The agreement between the two methods seen in Fig. 15(c) serves as a check for our p2TDVP-LBO algorithm. As explained in Sec. IV, the real-time evolution is carried out on the state $|\phi_T\rangle = \hat{J}\,|\psi_T\rangle$. In Fig. 15(a), we show the maximum bond dimension of $|\phi_T\rangle$ as a function of time with $\epsilon_{\text{Bond}} = \epsilon_{\text{LBO}} = 10^{-9}$ for both time-evolution methods. The need for a smaller bond dimension for p2TDVP is apparent, consistent with previous benchmarks of MPS time-evolution algorithms [81]. Figure 15(b) displays the maximum LBO dimension used in the SVD after applying the time-evolution gate in the tDMRG-LBO algorithm and step two of the p2TDVP-LBO algorithm (see Sec. IV for details). In both cases, using LBO is beneficial for the parameters chosen here. In Fig. 15(d), we plot the norm of the state $|\phi_T\rangle$. Note that $\sqrt{\langle\phi_T|\,|\phi_T\rangle} \neq 1$ since we already applied $\hat{J}$. The initial norm deviates between the two methods since the initial states are obtained using the different time-evolution schemes. Neither norm changes significantly during the reachable times. The reason why the time evolution is carried out until different times is the difference in computational cost. Note that this analysis does not account for the advantage of being able to distribute the computations onto several processes in the p2TDVP-LBO algorithm.

We now demonstrate that the calculations of the correlation function at finite temperatures can be homogeneously distributed onto several processes. In Fig. 16, we show that the bond dimension is roughly equal on all the bonds at different times for the bulk of the system. There, we plot the bond dimension between the different sites at the times $t\omega_0 = 8,\ 12,$ and 13 for the Holstein polaron. The parameters are given in the caption of Fig. 16. Furthermore, the grey dashed lines show where the partitioning of the

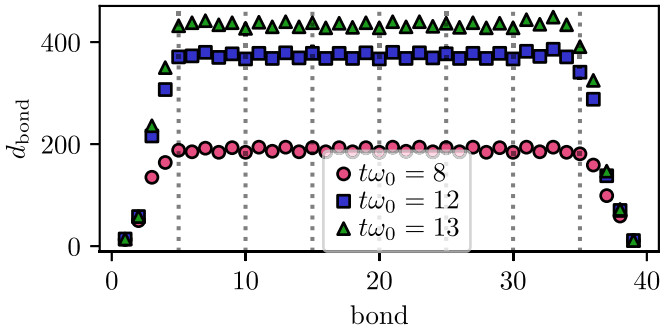

FIG. 16. Bond dimension between different sites at different times for the matrix-product state $|\phi_T\rangle$ for the Holstein polaron during time-evolution with p2TDVP-LBO. The calculations are done at the temperature $T/\omega_0 = 0.2$ and with the parameters $\lambda = 1$, $t_{\text{ph}}/\omega_0 = 0.1$, $M = 20$, $L = 20$, $\epsilon_{\text{bond}} = 5 \times 10^{-9}$, and $\epsilon_{\text{LBO}} = 10^{-9}$. The dashed vertical lines show the partitioning of the system onto eight processes.

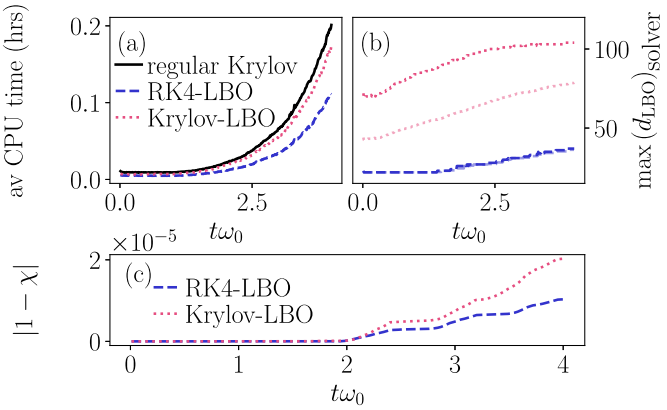

FIG. 17. Different local basis optimization schemes for two-site TDVP when calculating the real-time evolution of the bipolaron ground state after applying the current operator. The parameters are $L = 13$, $M = 25$, $\gamma/\omega_0 = 1$, $t_{\text{ph}}/\omega_0 = 0.0$, and $\epsilon_{\text{bond}} = \epsilon_{\text{LBO}} = 10^{-9}$. (a) Average CPU time for the different implementations in step one of the two-site TDVP algorithm, see Sec. IV for details. Black solid line: regular Krylov solver. Red dotted line: Krylov-LBO. Blue dashed line: RK4-LBO. (b) Maximum optimal basis dimension in the two-site TDVP with the Krylov-LBO (red dotted line) and with the RK4-LBO (blue dashed line) solver. The light lines are calculated by averaging the LBO dimension in all the Krylov vectors or all the k^j in the RK4 algorithm, and then taking the maximum of all the sites. (c) Absolute value of the overlap $\chi - 1$ of the wave function with a LBO solver and with the regular Krylov solver. Red dotted line: Krylov-LBO. Blue dashed line: RK4-LBO. All simulations use two cores.

system is done. Therefore, a need for dynamically adapting the boundaries as suggested for pDMRG in Ref. [137] does not seem necessary for our applications.

Lastly, in our discussion of the numerical details of p2TDVP-LBO, we illustrate the difference between using a regular Krylov solver, a Krylov solver with LBO (Krylov-LBO), and RK4 with LBO (RK4-LBO) in step one of the algorithm (see Sec. IV for details). In our test case, we apply the three versions of the algorithm to the real-time evolution of the bipolaron ground state after applying the current operator $|\phi_0\rangle = \hat{J}\,|\psi_0\rangle$. Note that the results, as in all LBO calculations, will be system and set-up dependent and a benchmark should be carried out in each case separately when feasible.

Figure 17(a) shows the average CPU time for each time step with the three methods. One first observes that the exponential increase in the bond dimension dominates the computation time in all cases. Still, using Krylov-LBO seems to be faster than using the regular Krylov solver. The RK4-LBO algorithm is significantly faster for the times reached here. We believe that this can be understood as follows: The Krylov vectors for a general state $|\psi\rangle$, are $|\psi\rangle_0 = |\psi\rangle$, $|\psi\rangle_1 = \hat{H}\,|\psi\rangle_0$, $|\psi\rangle_2 = \hat{H}\,|\psi\rangle_1 = \hat{H}^2\,|\psi\rangle_0$, and so on. The LBO basis is found before $\hat{H}$ is applied. Through the polynomial application of $\hat{H}$, we expect a larger phonon Hilbert space to be explored, which requires a larger number of LBO states. However, for the RK4 algorithm, $|k^1\rangle = \hat{H}\,|\psi\rangle$, but $|k^2\rangle = \hat{H}(|\psi\rangle + \alpha dt\,|k^1\rangle) = (\hat{H}\,|\psi\rangle + \alpha dt\hat{H}^2\,|\psi\rangle)$ etc, where α is a number. Now, the term including $\hat{H}^2$ is scaled with dt. We thus believe that for small dt, the optimal basis changes less drastically than for the Krylov vector $|\psi\rangle_2$. This seems plausible when inspecting the LBO dimensions needed in the calculations.

In Fig. 17(b), we show the maximum LBO dimension needed in the different algorithms. The red dotted line are the maximum LBO dimension used in the Krylov-LBO steps whereas the light red dotted line is the average. The maximum LBO dimension in the Krylov algorithm quickly reaches the maximum, which we already attributed to the fact that one must apply the effective Hamiltonian several times. The average remains somewhat lower. The required LBO dimension is significantly smaller in RK4-LBO (the average and maximum almost perfectly overlap), making the algorithm more efficient.

We also observe that the difference between RK4-LBO and Krylov-LBO is negligible for the time scales studied here. Figure 17(c) shows the absolute value of $1 - \chi$, where χ is the overlap between either the state using Krylov-LBO (red dotted line) or RK4-LBO (blue dashed line) with the state which uses a Krylov method without LBO. The difference is small for all times in our test case. We further want to point out that the RK4 solver, in general, is not as stable as the Krylov solver. For example, it did not converge well for the imaginary-time evolution in our calculations (which is why we use the regular Krylov solver in that case). For that reason, we also compared our results computed with the RK4-LBO solver to those obtained with a Krylov solver without LBO.

APPENDIX B: COMPARING THE MOMENTS

We now want to estimate the accuracy of the Fourier transform of the time-evolved current-current correlation function, see Eq. (8), which we use to extract $\sigma'(\omega)$. To do that, we compare the moments of the correlation function calculated in two ways: by calculating a thermal expectation value of the initial state and integrating the correlation function over ω. Computing the moments to assess the accuracy of the calculations for the Holstein polaron has already been used for the spectral functions, see, e.g., Refs. [33,35,138,139]. We

define the kth moment to be

$$\tilde{M}_k = \int_{-\infty}^{\infty} d\omega (\omega)^k C(\omega)_T. \tag{B1}$$

The zeroth moment is then

$$\tilde{M}_0 = \int_{-\infty}^{\infty} d\omega C(\omega)_T = \pi \langle \hat{J}^2 \rangle_T. \tag{B2}$$

The first moment becomes

$$\tilde{M}_1 = \int_{-\infty}^{\infty} d\omega \omega C(\omega)_T = \pi \langle [\hat{J}, \hat{H}] \hat{J} \rangle_T, \tag{B3}$$

where $[\hat{J}, \hat{H}] = [\hat{J}, \hat{H}_{\text{kin}}] + [\hat{J}, \hat{H}_{\text{e-ph}}]$ with

$$[\hat{J}, \hat{H}_{\text{kin}}] = -it_0^2 \sum_s (2\hat{c}^\dagger_{1,s}\hat{c}_{1,s} - 2\hat{c}^\dagger_{L,s}\hat{c}_{L,s}) \tag{B4}$$

and

$$\begin{aligned}[\hat{J}, \hat{H}_{\text{e-ph}}] = \gamma t_0 i \Bigg(& \sum_{j=2,s}^{L} (\hat{c}^\dagger_{j-1,s}\hat{c}_{j,s} + \hat{c}^\dagger_{j}\hat{c}_{j-1,s})(\hat{b}^\dagger_j + \hat{b}_j) \\ & - \sum_{j=1,s}^{L-1} (\hat{c}^\dagger_{j,s}\hat{c}_{j+1,s} + \hat{c}^\dagger_{j+1,s}\hat{c}_{j,s})(\hat{b}^\dagger_j + \hat{b}_j) \Bigg).\end{aligned} \tag{B5}$$

Lastly, the second moment becomes

$$\tilde{M}_2 = \int_{-\infty}^{\infty} d\omega \omega^2 C(\omega)_T = \pi \langle [[\hat{J}, \hat{H}], \hat{H}] \hat{J} \rangle_T, \tag{B6}$$

with

$$\begin{aligned}[[\hat{J}, \hat{H}], \hat{H}] = & it_0^3 2 \Bigg(\sum_{s=\uparrow,\downarrow} \Big(\hat{c}^\dagger_{1,s}\hat{c}_{2,s} - \hat{c}^\dagger_{2,s}\hat{c}_{1,s} \\ & + \hat{c}^\dagger_{L-1,s}\hat{c}^\dagger_{L,s} - \hat{c}^\dagger_{L,s}\hat{c}_{L-1,s} \Big) \Bigg) \\ & + \gamma t_0 \omega_0 i \Bigg(\sum_{j=2,s=\uparrow,\downarrow}^{L} \Big(\hat{c}^\dagger_{j-1,s}\hat{c}_{j,s}\hat{b}_j + \hat{c}^\dagger_{j,s}\hat{c}_{j-1,s}\hat{b}_j \\ & - \hat{c}^\dagger_{j-1,s}\hat{c}_{j,s}\hat{b}^\dagger_j - \hat{c}^\dagger_{j,s}\hat{c}_{j-1,s}\hat{b}^\dagger_j \Big) \\ & + \sum_{j=1,s=\uparrow,\downarrow}^{L-1} \Big(- \hat{c}^\dagger_{j,s}\hat{c}_{j+1,s}\hat{b}_j - \hat{c}^\dagger_{j+1,s}\hat{c}_{j,s}\hat{b}_j \\ & + \hat{c}^\dagger_{j,s}\hat{c}_{j+1,s}\hat{b}^\dagger_j + \hat{c}^\dagger_{j+1,s}\hat{c}_{j,s}\hat{b}^\dagger_j \Big) \Bigg) \\ & + it_0\gamma t_{\text{ph}} \Bigg(\sum_{j=2,s=\uparrow,\downarrow}^{L-1} \Big(\hat{c}^\dagger_{j-1,s}\hat{c}_j\hat{b}_{j+1} + \hat{c}^\dagger_{j,s}\hat{c}_{j-1,s}\hat{b}_{j+1} \\ & - \hat{c}^\dagger_{j-1,s}\hat{c}_{j,s}\hat{b}^\dagger_{j+1} - \hat{c}^\dagger_{j,s}\hat{c}_{j-1,s}\hat{b}^\dagger_{j+1} \Big) \Bigg) \\ & - it_0\gamma t_{\text{ph}} \Bigg(\sum_{j=2,s=\uparrow,\downarrow}^{L-1} \Big(\hat{c}^\dagger_{j,s}\hat{c}_{j+1,s}\hat{b}_j + \hat{c}^\dagger_{j+1,s}\hat{c}_{j,s}\hat{b}_j \\ & - \hat{c}^\dagger_{j,s}\hat{c}_{j+1,s}\hat{b}^\dagger_j - \hat{c}^\dagger_{j+1,s}\hat{c}_{j,s}\hat{b}^\dagger_j \Big) \Bigg) \\ & - it_0\gamma^2 \Bigg(\sum_{j=1,s=\uparrow,\downarrow}^{L-1} \Big(\hat{c}^\dagger_{j+1,s}\hat{c}_{j,s}(\hat{X}_j)^2 \\ & - \hat{c}^\dagger_{j+1,s}\hat{c}_{j,s}\hat{X}_j\hat{X}_{j+1} \\ & + \hat{c}^\dagger_{j,s}\hat{c}_{j+1,s}\hat{X}_j\hat{X}_{j+1} - \hat{c}^\dagger_{j,s}\hat{c}_{j+1,s}(\hat{X}_j)^2 \Big) \Bigg) \\ & + it_0\gamma^2 \Bigg(\sum_{j=2,s=\uparrow,\downarrow}^{L} \Big(\hat{c}^\dagger_{j-1,s}\hat{c}_{j,s}(\hat{X}_j)^2 - \hat{c}^\dagger_{j-1,,s}\hat{c}_{j,s}\hat{X}_j\hat{X}_{j-1} \\ & + \hat{c}^\dagger_{j,s}\hat{c}_{j-1,s}\hat{X}_j\hat{X}_{j-1} - \hat{c}^\dagger_{j,s}\hat{c}_{j-1,s}(\hat{X}_j)^2 \Big) \Bigg) \\ & - \gamma t_0^2 i \Bigg(\sum_{j=1,s=\uparrow,\downarrow}^{L-2} \Big(\hat{c}^\dagger_{j+2,s}\hat{c}_{j,s} - \hat{c}^\dagger_{j,s}\hat{c}_{j+2,s} \Big) \hat{X}_j \\ & + \sum_{j=1,s=\uparrow,\downarrow}^{L-2} \Big(\hat{c}^\dagger_{j,s}\hat{c}_{j+2,s} - \hat{c}^\dagger_{j+2,s}\hat{c}_{j,s} \Big) \hat{X}_{j+1} \Bigg) \\ & - \gamma t_0^2 i \Bigg(\sum_{j=2}^{L-1} \Big(\hat{c}^\dagger_{j-1,s}\hat{c}_{j+1,s} - \hat{c}^\dagger_{j+1,s}\hat{c}_{j-1,s} \Big) X_j \\ & + \sum_{j=2,s=\uparrow,\downarrow}^{L-1} \Big(\hat{c}^\dagger_{j+1,s}\hat{c}_{j-1,s} - \hat{c}^\dagger_{j-1,s}\hat{c}_{j+1,s} \Big) \hat{X}_{j+1} \Bigg),\end{aligned} \tag{B7}$$

with $\hat{X}_i = \hat{b}^\dagger_i + \hat{b}_i$. Figure 18 shows $\tilde{M}_1$, $\tilde{M}_2$, and $\tilde{M}_3$ for the same data as plotted in Fig. 11. We display both the integrated correlation functions (integrated for $\omega/\omega_0 \in [-15, 15]$) and the thermal expectation values. The relative difference is at maximum of the order of $\mathcal{O}(10^{-3})$. For the data shown in Fig. 10, the relative difference is also at maximum of the order of $\mathcal{O}(10^{-3})$. The moments without zero padding are in some cases just as good as for the data with zero padding. For the DMRG data in Fig. 12, we integrated for $\omega/\omega_0 \in [-80, 80]$ and obtain a relative difference at maximum of the order $\mathcal{O}(10^{-3})$. For the bipolaron data in Fig. 13, the difference in the moments are at most of the order $\mathcal{O}(10^{-3})$ when integrated for $\omega/\omega_0 \in [-15, 15]$. In Fig. 14, the relative difference is of order $\mathcal{O}(10^{-3})$ when we integrate for $\omega/\omega_0 \in [-50, 50]$.

To quantify the influence of the phonon cutoff M for large coupling and large temperatures ($T/\omega_0 = 1$), we compare several quantities in Fig. 19. Figure 19(a) shows the relative difference in the f-sum rule between the initial state and the integrated real part of the optical conductivity:

$$d(\text{f-sum}) = \frac{\left| \int_0^\infty d\omega \sigma'(\omega) - \frac{-\pi \langle E_{\text{kin}} \rangle_T}{2} \right|}{\left| \frac{-\pi \langle E_{\text{kin}} \rangle_T}{2} \right|}. \tag{B8}$$

Note that all terms in Eq. (B8) are evaluated with the same phonon truncation M and that we integrate for $\omega/\omega_0 \in [0, 80]$. We observe that the result improves as M is increased. The empty symbols show the same data but without zero padding. As can be seen, the sparse number of integration points produces inaccurate results. We also mention that the type of methods used has difficulties correctly capturing the low-frequency physics due to the limitations in reachable times.

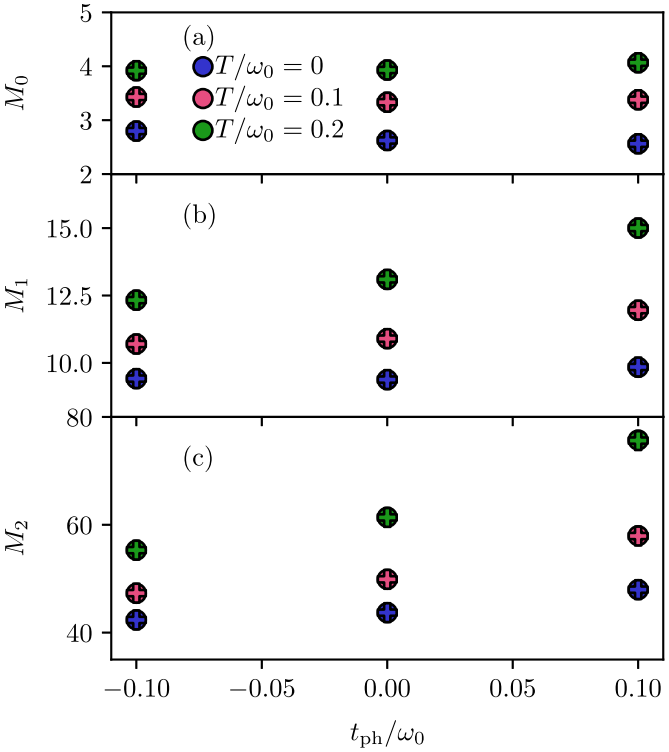

FIG. 18. Moments of the correlation function for the same parameters as in Fig. 11. (a) Zeroth moment, (b) first moment, (c) second moment. The circles are calculated by integrating the Fourier transformed data obtained with time evolution and the plus signs from evaluating the commutators at finite temperatures. For details, see Appendix B.

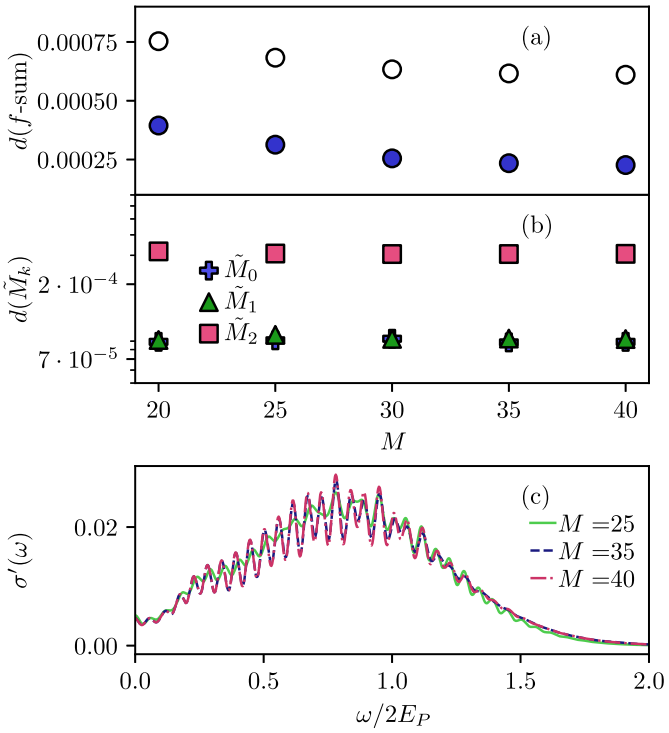

FIG. 19. (a) Relative difference in the f-sum rule, see Appendix B for details. (b) Relative difference in the moments, also see Appendix B. (c) Real part of the optical conductivity. All data are at $T/\omega_0 = 1$ and with different phonon cutoff M. The rest of the parameters are the same as in Fig. 12. The open circles in (a) show the data when no zero padding is used.

This can also lead to inaccurate results for the f-sums rule, in particular for systems with a significant Drude weight. In Fig. 19(b), we illustrate how the moments behave when M is varied. There, we show the relative difference between the integral over the correlation function (integrated for $\omega/\omega_0 \in [-80, 80]$) and the thermal expectation value (i.e., right-hand side of Eq. (B2) for $\tilde{M}_0$) denoted as $\langle\hat{\tilde{M}}_k\rangle_T$:

$$d(\tilde{M}_k) = \frac{\left|\int_{-\infty}^{\infty} d\omega(\omega)^k C(\omega)_T - \langle\hat{\tilde{M}}_k\rangle_T\right|}{|\langle\hat{\tilde{M}}_k\rangle_T|}. \tag{B9}$$

We first see that all moments have similar accuracy. Still, while not shown here, the moments do seem to converge individually when M is increased. We wish to emphasize that the moments are very accurate with and without zero padding and thus must be used with caution as convergence criteria.

One sees the influence of the different M on the optical conductivity in Fig. 19(c). Even for the largest M used here, small differences in some of the peak amplitudes can be observed. Still, the spectrum is quantitatively well captured. We also want to note that the real part of the optical conductivity in Fig. 19(c) has an η dependence as well. This can be understood by inspecting the current-current correlation function (not shown here). There are still some M dependent oscillations at longer times which get suppressed when η is large. This is not the case for $t_{\mathrm{ph}}/\omega_0 \neq 0$, where the correlation functions have no notable oscillations for large times t/ω_0. Similar behavior is seen for the ground-state calculations in Fig. 9. In some cases, we also observe some L dependence in the amplitudes of the optical conductivities. This is illustrated in Fig. 20.

We further want to remark that the use of zero padding is not strictly necessary when using single-site TDVP as is done for $T/\omega_0 = 1$. This is because the computational cost does not increase with time. However, we do this to justifiably compare it to the ground-state data, for which we use p2TDVP-LBO, and which has an increased computational cost with time. We can conclude that for our data, the convergence of the integral and the expectation values is a necessary but not a sufficient criterion to ensure proper convergence of the optical conductivity for parameters of the initial state. The convergence of the moments relative to each other seems to work better.

Furthermore, the moments and the kinetic energy are used to ensure that the initial thermal state is converged with respect to ρ_{LBO}, ρ_{bond}, M, and the imaginary-time step. The largest relative difference is of order $\mathcal{O}(10^{-3})$ and is found for some quantities for the large coupling polaron and bipolaron at $T/\omega_0 = 1$. We also computed the relative overlap between states with different ρ_{LBO}, ρ_{bond} and imaginary time steps and found a maximum difference from one of the order of $\mathcal{O}(10^{-5})$ for strong coupling and $T/\omega_0 = 1.0$ and $\mathcal{O}(10^{-6})$ for the rest of our finite T/ω_0 data.

APPENDIX C: BORN-OPPENHEIMER SURFACES

In order to derive an analytic expression for the real part of the optical conductivity for strong electron-phonon coupling,

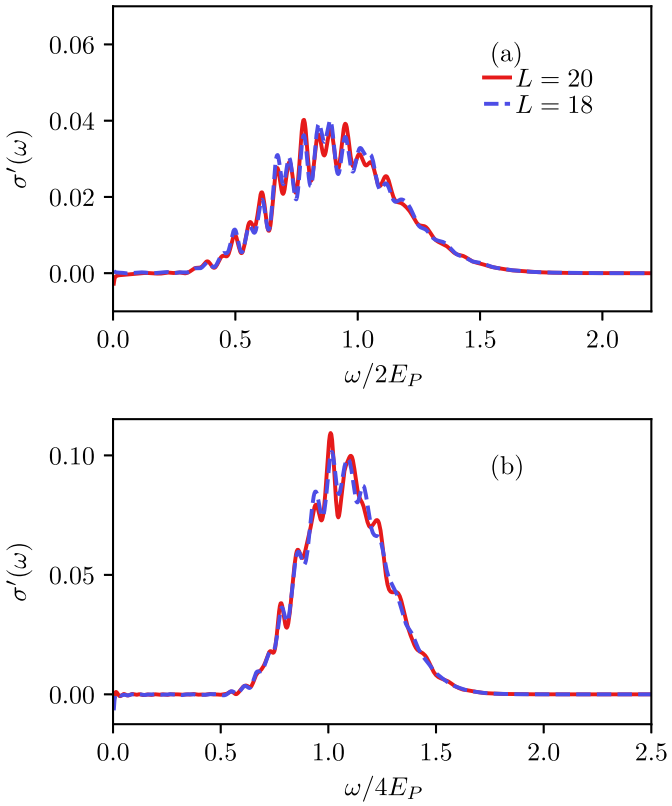

FIG. 20. (a) Ground-state optical conductivity for the polaron from Fig. 12(b) for two different system sizes. All other parameters are the same as in Fig. 12(b). (b) Ground-state optical conductivity for the bipolaron from Fig. 14(c) for the same system sizes as in (a). All other parameters are the same as in Fig. 14(c).

we first obtain the Born-Oppenheimer Hamiltonian [91,92] from Eq. (15). For a fixed $\bar{q}$ this becomes a 2×2 matrix, in the polaron case, which can be diagonalized

$$H_{\mathrm{BO}} = \begin{pmatrix} \frac{\bar{q}^2}{2}\tilde{\omega}_0 + \gamma\bar{q} & -t_0 \\ -t_0 & \frac{\bar{q}^2}{2}\tilde{\omega}_0 - \gamma\bar{q} \end{pmatrix}, \tag{C1}$$

where $\tilde{\omega}_0 = \omega_0 - t_{\mathrm{ph}}$. The Hamiltonian has the energies $E_{\pm}^{\mathrm{BO}} = \frac{1}{2}(\bar{q}^2\tilde{\omega}_0 \pm 2\sqrt{(\gamma\bar{q})^2 + t_0^2})$. These energies give the Born-Oppenheimer surfaces. Their extrema with respect to $\bar{q}$ can be found by setting their derivatives to zero and one obtains $\bar{q} = 0$, and $\bar{q}_{\mathrm{min},\pm} = \pm\frac{\sqrt{\gamma^4 - \tilde{\omega}_0^2 t_0^2}}{\tilde{\omega}_0\gamma}$. The Born-Oppenheimer surfaces can be seen in Fig. 2(a) for different phonon dispersion relations. The minima of the lower surface decrease as the phonon hopping goes from $t_{\mathrm{ph}}/\omega_0 = -0.1$ to $+0.1$. We obtain $\Delta^{\mathrm{BO}} = E_+^{\mathrm{BO}}(q_{\mathrm{min},\pm}) - E_-^{\mathrm{BO}}(q_{\mathrm{min},\pm}) = 2\sqrt{\frac{\gamma^4 - \tilde{\omega}_0^2 t_0^2}{\tilde{\omega}_0^2} + t_0^2}$. For the bipolaron, we have a 4×4 matrix

$$H_{\mathrm{BO}} = \begin{pmatrix} \frac{\bar{q}^2}{2}\tilde{\omega}_0 + 2\gamma\bar{q} & -t_0 & -t_0 & 0 \\ -t_0 & \frac{\bar{q}^2}{2}\tilde{\omega}_0 & 0 & -t_0 \\ -t_0 & 0 & \frac{\bar{q}^2}{2}\tilde{\omega}_0 & -t_0 \\ 0 & -t_0 & -t_0 & \frac{\bar{q}^2}{2}\tilde{\omega}_0 - 2\gamma\bar{q} \end{pmatrix}, \tag{C2}$$

using the convention $|\uparrow\downarrow, 0\rangle, |\uparrow, \downarrow\rangle, |\downarrow, \uparrow\rangle, |0, \uparrow\downarrow\rangle$ for the electron occupation basis. Here, the surfaces are obtained by solving for the eigenvalues numerically.

To obtain Eq. (16), one uses the fact that the current operator connects the lowest and the first excited surfaces for a fixed $\bar{q}$. To calculate the current-current correlation function, one must then compute [140]

$$\begin{aligned} \langle e^{i\hat{H}_g t} e^{-i\hat{H}_e t}\rangle_T &= \langle e^{-\hat{S}} e^{\hat{S}} e^{i\hat{H}_g t} e^{-\hat{S}} e^{\hat{S}} e^{-i\hat{H}_e t} e^{-\hat{S}} e^{\hat{S}}\rangle_T \\ &= \langle e^{i\hat{H}_e t} e^{\hat{S}} e^{-i\hat{H}_e t} e^{-\hat{S}}\rangle_T = \langle e^{\hat{S}(t)} e^{-\hat{S}}\rangle_T, \end{aligned} \tag{C3}$$

where $\hat{H}_g$ is the harmonic oscillator Hamiltonian with frequencies $\tilde{\omega}_0 = \omega_0 - t_{\mathrm{ph}}$ and ladder operators $\hat{a}$ and $\hat{a}^\dagger$. $\hat{H}_e$ is the harmonic oscillator Hamiltonian shifted with the distance d and $e^{-\hat{S}}$ is the Lang-Firsov transformation operator, see Ref. [125], with $\hat{S} = d\sqrt{\frac{1}{2}}(\hat{a} - \hat{a}^\dagger)$. Evaluating Eq. (C3), see, e.g., Ref. [96], rescaling with a factor of two for $L > 2$, and expanding $e^{i\tilde{\omega}_0 t} = 1 + i\tilde{\omega}_0 t - \frac{1}{2}\tilde{\omega}_0^2 t^2 + \mathcal{O}(\tilde{\omega}_0^3)$ before the Fourier transformation leads to Eq. (16).

[1] C. Franchini, M. Reticcioli, M. Setvin, and U. Diebold, Polarons in materials, Nat. Rev. Mater. **6**, 560 (2021).

[2] A. J. Millis, P. B. Littlewood, and B. I. Shraiman, Double Exchange Alone does not Explain the Resistivity of $La_{1-x}Sr_xMnO_3$, Phys. Rev. Lett. **74**, 5144 (1995).

[3] A. Lanzara, N. L. Saini, M. Brunelli, F. Natali, A. Bianconi, P. G. Radaelli, and S.-W. Cheong, Crossover from Large to Small Polarons across the Metal-Insulator Transition in Manganites, Phys. Rev. Lett. **81**, 878 (1998).

[4] C. Jooss, L. Wu, T. Beetz, R. F. Klie, M. Beleggia, M. A. Schofield, S. Schramm, J. Hoffmann, and Y. Zhu, Polaron melting and ordering as key mechanisms for colossal resistance effects in manganites, Proc. Natl. Acad. Sci. USA **104**, 13597 (2007).

[5] S. Schramm, J. Hoffmann, and C. Jooss, Transport and ordering of polarons in CER manganites PrCaMnO, J. Phys.: Condens. Matter **20**, 395231 (2008).

[6] K. Miyata, D. Meggiolaro, M. T. Trinh, P. P. Joshi, E. Mosconi, S. C. Jones, F. D. Angelis, and X.-Y. Zhu, Large polarons in lead halide perovskites, Sci. Adv. **3**, e1701217 (2017).

[7] D. Cortecchia, J. Yin, A. Bruno, S.-Z. A. Lo, G. G. Gurzadyan, S. Mhaisalkar, J.-L. Brédas, and C. Soci, Polaron self-localization in white-light emitting hybrid perovskites, J. Mater. Chem. C **5**, 2771 (2017).

[8] E. Cinquanta, D. Meggiolaro, S. G. Motti, M. Gandini, M. J. P. Alcocer, Q. A. Akkerman, C. Vozzi, L. Manna, F. De Angelis, A. Petrozza, and S. Stagira, Ultrafast THz Probe of Photoinduced Polarons in Lead-Halide Perovskites, Phys. Rev. Lett. **122**, 166601 (2019).

[9] D. Ghosh, E. Welch, A. J. Neukirch, A. Zakhidov, and S. Tretiak, Polarons in halide perovskites: A perspective, J. Phys. Chem. Lett. **11**, 3271 (2020).

[10] S. Yoon, H. L. Liu, G. Schollerer, S. L. Cooper, P. D. Han, D. A. Payne, S.-W. Cheong, and Z. Fisk, Raman and

optical spectroscopic studies of small-to-large polaron crossover in the perovskite manganese oxides, Phys. Rev. B **58**, 2795 (1998).

[11] M. Quijada, J. Černe, J. R. Simpson, H. D. Drew, K. H. Ahn, A. J. Millis, R. Shreekala, R. Ramesh, M. Rajeswari, and T. Venkatesan, Optical conductivity of manganites: Crossover from Jahn-Teller small polaron to coherent transport in the ferromagnetic state, Phys. Rev. B **58**, 16093 (1998).

[12] S. Mildner, J. Hoffmann, P. E. Blöchl, S. Techert, and C. Jooss, Temperature- and doping-dependent optical absorption in the small-polaron system $Pr_{1-x}Ca_xMno_3$, Phys. Rev. B **92**, 035145 (2015).

[13] K. H. Kim, J. Y. Gu, H. S. Choi, G. W. Park, and T. W. Noh, Frequency Shifts of the Internal Phonon Modes in $La_{0.7}Ca_{0.3}MnO_3$, Phys. Rev. Lett. **77**, 1877 (1996).

[14] C. Hartinger, F. Mayr, A. Loidl, and T. Kopp, Polaronic excitations in colossal magnetoresistance manganite films, Phys. Rev. B **73**, 024408 (2006).

[15] A. Machida, Y. Moritomo, and A. Nakamura, Spectroscopic evidence for formation of small polarons in doped manganites, Phys. Rev. B **58**, R4281 (1998).

[16] C. Zhang, J. Sous, D. R. Reichman, M. Berciu, A. J. Millis, N. V. Prokof'ev, and B. V. Svistunov, Bipolaronic high-temperature superconductivity, arXiv:2203.07380.

[17] Y. Zhang, T. Kafle, W. You, X. Shi, L. Min, H. (Hugo)Wang, N. Li, V. Gopalan, K. Rossnagel, L. Yang, Z. Mao, R. Nandkishore, H. Kapteyn, and M. Murnane, Bipolaronic nature of the pseudogap in (TaSe4)2I revealed via weak photoexcitation, arXiv:2203.05655.

[18] T. Holstein, Studies of polaron motion: Part I. The molecular-crystal model, Ann. Phys. (NY) **8**, 325 (1959).

[19] R. J. Bursill, R. H. McKenzie, and C. J. Hamer, Phase Diagram of the One-Dimensional Holstein Model of Spinless Fermions, Phys. Rev. Lett. **80**, 5607 (1998).

[20] C. E. Creffield, G. Sangiovanni, and M. Capone, Phonon softening and dispersion in the 1D Holstein model of spinless fermions, Eur. Phys. J. B **44**, 175 (2005).

[21] S. Fratini and S. Ciuchi, Dynamical Mean-Field Theory of Transport of Small Polarons, Phys. Rev. Lett. **91**, 256403 (2003).

[22] O. S. Barišić, Variational study of the Holstein polaron, Phys. Rev. B **65**, 144301 (2002).

[23] O. S. Barišić, Calculation of excited polaron states in the Holstein model, Phys. Rev. B **69**, 064302 (2004).

[24] O. S. Barišić, Holstein light quantum polarons on the one-dimensional lattice, Phys. Rev. B **73**, 214304 (2006).

[25] O. S. Barišić and S. Barišić, Phase diagram of the Holstein polaron in one dimension, Eur. Phys. J. B **64**, 1 (2008).

[26] J. Loos, M. Hohenadler, A. Alvermann, and H. Fehske, Phonon spectral function of the Holstein polaron, J. Phys.: Condens. Matter **18**, 7299 (2006).

[27] J. Loos, M. Hohenadler, and H. Fehske, Spectral functions of the spinless Holstein model, J. Phys.: Condens. Matter **18**, 2453 (2006).

[28] L. Vidmar, J. Bonča, and S. A. Trugman, Emergence of states in the phonon spectral function of the Holstein polaron below and above the one-phonon continuum, Phys. Rev. B **82**, 104304 (2010).

[29] L. Vidmar, J. Bonča, M. Mierzejewski, P. Prelovšek, and S. A. Trugman, Nonequilibrium dynamics of the Holstein polaron driven by an external electric field, Phys. Rev. B **83**, 134301 (2011).

[30] F. Dorfner, L. Vidmar, C. Brockt, E. Jeckelmann, and F. Heidrich-Meisner, Real-time decay of a highly excited charge carrier in the one-dimensional Holstein model, Phys. Rev. B **91**, 104302 (2015).

[31] C. Brockt and E. Jeckelmann, Scattering of an electronic wave packet by a one-dimensional electron-phonon-coupled structure, Phys. Rev. B **95**, 064309 (2017).

[32] D. Jansen, J. Stolpp, L. Vidmar, and F. Heidrich-Meisner, Eigenstate thermalization and quantum chaos in the Holstein polaron model, Phys. Rev. B **99**, 155130 (2019).

[33] J. Bonča, S. A. Trugman, and M. Berciu, Spectral function of the Holstein polaron at finite temperature, Phys. Rev. B **100**, 094307 (2019).

[34] L. Chen-Yen and S. A. Trugman, Absence of diffusion and fractal geometry in the Holstein model at high temperature, arXiv:2007.00817.

[35] D. Jansen, J. Bonča, and F. Heidrich-Meisner, Finite-temperature density-matrix renormalization group method for electron-phonon systems: Thermodynamics and Holstein-polaron spectral functions, Phys. Rev. B **102**, 165155 (2020).

[36] J. Bonča and S. A. Trugman, Dynamic properties of a polaron coupled to dispersive optical phonons, Phys. Rev. B **103**, 054304 (2021).

[37] E. Jeckelmann, C. Zhang, and S. R. White, Metal-insulator transition in the one-dimensional Holstein model at half filling, Phys. Rev. B **60**, 7950 (1999).

[38] C. Zhang, E. Jeckelmann, and S. R. White, Dynamical properties of the one-dimensional Holstein model, Phys. Rev. B **60**, 14092 (1999).

[39] H. Zhao, C. Q. Wu, and H. Q. Lin, Spectral function of the one-dimensional Holstein model at half filling, Phys. Rev. B **71**, 115201 (2005).

[40] H. Hashimoto and S. Ishihara, Photoinduced charge-order melting dynamics in a one-dimensional interacting Holstein model, Phys. Rev. B **96**, 035154 (2017).

[41] J. Stolpp, J. Herbrych, F. Dorfner, E. Dagotto, and F. Heidrich-Meisner, Charge-density-wave melting in the one-dimensional Holstein model, Phys. Rev. B **101**, 035134 (2020).

[42] M. Weber and J. K. Freericks, Field tuning beyond the heat death of a charge-density-wave chain, arXiv:2107.04096.

[43] D. Jansen, C. Jooss, and F. Heidrich-Meisner, Charge density wave breakdown in a heterostructure with electron-phonon coupling, Phys. Rev. B **104**, 195116 (2021).

[44] H. Fehske, D. Ihle, J. Loos, U. Trapper, and H. Büttner, Polaron formation and hopping conductivity in the Holstein-Hubbard model, Z. Phys. B **94**, 91 (1994).

[45] D. Ihle, H. Fehske, J. Loos, and U. Trapper, Bi-/polaron formation and optical conductivity in the Holstein-Hubbard model, Physica C: Superconductivity **235-240**, 2363 (1994).

[46] G. Wellein, H. Röder, and H. Fehske, Polarons and bipolarons in strongly interacting electron-phonon systems, Phys. Rev. B **53**, 9666 (1996).

[47] J. Bonča, T. Katrašnik, and S. A. Trugman, Mobile Bipolaron, Phys. Rev. Lett. **84**, 3153 (2000).

[48] J. Bonča and S. A. Trugman, Bipolarons in the extended Holstein Hubbard model, Phys. Rev. B **64**, 094507 (2001).

[49] P. Werner and A. J. Millis, Efficient Dynamical Mean Field Simulation of the Holstein-Hubbard Model, Phys. Rev. Lett. **99**, 146404 (2007).

[50] H. Fehske, G. Hager, and E. Jeckelmann, Metallicity in the half-filled Holstein-Hubbard model, Europhys. Lett. **84**, 57001 (2008).

[51] D. Golež, J. Bonča, and L. Vidmar, Dissociation of a Hubbard-Holstein bipolaron driven away from equilibrium by a constant electric field, Phys. Rev. B **85**, 144304 (2012).

[52] A. Nocera, M. Soltanieh-ha, C. A. Perroni, V. Cataudella, and A. E. Feiguin, Interplay of charge, spin, and lattice degrees of freedom in the spectral properties of the one-dimensional Hubbard-Holstein model, Phys. Rev. B **90**, 195134 (2014).

[53] P. Werner and M. Eckstein, Field-induced polaron formation in the Holstein-Hubbard model, Europhys. Lett. **109**, 37002 (2015).

[54] F. Marsiglio, Impact of retardation in the Holstein-Hubbard model: a two-site calculation, arXiv:2205.10352.

[55] L. Vidmar, J. Bonča, S. Maekawa, and T. Tohyama, Bipolaron in the t-J Model Coupled to Longitudinal and Transverse Quantum Lattice Vibrations, Phys. Rev. Lett. **103**, 186401 (2009).

[56] L. Vidmar, J. Bonča, T. Tohyama, and S. Maekawa, Quantum Dynamics of a Driven Correlated System Coupled to Phonons, Phys. Rev. Lett. **107**, 246404 (2011).

[57] A. Szabó, S. A. Parameswaran, and A. Gopalakrishnan, High-temperature transport and polaron speciation in the anharmonic Holstein model, arXiv:2110.10170.

[58] J. H. Fetherolf, P. Shih, and T. C. Berkelbach, Conductivity of an electron coupled to anharmonic phonons, arXiv:2205.09811.

[59] N. C. Costa, T. Blommel, W.-T. Chiu, G. Batrouni, and R. T. Scalettar, Phonon Dispersion and the Competition between Pairing and Charge Order, Phys. Rev. Lett. **120**, 187003 (2018).

[60] C. Schönle, D. Jansen, F. Heidrich-Meisner, and L. Vidmar, Eigenstate thermalization hypothesis through the lens of autocorrelation functions, Phys. Rev. B **103**, 235137 (2021).

[61] D. J. J. Marchand and M. Berciu, Effect of dispersive optical phonons on the behavior of a Holstein polaron, Phys. Rev. B **88**, 060301(R) (2013).

[62] P. J. Robinson, I. S. Dunn, and D. R. Reichman, Cumulant methods for electron-phonon problems ii: The self-consistent cumulant expansion, Phys. Rev. B **105**, 224305 (2022).

[63] M. Capone, W. Stephan, and M. Grilli, Small-polaron formation and optical absorption in Su-Schrieffer-Heeger and Holstein models, Phys. Rev. B **56**, 4484 (1997).

[64] S. Fratini, F. de Pasquale, and S. Ciuchi, Optical absorption from a nondegenerate polaron gas, Phys. Rev. B **63**, 153101 (2001).

[65] G. Schubert, G. Wellein, A. Weisse, A. Alvermann, and H. Fehske, Optical absorption and activated transport in polaronic systems, Phys. Rev. B **72**, 104304 (2005).

[66] S. Fratini and S. Ciuchi, Optical properties of small polarons from dynamical mean-field theory, Phys. Rev. B **74**, 075101 (2006).

[67] G. Wellein and H. Fehske, Self-trapping problem of electrons or excitons in one dimension, Phys. Rev. B **58**, 6208 (1998).

[68] G. L. Goodvin, A. S. Mishchenko, and M. Berciu, Optical Conductivity of the Holstein Polaron, Phys. Rev. Lett. **107**, 076403 (2011).

[69] B. Bertini, F. Heidrich-Meisner, C. Karrasch, T. Prosen, R. Steinigeweg, and M. Žnidarič, Finite-temperature transport in one-dimensional quantum lattice models, Rev. Mod. Phys. **93**, 025003 (2021).

[70] S. R. White, Density Matrix Formulation for Quantum Renormalization Groups, Phys. Rev. Lett. **69**, 2863 (1992).

[71] U. Schollwöck, The density-matrix renormalization group, Rev. Mod. Phys. **77**, 259 (2005).

[72] U. Schollwöck, The density-matrix renormalization group in the age of matrix product states, Ann. Phys. (NY) **326**, 96 (2011).

[73] F. Verstraete, J. J. García-Ripoll, and J. I. Cirac, Matrix Product Density Operators: Simulation of Finite-Temperature and Dissipative Systems, Phys. Rev. Lett. **93**, 207204 (2004).

[74] A. J. Daley, C. Kollath, U. Schollwöck, and G. Vidal, Time-dependent density-matrix renormalization-group using adaptive effective Hilbert spaces, J. Stat. Mech. (2004) P04005.

[75] S. R. White and A. E. Feiguin, Real-Time Evolution Using the Density Matrix Renormalization Group, Phys. Rev. Lett. **93**, 076401 (2004).

[76] G. Vidal, Efficient Simulation of One-Dimensional Quantum Many-Body Systems, Phys. Rev. Lett. **93**, 040502 (2004).

[77] A. E. Feiguin and S. R. White, Finite-temperature density matrix renormalization using an enlarged Hilbert space, Phys. Rev. B **72**, 220401(R) (2005).

[78] T. Barthel, U. Schollwöck, and S. R. White, Spectral functions in one-dimensional quantum systems at finite temperature using the density matrix renormalization group, Phys. Rev. B **79**, 245101 (2009).

[79] E. M. Stoudenmire and S. R. White, Minimally entangled typical thermal state algorithms, New J. Phys. **12**, 055026 (2010).

[80] A. E. Feiguin and G. A. Fiete, Spectral properties of a spin-incoherent Luttinger liquid, Phys. Rev. B **81**, 075108 (2010).

[81] S. Paeckel, T. Köhler, A. Swoboda, S. R. Manmana, U. Schollwöck, and C. Hubig, Time-evolution methods for matrix-product states, Ann. Phys. (NY) **411**, 167998 (2019).

[82] C. Zhang, E. Jeckelmann, and S. R. White, Density Matrix Approach to Local Hilbert Space Reduction, Phys. Rev. Lett. **80**, 2661 (1998).

[83] E. Jeckelmann and S. R. White, Density-matrix renormalization-group study of the polaron problem in the Holstein model, Phys. Rev. B **57**, 6376 (1998).

[84] T. Köhler, J. Stolpp, and S. Paeckel, Efficient and flexible approach to simulate low-dimensional quantum lattice models with large local hilbert spaces, SciPost Phys. **10**, 058 (2021).

[85] S. Mardazad, Y. Xu, X. Yang, M. Grundner, U. Schollwöck, H. Ma, and S. Paeckel, Quantum dynamics simulation of intramolecular singlet fission in covalently linked tetracene dimer, J. Chem. Phys. **155**, 194101 (2021).

[86] J. Haegeman, J. I. Cirac, T. J. Osborne, I. Pižorn, H. Verschelde, and F. Verstraete, Time-Dependent Variational Principle for Quantum Lattices, Phys. Rev. Lett. **107**, 070601 (2011).

[87] J. Haegeman, C. Lubich, I. Oseledets, B. Vandereycken, and F. Verstraete, Unifying time evolution and optimization with matrix product states, Phys. Rev. B **94**, 165116 (2016).

[88] P. Secular, N. Gourianov, M. Lubasch, S. Dolgov, S. R. Clark, and D. Jaksch, Parallel time-dependent variational principle algorithm for matrix product states, Phys. Rev. B **101**, 235123 (2020).

[89] C. Lanczos, An iteration method for the solution of the eigenvalue problem of linear differential and integral operators, J. Res. Natl. Bur. Stand. **45**, 255 (1950).

[90] P. Prelovšek and J. Bonča, *Ground State and Finite Temperature Lanczos Methods, Ground State and Finite Temperature Lanczos Methods* (Springer, Berlin, Heidelberg, 2013), pp. 1–30.

[91] M. Born and R. Oppenheimer, Zur Quantentheorie der Molekeln, Annalen der Physik **389**, 457 (1927).

[92] M. Born and K. Huang, *Dynamical Theory of Crystal Lattices* (Clarendon Press, Oxford, 1954).

[93] M. Stone and P. Goldbart, *Mathematics for Physics: A Guided Tour for Graduate Students* (Cambridge University Press, New York, 2009).

[94] H. Reik and D. Heese, Frequency dependence of the electrical conductivity of small polarons for high and low temperatures, J. Phys. Chem. Solids **28**, 581 (1967).

[95] D. Emin, Optical properties of large and small polarons and bipolarons, Phys. Rev. B **48**, 13691 (1993).

[96] G. Mahan, *Many-Particle Physics* (Plenum, New York, 2000).

[97] G. C. Schatz and M. A. Ratner, *Quantum Mechanics in Chemestry* (Dover, Mineola, New York, 2002).

[98] A. Nitzan, *Chemical Dynamics in Condensed Phases* (Oxford University Press, New York, 2006).

[99] Y. A. Firsov and E. K. Kudinov, The polaron state of a crystal, Phys. Solid State **43**, 447 (2001).

[100] L. K. McKemmish, R. H. McKenzie, N. S. Hush, and J. R. Reimers, Electronvibration entanglement in the Born-Oppenheimer description of chemical reactions and spectroscopy, Phys. Chem. Chem. Phys. **17**, 24666 (2015).

[101] S. R. White, Minimally Entangled Typical Quantum States at Finite Temperature, Phys. Rev. Lett. **102**, 190601 (2009).

[102] M. Binder and T. Barthel, Minimally entangled typical thermal states versus matrix product purifications for the simulation of equilibrium states and time evolution, Phys. Rev. B **92**, 125119 (2015).

[103] T. Barthel, Matrix product purifications for canonical ensembles and quantum number distributions, Phys. Rev. B **94**, 115157 (2016).

[104] A. Nocera and G. Alvarez, Symmetry-conserving purification of quantum states within the density matrix renormalization group, Phys. Rev. B **93**, 045137 (2016).

[105] M. Urbanek and P. Soldán, Parallel implementation of the time-evolving block decimation algorithm for the bosehubbard model, Comput. Phys. Commun. **199**, 170 (2016).

[106] B. Kloss, Y. B. Lev, and D. Reichman, Time-dependent variational principle in matrix-product state manifolds: Pitfalls and potential, Phys. Rev. B **97**, 024307 (2018).

[107] B. Kloss, D. R. Reichman, and R. Tempelaar, Multiset Matrix Product State Calculations Reveal Mobile Franck-Condon Excitations Under Strong Holstein-Type Coupling, Phys. Rev. Lett. **123**, 126601 (2019).

[108] M. Yang and S. R. White, Time-dependent variational principle with ancillary Krylov subspace, Phys. Rev. B **102**, 094315 (2020).

[109] Y. Xu, Z. Xie, X. Xie, U. Schollwöck, and H. Ma, Stochastic adaptive single-site time-dependent variational principle, JACS Au **2**, 335 (2022).

[110] E. M. Stoudenmire and S. R. White, Real-space parallel density matrix renormalization group, Phys. Rev. B **87**, 155137 (2013).

[111] G. Vidal, Efficient Classical Simulation of Slightly Entangled Quantum Computations, Phys. Rev. Lett. **91**, 147902 (2003).

[112] C. Guo, A. Weichselbaum, J. von Delft, and M. Vojta, Critical and Strong-Coupling Phases in One- and Two-Bath Spin-Boson Models, Phys. Rev. Lett. **108**, 160401 (2012).

[113] C. Brockt, F. Dorfner, L. Vidmar, F. Heidrich-Meisner, and E. Jeckelmann, Matrix-product-state method with a dynamical local basis optimization for bosonic systems out of equilibrium, Phys. Rev. B **92**, 241106(R) (2015).

[114] A. E. Feiguin and S. R. White, Time-step targeting methods for real-time dynamics using the density matrix renormalization group, Phys. Rev. B **72**, 020404(R) (2005).

[115] C. Karrasch, J. H. Bardarson, and J. E. Moore, Finite-Temperature Dynamical Density Matrix Renormalization Group and the Drude Weight of Spin-1/2 Chains, Phys. Rev. Lett. **108**, 227206 (2012).

[116] T. Barthel, U. Schollwöck, and S. Sachdev, Scaling of the thermal spectral function for quantum critical bosons in one dimension, arXiv:1212.3570.

[117] T. Barthel, Precise evaluation of thermal response functions by optimized density matrix renormalization group schemes, New J. Phys. **15**, 073010 (2013).

[118] C. Karrasch, J. H. Bardarson, and J. E. Moore, Reducing the numerical effort of finite-temperature density matrix renormalization group calculations, New J. Phys. **15**, 083031 (2013).

[119] D. Kennes and C. Karrasch, Extending the range of real time density matrix renormalization group simulations, Comput. Phys. Commun. **200**, 37 (2016).

[120] J. Hauschild, E. Leviatan, J. H. Bardarson, E. Altman, M. P. Zaletel, and F. Pollmann, Finding purifications with minimal entanglement, Phys. Rev. B **98**, 235163 (2018).

[121] P. P. Vaidyanathan, *The Theory of Linear Prediction*, Synthesis Lectures on Engineering Series (Morgan & Claypool, San Rafael, 2008).

[122] S. R. White and I. Affleck, Spectral function for the $S = 1$ Heisenberg antiferromagetic chain, Phys. Rev. B **77**, 134437 (2008).

[123] Y. Tian and S. R. White, Matrix product state recursion methods for computing spectral functions of strongly correlated quantum systems, Phys. Rev. B **103**, 125142 (2021).

[124] M. Fishman, S. R. White, and E. M. Stoudenmire, The ITensor software library for tensor network calculations, arXiv:2007.14822 (2020).

[125] I. G. Lang and Yu. A. Firsov, Kinetic theory of semiconductors with low mobility, Zh. Eksp. Teor. Fiz. **43**, 1843 (1963) [Sov. Phys. JETP **16**, 1301 (1963)].

[126] P. Ehrenfest, Bemerkung über die angenäherte Gültigkeit der klassischen Mechanik innerhalb der Quantenmechanik, Z. Phys. **45**, 455 (1927).

[127] J. C. Tully, Molecular dynamics with electronic transitions, J. Chem. Phys. **93**, 1061 (1990).

[128] D. V. Shalashilin, Quantum mechanics with the basis set guided by Ehrenfest trajectories: Theory and application to spin-boson model, J. Chem. Phys. **130**, 244101 (2009).

[129] D. V. Shalashilin, Nonadiabatic dynamics with the help of multiconfigurational Ehrenfest method: Improved theory and fully quantum 24d simulation of pyrazine, J. Chem. Phys. **132**, 244111 (2010).

[130] G. Li, B. Movaghar, A. Nitzan, and M. A. Ratner, Polaron formation: Ehrenfest dynamics vs. exact results, J. Chem. Phys. **138**, 044112 (2013).

[131] P. Mitrić, V. Janković, N. Vukmirović, and D. Tanasković, Spectral Functions of the Holstein Polaron: Exact and Approximate Solutions, Phys. Rev. Lett. **129**, 096401 (2022).

[132] P. J. Robinson, I. S. Dunn, and D. R. Reichman, Cumulant methods for electron-phonon problems i: Perturbative expansions, Phys. Rev. B **105**, 224304 (2022).

[133] J. L. Alonso, C. Bouthelier-Madre, A. Castro, J. Clemente-Gallardo, and J. A. Jover-Galtier, About the computation of finite temperature ensemble averages of hybrid quantum-classical systems with molecular dynamics, New J. Phys. **23**, 063011 (2021).

[134] V. Janković and N. Vukmirović, Spectral and thermodynamic properties of the Holstein polaron: Hierarchical equations of motion approach, Phys. Rev. B **105**, 054311 (2022).

[135] M. ten Brink, S. Gräber, M. Hopjan, D. Jansen, J. Stolpp, F. Heidrich-Meisner, and P. E. Blöchl, Real-time non-adiabatic dynamics in the one-dimensional Holstein model: Trajectory-based vs exact methods, J. Chem. Phys. **156**, 234109 (2022).

[136] T. Hotta and E. Dagotto, *Theory of Manganites* (Springer, Dordrecht, 2004).

[137] F.-Z. Chen, C. Cheng, and H.-G. Luo, Real-space parallel density matrix renormalization group with adaptive boundaries, Chin. Phys. B **30**, 080202 (2021).

[138] P. E. Kornilovitch, Photoemission spectroscopy and sum rules in dilute electron-phonon systems, Europhys. Lett. **59**, 735 (2002).

[139] G. L. Goodvin, M. Berciu, and G. A. Sawatzky, Green's function of the Holstein polaron, Phys. Rev. B **74**, 245104 (2006).

[140] A. Tokmakoff, Lecture notes on time-dependent quantum mechanics and spectroscopy (unpublished).

5.3 Optical conductivity for bipolarons with repulsive electron-electron interaction

In this section, I demonstrate how the bipolaron Born-Oppenheimer surfaces can be utilized to interpret the optical conductivity, even when electron-electron interaction is included. The four Born-Oppenheimer surfaces are obtained by diagonalizing the matrix in Eq. (2.16).

In Fig. 5.1(a), I show the Born-Oppenheimer surfaces for the bipolaron with different interaction strengths U/t_0. For $U/t_0 = 0$, one can detect two possible transitions. One at the energy difference between the lowest and the two degenerate first excited surfaces, and one thermally activated transition at $\bar{q} \approx 0$ with an energy difference $\omega \approx 2t_0$. The latter transition has already been observed for the polaron in Ref. [56]. One can understand this process for the bipolaron by looking at the matrix from Eq. (2.16) with $|\bar{q}| = 0$ and $U/t_0 = 0$. One obtains a matrix that can be diagonalized:

$$\hat{H}_{\mathrm{BO},|\bar{q}|=0,U=0} \begin{pmatrix} 0 & -t_0 & -t_0 & 0 \\ -t_0 & 0 & 0 & -t_0 \\ -t_0 & 0 & 0 & -t_0 \\ 0 & -t_0 & -t_0 & 0 \end{pmatrix}, \tag{5.1}$$

which has the eigenvalues $E_0 = -2t_0$, $E_1 = 0$,$E_2 = 0$ and $E_3 = 2t_0$. In this case, the current operator can only connect the lowest surface state to the first excited state, and not to the eigenstate belonging to the E_3. The eigenvector belonging to eigenvalue E_0 is

$$|\phi_1\rangle = \frac{1}{2} \begin{pmatrix} 1 \\ 1 \\ 1 \\ 1 \end{pmatrix}. \tag{5.2}$$

When applying the current operator, one gets

$$\hat{J}\,|\phi_1\rangle = it_0 \begin{pmatrix} 1 \\ 0 \\ 0 \\ -1 \end{pmatrix}. \tag{5.3}$$

This illustrates that the thermally activated process corresponds to taking two delocalized electrons and binding them together in an antisymmetric wave function for a fixed phonon configuration. In contrast, for the polaron, this process corresponds to going from a symmetric to an antisymmetric wave function with a delocalized electron [56].

Figure 5.1(a) depicts the Born-Oppenheimer surfaces for various U/t_0. When U/t_0 is increased, several observations can be made. Most notably is that the lowest surface is shifted upwards. For large $|\bar{q}|$, the first excited surfaces remain approximately constant, indicating that the center of the optical conductivity will shift to smaller frequencies.

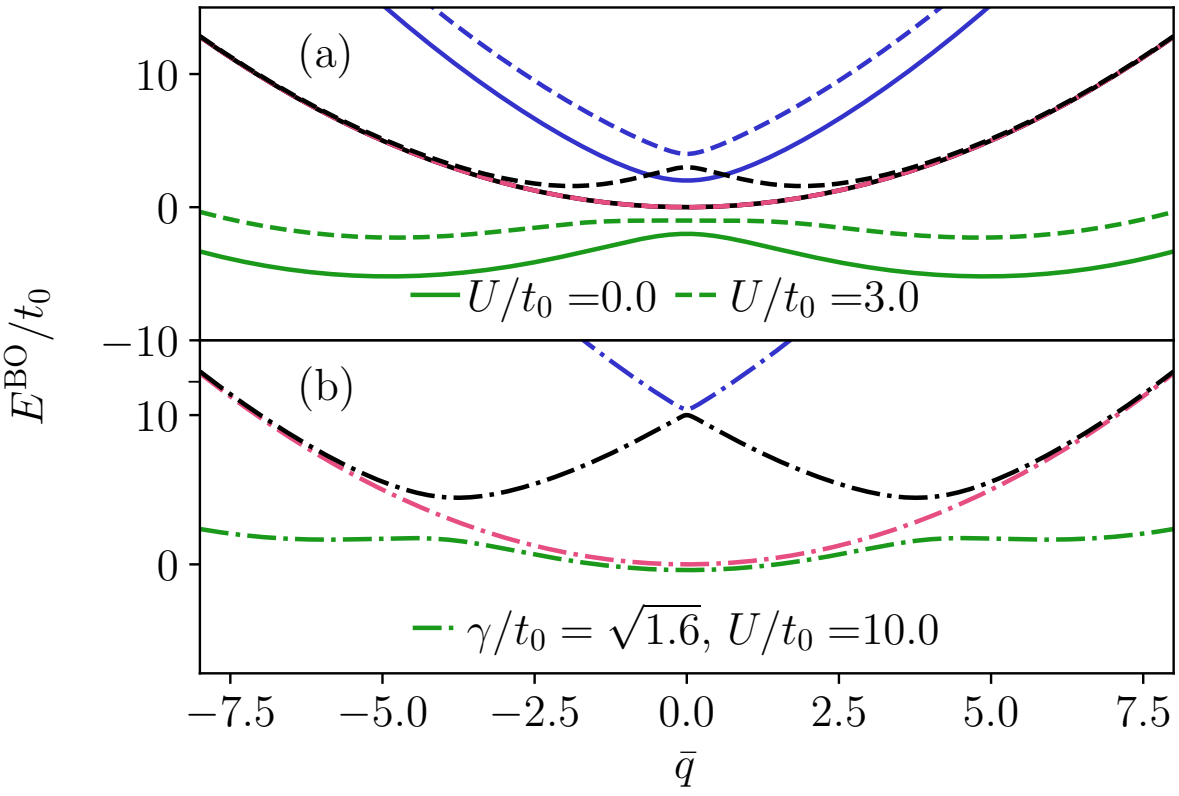

Figure 5.1: (a) Born-Oppenheimer surfaces for the Holstein-Hubbard bipolaron with different electron-electron interaction strengths U/t_0 and with $\gamma/t_0 = 1$ and $\omega_0/t_0 = 0.4$. (b) Same as (a) but with $U/t_0 = 10$ and $\gamma/t_0 = \sqrt{1.6}$.

Furthermore, the degeneracy of the first excited states is lifted for small $\bar{q}$. We also see that the energy difference between the minimum and maximum in the lowest surface decreases, which leads to larger values for the optical conductivity at small frequencies. The upwards shift of the lowest surface also indicates that the thermally activated peaks can occur at lower temperatures.

In Fig. 5.1(b), I show the Born-Oppenheimer surfaces for strong repulsion $U/t_0 = 10$ and $\gamma/t_0 = \sqrt{1.6}$. Now, the lowest surface has a minimum at $\bar{q} = 0$ and one can expect two separate polarons. In this case, the polaron Born-Oppenheimer surfaces should be used to describe the physics.

Before I present the numerical results, I want to give some technical details for the calculations. In this section, $\epsilon_{\mathrm{bond},J}$ is the truncation used when the current operator is applied to the matrix-product state before the real-time evolution, which is with single-site TDVP. The exact definition of $\epsilon_{\mathrm{bond},J}$ can be found in Appendix D. For the imaginary time-evolution, I used 2TDVP-LBO with $\epsilon_{\mathrm{bond}} = \epsilon_{\mathrm{LBO}} = 10^{-9}$ for the polaron and $\epsilon_{\mathrm{bond}} = \epsilon_{\mathrm{LBO}} = 10^{-8}$ for the bipolaron data. I further use $d\tau t_0 = 0.1$. All the real-time calculations are done with $dtt_0 = 0.01$ and I add $4t_{\mathrm{tot}}t_0$ zeros to the signal before the Fourier transformation.

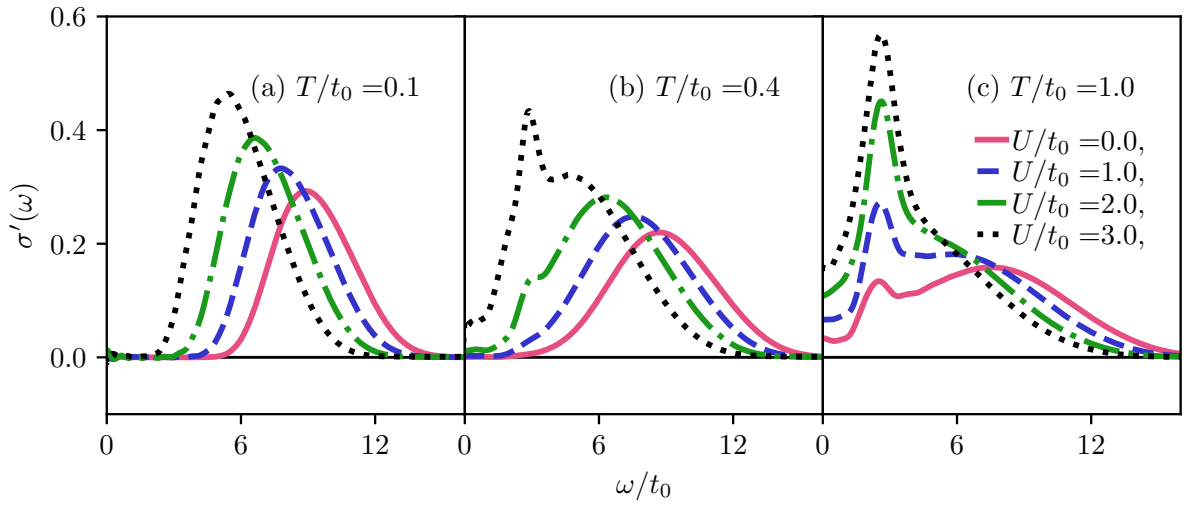

Figure 5.2: Real part of the optical conductivity for $\gamma/t_0 = 1$, $\omega_0/t_0 = 0.4$ and different U/t_0. The simulations are done with $\epsilon_{\text{bond},J} = 10^{-7}$, $M = 40$, $\eta = 0.05/(4\pi)$, and $t_{\text{tot}}t_0 = 10$.

Figure 5.2 shows the optical conductivity for $\gamma/t_0 = 1$, $\omega_0/t_0 = 0.4$ but with different U/t_0 and at different temperatures. One can see that the Born-Oppenheimer picture fits well by first looking at the non-interacting case ($U/t_0 = 0$, red curve) for $T/t_0 = 0.1$ in Fig. 5.2(a), $T/t_0 = 0.4$ in Fig. 5.2(b), and $T/t_0 = 1.0$ in Fig. 5.2(c). Initially, there is a Gaussian-like curve which broadens when the temperature is increased. For $T/t_0 = 1.0$ in Fig. 5.2(c), the resonance stemming from the thermally activated $\omega \approx 2t_0$ transition becomes visible.

When interaction is turned on, the center of the optical conductivity curve is shifted to lower frequencies [Fig. 5.2(a)], exactly as predicted by studying the Born-Oppenheimer surfaces in Fig. 5.1(a). Figure 5.2(b) shows that at $T/t_0 = 0.4$, the thermally activated resonance is already visible for the larger values of U/t_0. This is also consistent with the potential well being shallower. Also, all curves demonstrate the thermally activated resonance at $T/t_0 = 1.0$, but it is much more prominent for large U/t_0. However, a clear trend for the exact position of the resonance with U/t_0 can not be determined from the data. The low-frequency values are also much larger for large U/t_0 for $T/t_0 = 0.4$ and $T/t_0 = 1.0$, consistent with the lowering of the $\bar{q} = 0$ potential barrier in the Born-Oppenheimer picture.

In Fig. 5.3(a), I show two typical current-current correlation functions for the bipolaron at different temperatures and with $\gamma/t_0 = \sqrt{1.6}$, $\omega_0/t_0 = 0.4$, and $U/t_0 = 10$. As can be seen by comparing them to the corresponding optical conductivities in Fig. 5.3(b), the key features can be determined by the short-time decay of the correlation functions.

Finally, I demonstrate that the system consists of two separated polarons for sufficiently large U/t_0. In Fig. 5.3(b), I plot the optical conductivity for the bipolaron and polaron (the latter is scaled by a factor of two). The optical conductivities match quantitatively

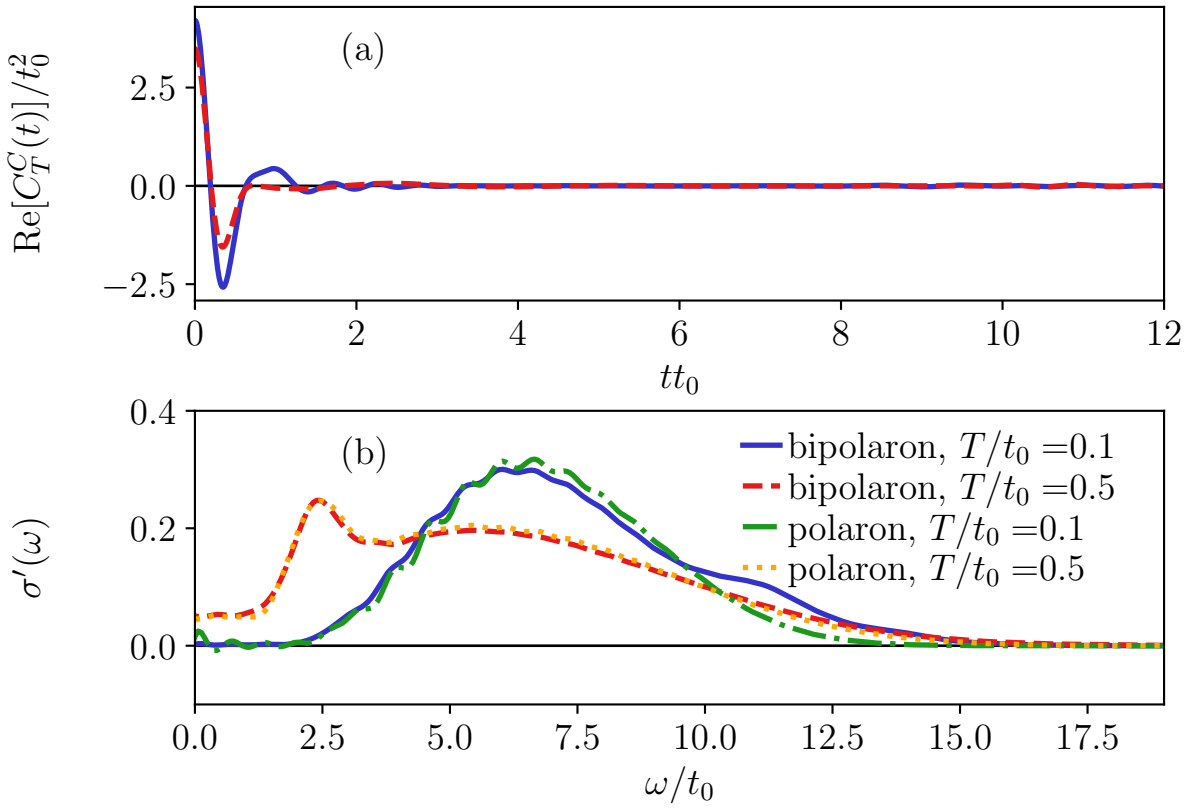

Figure 5.3: (a) Real part of the current-current correlation functions for the bipolaron with $\gamma/t_0 = \sqrt{1.6}$, $\omega_0/t_0 = 0.4$, and $U/t_0 = 10$. The blue solid line is for $T/t_0 = 0.1$ and the red dashed line is for $T/t_0 = 0.5$. (b) The optical conductivity for the polaron and bipolaron for the same parameters as (a). The polaron curve is scaled by a factor of two. The simulations are done using $\epsilon_{\mathrm{bond},J} = 10^{-7}$, $M = 35$, $\eta = 0.05/(4\pi)$, and $t_{\mathrm{tot}}t_0 = 10$.

well with minor differences at large frequencies, and in total, the physics are described by the single polaron Born-Oppenheimer surfaces from Eq. (2.15).

5.4 Energy transport coefficients

After having presented results for the optical conductivity for the Holstein polaron and bipolaron, I will now shift the focus to the energy transport coefficients at finite filling n. Energy transport is closely related to thermal conductivity, and having an efficient way to calculate the first quantity is a crucial step on the way to being able to compute the thermal conductivity in the Holstein model.

Understanding thermal and energy transport in models where phonons play a significant role is important for several reasons. For example, there are a series of low-dimensional cuprate-compound-materials that show interesting thermal properties, see, e.g., Refs. [263–266]. These materials are well described by Heisenberg spin chains, but to determine whether their large thermal conductivity can be traced back to the integrability of the Heisenberg model, we need a thorough understanding of the phononic contributions [267–270]. Furthermore, the development of novel experimental techniques to measure thermal conductivity [97–99] has enhanced the need for good theoretical models to account for general phononic effects. This is needed in both material engineering and to understand the relevant heating processes in molecular devices, see, e.g., Refs. [271–274].

The goal of this section is to present the first numerically exact matrix-product-state-based study of the finite-frequency energy-transport coefficients and thermal conductivity at finite temperatures for a Holstein system at a finite density and fixed particle number. Whereas the thermal conductivity zero-frequency contribution for the Holstein model was studied with a self-consistent perturbation theory in a zigzag carbon tube in Ref. [275], this work will help us to better understand which processes contribute to the spectrum, and what role the phonons and polaron formation play in a broad range of parameters.

Here, I use the methods from Sec. 5.1 and Ch. 3 to calculate the energy transport coefficient and optical conductivity for the Holstein model at $n = 1/3$ and $n \approx 1/2$ filling. Even though this extension is strightforward in principle, it comes with several practical complications. As I explained in Ch. 3, the generation of the $T = \infty$ states gets more involved due to the conservation of the particle number. The real-time evolution is also more complex since the energy current couples to the nearest and next-nearest neighboring sites and both phononic and electronic degrees of freedom [see Eq. (2.30)]. This leads to more highly entangled initial states, which again makes the time-evolution with matrix product states more difficult.

Before I present the results, I want to give some technical details. For the data in this section, the imaginary-time evolution is done with 2TDVP-LBO (with $\epsilon_{\text{bond}} = \epsilon_{\text{LBO},J} = 10^{-9}$ and imaginary time-step $d\tau t_0 = 0.1$) and the real-time evolution with single-site TDVP. Since the bond dimension of the matrix-product state does not increase with single-site TDVP, it is important that it is sufficiently large in the initial state. I define $\epsilon_{\text{bond},J}$ to be the truncation of the matrix-product state when I apply the matrix-product operator $\hat{J}$ before the real-time evolution. In Appendix D, I demonstrate how the convergence of the data is controlled. All the real-time calculations are done with $dtt_0 = 0.01$ and I add $4t_{\text{tot}}t_0$ zeros to the signal before the Fourier transformation.

In Fig. 5.4, I show the optical conductivity and the energy transport coefficient com-

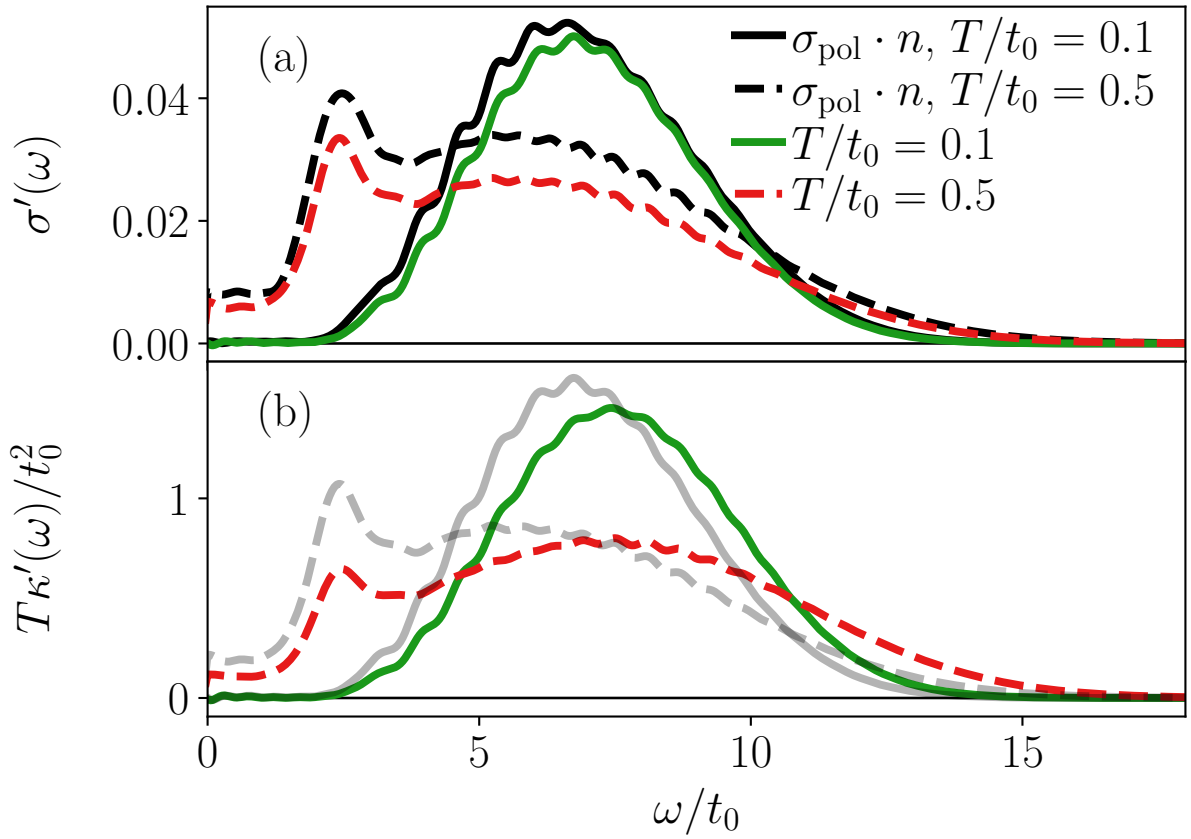

Figure 5.4: (a) Optical conductivity for the Holstein model at $n = 1/3$ filling for $L = 9$, $\gamma/t_0 = \sqrt{1.6}$, $\omega_0/t_0 = 0.4$, and $M = 40$ and different temperatures. I use $\epsilon_{\mathrm{bond},J} = 10^{-8}$, $t_{\mathrm{tot}}t_0 = 14$, $\eta = 0.1/(4\pi)$, and Gaussian broadening. The black lines correspond to the polaron data from Fig. 5.3 rescaled by the filing n. (b) Energy transport coefficient for the same parameters as (a). The gray lines are the optical conductivity data rescaled by $(2\gamma/\omega)^2$.

puted with Eqs. (2.31) and (2.32), respectively, in the strong coupling and adiabatic regime ($\gamma/t_0 = \sqrt{1.6}$ and $\omega_0/t_0 = 0.4$). Figure 5.4(a) shows the optical conductivity at $T/t_0 = 0.1$ and $T/t_0 = 0.5$. One can see that many of the features from the polaron (Fig. 5.3) carry over to the $n = 1/3$ filling. In particular the asymmetric Gaussian shape and the thermally activated resonance at $\omega \sim 2t_0$. The black lines in Fig. 5.4 correspond to the rescaled polaron data from Fig. 5.3 and further demonstrate that the optical conductivity spectra are dominated by polaron physics, although the spectrum is impacted by going to finite filling.

In Fig. 5.4(b), I show the energy transport coefficient and the optical conductivity data (gray lines) rescaled by the factor $(2\gamma/\omega)^2$ (this factor is chosen arbitrary to compare the data on the same scale). One sees that the main features from $\sigma'(\omega)$ carry over to $\kappa'(\omega)$ with a shift in amplitude and minor shifts in frequencies. This can be understood by inspecting

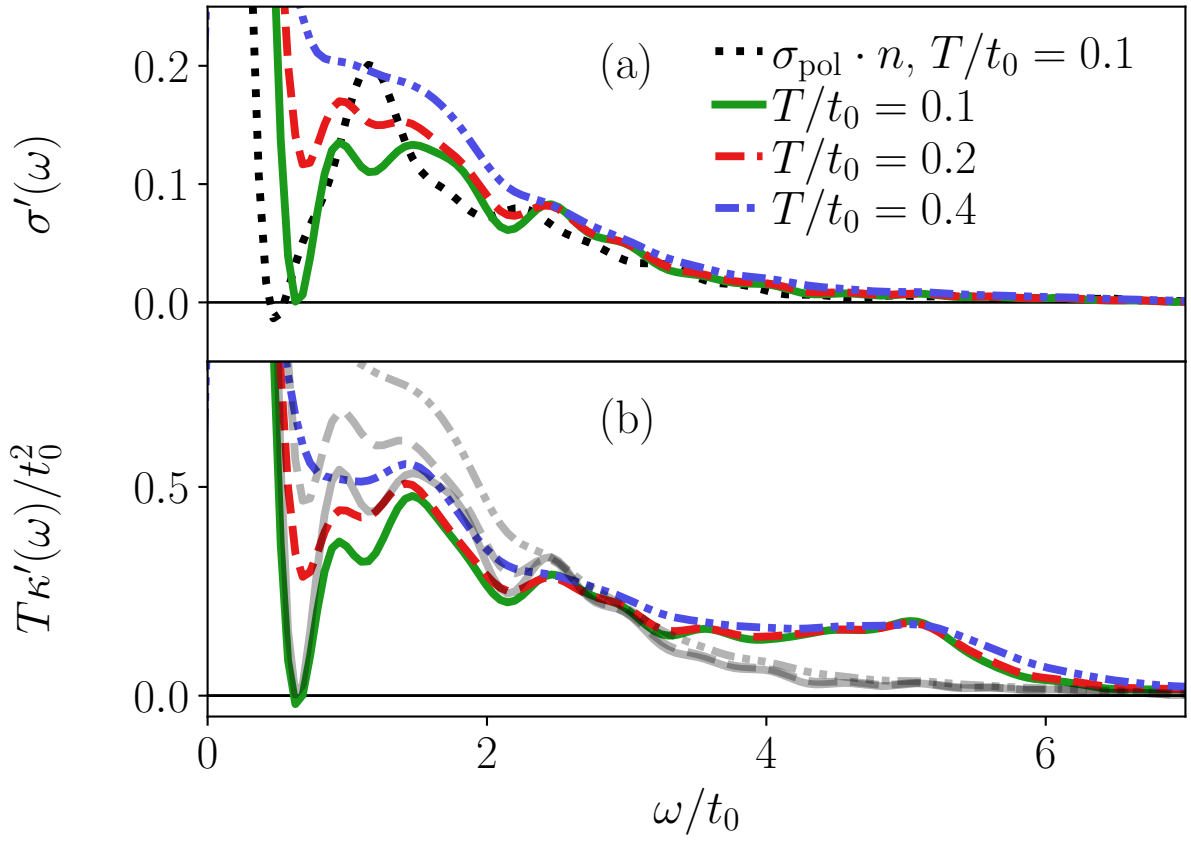

Figure 5.5: (a) Optical conductivity for the Holstein model at $n = 1/3$ filling for $L = 15$, $\gamma/t_0 = 1$, $\omega_0/t_0 = 1$, $M = 20$, and different temperatures. I use $\epsilon_{\mathrm{bond},J} = 10^{-9}$, $t_{\mathrm{tot}}t_0 = 12$, $\eta = 0.05/(4\pi)$, and Gaussian broadening. The black line is polaron data from 5.1 at $T/t_0 = 0.1$ rescaled by the fillng n. (b) Energy transport coefficient for the same parameters as (a). The gray lines are the optical conductivity data rescaled with $(2\gamma/\omega)^2$.

the energy-current operator in Eq. (2.30) and taking the Holstein dimer limit ($L = 2$). In this case, $\hat{J}^E = -it_0\gamma(c_1^\dagger \hat{c}_2 - c_2^\dagger \hat{c}_1)(\hat{b}_2 + \hat{b}_2^\dagger) = -\gamma \hat{J}\hat{X}_2$, and in a regime where the Born-Oppenheimer approximation is valid, this should lead to a rescaled optical conductivity if the eigenstates are close to eigenstates of $\hat{X}_2$. In Appendix D, I demonstrate that there are only minor system size effects in the data.

I will now show results for $\sigma'(\omega)$ and $\kappa'(\omega)$ for $L = 15$, $\gamma/t_0 = 1$ and $\omega_0/t_0 = 1$. As can be seen in Fig. 5.5(a), the optical conductivity data at finite filling deviate from the rescaled polaron data (black dashed line). The spectrum is broader, but the one- and two-phonon emission peaks are still visible. The energy transport coefficients in Fig. 5.5(b) now differ from the optical conductivity (grey lines rescaled with a factor $(2\gamma/\omega)^2$). Most significantly, a plateau is emerging for high frequencies where the optical conductivity has decayed to zero. I also address the finite size dependencies for these parameters in Appendix D.

To better understand the energy-transport-coefficient spectra, I define a reduced energy

current that only consists of the term proportional to $t_0\gamma$:

$$\hat{J}_R^E = -it_0\gamma\Big(\sum_{j=2}^{L}(\hat{c}_{j-1}^\dagger\hat{c}_j - \hat{c}_j^\dagger\hat{c}_{j-1})(\hat{b}_j + \hat{b}_j^\dagger)\Big)\,. \tag{5.4}$$

The energy transport coefficients calculated with $\hat{J}^E$ and $\hat{J}_R^E$ are shown in Fig. 5.6 for the same parameters as in Fig. 5.4 [Fig. 5.6(a)] and the same as in Fig. 5.5 [Fig. 5.6(b)]. In Fig. 5.6(a), one can see that almost the complete energy transport coefficient is determined by the term $\sim t_0\gamma$, with only minor deviations in the amplitudes. In Fig. 5.6(b) on the other hand, the low frequency behavior is dominated by the next nearest-neighbor current $\sim t_0^2$ and or cross terms. For these parameters, the $\hat{J}_R^E$ conductivity has a plateau spanning over a large frequency range. For high frequencies, the conductivities almost completely overlap, signaling that the high-frequency behavior is dominated by the current-phonon displacement terms in Eq. (5.4). The data also verify that the decay in the optical conductivity in Fig. 5.5 can be attributed to the decay of the operator matrix elements.

In Appendix D, I also show results for a small but finite phonon bandwidth, which significantly complicates the energy-current operator [195] and thereby the numerical simulations. There, I demonstrate that this changes the optical conductivity but that the differences between optical conductivity and energy transport coefficients are similar to what is seen in the data in this chapter.

Now, I will present results for filling $n = (L-1)/(2L)$ which goes to $n = 1/2$ for $L \to \infty$. In Fig. 5.7(a), the optical conductivity is plotted for $n = (L-1)/(2L)$, $L = 15$, $\gamma/t_0 = 1$, $\omega_0/t_0 = 1$, and $M = 20$, which is in the metallic regime for the Holstein model. The spectra share most of its features with the $n = 1/3$ spectra shown in Fig. 5.5. The energy transport coefficient for $n \approx 1/2$ is shown in Fig. 5.7(b). Much of the analysis from the $n = 1/3$ data carries over to $n \approx 1/2$, such as that of the plateau stretching over a wide range of frequencies. However, the data seems to indicate that that using $\hat{J}_R^E$ reproduces the spectra much better at low frequencies (at $T/t_0 = 0.2$) than was seen for $n = 1/3$ in Fig. 5.6(b). Note that data for $n \approx 1/2$ in the charge-density-wave parameter regime is shown in Appendix D.

Whereas this section focused on the finite-frequency part of the energy transport coefficient and thermal conductivity, it would also be interesting to do an extensive study of the direct-current conductivities (the zero-frequency contribution of the conductivities without the Drude weight). While this might be possible in some parameter regimes, it is generally difficult with the methods used here due to the limitations of the real-time evolution. For this, other methods are better suited, such as, e.g., the one used by Bischoff and Jeckelmann in Ref. [276]. Additionally, motivated by the aforementioned spin-lattice experiments, either considering a Heisenberg chain coupled to phonons or adding a Heisenberg chain to the Holstein model, see, e.g., Refs. [269, 270, 277], could provide new insights into the competition between phononic and spin degrees of freedom.

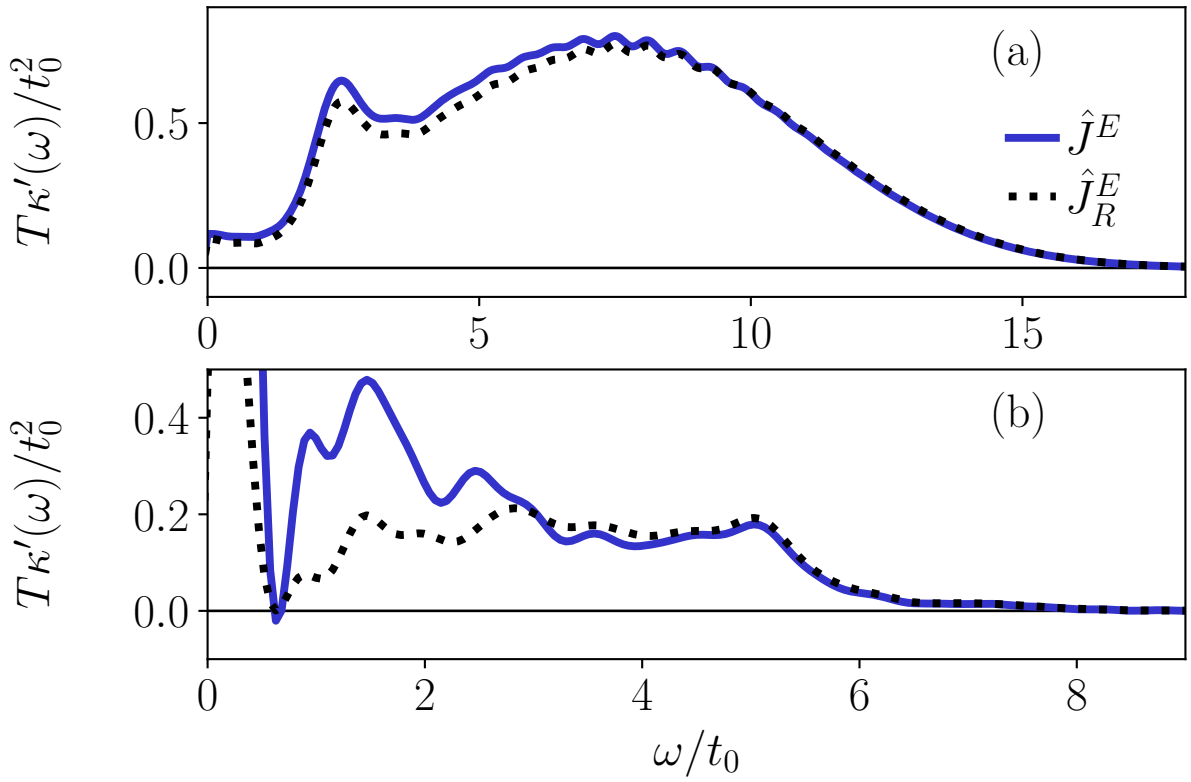

Figure 5.6: (a) Energy transport coefficient computed with $\hat{J}^E$ and $\hat{J}^E_R$ for the same parameters as in Fig. 5.4 for $T/t_0 = 0.5$. (b) Same as (a) but with the parameters from Fig. 5.5 at $T/t_0 = 0.2$.

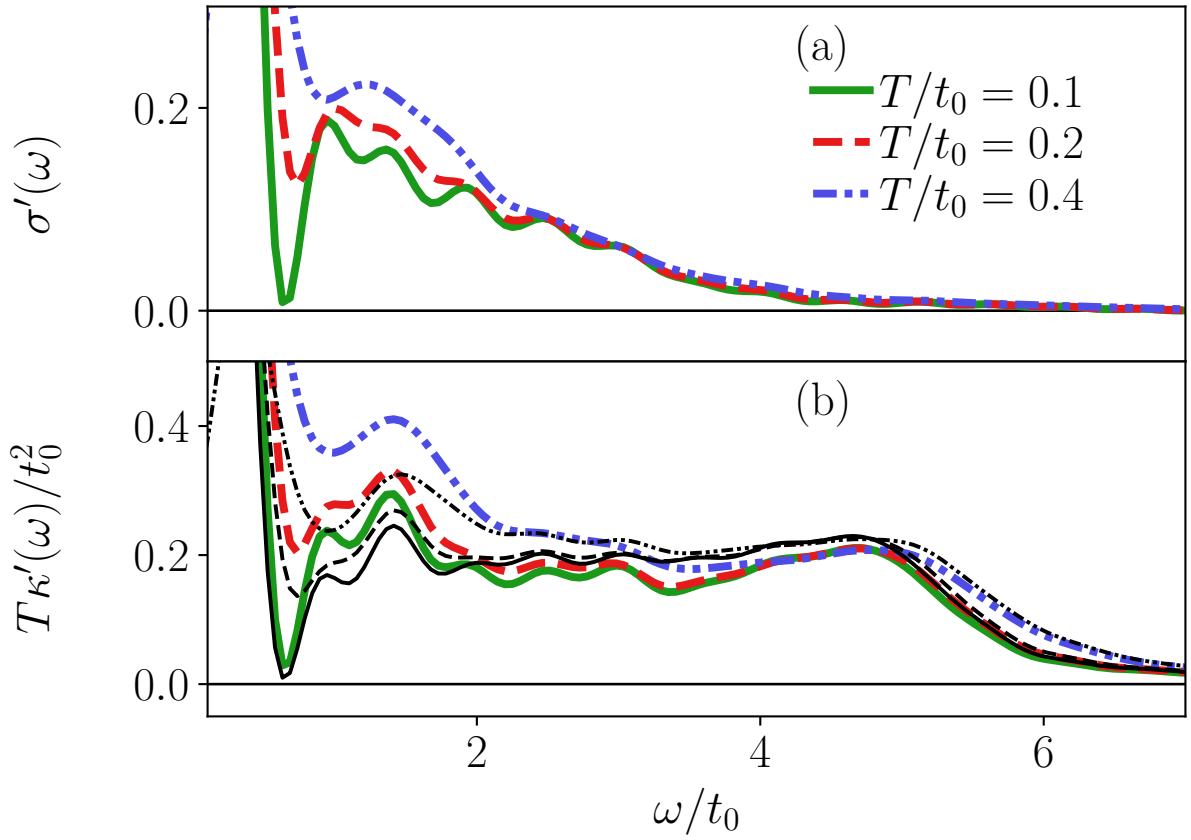

Figure 5.7: (a) Optical conductivity for $L = 15$, $\gamma/t_0 = 1$, $\omega_0/t_0 = 1$, $M = 20$, and filling $n = (L-1)/(2L)$. (b) Energy transport coefficient calculated with $\hat{J}^E$ [same color labels as in (a)] and $\hat{J}^E_R$ [black lines and the linestyle indicates the corresponding temperature as in (a)] for the same parameters as in (a). All simulations are done with $\epsilon_{\mathrm{bond},J} = 10^{-8}$, $t_{\mathrm{tot}}t_0 = 12$, and $\eta = 0.05/(4\pi)$.

Chapter 6

Transport and charge density wave breakdown in heterostructures

So far, the focus of this thesis has been on the influence of electron-phonon coupling and temperature on dynamical quantities such as spectral functions and transport coefficients for polarons, bipolarons, and systems at finite filling. In this chapter, the topic will change to charge density waves (CDWs) and heterostructures.

Electron-phonon interaction can not only lead to polaron formation [6] but also to the emergence of charge ordered and CDW states [6, 7]. Since this occurs in materials with technological applications, such as photovoltaics [278], it has sparked a great interest in these states and their melting. For example, Chávez-Cervantes et al. studied the melting of a CDW in quasi-one dimensional indium wires in Ref. [279], Polli et al. looked at the insulator to metal transition in a charge-ordered system in Ref. [280], and Jooss et al. studied the polaron solid to liquid transition in Ref. [29].

Materials with polarons are also promising candidates for efficient energy harvesting, which has led to investigations of the specific role of the phonons in relaxations processes and the life time of excitations. For example, Kressdorf et al. demonstrated a reduction of energy loss and long-lived hot polarons (above the band gap) in a charge-ordered system in Ref. [35], and the current-voltage characteristics in heterojunctions where polaron physics plays an important role was investigated in, e.g., Refs. [281, 282]. Motivated by these experiments, the question emerges: to what degree can we study non-equilibrium physics in heterostructure models with CDW and polaron formation?

How to investigate these systems theoretically can actually be motivated by transport in molecular junctions, which has led to a lot of research on understanding the role of the molecular vibrations, see Refs. [272, 283] for reviews. One simple microscopic model used to simulate such junctions is a one-site Holstein model coupled to metallic leads. This is known as the spinless Anderson-Holstein model and it is well-studied using a variety of methods, e.g., in Refs. [168–170, 174, 284–286]. In this chapter, I ask whether a nine-site Holstein model coupled to metallic leads can be used to study transport properties of heterostructures with electron-phonon interactions.

One of the methods that has been used to study such nanostructures is the density-

matrix renormalization group (DMRG) [287–294], which I introduced in Ch. 3. The idea in some of these studies is to couple the structure to very large leads. Then, one applies a voltage and time evolves until a quasi-steady state current emerges. By doing this for different voltages, one can then extract current-voltage diagrams.

By sandwiching an insulating model between the leads, these approaches can also been used to study the breakdown of insulating states. For example, the melting of Mott insulating states was studied by, e.g., Heidrich-Meisner et al. in Ref. [172] and Kirini and Ueda in Ref. [173]. How an insulating state (not coupled to leads) breaks due to electric fields has also been widely investigated, for example, for Mott insulating states in Refs. [295–298] and for CDWs in electron-phonon systems in Refs. [75–77, 177, 178]. In the context of electron-phonon models coupled to metallic leads, the focus has either been on the scattering of a wave packet on a Holstein structure as done by Brockt and Jeckelmann in Ref. [63], or on computing the linear conductance as done by Bischoff and Jeckelmann in Ref. [299]. Recently, in Ref. [300], Zhang et al. also conducted a theoretical investigation of an electron-phonon model coupled to metallic leads motivated by the perspectives of quantum simulators [301].

Here, I will present a publication where we address the effects of an applied voltage on electron-phonon systems. In the first part, we consider a Holstein model in the ground state in the CDW parameter regime and apply a voltage that changes linearly through the system. By using tDMRG with local basis optimization (LBO), see Ch. 3, we show that local voltage differences of the order of the polaron binding energy are necessary for the CDW order parameters to decay. The decay is qualitatively similar to that of a polaron in the Holstein dimer with a chemical potential on one site, indicating that it is dominated by polaron physics on short time scales.

We then couple the Holstein model with nine sites to two metallic leads so that the total system size is $L = 236$. We first establish that the Holstein-structure ground state goes from a metallic to a CDW state by tuning the electron-phonon coupling and the local gate voltage. We start our analysis in the metallic regime, and compute a current-voltage diagram for small bias voltages. We find that the currents through the structure significantly decrease when the electron-phonon coupling is increased. Additionally, we can extract the Luttinger parameter from the data. By analyzing the local phonon modes, we see that the structure is not significantly impacted by going from the ground state to a state where a quasi-steady current flows. For all calculations in this parameter regime, we find that incorporating LBO significantly speeds up the calculations.

After that, we investigate the structure in the CDW parameter regime. Similar to the regular Holstein model, we find that large local voltage differences are needed for the electrons to start tunneling to their neighboring sites. When we inspect the local modes in the Holstein structure, an interesting picture emerges. For small voltage differences, the Poisson distribution is mostly unaffected (except at the boundary). For large bias voltages, however, the first optimal basis state remains well described by the coherent state as the electron tunnels out. On the previously empty sites, a variety of phonon modes get occupied, and no clear polaronic formation can be reported on the time scales accessible to us. This is also a regime which is difficult for LBO based methods.

Our results in this chapter demonstrate the ability of DMRG with LBO to give us new insights into systems with electron-phonon coupling out of equilibrium. The formalism can also be extended to include finite phonon bandwidths, see, e.g., Ref. [67, 92], or electron-electron interaction, though this might impact the accessible time scales. Whereas LBO is very useful in the metallic regime, it has problems in the CDW regime due to the vast amount of modes needed to capture the electronic tunneling into new sites. The setups studied here could be interesting tasks for trajectory-based methods, see Refs. [122, 123, 178, 239] or Ch. 3, or other phonon tailored matrix-product-state algorithms [153]. One could both benchmark the current-voltage diagrams and try to study the CDWs for longer times.

6.1 Publication: Charge density wave breakdown in a heterostructure with electron-phonon coupling

Reprinted article with permission from
David Jansen, Christian Jooss, and Fabian Heidrich-Meisner
Phys. Rev. B 104, 195116 (2021)
https://doi.org/10.1103/PhysRevB.104.195116

Author contributions: D. J. did all the numerical calculations and wrote the article. F. H.-M. and C. J. suggested working on the model and setup and revised the manuscript. All authors discussed the data.

Charge density wave breakdown in a heterostructure with electron-phonon coupling

David Jansen,[1] Christian Jooss,[2] and Fabian Heidrich-Meisner[1]
[1]*Institut für Theoretische Physik, Georg-August-Universität Göttingen, D-37077 Göttingen, Germany*
[2]*Institut für Materialphysik, Georg-August-Universität Göttingen, D-37077 Göttingen, Germany*

(Received 16 September 2021; accepted 25 October 2021; published 10 November 2021)

Understanding the influence of vibrational degrees of freedom on transport through a heterostructure poses considerable theoretical and numerical challenges. In this work, we use the density-matrix renormalization group method together with local basis optimization to study the half-filled Holstein model in the presence of a linear potential, either isolated or coupled to tight-binding leads. In both cases, we observe a decay of charge density wave states at a sufficiently strong potential strength. Local basis optimization selects the most important linear combinations of local oscillator states to span the local phonon space. These states are referred to as optimal modes. We show that many of these local optimal modes are needed to capture the dynamics of the decay, that the most significant optimal mode on the initially occupied sites remains well described by a coherent state typical for small polarons, and that those on the initially empty sites deviate from the coherent-state form. Additionally, we compute the current through the structure in the metallic regime as a function of voltage. For small voltages, we reproduce results for the Luttinger parameters. As the voltage is increased, the effect of larger electron-phonon coupling strengths becomes prominent. Further, the most significant optimal mode remains almost unchanged when going from the ground state to the current-carrying state in the metallic regime.

DOI: 10.1103/PhysRevB.104.195116

I. INTRODUCTION

There is an increased technological and scientific importance of devices that are so small that quantum effects play an important role, see, e.g., Refs. [1–4]. Thus, a detailed understanding of charge transport and the nonequilibrium properties of such quantum structures is desirable. In particular, the formation of electron-phonon bound states, polarons, can give rise to the emergence of new electronic phases with electric transport characteristics different from metals or band semiconductors [5].

For example, at sufficient doping, charge density waves (CDWs) or charge-ordered (CO) states can evolve. Under strong electric fields, such states can break down, as, e.g., in CDW wires [6] or in CO manganites [7]. *In situ* transport experiments with CO manganites in an electron microscope revealed a complex transient behavior with movement of entire CO domains and subsequent melting into a metallic state [8]. Polaron transport, binding, and dissociation in electric fields also have an impact on the performance of polymer solar cells [9]. Notably, CO can enhance the lifetime of polaron excitations in junctions and thus enable hot-polaron-type solar cells [10]. Understanding these experiments makes a comprehensive study of polaron transport and melting of CDW/CO states highly desirable. An improved and fully quantum-mechanical modeling of vibrational degrees of freedom [11–15] can help interpret the behavior of molecules, see, e.g., Refs. [16–18], and charge transport and thermalization in heterostructures, see, e.g., Refs. [10,19,20].

In general, CDW and CO states can hardly be distinguished in their ground states, since they have the same order parameter. However, the mechanism of forming the two ordered states is very different, i.e., a Peierls-type lattice instability (CDW) [21] versus crystallization of localized charge carriers (CO) [22,23]. The difference is visible by the different phase transitions and nonequilibrium behavior: on the one hand, CDWs display metallic behavior above their transition temperature. Below this temperature, collective phenomena [24–27], such as sliding, lead to nonlinear behavior in the current-voltage relation if a sufficiently strong electric field is applied. In CO systems, on the other hand, charge transport above the transition temperature is due to the hopping of localized polarons [8,28]. The CDW states will be the main focus of this work and one of our goals is to better understand the CDW behavior under an applied voltage.

From a theoretical point of view, one possible setup consists of a one-dimensional quantum structure sandwiched between two metals (see Fig. 1). Then, the transport properties of this structure can be investigated by applying a voltage difference to the two conducting leads. Whereas the simplest case is to model a quantum dot with a certain energy level, many interesting and complicated extensions exist [12,29,30].

One important example is to allow for local vibrational degrees of freedom on the quantum dot (see, e.g., Refs. [11,13–15,31–34]). If these are modeled by a harmonic oscillator, one gets the single-level spinless Anderson-Holstein model (SAHM), which has been studied extensively in, e.g., Refs. [35–42]. One of the main goals of this work is to go beyond the SAHM and study a Holstein model, extending over several sites and coupled to leads.

Our main motivation is to get a better understanding of the effect of phonons on charge transport. The one-dimensional

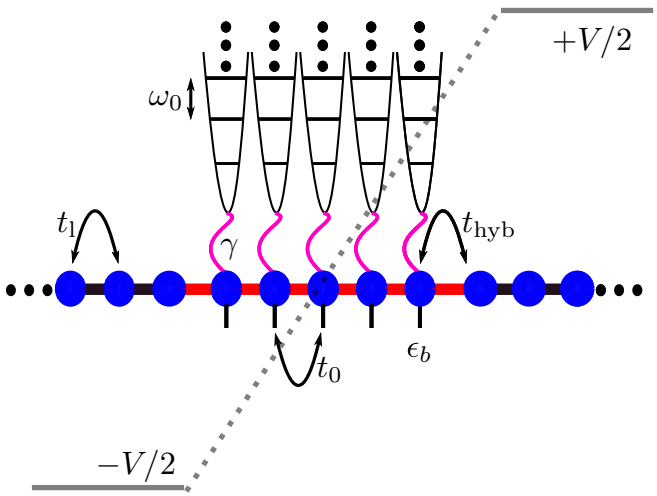

FIG. 1. Two leads connected to a Holstein-model structure. The leads have hopping amplitude t_1. In the structure, the electrons couple to the phonons with a coupling strength γ and have a hopping amplitude t_0. The phonons have the frequency ω_0 and there is a local gate voltage ϵ_b. The electrons can tunnel between the leads and the structure with an tunneling amplitude t_{hyb}. At time $t = 0$, a voltage V is applied, with a linear interpolation through the structure.

Holstein model has a complex ground-state phase diagram (see, e.g., Refs. [43,44]) and, at half-filling, undergoes a transition from a Tomanga-Luttinger liquid (TLL) to a CDW depending on the parameters. We address two main questions: How does the CDW phase behave when subjected to a linear potential and how do the different phases behave when the Holstein model is coupled to leads and a bias voltage is switched on?

The immense complexity of these types of nonequilibrium problems has driven the development of analytical and numerical methods such as the density-matrix renormalization group (DMRG) (see, e.g., Refs. [29,45–56]), the numerical-renormalization group (NRG) (see, e.g., Refs. [57–60]), real-time renormalization group (RTRG) [61], functional-renormalization group (FRG) [38–40,42,62,63], and quantum Monte Carlo (QMC) (as done in, e.g., Refs. [64–66]). In this work, we utilize DMRG for both ground-state search and time evolution [67–73]. A comparison between several of these methods for the single-impurity Anderson model is contained in Ref. [30].

Here, we are particularly interested in modeling the influence of phonons, requiring large local Hilbert spaces to capture the relevant physics in different parameter regimes. Although this can, in principle, be problematic for DMRG-based methods, techniques have been developed to treat these cases more efficiently (see also Refs. [74,75]). One approach, introduced in Ref. [76], consists of mapping the bosonic degrees of freedom onto pseudosites in the lattice, thus replacing the large local Hilbert space with long-range interactions. Another method consists of finding a basis where the local Hilbert space can be truncated significantly with negligible error [77], called the local basis optimization (LBO). Recently, in Ref. [78], Köhler *et al.* suggested introducing bath sites, thus treating a doubled system but with a restored U(1) symmetry. The methodology was further applied to time-evolution calculations in Ref. [79]. These methods were benchmarked against each other for the ground-state search in Ref. [80]. For the problems at hand, we use LBO, which has already been successfully applied to a wide range of problems, e.g., in Refs. [81–87].

We first investigate the regular Holstein model (not coupled to leads) in the CDW phase, and focus on the breakdown of the charge order. When we apply a linear potential, the CDW order parameters defined in the electron and phonon sector decay rapidly if the intersite potential difference is of similar magnitude as the polaron binding energy. We further illustrate that the picture is similar to that in the Holstein dimer for short times. Related studies have been done of the breakdown of a Mott insulator coupled to two leads in Ref. [50], of a Mott insulator due to an electric field in Refs. [88–91], and of the Falicov-Kimball model, e.g., in Refs. [92–94]. Our work complements previous studies on the Holstein model where the CDW breakdown has been investigated by quenching parameters (e.g., in Ref. [86]) and applying a light pulse (e.g., in Ref. [95]). Additionally, there have been studies of single and bipolarons in a linear potential (see, e.g., Refs. [96,97]), and recently, on the heating of a CDW [98] and a CDW with pulsed electric fields [99] and classical phonons.

We then couple the Holstein model to leads. Using time-dependent DMRG with LBO, we compute the current-voltage diagram of the structure in the metallic phase and demonstrate that using LBO leads to a significant computational speed up. Note that the linear conductance of the model in the metallic phase has been computed in a similar setup in Ref. [100]. There, the authors used a Kubo-formalism-based DMRG approach [101,102]. They also computed the Luttinger parameters [103–105] for the model and obtained quantitative agreement with Ref. [106], which computed the parameters from the structure factor. We reproduce their results by analyzing the steady-state current at low voltages. Further, we illustrate that the first optimal-basis state remains approximately constant in the current-carrying state as a function of time.

In the CDW phase, large voltages are required for a clear decay of the order parameter to be seen at the time scales reached with our method. Further, the properties of the most significant optimal-basis state change in the initially empty site but remain well described by a coherent state in the initially occupied sites.

The main results of this paper can be summarized as follows: In the charge density wave regime of the Holstein model, we simulate the CDW breakdown at large voltages. We explicitly demonstrate the decay of order parameters in both the phonon and electron sector. This is done for the Holstein model, as well as the Holstein model coupled to leads. Further, we show that the local phonon states of the initially empty sites in the CDW deviate from the coherent state, usually used to describe the small polaron. In the metallic regime, we compute the current-voltage diagram and observe a significant dependence on the electron-phonon coupling at small voltages. We additionally illustrate that the local phonon distribution remains largely unaffected by the voltage in the current-carrying state compared to the ground state and

we reproduce literature values [102,106] for the Luttinger parameter.

This paper is organized as follows: In Sec. II, we introduce the model. In Sec. III, we briefly review DMRG with LBO and how it can be applied to the systems studied here. In Sec. IV, we discuss CDW order in the ground state of the Holstein model with and without a coupling to the leads. Section V looks at the usual Holstein model and Sec. VI at the Holstein model coupled to the leads. We summarize and give a brief outlook in Sec. VII.

II. MODEL

When investigating how vibrating degrees of freedom affect the transport properties of a structure attached to two leads we can write down a three-term model:

$$\hat{H} = \hat{H}_{\text{leads}} + \hat{H}_{\text{hyb}} + \hat{H}_{\text{s}}. \tag{1}$$

We use open-boundary conditions and set $\hbar = 1$ throughout this paper. If the structure starts at site L_0 and is of length L_{s}, the Hamiltonian of the leads becomes

$$\begin{aligned}\hat{H}_{\text{leads}} = &-t_{\text{l}} \sum_{j=1}^{L_0-2} (\hat{c}_j^\dagger \hat{c}_{j+1} + \hat{c}_{j+1}^\dagger \hat{c}_j) \\ &- t_{\text{l}} \sum_{j=L_0+L_{\text{s}}}^{L-1} (\hat{c}_j^\dagger \hat{c}_{j+1} + \hat{c}_{j+1}^\dagger \hat{c}_j),\end{aligned} \tag{2}$$

where $\hat{c}_j^{(\dagger)}$ is the electron annihilation (creation) operator on the jth site, L is the total length of the system, and t_l the hopping amplitude in the leads. The hybridization term is

$$\begin{aligned}\hat{H}_{\text{hyb}} = &-t_{\text{hyb}} (\hat{c}_{L_0-1}^\dagger \hat{c}_{L_0} + \text{H.c.}) \\ &- t_{\text{hyb}} (\hat{c}_{L_0+L_{\text{s}}-1}^\dagger \hat{c}_{L_0+L_{\text{s}}} + \text{H.c.}),\end{aligned} \tag{3}$$

and t_{hyb} is the hopping amplitude between the structure and the leads. To model vibrational degrees of freedom in the structure, we choose the Holstein model [107], which contains a coupling between electrons and local optical phonons. The structure's Hamiltonian then takes the form:

$$\begin{aligned}\hat{H}_{\text{s}} = &-t_0 \sum_{j=L_0}^{L_0+L_{\text{s}}-2} (\hat{c}_j^\dagger \hat{c}_{j+1} + \text{H.c.}) \\ &+ \sum_{j=L_0}^{L_0+L_{\text{s}}-1} (\omega_0 \hat{b}_j^\dagger \hat{b}_j + \gamma \hat{n}_j (\hat{b}_j^\dagger + \hat{b}_j) + \epsilon_b \hat{n}_j),\end{aligned} \tag{4}$$

with $\hat{b}_j^{(\dagger)}$ being the phonon annihilation (creation) operator on site j and $\hat{n}_j = \hat{c}_j^\dagger \hat{c}_j$. Further, we have the gate voltage ϵ_b, the harmonic-oscillator frequency ω_0 and the coupling strength between the electrons and the phonons γ. For $L_{\text{s}} = 1$, the model turns into the well-studied spinless Anderson-Holstein model. The complete model is illustrated in Fig. 1. We also define

$$\tilde{\epsilon} = \epsilon_b - \frac{\gamma^2}{\omega_0}, \tag{5}$$

and in this work, we set $\tilde{\epsilon} = 0$ so that ϵ_b corresponds to the polaron binding energy in the single-site limit of the model. In this regime, we can detect a clear distinction between the metallic and CDW phase in the ground state for the parameters investigated here. When we refer to the regular Holstein model, we mean the Hamiltonian in Eq. (4) without leads.

When studying the Holstein structure coupled to leads, we always start with the ground state of the Hamiltonian in Eq. (1), and at time $t\omega_0 > 0$, we apply a voltage by adding the term

$$\begin{aligned}\hat{H}_{\text{V}} = &\frac{-V\theta(t)}{2} \sum_{j=1}^{L_0-1} \hat{n}_j + \frac{V\theta(t)}{2} \sum_{j=L_0+L_{\text{s}}}^{L} \hat{n}_j \\ &+ \sum_{j=L_0}^{L_0+L_{\text{s}}-1} \theta(t)(i - L_x)\Delta V \hat{n}_j\end{aligned} \tag{6}$$

to the Hamiltonian. Here, $\Delta V = V/(L_{\text{s}} + 1)$ and $L_x = L_0 - 1 + (L_{\text{s}} + 1)/2$. For the regular Holstein model, we only apply the linear potential [i.e., the last term in Eq. (6)].

We further define the hybridization parameter

$$\Gamma = 2(t_{\text{hyb}})^2. \tag{7}$$

We are interested in the expectation values of several observables. We calculate the expectation value of the current through the structure defined as

$$\hat{j} = \frac{i}{2} t_{\text{hyb}} (\hat{c}_{L_0-1}^\dagger \hat{c}_{L_0} - \text{H.c.} + \hat{c}_{L_0+L_{\text{s}}-1}^\dagger \hat{c}_{L_0+L_{\text{s}}} - \text{H.c.}), \tag{8}$$

where we take the average of the incoming and outgoing currents. Additionally, we compute an order parameter in the electron sector

$$O_n = \frac{1}{N_e} \sum_{i=L_0}^{L_0+L_{\text{s}}-1} (-1)^{i-L_0} \langle \hat{n}_i \rangle, \tag{9}$$

and in the phonon sector

$$\mathcal{O}_X = \frac{-1}{N_e} \sum_{i=L_0}^{L_0+L_{\text{s}}-1} (-1)^{i-L_0} \langle \hat{X}_i \rangle, \tag{10}$$

where $\hat{X}_i = \hat{b}_i^\dagger + \hat{b}_i$ and $N_e = (L_{\text{s}} + 1)/2$ for odd L_{s}. In Eq. (10), we include an additional minus sign to ensure that $O_X > 0$ in the ground state for $\gamma > 0$. These parameters characterize the transition from a TLL to a CDW phase.

III. METHODS

In this section, we briefly explain the main numerical method used in this work, namely the time-dependent density-matrix renormalization group using LBO. DMRG-based methods [67,71,72] have proven to be an extremely valuable tool to study one-dimensional systems and have already been applied extensively to a wide range of problems (see Refs. [71–73] for reviews). This work uses time-dependent DMRG [68–70] with local basis optimization [77]. LBO has been combined with both exact-diagonalization methods [81] and matrix-product state methods [83–87] and has enabled the study of electron-phonon systems in previously inaccessible regimes for other wave-function-based methods, e.g., for finite-temperature spectral functions of the Holstein polaron [87], quench dynamics of charge-density waves with a completely quantum mechanical treatment of the phonons [86],

and the scattering of an electronic wave packet on a structure with electron-phonon interaction [85]. Other Hilbert-space-based methods used in the field are exact diagonalization, see, e.g., in Refs. [81,108,109], diagonalization in a limited functional space, e.g., in Refs. [96,110,111], and the Lanczos method, e.g., in Refs. [112–114].

Here, for the Holstein model coupled to leads, we use matrix-product states consisting of both sites with only fermionic (indicated by σ) and sites with both fermionic and bosonic degrees of freedom (indicated by η). We write $|\vec{\sigma}\rangle_{\text{left}} = |\sigma_1, \ldots, \sigma_{L_0-1}\rangle$, $|\vec{\sigma}\rangle_{\text{right}} = |\sigma_{L_0+L_s}, \ldots, \sigma_L\rangle$, and $|\vec{\eta}\rangle_R = |\eta_{L_0}, \ldots, \eta_{L_0+L_s-1}\rangle$. We truncate the phonon Hilbert space by allowing maximum M phonons on each site. The total matrix-product state can be written as:

$$|\psi\rangle = \sum_{|\vec{\sigma}\rangle_{\text{left}}, |\vec{\sigma}\rangle_{\text{right}}, |\vec{\eta}\rangle} A^{\sigma_1} \ldots A^{\sigma_{L_0-1}} A^{\eta_{L_0}} \ldots A^{\eta_{L_0+L_s-1}} A^{\sigma_{L_0+L_s}} \ldots A^{\sigma_L} |\vec{\sigma}\rangle_{\text{left}} |\vec{\eta}\rangle |\vec{\sigma}\rangle_{\text{right}} . \quad (11)$$

For the time evolution, the Hamiltonian is first written as a sum of terms $\hat{h}_l$ acting on the two neighboring sites l and $l+1$. For a time step dt, we carry out a second-order Trotter-Suzuki decomposition into even and odd terms

$$e^{-idt\hat{H}} = e^{-idt\hat{H}_{\text{even}}/2} e^{-idt\hat{H}_{\text{odd}}} e^{-idt\hat{H}_{\text{even}}/2} + O(dt^3). \quad (12)$$

The gates can now be applied directly to the matrix-product state.

To treat the large number of local degrees of freedom efficiently we apply a transformation into a local optimal basis. This is done by obtaining the local reduced density matrix ρ at each time step after applying the time-evolution gate to a site with bosonic degrees of freedom. As described in detail in Refs. [83,85–87], this is used to obtain the transformation matrices into the new, called the optimal local basis by diagonalizing ρ such that

$$\rho = U^\dagger W U. \quad (13)$$

In Eq. (13), W is a diagonal matrix containing the eigenvalues w_α and U is the transformation matrix with the eigenvectors $|\phi_\alpha\rangle$ such that

$$\rho |\phi_\alpha\rangle = w_\alpha |\phi_\alpha\rangle . \quad (14)$$

The matrices U transform between the phonon bare mode basis and the optimal basis on a given site. Note that they are therefore site dependent and are stored as part of the MPS as objects connecting the local degrees of freedom to the optimal phonon modes that enter into the A matrices of the MPS. The number of optimal states one needs to keep while allowing for a certain error is set by the eigenvalues w_α. In the single-site limit of the Holstein model, it is well known that the system can be described by only two optimal states, the coherent and the empty state. In this case, the optimal basis has an obvious physical meaning. Since the system conserves the number of electrons we can split up the reduced density matrices into block matrices in the one-electron sector ρ^1 and the zero-electron sector ρ^0 with the sum of the traces $\text{Tr}[\rho^1] + \text{Tr}[\rho^0] = 1$. We further denote the corresponding eigenvalues and eigenvectors with an additional index so that, e.g., $\rho^1 |\phi^1_\alpha\rangle = w^1_\alpha |\phi^1_\alpha\rangle$. The weights w^1_α in our system are analysed in the Appendix. One important result of this work is that the local basis optimization works very well for the calculations done in the metallic phase (only ∼3 local states are needed in one particle number sector, compared to $M+1$ (in this case $M = 30$) in the bare phonon-number basis). There, only relatively small voltages are needed to obtain a steady-state current and a current-voltage diagram. In contrast, in all cases where the CDW is found to break down, large voltages and many local states are required.

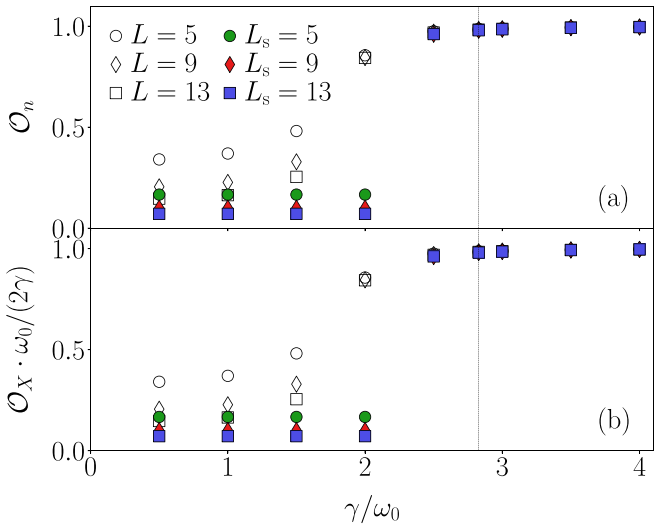

FIG. 2. (a) Order parameter in the electron sector for the ground states of the Holstein model (open symbols) and the Holstein model coupled to leads (filled symbols) for different γ/ω_0. L refers to the system size of the Holstein model and L_s to the length of the structure, which is coupled to the leads. In both cases, we set $t_0/\omega_0 = 1$, $\tilde{\epsilon} = 0$, $M = 35$ for $\gamma/\omega_0 \leqslant 2$, and $M = 50$ for $\gamma/\omega_0 > 2$. For the Holstein model coupled to leads, we further use a total $L = 236$, $t_l/\omega_0 = 2$, and $\Gamma/\omega_0 = 1$. The dashed line indicates $\gamma/\omega_0 = 2\sqrt{2}$, which is predominately used later in this work. (b) Order parameter in the phonon sector for the same parameters as in (a). Note that we do not show the data point for $L_s = 5$, and $\gamma/\omega_0 = 2.5$, since it is not converged conclusively with respect to the criteria in the main text.

In the time-dependent DMRG method with LBO we first apply the time-evolution gate, then obtain the transformation matrices and transform into the optimal basis before the subsequent singular value decomposition. A thorough discussion of the method can be found in Ref. [83].

When diagonalizing the reduced density matrix to obtain the optimal basis, the smallest eigenvalues w_α are discarded such that the truncation error is below a threshold: $\sum_{\text{discarded }\alpha} w_\alpha / (\sum_{\text{all }\alpha} w_\alpha) < \epsilon_{\text{LBO}}$. For the truncation done in the time-evolution scheme, we discard all singular values such that $\sum_{\text{discarded }\alpha} s^2_\alpha / (\sum_{\text{all }\alpha} s^2_\alpha) < \epsilon_{\text{bond}}$. All calculations were done using Ref. [115] and with $dt\omega_0 = 0.025$.

IV. CDW ORDER IN THE GROUND AND INITIAL STATE

We first look at the ground-state properties of the two setups. In Fig. 2, we show O_X and O_n for the ground state

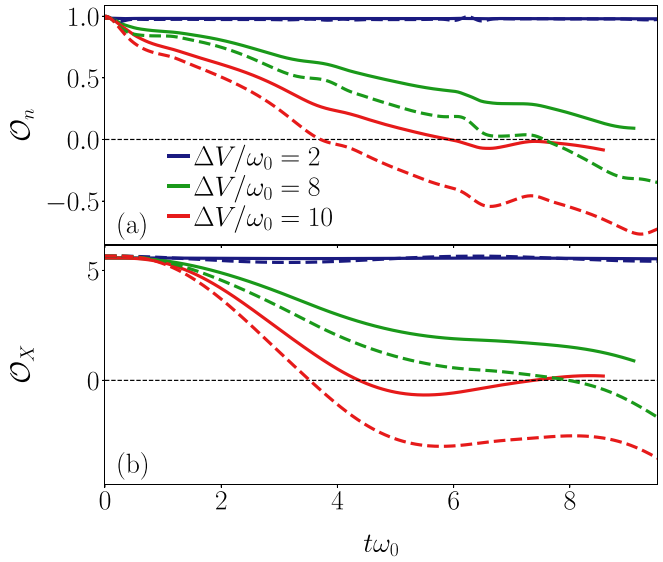

FIG. 3. Order parameters for the Holstein model with $L = 9$, $\gamma/\omega_0 = 2\sqrt{2}$, $\tilde{\epsilon} = 0$, $t_0/\omega_0 = 1$, $M = 50$, and different voltages V/ω_0 (ΔV is the potential difference between consecutive sites in the structure). For the calculations, we use $\epsilon_{\text{LBO}} = 10^{-7}$ and $\epsilon_{\text{bond}} = 10^{-7}$. (a) Order parameter in the fermion sector, see Eq. (9). (b) Order parameter in the bosonic sector, see Eq. (10). The dashed lines are the exact data for the Holstein dimer.

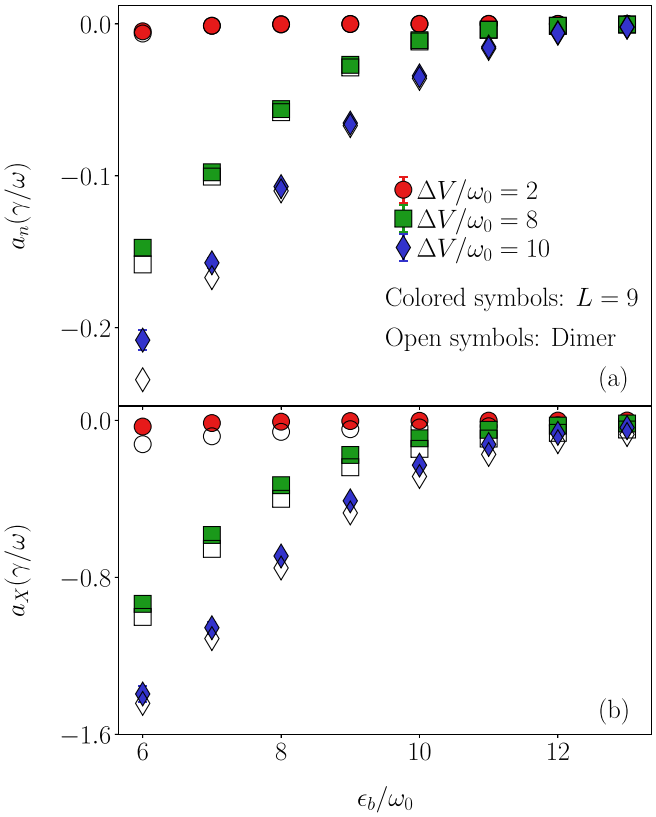

FIG. 4. Slopes of the linear fit to the initial decay of the order parameters (see main text for details) in the Holstein model. We use $L = 9$, $\gamma/\omega_0 = 2\sqrt{2}$, $\tilde{\epsilon} = 0$, $t_0/\omega_0 = 1$, $M = 50$, and different voltages V/ω_0. For the calculations, we use $\epsilon_{\text{LBO}} = 10^{-7}$, $\epsilon_{\text{bond}} = 10^{-7}$. The error bars indicate the standard deviation of the errors with maximum values of the order of 10^{-2} and thereby can not be seen for most points on the scale of the figure. Note that the $L = 9$ data are rescaled with the factor 5/4 to make the number of electrons participating in the CDW breakdown commensurate with the Holstein dimer.

obtained with DMRG for both the Holstein model and the Holstein model coupled to leads. The relative variance of the ground-state energy, $\sigma_E^2 = (\langle H^2\rangle - \langle H\rangle^2)/\langle H\rangle^2$, is converged up to the order $\leqslant 10^{-6}(10^{-12})$ for the regular Holstein model (Holstein model coupled to leads). We further verify that the obtained state is robust with respect to different initial states. The data are shown for both the structure coupled to leads and the regular Holstein model for different γ/ω_0 with $M = 35$ local phonon states for $\gamma/\omega_0 \leqslant 2$ and $M = 50$ for $\gamma/\omega_0 > 2$. One can observe a clear distinction between the charge density wave phase and the metallic phase. For small γ/ω_0, the order parameters decrease as the system size is increased. Note that in the metallic case, the values for the Holstein model coupled to leads are smaller than for the Holstein chain itself at the same length since for the structure, the total system size is even while the number of sites in the structure is odd. As γ/ω_0 is increased, both O_n and $O_X \cdot \gamma/\omega_0$ approach a constant for all systems, indicating the charge density wave phase. We further confirm that the results remain consistent as the maximum local phonon occupation number M is increased.

V. HOLSTEIN MODEL WITH A LINEAR POTENTIAL

In this section, we focus on the Holstein model without coupling to any leads [i.e., just Eq. (4)]. To investigate the dynamics of the CDW, we initially compute the ground state of the Holstein model and at time $t\omega_0 = 0$ we apply the linear potential. We focus on the strong-coupling regime, $\gamma/\omega_0 = 2\sqrt{2}$, $t_0/\omega_0 = 1$, where the ground state is known to be a charge density wave [43,44] (see Fig. 2). In Fig. 3, we show the order parameters for different voltages. Since a single polaron has a binding energy of $\epsilon_b = \gamma^2/\omega_0$, one expects that local voltage differences of $\Delta V/\omega_0 \sim \gamma^2/\omega_0^2$ are needed for the order parameter to decay on the time scales reachable here. This is confirmed for both the order parameter in the electron [Fig. 3(a)] and phonon sector [Fig. 3(b)]. There, we observe almost no decay for $V/\omega_0 = 20$, which corresponds to $\Delta V/\omega_0 = 2 \ll \gamma^2/\omega_0^2 = 8$. However, for both $V/\omega_0 = 80$ ($\Delta V/\omega_0 = 8$) and $V/\omega_0 = 100$ ($\Delta V/\omega_0 = 10$), the order parameters decay substantially. Since one could expect that only the voltage difference between two neighboring sites should dominate the order-parameter decay, we also show the data for the same voltage differences in the Holstein dimer. The dynamics are indeed similar, indicating that the dimer picture gives a reasonable qualitative description for the short-time dynamics.

To quantify how the change of the order parameter is affected by the electron-phonon coupling strength, we fit O_n and O_X in the interval $t\omega_0 \in [0, 6]$ with the function $f(t) = at + b$. In Fig. 4, we show the resulting values of a as a function of $\epsilon_b = \gamma^2/\omega_0$ for different voltages for the Holstein model and the dimer. The figure indicates that the decrease of the order parameters strongly depends on the polaron binding energies and the intersite voltage ΔV. In all cases, the decay gets suppressed when the binding energy gets large. Further,

the figure illustrates that the functional dependence of the a's are similar for both the Holstein model and the dimer. To conclude, our results suggest that a breakdown of the CDW can already be seen for $\Delta V \approx \epsilon_b$, but gets more prominent for $\Delta V \gg \epsilon_b$. For $\Delta V \ll \epsilon_b$, the CDW is stable.

VI. HOLSTEIN STRUCTURE COUPLED TO LEADS

In this section, we move on to study the Holstein structure coupled to leads with $L_s = 9$. In the first part, we focus on coupling strengths, which lie in the TLL regime before we go to the charge density wave regime.

A. Metallic phase

1. Currents

We first compute the current-voltage curve for the model with coupling strengths γ/ω_0 in the TLL regime. To do this, we apply the commonly used technique, see, e.g., Refs. [29,47,50], of averaging the expectation values of $\langle \hat{j}(t) \rangle$ in a time interval where a quasi-steady-state current is reached. We call this quantity $\langle \hat{j}(t) \rangle_{\rm av}$. We choose the interval $t\omega_0 \in [20, 30]$. Typical data for the time dependence of the current $\langle \hat{j}(t) \rangle$ is shown in the Appendix. For our data, the standard deviation is defined as

$$\sigma_{\rm STD}(\langle \hat{j} \rangle) = \sqrt{\sum_{t_i\omega_0 \in [20,30]} \frac{1}{N} |\langle \hat{j}(t_i) \rangle - \langle \hat{j}(t) \rangle_{\rm av}|^2}, \qquad (15)$$

where t_i is a point in time depending on the time step, N is the number of terms in the sum $\sum_{t_i\omega_0 \in [20,30]}$, and we have $\sigma_{\rm STD}(\langle \hat{j} \rangle)/\langle \hat{j}(t) \rangle_{\rm av}$ of order $\leqslant 10^{-3}$.

The current-voltage diagram is plotted in Fig. 5(a). The data show that in the low-voltage regime, the currents decrease as γ/ω_0 is increased. Similar behavior is observed in the SAHM in Ref. [40]. This is even more clearly illustrated in Fig. 5(b), where $\langle \hat{j}(t) \rangle_{\rm av}/V$ is plotted. As γ/ω_0 is increased, a steady-state current can not be estimated for large V/ω_0 from our data. For this reason, we show fewer points in those cases.

In the SAHM, the equilibrium spectral function of the dot at the particle-hole symmetric point displays a main peak at zero frequency accompanied by additional peaks separated by ω_0 [36]. When the electron-phonon coupling is increased, the width of the main peak starts decreasing as spectral weight is shifted to larger frequencies. Since the current contains the integral over the spectral function (for the voltages studied here, one would expect the spectral function to remain approximately unaffected), the current will decrease at small voltages. Although the spectral function of the Holstein structure extending over several sites is likely more complicated (see, e.g., Refs. [81,116,117] for spectral functions of half-filled Holstein chains), it is plausible that this picture still holds. This is further supported by the fact that for the noninteracting model and at small voltages, increasing $t_0/t_{\rm hyb}$ leads to a decrease in the current. Decreasing $t_0/t_{\rm hyb}$, however, increases the current. This is because at a fixed small voltage, a larger portion of states of the structure participates in transport as the band width decreases. Note that if both t_0 and $t_{\rm hyb}$ are decreased but their ratio is kept constant, the current also decreases. For the Holstein structure, one expects that both the

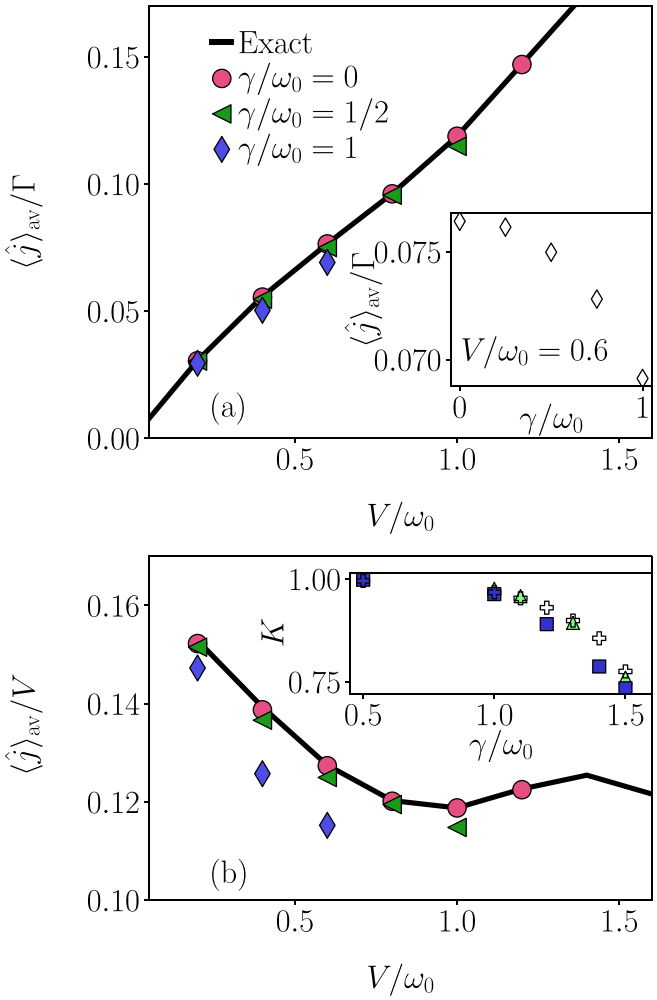

FIG. 5. (a) Average current $\langle \hat{j} \rangle_{\rm av}$, see text for details, for the structure with $L_s = 9, L = 236, \Gamma/\omega_0 = 1, t_l/\omega_0 = 2, \epsilon_{\rm bond} = 10^{-8}, \epsilon_{\rm LBO} = 10^{-7}, \tilde{\epsilon} = 0$, and different γ/ω_0 in the metallic phase. We further show exact results for $\gamma/\omega_0 = 0$ (black solid line). The inset in (a) shows $\langle \hat{j} \rangle_{\rm av}$ at fixed $V/\omega_0 = 0.6$ as a function of γ/ω_0. (b) Same data as in (a) but divided by V. The inset in (b) shows the Luttinger-liquid parameter, see main text for details, together with values obtained with different methods. The plus signs are calculated from our data, the green triangles are from Ref. [106], and the blue squares from Ref. [100].

tunneling in and out of the structure as well as the band width is reduced when electron-phonon interactions are turned on. Since we clearly see a decrease in the current, we assume that the dominating effect of the electron-phonon coupling is on the tunneling from the structure into the leads in the parameter regimes studied here.

In the inset of Fig. 5(b), we show the Luttinger-liquid parameter computed from our data together with those obtained by studying the structure factor in Ref. [106] and from the Kubo formalism in Ref. [100]. The Luttinger parameter K renormalizes the conductance G in a Luttinger liquid [103–105],

$$G = KG_0, \qquad (16)$$

where G_0 is the conductance of free fermions in a tight-binding chain. We calculate K as the ratio of $\langle \hat{j} \rangle_{\rm av}$ at finite

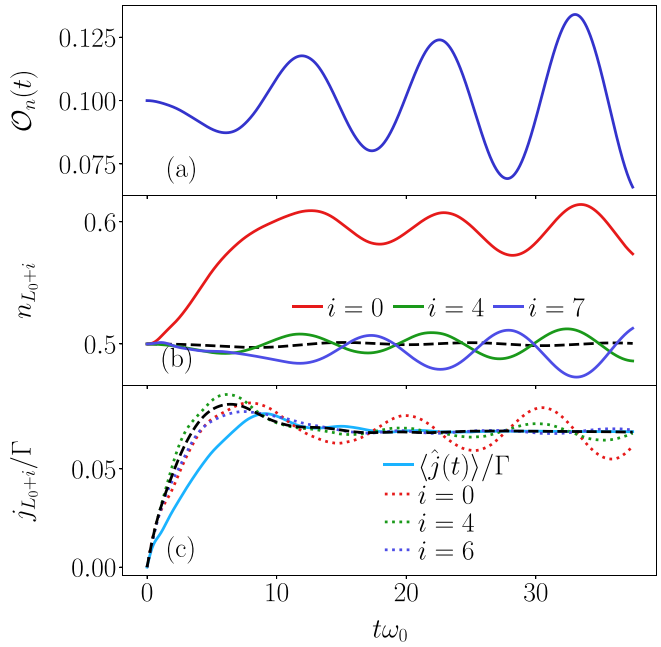

FIG. 6. (a) Order parameter in the electron sector, see Eq. (9), of the Holstein structure with $L_s = 9, L = 236, t_l/\omega_0 = 2, \gamma/\omega_0 = 1, \Gamma/\omega_0 = 1, \tilde{\epsilon} = 0$, and $V/\omega_0 = 0.6$. For the calculations, we use $\epsilon_{\text{LBO}} = 10^{-7}$, $\epsilon_{\text{bond}} = 10^{-8}$. (b) Selected local densities in the structure, see main text for details. (c) Current from Eq. (8) together with selected local currents in the structure, see main text for details. The black dashed lines are the average over local densities (b) and local currents (c).

γ and at $\gamma = 0$ with $V/\omega_0 = 0.2$

$$K = \frac{\langle\hat{j}\rangle_{\text{av}}}{\langle\hat{j}\rangle_{\text{av},\gamma/\omega_0=0}}\bigg|_{V/\omega_0=0.2}. \tag{17}$$

Note that we changed the averaging interval to $t\omega_0 \in [25, 32.5]([30, 32.5])$ for $\gamma/\omega_0 = 1.4(1.5)$ due to the longer relaxation time. We see that this method qualitatively reproduces K from our time-dependent calculations.

We now take a closer look at the current-carrying state at $V/\omega_0 = 0.6$ and $\gamma/\omega_0 = 1$. Figure 6(a) shows the order parameter, which oscillates around 0.1. Further, the local electron densities $n_{L_0+i} = \langle\hat{n}_{L_0+i}\rangle$ on selected sites are plotted in Fig. 6(b). As expected, their average increases for i going from small to large due to the inhomogeneous bias voltage. Still, their mean value is $1/L_s \sum_{i=0}^{L_s-1} \langle\hat{n}_{L_0+i}\rangle \approx 0.5$, as illustrated by the black dashed line. Selected local currents $j_{L_0+i} = i\langle\hat{c}^\dagger_{L_0+i}\hat{c}_{L_0+i+1} - \text{H.c.}\rangle$ and the total current, see Eq. (8), can be seen in Fig. 6(c). There, the steady-state current and the mean of the local currents (black dashed line) overlap after some initial dynamics, consistent with having a constant flow of current through the structure. The local currents all oscillate around the mean value. Both the local currents and densities are also representative for those not shown in this paper.

2. Reduced density matrices in the metallic phase

Lastly, we look at the diagonal elements of the reduced density matrix in the one-electron sector ρ^1 and the most significant eigenvector $\rho^1 |\phi_1^1\rangle = w_1^1 |\phi_1^1\rangle$ at site $L_0 + i$, where

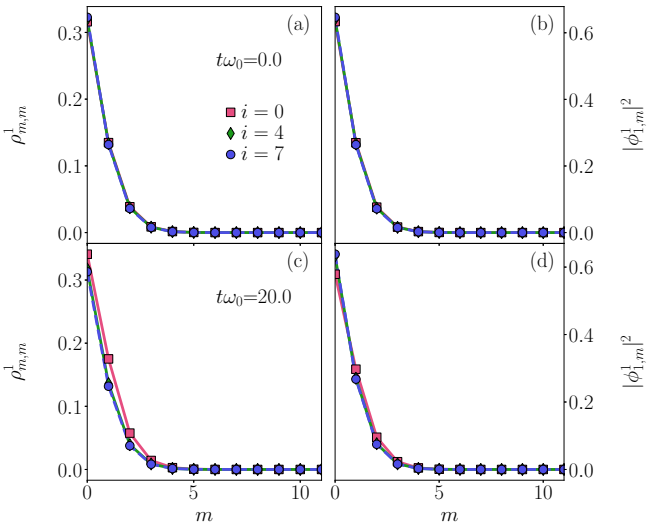

FIG. 7. (a) Diagonal elements of the reduced density matrix in the Holstein structure with $L_s = 9, L = 236, t_l/\omega_0 = 2, \gamma/\omega_0 = 1, \Gamma/\omega_0 = 1, \tilde{\epsilon} = 0, M = 30$ at different sites and different times with $V/\omega_0 = 0.6$. Further, $\epsilon_{\text{LBO}} = 10^{-7}$ and $\epsilon_{\text{bond}} = 10^{-8}$ are used for the calculations. (b) Absolute value squared of the components of the most significant optimal-basis state. All data are from the block matrix with an electron and the times are $t\omega_0 = 0$ in (a) and (b), and $t\omega_0 = 20$ in (c) and (d).

w_1^1 is the largest eigenvalue. The diagonal elements of ρ were already studied for the SAHM in different parameter regimes in Ref. [37] and the optimal-basis states in the Holstein model in, e.g., Ref. [111]. Both are shown for selected sites for $V/\omega_0 = 0.6$ and $\gamma/\omega_0 = 1$ at different times in Fig. 7. We see that both the diagonal elements of the reduced density matrix and the component of the optimal basis are strongly peaked at the zero phonon mode and decay rapidly for larger modes. We also observe that the distributions remain approximately the same during the time evolution (here, we only show the data for $t\omega_0 = 0, 20$) with some oscillations for the different sites, stemming from the oscillating local densities. Physically, this means that the electrons are being transported through the structure without significantly impacting the phonon distributions. Indeed, our results indicate that the current-carrying state can be well described by a few local modes that do not display much change compared to the ground state. The most significant eigenvalues of the reduced density matrix can be seen in the Appendix and decay exponentially. This illustrates the computational benefit of using LBO.

B. Charge density wave phase

1. Charge density wave breakdown

We now go into the strong electron-phonon coupling (CDW) regime where the order parameters, see Eqs. (9) and (10), remain nonzero as L_s is increased. Since the polaron binding energy is γ^2/ω_0, we expect that voltages with $\Delta V \sim \gamma^2/\omega_0$ are needed to break up the CDW as we saw in Sec. V. Here, we also choose $\gamma/\omega_0 = 2\sqrt{2}$ and study the breakdown of the CDW at large V/ω_0. In Fig. 8, we show the order parameters for $\Delta V/\omega_0 = 2, 8, 10$. We observe a similar

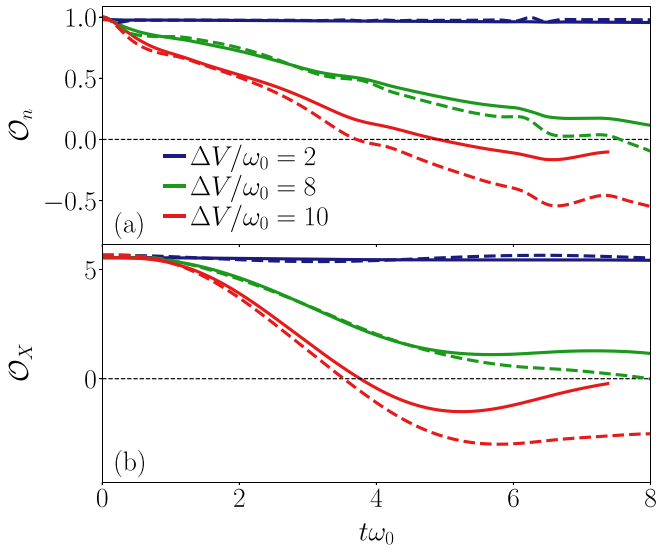

FIG. 8. Order parameters for the Holstein structure with $L_s = 9, L = 236, t_l/\omega_0 = 2, \gamma/\omega_0 = 2\sqrt{2}, \Gamma/\omega_0 = 1, \tilde{\epsilon} = 0$, and voltage gradients with different $\Delta V/\omega_0$. For the calculations we use $\epsilon_{\text{LBO}} = 10^{-7}$ and $\epsilon_{\text{bond}} = 10^{-7}$. (a) Order parameter in the fermion sector, see Eq. (9). (b) Order parameter in the phonon sector, see Eq. (10). The dashed lines show the exact data for the Holstein dimer.

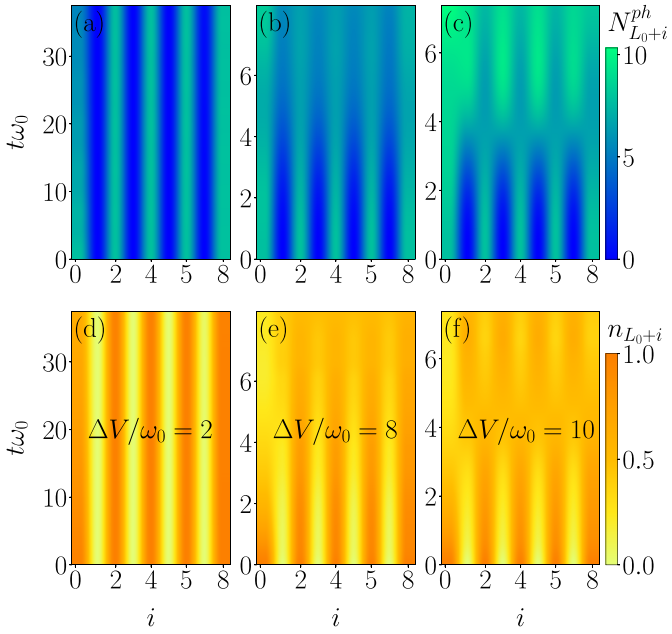

FIG. 9. Local densities for the Holstein structure with $L_s = 9, L = 236, t_l/\omega_0 = 2, \gamma/\omega_0 = 2\sqrt{2}, \Gamma/\omega_0 = 1, \tilde{\epsilon} = 0, M = 50$, and different local voltage differences $\Delta V/\omega_0$. We use $\epsilon_{\text{LBO}} = 10^{-7}$ and $\epsilon_{\text{bond}} = 10^{-7}$ for the calculations. (a)–(c) Local phonon number for $\Delta V/\omega_0 = 2, 8, 10$. (d)–(f) Local electron occupation for the same values of ΔV.

behavior as for the regular Holstein model, namely that they decrease as the applied voltage is increased. Further, we see that the initial dynamics are quantitatively similar to those of the dimer. However, as was the case in Sec. V, their decay is qualitatively different, in particular for larger times. Whereas the dimer data go far below zero, our data indicate that for the structure, both order parameters decay to zero with a stronger damping. While not shown here, when fitting the decay of the order parameters with a linear function for the initial dynamics, as done in Sec. V, we see a similar behavior as for the Holstein model. The difference is that no rescaling is needed since all electrons can contribute to the decay. Further, the data points for the structure tend to lie above the dimer points due to boundary effects, which we elaborate on in the next paragraph.

The local electron and phonon occupations are shown as functions of the sites in the structure and of time in Fig. 9. The figure confirms the results from the order parameters by illustrating how the electron densities remain constant for $\Delta V/\omega_0 = 2$ [Fig. 9(d)] and start to spread out for $\Delta V/\omega_0 = 8, 10$ [Figs. 9(e) and 9(f)]. Further, the change in electron densities is accompanied by a change and a shift of the maximum phonon occupation to the previously empty sites. Indeed, once the electrons can tunnel to an empty site, the excess energy first goes into generating a large number of new phonons. Additionally, the coupling to the leads allow the electron farthest to the left to tunnel out of the structure. This boundary effect also leads to a small decay of the order parameter for $\Delta V/\omega_0 = 2$ as well. We also observe that there are no local currents present for $\Delta V/\omega_0 = 2$, but that they become finite for large $\Delta V/\omega_0$.

2. *Reduced density matrices in the charge density wave phase*

We continue by looking at the diagonal elements of the reduced density matrix and the first optimal-basis state and contrast them to what we observed for the current-carrying state in Sec. VI A. In Fig. 10, we show the data for different voltages at different times. The first thing that stands out are the initial distributions at $t\omega_0 = 0$ in Figs. 10(a) and 10(b). On the sites occupied by electrons, namely sites $i = 4, 7$, both the diagonal elements of the density matrix and the most significant optimal-basis state are well described by the Poisson distribution, indicating a coherent local phonon state, as expected in the large-coupling limit. To illustrate this, we also plot

$$P_{\text{Poisson}}(m) = \frac{|\lambda|^{2m}}{m!} e^{-|\lambda|^2}, \tag{18}$$

where $\lambda = \gamma/\omega_0$. The empty sites have almost no weight except for at the $m = 0$ mode. As the system evolves in time with a small bias voltage we make several interesting observations. As illustrated in Figs. 10(c) and 10(d), at $t\omega_0 = 20$, the system remains well described by coherent states. Both the most significant optimal-basis state and the diagonal elements of the density matrix keep their Poisson form. Whereas $|\phi^1_{1,m}|^2$ remains perfectly described by the Poisson distribution on the occupied sites, the amplitude of the $\rho^1_{m,m}$ at $i = 0$ decreases due to the boundary effect previously described. We further note some change in $|\phi^1_{1,m}|^2$ for $i = 4$.

More dramatic changes can be seen for the large bias voltage $\Delta V/\omega_0 = 10$ in Figs. 10(e) and 10(f). At $t\omega_0 = 6$, the amplitude of the diagonal elements of ρ^1 have decreased significantly compared to the original distribution at sites

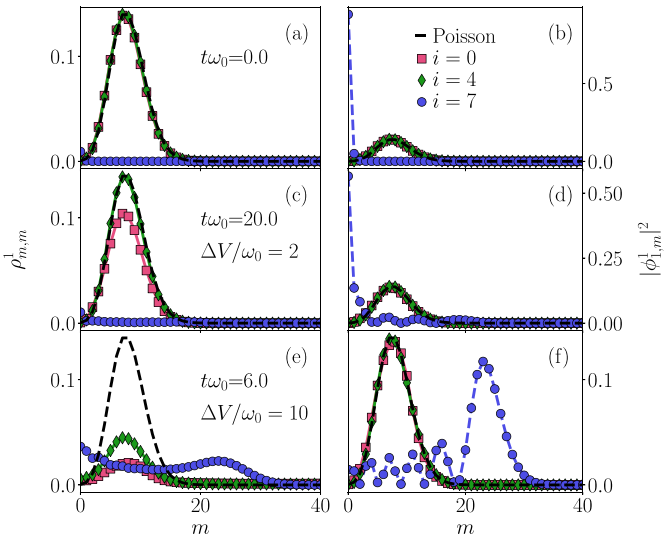

FIG. 10. (a) Diagonal elements of the reduced density matrix in the Holstein structure with $L_s = 9, L = 236, t_l/\omega_0 = 2, \gamma/\omega_0 = 2\sqrt{2}, \Gamma/\omega_0 = 1, \tilde{\epsilon} = 0, M = 50$. (b) Components of the most significant local optimal-basis state. (c) Same as in (a) but at $t\omega_0 = 20$ and $\Delta V/\omega_0 = 2$. (d) Same as in (a) but at $t\omega_0 = 6$ and $\Delta V/\omega_0 = 10$. (d) Same as in (b) but at $t\omega_0 = 20$ and $\Delta V/\omega_0 = 2$. (f) Same as in (b) but at $t\omega_0 = 6$ and $\Delta V/\omega_0 = 10$. We use $\epsilon_{\text{LBO}} = 10^{-7}$ and $\epsilon_{\text{bond}} = 10^{-7}$ for the calculations. The black dashed line corresponds to the Poisson distribution from Eq. (18).

$i = 0, 4$. This is a consequence of the electron density getting distributed to other sites, leading to an increase of the weights in the zero-electron density matrix ρ^0, which is not shown here. Also, $|\phi^1_{1,m}|^2$ remains well described by the coherent state on all initially occupied sites, but with some oscillations between modes. However, the previously empty sites gain a large amplitude spreading out across several modes as can be seen for $i = 7$. This is due to the electron density increasing and phonons being generated with the excess energy. Further, the $|\phi^1_{1,m}|^2$ seems to resemble a shifted coherent state with additional oscillations at the times reachable here. Figures 10(e) and 10(f) also illustrate that the system is notoriously more complex to simulate due to the large number of bare modes needed to capture the dynamics on the initially unoccupied sites. We further looked at the second most significant optimal-basis state in the one-electron sector, but there, no physical interpretation could be extracted. In the Appendix, we additionally illustrate that a large number of optimal modes are needed to keep the error small and thus LBO loses some of its advantage.

VII. CONCLUSION

In this paper, we used time-dependent DMRG with local basis optimization to investigate both the Holstein model in the CDW phase and the Holstein model sandwiched between conducting leads in the CDW and TLL phase under an applied bias voltage. For the regular Holstein model, we first saw that when a strong enough bias voltage is applied, the order parameters in both the electron and phonon sector clearly decay. We further demonstrated a clear dependence between the applied voltage and the initial decay rate of the order parameters and that the dynamics resemble those in the Holstein dimer for short times but later deviate.

We then proceeded to look at the Holstein model coupled to conducting leads. After establishing that a clear separation between the TLL and CDW phase can be seen at different coupling strengths we first focused on the system in the TLL phase. Studying the steady-state currents for small voltages, we were able to compute current-voltage curves, showing that charge transport at small voltages is reduced when the phonon coupling is increased. Similar behavior has been reported for the SAHM model by Ref. [40]. Our data also reproduce the Luttinger-liquid parameters from Refs. [100,106]. We additionally looked at the diagonal elements and the most significant optimal-basis state in the one-electron sector for the current-carrying state. Our data indicate that the local phonon distribution is not significantly impacted by the applied voltage in the steady-state current. Further, the same is seen for the most significant optimal mode.

We then continued our study of the Holstein model coupled to leads by working with an electron-phonon coupling in the CDW regime. We could report similar behavior as for the regular Holstein model, namely that large voltages are needed for the CDW to break down. At small voltages, the CDW remains unchanged except for boundary effects. This is also seen in the properties of the reduced density matrices. Initially, the occupied sites were well described by the Poisson distribution. This remained true during the time evolution for small bias voltages, except for the aforementioned boundary effects. However, for strong voltages, the amplitudes of the reduced density matrix in the one-electron sector, ρ^1, started to decrease as expected since the electron densities spread out. Further, a wide range of bare modes displayed large weights in the previously unoccupied sites as a consequence of the phonons being generated with the excess energy. In this case, the most significant optimal-basis states remain well described by the coherent distribution for all times reached here in the initially occupied sites. In contrast, the previously empty sites obtained a distribution centered around the larger bare phonon modes.

There are many possible continuations building on the results of this work. After having established that local basis optimization can simplify the calculations significantly in the metallic phase, one could make the structure more complex by either adding phonon dispersion (see, e.g., Refs. [118,119]) or trying to capture more aspects of manganites (see, e.g., Refs. [19,120] and Ref. [121] for a theory review) by adding electron interaction or interaction with local spins. Also, analyzing how energy is transferred into the different degrees of freedom, complementary to Ref. [98], would be of great interest. Further, applying a thermal gradient to the system would allow for the study of thermal transport through such quantum structures, see, e.g., Refs. [39–41,122–124]. Lastly, being able to compute a current-voltage diagram for the CDW phase, its dynamics, and its properties at finite temperature would be of great interest, e.g., in the context of recent experiments [8,25,27]. In particular, it would be desirable to see if one can reach a state where the electron densities are equally distributed through the system and to better understand the time scales of any collective behavior. Since the reachable times of our CDW calculations are greatly limited by the

large number of optimal-basis states required, this might be a task for other phonon-specialized matrix-product-state-based time-evolution techniques [79]. Here, also insights into different behaviors of CDW and CO states are of interest.

ACKNOWLEDGMENTS

We acknowledge useful discussions with P. Blöchl, J. Hoffmann, E. Jeckelmann, B. Kressdorf, V. Meden, and J. Stolpp. This work was funded by the Deutsche Forschungsgemeinschaft (DFG, German Research Foundation) - 217133147 via SFB 1073 (Project No. B09 and Project No. B02). We further thank E. Jeckelmann and V. Meden for providing us data to benchmark our results from Refs. [100] and [40], respectively.

APPENDIX: NUMERICAL DETAILS

Here, we illustrate several numerical details of our calculations. As explained in Sec. III, we control the truncation of the bond dimension with the parameter ϵ_{bond} and the truncation of the local basis optimization with ϵ_{LBO}. Figure 11 shows the expectation value of the current for fixed ϵ_{bond} and different ϵ_{LBO} in Fig. 11(a) and fixed ϵ_{bond} and different ϵ_{LBO} in Fig. 11(b). Clearly, the current is converged for the parameters used in this work, which also was verified for the other data shown. Additionally, we observe that using a very large ϵ_{bond} unequivocally leads to the false expectation values for $\langle \hat{j}(t) \rangle$. In contrast, very large ϵ_{LBO} can be used. Further, even a too large ϵ_{LBO} seems to approximately reproduce the steady-state current for the parameters shown here, and therefore, more care must be taken when determining if ϵ_{LBO} is sufficiently converged. To compute the current-voltage diagram we average $\langle \hat{j}(t) \rangle$ in the interval $t\omega_0 \in [20, 30]$, which is illustrated by the black dashed lines in Fig. 11(b).

To demonstrate that sufficiently large local phonon Hilbert spaces are included in the calculations we show the order

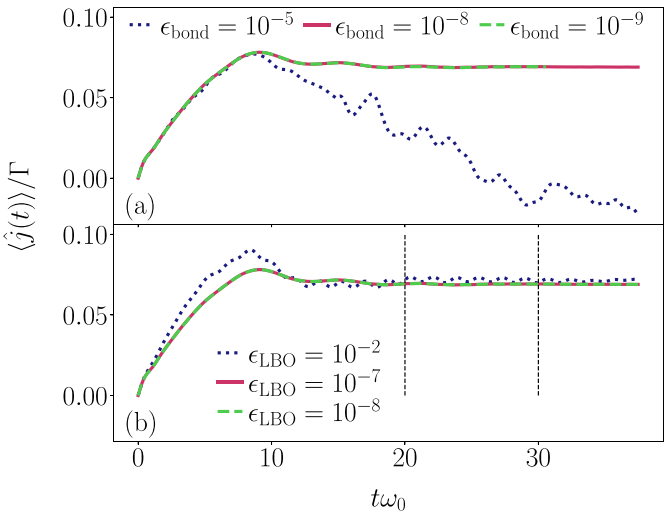

FIG. 11. Current $\langle \hat{j}(t) \rangle$ from Eq. (8) for the Holstein structure with $L_s = 9, L = 236, V/\omega_0 = 0.6, t_l/\omega_0 = 2, \Gamma/\omega_0 = 1, \tilde{\epsilon} = 0, M = 30$, and $\gamma/\omega_0 = 1$. (a) Fixed $\epsilon_{\text{LBO}} = 10^{-7}$ and different ϵ_{bond}. (b) Fixed $\epsilon_{\text{bond}} = 10^{-8}$ and different values of ϵ_{LBO}.

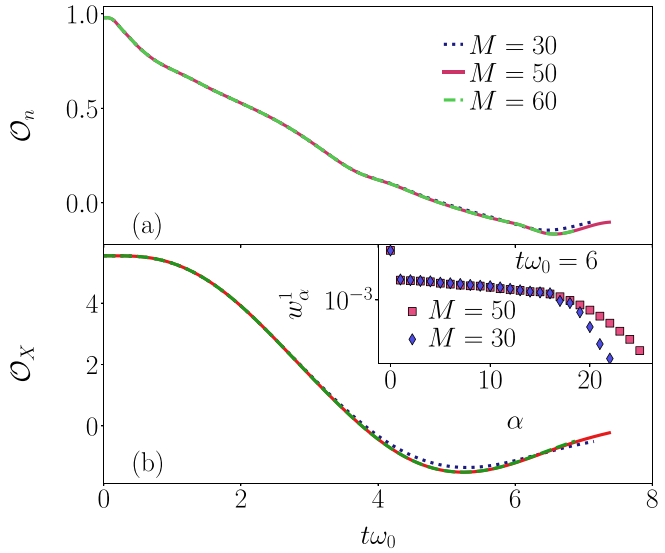

FIG. 12. Order parameters for the Holstein structure with $L_s = 9, L = 236, t_l/\omega_0 = 2, \gamma/\omega_0 = \sqrt{2}, \Gamma/\omega_0 = 1, \tilde{\epsilon} = 0, \Delta V/\omega_0 = 10$, and different M. For the calculations, we use $\epsilon_{\text{LBO}} = \epsilon_{\text{bond}} = 10^{-7}$. (a) Order parameter in the fermion sector, see Eq. (9). (b) Order parameter in the bosonic sector, see Eq. (10). The inset shows the eigenvalues of the reduced density matrix in the one-electron sector at time $t\omega_0 = 6$ on a log scale.

parameter computed with different local phonon-number truncations M in Fig. 12. For the parameters shown here, $M = 50$ is more than sufficient to capture the relevant physics of the order-parameter decay. Further, we see that the $M = 30$ data start to deviate on the scale of the figure. Also, inspecting the

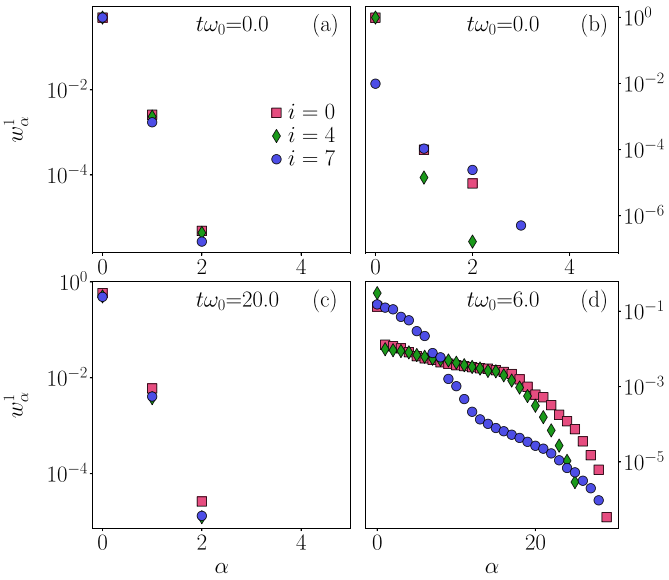

FIG. 13. Eigenvalues of the reduced density matrices at different sites i for the Holstein structure with $L_s = 9, L = 236, t_l/\omega_0 = 2, \Gamma/\omega_0 = 1, \tilde{\epsilon} = 0$, and different γ/ω_0 and M and at different times. (a) $t\omega_0 = 0, M = 30$ and $\gamma/\omega_0 = 1$. (b) $t\omega_0 = 0, M = 50$ and $\gamma/\omega_0 = 2\sqrt{2}$. (c) Same as (a) but at $t\omega_0 = 20$ and $V/\omega_0 = 0.6$. (d) Same as (b) but at $t\omega_0 = 6$ and $V/\omega_0 = 100$ ($\Delta V/\omega_0 = 10$). We use $\epsilon_{\text{LBO}} = 10^{-7}$ in all plots and $\epsilon_{\text{bond}} = 10^{-8}[10^{-7}]$ in (a) and (c) [(b) and (d)]. We only show $w_\alpha^1 > \epsilon_{\text{LBO}}$.

optimal weights in the inset of Fig. 12 reveals that $M = 30$ and $M = 50$ differ with respect to the larger optimal-basis state weights w_α^1 in the one-electron sector.

In Fig. 13, we show the eigenvalues w_α^1 of the reduced density matrix ρ^1 for different sites i on a logarithmic scale. In the TLL regime, displayed in Figs. 13(a) and 13(c), it becomes clear that LBO can be a powerful tool to further study the current-carrying state. For all times calculated here, only a few optimal modes are needed to accurately represent it. The situation for the CDW breakdown is quite different. Figures 13(b) and 13(d) show the weights in this regime. Despite being able to represent the state accurately with only a few modes at $t\omega_0 = 0$, almost the complete set of modes is needed for $t\omega_0 = 6$. This could in theory make the optimal-basis calculations even more costly than just the regular time-evolution method. However, that is not observed for our calculations with $M = 50$. This regime is still clearly a candidate for other schemes to efficiently treat phonons, such as the one of Ref. [78]. In total, the limiting factor for our calculations in the metallic regime is the local bond dimension and obtaining a steady state. For the CDW regime, the amount of local modes needed becomes an issue before the bond dimension matters.

[1] A. Majumdar, Thermoelectricity in semiconductor nanostructures, Science **303**, 777 (2004).

[2] A. Shakouri, Nanoscale thermal transport and microrefrigerators on a chip, Proc. IEEE **94**, 1613 (2006).

[3] F. Giazotto, T. T. Heikkilä, A. Luukanen, A. M. Savin, and J. P. Pekola, Opportunities for mesoscopics in thermometry and refrigeration: Physics and applications, Rev. Mod. Phys. **78**, 217 (2006).

[4] P. Rodgers, Silicon goes thermoelectric, Nature Nanotechnol. **3**, 76 (2008).

[5] C. Franchini, M. Reticcioli, M. Setvin, and U. Diebold, Polarons in materials, Nature Rev. Mater. **6**, 560 (2021).

[6] M. Chávez-Cervantes, G. E. Topp, S. Aeschlimann, R. Krause, S. A. Sato, M. A. Sentef, and I. Gierz, Charge Density Wave Melting in One-Dimensional Wires with Femtosecond Subgap Excitation, Phys. Rev. Lett. **123**, 036405 (2019).

[7] D. Polli, M. Rini, S. Wall, R. W. Schoenlein, Y. Tomioka, Y. Tokura, G. Cerullo, and A. Cavalleri, Coherent orbital waves in the photo-induced insulator-metal dynamics, Nature Mater. **6**, 643 (2007).

[8] C. Jooss, L. Wu, T. Beetz, R. F. Klie, M. Beleggia, M. A. Schofield, S. Schramm, J. Hoffmann, and Y. Zhu, Polaron melting and ordering as key mechanisms for colossal resistance effects in manganites, Proc. Natl. Acad. Sci. USA **104**, 13597 (2007).

[9] J. M. Szarko, B. S. Rolczynski, S. J. Lou, T. Xu, J. Strzalka, T. J. Marks, L. Yu, and L. X. Chen, Photovoltaic function and exciton/charge transfer dynamics in a highly efficient semiconducting Copolymer, Adv. Funct. Mater. **24**, 10 (2014).

[10] B. Kressdorf, T. Meyer, A. Belenchuk, O. Shapoval, M. ten Brink, S. Melles, U. Ross, J. Hoffmann, V. Moshnyaga, M. Seibt, P. Blöchl, and C. Jooss, Room-Temperature Hot-Polaron Photovoltaics in the Charge-Ordered State of a Layered Perovskite Oxide Heterojunction, Phys. Rev. Appl. **14**, 054006 (2020).

[11] M. Galperin, M. A. Ratner, and A. Nitzan, Molecular transport junctions: vibrational effects, J. Phys. Condens. Matter **19**, 103201 (2007).

[12] S. Andergassen, V. Meden, H. Schoeller, J. Splettstoesser, and M. R. Wegewijs, Charge transport through single molecules, quantum dots and quantum wires, Nanotechnol. **21**, 272001 (2010).

[13] J. C. Cuevas and E. Scheer, *Molecular Electronics*, 2nd ed. (World Scientific, Singapore, 2017).

[14] Y. Dubi and M. Di Ventra, Colloquium: Heat flow and thermoelectricity in atomic and molecular junctions, Rev. Mod. Phys. **83**, 131 (2011).

[15] M. Thoss and F. Evers, Perspective: Theory of quantum transport in molecular junctions, J. Chem. Phys. **148**, 030901 (2018).

[16] H. Park, J. Park, A. K. L. Lim, E. H. Anderson, A. P. Alivisatos, and P. L. McEuen, Nanomechanical oscillations in a single-C60 transistor, Nature (London) **407**, 57 (2000).

[17] R. H. M. Smit, Y. Noat, C. Untiedt, N. D. Lang, M. C. van Hemert, and J. M. van Ruitenbeek, Measurement of the conductance of a hydrogen molecule, Nature (London) **419**, 906 (2002).

[18] T. L. Cocker, D. Peller, P. Yu, J. Repp, and R. Huber, Tracking the ultrafast motion of a single molecule by femtosecond orbital imaging, Nature (London), **539** 263 (2016).

[19] B. Ifland, P. Peretzki, B. Kressdorf, P. Saring, A. Kelling, M. Seibt, C. Jooss, and J. Beilstein, Current-voltage characteristics of manganite-titanite perovskite junctions, Nanotechnol. **6**, 1467 (2015).

[20] B. Ifland, J. Hoffmann, B. Kressdorf, V. Roddatis, M. Seibt, and C. Jooss, Contribution of Jahn-Teller and charge transfer excitations to the photovoltaic effect of manganite/titanite heterojunctions, New J. Phys. **19**, 063046 (2017).

[21] R. Peierls, *Quantum Theory of Solids* (Clarendon Press, Oxford, 1955), p. 108.

[22] D. Volja, W.-G. Yin, and W. Ku, Charge ordering in half-doped manganites: Weak charge disproportion and leading mechanisms, Europhys. Lett. **89**, 27008 (2010).

[23] M. Sotoudeh, S. Rajpurohit, P. Blöchl, D. Mierwaldt, J. Norpoth, V. Roddatis, S. Mildner, B. Kressdorf, B. Ifland, and C. Jooss, Electronic structure of $Pr_{1-x}Ca_xMnO_3$, Phys. Rev. B **95**, 235150 (2017).

[24] N. Kida and M. Tonouchi, Spectroscopic evidence for a charge-density-wave condensate in a charge-ordered manganite: Observation of a collective excitation mode in $Pr_{0.7}Ca_{0.3}MnO_3$ by using THz time-domain spectroscopy, Phys. Rev. B **66**, 024401 (2002).

[25] A. Wahl, S. Mercone, A. Pautrat, M. Pollet, C. Simon, and D. Sedmidubsky, Nonlinear electrical response in a charge/orbital ordered $Pr_{0.63}Ca_{0.37}MnO_3$ crystal: The charge density wave analogy, Phys. Rev. B **68**, 094429 (2003).

[26] S. Cox, J. Singleton, R. D. McDonald, A. Migliori, and P. B. Littlewood, Sliding charge-density wave in manganites, Nature Mater. **7**, 25 (2008).

[27] C. Barone, A. Galdi, N. Lampis, L. Maritato, F. M. Granozio, S. Pagano, P. Perna, M. Radovic, and U. Scotti di Uccio, Charge density waves enhance the electronic noise of manganites, Phys. Rev. B **80**, 115128 (2009).

[28] R. Schmidt, Investigation of the electronic structure of the charge-ordered phase in epitaxial and polycrystalline $La_{1-x}Ca_xMnO_3 (x = 0.55, 0.67)$ perovskite manganites, Phys. Rev. B **77**, 205101 (2008).

[29] A. Branschädel, G. Schneider, and P. Schmitteckert, Conductance of inhomogeneous systems: Real-time dynamics, Ann. Phys. (NY) **522**, 657 (2010).

[30] J. Eckel, F. Heidrich-Meisner, S. G. Jakobs, M. Thorwart, M. Pletyukhov, and R. Egger, Comparative study of theoretical methods for non-equilibrium quantum transport, New J. Phys. **12**, 043042 (2010).

[31] M. Galperin, M. A. Ratner, and A. Nitzan, Inelastic electron tunneling spectroscopy in molecular junctions: Peaks and dips, J. Chem. Phys. **121**, 11965 (2004).

[32] M. Galperin, M. A. Ratner, and A. Nitzan, Hysteresis, switching, and negative differential resistance in molecular junctions: A polaron model, Nano Lett. **5**, 125 (2005).

[33] M. Galperin, A. Nitzan, and M. A. Ratner, Resonant inelastic tunneling in molecular junctions, Phys. Rev. B **73**, 045314 (2006).

[34] M. Galperin, A. Nitzan, and M. A. Ratner, Heat conduction in molecular transport junctions, Phys. Rev. B **75**, 155312 (2007).

[35] T. Koch, J. Loos, A. Alvermann, A. R. Bishop, and H. Fehske, Transport through a vibrating quantum dot: Polaronic effects, J. Phys. Conf. Ser. **220**, 012014 (2010).

[36] A. Jovchev and F. B. Anders, Influence of vibrational modes on quantum transport through a nanodevice, Phys. Rev. B **87**, 195112 (2013).

[37] E. Eidelstein, D. Goberman, and A. Schiller, Crossover from adiabatic to antiadiabatic phonon-assisted tunneling in single-molecule transistors, Phys. Rev. B **87**, 075319 (2013).

[38] A. Khedri, T. A. Costi, and V. Meden, Exponential and power-law renormalization in phonon-assisted tunneling, Phys. Rev. B **96**, 195155 (2017).

[39] A. Khedri, V. Meden, and T. A. Costi, Influence of phonon-assisted tunneling on the linear thermoelectric transport through molecular quantum dots, Phys. Rev. B **96**, 195156 (2017).

[40] A. Khedri, T. A. Costi, and V. Meden, Nonequilibrium thermoelectric transport through vibrating molecular quantum dots, Phys. Rev. B **98**, 195138 (2018).

[41] T. Shi, J. I. Cirac, and E. Demler, Ultrafast molecular dynamics in terahertz-STM experiments: Theoretical analysis using the Anderson-Holstein model, Phys. Rev. Res. **2**, 033379 (2020).

[42] M. Caltapanides, D. M. Kennes, and V. Meden, Finite-bias transport through the interacting resonant level model coupled to a phonon mode: A functional renormalization group study, Phys. Rev. B **104**, 085125 (2021).

[43] R. J. Bursill, R. H. McKenzie, and C. J. Hamer, Phase Diagram of the One-Dimensional Holstein Model of Spinless Fermions, Phys. Rev. Lett. **80**, 5607 (1998).

[44] C. E. Creffield, G. Sangiovanni, and M. Capone, Phonon softening and dispersion in the 1D Holstein model of spinless fermions, Eur. Phys. J. B **44**, 175 (2005).

[45] P. Schmitteckert, Nonequilibrium electron transport using the density matrix renormalization group method, Phys. Rev. B **70**, 121302(R) (2004).

[46] K. A. Al-Hassanieh, A. E. Feiguin, J. A. Riera, C. A. Büsser, and E. Dagotto, Adaptive time-dependent density-matrix renormalization-group technique for calculating the conductance of strongly correlated nanostructures, Phys. Rev. B **73**, 195304 (2006).

[47] S. Kirino, T. Fujii, J. Zhao, and K. Ueda, Time-dependent dmrg study on quantum dot under a finite bias voltage, J. Phys. Soc. Jpn. **77**, 084704 (2008).

[48] A. Weichselbaum, F. Verstraete, U. Schollwöck, J. I. Cirac, and J. von Delft, Variational matrix-product-state approach to quantum impurity models, Phys. Rev. B **80**, 165117 (2009).

[49] C. Guo, A. Weichselbaum, S. Kehrein, T. Xiang, and J. von Delft, Density matrix renormalization group study of a quantum impurity model with Landau-Zener time-dependent Hamiltonian, Phys. Rev. B **79**, 115137 (2009).

[50] F. Heidrich-Meisner, I. González, K. A. Al-Hassanieh, A. E. Feiguin, M. J. Rozenberg, and E. Dagotto, Nonequilibrium electronic transport in a one-dimensional Mott insulator, Phys. Rev. B **82**, 205110 (2010).

[51] M. Einhellinger, A. Cojuhovschi, and E. Jeckelmann, Numerical method for nonlinear steady-state transport in one-dimensional correlated conductors, Phys. Rev. B **85**, 235141 (2012).

[52] C. A. Büsser and F. Heidrich-Meisner, Inducing Spin Correlations and Entanglement in a Double Quantum Dot Through Nonequilibrium Transport, Phys. Rev. Lett. **111**, 246807 (2013).

[53] M. Ganahl, P. Thunström, F. Verstraete, K. Held, and H. G. Evertz, Chebyshev expansion for impurity models using matrix product states, Phys. Rev. B **90**, 045144 (2014).

[54] A. Dorda, M. Ganahl, H. G. Evertz, W. von der Linden, and E. Arrigoni, Auxiliary master equation approach within matrix product states: Spectral properties of the nonequilibrium Anderson impurity model, Phys. Rev. B **92**, 125145 (2015).

[55] F. Schwarz, I. Weymann, J. von Delft, and A. Weichselbaum, Nonequilibrium Steady-State Transport in Quantum Impurity Models: A Thermofield and Quantum Quench Approach Using Matrix Product States, Phys. Rev. Lett. **121**, 137702 (2018).

[56] M. M. Rams and M. Zwolak, Breaking the Entanglement Barrier: Tensor Network Simulation of Quantum Transport, Phys. Rev. Lett. **124**, 137701 (2020).

[57] K. G. Wilson, The renormalization group: Critical phenomena and the kondo problem, Rev. Mod. Phys. **47**, 773 (1975).

[58] H. R. Krishna-murthy, J. W. Wilkins, and K. G. Wilson, Renormalization-group approach to the anderson model of dilute magnetic alloys. I. static properties for the symmetric case, Phys. Rev. B **21**, 1003 (1980).

[59] F. B. Anders and A. Schiller, Real-Time Dynamics in Quantum-Impurity Systems: A Time-Dependent Numerical Renormalization-Group Approach, Phys. Rev. Lett. **95**, 196801 (2005).

[60] R. Bulla, T. A. Costi, and T. Pruschke, Numerical renormalization group method for quantum impurity systems, Rev. Mod. Phys. **80**, 395 (2008).

[61] H. Schoeller, An introduction to real-time renormalization group, *Low-Dimensional Systems*, edited by T. Brandes (Springer, Berlin, 2000), pp. 137–166.

[62] H. Schmidt and P. Wölfle, Transport through a kondo quantum dot: Functional RG approach, Ann. Phys. (Berlin) **19**, 60 (2010).

[63] W. Metzner, M. Salmhofer, C. Honerkamp, V. Meden, and K. Schönhammer, Functional renormalization group approach to correlated fermion systems, Rev. Mod. Phys. **84**, 299 (2012).

[64] J. E. Han and R. J. Heary, Imaginary-Time Formulation of Steady-State Nonequilibrium: Application to Strongly Correlated Transport, Phys. Rev. Lett. **99**, 236808 (2007).

[65] P. Werner, T. Oka, and A. J. Millis, Diagrammatic Monte Carlo simulation of nonequilibrium systems, Phys. Rev. B **79**, 035320 (2009).

[66] P. Werner, T. Oka, M. Eckstein, and A. J. Millis, Weak-coupling quantum Monte Carlo calculations on the Keldysh contour: Theory and application to the current-voltage characteristics of the Anderson model, Phys. Rev. B **81**, 035108 (2010).

[67] S. R. White, Density Matrix Formulation for Quantum Renormalization Groups, Phys. Rev. Lett. **69**, 2863 (1992).

[68] A. J. Daley, C. Kollath, U. Schollwöck, and G. Vidal, Time-dependent density-matrix renormalization-group using adaptive effective Hilbert spaces, J. Stat. Mech. (2004) P04005.

[69] S. R. White and A. E. Feiguin, Real-Time Evolution using the Density Matrix Renormalization Group, Phys. Rev. Lett. **93**, 076401 (2004).

[70] G. Vidal, Efficient Simulation of One-Dimensional Quantum Many-Body Systems, Phys. Rev. Lett. **93**, 040502 (2004).

[71] U. Schollwöck, The density-matrix renormalization group, Rev. Mod. Phys. **77**, 259 (2005).

[72] U. Schollwöck, The density-matrix renormalization group in the age of matrix product states, Ann. Phys. (NY) **326**, 96 (2011).

[73] S. Paeckel, T. Köhler, A. Swoboda, S. R. Manmana, U. Schollwöck, and C. Hubig, Time-evolution methods for matrix-product states, Ann. Phys. (NY) **411**, 167998 (2019).

[74] B. Kloss, D. R. Reichman, and R. Tempelaar, Multiset Matrix Product State Calculations Reveal Mobile Franck-Condon Excitations under Strong Holstein-Type Coupling, Phys. Rev. Lett. **123**, 126601 (2019).

[75] M. L. Wall, A. Safavi-Naini, and A. M. Rey, Simulating generic spin-boson models with matrix product states, Phys. Rev. A **94**, 053637 (2016).

[76] E. Jeckelmann and S. R. White, Density-matrix renormalization-group study of the polaron problem in the Holstein model, Phys. Rev. B **57**, 6376 (1998).

[77] C. Zhang, E. Jeckelmann, and S. R. White, Density Matrix Approach to Local Hilbert Space Reduction, Phys. Rev. Lett. **80**, 2661 (1998).

[78] T. Köhler, J. Stolpp, and S. Paeckel, Efficient and flexible approach to simulate low-dimensional quantum lattice models with large local Hilbert spaces, SciPost Phys. **10**, 58 (2021).

[79] S. Mardazad, Y. Xu, X. Yang, M. Grundner, U. Schollwöck, H. Ma, and S. Paeckel, Quantum dynamics simulation of intramolecular singlet fission in covalently linked tetracene dimer, arXiv:2107.13948.

[80] J. Stolpp, T. Köhler, S. R. Manmana, E. Jeckelmann, F. Heidrich-Meisner, and S. Paeckel, Comparative study of state-of-the-art matrix-product-state methods for lattice models with large local hilbert spaces without u(1) symmetry, Comput. Phys. Commun. **269**, 108106 (2021).

[81] C. Zhang, E. Jeckelmann, and S. R. White, Dynamical properties of the one-dimensional Holstein model, Phys. Rev. B **60**, 14092 (1999).

[82] C. Guo, A. Weichselbaum, J. von Delft, and M. Vojta, Critical and Strong-Coupling Phases in One- and Two-Bath Spin-Boson Models, Phys. Rev. Lett. **108**, 160401 (2012).

[83] C. Brockt, F. Dorfner, L. Vidmar, F. Heidrich-Meisner, and E. Jeckelmann, Matrix-product-state method with a dynamical local basis optimization for bosonic systems out of equilibrium, Phys. Rev. B **92**, 241106(R) (2015).

[84] F. A. Y. N. Schröder and A. W. Chin, Simulating open quantum dynamics with time-dependent variational matrix product states: Towards microscopic correlation of environment dynamics and reduced system evolution, Phys. Rev. B **93**, 075105 (2016).

[85] C. Brockt and E. Jeckelmann, Scattering of an electronic wave packet by a one-dimensional electron-phonon-coupled structure, Phys. Rev. B **95**, 064309 (2017).

[86] J. Stolpp, J. Herbrych, F. Dorfner, E. Dagotto, and F. Heidrich-Meisner, Charge-density-wave melting in the one-dimensional Holstein model, Phys. Rev. B **101**, 035134 (2020).

[87] D. Jansen, J. Bonča, and F. Heidrich-Meisner, Finite-temperature density-matrix renormalization group method for electron-phonon systems: Thermodynamics and Holstein-polaron spectral functions, Phys. Rev. B **102**, 165155 (2020).

[88] T. Oka, R. Arita, and H. Aoki, Breakdown of a Mott Insulator: A Nonadiabatic Tunneling Mechanism, Phys. Rev. Lett. **91**, 066406 (2003).

[89] T. Oka and H. Aoki, Ground-State Decay Rate for the Zener Breakdown in Band and Mott Insulators, Phys. Rev. Lett. **95**, 137601 (2005).

[90] T. Oka and H. Aoki, Dielectric breakdown in a Mott insulator: Many-body Schwinger-Landau-Zener mechanism studied with a generalized Bethe ansatz, Phys. Rev. B **81**, 033103 (2010).

[91] M. Eckstein, T. Oka, and P. Werner, Dielectric Breakdown of Mott Insulators in Dynamical Mean-Field Theory, Phys. Rev. Lett. **105**, 146404 (2010).

[92] J. K. Freericks, V. M. Turkowski, and V. Zlatić, Nonequilibrium Dynamical Mean-Field Theory, Phys. Rev. Lett. **97**, 266408 (2006).

[93] V. Turkowski and J. K. Freericks, Nonequilibrium perturbation theory of the spinless Falicov-Kimball model: Second-order truncated expansion in U, Phys. Rev. B **75**, 125110 (2007).

[94] J. K. Freericks, Quenching Bloch oscillations in a strongly correlated material: Nonequilibrium dynamical mean-field theory, Phys. Rev. B **77**, 075109 (2008).

[95] H. Hashimoto and S. Ishihara, Photoinduced charge-order melting dynamics in a one-dimensional interacting Holstein model, Phys. Rev. B **96**, 035154 (2017).

[96] D. Golež, J. Bonča, and L. Vidmar, Dissociation of a Hubbard-Holstein bipolaron driven away from equilibrium by a constant electric field, Phys. Rev. B **85**, 144304 (2012).

[97] L. Vidmar and J. Bonča, Real-time current of a charge carrier in a strongly correlated system coupled to phonons, driven by a uniform electric field, J. Supercond. Nov. Magn. **25**, 1255 (2012).

[98] M. Weber and J. K. Freericks, Field tuning beyond the heat death of a charge-density-wave chain, arXiv:2107.04096.

[99] M. Weber and J. K. Freericks, Real-time evolution of static electron-phonon models in time-dependent electric fields, arXiv:2108.05431.

[100] J.-M. Bischoff and E. Jeckelmann, Density-matrix renormalization group study of the linear conductance in quantum wires coupled to interacting leads or phonons, Phys. Rev. B **100**, 075151 (2019).

[101] D. Bohr, P. Schmitteckert, and P. Wölfle, DMRG evaluation of the Kubo formula —conductance of strongly interacting quantum systems, Europhy. Lett. **73**, 246 (2006).

[102] J.-M. Bischoff and E. Jeckelmann, Density-matrix renormalization group method for the conductance of one-dimensional correlated systems using the Kubo formula, Phys. Rev. B **96**, 195111 (2017).

[103] W. Apel and T. M. Rice, Combined effect of disorder and interaction on the conductance of a one-dimensional fermion system, Phys. Rev. B **26**, 7063 (1982).

[104] C. L. Kane and M. P. A. Fisher, Transmission through barriers and resonant tunneling in an interacting one-dimensional electron gas, Phys. Rev. B **46**, 15233 (1992).

[105] C. L. Kane and M. P. A. Fisher, Transport in a One-Channel Luttinger Liquid, Phys. Rev. Lett. **68**, 1220 (1992).

[106] S. Ejima and H. Fehske, Luttinger parameters and momentum distribution function for the half-filled spinless fermion Holstein model: A DMRG approach, Europhys. Lett. **87**, 27001 (2009).

[107] T. Holstein, Studies of polaron motion: Part I. The molecular-crystal model, Ann. Phys. (NY) **8**, 325 (1959).

[108] M. Capone, W. Stephan, and M. Grilli, Small-polaron formation and optical absorption in Su-Schrieffer-Heeger and Holstein models, Phys. Rev. B **56**, 4484 (1997).

[109] D. Jansen, J. Stolpp, L. Vidmar, and F. Heidrich-Meisner, Eigenstate thermalization and quantum chaos in the Holstein polaron model, Phys. Rev. B **99**, 155130 (2019).

[110] J. Bonča, S. A. Trugman, and I. Batistić, Holstein polaron, Phys. Rev. B **60**, 1633 (1999).

[111] F. Dorfner, L. Vidmar, C. Brockt, E. Jeckelmann, and F. Heidrich-Meisner, Real-time decay of a highly excited charge carrier in the one-dimensional Holstein model, Phys. Rev. B **91**, 104302 (2015).

[112] G. Wellein, H. Röder, and H. Fehske, Polarons and bipolarons in strongly interacting electron-phonon systems, Phys. Rev. B **53**, 9666 (1996).

[113] G. Wellein and H. Fehske, Self-trapping problem of electrons or excitons in one dimension, Phys. Rev. B **58**, 6208 (1998).

[114] J. Bonča, S. A. Trugman, and M. Berciu, Spectral function of the Holstein polaron at finite temperature, Phys. Rev. B **100**, 094307 (2019).

[115] M. Fishman, S. R. White, and E. M. Stoudenmire, The ITensor software library for tensor network calculations, arXiv:2007.14822.

[116] S. Sykora, A. Hübsch, K. W. Becker, G. Wellein, and H. Fehske, Single-particle excitations and phonon softening in the one-dimensional spinless Holstein model, Phys. Rev. B **71**, 045112 (2005).

[117] H. Zhao, C. Q. Wu, and H. Q. Lin, Spectral function of the one-dimensional Holstein model at half filling, Phys. Rev. B **71**, 115201 (2005).

[118] J. Bonča and S. A. Trugman, Dynamic properties of a polaron coupled to dispersive optical phonons, Phys. Rev. B **103**, 054304 (2021).

[119] N. C. Costa, T. Blommel, W.-T. Chiu, G. Batrouni, and R. T. Scalettar, Phonon Dispersion and the Competition between Pairing and Charge Order, Phys. Rev. Lett. **120**, 187003 (2018).

[120] M. Kalla, N. R. Chebrolu, and A. Chatterjee, Magneto-transport properties of a single molecular transistor in the presence of electron-electron and electron-phonon interactions and quantum dissipation, Sci. Rep. **9**, 16510 (2019).

[121] T. Hotta and E. Dagotto, *Theory of Manganites* (Springer, Dordrecht, 2004).

[122] T. Koch, J. Loos, and H. Fehske, Thermoelectric effects in molecular quantum dots with contacts, Phys. Rev. B **89**, 155133 (2014).

[123] C. Schinabeck, R. Härtle, and M. Thoss, Hierarchical quantum master equation approach to electronic-vibrational coupling in nonequilibrium transport through nanosystems: Reservoir formulation and application to vibrational instabilities, Phys. Rev. B **97**, 235429 (2018).

[124] P. Roura-Bas, F. Güller, L. Tosi, and A. A. Aligia, Destructive quantum interference in transport through molecules with electron–electron and electron-vibration interactions, J. Phys. Condens. Matter **31**, 465602 (2019).

Chapter 7

Comparing trajectory-based to exact methods

So far in this thesis, I have shown results obtained with matrix-product-state algorithms tailored for electron-phonon problems with local basis optimization. These algorithms utilize the low entanglement in the system to approximate the quantum state. Furthermore, the approach treats the phonons quantum mechanically but truncates the phonon Hilbert space based on eigenvalues of the reduced density matrices.

As I have demonstrated, these algorithms can be used to study a series of problems inspired by solid-state physics, such as computing spectral functions and transport coefficients, and studying charge-density-wave (CDW) melting and transport in heterostructures. However, solid-state physics is not the only field where systems with electron-boson interaction play an important role. In chemical physics, for example, studying molecular dynamics in regimes where the Born-Oppenheimer approximation does not suffice [302] has led to the development of a series of algorithms based on different approximations. These algorithms include multitrajectory Ehrenfest (MTE) [122, 123], surface hopping algorithms [124–126], and multiconfigurational Ehrenfest (MCE) [120, 121], which were introduced in Ch. 3.

This raises the interesting question, to what degree can one incorporate computationally cheaper but approximative algorithms from the chemical physics community into canonical solid-state problems such as those studied here? Some setups have already been addressed. For example, Chen et al. studied polaron dynamics with MCE in Ref. [180]. Another example is Ref. [303], where Li et al. obtained different relaxation times for the polaron formation when comparing Ehrenfest and quantum algorithms. In Ref. [178], Petrović et al. used Monte Carlo with classical phonons to investigate the time-resolved photoemission for a CDW in the Holstein model, which allowed them to study times long enough to capture relaxation at finite temperatures after an excitation.

Here, the goal is to better understand the validity of these methods for two typical condensed matter questions: how does the electron density spread in a lattice [62, 66], and what are the effects leading to CDW melting [76, 178]. In the presented results, we start with different initial states and systems, and study the time-evolution of both electronic

and phononic observables (some of the initial states are motivated by Stolpp et al. in Ref. [76]).

We start with the Holstein dimer and trimer. For these systems, exact diagonalization results are available, which allows us to estimate the accuracy of the different algorithms. This also gives us insight into why certain algorithms work well or fail based on the Born-Oppenheimer surfaces (the Born-Oppenheimer Hamiltonian was introduced in Ch. 2 for the Holstein dimer). We then look at extended systems and study the spread of an electron in the lattice. The two initial states we study are one with a free electron and one with an electron dressed with phonons. In both cases, the electron starts in the center of the lattice. In this situation, we use tDMRG with LBO (tDMRG-LBO), see Ch. 3, to assess the accuracy of the algorithms. Even though the available time for tDMRG-LBO is limited, we still get a good indication of which algorithms are best suited for these types of setups. Finally, we compare tDMRG-LBO and MTE for CDW initial states.

For the bare-electron initial state, we find that for large systems, all methods correctly capture the reduced mean-squared displacement (RMSD) of the electron density at initial times, but later, they all deviate from the tDMRG-LBO results. When looking at the phonon number, we observe that the different versions of the fewest-switches surface hopping algorithm (FSSH) and MCE capture the observable qualitatively well, whereas MTE displays large deviations. Many of our conclusions also apply to the dressed-electron initial state, but we report better short time dynamics for FSSH than for MTE for the central nuclei-coordinate observable.

Finally, for CDW initial states, we find that MTE captures the physics of some observables very well. In the adiabatic regime, the order parameter is exactly reproduced by MTE for both the dressed and bare initial states. In the anti-adiabatic regime, however, the initial plateau of the order parameter is only quantitatively captured for the bare initial state. For the phonon number, we always observe some deviations, indicating that it could be problematic to use MTE to study the energy transfer between the phononic and electronic degrees of freedom.

These results help us assess how reliable the trajectory-based methods are for condensed-matter problems such as the spread of electron density in a lattice and CDW melting. A possible next step would be to test how good the approximations are for the equilibrium correlation functions relevant for the spectral functions and transport coefficients discussed in Ch. 4 and Ch. 5. This could help us better understand which, if any, quasi-particle properties remain in the trajectory-based approach (see Ref. [304] for a discussion of Ehrenfest methods at finite temperature). As explained in Ch. 2, the integral over the optical conductivity can be related to thermal expectation values via the f-sum rule. For the Holstein model, this is proportional to the electron kinetic energy. It would thus also be interesting to analyze how differences between the exact and approximate kinetic-energy expectation value manifest themselves in the optical conductivity spectra.

7.1 Publication: Real-time non-adiabatic dynamics in the one-dimensional Holstein model: Trajectory-based vs exact methods

Reprinted article with permission from
Michael ten Brink, Stefan Gräber, Miroslav Hopjan, David Jansen, Jan Stolpp, Fabian Heidrich-Meisner, and Peter E. Blöchl
J. Chem. Phys. 156, 234109 (2022)
https://doi.org/10.1063/5.0092063

Author contributions: M. t. B. wrote the bulk of the manuscript, implemented the surface hopping algorithms, and produced some of the exact data and the single electron MTE data. S. G. implemented the Ehrenfest algorithms and wrote the multiconfigurational Ehrenfest part of the manuscript together with M. H.. M. H. also wrote the introduction and conclusion together with M. t. B.. The single electron MTE data from M. t. B. were compared to the results of S. G.. The multi-electron MTE results were also computed by S. G.. D. J. computed the DMRG data, did the exact calculations in second quantization, and wrote the DMRG and CDW parts of the manuscript. J. S. also provided DMRG data for the CDW part which was compared to the data from D. J.. M. H., F. H.-M., and P. B. conceived the idea of the project. J. S., F. H.-M., and P. B. revised the manuscript. All authors contributed to interpreting the results and discussed the data.

Real-time non-adiabatic dynamics in the one-dimensional Holstein model: Trajectory-based vs exact methods

Cite as: J. Chem. Phys. **156**, 234109 (2022); https://doi.org/10.1063/5.0092063
Submitted: 20 March 2022 • Accepted: 16 May 2022 • Published Online: 17 June 2022

M. ten Brink, S. Gräber, M. Hopjan, et al.

The Journal of Chemical Physics ARTICLE scitation.org/journal/jcp

Real-time non-adiabatic dynamics in the one-dimensional Holstein model: Trajectory-based vs exact methods

Cite as: J. Chem. Phys. 156, 234109 (2022); doi: 10.1063/5.0092063
Submitted: 20 March 2022 • Accepted: 16 May 2022 •
Published Online: 17 June 2022

M. ten Brink,[1,2,a)] S. Gräber,[1] M. Hopjan,[1,3] D. Jansen,[1] J. Stolpp,[1] F. Heidrich-Meisner,[1] and P. E. Blöchl[1,2]

AFFILIATIONS

[1] Institut für Theoretische Physik, Georg-August-Universität Göttingen, Friedrich-Hund-Platz 1, 37077 Göttingen, Germany
[2] Institut für Theoretische Physik, Technische Universität Clausthal, Leibnizstr. 10, 38678 Clausthal-Zellerfeld, Germany
[3] Department of Theoretical Physics, J. Stefan Institute, Jamova cesta 39, SI-1000 Ljubljana, Slovenia

[a)] Author to whom correspondence should be addressed: m.tenbrink@theorie.physik.uni-goettingen.de

ABSTRACT

We benchmark a set of quantum-chemistry methods, including multitrajectory Ehrenfest, fewest-switches surface-hopping, and multiconfigurational-Ehrenfest dynamics, against exact quantum-many-body techniques by studying real-time dynamics in the Holstein model. This is a paradigmatic model in condensed matter theory incorporating a local coupling of electrons to Einstein phonons. For the two-site and three-site Holstein model, we discuss the exact and quantum-chemistry methods in terms of the Born–Huang formalism, covering different initial states, which either start on a single Born–Oppenheimer surface, or with the electron localized to a single site. For extended systems with up to 51 sites, we address both the physics of single Holstein polarons and the dynamics of charge-density waves at finite electron densities. For these extended systems, we compare the quantum-chemistry methods to exact dynamics obtained from time-dependent density matrix renormalization group calculations with local basis optimization (DMRG-LBO). We observe that the multitrajectory Ehrenfest method, in general, only captures the ultrashort time dynamics accurately. In contrast, the surface-hopping method with suitable corrections provides a much better description of the long-time behavior but struggles with the short-time description of coherences between different Born–Oppenheimer states. We show that the multiconfigurational Ehrenfest method yields a significant improvement over the multitrajectory Ehrenfest method and can be converged to the exact results in small systems with moderate computational efforts. We further observe that for extended systems, this convergence is slower with respect to the number of configurations. Our benchmark study demonstrates that DMRG-LBO is a useful tool for assessing the quality of the quantum-chemistry methods.

I. INTRODUCTION

In quantum chemistry, the joint dynamics of electronic excitations coupled to nuclear degrees of freedom can lead to complex non-adiabatic effects, which cannot be described within the Born–Oppenheimer (BO) approximation.[1–3] The correct description of non-adiabatic effects is essential to understand the resulting intricate processes, such as interference close to and transitions through avoided crossings and conical intersections,[4,5] intraband relaxation, or energy transfer.[6] This coupled dynamics of an electron–bosonic composite system is often initiated by the excitation with an electromagnetic field, and complexity can further increase if the quantum nature of the electromagnetic field and its bosonic excitations are taken into account explicitly.[7–12]

Bosonic excitations naturally emerge in condensed matter, e.g., plasmons,[13] phonons,[14–16] or magnons.[13] Here, such excitations can couple to electrons and influence the electronic properties. For example, exciton–phonon coupling[17–22] in semiconductors affects exciton mobilities, the phonon–bottleneck mechanism reduces energy loss of hot carriers,[23–27] and phonon–magnon scattering[28,29] induced by electron–phonon coupling can lead to ultrafast demagnetization,[30] to mention a few examples. Clearly, there is an increasing interest in the theoretical description of such multi-component systems involving bosons, also in view of recent

ultrafast dynamics experiments,[31–33] where, for example, light excitations in electron–phonon coupled systems have been claimed to enhance superconductivity[34–40] or where phase transitions to a charge-density-wave phase[41–43] or a metal–insulator structural phase transition[44] can be driven.

Exact solutions to the real-time dynamics of composite electron–nuclear systems are scarce. Among the few systems for which numerically exact solutions exist, we mention, e.g., the dissipative spin-boson model,[45–57] Tully's set of problems,[58–62] the Shin–Metiu model of proton-charge transfer,[63–68] and its variant for desorption.[69,70] Recently, some exactly solvable models for cavity quantum electrodynamics (QED) have been presented.[12] To describe more complex systems, a quite large palette of quantum-chemical approximate methods has been devised so far.[1] Examples are Ehrenfest and surface-hopping methods, which are widely used and computationally favorable algorithms.[1,59] They use independent classical trajectories for the nuclei and restore some quantum effects by averaging over the trajectories. Their low computational costs allow for treating rather large molecular systems.

In condensed matter physics, the description of coupled electron–bosonic systems is naturally done within the formalism of diagrammatic quantum field methods,[14,71–73] which has recently been extended to the description of non-equilibrium real-time dynamics.[74–77] A related method based on the Bogoliubov–Born–Green–Kirkwood–Yvon hierarchy for the correlation matrices has recently been applied to the bosonic excitation of the cavity field in cavity QED.[78] We also mention parallel efforts with two-component density-functional theory,[79] density-matrix embedding theory,[80] and quantum Monte Carlo methods.[81,82] Combinations of Ehrenfest and surface-hopping dynamics with time-dependent density functional theory are popular as well.[83–85]

For condensed matter problems, numerically exact solutions for the real-time dynamics of electron–phonon coupled systems based on the matrix–product representation of many-body states have started to emerge.[86–88] Such methods can efficiently handle large bosonic Hilbert spaces. This effort to develop efficient methods for (quasi) one-dimensional (1D) coupled electron–nuclear models based on the density matrix renormalization group (DMRG)[89–91] is ongoing.[86–88,92–94] Specific methods are the pseudosite DMRG method,[95] DMRG with local basis optimization (DMRG-LBO),[96–98] and the projected purified DMRG.[93] DMRG methods use an efficient matrix–product state (MPS) representation of the truncated wave function and DMRG-LBO adds the determination of an optimal basis for the local degrees of freedom obtained from diagonalizing local reduced density matrices. This optimal basis can, in many cases, be truncated with a negligible error, thereby making many algorithms computationally more efficient.[86,88,96–102]

Naturally, one can ask if the approximate methods devised for quantum chemistry could be applied in condensed matter[57,103–105] and vice versa.[106] To answer such questions, benchmarks, such as the ones that have been carried out in the context of cavity QED[78] or the spin-boson model,[57,107] are desirable. We also mention a recent comparative study of several quantum-chemistry methods performed in large chromophores.[108] Applications of surface-hopping algorithms in extended condensed matter systems have started to appear (see Ref. 109 and references therein). However, there is a need for systematic studies comparing such independent-trajectory methods to unbiased numerically exact results in extended condensed matter systems. One recent effort along these lines has been presented in Ref. 110. Therefore, in our work, we study the real-time dynamics in a paradigmatic condensed matter system, the Holstein model,[111] with methods of quantum chemistry, specifically the Ehrenfest and fewest-switches surface-hopping algorithms,[1,58,59] and the multiconfigurational Ehrenfest (MCE) algorithm[112,113] and we benchmark them against exact diagonalization (ED) for small systems and DMRG-LBO[86,88] for large systems. We note that the multiconfigurational Ehrenfest method has recently been compared against the hierarchy equation of motion method[114,115] and the multiple Davydov D2 ansatz[116] in a similar model for up to 16 sites.[117]

The Holstein model[111] is one of the prototypical systems to describe the formation of polarons,[118,119] which were originally thought of as electrons that cause distortions in their surrounding polar lattice, now broadly understood as electronic quasi-particles. The key ingredients of the Holstein model are the local interaction of electrons and Einstein phonons. The model consists of one harmonic oscillator on every lattice site, which is bi-linearly coupled to the electronic density on that site. The only coupling between lattice sites and hence oscillators originates from the electronic hopping between sites, which is often restricted to nearest-neighbor hopping. Consequently, the oscillators interact only indirectly via electrons. Despite its simplicity, the Holstein model has been used to describe polaronic signatures in materials.[15] Apart from the polarons, the Holstein model can also host a Peierls-type lattice instability,[120] the so-called charge-density wave (CDW) phase at half filling.[121–128] By tuning parameters of the 1D Holstein model, one can predict a transition between the CDW and Luttinger-liquid metallic phases.[125,126] The CDW-to-metallic transition has recently been observed in experiments.[16] The physics of polarons and the CDW-to-metallic transition described in the Holstein model generally involve a strong coupling between oscillators and electrons, for whose description non-perturbative theoretical methods are necessary even in equilibrium (see Ref. 15 and references therein).

To connect our model to the concepts of quantum chemistry, we first consider the two-site Holstein model[129–138] [see Figs. 1(a)–1(c)] as it can be seen as a limit of both the spin-boson model and the Shin–Metiu model, i.e., the quantum-chemistry models mentioned above. For the Shin–Metiu problem, one arrives at the two-site Holstein model by taking its first two Born–Oppenheimer surfaces into account, leading to a similar Born–Oppenheimer Hamiltonian as for the Holstein model.[3] For the spin-boson model, the two-site Holstein model is obtained by limiting the number of bath oscillators to one, leading to the so-called one-mode spin-boson model.[139] Moreover, the two-site Holstein model can also be seen as the simplest appropriate model system in which two diabatic states, representing reactants and products, are coupled through a single harmonic oscillator.[140,141] It is thus natural to start with the two-site Holstein model and discuss the non-adiabatic dynamics from the perspective of the Born–Huang formalism as it is common in quantum chemistry.

For the two-site Holstein model, we consider both initial states that have contributions only on a single Born–Oppenheimer surface [see Fig. 1(a)] and local initial states [see Figs. 1(b) and 1(c)]. The former is typically used in quantum chemistry to study the dynamics

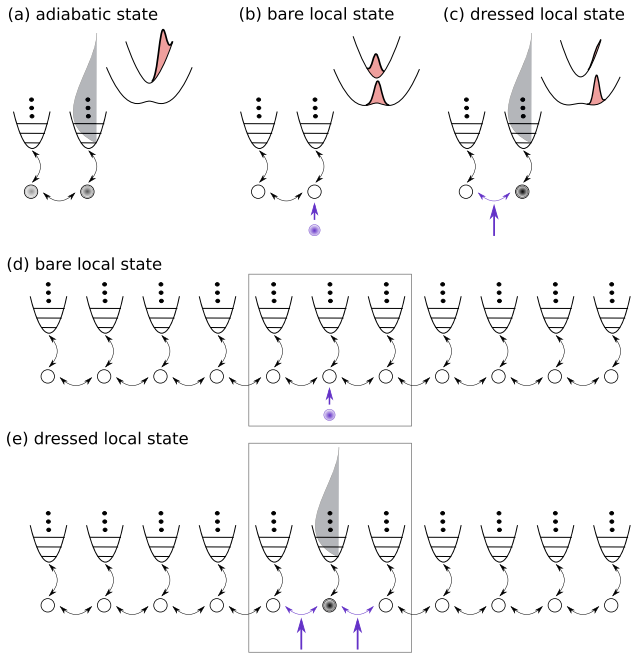

FIG. 1. Examples of initial conditions considered in this work: (a)–(c) the two-site Holstein model and (d) and (e) the extended Holstein model. For the two-site Holstein model, we also sketch the initial nuclear wave function densities on the potential energy (Born–Oppenheimer) surfaces in the Born–Huang formalism. (a) The adiabatic initial state has contributions only on the upper Born–Oppenheimer surface, (b) the bare local state represents the addition of an electron on one of the sites of an empty Holstein dimer, and (c) the dressed local state represents a quench of the hopping matrix element between the empty site and a local polaron on the other site. (d) This bare local state represents an electron added to an empty Holstein lattice and addresses the formation of a polaron. (e) The dressed local initial state represents a polaron localized to one site, which can be understood again as a quench of the hopping parameter. We note that conditions (d) and (e) have been studied in Refs. 77 and 87. The rectangles denote the reduction to the three-site Holstein model, for which the Born–Huang formalism in terms of potential energy surfaces is still practically tractable.

of a wave packet near an avoided crossing. Since the wave function at each nuclear position has contributions only in a single (adiabatic) Born–Oppenheimer state, we also call this an adiabatic initial state. The latter two have recently been studied in condensed-matter-theory studies, for example, for the Holstein model (see Refs. 77 and 87). The local initial conditions start in a coherent superposition of different adiabatic states, which poses a challenge for fewest-switches surface hopping (FSSH).[142] We note that both the adiabatic initial state, which has contributions on a single Born–Oppenheimer surface, and the local states are idealized initial states and a generic initial state realized in an experiment, e.g., after optical excitation, is probably in between the two initial conditions. Even though idealized, the nuclear wave functions of all initial conditions can be exactly represented as well-defined probability distributions in phase space for the Ehrenfest and surface-hopping trajectory methods. In this way, we test the inherent approximations of the dynamics alone and not approximations of the nuclear initial state. The findings from the two-site Holstein model will help us to interpret the dynamics in larger Holstein chains, where the exact Born–Huang formalism is not practically tractable.

In the Holstein chain, the coupling between bosons and electrons can lead to strong non-adiabatic effects, similar to those in the two-site Holstein model. Thus, out-of-equilibrium dynamics in the Holstein model constitute a challenging problem for which several methods have been developed. A straightforward way to solve the problem is to use exact diagonalization;[97,143–146] however, one quickly reaches memory limits due to the huge Hilbert space that needs to be considered. Therefore, one has to resort to efficient methods that seek to determine the relevant part of the Hilbert space, such as diagonalization in a limited functional space,[147–149] its recent extension,[150] and tailored implementations of the Lanczos method.[151–154] These methods can still describe only moderately large system sizes. To increase the system sizes even further, matrix–product–state (e.g., the density matrix renormalization group) methods[86–88,101,155,156] adapted to the large phononic Hilbert space can be used. These methods allow us to study both single polarons[87,101] and charge-density wave states[88] in systems with a finite electronic density. For the polaron problem, alternative quantum-chemistry methods are the hierarchical equation-of-motion method[114,115,157] or the Davydov D_1 or D_2 ansatz.[116,117,158,159] Recently, the multiconfigurational Ehrenfest method has been applied to the polaron problem with promising results.[117] In this work, we consider some of these methods and apply them to initial conditions that probe the relevant physics of the Holstein model, i.e., polaron physics in chains with up to 51 sites [see Figs. 1(d) and 1(e)] and CDW physics [see Figs. 2(a) and 2(b)] in chains with 13 sites.

We provide a brief account of our main observations. Starting with the two-site system (the Holstein dimer) and the three-site system (the Holstein trimer), we show that the multitrajectory Ehrenfest (MTE) method, which is the cheapest method to implement, has serious drawbacks and, in general, only the ultrashort time dynamics is correctly described. The surface-hopping method

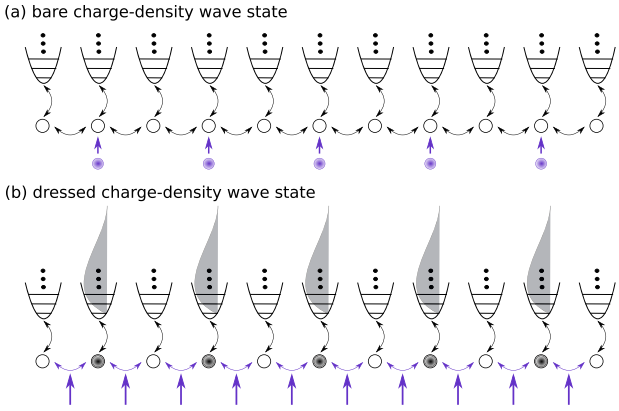

FIG. 2. Examples of charge-density wave initial conditions considered in this work for the Holstein chains mimicking ideal CDW orders. (a) The bare CDW represents the addition of electrons on every second site. (b) The dressed CDW represents maximally localized polarons placed on every second site. We note that conditions (a) and (b) have been studied in Ref. 88 using DMRG-LBO.

improves the description of non-adiabatic effects, such as wave-packet splitting. Even though the coherences included in the local initial states are not well suited for the surface-hopping method, the approach still gives a better qualitative description than the multitrajectory Ehrenfest method for later times in most cases. For the multiconfigurational Ehrenfest method, we demonstrate convergence to exact dynamics with an increasing number of configurations, confirming that the method is, in principle, exact. For instance, it is able to describe quantum tunneling processes.

For the polaron problem in Holstein chains with up to 51 sites, the multitrajectory Ehrenfest method is incapable of sufficiently relaxing excitations back to the lower energy surfaces and cannot describe the local trapping of the charge carrier. Contrarily, the surface-hopping method yields a significantly better agreement with DMRG than MTE, and certain physics in the long-time behavior, such as local trapping, is captured qualitatively by this method. We observe a slower convergence for the multiconfigurational Ehrenfest (MCE) method than for the dimer or trimer. In practical calculations using MCE, we are able to converge most observables only in the short-time dynamics, while at later times, some of the observables deviate from the results of the exact DMRG-LBO method.

Finally, for the charge-density-wave physics for which we consider multi-electron systems, we demonstrate the failure of the multitrajectory Ehrenfest dynamics to describe energy transfer and the evolution of the total phonon number after ultrashort dynamics by comparison to the exact DMRG-LBO method. In contrast, in an adiabatic parameter regime, the charge-density wave order parameter is reasonably well described by MTE.

The plan of this work is as follows. We introduce the 1D Holstein model in Sec. II. We review the Born–Huang formalism in Sec. III. In Sec. IV, we discuss exact numerical methods, the exact diagonalization in second quantization and the Born–Huang basis, and the density matrix renormalization group. The independent-trajectory methods are discussed in Sec. V. In Sec. VI, we follow up with the multiconfigurational Ehrenfest method. We then present our results for the two-site model in Sec. VII and for the three-site Holstein model in Sec. VIII. The polaron physics for Holstein chains is considered in Sec. IX. Finally, CDW physics is covered in Sec. X. We conclude and give prospects in Sec. XI.

II. THE HOLSTEIN MODEL

A. The Holstein chain

In this work, we consider the Holstein model[111] for the special case of one dimension. The Hamiltonian in the occupation number formalism with the phonon creation and annihilation operators $\hat{b}_i^\dagger$ and $\hat{b}_i$ for site i and the corresponding spinless electronic operators $\hat{c}_i^\dagger$ and $\hat{c}_i$ can be written as

$$\hat{H} = \sum_i \Big[-t_0(\hat{c}_i^\dagger \hat{c}_{i+1} + \hat{c}_{i+1}^\dagger \hat{c}_i) + \hbar\omega_0(\hat{b}_i^\dagger \hat{b}_i + 1/2) - \gamma \hat{n}_i \Big(\hat{b}_i^\dagger + \hat{b}_i\Big)\Big], \tag{1}$$

with $\hat{n}_i = \hat{c}_i^\dagger \hat{c}_i$. Here, we can identify the three fundamental model parameters: the hopping matrix element t_0, the phonon frequency ω_0, and the electron–phonon coupling γ.

It is instructive to transform the phonon operators to their position $\hat{x}_i$ and momentum $\hat{p}_i$ operators to get real-space representations for the solutions to this model. For this purpose, we insert the definition of the phonon ladder operators used above: $\hat{b}_i = \sqrt{\frac{m\omega_0}{2\hbar}}\Big(\hat{x}_i + \frac{i}{m\omega_0}\hat{p}_i\Big)$ (and $\hat{b}_i^\dagger$ accordingly), with the nuclear mass m, to write the Hamiltonian (1) equivalently as

$$\hat{H} = \sum_i \left[-t_0(\hat{c}_i^\dagger \hat{c}_{i+1} + \hat{c}_{i+1}^\dagger \hat{c}_i) + \frac{m\omega_0^2}{2}\hat{x}_i^2 + \frac{1}{2m}\hat{p}_i^2 - \sqrt{\frac{2m\omega_0}{\hbar}}\gamma \hat{x}_i \hat{n}_i \right]. \tag{2}$$

Sometimes, in this work, we use a simplified dimensionless notation, which will always be indicated by a bar over a symbol: $\bar{X}$. The dimensionless variables are defined by setting $\hbar\omega_0$ as the energy unit: $\bar{\hat{H}} = \frac{\hat{H}}{\hbar\omega_0}$, $\bar{t}_0 = \frac{t_0}{\hbar\omega_0}$, and $\bar{\gamma} = \frac{\gamma}{\hbar\omega_0}$, and by using the natural length scale for the harmonic oscillators: $\bar{\hat{x}}_i = \hat{x}_i / \sqrt{\frac{\hbar}{m\omega_0}}$.

B. Holstein dimer and trimer

When visualizing potential energy surfaces later in this work, but also for the numerically exact calculation of eigenstates of the system, it is useful to reduce the number of phonon degrees of freedom for the small Holstein systems.

For this, the phonon coordinates of the dimer Hamiltonian can be transformed into a relative and a center-of-mass coordinate, $\hat{\bar{q}} = (\hat{\bar{x}}_1 - \hat{\bar{x}}_2)/\sqrt{2}$ and $\hat{\bar{Q}} = (\hat{\bar{x}}_1 + \hat{\bar{x}}_2)/\sqrt{2}$, to obtain

$$\begin{aligned}\hat{\bar{H}}_{Dimer} = &-\bar{t}_0(\hat{c}_1^\dagger \hat{c}_2 + \hat{c}_2^\dagger \hat{c}_1) + \frac{\hat{\bar{Q}}^2}{2} + \frac{\hat{\bar{p}}_Q^2}{2} + \frac{\hat{\bar{q}}^2}{2} + \frac{\hat{\bar{p}}_q^2}{2} \\ &- \bar{\gamma}[\hat{\bar{q}}(\hat{n}_1 - \hat{n}_2) + \hat{\bar{Q}}(\hat{n}_1 + \hat{n}_2)].\end{aligned} \tag{3}$$

If we keep the total electron density constant at $\langle \hat{n}_1 \rangle + \langle \hat{n}_2 \rangle = const.$, the equation for the center-of-mass coordinate $\bar{Q}$ is a simple harmonic oscillator and independent of the rest of the system. We are then left with a single phonon coordinate $\bar{q}$:

$$\hat{\bar{H}}_{\bar{q}} = -\bar{t}_0(\hat{c}_1^\dagger \hat{c}_2 + \hat{c}_2^\dagger \hat{c}_1) + \frac{\hat{\bar{q}}^2}{2} + \frac{\hat{\bar{p}}_q^2}{2} - \bar{\gamma}\hat{\bar{q}}(\hat{n}_1 - \hat{n}_2). \tag{4}$$

The center-of-mass coordinate can be removed for the Holstein model of any size, but we do this explicitly only for the dimer and trimer ($L = 3$). For the trimer, the phonon coordinates can be transformed into

$$\begin{aligned}\hat{\bar{X}} &= \frac{1}{\sqrt{3}}\Big(\hat{\bar{x}}_1 + \hat{\bar{x}}_2 + \hat{\bar{x}}_3\Big), \\ \hat{\bar{x}}_s &= \frac{2}{\sqrt{6}}\left(\hat{\bar{x}}_2 - \frac{\hat{\bar{x}}_1 + \hat{\bar{x}}_3}{2}\right), \\ \hat{\bar{x}}_a &= \frac{1}{\sqrt{2}}\Big(\hat{\bar{x}}_3 - \hat{\bar{x}}_1\Big).\end{aligned} \tag{5}$$

Here, $\hat{\bar{X}}$ is a center-of-mass coordinate, which, like in the Holstein dimer, does not couple to the rest of the system if we have a constant electron number. $\hat{\bar{x}}_s$ is a symmetric phonon mode around the central site and couples to the difference of the electron population on the

central site and the average population on the edge sites. Finally, $\hat{\tilde{x}}_a$ is an anti-symmetric phonon mode, which couples to the difference of the electronic populations on the edge Holstein sites ($\hat{\tilde{x}}_1$ and $\hat{\tilde{x}}_3$).

III. THE BORN–HUANG FORMALISM

A. General recapitulation of the Born–Huang approach

In this section, we provide a short recapitulation of the Born–Huang approach,[160] which can be described as an expansion of the wave function in adiabatic electronic eigenstates. In this Born–Huang formalism, we can understand the notion of non-adiabatic effects, which can lead to transitions between different adiabatic electronic states.

We start by expanding the total state $|\Psi\rangle$ of the system in nuclear and electron basis states, $|R\rangle$ and $|\phi_a(R)\rangle$, where the nuclear state is defined by its (many-particle) position vector R, and the electron state, which might depend on the nuclear position, is labeled by a general (many-particle) index a,

$$|\Psi\rangle = \int \mathrm{d}R \sum_a |R, \phi_a(R)\rangle \Psi_a(R). \tag{6}$$

The idea of the Born–Huang approach is to use a special set of electronic basis states: the eigenstates of the Born–Oppenheimer[161] (BO) Hamiltonian $\hat{H}^{BO}$, which is obtained from the total Hamiltonian $\hat{H}$ by removing the kinetic energy term of the phonons,

$$\begin{aligned} \hat{H} &= \sum_k \frac{\hat{P}_k^2}{2m_k} + \hat{H}^{BO}(\hat{R}), \\ \hat{H}^{BO}(R)|\phi_a^{BO}(R)\rangle &= E_a^{BO}(R)|\phi_a^{BO}(R)\rangle. \end{aligned} \tag{7}$$

Here, $\hat{P}_k$ and m_k are the nuclear momentum operators and nuclear masses. Note that in the second line of Eq. (7), the Born–Oppenheimer Hamiltonian is a purely electronic operator: $\hat{H}^{BO}(R) = \langle R|\hat{H}^{BO}(\hat{R})|R\rangle$. Its electronic eigenstates, called Born–Oppenheimer states, form a complete basis for every R.

Using the Born–Oppenheimer states $|\phi_a^{BO}(R)\rangle$ as electronic basis, the time-dependent Schrödinger equation for the wave function $\Psi_a(R)$ of the full system can be written as

$$i\hbar \frac{\partial}{\partial t}\Psi_a(R) = \sum_b \left[\sum_k \frac{1}{2m_k} \left(\mathbf{1}\frac{\hbar}{i}\nabla_k + \mathbf{A}_{(k)}(R) \right)^2 + \mathbf{E}^{BO}(R) \right]_{a,b} \Psi_b(R), \tag{8}$$

where boldface symbols represent matrices in the basis of Born–Oppenheimer states, with $\mathbf{E}^{BO}(R)$ being the diagonal matrix containing the Born–Oppenheimer energies, $\mathbf{1}$ the unit matrix and $\mathbf{A}_{(k)}(R)$ a new contribution called the derivative couplings,

$$A_{a,b,(k)}(R) = \langle \phi_a^{BO}(R)| \frac{\hbar}{i}\nabla_k |\phi_b^{BO}(R)\rangle. \tag{9}$$

We note that the derivative couplings are often defined without the factor $\hbar/i$. The Schrödinger equation (8) takes the form of a wave function evolving in a set of potential energy surfaces $E_a^{BO}(R)$, also called Born–Oppenheimer surfaces, which are coupled via a vector potential $\mathbf{A}_{(k)}(R)$.

The Born–Oppenheimer basis is also called the adiabatic basis. This is rooted in the adiabatic approximation, or sometimes called the Born–Oppenheimer approximation, which amounts to neglecting the derivative couplings in Eq. (8).[162,163] Within this approximation, the wave function evolves independently on all potential energy surfaces $E_a^{BO}(R)$, and the Born–Oppenheimer states $|\phi_a^{BO}(R)\rangle$ are treated like electronic eigenstates of the system. The methods studied in this work go beyond the adiabatic approximation to account for the influence of the derivative couplings on the wave function dynamics. Any effect induced by the derivative couplings is called a *non-adiabatic* effect, and they often couple different adiabatic (Born–Oppenheimer) states.

These non-adiabatic effects become especially important when two Born–Oppenheimer surfaces $E_a^{BO}(R)$ and $E_b^{BO}(R)$ come close in energy, as can be seen from a different representation of the derivative couplings,

$$A_{a,b,(k)}(R) = \frac{\langle \phi_a^{BO}(R)| \left(\frac{\hbar}{i}\nabla_k \hat{H}^{BO}(R) \right) |\phi_b^{BO}(R)\rangle}{E_a^{BO}(R) - E_b^{BO}(R)}, \quad a \neq b. \tag{10}$$

Instead of an adiabatic electronic basis, which diagonalizes the Born–Oppenheimer Hamiltonian, one could also choose an electronic basis in which the derivative couplings defined in Eq. (9) vanish. Such a basis is called a *diabatic* electronic basis.[164–166] The obvious choice is a phonon-independent basis, in the following denoted as $|\chi_a\rangle$, which will also be used later in one of our implementations of exact diagonalization and the density matrix renormalization group. Note that such a phonon-independent, "trivial diabatic" basis is, in general, the only strictly diabatic basis.[167] In this work, when we refer to diabatic basis states, we always consider them as phonon-independent or at least with a negligible R-dependence.

For later reference, the expansion of the state of the system in both the adiabatic Born–Oppenheimer and the diabatic phonon-independent basis is stated explicitly,

$$|\Psi\rangle = \int \mathrm{d}R \sum_a |R, \phi_a^{BO}(R)\rangle \Psi_a^{(a)}(R), \tag{11}$$

$$= \int \mathrm{d}R \sum_a |R, \chi_a\rangle \Psi_a^{(d)}(R). \tag{12}$$

Here, the superscripts (a) and (d) of the wave function refer to the adiabatic and diabatic basis, respectively, and the index a refers to the Born–Oppenheimer and diabatic electronic states in the two cases. We can understand the $\Psi_a(R)$ as a multi-component nuclear wave function.

Different diabatic states are coupled by the off-diagonal elements of the Born–Oppenheimer Hamiltonian, $V_{a,b} = \langle \chi_a|\hat{H}^{BO}|\chi_b\rangle$, which usually change smoother with respect to variations in the nuclear coordinates than the derivative couplings in an adiabatic basis,[165,166,168,169] thus, in some cases, leading to a more stable numerical integration (see also Sec. V E 2). Then again, the peaked structure of the derivative couplings in the adiabatic basis allows for the identification of strong non-adiabatic coupling regions in nuclear configuration space R and other regions where the adiabatic surfaces are mostly isolated. This insight can be used to motivate approximations and restrictions to certain adiabatic states, which is not as easily obtained from a diabatic basis.

B. Born–Huang approach for the Holstein dimer

The Born–Oppenheimer Hamiltonian of the Holstein dimer $\hat{\bar{H}}^{BO}_{\bar{q}}$ [see Eq. (4)] can be diagonalized analytically (see, e.g., Ref. 140) for which we will assume a system with exactly one electron. In the basis of the two site-local electronic states $|\chi_1\rangle$ and $|\chi_2\rangle$ (where $|\chi_i\rangle = c_i^\dagger|0\rangle$), it becomes

$$\hat{\bar{H}}^{BO}(\bar{q}) = \begin{pmatrix} \frac{\bar{q}^2}{2} - \bar{\gamma}\bar{q} & -\bar{t}_0 \\ -\bar{t}_0 & \frac{\bar{q}^2}{2} + \bar{\gamma}\bar{q} \end{pmatrix}, \tag{13}$$

which we solve for the Born–Oppenheimer eigenenergies

$$\bar{E}^{BO}_{\pm}(\bar{q}) = \frac{\bar{q}^2}{2} \pm \sqrt{\bar{q}^2\bar{\gamma}^2 + \bar{t}_0^2} \tag{14}$$

and the corresponding eigenstates

$$\begin{pmatrix} \phi^{BO}_{\pm,1}(\bar{q}) \\ \phi^{BO}_{\pm,2}(\bar{q}) \end{pmatrix} = \begin{pmatrix} \sqrt{1 + \left(\frac{\bar{q}\bar{\gamma}}{\bar{t}_0} \pm \sqrt{\left(\frac{\bar{q}\bar{\gamma}}{\bar{t}_0}\right)^2 + 1}\right)^2}^{-1} \\ \mp\sqrt{1 + \left(\frac{\bar{q}\bar{\gamma}}{\bar{t}_0} \mp \sqrt{\left(\frac{\bar{q}\bar{\gamma}}{\bar{t}_0}\right)^2 + 1}\right)^2}^{-1} \end{pmatrix}. \tag{15}$$

The Born–Oppenheimer surfaces $\bar{E}^{BO}(\bar{q})$ of the Holstein dimer are shown in Fig. 3 for $\frac{\bar{\gamma}^2}{\bar{t}_0} > 1$. For $\frac{\bar{\gamma}^2}{\bar{t}_0} < 1$, the lower surface has only a single minimum at $\bar{q} = 0$, a case studied, for example, in

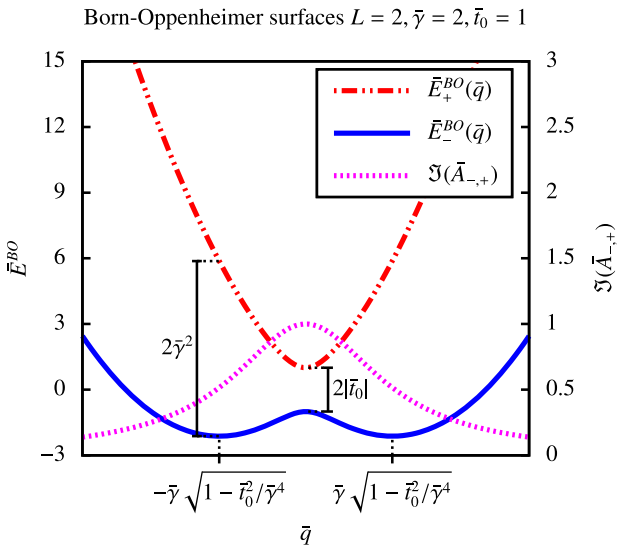

FIG. 3. Born–Oppenheimer surfaces of the Holstein dimer according to Eq. (14) and the imaginary part of the derivative couplings from Eq. (16) for the parameters $\bar{\gamma} = 2$ and $\bar{t}_0 = 1$. The splitting of the surfaces is $2\bar{t}_0$ at $\bar{q} = 0$, while at the minimum of the lower surface ($\bar{q} = \pm\sqrt{\bar{\gamma}^2 - \bar{t}_0^2/\bar{\gamma}^2}$), the difference in Born–Oppenheimer energies amounts to $2\bar{\gamma}^2$ (for $\frac{\bar{\gamma}^2}{\bar{t}_0} > 1$).

Refs. 170 and 171. This regime is not studied in this work but is of interest for future investigations.

In the case of a slowly moving nuclear wave function, we can expect the system to evolve along these potential energy surfaces as long as they are sufficiently separated, i.e., for q far away from zero. The non-adiabatic effects can be quantified by calculating the derivative couplings $\bar{A}$ via Eq. (9). The diagonal elements vanish, and we obtain for the off-diagonal elements[172,173]

$$\bar{A}_{+,-} = \bar{A}^*_{-,+} = -i\frac{\bar{\gamma}}{2\bar{t}_0}\frac{1}{1 + (\bar{q}\bar{\gamma}/\bar{t}_0)^2}. \tag{16}$$

They are also depicted in Fig. 3. We see that the coupling is peaked with a Lorentzian curve around $\bar{q} = 0$. The curve becomes more localized as $\bar{\gamma}/\bar{t}_0$ becomes large, i.e., a small hopping matrix element between the sites will lead to highly peaked derivative couplings around the avoided crossing point.[109] The easiest estimate for non-adiabatic transitions between the Born–Oppenheimer surfaces is the Landau–Zener formula,[174,175] which assumes a predefined classical nuclear path $q(t)$ that evolves with constant velocity $\dot{q}$ through the avoided crossing region. Starting on the lower Born–Oppenheimer surface at $q \approx -\infty$, the transition probability to the upper Born–Oppenheimer surface at $q \approx \infty$ is then dominated by the avoided crossing point and can be approximated as[175]

$$P^{LZ}_{-\to+} = \exp\left(\frac{-\pi|\bar{t}_0|^2}{\dot{\bar{q}}\bar{\gamma}}\right). \tag{17}$$

The Landau–Zener formula (17) illustrates that we can expect non-adiabatic effects to become relevant for a small hopping matrix element, i.e., for large derivative couplings at the crossing region $q \approx 0$.

C. Born–Huang approach for the Holstein trimer

Similar to the dimer, we can write the Born–Oppenheimer Hamiltonian of the Holstein trimer with one electron in the basis of the three local electronic states as

$$\hat{\bar{H}}^{BO}_{Trimer}(\bar{x}_s, \bar{x}_a) = \frac{\bar{x}_s^2}{2} + \frac{\bar{x}_a^2}{2}, + \begin{pmatrix} \bar{\gamma}\left(\bar{x}_a + \frac{1}{\sqrt{3}}\bar{x}_s\right) & -\bar{t}_0 & 0 \\ -\bar{t}_0 & -\bar{\gamma}\frac{2}{\sqrt{3}}\bar{x}_s & -\bar{t}_0 \\ 0 & -\bar{t}_0 & \bar{\gamma}\left(-\bar{x}_a + \frac{1}{\sqrt{3}}\bar{x}_s\right) \end{pmatrix}, \tag{18}$$

where we again discarded the center-of-mass phonon coordinate. $\bar{x}_s$ and $\bar{x}_a$ are the symmetric and anti-symmetric phonon mode defined in Eq. (5).

The Born–Oppenheimer surfaces in the nuclear space spanned by $\bar{x}_s$ and $\bar{x}_a$ can be calculated analytically or by numerical diagonalization of the Born–Oppenheimer Hamiltonian. We show contours of the Born–Oppenheimer surfaces calculated from diagonalization for $\bar{\gamma} = \bar{t}_0 = 2.5$ in Fig. 4. The energy-separation of the different Born–Oppenheimer surfaces can be seen the best in a surface-plot, which is illustrated in Fig. 5. Since the surfaces are symmetric with respect to $\bar{x}_a$, we include only positive values for the anti-symmetric phonon mode in Fig. 5.

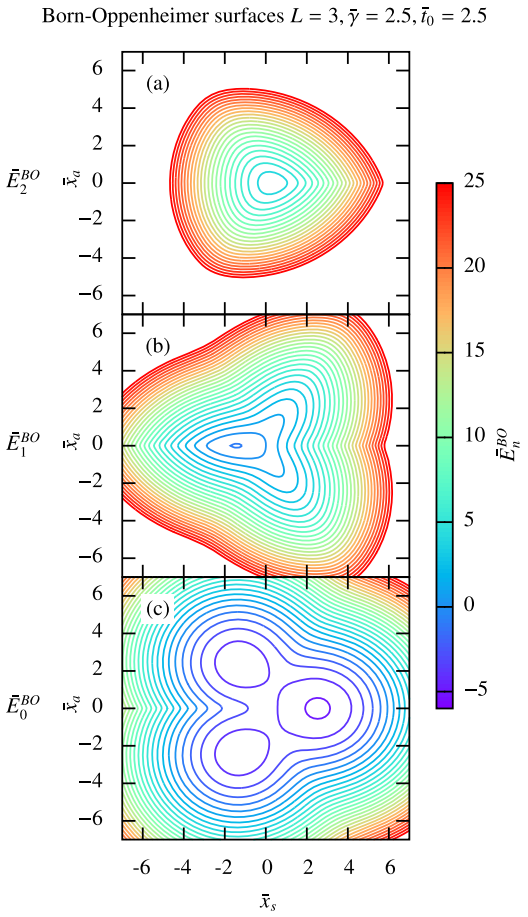

FIG. 4. Contours of the Born–Oppenheimer surfaces of the Holstein trimer, obtained from the diagonalization of the Hamiltonian (18) for $\bar{\gamma} = \bar{t}_0 = 2.5$ in the nuclear coordinate space of the symmetric $\bar{x}_s$ and anti-symmetric $\bar{x}_a$ phonon mode. We draw the contours for every $\Delta\bar{E}_i^{BO} = 1$ for the (a) highest, (b) middle, and (c) lowest Born–Oppenheimer surface.

The lowest Born–Oppenheimer surface [Fig. 4(c)] has three local minima, corresponding to the three different Holstein sites. The lowest (global) minimum is at positive $\bar{x}_s$ and at $\bar{x}_a = 0$, i.e., here mainly the central site has a large phonon distortion. The other two minima correspond to large phonon distortions on the left and right edge sites of the Holstein trimer, respectively. The higher Born–Oppenheimer surfaces [Figs. 4(a) and 4(b)] each have only one minimum, which for the highest surface, similar to the dimer case, is located at the symmetric point $\bar{x}_s = \bar{x}_a = 0$.

Using the language of chemical bonds, we can associate the three Born–Oppenheimer states with a bonding, non-bonding, and antibonding state. Note that technically, the middle Born–Oppenheimer state is only truly non-bonding, with zero electronic population on the central site, for $\bar{x}_a = 0$ (the red lines in Fig. 5). At the three minima of the lowest Born–Oppenheimer surface, the bonding state corresponds to the electron mostly localized to the site with a large nuclear coordinate $\bar{x}_i$, which one might consider as a small polaron state.

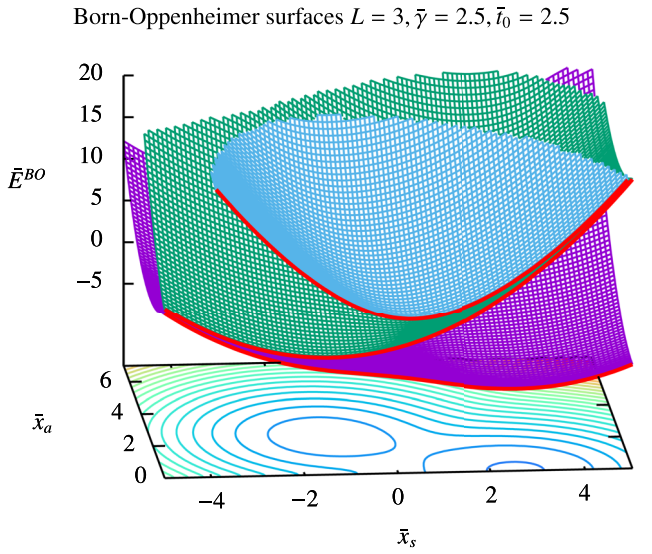

FIG. 5. Born–Oppenheimer surfaces of the Holstein trimer, obtained from diagonalization of the Hamiltonian (18) for $\bar{\gamma} = \bar{t}_0 = 2.5$ in the nuclear coordinate space of the symmetric $\bar{x}_s$ and anti-symmetric $\bar{x}_a$ phonon mode. Since the surfaces are invariant under the operation $\bar{x}_a \to -\bar{x}_a$, we show only non-negative values for the anti-symmetric mode. The lowest surface is drawn in magenta, the middle in green, and the highest in blue. The Born–Oppenheimer energies along the symmetric phonon slice $\bar{x}_a = 0$ are included as red lines. In the x–y plane, a contour plot of the lowest (magenta) surface is included, corresponding to Fig. 4(c).

In this work, we investigate symmetric initial states, with a phonon distribution around $\bar{x}_a = 0$. The corresponding slice of the Born–Oppenheimer surfaces is included as red lines in Fig. 5. Here, the lowest (bonding) Born–Oppenheimer electronic wave function has the same sign on all three trimer sites, the middle (non-bonding) Born–Oppenheimer state has contributions only on the edge sites and changes sign between them, and the upper (antibonding) Born–Oppenheimer state changes its sign twice between the sites. The energy of the non-bonding state is near degenerate with the antibonding state for large positive $\bar{x}_s$, where the antibonding state has an only little contribution on the central site. At the same time, for large negative values of the symmetric phonon mode, the non-bonding state becomes near degenerate with the bonding state. These near degeneracies are lifted if the anti-symmetric phonon mode is shifted away from zero.

The qualitative picture of these asymptotically approaching surfaces stays the same for any parameter choice with $\bar{t}_0$ and $\bar{\gamma}$ positive. In contrast to the Holstein dimer, we thus cannot achieve a complete separation of the Born–Oppenheimer surfaces by tuning the parameters of the system.

IV. EXACT DIAGONALIZATION AND DENSITY MATRIX RENORMALIZATION GROUP METHODS

A. Exact diagonalization in second quantization

In order to obtain exact results, we diagonalize the Hamiltonian in its second quantized form Eq. (1). This is briefly reviewed here since the notation also appears in the description of the DMRG

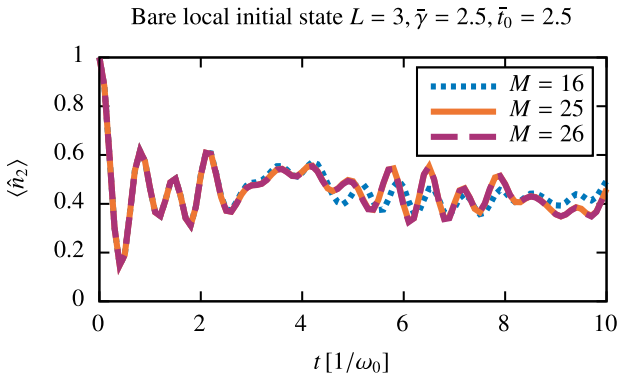

FIG. 6. Convergence of exact diagonalization in second quantization with respect to the used local phonon cutoff M. We show the electron occupation on the central site for the Holstein trimer with $\bar{\gamma} = \bar{t}_0 = 2.5$, starting from the bare local initial state.

algorithm. A thorough review on exact diagonalization and how it can be improved for larger systems can be found in Ref. 176. To diagonalize Eq. (1), we first set up a basis for the Hilbert space. For the dimer, each state in the real-space occupation number basis takes the form $|\alpha\rangle = |n_1^e, n_1^{ph}, n_2^e, n_2^{ph}\rangle$. We further truncate the local phonon number to M so that $n_i^{ph} \in \{0, 1, \ldots, M\}$. With $n_i^e \in \{0, 1\}$ and the constraint $n_1^e + n_2^e = 1$, we have a total Hilbert-space dimension $D_H = L(M+1)^L$, where $L = 2$ for the dimer. The complete sparse Hamiltonian can now be easily generated by iterating through the basis and determining which elements are nonzero $\langle\alpha|\hat{H}|\beta\rangle \neq 0$. The Hamiltonian can then be diagonalized, and the time evolution of an initial state carried out exactly. In this work, exact diagonalization in second quantization is used for $L = 2$ and $L = 3$.

Since we are working in the real-space phonon occupation-number basis, it is important to include enough phonons M to capture the correct physics for a given set of parameters. In Fig. 6, we illustrate this for the Holstein trimer. One sees that the observable deviates from its correct value if M is chosen too small, as is the case for $M = 16$. Once the data have been converged with respect to M, the expectation value should no longer change upon increasing M further.

B. Grid-based calculation of eigenstates in the Born–Oppenheimer basis

Another approach is to solve the eigenproblem of the Holstein dimer directly in the Born–Oppenheimer (adiabatic) electronic basis via the Schrödinger equation (8). This will lead to the same eigenenergies as in the exact diagonalization in the second quantization method but gives easier access to adiabatic observables, for example, the occupation of the different Born–Oppenheimer electronic states. Since the Holstein dimer has only one relevant nuclear coordinate, we can solve the Schrödinger equation (8) directly on a grid and calculate the lowest m eigenstates $|\Psi^n\rangle, n = 1, \ldots, m$ of the system. For sufficiently large m, we can then represent any initial state in these eigenstates and time evolve the state to arbitrary long times.

Using the Born–Oppenheimer energies and derivative couplings of Eqs. (14) and (16), we can write the time-independent version of the Schrödinger equation in the adiabatic electronic basis (8) as

$$\tilde{E}^n \Psi_\pm^n(\tilde{q}, \tilde{t}) = \left[-\frac{1}{2}\nabla_{\tilde{q}}^2 + \frac{\tilde{a}(\tilde{q})^2}{2} + \tilde{E}_\pm^{BO}(\tilde{q})\right]\Psi_\pm^n(\tilde{q}, \tilde{t}) \mp \left[\frac{1}{2}\frac{\partial a(\tilde{q})}{\partial \tilde{q}} + \tilde{a}(\tilde{q})\nabla_{\tilde{q}}\right]\Psi_\mp^n(\tilde{q}, \tilde{t}), \tag{19}$$

where $\tilde{a}(\tilde{q})$ is the imaginary part of $\tilde{A}_{-,+}$.

There are many ways to solve the differential equations (19). Here, we use an iterative procedure to obtain the lowest m eigenstates in a Car–Parrinello inspired scheme.[177]

In this process, the two-component wave functions $\Psi_\pm^n(\tilde{q})$ time evolve with a fictitious kinetic energy on the instantaneous energy surfaces $\langle\phi_\pm^{BO}(\tilde{q}), \tilde{q}|\hat{\tilde{H}}|\Psi^n\rangle$, discretized on a grid. For higher energy states, the wave functions and forces acting on them are orthogonalized to lower states, to ensure relaxation to eigenstates. A friction term dampens the fictitious kinetic energy until the potential energy is minimized under the orthogonalization constraints. We use a Verlet-algorithm for the propagation in this relaxation process.[178] We finally end up with the lowest m eigenstates, which can be used to represent the initial state and its time evolution at any later time. One needs to ensure that enough eigenstates m are used to accurately represent the desired initial state, which is the case if the norm of the projected state is close to 1.

C. Density matrix renormalization group methods

1. Brief review

Exactly diagonalizing Eq. (1) works well in many parameter regimes for the Holstein dimer and gives direct access to eigenstates and energies. However, due to the exponential scaling of the Hilbert-space dimension with the system size $[\sim (M+1)^L]$, the method quickly reaches its limits when larger systems and a large local phonon truncation M are needed. Taking all symmetries of the model into consideration[176] only gives access to slightly larger systems. One type of method, which has proven extremely powerful when dealing with one-dimensional systems, is density matrix renormalization group (DMRG) algorithms. In this work, we describe the key ideas of DMRG, but there exist many comprehensive reviews, e.g., Refs. 90, 91, and 179 specifically for time evolution.

DMRG, though originally developed for the ground-state search,[89] has proven to be useful for a wide range of other applications, such as time evolution[180–184] and finite-temperature[185–190] calculations. Even though DMRG is primarily used in one dimension, there exist generalizations to two-dimensional systems (see, e.g., Refs. 191–195).

The key insight in DMRG is that in many situations, the knowledge of the whole Hilbert space is not needed to capture the relevant physics. Rather, one only needs to focus on states in a small part of it which can be clearly identified based on the reduced-density matrices of the sub-system obtained by tracing out the remaining physical degrees of freedom. In the eigenbasis of the reduced-density matrix of a system partitioned into subsystems A and B, the state $|\psi\rangle$ can be truncated to $|\psi\rangle_{\text{trunc}}$ in a controlled way with a minimal distance $\||\psi\rangle - |\psi\rangle_{\text{trunc}}\|_2$. The reason why this approximation works is rooted in the sufficiently fast decay of reduced density-matrix eigenvalues

in typical ground states of one-dimensional systems. This, in turn, is related to the spatial entanglement encoded in many-body ground states, which under certain conditions obey an area law instead of a volume law, where the latter is typical in generic excited states.[91,196]

Such a bi-partitioned state on a one-dimensional lattice can be written as

$$|\psi\rangle = \sum_{\vec{\sigma}_i,\vec{\sigma}_j} \psi^{\vec{\sigma}_i\vec{\sigma}_j} |\vec{\sigma}_i\rangle_A |\vec{\sigma}_j\rangle_B, \tag{20}$$

where $|\vec{\sigma}_i\rangle_A = |\sigma_1, \sigma_2, \ldots, \sigma_w\rangle_A$, $|\vec{\sigma}_j\rangle_B = |\sigma_{w+1}, \sigma_{w+2}, \ldots, \sigma_L\rangle_B$, and σ_l corresponds to the physical state at site l. Now, one can perform a singular-value decomposition of $\psi^{\vec{\sigma}_i\vec{\sigma}_j} = \sum_{\alpha,\beta} U_\alpha^{\vec{\sigma}_i} s_{\alpha\beta} V_\beta^{\dagger\vec{\sigma}_j}$. $s_{\alpha\beta}$ are the r non-zero singular values. By rotating the states using $|\alpha\rangle_A = \sum_{\vec{\sigma}_i} U_\alpha^{\vec{\sigma}_i} |\vec{\sigma}_i\rangle_A$ and $|\beta\rangle_B = \sum_{\vec{\sigma}_j} V_\beta^{\dagger\vec{\sigma}_j} |\vec{\sigma}_j\rangle_B$ and using the fact that $s_{\alpha\beta}$ (s_α for brevity) is a diagonal matrix, one gets

$$|\psi\rangle = \sum_{\alpha=1}^{r} s_\alpha |\alpha\rangle_A |\alpha\rangle_B. \tag{21}$$

After ordering the singular values $s_\alpha > 0$ according to their magnitude such that $s_1 \geq s_2 \geq s_3 \ldots$, $|\psi\rangle$ can now be truncated by neglecting states, depending on their singular value s_α. For example, if there are r singular values and one wants to truncate at the dimension $m+1$, one cuts off all states belonging to s_α with $m < \alpha \leq r$. The state can now be written as

$$|\psi\rangle_{\text{trunc}} = \sum_{\alpha=1}^{m} s_\alpha |\alpha\rangle_A |\alpha\rangle_B. \tag{22}$$

The s_α^2 are also the eigenvalues of the reduced density matrix of either subsystem and $\| |\psi\rangle - |\psi\rangle_{\text{trunc}} \|_2^2 = \sum_{\gamma=m+1}^{r} s_\gamma^2$. We refer to this truncation as the standard DMRG truncation, affecting the so-called bond dimension, as opposed to the truncation of the local Hilbert space discussed next.

With this in mind, a state $|\psi\rangle$ can be represented as a matrix–product state (MPS) by iterating through the system and performing a series of singular-value decompositions. It can then be written in its final form as a so-called mixed canonical MPS,

$$|\psi\rangle = \sum_{\vec{\sigma},\alpha_1,\ldots,\alpha_{L-1}} A^{\sigma_1}_{\alpha_0\alpha_1} \ldots A^{\sigma_{i-1}}_{\alpha_{i-2}\alpha_{i-1}} M^{\sigma_i\sigma_{i+1}}_{\alpha_{i-1}\alpha_{i+1}} B^{\sigma_{i+2}}_{\alpha_{i+1}\alpha_{i+2}} \ldots B^{\sigma_L}_{\alpha_{L-1}\alpha_L} |\vec{\sigma}\rangle, \tag{23}$$

where $A^{\sigma_j}, B^{\sigma_l}, M^{\sigma_i\sigma_{i+1}}$ are matrices with bond indices α_j and $\alpha_0 = \alpha_L = 1$, $|\vec{\sigma}\rangle = |\sigma_1, \sigma_2, \ldots, \sigma_L\rangle$ are the state vectors, and the σ_i are the local degrees of freedom. For the Holstein model, we have $|\vec{\sigma}\rangle = |n_1^{\text{e}} n_1^{\text{ph}}, n_2^{\text{e}} n_2^{\text{ph}}, \ldots, n_L^{\text{e}} n_L^{\text{ph}}\rangle$. The A (B) matrices are left (right) normalized, meaning that $\sum_{\sigma_i} A^{\dagger\sigma^i} A^{\sigma^i} = \mathbb{I}$ ($\sum_{\sigma_i} B^{\sigma^i} B^{\dagger\sigma^i} = \mathbb{I}$), where $\mathbb{I}$ is the identity matrix. This representation is exact if no truncation has taken place but is also valid for a truncated state. Truncation of the MPS can be done variationally or through a series of singular-value decompositions.[91] In practice, it is unfeasible to obtain the MPS from a general state, and therefore, one often starts from one that can easily be written down in MPS form or is obtained efficiently by a ground-state search. This representation now serves as the starting point for the time-evolution algorithm with local basis optimization.

2. Time evolution with local basis optimization

To time evolve the matrix–product state $|\psi\rangle$ with a Hamiltonian that only acts on neighboring sites, we first write it as a sum of local energy terms $\hat{H} = \sum_i \hat{h}_i$ with $\hat{h}_i$ connecting two neighboring sites. We then carry out a Trotter–Suzuki decomposition to second order so that our time-evolution operator becomes

$$e^{-i\Delta t\hat{H}/\hbar} = e^{-i\Delta t\hat{H}_{\text{even}}/(2\hbar)} e^{-i\Delta t\hat{H}_{\text{odd}}/\hbar} e^{-i\Delta t\hat{H}_{\text{even}}/(2\hbar)} + O(\Delta t^3), \tag{24}$$

where $\hat{H}_{\text{even (odd)}} = \sum_{l:even(odd)} \hat{h}_l$, and Δt is the time step. Since the even (odd) $\hat{h}_l$ commute, we can write each exponential as a product of Trotter gates, e.g., $e^{-i\Delta t\hat{H}_{\text{even}}/(2\hbar)} = \prod_{l:even} e^{-i\Delta t\hat{h}_l/(2\hbar)}$. To apply the time-evolution gate acting on sites i and $i+1$, we first bring the matrix–product state into the mixed canonical form of Eq. (23) for those sites. We then apply the corresponding time-evolution operator directly

$$\Phi^{\sigma_i'\sigma_{i+1}'}_{\alpha_{i-1}\alpha_{i+1}} = \sum_{\sigma_i,\sigma_{i+1}} U^{\sigma_i'\sigma_{i+1}'\sigma_i\sigma_{i+1}} M^{\sigma_i\sigma_{i+1}}_{\alpha_{i-1}\alpha_{i+1}}, \tag{25}$$

where $U^{\sigma_i'\sigma_{i+1}'\sigma_i\sigma_{i+1}}$ is a Trotter gate. By carrying out a singular-value decomposition of $\Phi^{\sigma_i'\sigma_{i+1}'}_{\alpha_{i-1}\alpha_{i+1}}$, the updated tensors are obtained and one can continue with the following sites.

Since the time evolution, and many other DMRG based algorithms, often scale polynomially with the local Hilbert-space dimension, they can become expensive when these are too large. This is also the case in the Holstein model where the local dimension is $2(M+1)$. Therefore, a number of methods have been introduced for a more efficient treatment of such large local dimensions.[93–96] In this work, we use local basis optimization,[96] which has already been combined with different numerical methods, including matrix–product states, e.g., in Refs. 86, 88, 98–102, and 156. The idea of the local basis optimization can be intuitively understood by looking at the Holstein model in the strong-coupling limit. For a site with a localized electron, the phonon distribution is that of a coherent state. Thus, the site can be described by two states, either the zero phonon or a coherent phonon state. This encourages the search for a basis where the state can be represented with a negligible error but with significantly fewer modes in generic parameter regimes. This basis can be found by diagonalizing the local, single-site reduced-density matrix $\rho = U^\dagger W U$, where $\rho^{\sigma_i\sigma_i'} = \sum_{\sigma_{i+1},\alpha_{i-1},\alpha_{i+1}} \Phi^{\sigma_i\sigma_{i+1}}_{\alpha_{i-1}\alpha_{i+1}} \Phi^{\dagger\sigma_{i+1}\sigma_i'}_{\alpha_{i-1}\alpha_{i+1}}$. Here, W is a diagonal matrix with elements w_α. The truncation can be done based on the w_α's, which are the eigenvalues of ρ. The transformation matrices U transform the site from the physical state $|\sigma_i\rangle$ to the optimal basis state $|\tilde{\sigma}_i\rangle = \sum_{\sigma_i} U^{\tilde{\sigma}_i\sigma_i} |\sigma_i\rangle$. When combining the local basis optimization with DMRG, which we refer to as DMRG-LBO, the transformation matrices can be applied to $\Phi^{\sigma_i'\sigma_{i+1}'}_{\alpha_{i-1}\alpha_{i+1}}$ from Eq. (25) before the subsequent singular-value decomposition. This singular-value decomposition

is done before moving to the next set of sites and applying the next Trotter gate. Due to the extra cost of the transformations, the procedure is only beneficial if the local basis can be truncated such that the dimension of the optimal basis is significantly smaller than the one of the physical basis (see Ref. 86 for technical details).

When diagonalizing the reduced density matrix to obtain the optimal basis, the smallest eigenvalues w_α are discarded such that the truncation error is below a threshold ϵ_{LBO} so that

$$\sum_{\text{discarded }\alpha} w_\alpha \Big/ \left(\sum_{\text{all }\beta} w_\beta\right) < \epsilon_{\text{LBO}}. \tag{26}$$

For the standard DMRG truncation done in the time-evolution scheme, we discard all singular values with a threshold ϵ_{bond} such that

$$\sum_{\text{discarded }\alpha} s_\alpha^2 \Big/ \left(\sum_{\text{all }\beta} s_\beta^2\right) < \epsilon_{\text{bond}}. \tag{27}$$

Note that the MPS representation of the state in Eq. (23) can indeed be exact for a fixed phonon cutoff M. This would, however, require exponentially large matrices and is unfeasible. By introducing a finite truncation, the representation is no longer exact but is an approximation of the state. Since this error can be made arbitrarily small, in principle, and often also in practical applications, we refer to DMRG as an exact method and convergence of the calculations must always be controlled with respect to ϵ_{bond} and ϵ_{LBO}. How to do this is demonstrated for one example in Fig. 7(a) for ϵ_{bond} and Fig. 7(b) for ϵ_{LBO}. Figure 7(a) shows the electron density for a fixed ϵ_{LBO} with different values for ϵ_{bond}. For ϵ_{bond} chosen too large (here, when $\epsilon_{\text{bond}} = 10^{-6}$), too many states are truncated away and the time-dependent expectation value of the observable is inaccurately captured by the MPS. However, if ϵ_{bond} is set to be sufficiently small, the data become independent of the truncation and the approximated state can be used to correctly calculate the expectation values. A similar check must be done for ϵ_{LBO}. This is illustrated in Fig. 7(b) with a fixed ϵ_{bond}. Now, a poorly chosen ϵ_{LBO} leads to an erroneous representation of the local state and the expectation value of the observable deviates from its correct form. As is the case for ϵ_{bond}, below a sufficiently small ϵ_{LBO}, the expectation values become independent thereof and the data are converged up to a certain accuracy. This convergence must be checked for each observable individually. We find that, in particular, the reduced mean-squared displacement (RMSD) and the total phonon number need smaller cutoffs to reach convergence.

Note that a convergence check with respect to the local phonon truncation M is also needed. This must be carried out by varying M as illustrated for exact diagonalization (see Fig. 6) in Sec. IV A. The DMRG-LBO calculations in this work are done using the ITensor Software Library.[197]

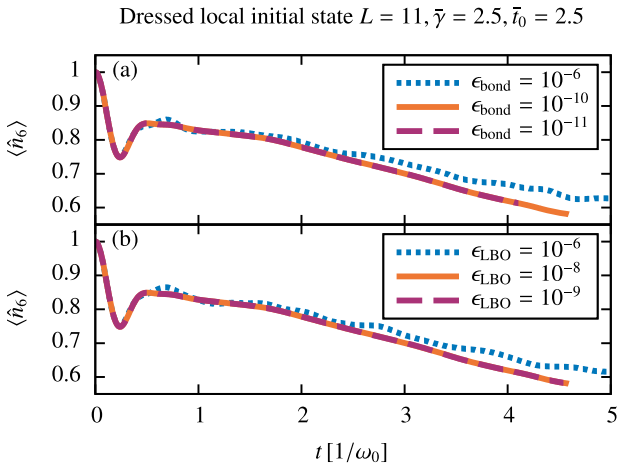

FIG. 7. Convergence of the DMRG data with ϵ_{bond} and ϵ_{LBO}. We show the electron occupation on the central site in the Holstein chain with $L = 11$, $\bar{\gamma} = \bar{t}_0 = 2.5$, starting from the dressed local initial state. (a) Fixed $\epsilon_{\text{LBO}} = 10^{-8}$ and different ϵ_{bond}. (b) Fixed $\epsilon_{\text{bond}} = 10^{-10}$ and different ϵ_{LBO}. We further use $M = 40$ and $\Delta t = 0.004/\omega_0$.

V. INDEPENDENT TRAJECTORY METHODS

In this section, we first briefly review the phase-space approach to quantum mechanics and the ansatz to describe the nuclear dynamics by a swarm of independent trajectories. We then describe the two independent-trajectory methods used in this work: multitrajectory Ehrenfest (MTE)[59,198,199] and fewest-switches surface hopping (FSSH).[58] For the latter, we also review some possible improvements to the algorithm, both for its general description and specific ones for its application to large systems. We conclude this section with a short discussion of our implementation of both methods and their internal convergence.

A. Phase space representation of quantum mechanics

The independent-trajectory methods combine a (classical) phase-space description of the nuclear degrees of freedom with a quantum mechanical wave-function (WF) formalism of the electronic subsystem. The partial phase-space description by itself is not an approximation and can be understood in the framework of the partial Wigner transform.[200–202] The Wigner transform (sometimes called the Weyl transform) maps an operator $\hat{O}$ to a function of phase-space $O_W(R,P)$.[203–207] For a composite electron–nuclear system, one can define the partial Wigner transform acting on the nuclear degrees of freedom by[202,208,209]

$$O_{a,b;W}(R,P) = \int \mathrm{d}Z \Big[e^{iP\cdot Z/\hbar} \times \left\langle R - \frac{Z}{2}, \phi_a\left(R - \frac{Z}{2}\right) \middle| \hat{O} \middle| R + \frac{Z}{2}, \phi_b\left(R + \frac{Z}{2}\right) \right\rangle \Big], \tag{28}$$

where the selected electronic basis $|\phi_a(R)\rangle$ can refer to both diabatic or adiabatic states and the integral is taken over the whole nuclear position space Z. Of special importance is the partial Wigner transform of the density matrix of the full system $\hat{\rho} = |\Psi\rangle\langle\Psi|$, which allows

us to calculate expectation values of any operator via a phase-space average

$$\langle \hat{O} \rangle = \sum_{a,b} \int \mathrm{d}R \int \mathrm{d}P \; O_{a,b:W}(R,P) \frac{\rho_{b,a:W}(R,P)}{(2\pi\hbar)^n}. \tag{29}$$

The term $W_{b,a}(R,P) := \frac{\rho_{b,a:W}(R,P)}{(2\pi\hbar)^n}$ looks like a probability distribution in phase space but can contain negative values. When we speak of the partially Wigner-transformed density matrix, we always refer to this object $W_{b,a}(R,P)$. For a pure state expanded in the same basis as used in Eq. (28), it can be written as

$$W_{a,b}(R,P) = \int \mathrm{d}Z \frac{e^{iP\cdot Z/\hbar}}{(2\pi\hbar)^n} \Psi_a\left(R - \frac{Z}{2}\right) \Psi_b^*\left(R + \frac{Z}{2}\right). \tag{30}$$

This form of the partial Wigner transform is basis dependent and allows us to describe both phonon-independent (diabatic) and adiabatic states easily, since only the wave function in the respective basis $\Psi_a^{(d)}$ or $\Psi_a^{(a)}$ [see Eqs. (11) and (12)] is needed. However, one also needs to represent the observable in the same basis [see Eq. (28)], which can be non-trivial in an adiabatic basis.

An alternative definition of the partial Wigner transform exists,[200,201,210] in which the electronic states in Eq. (28) do not depend on Z and are evaluated at position R. For a phonon-independent electronic basis, both definitions are equivalent, while the R-dependence of adiabatic states is treated differently. One can think of this alternative, the so-called "Wigner-then-adiabatic"[211] definition, as if one first performs the partial Wigner transform in a phonon-independent basis, and afterward represents it in another, e.g., adiabatic, basis. It is frequently used when relating the quantum–classical Liouville approach,[200] which is an approximate solution to the time evolution of the Wigner function, to trajectory-based descriptions of the phase-space evolution, such as MTE and FSSH.[201,210]

Adiabatic initial states can be much easier represented in the variant of Eq. (30), and this definition will be used later when sampling the independent-trajectory methods (see Secs. V B and V F).

B. Independent-trajectory methods

Independent-trajectory methods approximate the partially Wigner-transformed density matrix (30) by an ensemble average over a number N_{traj} of classical nuclear trajectories (indexed by r) described in nuclear phase space by $R^r(t), P^r(t)$, each with an attached electronic density matrix $\hat{\rho}_{el}^r$, and potentially a weight-factor w^r,

$$\hat{W}(R,P,t) \approx \frac{1}{N_{traj}} \sum_r^{N_{traj}} w^r \delta(R - R^r(t)) \delta(P - P^r(t)) \cdot \hat{\rho}_{el}^r(t). \tag{31}$$

Expectation values of observables can then be calculated via Eq. (29). The two most common approaches to obtain initial conditions in the trajectory-simulations are to sample them either from the partial Wigner transform of a given density matrix or from a classical molecular dynamics simulation, where often the former approach is preferred.[212–216] The implementation of the Wigner sampling used in this work is described in more detail in Sec. V F.

The nuclear trajectory r is propagated via classical Newtonian equations of motion under some method-specific classical Hamiltonian $H^{nuc,r}$, which is independently obtained for each trajectory,

$$\frac{\partial R_k^r}{\partial t} = \frac{\partial H^{nuc,r}}{\partial P_k^r}, \quad \frac{\partial P_k^r}{\partial t} = -\frac{\partial H^{nuc,r}}{\partial R_k^r}. \tag{32}$$

Here, R_k^r and P_k^r are the kth-component of the nuclear position and momentum of the trajectory r. Without the attached electronic density matrix and when using a Wigner sampling of the initial nuclear quantum state, this approach is equivalent to the truncated Wigner approximation in a phase-space representation.[217] The electronic density matrix is time evolved under the influence of the classical nuclear positions $R^r(t)$ and momenta $P^r(t)$, and the explicit form is given in Secs. V C and V D.

As the name implies, different trajectories with their attached electronic density matrices are not allowed to interact during the time evolution. This approximation is at the core of these methods and allows easy, distributed parallel calculations. In this paper, we will use two well-established independent-trajectory methods with different underlying approximations and equations of motion: multitrajectory Ehrenfest[59,198,199] and fewest-switches surface hopping.[58] More details on the initial sampling used in this work, and convergence analysis of both methods is given at the end of this section (see Sec. V F).

C. Multitrajectory Ehrenfest dynamics

In the first method, the multitrajectory Ehrenfest (MTE) approach, the coupling of each nuclear trajectory with its attached electronic density matrix, is described on a mean-field level, called Ehrenfest dynamics,[59,198,199] or sometimes mixed quantum/classical time-dependent self-consistent-field.[218,219] Here, the nuclear trajectory is propagated via the Newtonian equations of motion (32) according to the mean-field nuclear Hamiltonian

$$H^{nuc,r} = T^{nuc}(P^r) + \mathrm{Tr}\left[\hat{H}^{BO}(R^r)\hat{\rho}_{el}^r\right]_e, \tag{33}$$

where $\mathrm{Tr}[\cdot]_e$ is a trace in the electronic subsystem only and $T^{nuc}(P)$ denotes the classical nuclear kinetic energy. The electronic density matrix is then propagated by the time-dependent electronic Hamiltonian $\hat{H}^{BO}(R^r(t))$,

$$\frac{d}{dt}\hat{\rho}_{el}^r(t) = -\frac{i}{\hbar}\left[\hat{H}^{BO}(R^r(t)), \hat{\rho}_{el}^r(t)\right]. \tag{34}$$

Ehrenfest dynamics is independent of the choice of the electronic basis, as can be seen from Eqs. (33) and (34), where we did not specify any basis. Ehrenfest dynamics can be derived from the exact quantum dynamics by first applying a mean-field approximation, the time-dependent self-consistent field method, and afterward a classical approximation for the nuclear coordinates (see also Refs. 59 and 220 and references therein). Alternatively, one can start from the (approximate) quantum–classical Liouville equation and neglect electron–phonon correlations in the total density matrix.[201,221] The time evolution is completely deterministic and the multitrajectory approach only serves as an accurate sampling of the initial state.

It is easier to see the limitations of the mean-field approximation and the ability of Ehrenfest dynamics to describe non-adiabatic effects if we write the electronic time-evolution in the (adiabatic) Born–Oppenheimer basis $|\phi_a^{BO}(R(t))\rangle$, which in the independent-trajectory approach is now explicitly time dependent. For a pure state described by $|\Psi_{el}^r(t)\rangle = \sum_a \Psi_{el,a}^{r,(a)}(t)|\phi_a^{BO}(R^r(t))\rangle$, the Schrödinger equation for the electronic wave function becomes

$$i\hbar\partial_t \Psi_{el,a}^{r,(a)}(t) = \sum_b \left(\delta_{a,b} E_b^{BO}(R^r(t)) + \sum_k \dot{R}_k^r(t) A_{a,b,(k)}(R^r(t))\right)\Psi_{el,b}^{r,(a)}(t), \tag{35}$$

where $\dot{R}_k$ is the time-derivative of the kth component of the nuclear coordinate and $A_{a,b,(k)}$ are the derivative couplings defined in Eq. (9).[58]

Similar to the Schrödinger equation in the Born–Huang approach [Eq. (8)], the derivative couplings are responsible for non-adiabatic transitions between different Born–Oppenheimer surfaces. However, these transitions are now described by a purely electronic Schrödinger equation (35), where the nuclear momenta enter only via the velocity term $\dot{R}_k$ in front of the derivative couplings. Hence, non-adiabatic transitions between Born–Oppenheimer surfaces are possible in Ehrenfest dynamics and are again peaked where the derivative couplings become large.

One problem of the mean-field description in Ehrenfest dynamics becomes apparent when considering an electron–nuclear wave packet initially localized to a certain Born–Oppenheimer state, which then passes through a region with strong non-adiabatic coupling. Beyond that region, the wave packet will have contributions on more than one surface, and, as shown in the exact Schrödinger equation (8), these contributions should evolve independently from each other when the derivative couplings become negligible again. This is not reproduced in Ehrenfest dynamics, where each nuclear trajectory will evolve in one effective potential built from the electronic contributions in all occupied surfaces, leading to possibly unphysical paths when the force-contributions of the involved surfaces differ strongly.[58,222,223] For more information on the implementation of MTE in this work and convergence analysis, see Sec. V F.

D. Fewest-switches surface hopping

Surface-hopping methods[224,225] try to circumvent the mean-field averaging problem by calculating the forces acting on the nuclei from a single energy surface $E_{\lambda^r}(R^r)$ in each time step, with the possibility of stochastic hops between surfaces. While it is not a mean-field method, it still uses an independent-trajectory approach, which, combined with the classical path assumption for the nuclei, leads to the same electronic time-evolution [Eqs. (34) and (35)] as MTE.[58,59]

Surface-hopping methods interpret the resulting electronic populations $|\Psi_{el,a}^r(t)|^2$ as the probability of the trajectory r to be on the electronic surface $E_a^r(R) = \langle\phi_a|\hat{H}^{BO}(R^r)|\phi_a\rangle$. Since the forces on the nuclei are calculated from a single diagonal entry of the electronic density matrix, they are strongly basis dependent. The typical choice is the Born–Oppenheimer basis (see, for example, the discussion in Ref. 59), which leads to the nuclear Hamiltonian

$$H^{nuc,r} = T^{nuc}(P^r) + E_{\lambda^r}^{BO}(R^r), \tag{36}$$

where T^{nuc} is the kinetic energy term of the classical nuclear Hamiltonian and λ^r is the currently active Born–Oppenheimer surface of trajectory r. The hopping algorithm is designed such that the distribution of trajectories on the surfaces approximately reproduces the electronic populations given by $|\Psi_{el,a}^r(t)|^2$. The most common form for the hopping algorithm is the fewest-switches surface hopping (FSSH),[58] which is also used in this work.

The time derivative of the electronic populations $|\Psi_{el,a}^r|^2 = \rho_{a,a}^r$ in the Born–Oppenheimer basis can be expressed by using Eq. (35) as $\dot{\rho}_{a,a}^r = \sum_{b\neq a} b_{a,b}^r$ with $b_{a,b}^r = -2\Re\left[\frac{i}{\hbar}(\Psi_{el,a}^r)^* \Psi_{el,b}^r \sum_k \dot{R}_k^r \cdot A_{a,b,(k)}(R^r)\right]$, where $\Re$ refers to the real part. From this expression, FSSH estimates the change of electronic population from surface a to surface b within a time step Δt as $-b_{a,b}^r \Delta t$. The FSSH algorithm, as the name fewest-switches implies, tries to use the minimum number of hops between surfaces to satisfy this relation. For that reason, a hop from an active surface λ to another surface λ' within a time step Δt is allowed with a probability equal to $p_{\lambda\to\lambda'}^r = \max\left\{\frac{-\Delta t b_{\lambda,\lambda'}^r}{\rho_{\lambda,\lambda}^r}, 0\right\}$, i.e., hops are only allowed in one direction between two surfaces.

In order to conserve the total energy of the system, a surface hop in the fewest-switches algorithm[58] is accompanied by a velocity adjustment of the nuclear degrees of freedom. The velocity adjustment happens in the direction of the derivative coupling $\vec{A}_{\lambda,\lambda'}$ between the surfaces. If the corresponding momentum is not sufficient to compensate for the energy increment of a hop, the hop is frustrated and ignored. When dealing with relatively low nuclear kinetic energies, this can lead to significant deviations in the distribution of trajectories from the propagated electronic populations $|\Psi_{el,a}^r(t)|^2$. The occurrence of frustrated hops can render FSSH inferior to an Ehrenfest approach in some cases.[226] Even without frustrated hops one cannot guarantee the internal consistency between the electronic populations and the trajectory distributions due to missing decoherence effects,[227] which might be remedied by introducing a decoherence correction (see Sec. V E 1).

It seems that each nuclear trajectory in FSSH has two quantities describing the electronic state: the electronic amplitudes Ψ_{el}^r, which determine the switching probabilities, and the currently active surface λ^r, which determines the nuclear Hamiltonian in Eq. (36).[228] Typically, the active-surface (AS) distributions are used to calculate populations of the Born–Oppenheimer states, $\langle\hat{n}_a^{BO}\rangle = \frac{1}{N_{traj}}\sum_r^{N_{traj}} \delta_{a,\lambda^r}$, as they approximately obey detailed balance.[229,230] In contrast, the calculation of electronic properties in other basis sets requires a proper definition of the full electronic density matrix $\hat{\rho}_{el}^r$ used in Eq. (31) to approximate the partially Wigner-transformed density matrix. In particular, a consistent approach to calculate diabatic populations $n_a = \mathrm{Tr}[\hat{n}_a] = \mathrm{Tr}[|\chi_a\rangle\langle\chi_a|]$ is not easily found in FSSH (see, for example, the discussions in Refs. 142, 210, and 228). Two simple possible definitions for the matrix elements of the density matrix in the Born–Oppenheimer basis are[142,210,228,231]

$$\rho_{el,a,b}^{r,(\mathrm{AS})} = \delta_{\lambda^r(t),a}\delta_{a,b}, \tag{37}$$

$$\rho^{r,(\mathrm{WF})}_{el,a,b} = \Psi^{r}_{el,a}\Psi^{r,*}_{el,b}. \tag{38}$$

The first definition $\hat{\rho}^{(\mathrm{AS})}_{el}$ corresponds to using only the distribution of active surfaces for the calculation of the electronic density matrix. With this ansatz, however, only a diagonal density matrix in the basis of Born–Oppenheimer states can be described for every nuclear configuration R. Thus, for an initial state that is a coherent superposition of several Born–Oppenheimer states, such as is the case for a typical diabatic state, this ansatz cannot capture the correct initial diabatic populations. The second ansatz $\hat{\rho}^{(\mathrm{WF})}_{el}$ relies on the electronic wave function amplitudes. Similar to MTE, electronic populations in any basis and for any initial state can be described with this ansatz. On the downside, the electronic amplitudes are not guaranteed to obey detailed balance and are unreliable for longer times.[142,228–230]

Based on an approximate derivation of surface hopping from the quantum–classical Liouville equation,[210] Landry *et al.* proposed the use of a mixed diabatic electronic density,[228] which corresponds to using

$$\rho^{r,(\mathrm{mixed})}_{el,a,b} = \begin{cases} \delta_{\lambda^r(t),a}, & \text{for } a = b, \\ \Psi^{r}_{el,a}\Psi^{r,*}_{el,b}, & \text{for } a \neq b, \end{cases} \tag{39}$$

for the electronic density matrix. Here, the active surface distribution is used for the diagonal elements of the electronic density matrix, while the off-diagonal elements are constructed from the electronic amplitudes. This expression combines the strengths of the long-time detailed balance given for the active-surface distributions and the short-time coherences of the electronic amplitudes.[228]

We note that the forces on the nuclei are still calculated from the active surfaces only, ignoring any coherences between adiabatic states, i.e., off-diagonal elements of the electronic density matrix in the adiabatic basis. When the coherences have a significant influence on the wave function dynamics, this will lead to deviations of the nuclear motion from the exact dynamics. This is, for example, the case for the (site-) local initial states studied in this work, which have non-zero coherences from the beginning. This deficiency is one consequence of the basis-dependence of surface hopping, which works best only when starting from an adiabatic (Born–Oppenheimer) initial state.

The mixed electronic density matrix defined by Eq. (39) provides a consistent way to calculate electronic populations in any basis. Unless stated otherwise in this work, we will use this definition for the calculation of diabatic populations. There is, however, one caveat to using the mixed electronic density matrix: the diabatic populations are not guaranteed to be positive.[228] We find this to be of relevance only in large systems starting from a local initial state, at sites far away from the initially occupied site with very low populations. Observables that put special focus on these small diabatic populations, such as the later investigated reduced mean-squared displacement [see Eq. (49)], cannot be calculated reliably by using the mixed electronic density matrix of Eq. (39) (see Appendix A). In these cases, one should consider to resort to the aforementioned definitions $\hat{\rho}^{(\mathrm{AS})}_{el}$ [Eq. (37)] or $\hat{\rho}^{(\mathrm{WF})}_{el}$ [Eq. (38)]. More information on our implementation of FSSH and convergence analysis is given in Sec. V F.

E. Improvements to fewest-switches surface hopping

Many improvements for surface-hopping algorithms have been proposed in the recent years, as portrayed in Refs. 104 and 105. We consider here only the very common decoherence correction and two further corrections specifically proposed for large systems (see also Ref. 109). In the following, the trajectory index r is omitted for clarity.

1. Decoherence correction

The assumption of independent-trajectories within the surface-hopping approach does not only discard the phase relation between different trajectories, but it also leads to overcoherence within the individual trajectories: the electronic amplitudes are evolved via Eq. (35) and without interactions with other trajectories. Therefore, they will keep the phase relation between different surfaces, which can lead to self-interference effects at later times. Already in the first proposal of the fewest-switches algorithm,[58] Tully mentioned the possibility of adding coherence damping terms to the time evolution of the electronic amplitudes. Since then, a large variety of decoherence corrections have been proposed (see, for example, Refs. 104, 109, 142, and 232). We use a force-based decoherence rate, proposed in Refs. 233 and 234, on the basis of a frozen Gaussian method,[235,236] where the electronic amplitudes of all non-active states $a \neq \lambda$ decay exponentially in each time step via $\Psi'_a = \Psi_a \cdot \exp(-\Delta t/\tau_a)$, with the decoherence rate

$$\frac{1}{\tau_a} = \sqrt{\sum_k \left(F^{\lambda}_k - F^{a}_k\right)^2/(4a_k\hbar^2)}. \tag{40}$$

Here, F^a_k is the kth component of the force acting on the ath potential energy surface and a_k is the width of the Gaussians used in the frozen Gaussian ansatz, which can be calculated in the Holstein model via $a_k = \frac{m\omega_0}{\hbar}$ (see also Ref. 109).

Subotnik *et al.* have proposed an advanced expression for decoherence rates of on- and off-diagonal elements of the electronic density matrix by deriving the surface-hopping approach from the quantum–classical Liouville equation.[210] We will not use their expression in this work, as it requires the propagation of additional variables.

Using a decoherence correction, in the following denoted by FSSH + D, simplifies the ambiguity of the electronic density matrix in FSSH, mentioned in Sec. V D. Since the electronic amplitudes are dampened toward the active surface distributions, all definitions of the density matrix become the same for long times. In order to recover the correct coherences of local initial states, one should thus resort to the mixed $\hat{\rho}^{(\mathrm{mixed})}_{el}$ [Eq. (39)] or the electronic amplitude (wave function) $\hat{\rho}^{(\mathrm{WF})}_{el}$ [Eq. (38)] definition.

2. Avoiding derivative couplings

Special care needs to be taken when dealing with large systems in FSSH (see Ref. 109). Here, different energy surfaces can come very close or even cross when different adiabatic states are localized to far separated regions of the system and are only very weakly coupled. The derivative couplings [see Eq. (10) or, for the dimer, Eq. (16)] then become very localized and cannot be sampled reliably unless very small time steps are used.[237–240] In the FSSH algorithm, the derivative couplings are used in three steps: the electronic propagation according to Eq. (35), the calculation of the

hopping probabilities, and the direction of the velocity adjustment after a successful surface hop.

Since the electronic propagation is basis independent [see Eq. (34)], it can be carried out in a diabatic basis $|\chi_a\rangle$ to avoid the derivative couplings altogether. In each time step, the adiabatic amplitudes are then calculated via $\Psi^{(a)}_{el,a}(t) = \sum_b \langle \phi^{BO}_a(R(t)) | \chi_b \rangle \Psi^{(d)}_{el,b}(t)$ [see Eqs. (11) and (12)].[237]

For calculating numerically stable hopping probabilities, also close to surface crossings, different schemes have been proposed (see Ref. 109 and references therein). In this work, we use an alternative expression for the hopping probability $p_{\lambda\to a} = \max\{g^{(\lambda)}_a, 0\}$ in systems with $L \geq 3$, which relies only on the general unitary adiabatic time propagator $\Psi_a(t+\Delta t) = \sum_b P_{a,b}(t, t+\Delta t)\Psi_b(t)$,

$$g^{(\lambda)}_a = \frac{|\Psi_\lambda(t)|^2 - |\Psi_\lambda(t+\Delta t)|^2}{|\Psi_\lambda(t)|^2} \times \frac{\Re\left[P^*_{a,\lambda}(t, t+\Delta t)\Psi_a(t+\Delta t)\Psi^*_\lambda(t)\right]}{|\Psi_\lambda(t)|^2 - \Re\left[P^*_{\lambda,\lambda}(t, t+\Delta t)\Psi_\lambda(t+\Delta t)\Psi^*_\lambda(t)\right]}, \quad (41)$$

and which was proposed in Ref. 241 as a numerically more stable variant of a similar expression proposed in Ref. 237.

The hopping probabilities defined by Eq. (41) fulfill the sum rule $\frac{|\Psi_\lambda(t)|^2 - |\Psi_\lambda(t+\Delta t)|^2}{|\Psi_\lambda(t)|^2} = \sum_{a\neq\lambda} g^{(\lambda)}_a$ in each time step exactly. This is necessary to obtain a self-consistent description between electronic amplitudes and active-surface distributions, as in the original FSSH algorithm.[58] Equation (41) can be evaluated without resorting to derivative couplings once the electronic wave-function propagation is obtained in the diabatic basis.

We compared our results also to the "crossing-corrected" algorithm proposed in Ref. 242 as an extension of a self-consistent correction suggested in Ref. 239, which also relies on exactly enforcing the sum-rule decomposition mentioned earlier. This method relies on identifying surface intersections, or near intersections, which can be insufficient for asymptotically approaching Born–Oppenheimer surfaces, as observed in the Holstein trimer (see Fig. 5). Then again, the crossing-corrected algorithm alleviates the difficult calculation of the velocity-adjustment while passing a surface intersection (by neglecting the velocity-adjustment). We could not observe a significant difference between using the crossing-corrected scheme and using Eq. (41) and employed the latter in this work. Hence, in our implementation, we still rely on the derivative couplings in the calculation of the velocity-adjustment.

3. Decoherence enhanced spurious charge transfer

Another problem appears when applying the decoherence correction in large systems: the "decoherence correction enhanced trivial crossing problem"[109,243] or also called "spurious charge transfer."[231,244] In large systems, different Born–Oppenheimer states might be localized to completely different parts of the system. A surface hop between these states, although rare, will correspond to an instantaneous jump in space. This becomes even more severe when surface crossings are not properly accounted for[109] (see Sec. V E 2). The electronic propagation via Eq. (34) is only indirectly, through the changing nuclear trajectory, affected by the jump, and subsequent hopping events can often still be well described. Hence, in normal FSSH, the erroneous jumps have only little effect, especially when calculating diabatic populations from the electronic amplitudes only [$\rho^{(\mathrm{WF})}$, see Eq. (38)]. The decoherence correction, however, collapses the electronic amplitudes to the active surface, resulting in the spurious charge transfer described in Refs. 109, 231, 243, and 244.

We note that this problem is even more severe when analyzing the real-time evolution of a local initial state in a large system, as done in this work. An example is the bare local state at the central site, with all phonon degrees of freedom in their ground state. This initial state has an almost equal weight on all Born–Oppenheimer surfaces. Thus, already the initial state has a large mismatch between local densities calculated according to the active surfaces (where the initial state is far spread) and the densities calculated according to the electronic amplitudes (where the local initial state is properly recovered). The decoherence correction then quickly removes the correct short-time coherences captured by the electronic amplitudes, resulting in an unphysical super-fast spreading of the wave function. This is shown in Appendix A.

Two ways to restrict the decoherence correction to avoid spurious charge transfer have been suggested: (i) allowing decoherence only when the currently active surface has a wave-function population above a threshold[243] or (ii) restricting the decoherence correction to a certain "active space" in the diabatic basis.[244] When describing the short-time evolution of local initial states, the first approach will have nearly no effect, since, as mentioned earlier, the adiabatic populations of most Born–Oppenheimer states will be above any reasonable threshold. We are thus left with the active-space ansatz of Ref. 244, which was already applied to calculating mobilities in organic semiconductors.[231,244]

This approach[244] introduces an additional step in the time evolution of every independent trajectory: After propagating the nuclei and electronic wave functions, but before the decoherence correction is applied, an "active region" in the diabatic states is defined, which should contain at least a fraction of $R = 0.999$ of the electronic charge density. In our implementation, we construct this region by subsequently adding diabatic basis states with decreasing electronic population to an active region subset, until the total electronic population of the subset exceeds the threshold R. Afterward, the decoherence correction is carried out, but all changes of the diabatic electronic amplitudes outside the active region are ignored, while the amplitudes inside the active region are rescaled to conserve the norm. Since R is close to 1, only diabatic states with a very low electronic population should be affected. As also pointed out in the original paper,[244] this active region only influences the decoherence correction step, while the propagation of the electronic wave functions is carried out in the usual way. This approach is well suited for our local initial states, where initially only a single diabatic state is occupied. We found quantitative changes in the time evolution depending on the exact value of the threshold R used (see Appendix A) and, in general, a value of $R = 0.99$ seems to improve the results over the originally suggested $R = 0.999$ for the local initial states in the large systems.

We can go one step further by completely turning off the decoherence correction in the short-time regime of a local initial state when we know that the coherences between Born–Oppenheimer states are still important. In this work, we take a simple approach

of delaying the use of a decoherence correction in large systems ($L \geq 11$) until a time of $\pi/(2\omega_0)$, i.e., a quarter phonon oscillation period, has passed. The effect of this delayed decoherence is shown in Appendix A. FSSH with this form of the restricted decoherence, i.e., an active region restriction with $R = 0.99$ and the delayed decoherence, will be denoted as FSSH + RD.

From the previous discussion, it is clear that in order to correctly describe the initial electronic state, all coherences between the adiabatic states need to be included. In the example of our local states in large systems, the initial adiabatic states are delocalized over many sites and only the coherences in the electronic wave function recover an electron density that is initially localized to a single site. This is also illustrated in Appendix A. Studies focusing on extracting mobilities and steady-state properties often discard these initial coherences or directly start from a relaxed adiabatic state.[231,243] Using this ansatz has the benefit that all definitions of the electronic density matrix are equivalent in the beginning and both types of restricted decoherence correction mentioned earlier can be used. Furthermore, it has been shown that, when using a crossing-corrected algorithm (see Sec. V E 2) and by including only a subset of all adiabatic states in the algorithm, system-size independent results could be obtained with surface hopping in very large systems, also without limitations to the decoherence correction.[245] Similar to the first restricted decoherence ansatz mentioned earlier, this approach is not suitable for our bare local initial states, which have an almost equal population of all adiabatic states. An alternative extension to ensure inherently system-size independent dynamics, which also works for our initial states, is a subsystem surface hopping ansatz,[246] which combines a surface hopping description for a dynamical subset of the lattice sites with molecular dynamics on the other sites. This can even be combined with an additional subsystem described on a purely statistical level.[247] In this work, where we focus on the initial real-time non-adiabatic dynamics, we stay with a pure surface hopping description, include all coherences for the local initial states, and use the restricted decoherence approach outlined earlier.

F. Computational details of the independent trajectory algorithms and convergence

The calculations presented in this work always start with the nuclear oscillators on every site in a coherent state and the electron either in a local or adiabatic state. The partially Wigner-transformed density matrix [Eq. (30)] has non-zero entries only in one diagonal matrix element of the diabatic or adiabatic electron basis, respectively: $W(R,P) := W_{a,a}(R,P) \neq 0$, corresponding to a normal Wigner transform of this component of the nuclear wave function [$\Psi_a^{(d)}(R)$ or $\Psi_a^{(a)}(R)$]. In both independent trajectory methods, we sample the initial nuclear positions and momenta from that Wigner transform, which for the coherent states leads to uncorrelated Gaussians in the positions and momenta, centered around their quantum mechanical averages $\langle \hat{x}_i \rangle$ and $\langle \hat{p}_i \rangle$. In the dimensionless variables, this can be expressed as

$$W(\tilde{x},\tilde{p}) = \frac{1}{(\pi)^L} \prod_{i=1}^{L} \exp\left(-(\tilde{x}_i - \langle \hat{\tilde{x}}_i \rangle)^2\right) \exp\left(-(\tilde{p}_i - \langle \hat{\tilde{p}}_i \rangle)^2\right). \quad (42)$$

Here, L is the number of sites. In particular, for all states studied here, we have $\langle \hat{\tilde{p}}_i \rangle = 0$, $\forall i$. For the bare states[see Figs. 1(b), 1(d), and 2(a)], all oscillators are centered around zero $\langle \hat{\tilde{x}}_i \rangle = 0$, $\forall i$, while the dressed and adiabatic states have $\langle \hat{\tilde{x}}_k \rangle = \sqrt{2}\tilde{y}$ for one site k [polaron states, Figs. 1(a), 1(c), and 1(e)] or every second site [dressed CDW state, Fig. 2(b)]. Taking $W(\tilde{x},\tilde{p})$ as the probability distribution for starting at a certain phase-space point, there is no need to keep track of any weighting factor in Eq. (31) for the different trajectories and all are weighted equally for calculating observables ($w^r = 1, \forall r$). All randomly drawn positions and momenta are moved and scaled to reproduce the correct mean and variance of the nuclear positions and momenta on each site. Only after the nuclear sampling, the electronic amplitudes are set to the predefined initial state $\Psi_{el}^{initial}(R)$, which, for an adiabatic state, depends on the nuclear positions R. In FSSH, the active surfaces are set to the initial adiabatic surface (for adiabatic initial states) or randomly sampled from the overlaps between the initial state with all adiabatic states at that nuclear position R (for local initial states).

After the initialization, in each time step, we first perform the integration of the nuclear equation of motion, and afterward that of the electronic wave function. In MTE [in a phonon-independent (diabatic) basis], we can integrate the nuclear positions on each site exactly for a constant electron density n on that site via $\tilde{x}(t+\Delta t) = \tilde{x}(t)\cos(\omega_0 \Delta t) + \tilde{p}(t)\sin(\omega_0 \Delta t) + \sqrt{2}\tilde{y}n[1-\cos(\omega_0 \Delta t)]$ and correspondingly for the momenta. Afterward, the vector of all new nuclear positions $\vec{x} := \vec{x}(t+\Delta t)$ is used to represent the electronic time-propagator in Born–Oppenheimer states to obtain $|\Psi_{el}(t+\Delta t)\rangle = \sum_a |\phi_a^{BO}(\vec{x})\rangle \exp(-i/\hbar \Delta t E_a^{BO}(\vec{x}))\langle \phi_a^{BO}(\vec{x})|\Psi_{el}(t)\rangle$, i.e., the electronic wave function is propagated for fixed nuclear positions.

In FSSH (in an adiabatic basis), the electron densities determining the nuclear forces change with the nuclear position $\vec{x}$ and we resort to a velocity-Verlet integration for the nuclear time step. To avoid using derivative couplings in the electronic integration (see Sec. V E 2), we propagate the electronic wave function in the diabatic basis and can use the same electronic propagation as for MTE. The overlap of Born–Oppenheimer eigenstates at different time steps (and thus different $\vec{x}$) is obtained in the diabatic basis. In addition, we make sure that the basis transformation between the diabatic and the Born–Oppenheimer basis, which is obtained by a numerical diagonalization of the Born–Oppenheimer Hamiltonian, does not change sign between subsequent time steps.

After the propagation, in FSSH, we allow for the surface hops, where the hopping probabilities in systems with $L \geq 3$ are calculated according to Eq. (41), with the adiabatic time propagator $P_{a,b}$ determined from the electron propagation step. Finally, if used, the decoherence correction is carried out in FSSH, with the restrictions mentioned in Sec. V E 3 for large systems ($L \geq 11$).

One needs to ensure internal convergence of the independent trajectory methods, both with the number of used trajectories and the used time step. However, even then, the calculated observables will not necessarily converge to the exact values. Since FSSH needs to sample both the initial state and the random surface hops, we can expect it to converge slower with the number of used trajectories than MTE, which only needs to sample the initial state. We can analyze the quality of the trajectory-ensemble average of the methods by repeating a simulation N_r times and investigating the standard deviation σ_O of an observable of interest O across the different runs, also

called the statistical error in the observable. This is illustrated for two typical cases in Fig. 8. The obtained data points can be well described by an inverse square-root dependence of the statistical error on the number of used trajectories. In general, we found that MTE needs fewer trajectories to obtain the same absolute statistical error as the FSSH methods, the factor depending on the system parameters, initial state, and investigated observables. Typical values obtained from linear fits of the log–log data are included in Fig. 8. Relative statistical errors might deviate from this observation, as the different methods converge the observables to different values. For the comparison to the ED, DMRG-LBO, and MCE results presented later, we use 20 000 trajectories for MTE and FSSH for all systems, with the exceptions of the dressed initial state in large systems $L \geq 11$ and for the data presented in Appendix B, where we could still observe a slight visible improvement by increasing to 50 000 trajectories.

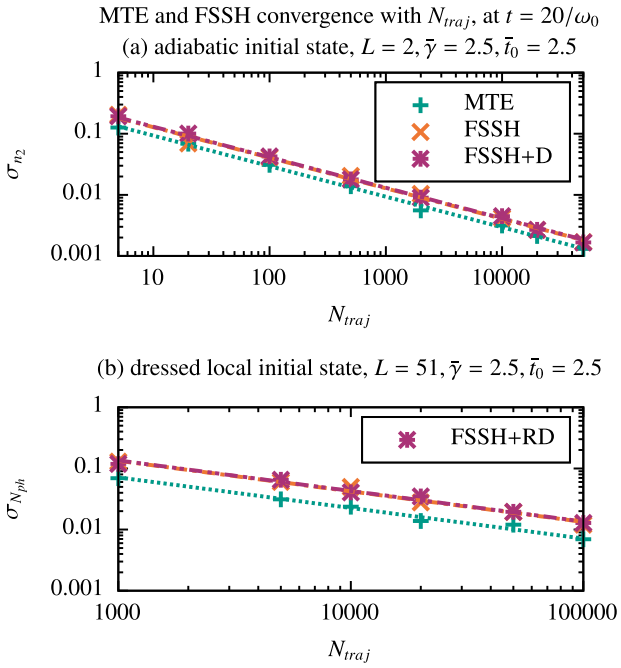

FIG. 8. Convergence of the absolute statistical error in MTE, FSSH, and FSSH + D/FSSH + RD with the number of used trajectories N_{traj} for $\bar{\gamma} = \bar{t}_0 = 2.5$ and $\Delta t = 0.001/\omega_0$ at $t = 20/\omega_0$ for two example systems and example observables. Dashed lines indicate linear fits of the log–log data with slope −0.5, corresponding to the expected inverse square-root decay of the statistical error with the number of used trajectories. The statistical error is calculated as the standard deviation from $N_r = 50$ simulation runs for data points with $N_{traj} \leq 20\,000$ and from $N_r = 25$ runs for a higher number of used trajectories. (a) Adiabatic initial state in the Holstein dimer, with the observable being the population on the second dimer site n_2. From the fitted intercepts of the dashed lines, we estimate that FSSH needs ≈1.88 times more trajectories than MTE for a similar convergence, and FSSH + D ≈1.96 times more trajectories than MTE. (b) Dressed local initial state in the Holstein chain with $L = 51$, where we analyze the total phonon number N_{ph}. The fitted intercepts indicate that FSSH needs ≈3.5 times more trajectories than MTE for a similar convergence, and FSSH + D ≈3.6 times more trajectories than MTE. For $L = 51$, the restricted version of the decoherence correction is used (see Sec. V E 3). Note that MTE, FSSH, and FSSH + D/RD converge to different values, especially for the second case (see Fig. 9).

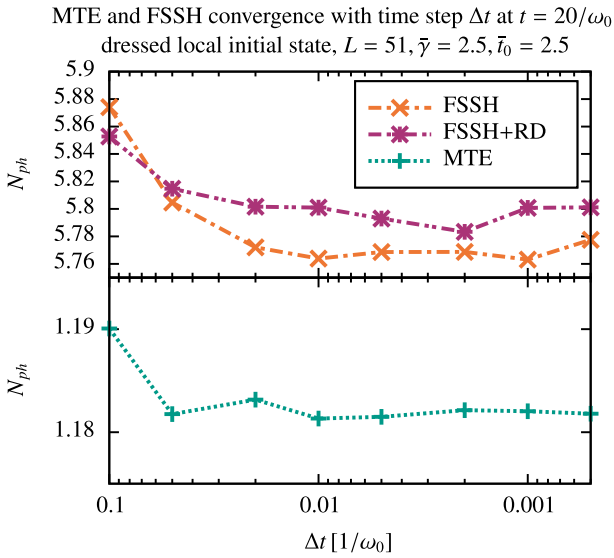

FIG. 9. Convergence of the total phonon number with the used integration time step Δt for MTE, FSSH, and FSSH + RD for $L = 51, \bar{\gamma} = \bar{t}_0 = 2.5$ with $N_{traj} = 100\,000$ at $t = 20/\omega_0$. The lines are guides for the eye.

In addition, a suitable integration time step needs to be used. One of the more difficult systems to converge with respect to the time step is shown in Fig. 9, with $L = 51, \bar{\gamma} = \bar{t}_0 = 2.5$ and $N_{traj} = 100\,000$. We can still observe variations in the total number of phonons for time steps smaller than $\Delta t = 0.01/\omega_0$, which are, however, in the order of magnitude of the statistical error for the 100 000 trajectories used (see Fig. 8). For results for the Holstein dimer $L = 2$ and for the many-electron calculations in Sec. X, we use $\Delta t = 0.01/\omega_0$, while for all one-electron results in systems with $L > 2$, we resort to a smaller time step of $\Delta t = 0.001/\omega_0$.

VI. MULTICONFIGURATIONAL EHRENFEST METHOD

In this section, we explain the method called "Multiconfigurational Ehrenfest" (MCE).[112,113] The method is based on (i) a wave-function ansatz constructed from multiple configurations and (ii) a Gaussian-state basis for oscillators, which is guided by Ehrenfest dynamics.

The MCE method is not a fully variational method, as opposed to, e.g., Gaussian-based Multi-Configuration time-dependent Hartree (G-MCTDH),[1,248–250] variational Multiconfigurational Gaussian (vMCG),[1,251–253] and the Davydov D2 ansatz.[116,117,254–256] The non-variational character, on the one hand, leads to a less complex equation of motion, while on the other hand, the resulting dynamics conserve energy only approximately.[257] MCE, in principle, converges to exact dynamics if the configurations form a complete, or sufficiently large, basis set.[257] A characteristic feature of MCE, which needs to be kept in mind, is that convergence has different rates for different observables. Observables linear in position or momenta converge much faster than observables with higher powers of position or momenta, e.g., the energy of the oscillators. As we confirm below, the convergence of these more difficult observables, as well as total energy conservation, can be reached for

short time intervals or small systems in practical applications. Even when the total energy still drifts, the average nuclear position and the electronic densities close to the initially occupied sites are captured quite well even for later times.

The MCE algorithm comes in two flavors called MCEv1,[112] where all electronic coefficients are coupled across the configurations, and MCEv2,[113] where each configuration has one additional global coefficient, and only these coefficients are coupled across different configurations. The MCEv1 is recommended for model Hamiltonians,[258] such as the Holstein model, to which it was already applied.[117] In this work, only MCEv1 results are included. However, some of the implementation strategies devised for the MCEv2, e.g., the initialization of the total state, are adapted to MCEv1.

A. Ansatz for the total state

The time-dependent basis used in both versions of MCE is constructed from coherent states and an electronic wave function.[112] For a single configuration r, the coherent state product of the oscillators can be written as

$$|\mathbf{z}^r\rangle := \exp\left(\sum_{i=1}^{L}\left(z_i^r\hat{b}_i^\dagger - z_i^{r*}\hat{b}_i - i\Re(z_i^r)\Im(z_i^r)\right)\right)|0\rangle_{ph} \tag{43}$$

and is fully characterized by the set of complex numbers $\{z_1^r,\ldots,z_L^r\}$ defined as the eigenvalues of the annihilation operators $\hat{b}_i|\mathbf{z}^r\rangle = z_i^r|\mathbf{z}^r\rangle$. The additional global phase factor $\Re(z_i^r)\Im(z_i^r)$, with $\Re$ and $\Im$ referring to the real and imaginary part, is introduced to simplify the phononic overlap matrix. A full configuration r is constructed by attaching an electronic state $|\phi^r\rangle$ to the coherent state product $|\mathbf{z}^r\rangle$, resulting in the total state $|\psi^r\rangle = |\phi^r\rangle \otimes |\mathbf{z}^r\rangle$ for the rth configuration.

In MCE, the ansatz can be written as $|\phi^r\rangle = \sum_{i=1}^{L} a_i^r(t)\hat{c}_i^\dagger|0\rangle_{el}$.[259] We note that, in this paper, we consider only single-particle electronic states. Representing many-body electronic states is possible; however, they require the use of a many-body basis instead of the single-particle basis. Putting all together, the ansatz for the total state, constructed from N_c configurations $|\psi^r\rangle$, can be written as[117]

$$|\Psi(t)\rangle = \sum_{r=1}^{N_c}|\psi^r\rangle = \sum_{r=1}^{N_c}\left(\sum_{i=1}^{L}a_i^r(t)\hat{c}_i^\dagger|0\rangle_{el}\right)\otimes|\mathbf{z}^r(t)\rangle. \tag{44}$$

The individual configurations in MCEv1 are not normalized $\langle\psi^r|\psi^r\rangle \neq 1$, but one can normalize the full state $|\Psi\rangle$.

B. Initialization

Initialization of the configurations in Eq. (44) is important to accurately represent the initial state $|\Psi_{initial}\rangle$ with the state ansatz of Eq. (44). Choosing a good subset $\{|\mathbf{z}^r\rangle\}_{r=1,\ldots,N_c}$ is crucial for the correctness and efficiency of MCE.[258] We have observed that MCEv1 is somewhat less sensitive to the initial sampling than MCEv2 due to the coupling between the configurations (see also Ref. 259).

For the initialization, first a set of normalized, but, in general, nonorthogonal, initial configurations $|\psi^r\rangle$ need to be found, onto which the initial state can be projected,[258] $|\Psi\rangle = \sum_{r=1}^{N_c}|\psi^r\rangle\sum_{s=1}^{N_c}\left(S^{-1}\right)^{rs}\langle\psi^s|\Psi_{initial}\rangle = \sum_{r=1}^{N_c}|\psi^r\rangle A^r$, with $S^{rs} = \langle\psi^r|\psi^s\rangle$. If the configurations form a complete basis, we have $|\Psi\rangle = |\Psi_{initial}\rangle$. The coefficients A^r are then absorbed into the electronic coefficients a_i^r of the configurations to obtain the non-normalized initial configurations used in the state ansatz of MCEv1 [Eq. (44)]. The norm of the resulting state deviates from unity $\langle\Psi|\Psi\rangle \neq 1$, in general, but the deviation from 1 can be used as a measure of how well $|\Psi_{initial}\rangle$ is represented. To find the set of initial configurations $\{|\psi^r\rangle\}_{r=1,\ldots,N_c}$, both the coherent state products $\mathbf{z}^r$ and the electronic coefficients a_i^r need to be specified.

We first start with the specification of the coherent state products $\mathbf{z}^r$. As mentioned in Sec. V F, the nuclear wave functions of all initial states studied in this work correspond to a coherent state on every site. In the coherent phonon basis of MCE, this can easily be described by coherent phonon states on every site i with z_i^{ini}. According to the "compressed coherent state swarms" method proposed in Ref. 260, we sample the values of the coherent state products $\{z_1^r,\ldots,z_L^r\}$ from a Gaussian distribution around these initial values, i.e., for the rth configuration,

$$P(\mathbf{z}^r) \propto \prod_i \exp\left(-2\alpha|z_i^r - z_i^{ini}|^2\right). \tag{45}$$

Here, α describes a compression parameter of the sampling width of the Gaussian, with $\alpha = 1$ corresponding to a sampling width equal to the width of the coherent states itself. As investigated in Ref. 260, increasing the compression parameter α can improve the sampling of the initial state and reduce the number of configurations needed to obtain a norm of the projected initial state close to 1. This can lead to more accurate dynamics at later times,[257] but also the opposite might be the case.[260]

We adjust the α-parameter in an iterative scheme, as in Ref. 258, here done by iteratively multiplying α by a constant factor $\gamma > 1$ until the total norm of the state reaches $1 - \langle\Psi|\Psi\rangle < 2e-5$. In addition, all sampled coherent state products are shifted and scaled to reproduce the correct mean and standard deviation of Eq. (45). For small systems with a large number of configurations, the sampled coherent states can be very dense and cause numerical problems in the inversion of the overlap matrix. To overcome this problem, the sampled configurations in systems with $L \leq 3$ are all moved very slightly according to a repulsive force, exponentially decaying with the distance between the coherent states. Afterward, if the overlap matrix is still ill-conditioned due to the dense configurations, which might result in erroneous total norms larger than 1, we allow for an expansion of the sampling region by iteratively reducing the compression parameter α, possibly even below 1. This never occurred for system sizes $L > 3$.

In each iteration of the compression scheme, after the $\mathbf{z}^r$ are obtained, the electronic coefficients are chosen and normalized within each configuration r for which several approaches are possible. One option is to choose the electronic coefficients as they are given by the initial wave function at the center point of the sampled coherent state. We observed a better convergence when using a random sampling of the electron state and employed the so-called "quantum superposition sampling" (QSS).[259] In this approach, the electronic coefficients are chosen randomly, and also initially unoccupied basis states are sampled. We use a slight variation in not choosing the electronic coefficients completely at random, but Gauss-distributed around its values at the coherent-state center point, with subsequent normalization. For the electronic Gaussian function, we choose a standard deviation of $\sigma_{el} = 0.5/\sqrt{\alpha}$, which

changes iteratively with the compression scheme of the nuclear sampling process. A value of $\sigma_{el} = 0$ corresponds to the deterministic electronic coefficients obtained from $|\Psi_{initial}\rangle$ at the center point of the selected phonon coherent state, while a value of $\sigma_{el} = \infty$ corresponds to completely random electronic coefficients. While we do not perform a systematic study, we find the choice $\sigma_{el} = 0.5/\sqrt{\alpha}$ to be a reasonable choice for most of our investigated initial states. The exception is the tunneling process (see Fig. 17), where a value of $\sigma_{el} = 1/\sqrt{\alpha}$ produces better results, as more basis states on the initially unoccupied site are helpful in recovering the tunneling transition.

In general, treating adiabatic initial states and related observables, such as the occupation of the Born–Oppenheimer states $\langle \hat{n}_a^{BO} \rangle$, is computationally demanding in our implementation of MCE. A single configuration in the state ansatz used here [Eq. (44)] contains one diabatic electronic state and a coherent phonon-state, which has a Gaussian shape in a phonon coordinate representation R. Thus, Gaussian integrals in the phonon coordinate space are needed to evaluate projections onto the Born–Oppenheimer states, which become demanding for large systems and are only done for small systems $L \leq 3$ in this work. Alternatively, one could directly implement MCE with an adiabatic electronic basis,[261] which is, however, not pursued in this work.

Finally, for large systems, we find it beneficial to use a site-dependent compression value α_i, similar to the pancake sampling.[260] In the pancake-sampling, the nuclear initial conditions on sites that are regarded as less important for the dynamics (e.g., bath sites in comparison to system sites) are sampled with higher compression. We use a pancake-like sampling for systems with $L > 3$, where the compression parameters α_i on each site i are scaled with an exponential of the distance from the initially occupied (central) site c, similar to the formula used in Ref. 262, $\alpha_i = \alpha \cdot \exp\left(|i - c|/\tau\right)^2$, with the characteristic decay-scale τ, which is set to 3 in this work. When using this pancake-like sampling for our large system studies $(L > 3)$, we find that the iterative compression of the coherent state sampling stopped very close to a value of $\alpha = 1$, i.e., the total norm of the state is already accurately described by the pancake compression, without any additional global compression.

C. Time propagation

The equation of motion for the electronic coefficients a_i^r can be obtained from the Dirac–Frenkel time-dependent variational principle[263] (using $\hbar = 1$ in this subsection) with the Lagrangian $\mathcal{L} = \langle \Psi | i \frac{\partial}{\partial t} - \hat{H} | \Psi \rangle$. Performing the variations $\frac{\partial \mathcal{L}}{\partial a_i^{r*}} - \frac{\mathrm{d}}{\mathrm{d}t} \frac{\partial \mathcal{L}}{\partial \dot{a}_i^{r*}} = 0$, the equation of motion for the electronic coefficients a_i^s reads[117]

$$i \sum_s R^{rs} \dot{a}_i^s = \frac{\partial}{\partial \dot{a}_i^{r*}} \langle \Psi | \hat{H} | \Psi \rangle - i \sum_s R^{rs} a_i^s \sum_j \left(z_j^{r*} \dot{z}_j^s - \frac{\dot{z}_j^{s*} z_j^s + z_j^{s*} \dot{z}_j^s}{2} \right), \tag{46}$$

with $R^{rs} = \langle \mathbf{z}^r | \mathbf{z}^s \rangle$.

We note that, at this point, we could apply the variational principle also to the z_i^{r*} coordinates to derive the equation of motion for z_i^r. This would lead to a fully variational method, the so-called multiple Davydov D_2 ansatz.[116,117,254–256] Instead, in the MCE method, a different choice for the equation of motion for z_i^r is used. Concretely, the Ehrenfest forces, $\dot{x}_i^r = \partial H^{nuc,r} / \partial p_i^r$ and $\dot{p}_i^r = -\partial H^{nuc,r} / \partial x_i^r$, from each configuration-averaged Hamiltonian $H^{nuc,r} = \langle \psi^r | \hat{H} | \psi^r \rangle / \langle \psi^r | \psi^r \rangle$ are used to evolve the coefficients z_i^r. For the Holstein Hamiltonian [Eq. (1)], this can be compactly written as

$$i \dot{z}_i^r = \frac{\partial H^{nuc,r}}{\partial \dot{z}_i^{r*}} = \omega_0 z_i^r - \gamma \underbrace{\frac{|a_i^r|^2}{\sum_j |a_j^r|^2}}_{n_i^r}, \tag{47}$$

where the second term is the force proportional to the electronic density n_i^r on site i in the configuration r. Inserting the equation of motion (47) into Eq. (46) and applying this to our Holstein model, we get a linear coupled system of equations of motion

$$\begin{aligned} i \sum_s R^{rs} \dot{a}_i^s = &- t_0 \sum_s R^{rs} (a_{n-1}^s + a_{n+1}^s) - \gamma \left(z_i^{r*} \sum_s R^{rs} a_i^s + \sum_s R^{rs} a_i^s z_i^s \right) \\ &+ \gamma \sum_s \left(R^{rs} \sum_j z_j^{r*} n_j^s \right) a_i^s + i\gamma \sum_s R^{rs} a_i^s \sum_j n_j^s \Im(z_j^s), \end{aligned} \tag{48}$$

resulting in a norm-conserving dynamics.[257] In this work, the equations of motion in Eqs. (47) and (48) are integrated with an adaptive time-step Runge–Kutta–Fehlberg4(5) integrator. The error tolerance is chosen sufficiently small to conserve the norm up to 1×10^{-6}.

D. Convergence properties and benchmark of MCE

Investigating the internal convergence in the MCE algorithm is important, since the calculated observables should approach the exact values when the basis at a certain time step becomes sufficiently large. Previous convergence tests of MCE and benchmarks to other methods exist, see, e.g., for the spin-boson model in Ref. 112 and for a donor–acceptor charge transfer system in Ref. 257. A comparative study in an extended periodic dispersive Holstein chain was carried out recently in Ref. 117 for up to 16 lattice sites. For the results presented in our work, we analyze the convergence of MCE for Holstein chains with up to $L = 51$ sites with a benchmark obtained from the numerically exact DMRG-LBO (denoted as DMRG) simulations.

We find that the convergence works well for small systems and also in large systems for certain observables, such as the average phonon position and electronic densities close to the initial position of the electron. However, as mentioned before, a good convergence is difficult to reach for long times in large systems for other observables,[257] e.g., subsystem energies and local quantities far away from the initially occupied sites. Since the aforementioned violation of total energy conservation is induced by the incomplete basis,[257] one can attempt to use the total-energy drift as an internal convergence criterion. For the convergence analysis, it is again helpful to repeat each simulation N_r times (see Sec. V F). We then obtain both the run-averaged observable $\langle O \rangle^r$ and its standard deviation σ_O.

As a typical scenario obtained for small systems, Fig. 10 shows the run-averaged number of phonons with its standard deviation as error bars over the number of used configurations at a time

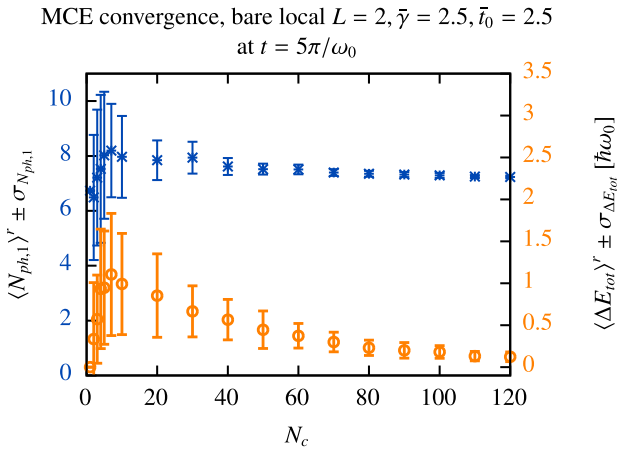

FIG. 10. MCE convergence of the phonon number on the initially occupied site $N_{ph,1}$ (blue stars) and total energy drift ΔE_{tot} (orange circles) vs the number of used configurations N_c for the bare local initial state in the Holstein dimer with $\bar{\gamma} = 2.5, \bar{t}_0 = 2.5$. We show the results at time $t = 5\pi/\omega_0$. The observables are run-averaged over $N_r = 50$ runs, and the resulting standard deviation is displayed as error bars.

$t = 5\pi/\omega_0$, starting from the bare local state [see Fig. 1(b)] in the Holstein dimer with $\bar{\gamma} = \bar{t}_0 = 2.5$. This is compared to the run-averaged total energy drift, with its standard deviation as error bars.

For a large number of configurations N_c, the total phonon number converges to a constant value and the energy drift tends to zero, as expected. In addition, the standard deviation across different runs becomes negligible and the dynamics thus independent of the random initial sampling. Interestingly, the behavior is different for small N_c, where, at first, the energy drift and its standard deviation increase with the number of configurations. We can understand this from the fact that, for far-separated configurations in the phonon Hilbert space, their dynamics become almost independent and similar to the MTE approach introduced in Sec. V C. Only when the configurations come close to each other, but are not yet dense enough to form a nearly complete basis, an energy drift is introduced. We note that we also enforce the correct mean and variance of the initial phonon sampling, up to the compression scheme mentioned in Sec. VI B, which influences the low-N_c regime. The total phonon number and its standard deviation converge only in the large-N_c limit when the energy drift approaches zero again. This is relevant for large systems, where this limit is difficult to reach (see Fig. 11): only looking at the energy drift, without its trend with increasing the number of configurations, could give a wrong impression of the internal convergence of MCE.

For small systems, $L = 2$ and $L = 3$, we could always reach the large-N_c limit. Here, we identify the energy drift as a useful tool to assess internal convergence. It grows with the simulation time t so that an increasing number of configurations N_c is needed to obtain correct results for later times. In our results for $L = 2$ and $L = 3$, we indicate the time $t^{MCE}_{0.2\hbar\omega_0}$, where the run-averaged energy drift exceeds $0.2\,\hbar\omega$. This is an arbitrary value, useful only for comparing the convergence between different system and method parameters.

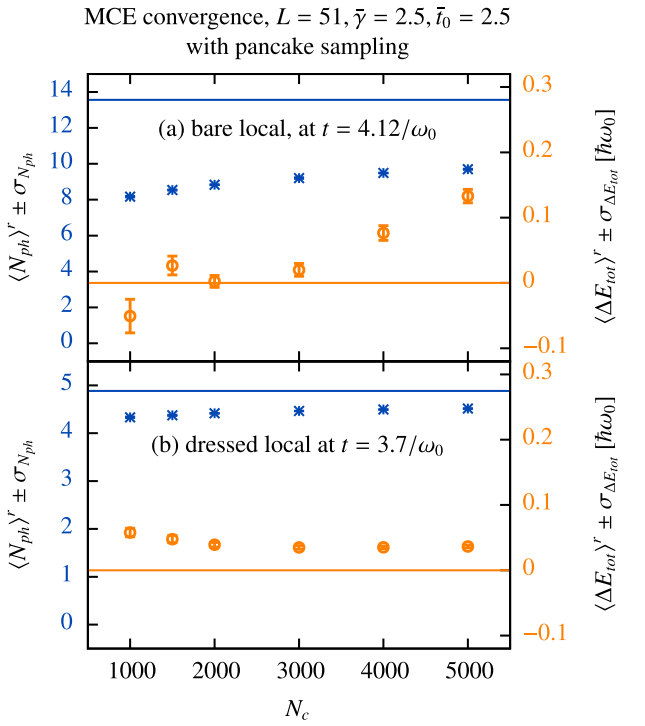

FIG. 11. MCE convergence of the total phonon number $N_{ph} = \langle \sum_i \hat{b}_i^\dagger \hat{b}_i \rangle$ (blue stars) and total energy drift ΔE_{tot} (orange circles) over the number of used configurations N_c for the (a) bare and (b) dressed local initial state in the Holstein chain with $L = 51, \bar{\gamma} = 2.5, \bar{t}_0 = 2.5$. The MCE initialization is done with the pancake-like sampling, which improves convergence. The observables are run-averaged over $N_r = 10$ runs, and the resulting standard deviation is included as error bars. The desired converged results are indicated by dashed lines: zero energy drift and the total phonon number obtained with DMRG at the selected time. We show the results at time (a) $t = 4.12/\omega_0$ and (b) $t = 3.7/\omega_0$, corresponding to the first major maximum (bare) or minimum (dressed) in the total phonon number obtained with DMRG (see Figs. 24 and 28).

For larger systems, we could only reach the large-N_c limit for very short times, while for most of the dynamics, the simulations are just beyond the energy-drift peak (for the dressed initial states) or even in the rising energy-drift regime (for the bare initial states). The MCE convergence of the total phonon number $N_{ph} = \langle \sum_i \hat{b}_i^\dagger \hat{b}_i \rangle$ and the total energy drift in the Holstein chain with $L = 51, \bar{\gamma} = \bar{t}_0 = 2.5$ is compared to the value obtained with DMRG (see Sec. IV C) in Fig. 11. We analyze the convergence at the time where the total phonon number obtained from DMRG reaches the first major maximum (bare) or minimum (dressed); see our results in Figs. 24 and 28 for the obtained time evolution.

For both the bare and dressed initial state in Fig. 11, we could not converge the total phonon number to the DMRG value for the number of configurations available. For the bare local initial state, the total energy drift is negative for small N_c, which in our simulations always indicates a poor sampling. For the dressed initial state, the total energy drift is already in the falling branch and only shows a small absolute total energy drift $\langle \Delta E^r_{tot}(N_c = 5000)\rangle \approx 0.036\,\hbar\omega_0$. While for small systems, such a value is completely sufficient, this is not the case for the Holstein chain ($L \gg 3$) with only one localized

electron: the total initial energy stays constant with the number of sites (ignoring the zero-point energy of the phonon harmonic oscillators), and thus the average energy per site becomes very small for large systems. A global quantity like the total phonon number is very difficult to converge in this case.

We will see later that some observables are still very well recovered in these regimes, for example, local observables around the initially occupied site. Thus, we consider the MCEv1 method used in this work as a promising technique, especially for small systems and some local observables with a larger energy scale, while global observables and questions of energy transfer between subsystems seem to be much more difficult to obtain or would require more extensive computational resources.

VII. RESULTS FOR THE HOLSTEIN DIMER

Before analyzing the Holstein chain, we first review the non-adiabatic dynamics in the Holstein dimer. As a prototypical system for an avoided crossing in a confining potential, this and similar models are already well studied in the literature[107] (see also Sec. I). Here, we concentrate on a few example cases to illustrate the influence of non-adiabatic effects on electron–nuclear dynamics and the ability of the trajectory-based methods to capture these effects. We will use our insights later in our interpretation of our results for the Holstein trimer and the Holstein chain, as many observations carry over to these systems. For the Holstein dimer, we compare the independent-trajectory methods multitrajectory Ehrenfest (MTE) and fewest-switches surface hopping (FSSH) to exact diagonalization (ED) and the multiconfigurational Ehrenfest approach (MCE). For the ED calculation, we include the results from the grid-based calculation in the Born–Oppenheimer basis (see Sec. IV B), which is, in all tested systems, identical to ED in second quantization (Sec. IV A).

We analyze the three different initial conditions shown in Figs. 1(a)–1(c). (i) The wave function has contributions only on the upper Born–Oppenheimer surface, which we call an adiabatic initial state, and then enters a region of significant derivative coupling, thus allowing for transitions between the surfaces [Fig. 1(a)]. (ii) The electron is initially localized to a single dimer site [Figs. 1(b) and 1(c)]. Here, the initial electron state does not depend on the nuclear position and populates a single (trivial) diabatic state. It is in a coherent superposition of both adiabatic states, which provides a challenge for the surface-hopping approach (see Sec. V D). One example of a comparative study in a similar system with initial conditions not restricted to a single adiabatic state is Ref. 228, where the mixed calculation of diabatic populations in FSSH was also suggested (see Sec. V D). In both the adiabatic and local initial states, the nuclear wave function in the respective adiabatic or diabatic basis [see Eqs. (11) and (12)] has only one non-zero component $\Psi_a(q) = \delta_{a,b}\Psi_{nuc}(q)$. For this component of the nuclear wave function, we always choose a coherent state centered around some $\bar{q}_0 := \langle \hat{\bar{q}}(t=0)\rangle$ and with $\bar{p}_{q,0} = 0$.

For the local initial conditions (ii), we analyze two types of such initial states: First, the bare local initial state, where the system starts with all phonon sites in the ground state $\bar{q}_0 = 0$, corresponding to a bare charge carrier injected locally into a Holstein chain, where no electron–phonon coupling or electron spreading could yet develop [see Fig. 1(b)]. Second, the localized electron can start with local phonon excitations already developed on the initial site $\bar{q}_0 = \bar{\gamma}$, which is called the dressed local initial state [see Fig. 1(c)]. For the Holstein dimer, we consider this state mainly to showcase the effect of a tunneling transition, but dressed local states will be analyzed in more detail for the larger systems. The dressed local state can, for example, be realized by a sudden parameter quench, where the electronic hopping matrix element is turned on for times $t > 0$.

A. Adiabatic initial state: Transition through the avoided crossing

In the adiabatic initial state, the electron initially occupies the upper Born–Oppenheimer state, while we choose the phonon distribution as a coherent state around $\bar{q}_0 = \bar{\gamma}$. In the spirit of the language of chemical bonds, this initial configuration corresponds to an antibonding initial state. As parameters, we choose an intermediate regime with $\bar{\gamma} = \bar{t}_0 = 2.5$, which allows for non-adiabatic transitions between the Born–Oppenheimer surfaces when the wave packet approaches the avoided crossing point at $\bar{q} = 0$.

To get an impression of the time-evolution predicted by the exact and independent-trajectory methods, we show the probability densities on the two Born–Oppenheimer surfaces in nuclear coordinate space $|\Psi_{\pm}^{(a)}(q,t)|^2$ [see Eq. (11)] in Fig. 12. For the independent-trajectory methods MTE and FSSH (here without decoherence correction), they are obtained from $|\Psi_{\pm}^{(a)}(q,t)|^2 = \int \mathrm{d}p_q \langle \phi_{\pm}^{BO}(q)|\hat{W}(q,p_q,t)|\phi_{\pm}^{BO}(q)\rangle$ using the approximate partially Wigner-transformed density matrix from Eq. (31). For each method, the Born–Oppenheimer probability densities are shown for four different time snapshots.

The first snapshot at $t = 0/\omega_0$ illustrates the starting configuration of each method [Figs. 12(a)–12(c)] where the initial Gaussian shape is roughly recovered by the random sampling of the 20 000 trajectories of the independent-trajectory methods. At $t = 2.5/\omega_0$ [Figs. 12(d)–12(f)], the initial wave packet has passed through the avoided crossing for the first time and now shows contributions on both Born–Oppenheimer surfaces. The FSSH method reproduces the separation of the upper and lower component of the nuclear wave function, while they are centered around the same q in the MTE method. Thus, MTE already fails to correctly describe the very first transition through the avoided crossing. The same holds for the second splitting at $t = 4/\omega_0$ [Figs. 12(g)–12(i)]. At this time, the mean nuclear position $\langle \hat{q}\rangle$ of MTE also starts to deviate significantly from the exact results, as illustrated in Fig. 13. Finally, at $t = 5.2/\omega_0$ [Figs. 12(j)–12(l)], the remaining upper part of the nuclear wave function interferes with its recurring lower component. The following interference pattern is not accurately captured by the surface-hopping method, and observables will start to deviate from the exact results at later times.

We can investigate the transition probabilities back into the lower Born–Oppenheimer state by looking at the occupation of the upper Born–Oppenheimer surface $\langle \hat{n}_+\rangle(t)$. This is depicted in Fig. 13(a), which also includes the results from the fewest-switches surface hopping with the force-based decoherence rate of Eq. (40) and the multiconfigurational Ehrenfest method (see Sec. VI). We can see the first three transitions through the avoided crossing, where every time a portion of the upper nuclear wave function

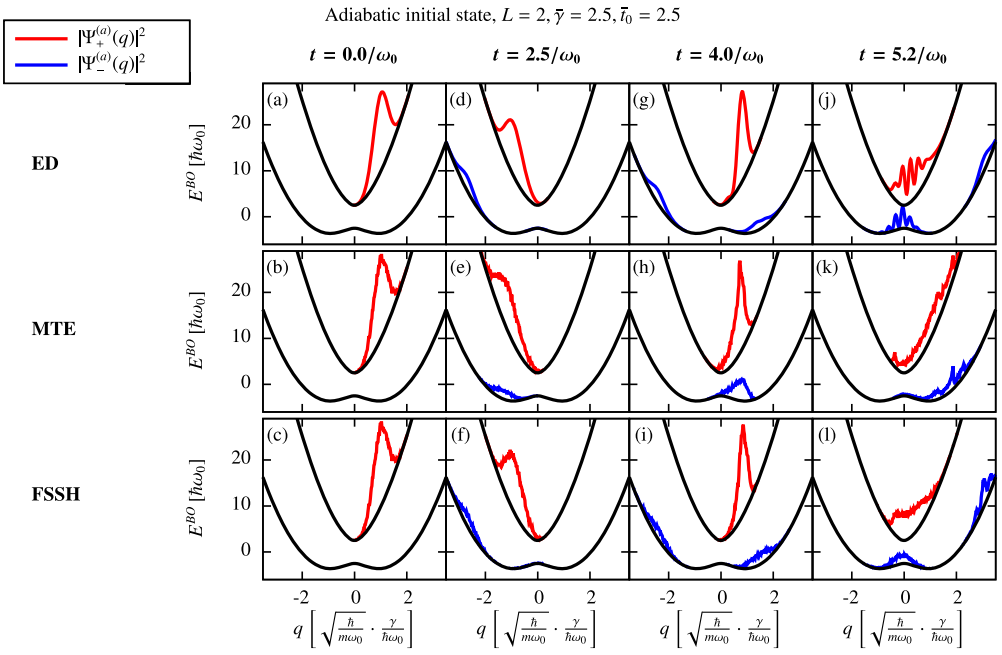

FIG. 12. Snapshots of the Born–Oppenheimer (adiabatic) probability densities $|\Psi_\pm^{(a)}(q,t)|^2$ [see Eq. (11)] for three different methods starting from the adiabatic initial state in the Holstein dimer with $\bar{\gamma} = \bar{t}_0 = 2.5$. In the first row, we show the numerically exact results obtained from exact diagonalization using the approach outlined in Sec. IV B. This is compared to the two independent-trajectory methods multitrajectory Ehrenfest (MTE) and fewest-switches surface hopping (FSSH), here without the decoherence correction, in the two rows below. For each method, the Born–Oppenheimer probability densities are depicted for four different time snapshots, (a)–(c) $t = 0/\omega_0$, (d)–(f) $t = 2.5/\omega_0$, (g)–(i) $t = 4/\omega_0$, and (j)–(l) $t = 5.2/\omega_0$. In each snapshot, the density on the upper and lower Born–Oppenheimer surface are represented as a red and blue line. Both are drawn on top of the respective Born–Oppenheimer energy surfaces with an arbitrary but constant scaling to improve visibility. MTE and FSSH use 20 000 trajectories and $\Delta t = 0.01/\omega_0$, and the ED method 250 eigenstates (see Secs. IV B and V).

passes to the lower surface, while $\langle \hat{n}_+ \rangle(t)$ stays plateau-like between the transitions. Already after the first transition, the MTE method overestimates the occupation of the upper Born–Oppenheimer surface, i.e., it underestimates the relaxation probability. FSSH exhibits deviations after the first transition as well but is capable of still giving qualitatively accurate results for the second, third, and fourth transition. The decoherence correction (FSSH + D) improves the quantitative descriptions of the first three plateaus but overestimates the relaxation for longer times more than the conventional FSSH. It was reported before that decoherence corrections can induce problems when describing recoherences, where previously separated parts of the wave function meet again.[142] All of the independent-trajectory methods fall short of correctly describing the long-time behavior for times $t > 10/\omega_0$ when the wave function is spread across most of the nuclear coordinate space.

In addition, we can look at the electronic densities on the two dimer sites, corresponding for the one-electron case to the populations in our diabatic basis, which is displayed for the first site $\langle \hat{n}_1 \rangle$ in Fig. 13(b). We observe that in the first few transitions through the avoided crossing, the electron, for the most part, switches the occupied site, while for later times, it is mostly delocalized between both dimer sites. Again, MTE reproduces the exact results to the least extent. The surface-hopping methods improve on that, with the decoherence correction again leading to a better quantitative description for short times. For times $t > 8/\omega_0$, both FSSH with and without decoherence deviate significantly from the exact results. The time evolution of both the diabatic and adiabatic populations is very close to the results obtained in Ref. 107 for a similar initial state.

Finally, we also compare a nuclear observable for which we choose the average nuclear position $\langle \hat{q} \rangle$ [see Fig. 13(c)]. This observable is slightly more robust than the electronic occupations, with even MTE showing larger deviations only for $t > 4/\omega_0$. FSSH + D reproduces the nuclear position to the largest extent.

MCE coincides with the ED results for most of the time evolution and only slight deviations can be seen at the end of the shown time interval for all observables in Fig. 13. It is thus a significant improvement over the MTE method. The energy drift of MCE reaches $0.2\,\hbar\omega_0$ at $t^{MCE}_{0.2\,\hbar\omega_0} = 6.37/\omega_0$.

B. Bare local initial state with large electron hopping

The bare local initial states start with the electron localized to one of the two dimer sites, while the phonons are in a coherent state around $\bar{q}_0 = 0$. For these small values of $\bar{q}$, the Born–Oppenheimer wave functions of the dimer [Eq. (15)] have almost an equal weight in both Born–Oppenheimer states. Thus, this initial state has, already from the beginning, coherent contributions in both Born–Oppenheimer surfaces. To disentangle the effects of the initial coherent superposition of the state and later non-adiabatic transitions, we choose the parameters $\bar{\gamma} = 4, \bar{t}_0 = 10$. In this large electron hopping parameter regime, non-adiabatic transitions are mostly excluded; see also the Landau–Zener formula (17).

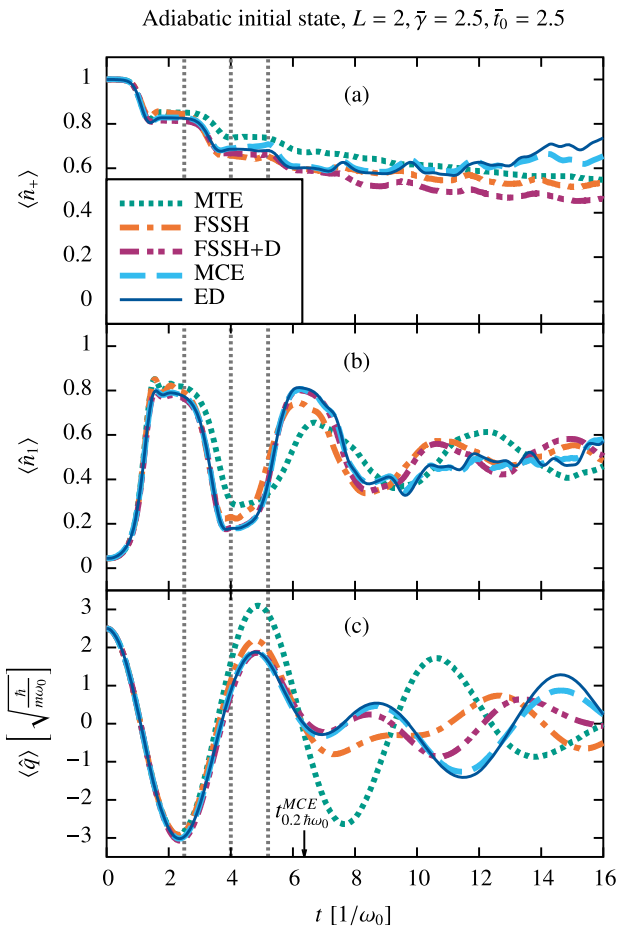

FIG. 13. Time evolution of three observables starting from the adiabatic initial state in the Holstein dimer with $\bar{\gamma} = 2.5$ and $\bar{t}_0 = 2.5$. We show the (a) electronic occupation of the upper Born–Oppenheimer surface $\langle \hat{n}_+ \rangle$, (b) electronic occupation of the first dimer site $\langle \hat{n}_1 \rangle$, and (c) average phonon coordinate $\langle \hat{q} \rangle$ for five different methods: Exact diagonalization (ED) as a dark blue solid line, multiconfigurational Ehrenfest (MCE) as a dashed light blue line, fewest-switches surface hopping without decoherence correction (FSSH) and with decoherence correction (FSSH + D) as dashed–dotted magenta and orange lines, and multitrajectory Ehrenfest (MTE) as a dotted green line. MTE, FSSH, and FSSH + D use 20 000 trajectories and $\Delta t = 0.01/\omega_0$, MCE uses 300 configurations, and ED 250 eigenstates. For the descriptions of the methods, see Secs. IV B, V, and VI. The energy drift of MCE reaches $0.2\,\hbar\omega_0$ at $t^{MCE}_{0.2\,\hbar\omega_0} = 6.37/\omega_0$. The times of the snapshots shown in Fig. 12 are indicated with vertical gray dashed lines.

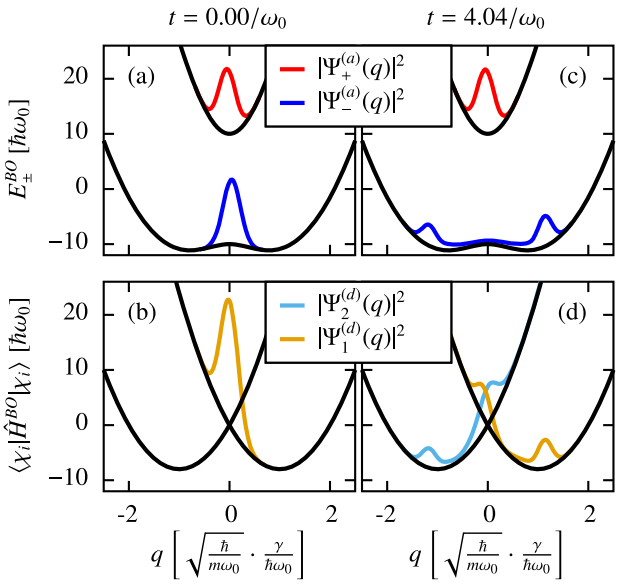

FIG. 14. Probability densities obtained from exact diagonalization (see Sec. IV B) in the Holstein dimer, starting from the bare local initial state with $\bar{\gamma} = 4, \bar{t}_0 = 10$. We show snapshots for the initial state $t = 0/\omega_0$ and at time $t = 4.04/\omega_0$. We display the Born–Oppenheimer (adiabatic) probability densities $|\Psi^{(a)}_\pm(q)|^2$ [(a) and (c)] and local (diabatic) probability densities $|\Psi^{(d)}_i(q)|^2$ [(b) and (d)] [see Eqs. (11) and (12)]. The probability densities are drawn on top of the diagonal elements of the Born–Oppenheimer Hamiltonian in the respective electronic bases $E^{BO}_\pm(q) = \langle \phi^{BO}_\pm(q) | \hat{H}^{BO}(q) | \phi^{BO}_\pm(q) \rangle$ and $\langle \chi_i | \hat{H}^{BO}(q) | \chi_i \rangle$ with an arbitrary but constant scaling to improve visibility.

The probability densities of the initial state in both the adiabatic and diabatic basis [see Eqs. (11) and (12)] are shown in Figs. 14(a) and 14(b), obtained from exact diagonalization. Figure 14 visualizes the problem of the basis-dependence of the FSSH method: since the forces on the atoms are calculated only from the adiabatic electron densities [Fig. 14(a)], ignoring the coherent superposition of the two states, we cannot expect FSSH to reproduce the atomic movement exactly, even for short times.

However, in later times, the nuclear wave function components on the two Born–Oppenheimer surfaces will evolve nearly independently from each other, due to the large electron hopping, as can be seen from Fig. 14(c). The antibonding contribution stays localized around $q = 0$, while the bonding (lower Born–Oppenheimer state) contribution separates into both potential energy minima. The electron in the bonding contribution is mostly localized on the different Holstein dimer sites, while in the antibonding contribution, the electron rapidly oscillates between the sites. The snapshot of the diabatic probability densities in Fig. 14(d) captures a moment in which the electron in the antibonding contribution is completely delocalized.

This specific local state poses an additional problem for the FSSH method: the occurrence of frustrated hops. Since the nuclear wave function is initialized around $q = 0$, almost all classical trajectories from the lower surface will never have enough kinetic energy to perform a hop to the upper surface. Only trajectories starting on the upper surface can hop to the lower surface and, since they keep their high kinetic energy, later hop back to the upper surface. This asymmetry leads to incorrect electronic occupations of the Born–Oppenheimer surfaces, as seen in Fig. 15(a). The decoherence correction dampens this effect to keep the electronic occupations of the Born–Oppenheimer surfaces close to 0.5, as ED, MCE, and also the MTE method obtain.

In addition to the long-time effect of the frustrated hops, the surface-hopping methods cannot reproduce the short-time evolution of the average phonon position $\langle \hat{q} \rangle$ [see the inset Fig. 15(c)]

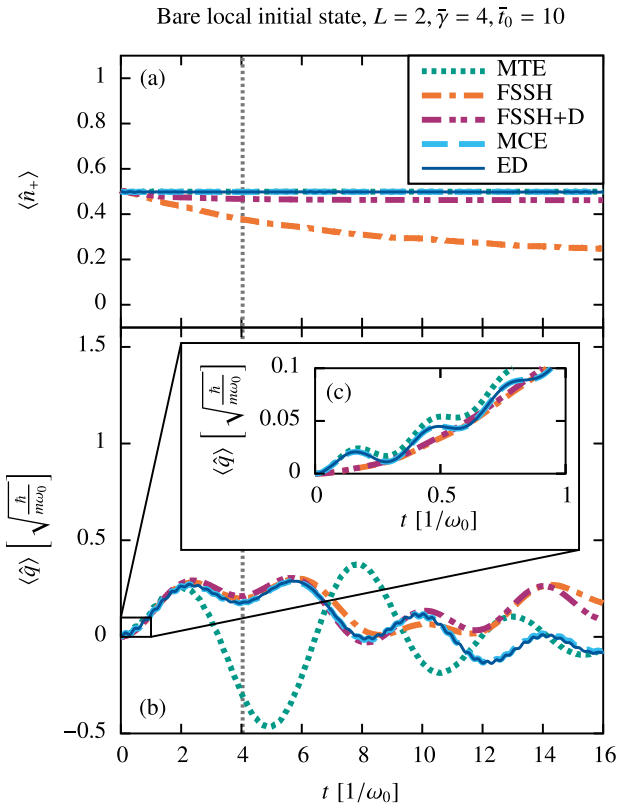

FIG. 15. Time evolution of the (a) electronic occupation of the upper Born–Oppenheimer surface $\langle \hat{n}_+ \rangle$ and (b) average phonon coordinate $\langle \hat{q} \rangle$, starting from the bare local initial state in the Holstein dimer with $\bar{\gamma} = 4$ and $\bar{t}_0 = 10$, for the methods MTE, FSSH, FSSH + D, ED, and MCE (see Secs. IV B, V, and VI). The inset (c) depicts the magnified short-time evolution of the average phonon coordinate. MTE, FSSH, and FSSH + D use 20 000 trajectories and $\Delta t = 0.01/\omega_0$, MCE uses 60 configurations, and ED 250 eigenstates. The energy drift of MCE does not reach $0.2\,\hbar\omega_0$ in the time window shown. The vertical gray line indicates the time of the snapshot shown in Figs. 14(c) and 14(d).

and fail to describe the initial small-scale oscillations of the average nuclear position. This deviation is caused by the aforementioned shortcoming of the adiabatic FSSH method to correctly calculate nuclear forces for an initial state with coherences between the adiabatic states. Intriguingly, the surface-hopping methods reproduce the average phonon position for longer times much better than MTE [see Fig. 15(b)]. The failure of the MTE method can be understood from its difficulties in reproducing the separation of the upper and lower part of the nuclear wave function visible in Fig. 14, as already seen for the adiabatic initial state in Sec. VII A.

None of the independent-trajectory methods is able to reproduce the small-scale oscillations of $\langle \hat{q} \rangle$ of the exact results for longer times. They correspond to the fast oscillation of the anti-bonding contribution of the nuclear wave function and thus to a fast oscillation of the electron between the Holstein sites. Thus, the long-term oscillations of the electron densities on the Holstein sites are also not reproduced (not shown here). The FSSH + D method loses this fast oscillation the quickest, while it is able to describe the average long-term behavior better than MTE and FSSH without decoherence.

Nonetheless, this initial configuration demonstrates that adiabatic surface-hopping methods have significant difficulties in describing initial states that already start with strong coherences between different Born–Oppenheimer states, i.e., off-diagonal elements in the adiabatic representation of the electronic density matrix. In addition, we see the effect of frustrated hops, which is the most severe when the nuclear trajectories have little momentum compared to the potential energy splitting in the non-adiabatic region.

MCE does not reach an energy drift of $0.2\,\hbar\omega_0$ in the time interval shown and is in excellent agreement with the exact results. Thus, it appears to be the method of choice.

C. Bare local initial state with small electron hopping

Next, we stay with the bare local initial state, but study a system with reduced electron hopping $\bar{t}_0 = 0.5$, also called the resonant regime (see, e.g., Ref. 139). This is far away from an adiabatic parameter regime, and surface transitions around $\bar{q} = 0$ are very likely. We stay in the strong-coupling regime with $\bar{\gamma} = 2$. Starting from the bare charge-density wave, published results for larger systems[88] suggest the formation of plateaus in the electronic occupations for these parameters. They can occur when most of the nuclear wave packet evolves away from $\bar{q} = 0$ to the local minima of the lower energy surface $\bar{q} \approx \sqrt{\bar{\gamma}^2 - \bar{t}_0^2/\bar{\gamma}^2}$. Therefore, the plateaus correspond to a transient local electron trapping. However, we can only expect them to occur for short times before the nuclear wave packet spreads in the whole nuclear configuration space.

The comparison of ED, MCE, and the independent-trajectory methods is shown in Fig. 16. We observe that among the independent-trajectory methods, only MTE reproduces the first electronic population plateau at roughly the correct height, while the surface-hopping methods both obtain a too low value. After the first plateau, all of the independent-trajectory methods start to largely

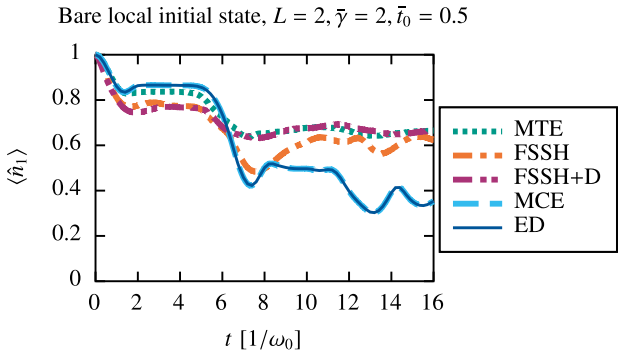

FIG. 16. Electronic occupation of the first, initially occupied, dimer site $\langle \hat{n}_1 \rangle$ for the bare local initial state in the Holstein dimer with $\bar{\gamma} = 2$ and $\bar{t}_0 = 0.5$. We compare the results of the methods MTE, FSSH, FSSH + D, ED, and MCE (see Secs. IV B, V, and VI). MTE, FSSH, and FSSH + D use 20 000 trajectories and $\Delta t = 0.01/\omega_0$, MCE uses 150 configurations, and ED 250 eigenstates. The energy drift of MCE does not reach $0.2\,\hbar\omega_0$ in the time window shown.

deviate from the numerically exact results. In particular, the decoherence correction of FSSH has a detrimental effect on the accuracy of describing the electron density $\langle \hat{n}_1 \rangle$: Since the wave function is relaxed to the adiabatic states, the coherences between these states are lost even faster than in the other independent-trajectory methods. The failure of the FSSH methods to describe the short-time evolution illustrates the difficulties of these methods to deal with these coherences, especially in such a fast-phonon parameter regime. We note that this initial state is a difficult scenario and that local initial states that start away from $\bar{q} = 0$ are already easier to describe with FSSH. Similar to the large electron-hopping case studied before (Sec. VII B), the energy drift of MCE does not reach $0.2\,\hbar\omega_0$ in the time interval shown, and we observe a very good agreement between MCE and exact diagonalization.

D. Tunneling transition of a dressed local initial state

As a last example for the dimer, we analyze the even more difficult question of the slow tunneling of an electron between the two dimer sites for the dressed local initial state. The long-time results are displayed in Fig. 17, again for $\bar{\gamma} = 2$ and $\bar{t}_0 = 0.5$. We observe slow tunneling with a period of $T \approx 100\pi/\omega_0$ between the two dimer sites. This fits the calculated eigenenergies obtained from our exact-diagonalization method, which predicts an energy splitting of the two lowest eigenstates of $\Delta E \approx 0.02\hbar\omega_0$. The dressed local initial state can be described well as a coherent superposition of these two eigenstates, which are a symmetric and an anti-symmetric combination of Gaussians localized to the two potential energy minima of the Holstein dimer, with an only very little contribution on the upper Born–Oppenheimer surface. Unsurprisingly, all of the independent-trajectory methods stay in the initial potential minimum and do not reproduce the tunneling to the other minimum at all. The classical nuclear kinetic energy of the bonding part of the nuclear wave function is too low to overcome the tunneling barrier. In contrast, the MCE method is able to partially capture the tunneling effect to the other dimer site. This is only possible because some configurations move to the other dimer site, which can be further facilitated in this method by using a larger initial electronic spread for the quantum superposition sampling (see Sec. VI B). We note that using the MCEv2 method (see Sec. VI) with additional initial configurations mirrored from the initially occupied to the unoccupied site, we could observe a complete recurrence of the density $\langle \hat{n}_1 \rangle \to 1$ after one tunneling period (results not shown here). This and other extensions of MCE that include tunneling, see, for example, Refs. 264 and 265, are not discussed further in this work. Extensions of the independent-trajectory methods to include tunneling effects[266,267] are beyond the scope of this work as well, where we will focus on the short-time dynamics in the following examples. However, one should keep the inherent lack of tunneling effects in the independent-trajectory methods in mind.

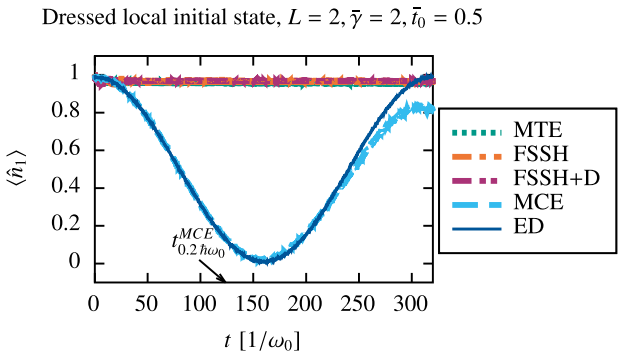

FIG. 17. Electronic occupation of the first, initially occupied, dimer site $\langle \hat{n}_1 \rangle$ for the dressed local initial state in the Holstein dimer with $\bar{\gamma} = 2$ and $\bar{t}_0 = 0.5$. We show the long-time results for the methods MTE, FSSH, FSSH + D, ED, and MCE (see Secs. IV B, V, and VI). MTE, FSSH, and FSSH + D use 20 000 trajectories and $\Delta t = 0.01/\omega_0$, MCE uses 200 configurations, and a larger standard-deviation in the initial quantum superposition sampling of the electronic coefficients of $\sigma_{el} = 1/\sqrt{\alpha}$, with the compression parameter α (see Sec. VI B for details). ED uses 250 eigenstates. The energy drift of MCE reaches $0.2\,\hbar\omega_0$ at $t^{MCE}_{0.2\,\hbar\omega_0} = 123.7/\omega_0$.

E. Summary for the Holstein dimer

In this section, we compared MTE, MCE, and FSSH to numerically exact results in the Holstein dimer. The presented examples illustrate some of the typical non-adiabatic effects trajectory-based methods need to look out for. This includes non-adiabatic transitions of an excited initial state (Sec. VII A), built-in coherences between different adiabatic basis states due to the choice of the initial state (Sec. VII B), and a combination of both, here in a fast-phonon regime (Sec. VII C). MTE, which is basis-independent, is able to describe the short-time dynamics in all cases but fails to capture independent dynamics on different adiabatic surfaces. Thus, as soon as this becomes relevant in the real-time dynamics, e.g., after the first surface transition in the adiabatic initial state (Fig. 13), after the initial build-up of phonons in the bare local initial state (Fig. 15), or after the end of the first local-trapping plateau in the fast-phonon regime (Fig. 16), the MTE results deviate significantly from the exact results.

The FSSH methods, in contrast, are well suited to describe independent components of the nuclear wave function on different energy surfaces and can capture non-adiabatic transitions between surfaces well. They are less accurate, however, when the coherences between the adiabatic states become important, either because previously separated portions of the nuclear wave function meet again (Fig. 12) or because the initial state is already in a highly coherent superposition of different adiabatic states, as for the bare local electron (Figs. 15 and 16). Intriguingly, the problematic coherences of the local initial states have a tendency to decay for later times, most pronounced in an approximately adiabatic parameter regime (Sec. VII B). Here, the qualities of FSSH, approximately obeying detailed balance and being able to describe a wave-function splitting, can lead to a much better long-time agreement with numerically exact results. The fast-phonon (slow electron) example (Fig. 16) shows that this is not true for all cases and one should analyze both system parameters and the initial state to make an assessment of the accuracy of the FSSH methods. The decoherence correction improves the average phonon quantities in the long-time regime and is able to remedy some of the frustrated-hop problem of FSSH for the very low nuclear kinetic energies studied in this work (Figs. 13 and 15). However, the artificial removal of coherences between the

adiabatic states can lead to detrimental results when exactly these coherences are important for describing the initial state (Fig. 16). Both MTE and the FSSH methods are not able to describe a slow tunneling transition in the classical energetically forbidden regime (Fig. 17). Combined with the problem of frustrated hops and, in general, the quantum nature of phonons, the independent-trajectory methods seem more promising if the phonons are initially prepared in a thermal state, which is, however, not studied in this work.

The MCE method produces remarkable results for all initial states and is in very good agreement with the ED data. In addition, it is, for the system and method parameters used, in most cases computationally even cheaper than the independent-trajectory methods (which, however, are easier to parallelize). In this small system, MCE, as an example of a coupled-trajectory method, seems to be the method of choice. It is even able to capture some of the tunneling transition, but special care must be taken in the choice of the initial basis and a perfect transition is difficult to achieve, at least in MCEv1 (Fig. 17).

VIII. RESULTS FOR THE HOLSTEIN TRIMER

For the extended systems ($L > 2$) with one electron, we concentrate on the parameters $\bar{\gamma} = \bar{t}_0 = 2.5$, which have already been used for the adiabatic initial state in the Holstein dimer (see Sec. VII A) and for the calculation of the Born–Oppenheimer surfaces of the Holstein trimer in Sec. III C. With these parameters, we stay in the strong-coupling regime and an intermediate electron hopping, which is neither in the near-adiabatic regime displayed in Sec. VII B nor in the rather unphysical fast-phonon regime of Sec. VII C. These parameters put all studied methods to a test, as both non-adiabatic transitions and high phonon numbers need to be captured correctly.

For the Holstein trimer, the Born–Oppenheimer surfaces are still easy to visualize, as illustrated in Figs. 4 and 5, which is useful to understand the qualitatively different behavior of the independent-trajectory methods MTE and FSSH, also for the Holstein chain (Sec. IX). These two methods are again compared to MCE and ED, where for the exact diagonalization, we now resort to the description in the second quantization from Sec. IV A. The occupation of the Born–Oppenheimer states $\langle \hat{n}_a^{BO} \rangle$, as well as adiabatic initial states, is not calculated in our implementation of this method. We nonetheless start with one adiabatic initial condition, as one would typically study in a quantum-chemistry problem and then turn to two different local initial states. These local states are typical initial conditions of one-electron problems studied in recent quantum-many body investigations, for example, in Refs. 87 and 88 for the Holstein chain, and will also be investigated for the Holstein chain in Sec. IX.

A. Adiabatic initial state

We start with an example where the wave function is initially restricted to one of the three Born–Oppenheimer energy surfaces of Fig. 5, which we again call an adiabatic initial state. We choose the middle, "non-bonding," Born–Oppenheimer surface E_1^{BO}. For the phonons, we choose a coherent state around $\bar{x}_a = 0, \bar{x}_s = 2\bar{\gamma}/\sqrt{3} \approx 2.887$, corresponding to a phonon cloud present on the central Holstein site, while the edge phonon modes are in their ground state. This phonon state is equivalent to the dressed local state investigated later (Sec. VIII B). We can understand this state as a dressed local state, where the electron has suddenly been removed and placed into the non-bonding adiabatic state, with its electron density concentrated on the edge sites. We depict the electronic density on the central site and the average symmetric phonon distortion in Fig. 18.

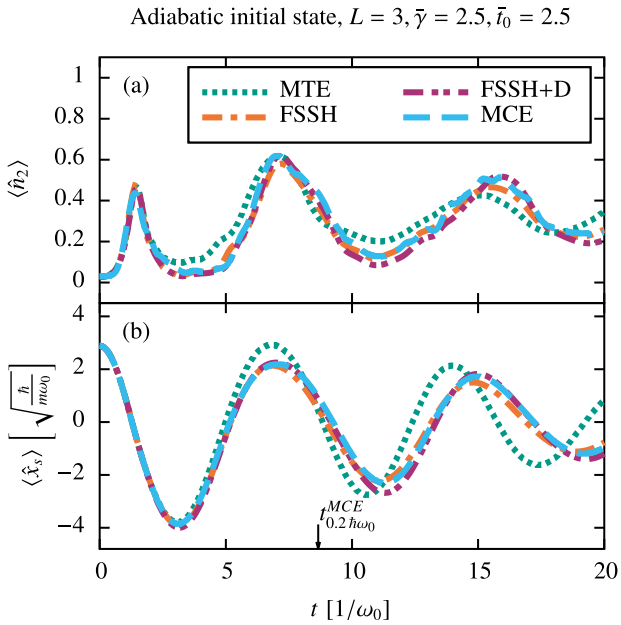

FIG. 18. Time evolution of (a) the electronic population on the central site $\langle \hat{n}_2 \rangle$ and (b) the symmetric phonon mode $\langle \hat{x}_s \rangle$, starting from the non-bonding initial state ($\langle \hat{n}_1^{BO}(\bar{t} = 0) \rangle = 1$) around $\bar{x}_a = 0, \bar{x}_s = 2\bar{\gamma}/\sqrt{3}$ in the Holstein trimer with $\bar{\gamma} = 2.5$ and $\bar{t}_0 = 2.5$. We show results obtained from the methods MTE, FSSH, FSSH + D, and MCE (see Secs. V and VI). The independent trajectory methods use 20 000 trajectories and $\Delta t = 0.001/\omega_0$, and MCE uses 1200 configurations. The energy drift of MCE reaches $0.2\,\hbar\omega_0$ at $t^{MCE}_{0.2\,\hbar\omega_0} = 8.66/\omega_0$.

The figure illustrates that about half of the electronic density quickly moves to the central site, as the symmetric phonon mode goes through zero, but oscillates back as the phonon mode continues to larger negative values. From the shape of the Born–Oppenheimer surfaces (Fig. 5), we know that the non-bonding and the bonding electronic state for these negative values of $\langle \hat{x}_s \rangle$ (and with $\langle \hat{x}_a \rangle \approx 0$) are almost equivalent and have only very little electronic contribution on the central site. After this initial transition, the electronic population on the central site and the symmetric phonon mode oscillate synchronously since now most of the electronic population has relaxed to the ground state.

We conclude that FSSH, especially with the decoherence correction, is able to describe this time evolution predicted from MCE very well. In addition, MTE exhibits not too large deviations from the MCE results for short times. However, for longer times, it is not able to predict the same oscillation frequency of

the symmetric phonon mode $\hat{x}_s$ as obtained from FSSH and MCE. For this adiabatic initial state, FSSH appears to be a very suitable independent-trajectory method, with even higher accuracy for later times than in the Holstein dimer (Fig. 13). We attribute this to the larger system size and the beneficial shape of the Born–Oppenheimer surfaces: The region where the non-bonding and the bonding surface come close to each other is also the region where they result in mostly the same forces. This might also lead to the rather good performance of MTE: even if the surface splitting is not perfectly described, the effect on the nuclear dynamics is only minor for short times. For later times, of course, this is not true anymore. We note that MCE shows an energy drift (with $t^{MCE}_{0.2\,\hbar\omega_0} = 8.66/\omega_0$), and data at later times should be interpreted with some caution.

B. Local initial states

Next, we analyze two local initial states, the bare and dressed local state [see Figs. 1(d) and 1(e)]. We start with the bare local initial state where all phonon harmonic oscillators are in the ground state and the electron is localized to one trimer site. We choose the electron to be localized initially to the central site: $\langle \hat{n}_2(t=0)\rangle = 1$. The results presented here differ only quantitatively when we choose an edge site instead.

The ground-state configuration of the phonons corresponds to a Gaussian distribution on each site centered around $\bar{x}_i = 0$. In the reduced trimer coordinates defined in Eq. (5), it is centered around $\bar{x}_s = \bar{x}_a = 0$. As described in Sec. III C, the second, non-bonding Born–Oppenheimer state has no electronic contribution on the central site for zero anti-symmetric distortion $\bar{x}_a = 0$ (the red lines in Fig. 5). Here, the localized electron occupies only the lowest, bonding and highest, anti-bonding Born–Oppenheimer state, in fact, with an equal weight. Due to the finite width of the Gaussian distribution, the electron will nonetheless have a (smaller) contribution in the non-bonding Born–Oppenheimer state. Similar to the bare local state in the dimer (Secs. VII B and VII C), this initial state is rather distinct from a pure adiabatic state and coherences between the adiabatic basis states are important.

The occupation of the lowest Born–Oppenheimer state is depicted in Fig. 19(a). MTE builds up a much smaller occupation of the lowest Born–Oppenheimer state compared to the surface-hopping methods or MCE. MCE predicts occupations of the lowest Born–Oppenheimer state between FSSH with and FSSH without decoherence for intermediate times. Note that the energy drift of MCE reaches $0.2\,\hbar\omega_0$ at $t^{MCE}_{0.2\,\hbar\omega_0} = 8.16/\omega_0$ (see Sec. VI D). FSSH without decoherence shows the largest relaxation to the lowest Born–Oppenheimer state, similar to the case of large electron hopping, investigated for the Holstein dimer in Sec. VII B.

For the dynamics of the electronic population on the central Holstein site, the independent-trajectory methods are again not able to reproduce the persisting fast oscillations between the sites at late times [see Fig. 19(b)]; however, the FSSH methods seem to describe the average occupation slightly better than MTE.

Finally, we observe large deviations in the average symmetric phonon distortion $\langle \hat{x}_s\rangle$ in Fig. 19(c). MTE deviates strongly from ED already after $t \approx 2.5/\omega_0$, and also the surface-hopping methods do not quantitatively reproduce the later time evolution. However, they recover the qualitative oscillations in the observable until $t \approx 15/\omega_0$.

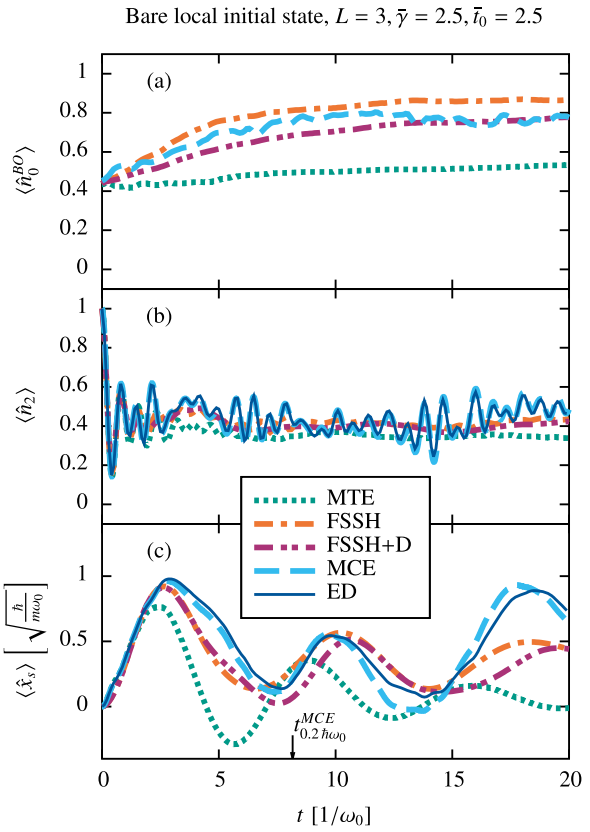

FIG. 19. Time evolution of three observables starting from the bare local initial state at the central site in the Holstein trimer with $\bar{\gamma} = 2.5$ and $\bar{t}_0 = 2.5$. We show (a) the occupation of the lowest Born–Oppenheimer state $\langle \hat{n}_0^{BO}\rangle$, (b) the electronic population on the central site $\langle \hat{n}_2\rangle$, and (c) the symmetric phonon mode $\langle \hat{x}_s\rangle$, for the methods MTE, FSSH, FSSH + D, ED, and MCE (see Secs. IV A, V, and VI). The independent trajectory methods use 20 000 trajectories and $\Delta t = 0.001/\omega_0$, ED uses 26 local phonon states, and MCE 1000 configurations. The energy drift of MCE reaches $0.2\,\hbar\omega_0$ at $t^{MCE}_{0.2\,\hbar\omega_0} = 8.16/\omega_0$.

We also see noticeable deviations between ED and MCE when the energy drift becomes too large at times $t > t^{MCE}_{0.2\,\hbar\omega_0}$.

Next, we consider the dressed local initial state where a coherent phonon state on the initially occupied central site dresses the electron. This corresponds to a Gaussian distribution around zero for the edge sites and around $\bar{x}_2 = \sqrt{2}\bar{\gamma}$ for the central site, or equivalently in the trimer coordinates, $\bar{x}_a = 0$ and $\bar{x}_s = 2\bar{\gamma}/\sqrt{3} \approx 2.887$, as for the adiabatic state studied before (Sec. VIII A).

The occupation of the initially occupied central Holstein site is displayed in Fig. 20(a). As always for the local initial states, the independent-trajectory methods cannot reproduce the small-scale oscillations of the electronic density for long times. MTE is also not able to reproduce the average electron density, i.e., too much electronic weight is shifted to the edge sites. Moreover, the average symmetric phonon distortion $\langle \hat{x}_s\rangle$ in Fig. 20(b) is not correctly described in MTE, while the FSSH methods show qualitatively the correct large-scale oscillations. There are no large deviations

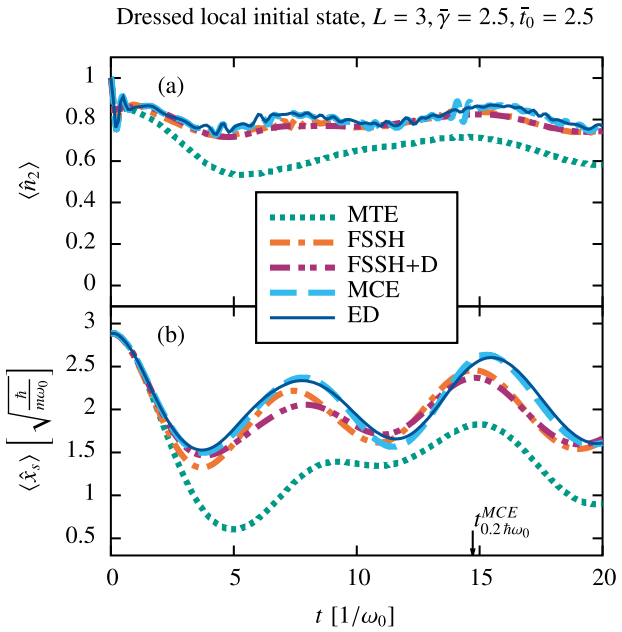

FIG. 20. Time evolution of (a) the electronic population on the central site $\langle \hat{n}_2 \rangle$ and (b) the symmetric phonon mode $\langle \hat{x}_s \rangle$ starting from the dressed local initial state at the central site in the Holstein trimer with $\bar{\gamma} = 2.5$ and $\bar{t}_0 = 2.5$, for MTE, FSSH, FSSH + D, ED, and MCE (see Secs. IV A, V, and VI). The independent trajectory methods use 20 000 trajectories and $\Delta t = 0.001/\omega_0$, ED uses 21 local phonon states, and MCE 1000 configurations. The energy drift of MCE reaches $0.2\,\hbar\omega_0$ at $t^{MCE}_{0.2\,\hbar\omega_0} = 14.72/\omega_0$.

between ED and MCE, consistent with a small energy drift that reaches $0.2\,\hbar\omega_0$ only at $t^{MCE}_{0.2\,\hbar\omega_0} \approx 14.72$.

For both local initial states, MTE has problems to even qualitatively describe the correct long-time behavior. We attribute this failure to the inability of MTE to correctly describe a wave-function splitting (see Fig. 12) because of the mean-field description of the electron–phonon coupling. Describing the wave-function splitting correctly is even important for these local initial states, as illustrated in the Holstein dimer (see Fig. 14). For the bare local initial state [Fig. 19(a)], we observe nearly no relaxation toward the lowest Born–Oppenheimer state in the MTE simulation. The dynamics are influenced too much by the large initial occupation of the highest Born–Oppenheimer state, which has its potential energy minimum at $\bar{x}_a = \bar{x}_s = 0$. In the dressed local initial state, too much electronic weight in the MTE simulation is able to escape the local trapping on the central site (Fig. 20). While the state has a large initial contribution in the lowest Born–Oppenheimer state $\langle \hat{n}_0^{BO}(t=0) \rangle \approx 0.922\,25$, the remaining weight in the higher states shifts part of the electron from the potential energy minimum corresponding to the central site ($\bar{x}_s = \bar{\gamma}$) to the other two minima (see the Born–Oppenheimer surfaces, Figs. 4 and 5). In summary, the dynamics in MTE are influenced too much by the higher Born–Oppenheimer states, as also observed in other comparative studies, e.g., Ref. 268, and the method has difficulties to describe the formation of stable localized charge carriers.

From the Holstein dimer, we have seen that FSSH faces challenges as well, in particular, for local initial states, which resurface in the Holstein trimer. The low kinetic energy of the phonons leads to frustrated hops, most pronounced without the decoherence correction, and thus to an overestimation of the relaxation to the lower Born–Oppenheimer surfaces [see Fig. 19(a)]. The effect is less severe here due to the moderate strength of the electron-hopping parameter and the different structures of the Born–Oppenheimer surfaces of the trimer (see Fig. 5). Second, FSSH has difficulties describing the correct short-time behavior of both electron densities and nuclear oscillations due to the missing coherences between the Born–Oppenheimer states for the calculation of the nuclear forces. The decoherence correction worsens this deficiency for the electron density, as it actively dampens out these coherences. This effect seems to be much less relevant for the two cases investigated here, compared to the Holstein dimer. The dressed local initial state is less affected by both problems, as it is much closer to an adiabatic initial state.

For the parameters chosen here, and in general for sufficiently fast electrons, the independent-trajectory methods seem to perform better if the wave function has initially contributions only in a single adiabatic state. Despite the difficulties of the surface-hopping methods in describing a local initial state, we observe a good qualitative agreement of the long-time behavior of the investigated observables, in contrast to the MTE method. The coupled-trajectory method MCE outperforms both independent-trajectory methods. As long as the energy drift is sufficiently small, it reveals a very good agreement with the ED results, at a still very low computational cost.

IX. RESULTS FOR THE HOLSTEIN CHAIN—ONE ELECTRON

We now turn to the spatial spreading of a single localized electron in Holstein chains of lengths $L = 11$ and 51. All observables and methods were also compared for $L = 101$, which, however, provides no new insight over the $L = 51$ results and is not shown here. We stay in the intermediate regime of $\bar{\gamma} = \bar{t}_0 = 2.5$, analyzed before for the Holstein trimer.

In our study, we want to investigate the detailed short-time evolution of a localized charge carrier when the phonon subsystem is not yet adjusted to the electron (bare initial state) or is only locally equilibrated (dressed initial state). These two cases correspond precisely to the "Franck–Condon excitation" and "relaxed excitation" analyzed in Ref. 87 with a matrix–product state method for $\bar{t}_0 = 1$. A comparison to the data of Ref. 87 is included in Appendix B. Our conclusions for the trajectory-based methods studied here also hold for that parameter set.

The evolution of such localized states has previously been investigated in a periodic dispersive Holstein model with the variational Davydov D2 ansatz for 32 sites,[256] which also considered off-diagonal electron–phonon coupling, and with the hierarchical equations of motion method for ten sites.[115] The latter was compared to MCE,[117] with a good agreement of both methods for the system parameters investigated in that study. Furthermore, the spreading, and relatedly the mobility, of a local initial state in a large system has been investigated using the surface-hopping methods (see, e.g., Refs. 231 and 243, and references therein). Typically, in

these studies, the phonons are initially prepared in a thermal state and the long-time behavior is analyzed. For an extensive discussion of such initial states and the classification of transport in strongly correlated 1D systems from the perspective of condensed matter theory and quantum many-body methods (see Ref. 269).

In all following sections, we compare the trajectory-based methods to the numerically exact DMRG-LBO results, which we will denote simply as DMRG. In FSSH without decoherence, we use the mixed definition of the electronic density matrix $\hat{\rho}_{el}^{(\mathrm{mixed})}$ [see Eq. (39)], while with the restricted decoherence correction, we use the wave-function definition of the density matrix $\hat{\rho}_{el}^{(\mathrm{WF})}$ [see Eq. (38)]. In contrast to the small systems studied before, we reach convergence of the MCE simulation for most observables only for very short times (see Sec. VI D). Identifying a useful total energy-drift convergence criterion, as done for the dimer and trimer case, is not easily done here, as the relevant energy scales of many of the studied observables become very small. The MCE simulations in this section are done with $N_c = 5000$ configurations. As can be seen from the convergence study in Fig. 11, this is not enough to consider MCE as an exact method for all observables studied here, and further convergence for even higher N_c is very slow. Similar to MTE and FSSH, we will thus judge the accuracy of the MCE results by comparing them to the DMRG simulation.

A. Bare local initial state

We start with the bare local initial state, with the electron placed on the central site of the Holstein chain [see Fig. 1(d)]. We show the time evolution of the electron densities on the different sites in Fig. 21 for the two system sizes obtained from the methods DMRG, MCE, MTE, and FSSH without and with restricted decoherence.

The DMRG results are only available for short times for all system sizes. During that time window, a part of the electron density first shows a ballistic spreading until $t \approx 2/\omega_0$, while it stays mostly localized after that. For $L = 11$ [Fig. 21(a)], the electron density already reaches the boundaries of the system by that time and is reflected there, while for $L = 51$ [Fig. 21(b)], it stays localized in the center for later times and does not reach the chain boundary in the simulated time interval.

All other methods reproduce the initial ballistic spreading at short times, but deviate from DMRG for later times. The electron densities obtained from MCE agree very well with the DMRG results for $L = 11$ [Fig. 21(c)], where almost no quantitative difference is visible. For $L = 51$ [Fig. 21(d)], we find a similar excellent agreement for the electron densities on sites close to the initially occupied central site. In contrast, MCE, at least with the number of configurations used here, is not able to contain the electron density in a localized region for later times in this larger system. Instead, a small portion of the electron density continues to spread ballistically through the system and reaches the chain boundaries. This ballistic escape comes along with a weak periodic modulation with the phonon oscillation period. The situation becomes much worse for MTE [see Figs. 21(e) and 21(f)], which displays a broad delocalization of the electron density for times $t > 2/\omega_0$ for both system sizes, not observed in any of the other methods. Since the nuclear trajectories of MCE follow the Ehrenfest equations of motion, this might explain the poor convergence of MCE in this setup, as illustrated in Sec. VI D.

FSSH without [Figs. 21(g) and 21(h)] and with decoherence [Figs. 21(i) and 21(j)] predict a very similar electronic density for $L = 11$ as MCE and DMRG. For $L = 51$, both FSSH methods reproduce the localization after the initial ballistic expansion, also observed in the DMRG results. The width of this localized electron

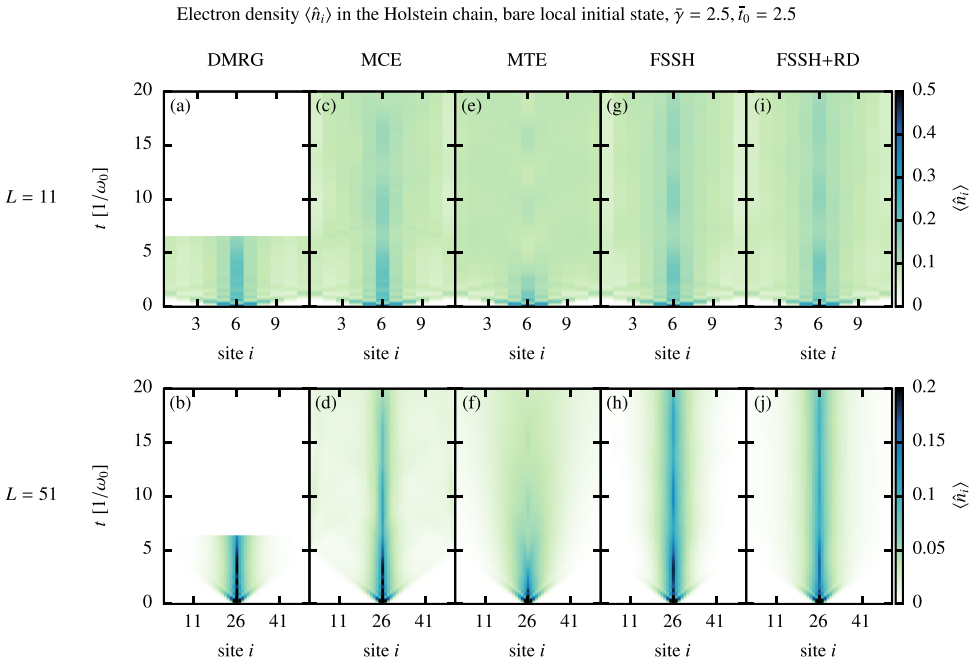

FIG. 21. Electron densities $\langle \hat{n}_i \rangle$ in the Holstein chain, starting from the bare local electron on the central site with $\bar{\gamma} = \bar{t}_0 = 2.5$. We show the results for $L = 11$ and 51 lattice sites in the two rows, obtained from the methods DMRG [(a) and (b)], MCE [(c) and (d)], MTE [(e) and (f)], and FSSH without [(g) and (h)] and with restricted decoherence [(i) and (j)] in the five columns (see Secs. IV C, V, and VI). For better visibility, the maximum color range is set to $\langle \hat{n}_i \rangle = 0.5$ for $L = 11$ and to $\langle \hat{n}_i \rangle = 0.2$ for $L = 51$. In DMRG, we use $\epsilon_{\mathrm{LBO}} = 10^{-8}, \epsilon_{\mathrm{bond}} = 10^{-8}$, $\Delta t = 0.004/\omega_0$, and $M = 40$. For MCE, we use 5000 configurations initialized with the pancake-like sampling, and for the independent trajectory methods, we use 20 000 trajectories and $\Delta t = 0.001/\omega_0$.

density does, however, not match the DMRG results exactly, as analyzed later with the reduced mean-squared displacement (Fig. 23). FSSH without decoherence recovers the dynamics of the electron density slightly better than with decoherence, which was already observed in the dimer (see Sec. VII C). The electron density obtained from FSSH without decoherence has small fluctuations on the sites far away from the center for $L = 51$, which are not visible in Fig. 21(h) because of their very small amplitude. They are caused by the mixed calculation of the electron density matrix via Eq. (39). While they seem unproblematic in Fig. 21(h), they prevent an accurate calculation of the reduced mean-squared displacement (see Appendix A). We note that the close agreement of FSSH with FSSH + RD in Fig. 21 is only achieved by using this mixed definition for calculating the electronic density matrix in FSSH without decoherence. The electron density calculated from the wave function spreads similar as in the MTE simulation (see Appendix A), but the distribution of active surfaces is very similar to the FSSH + RD simulation, mostly due to the occurrence of frustrated hops. As pointed out in Ref. 142, frustrated hops help to approximately recover detailed balance. For initial states starting from a thermal phonon distribution, frustrated hops might occur less often and FSSH without restricted decoherence could deviate strongly from the FSSH + RD results.

The agreement of MCE and the FSSH methods with the DMRG results appears to be more reliable close to the initially occupied central site in Fig. 21. We analyze this further for the time evolution of the phonon position on that central site $x_{central}$ in Fig. 22 for $L = 51$ sites. We do not include the $L = 11$ results here, which differ only slightly from the $L = 51$ results for this observable. In this observable, there is no significant difference between MCE and DMRG for the times available. Similar to most local initial states observed in this work, MTE describes the evolution at very short times the best among the independent-trajectory methods. For later times, however, the phonon position obtained with MTE oscillates almost around zero, indicating that the electron does not stay sufficiently localized, with most of the electron lost in the broad spreading observed before [Fig. 21(f)]. In contrast, FSSH + RD reveals a remarkable agreement with MCE for the phonon position for later times, albeit not capturing the first maximum at the correct height. FSSH without decoherence correction deviates stronger for later times but still captures the qualitative oscillations of the MCE calculation much better than MTE. Similar to our study in the dimer (Fig. 15), both FSSH methods can reproduce the long-time dynamics surprisingly well, even if the initial state includes coherences between different adiabatic states, thus preventing a completely accurate description of the short-time dynamics.

A good quantitative description of the spread of the electron density is given by the reduced mean-squared displacement (RMSD),

$$\mathrm{RMSD}(t) = \sqrt{\sum_{i=1}^{L} \langle \hat{n}_i(t) \rangle \left(ai - x_0^{el} \right)^2}, \tag{49}$$

where $a \cdot i$ denotes the position of the ith site in the Holstein chain, with a the distance between Holstein sites. $x_0^{el} = \left[\sum_{i=1}^{L} \langle \hat{n}_i(t=0) \rangle ai \right]$ is the average initial electron position, i.e., here the center of the chain. In the following, we set $a = 1$. The reduced mean-squared displacement is depicted in Fig. 23. Note that the reduced mean-squared displacement weights the electronic density on the edge sites much higher than on the central site (with a factor of 625 for the $L = 51$ system). Thus, deviations in the electron density away from

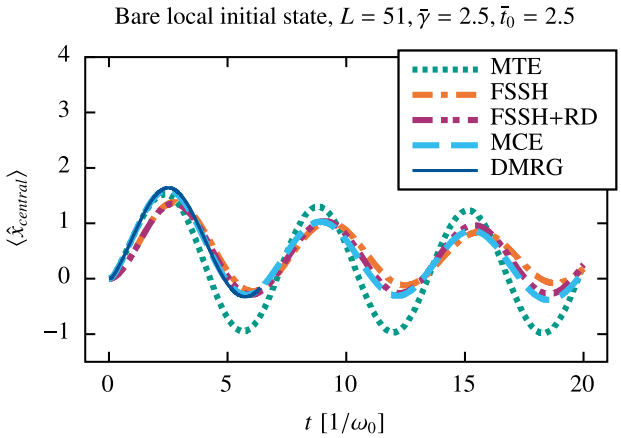

FIG. 22. Phonon position $\langle \hat{x}_{central} \rangle$ on the central, initially occupied site in the Holstein chain, starting from the bare local electron on the central site with $\bar{\gamma} = \bar{t}_0 = 2.5$ for $L = 51$, obtained from the methods MTE, FSSH, FSSH + RD, DMRG, and MCE (see Secs. IV C, V, and VI). We use the same method parameters as in Fig. 21.

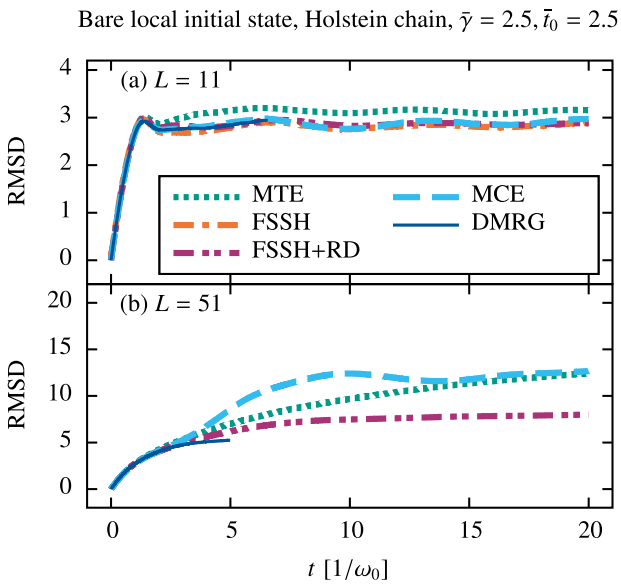

FIG. 23. Reduced mean-squared displacement RMSD in the Holstein chain given via Eq. (49), starting with the bare local electron on the central site with $\bar{\gamma} = \bar{t}_0 = 2.5$ for (a) $L = 11$ and (b) $L = 51$, obtained from the methods MTE, FSSH + RD, DMRG, and MCE (see Secs. IV C, V, and VI). For FSSH without decoherence, only the results for $L = 11$ are included (see Appendix A). We use the same method parameters as in Fig. 21, with the exception of the DMRG cutoffs, which are decreased to $\epsilon_{\mathrm{LBO}} = 10^{-9}$, $\epsilon_{\mathrm{bond}} = 10^{-9}$ for $L = 51$.

the initially occupied site are magnified. This also makes the use of FSSH without decoherence difficult (see Appendix A).

For $L = 11$ [Fig. 23(a)], the FSSH, MCE, and DMRG methods show a very good agreement and seem to converge to the same value. MTE, in contrast, obtains a too high long-time value, consistent with the loss of the local electron on the central site, also visible in Fig. 21(e). For $L = 51$ [Fig. 23(b)], we observe that the RMSD obtained from MTE follows a mostly square-root behavior for later times, indicating that the spreading of the density is of a diffusive type. The FSSH + RD data follow the same curve for some time, while the RMSD stays almost constant and thus localized for later times. The long-time value is slightly higher than what is obtained with DMRG for the times available. Note that we sometimes use different cutoffs for the DMRG simulations, since some observables, e.g., the RMSD, converge slower than others. The MCE data exhibit a strong increase of the RMSD for times greater than $t \approx 5/\omega_0$ in this larger system, representative of the ballistic escape of the electron density at those times. We note that this ballistic behavior is observed only for a small portion of the electron density, which, however, becomes the dominant term in the RMSD due to the aforementioned quadratic scaling with the distance from the center of the chain.

Finally, in Fig. 24, we analyze the total phonon number in the system, which is proportional to the energy stored in the phonon subsystem alone (discounting the zero-point oscillator energies). First, the total phonon number in the system is mostly independent of the system size, as expected, since the total initial energy, without the zero-point phonon energy, is the same for all system sizes. No method is able to reproduce the total phonon number obtained in the DMRG simulations, not even for the $L = 11$ system. Even MCE has difficulties in computing this quantity, as it is quadratic in the phonon positions and momenta and is directly influenced by the energy drift (see Sec. VI D). The most significant deviation is observed in MTE, where the total phonon number stays very small. In contrast, the FSSH methods obtain a similar phonon number as MCE for the first maximum, but then stay at these high values, corresponding to the long-time localization observed before. Unfortunately, we cannot unambiguously determine which long-time behavior is correct, as the DMRG data are not available until late times, and all other methods deviate from DMRG before that. From the figure, we observe that FSSH methods are the closest to the DMRG data and we may, therefore, speculate that the FSSH methods also approximate the long-time behavior the closest. However, numerically exact simulations for longer times are needed for further analysis.

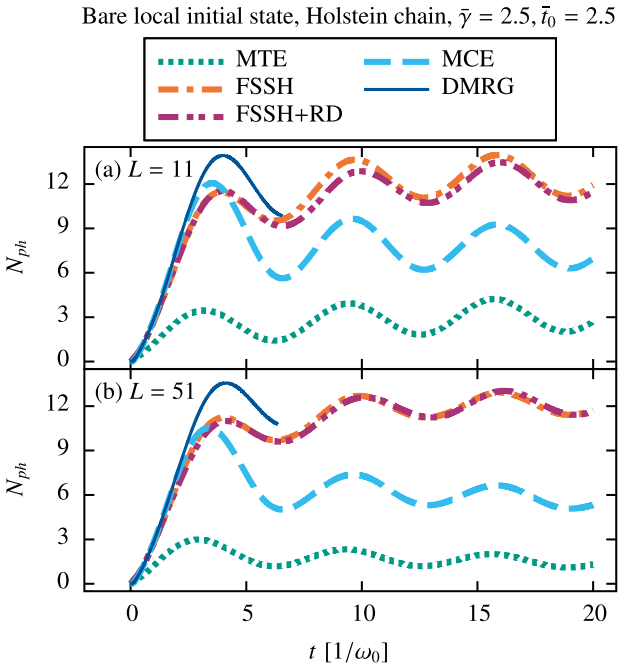

FIG. 24. Total phonon number $N_{ph} = \langle \sum_i \hat{b}_i^\dagger \hat{b}_i \rangle$ in the Holstein chain, starting with the bare local electron on the central site with $\bar{\gamma} = \bar{t}_0 = 2.5$ for (a) $L = 11$ and (b) $L = 51$, obtained from the methods MTE, FSSH, FSSH + RD, DMRG, and MCE (see Secs. IV C, V, and VI). We use the same method parameters as in Fig. 21.

Overall, in the global quantities of the RMSD and the total phonon number, no consistent picture arises from the trajectory-based methods. It remains a promising question for future studies to further investigate the validity of FSSH within the long-time limit, building on existing research on steady-state properties, such as mobilities at finite temperatures.[231,243] As illustrated in various examples in the Holstein dimer and trimer (Secs. VII and VIII), the difficulties of the FSSH method in describing the short-time behavior stem from the local initial state. Here, the bare local initial state is a near-worst-case scenario, as it has an almost equal electronic weight in all Born–Oppenheimer states. Since MTE fails in describing any of the analyzed global quantities, a pure mean-field solution seems to be of limited use for the parameters studied here. A mixture of MTE with a form of decoherence, e.g., the coherent switching with the decay-of-mixing method,[270] might be a promising compromise. Finally, even a coupled-trajectory method, such as MCE, can fail in such large systems, where a good sampling of the relevant Hilbert space is non-trivial. Using an alternative algorithm, which is not based on MTE-guided trajectories, might be beneficial here (see Sec. VI). However, for $L = 11$, MCE still recovers the electron densities, including the RMSD, very well and the phonon position at the central site shows excellent agreement with DMRG for both system sizes. Our assessment of the trajectory-based methods also holds for the parameter regime $\bar{t}_0 = 1$, shown in Appendix B in a comparison with the data from Ref. 87.

B. Dressed local initial state

We now turn to the dressed initial state, again with the electron initially localized to the central site and $\bar{\gamma} = \bar{t}_0 = 2.5$ for $L = 11$ and $L = 51$. We start with the evolution of the electron density displayed in Fig. 25. In contrast to the bare local initial state, we obtain a much stronger localization in all methods, and therefore, we switch to a logarithmic scale for $L = 51$. Most of the observations from the bare local initial state carry over to the dressed initial state.

For $L = 11$, the MCE, FSSH, and FSSH + RD results agree well with the DMRG data for the times available. MTE shows a broad spreading for late times, which deviates from all other methods starting after the first half phonon period in both system sizes. This is similar to the dressed initial state in the trimer (Fig. 20), where the

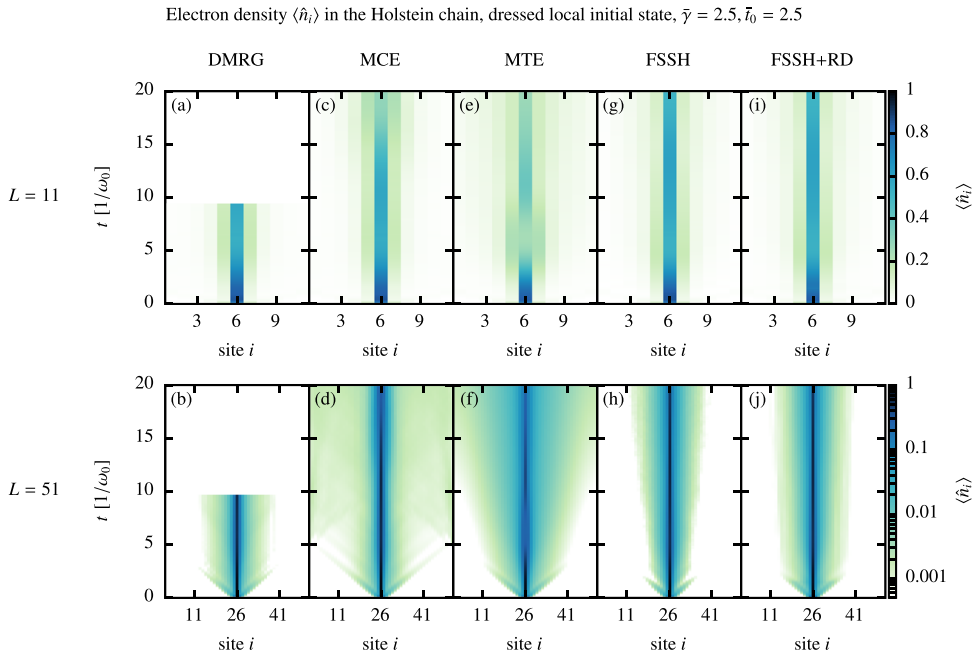

FIG. 25. Electron densities $\langle \hat{n}_i \rangle$ in the Holstein chain, starting from the dressed local electron on the central site with $\bar{\gamma} = \bar{t}_0 = 2.5$. We show the results for $L = 11$ and 51 lattice sites in the two rows, obtained from the methods DMRG [(a) and (b)], MCE [(c) and (d)], MTE [(e) and (f)], FSSH [(g) and (h)], and FSSH + RD [(i) and (j)] (see Secs. IV C, V, and VI) in the five columns. In DMRG, we use $\epsilon_{\text{LBO}} = 10^{-8}$, $\epsilon_{\text{bond}} = 10^{-8}$, $\Delta t = 0.004/\omega_0$, and $M = 40$. MCE uses 5000 configurations initialized with the pancake-like sampling and the independent trajectory methods use 50 000 trajectories and $\Delta t = 0.001/\omega_0$.

initial localization of the electron was partially lost in the time evolution. For $L = 51$, MCE reproduces the electron density around the center well, while it features a small ballistic escape of the electron density to the chain boundaries, not predicted from the DMRG calculation. The width of the electronic density distribution at longer times for $L = 51$ appears to be better recovered with FSSH + RD here [Fig. 27(h)] than for the bare local initial state studied before. FSSH without decoherence, however, apparently produces a more localized electron density compared to the DMRG data after the initial ballistic expansion and features a slow spreading of the electronic density for later times. Note that, due to the logarithmic scale, very small electronic contributions (below 0.0005) are cut off. This hides very small electronic populations developing outside of the localized region in the FSSH method without decoherence (similar to the bare local initial state), only relevant for observables such as the RMSD.

Next, we analyze the nuclear position on the central site for $L = 51$ in Fig. 26. Again, the MCE results for this observable are very close to the DMRG simulation for the times available, while MTE predicts much too low values for the phonon position, similar to the bare local case. We observe that the FSSH methods follow the dynamics of DMRG closely and even outperform MTE in the short-time regime. This is in contrast to the bare local state studied before, where MTE provides a better description for the first phonon oscillation (see Fig. 22), reflecting that the dressed initial state is easier to describe for the FSSH methods than the bare initial state. For long times, MCE, at least for a short duration, appears to come closer to the MTE simulation. We cannot judge whether this is captured correctly, since MCE is less reliable for these times, as mentioned in the convergence analysis from Sec. VI D.

For the global evolution, we again look at the reduced mean-squared displacement in Fig. 27. For $L = 11$, we observe a good agreement of FSSH + RD, MCE, and DMRG, similar to the bare local case. FSSH without decoherence correction displays slight deviations and MTE predicts much too high values. For $L = 51$, we can see a continuous expansion of the RMSD in the MTE data, which increases slightly faster than a pure diffusion curve (a linear fit of the log–log curve reveals a slope of ≈0.6 for times $t > 1/\omega_0$). FSSH + RD is the closest to the DMRG results from the trajectory-based methods and shows only a very small spreading for later times. In the MCE calculation, we have a second increment of the RMSD for intermediate times, similar to the bare local case, but then a transition to a mostly flat value soon after the ballistic part of the density reaches the boundaries of the system.

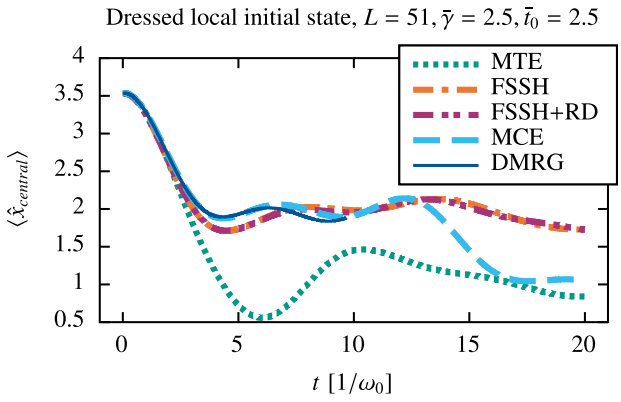

FIG. 26. Phonon position $\langle \hat{x}_{central} \rangle$ on the central, initially occupied site in the Holstein chain, starting from the dressed local electron on the central site with $\bar{\gamma} = \bar{t}_0 = 2.5$ for $L = 51$, obtained from the methods MTE, FSSH, FSSH + RD, DMRG, and MCE (see Secs. IV C, V, and VI). We use the same method parameters as in Fig. 25.

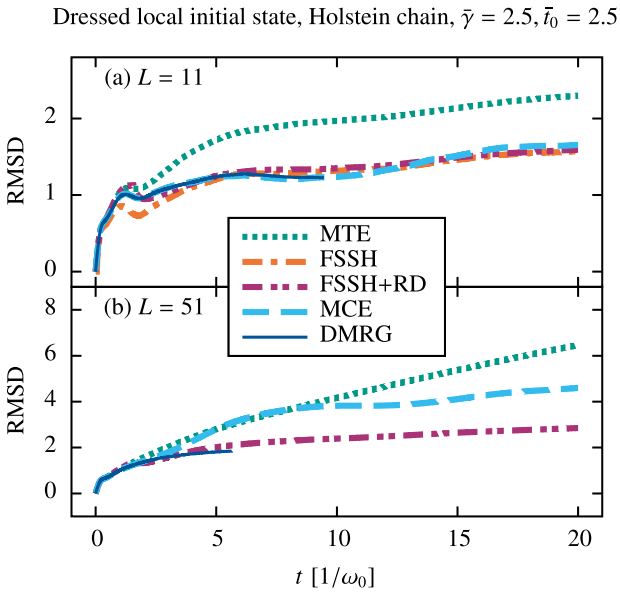

FIG. 27. Reduced mean-squared displacement RMSD in the Holstein chain given via Eq. (49), starting with the dressed local electron on the central site with $\bar{\gamma} = \bar{t}_0 = 2.5$ for (a) $L = 11$ and (b) $L = 51$. We show the results obtained from DMRG, MCE, MTE, and FSSH + RD (see Secs. IV C, V, and VI). For FSSH without decoherence, only the results for $L = 11$ are included (see Appendix A). We use the same method parameters as in Fig. 25, with the exception of the DMRG cutoffs, which are decreased to $\epsilon_{\mathrm{LBO}} = 10^{-9}$, $\epsilon_{\mathrm{bond}} = 10^{-9}$ for $L = 51$.

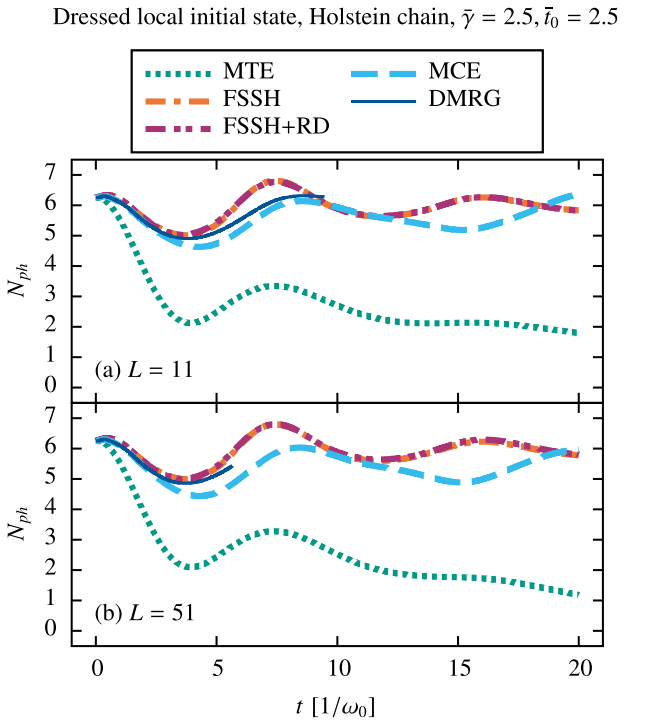

FIG. 28. Total phonon number $N_{ph} = \langle \sum_i \hat{b}_i^\dagger \hat{b}_i \rangle$ in the Holstein chain, starting with the dressed local electron on the central site with $\bar{\gamma} = \bar{t}_0 = 2.5$ for (a) $L = 11$ and (b) $L = 51$, obtained from the methods MTE, FSSH, FSSH + RD, DMRG, and MCE (see Secs. IV C, V, and VI). We use the same method parameters as in Fig. 25, with the exception of the DMRG cutoffs, which are decreased to $\epsilon_{\mathrm{LBO}} = 10^{-9}$, $\epsilon_{\mathrm{bond}} = 10^{-9}$ for $L = 51$.

As the second global quantity, we analyze the total phonon number in Fig. 28. Here, DMRG, MCE, FSSH, and FSSH + RD stay close to the initial value, while MTE completely loses the energy initially stored in the phonon sector, consistent with the broad spreading of the electronic density observed before. Similar to the case of the bare local state, the evolution of the total phonon number is almost independent of the system size. For the dressed local state studied here, however, MCE, FSSH, and FSSH + RD are able to recover the short-time dynamics of DMRG much better.

In summary, for both local initial states, MTE does not form a stable localized phonon-dressed electron distribution. In the Born–Huang notation, we interpret this as an insufficient relaxation to the lowest Born–Oppenheimer state, as already observed in the Holstein trimer (see Sec. VIII). This also poses a challenge for coupled-trajectory methods based on MTE, such as the analyzed MCEv1, where convergence is very difficult to achieve in some observables. While the results of the FSSH methods are still more in a qualitative rather than a quantitative agreement with the DMRG data, at least for $L = 51$, we see a strong improvement in the short-time dynamics of the dressed local state, compared to the bare local case analyzed before (Sec. IX A). We note that a good description of FSSH relies on the improvements mentioned in Sec. V E, especially the decoherence correction, which allows a consistent calculation of the diabatic electronic populations and the RMSD, and the restriction of exactly that decoherence to avoid an unphysical super-fast spreading of the wave function (see Appendix A).

From the results presented here, we conclude that MTE is not well suited to describe the real-time dynamics of an initially localized electron, neither with nor without a phonon dressed state, at least for the system parameters studied here. FSSH is, for many observables, the closest to DMRG and we may thus expect it to provide a reasonable account of the long-time dynamics. Moreover, FSSH works better for the dressed than the bare initial state. The promising coupled-trajectory technique MCE is in excellent agreement with the DMRG results where it can be converged. While the short-time dynamics are well represented for all cases, the Ehrenfest-guided dynamics of the underlying basis set seem insufficient to accurately reproduce the correct long-times values for some observables. Still, for $L = 11$, it is the best trajectory-based method for all studied observables, except for the total phonon number, and for $L = 51$, it shows the most accurate agreement with the DMRG results for the electron density and phonon position on the central site.

The DMRG results give access only to a limited time scale in which the results clearly do not show a diffusive behavior. This is different from some previous studies using, for example, surface hopping for an initial state with the phonons prepared in a thermal state.[231,243] The general transport behavior of 1D correlated models is non-trivial to predict (see Ref. 269). It is possible that our quenched initial states are still in a pre-thermal regime for the time-scales investigated, but with the methods and results available

we cannot yet determine the correct physical long-time behavior of, e.g., the RMSD. Since, for $L = 11$, the electron density quickly reaches the boundaries of the system (see Figs. 21 and 25), our results differ qualitatively between both studied system sizes. Out of all studied examples studied in our work, the results for the time-evolution of local electron states in the Holstein chain (Sec. IX) are the least satisfactory, and further studies are needed in the future.

X. RESULTS FOR THE HOLSTEIN CHAIN—CHARGE-DENSITY WAVES

In this section, we compare the MTE method to DMRG data for the extended Holstein chain close to half filling. This system is known to have a phase transition from a Tomonaga–Luttinger-liquid state to a charge-density wave.[125,126] The non-equilibrium breakdown of the charge-density wave has already been the subject of several studies, e.g., Refs. 88, 102, and 271. To test the MTE method, we compare the results to DMRG data in setups strongly motivated by the results of Ref. 88. Our main goal is to find out whether the MTE method captures the decay of the order parameter and the energy transfer from electronic to vibrational degrees of freedom. The two initial states are similar to those considered in previous sections. Now, however, both the bare and the dressed states have electrons on every other site (see Fig. 2). In Figs. 29(a)–29(c), we show (a) the average phonon number N_{ph}/N, with N the number of electrons, (b) the CDW order parameter O_{CDW}, defined as

$$O_{\mathrm{CDW}} = \frac{1}{N}\sum_{i=1}^{L}(-1)^i\langle\hat{n}_i\rangle, \tag{50}$$

and (c) the electron kinetic energy E_{kin}, calculated with DMRG and MTE. The initial state is the bare CDW, and we use $\bar{\gamma} = 4$ and $\bar{t}_0 = 10$. In Fig. 29(b), we see that the order parameter is well described by the MTE method. The rapid decay due to the large hopping amplitude and the following oscillations are all correctly captured. In fact, the DMRG and MTE data are indistinguishable on the scale of the figure. For the phonon number [Fig. 29(a)] and the kinetic energy [Fig. 29(c)], we observe a quite different picture. The MTE results conserve the total energy, but this results from underestimating the phonon energy and, at the same time, overestimating the kinetic energy of the electron. In fact, the physically very interesting relaxation process of the electrons to lower quasi-momentum states does not seem to be captured by MTE at all for the parameters chosen here.

In Figs. 30(a)–30(c), we show the same observables for the same initial state but for $\bar{\gamma} = 2$ and $\bar{t}_0 = 0.5$. Here, we also observe

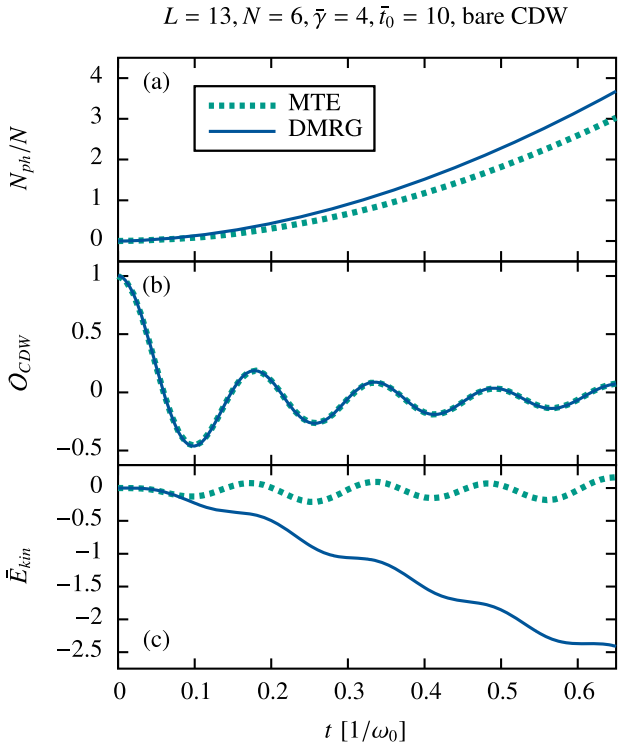

FIG. 29. Observables of the Holstein chain with $L = 13$, $N = 6$ electrons, $\bar{\gamma} = 4$, and $\bar{t}_0 = 10$. We show (a) the average phonon number, (b) the order parameter, and (c) the kinetic energy of the electrons. The initial state is the bare charge-density wave (see Sec. I for details). For the MTE method, we use 4000 trajectories and $\Delta t = 0.01/\omega_0$, and for the DMRG data, we use $\epsilon_{\mathrm{LBO}} = 10^{-8}$, $\epsilon_{\mathrm{bond}} = 10^{-8}$, $\Delta t = 0.001/\omega_0$, and $M = 35$.

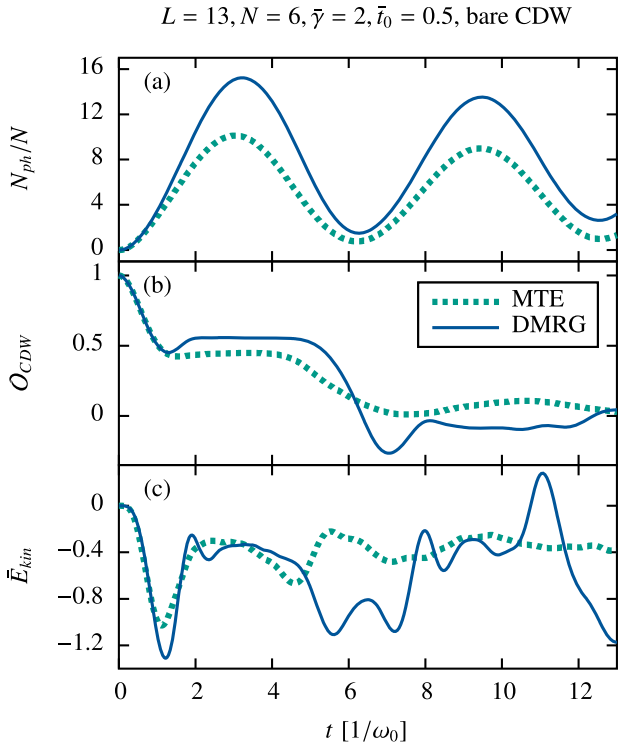

FIG. 30. Observables of the Holstein chain with $L = 13$, $N = 6$ electrons, $\bar{\gamma} = 2$, and $\bar{t}_0 = 0.5$. We show (a) the average phonon number, (b) the order parameter, and (c) the kinetic energy of the electrons. The initial state is the bare charge-density wave (see Sec. I for details). For the MTE method, we use 4000 trajectories and $\Delta t = 0.01/\omega_0$, and for the DMRG data, we use $\epsilon_{\mathrm{LBO}} = 10^{-7}$, $\epsilon_{\mathrm{bond}} = 10^{-7}$, $\Delta t = 0.02/\omega_0$, and $M = 35$.

significant differences between the MTE and the DMRG data. The CDW order parameter is not simulated correctly by MTE, even though the physically interesting plateau is captured. A similar picture as before emerges for the phonon number even though no clear trend can be seen for the kinetic energy. Beyond small time scales, there is a significant deviation between the DMRG and MTE data. We note that for these parameters, much longer times are reached in the DMRG simulation.

Finally, we look at the $\bar{\gamma} = 4$ and $\bar{t}_0 = 10$ data but starting from a dressed CDW. The three observables are displayed in Figs. 31(a)–31(c). Apparently, MTE captures the correct physical behavior for these parameters in the time interval where DMRG results are available. This includes the initial decay followed by a saturation for the CDW order parameter in Fig. 31(b) and the decrease of both the phonon energy in Fig. 31(a) and the electron kinetic energy in Fig. 31(c). Note that the relative error is much smaller in this setup, compared to the bare CDW shown in Fig. 29. Our data indicate that MTE captures the correct physics quantitatively for the dressed CDW with a large hopping amplitude but fails to describe the correct physics of the electron relaxation of the bare CDW state, seen in the kinetic energy. One reason might be that the dressed CDW is closer to an adiabatic initial state, which for the large electron-hopping parameters used in Fig. 31 is easier to describe for MTE.

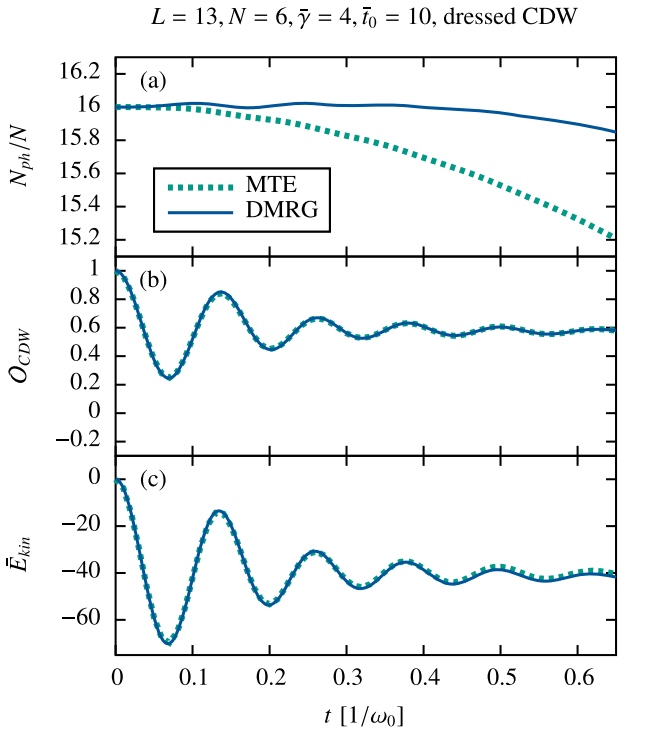

FIG. 31. Observables of the Holstein chain with $L = 13$, $N = 6$ electrons, $\bar{\gamma} = 4$, and $\bar{t}_0 = 10$. We show (a) the average phonon number, (b) the order parameter, and (c) the kinetic energy of the electrons. The initial state is the dressed charge-density wave (see Sec. I for details). For the MTE method, we use 4000 trajectories and $\Delta t = 0.01/\omega_0$, and for the DMRG data, we use $\epsilon_{\text{LBO}} = 10^{-7}$, $\epsilon_{\text{bond}} = 10^{-7}$, $\Delta t = 0.001/\omega_0$, and $M = 40$.

XI. CONCLUSIONS

In this work, we benchmarked several trajectory-based quantum-chemistry methods, MTE, FSSH, and MCE, against the numerically exact algorithms ED and DMRG-LBO. Our focus was on the real-time dynamics in the Holstein model, a prototypical electron–phonon system often studied in condensed-matter physics. We analyzed the methods in the framework of the Born–Huang formalism to better understand their qualitatively different behavior and the influence of non-adiabatic effects on their dynamics.

Compared to previous benchmark studies of trajectory-based methods, see, e.g., Refs. 57, 78, 107, 108, 110, and 117, a special focus was put on the influence of the initial state and of coherences on the non-adiabatic dynamics and the trajectory-based methods. We provide a new systematic comparison to exact DMRG-LBO data for quenched initial states in the extended Holstein model. While the MTE simulation always recovered the ultra-short time dynamics of the exact data, we found, in general, a better long-time description using a surface hopping approach, even for initial states with significant coherences between many adiabatic states. The coupled-trajectory method MCE provides excellent results for small systems, but converging this method can become difficult for large systems. We presented a detailed convergence analysis of MCE based on the criterion of energy conservation and by comparing it to the exact DMRG-LBO results. We will now conclude by discussing each method in detail.

In contrast to classical-trajectory methods that employ the Born–Oppenheimer approximation (see Sec. III A), both MTE and FSSH are, in principle, able to capture some non-adiabatic effects, such as transitions between adiabatic energy surfaces (see Figs. 12 and 13).

MTE works independently of the initial state and can recover the ultra-short dynamics for all investigated states. The method fails, however, in describing independent dynamics on different adiabatic energy surfaces due to the inherent mean-field approximation (which is a known result[58,199]). This is true both, when the time-evolution leads to an avoided crossing and a wave-function splitting (see Figs. 12, 13, and 18), as well as when different adiabatic states are populated from the beginning, as for the local states studied in this work. Even in an adiabatic parameter regime, where the contributions on the different surfaces should influence each other only very little (see Sec. III A), such initial states can lead to qualitatively wrong long-time dynamics (see, e.g., Fig. 15). Our interpretation is that the dynamics are often too much influenced by the high Born–Oppenheimer states, as discussed for the Holstein trimer (Sec. VIII) and cannot correctly describe the relaxation back to low-energy surfaces. This is also observed in the extended systems with one electron, where the bare and dressed local states both show a broad spreading of the electron density, not seen by the other methods. Our results confirm the known fact[103] that MTE is a questionable choice for analyzing energy transfer between the electronic and phononic subsystems, as can be seen from the total phonon number, which is described poorly (see Figs. 24 and 25, and Sec. X). Then again, for the charge-density wave states in a half-filled system, the electronic order parameter is captured reasonably well (Sec. X), especially in the adiabatic parameter regime. Here, for the dressed CDW, even the electron kinetic energy is accurately predicted, which we attribute to the fact that the state is close to an adiabatic state

in an adiabatic parameter regime. In addition, MTE is the computationally cheapest of all studied methods in large systems and can easily be extended to many-electron systems. It is thus a straightforward first method to implement also in condensed-matter problems. However, if one wants to accurately study systems with relevant non-adiabatic effects, either due to the parameter choice or due to initial states, one should consider using an improved method. It might be beneficial to use a mixture of MTE and the adiabatic basis of surface hopping, by introducing some form of decoherence in an MTE approach,[270,272] which, however, reintroduces a basis-dependence and was not studied in this work.

The FSSH method is strongly basis dependent and works best for adiabatic initial states, as shown in the Holstein dimer and trimer (see Figs. 13 and 18). There, it can correctly describe wave-function splitting and independent dynamics on the energy surfaces. One can question its use for initial states with non-zero off-diagonal elements of the adiabatic electronic density matrix, so-called "coherences," as for the local initial states studied in this work. FSSH cannot completely capture the correct short-time dynamics for these initial states, since the method ignores the coherences in its calculation of the nuclear forces, illustrated in Figs. 14 and 15. It has been suggested that for such coherent initial states, e.g., created by an attosecond light-pulse, a mean-field description, such as MTE, might be a better choice.[199] Nonetheless, we observed, in almost all systems, a better long-time description with FSSH than with MTE. For not too slow phonons, the initial coherences dampen out fast enough to recover reasonable long-time dynamics. The decoherence corrections improve the internal consistency of the different definitions of the electronic density matrix available and, in general, seem to reproduce the nuclear trajectories better. It also reduces the problem of frustrated hops in setups with very low nuclear kinetic energy around the avoided crossing, as seen in Fig. 15. When using a restricted decoherence correction and with proper treatment of the derivative couplings (see Sec. V E), any unphysical spurious charge transfer in large systems can be avoided. In these large systems, out of the tested trajectory-based methods, the FSSH + RD results for the RMSD were the closest to the DMRG results (see Figs. 23 and 27) and the method reproduced the local trapping of the electron. Further comparisons to numerically exact methods, in particular, in the long-time limit and for large systems, are needed in the future.

Here, we studied the most common form of a surface-hopping method and included only the corrections necessary to obtain reasonable results for the extended systems (see Sec. V E). The field of surface-hopping methods is still rapidly evolving, and many variations and improvements have been suggested in the recent years, for which we refer to the reviews Refs. 104 and 105. In that regard, our study serves as a starting point for a possible future comparison of these methods against the simple FSSH and DMRG-LBO.

The theoretical foundation of FSSH works with general many-particle states[58] and can readily be applied to many-electron systems. Due to the exponential growth of the electronic Hilbert space, this is limited in practice. The variant "independent-electron surface hopping" was suggested[273] for systems where the electrons are not subject to direct electronic correlations, as in the Holstein model. Here, a single Slater determinant is taken as the ansatz for the many-particle state, and derivative couplings and hopping probabilities are expressed in terms of the single-particle orbitals, which drastically reduces the computational cost. While this was not studied in this work, it is a natural next step in the analysis of the charge-density wave states of Sec. X.

The coupled-trajectory method MCE produces very accurate results whenever it can be converged and is even computationally cheap for small systems. It can also, at least partially, capture a tunneling transition in a classical energetically forbidden regime, which is not the case for our implementations of MTE and FSSH. Such a coupled-trajectory method seems to be the quantum-chemistry method of choice for the small systems studied here. For large systems, it is more difficult to converge for physically reasonable parameters and cannot be regarded as an exact method for the $N_c \sim 5 \cdot 10^3$ configurations used in this work. The computational cost scales with the third power of the number of configurations. While including more configurations is definitely feasible using longer computation times, the very slow convergence of MCE for $L = 51$ analyzed in Fig. 11 suggests that the implementation of alternative coupled-trajectory methods might also be worth trying. Nevertheless, even though we could not reach convergence according to our criteria, local observables around the initially occupied sites were still recovered very well (see Figs. 22 and 26). In the future, it would be interesting to apply MCE also to the charge-density wave states of Sec. X. Another direction could be the implementation of MCE in the adiabatic basis (see, e.g., Ref. 261). As alternative coupled-trajectory methods, one might consider Gaussian-based Multi-Configuration time-dependent Hartree (G-MCTDH),[1,248–250] variational Multiconfigurational Gaussian (vMCG)[1,251–253] the Davydov D2 ansatz,[116,117,254–256] MCEv2 with trajectory cloning,[264,274] and more adiabatic-surface guided methods, such as full multiple spawning,[275] or *ab initio* multiple spawning,[276] to name a few examples. Furthermore, multilayer multiconfiguration time-dependent Hartree[55,277] is a promising coupled-trajectory method for benchmarks.

Out of the tested methods, DMRG-LBO, although costly and due to entanglement growth limited to short times,[91] is the exact method of choice for the larger 1D systems. By construction, DMRG is a many-body technique and can therefore include electronic correlations. In contrast to MCE, the DMRG-LBO method used in our work could be converged in all cases, although the simulation time is limited. DMRG is, regardless of the specific algorithm, designed for many-electron systems for which we showed examples in our work. The recently introduced projected-purification method[93] might be another avenue toward reaching longer times, but time-dependent simulations of this method have not been systematically explored yet (see Ref. 106 for an application). Extensions of DMRG or generalizations of matrix–product states to two-dimensional systems exist,[90,91,191–195] yet are more expensive algorithms and combinations with efficient treatments of phonons have not been attempted or systematically tested. In the future, it would be interesting to apply the DMRG-LBO algorithm to systems with time-dependent external fields, e.g., for optical excitations, or interacting electrons. Another direction would be to extend the initial conditions to phonon distributions at finite temperature.[101]

To conclude, in this work, we provide unbiased data with numerically exact DMRG-LBO for 1D Holstein chains of large system sizes that serve as a new benchmark for approximate quantum-chemistry or condensed-matter methods. We provide comparisons of several trajectory-based quantum-chemistry methods, MTE,

FSSH, and MCE to the DMRG-LBO data. This allows us to explicitly quantify their strengths and weaknesses beyond relying on internal consistency checks. The initial conditions studied in this work start with many (or all) phonon oscillators in their ground state. In combination with the intermediate electron–phonon coupling and electron-hopping parameter choices, this provides a challenging testbed for all trajectory-based methods and we carefully studied the influence of the initial conditions. The MCE method can be converged to exact data for many systems and observables and is the most promising among the approximate methods tested here. More efficient implementations or alternative coupled-trajectory algorithms are needed for larger systems. In the future, comparative large-system studies with the phonons prepared in a thermal state, possibly combined with initial conditions created from an explicit optical excitation, would yield additional insight into the qualities of the trajectory-based methods.

ACKNOWLEDGMENTS

The authors are grateful to S. Kehrein, A. Osterkorn, and E. Paprotzki for fruitful discussions. We thank Kloss *et al.* for sending us their data. This paper was funded by the Deutsche Forschungsgemeinschaft (DFG, German Research Foundation) - SFB 1073 - 217133147 (projects B03, B09).

AUTHOR DECLARATIONS

Conflict of Interest

The authors have no conflicts to disclose.

DATA AVAILABILITY

The data that support the findings of this study are openly available at https://doi.org/10.25625/YDU1XT, Göttingen Research Online / Data.

APPENDIX A: SURFACE HOPPING FOR LOCAL INITIAL STATES IN LARGE SYSTEMS

For almost all observables and systems investigated in this work, the mixed definition of the electronic density matrix for FSSH according to Eq. (39) produces good results and could recover the diabatic populations at least approximately even for local initial states. The exceptions are very large systems with a local initial state, where small negative and positive electronic populations occur after some time throughout the whole system. While most of the density is still well recovered (see Figs. 21 and 25), this poses a problem for quantities that emphasize the small occupations on the borders of the chain such as the reduced mean-squared displacement [Eq. (49)]. This is shown in Fig. 32(a) for a very large example system with $L = 101$ sites.

The mixed definition partially even leads to negative values in the square-root for the RMSD and is also otherwise unreliable. One could resort to the active-surface [AS, Eq. (37)] definition, which seems to provide better long-time results, but does not reproduce the correct initial value. In contrast, the wave-function [WF, Eq. (38)] definition does not capture the localization for longer times. We note that if one discards the coherences in the initial state, all definitions

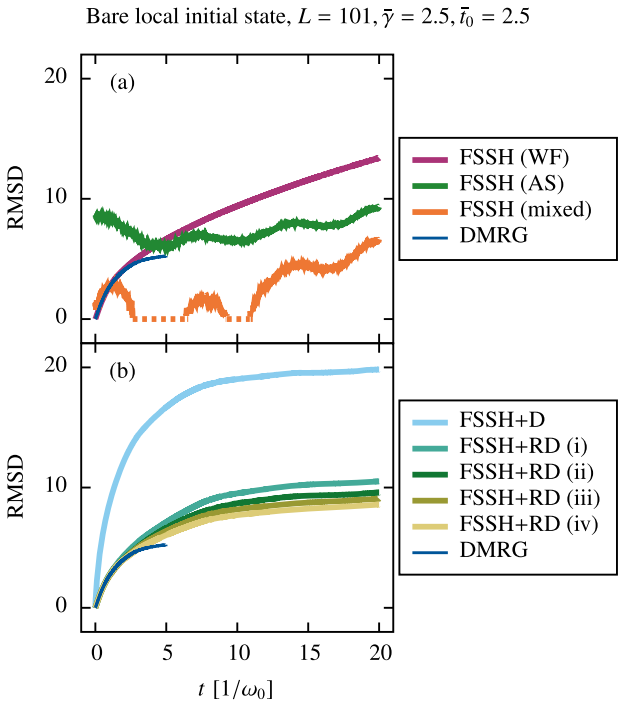

FIG. 32. (a) Reduced mean-squared displacement [see Eq. (49)] calculated with the three different possible definitions of the electronic density matrix (see Sec. V D) for FSSH without decoherence and compared to the DMRG results for the bare local initial state with $L = 101$, $\bar{\gamma} = \bar{t}_0 = 2.5$. The dashed line in the mixed definition indicated negative values in the square-root. (b) The RMSD for FSSH with a decoherence correction without restriction (FSSH + D) and with four different variations of restricted decoherence (see Sec. V E 3) (FSSH + RD): (i) $R = 0.999$ without delay, (ii) $R = 0.999$ with delay, (iii) $R = 0.99$ without delay, and (iv) $R = 0.99$ with delay. We use the same parameters as in Fig. 21, with the exception of the DMRG cutoffs, which are decreased to $\epsilon_{\text{LBO}} = 10^{-9}$ and $\epsilon_{\text{bond}} = 10^{-9}$.

of the electronic density matrix give the same result. In Fig. 32(a), this corresponds to the RMSD of the FSSH (AS) curve at $t = 0/\omega_0$. With the electron density delocalized significantly already from the beginning, this simplification is not suitable for describing the short-time non-adiabatic dynamics in quenched large systems and was not used in this work.

Using a decoherence correction allows us to use the wave-function definition and still recover the long-time localization, as described in Sec. V D. However, since the adiabatic states in the bare local initial state are strongly delocalized, this decoherence correction leads to the enhanced effect of the spurious charge transfer mentioned in Sec. V E 3, which results in an unphysical fast spreading of the wave function [see Fig. 32(b)] (FSSH + D). This can be remedied by using a restricted decoherence correction (FSSH + RD), as described in Sec. V E 3. We show results for four types of restrictions: (i) using the active-space threshold value of $R = 0.999$, suggested by Ref. 244 without delay and (ii) with delay, and using a reduced threshold of $R = 0.99$ (which corresponds to an even stronger restriction) without (iii) and with delay (iv). In this work, the restriction (iv) is used for system sizes of $L \geq 11$.

APPENDIX B: REDUCED ELECTRON HOPPING PARAMETER REGIME, $\bar{t}_0 = 1$

Here, we compare MTE, FSSH + RD, MCE, and DMRG for $\bar{t}_0 = 1$, which was already studied in Ref. 87 with another matrix–product state method designed for electron–phonon problems. We compute the reduced mean-squared displacement [see Eq. (49)] in a Holstein chain with $L = 25$ for both $\bar{\gamma} = 4$ and $\bar{\gamma} = 2.5$ for the bare local initial state. This initial state corresponds to the "Franck–Condon" excitation studied in Ref. 87 for the same parameters and we compare our results to their data. The results are shown in Figs. 33 and 34.

We observe a slightly different time evolution than for the parameters investigated in Sec. IX: The DMRG time evolution shows a step-like increment of the RMSD, similar to the intermediate plateau formation that we observe in the slow electron regime (see Figs. 16 and 30), and which we attributed to transient local trapping. The transient trapping resurfaces here with several steps in the RMSD at multiples of the phonon oscillation period, as already observed in Ref. 87. For the times available, DMRG and the data of Ref. 87 agree very well.

In both cases ($\bar{\gamma} = 4$ and $\bar{\gamma} = 2.5$), MCE displays the best short-time description of all trajectory-based methods. The method is again difficult to converge and cannot completely capture the formation of the second plateau for the used number of configurations, and the RMSD is drastically overestimated for later times. MTE cannot reproduce the formation of plateaus at all, which are only visible as wiggles in a growing RMSD. FSSH with the restricted decoherence correction (see Sec. V E 3) reproduces the formation of several plateaus. For short times, the method overestimates the height of the first RMSD plateau for both values of $\bar{\gamma}$, while the RMSD is better described for later times, especially for $\bar{\gamma} = 4$, but also for $\bar{\gamma} = 2.5$.

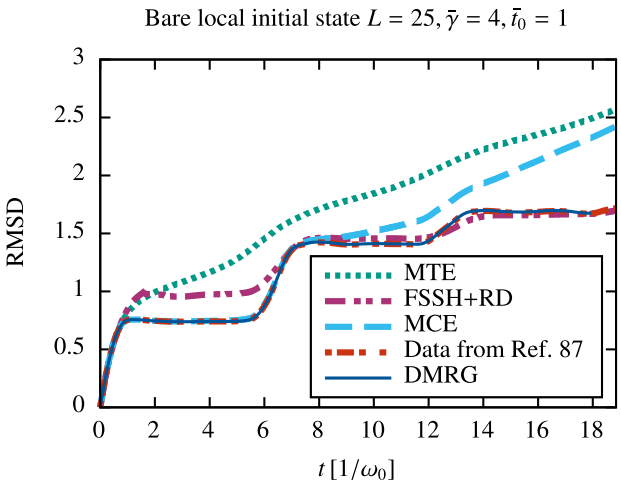

FIG. 33. Reduced mean-squared displacement [see Eq. (49)] obtained from the bare local initial state in the Holstein chain with $L = 25, \bar{t}_0 = 1, \bar{\gamma} = 4$, obtained with MTE, FSSH + RD, MCE, and DMRG (see Secs. IV C, V, and VI). This is compared to the data presented in Ref. 87. In the DMRG runs, we use $\epsilon_{\mathrm{LBO}} = 10^{-8}$, $\epsilon_{\mathrm{bond}} = 10^{-8}$, $\Delta t = 0.01/\omega_0$, and $M = 90$. MCE uses 4500 configurations initialized with the pancake-like sampling, and the independent trajectory methods use 50 000 trajectories. In the FSSH + RD runs, the RMSD is calculated from the wave-function definition of the density matrix [see Eq. (38)].

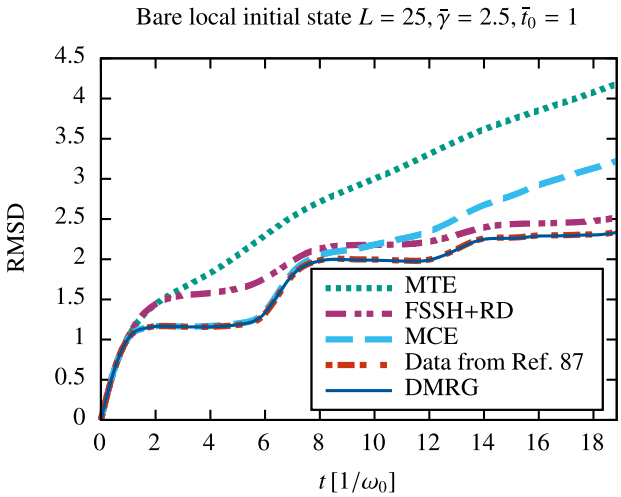

FIG. 34. Reduced mean-squared displacement [see Eq. (49)] obtained from the bare local initial state in the Holstein chain with $L = 25, \bar{t}_0 = 1, \bar{\gamma} = 2.5$, obtained with MTE, FSSH + RD, MCE, and DMRG (see Secs. IV C, V, and VI). This is compared to the data presented in Ref. 87. In our DMRG simulations, we use $\epsilon_{\mathrm{LBO}} = 10^{-8}$, $\epsilon_{\mathrm{bond}} = 10^{-8}$, $\Delta t = 0.01/\omega_0$, and $M = 35$. MCE uses 4500 configurations initialized with the pancake-like sampling, and the independent trajectory methods use 50 000 trajectories. In the FSSH + RD runs, the RMSD is calculated from the wave-function definition of the density matrix [see Eq. (38)].

Thus, all trajectory-based methods show a similar capability to describe the exact time evolution as already for the parameters investigated in Sec. IX: MTE cannot capture the local (transient) trapping of the electron, MCE works the best for short times, but is very difficult to converge for longer times, when also MTE fails, and FSSH cannot correctly describe the short-time evolution due to the build-in coherences of the local initial state but is able to predict a reasonable long-time behavior of the spreading of the electron.

REFERENCES

[1] L. González and R. Lindh, *Quantum Chemistry and Dynamics of Excited States: Methods and Applications* (John Wiley & Sons, Ltd, 2020).
[2] B. F. E. Curchod and T. J. Martínez, Chem. Rev. **118**, 3305 (2018).
[3] F. Agostini and B. F. E. Curchod, Wiley Interdiscip. Rev.: Comput. Mol. Sci. **9**, e1417 (2019).
[4] W. Domcke, D. R. Yarkony, and H. Köppel, *Conical Intersections: Theory, Computation and Experiment*, Advanced Series in Physical Chemistry Vol. 17 (World Scientific, 2011).
[5] D. R. Yarkony, Rev. Mod. Phys. **68**, 985 (1996).
[6] T. Nelson, S. Fernandez-Alberti, V. Chernyak, A. E. Roitberg, and S. Tretiak, J. Phys. Chem. B **115**, 5402 (2011).
[7] D. M. Coles, Y. Yang, Y. Wang, R. T. Grant, R. A. Taylor, S. K. Saikin, A. Aspuru-Guzik, D. G. Lidzey, J. K.-H. Tang, and J. M. Smith, Nat. Commun. **5**, 5561 (2014).
[8] J. A. Hutchison, T. Schwartz, C. Genet, E. Devaux, and T. W. Ebbesen, Angew. Chem., Int. Ed. **51**, 1592 (2012).
[9] E. Orgiu, J. George, J. A. Hutchison, E. Devaux, J. F. Dayen, B. Doudin, F. Stellacci, C. Genet, J. Schachenmayer, C. Genes, G. Pupillo, P. Samorì, and T. W. Ebbesen, Nat. Mater. **14**, 1123 (2015).
[10] A. Thomas, J. George, A. Shalabney, M. Dryzhakov, S. J. Varma, J. Moran, T. Chervy, X. Zhong, E. Devaux, C. Genet, J. A. Hutchison, and T. W. Ebbesen, Angew. Chem., Int. Ed. **55**, 11462 (2016).

[11] A. Bienfait, J. J. Pla, Y. Kubo, X. Zhou, M. Stern, C. C. Lo, C. D. Weis, T. Schenkel, D. Vion, D. Esteve, J. J. L. Morton, and P. Bertet, Nature **531**, 74 (2016).
[12] J. Flick, M. Ruggenthaler, H. Appel, and A. Rubio, Proc. Natl. Acad. Sci. U. S. A. **114**, 3026 (2017).
[13] D. Nabok, S. Blügel, and C. Friedrich, npj Comput. Mater. **7**, 178 (2021).
[14] F. Giustino, Rev. Mod. Phys. **89**, 015003 (2017).
[15] C. Franchini, M. Reticcioli, M. Setvin, and U. Diebold, Nat. Rev. Mater. **6**, 560 (2021).
[16] L. Kang, X. Du, J. S. Zhou, X. Gu, Y. J. Chen, R. Z. Xu, Q. Q. Zhang, S. C. Sun, Z. X. Yin, Y. W. Li, D. Pei, J. Zhang, R. K. Gu, Z. G. Wang, Z. K. Liu, R. Xiong, J. Shi, Y. Zhang, Y. L. Chen, and L. X. Yang, Nat. Commun. **12**, 6183 (2021).
[17] A. Raja, M. Selig, G. Berghäuser, J. Yu, H. M. Hill, A. F. Rigosi, L. E. Brus, A. Knorr, T. F. Heinz, E. Malic, and A. Chernikov, Nano Lett. **18**, 6135 (2018).
[18] S. Shree, M. Semina, C. Robert, B. Han, T. Amand, A. Balocchi, M. Manca, E. Courtade, X. Marie, T. Taniguchi, K. Watanabe, M. M. Glazov, and B. Urbaszek, Phys. Rev. B **98**, 035302 (2018).
[19] D. Werdehausen, T. Takayama, M. Höppner, G. Albrecht, A. W. Rost, Y. Lu, D. Manske, H. Takagi, and S. Kaiser, Sci. Adv. **4**, eaap8652 (2018).
[20] H.-Y. Chen, D. Sangalli, and M. Bernardi, Phys. Rev. Lett. **125**, 107401 (2020).
[21] S. Mor, V. Gosetti, A. Molina-Sánchez, D. Sangalli, S. Achilli, V. F. Agekyan, P. Franceschini, C. Giannetti, L. Sangaletti, and S. Pagliara, Phys. Rev. Res. **3**, 043175 (2021).
[22] D. Li, C. Trovatello, S. Dal Conte, M. Nuß, G. Soavi, G. Wang, A. C. Ferrari, G. Cerullo, and T. Brixner, Nat. Commun. **12**, 954 (2021).
[23] J. M. Frost, L. D. Whalley, and A. Walsh, ACS Energy Lett. **2**, 2647 (2017).
[24] D. Raiser, S. Mildner, B. Ifland, M. Sotoudeh, P. Blöchl, S. Techert, and C. Jooss, Adv. Energy Mater. **7**, 1602174 (2017).
[25] M. Park, A. J. Neukirch, S. E. Reyes-Lillo, M. Lai, S. R. Ellis, D. Dietze, J. B. Neaton, P. Yang, S. Tretiak, and R. A. Mathies, Nat. Commun. **9**, 2525 (2018).
[26] D. Ghosh, E. Welch, A. J. Neukirch, A. Zakhidov, and S. Tretiak, J. Phys. Chem. Lett. **11**, 3271 (2020).
[27] B. Kressdorf, T. Meyer, A. Belenchuk, O. Shapoval, M. ten Brink, S. Melles, U. Ross, J. Hoffmann, V. Moshnyaga, M. Seibt, P. Blöchl, and C. Jooss, Phys. Rev. Appl. **14**, 054006 (2020).
[28] C. Berk, M. Jaris, W. Yang, S. Dhuey, S. Cabrini, and H. Schmidt, Nat. Commun. **10**, 2652 (2019).
[29] F. Godejohann, A. V. Scherbakov, S. M. Kukhtaruk, A. N. Poddubny, D. D. Yaremkevich, M. Wang, A. Nadzeyka, D. R. Yakovlev, A. W. Rushforth, A. V. Akimov, and M. Bayer, Phys. Rev. B **102**, 144438 (2020).
[30] B. Frietsch, A. Donges, R. Carley, M. Teichmann, J. Bowlan, K. Döbrich, K. Carva, D. Legut, P. M. Oppeneer, U. Nowak, and M. Weinelt, Sci. Adv. **6**, eabb1601 (2020).
[31] J. Orenstein, Phys. Today **65**(9), 44 (2012).
[32] C. Giannetti, M. Capone, D. Fausti, M. Fabrizio, F. Parmigiani, and D. Mihailovic, Adv. Phys. **65**, 58 (2016).
[33] J. Lloyd-Hughes, P. M. Oppeneer, T. Pereira dos Santos, A. Schleife, S. Meng, M. A. Sentef, M. Ruggenthaler, A. Rubio, I. Radu, M. Murnane, X. Shi, H. Kapteyn, B. Stadtmüller, K. M. Dani, F. H. da Jornada, E. Prinz, M. Aeschlimann, R. L. Milot, M. Burdanova, J. Boland, T. Cocker, and F. Hegmann, J. Phys.: Condens. Matter **33**, 353001 (2021).
[34] R. Mankowsky, A. Subedi, M. Först, S. O. Mariager, M. Chollet, H. T. Lemke, J. S. Robinson, J. M. Glownia, M. P. Minitti, A. Frano, M. Fechner, N. A. Spaldin, T. Loew, B. Keimer, A. Georges, and A. Cavalleri, Nature **516**, 71 (2014).
[35] W. Hu, S. Kaiser, D. Nicoletti, C. R. Hunt, I. Gierz, M. C. Hoffmann, M. Le Tacon, T. Loew, B. Keimer, and A. Cavalleri, Nat. Mater. **13**, 705 (2014).
[36] M. Mitrano, A. Cantaluppi, D. Nicoletti, S. Kaiser, A. Perucchi, S. Lupi, P. Di Pietro, D. Pontiroli, M. Riccò, S. R. Clark, D. Jaksch, and A. Cavalleri, Nature **530**, 461 (2016).
[37] M. A. Sentef, A. F. Kemper, A. Georges, and C. Kollath, Phys. Rev. B **93**, 144506 (2016).
[38] M. Babadi, M. Knap, I. Martin, G. Refael, and E. Demler, Phys. Rev. B **96**, 014512 (2017).
[39] S. Paeckel, B. Fauseweh, A. Osterkorn, T. Köhler, D. Manske, and S. R. Manmana, Phys. Rev. B **101**, 180507 (2020).
[40] M. Buzzi, D. Nicoletti, M. Fechner, N. Tancogne-Dejean, M. A. Sentef, A. Georges, T. Biesner, E. Uykur, M. Dressel, A. Henderson, T. Siegrist, J. A. Schlueter, K. Miyagawa, K. Kanoda, M.-S. Nam, A. Ardavan, J. Coulthard, J. Tindall, F. Schlawin, D. Jaksch, and A. Cavalleri, Phys. Rev. X **10**, 031028 (2020).
[41] S. Vogelgesang, G. Storeck, J. G. Horstmann, T. Diekmann, M. Sivis, S. Schramm, K. Rossnagel, S. Schäfer, and C. Ropers, Nat. Phys. **14**, 184 (2018).
[42] G. Storeck, J. G. Horstmann, T. Diekmann, S. Vogelgesang, G. von Witte, S. V. Yalunin, K. Rossnagel, and C. Ropers, Struct. Dyn. **7**, 034304 (2020).
[43] G. Storeck, K. Rossnagel, and C. Ropers, Appl. Phys. Lett. **118**, 221603 (2021).
[44] J. G. Horstmann, H. Böckmann, B. Wit, F. Kurtz, G. Storeck, and C. Ropers, Nature **583**, 232 (2020).
[45] A. J. Leggett, S. Chakravarty, A. T. Dorsey, M. P. A. Fisher, A. Garg, and W. Zwerger, Rev. Mod. Phys. **59**, 1 (1987).
[46] D. E. Makarov and N. Makri, Chem. Phys. Lett. **221**, 482 (1994).
[47] R. Egger and C. H. Mak, Phys. Rev. B **50**, 15210 (1994).
[48] S. K. Kehrein and A. Mielke, Phys. Lett. A **219**, 313 (1996).
[49] K. Thompson and N. Makri, J. Chem. Phys. **110**, 1343 (1999).
[50] H. Wang, J. Chem. Phys. **113**, 9948 (2000).
[51] D. MacKernan, R. Kapral, and G. Ciccotti, J. Phys.: Condens. Matter **14**, 9069 (2002).
[52] H. Wang and M. Thoss, J. Chem. Phys. **119**, 1289 (2003).
[53] H. Wang and M. Thoss, New J. Phys. **10**, 115005 (2008).
[54] D. Mac Kernan, G. Ciccotti, and R. Kapral, J. Phys. Chem. B **112**, 424 (2008).
[55] H. Wang and M. Thoss, "Multilayer formulation of the multiconfiguration time-dependent Hartree theory," in *Multidimensional Quantum Dynamics*, edited by H.-D. Meyer, F. Gatti, and G. A. Worth (Wiley, 2009), Chap. 14, pp. 131–147.
[56] A. A. Kananenka, C.-Y. Hsieh, J. Cao, and E. Geva, J. Phys. Chem. Lett. **7**, 4809 (2016).
[57] H.-T. Chen and D. R. Reichman, J. Chem. Phys. **144**, 094104 (2016).
[58] J. C. Tully, J. Chem. Phys. **93**, 1061 (1990).
[59] J. C. Tully, Faraday Discuss. **110**, 407 (1998).
[60] F. Agostini, S. K. Min, A. Abedi, and E. K. U. Gross, J. Chem. Theory Comput. **12**, 2127 (2016).
[61] F. Agostini, Eur. Phys. J. B **91**, 143 (2018).
[62] L. M. Ibele and B. F. E. Curchod, Phys. Chem. Chem. Phys. **22**, 15183 (2020).
[63] S. Shin and H. Metiu, J. Chem. Phys. **102**, 9285 (1995).
[64] A. Abedi, F. Agostini, Y. Suzuki, and E. K. U. Gross, Phys. Rev. Lett. **110**, 263001 (2013).
[65] F. Agostini, A. Abedi, Y. Suzuki, S. K. Min, N. T. Maitra, and E. K. U. Gross, J. Chem. Phys. **142**, 084303 (2015).
[66] F. G. Eich and F. Agostini, J. Chem. Phys. **145**, 054110 (2016).
[67] G. H. Gossel, L. Lacombe, and N. T. Maitra, J. Chem. Phys. **150**, 154112 (2019).
[68] P. Martinez, B. Rosenzweig, N. M. Hoffmann, L. Lacombe, and N. T. Maitra, J. Chem. Phys. **154**, 014102 (2021).
[69] E. Boström, A. Mikkelsen, and C. Verdozzi, Phys. Rev. B **93**, 195416 (2016).
[70] E. Boström, M. Hopjan, A. Kartsev, C. Verdozzi, and C.-O. Almbladh, J. Phys.: Conf. Ser. **696**, 012007 (2016).
[71] N. Säkkinen, Y. Peng, H. Appel, and R. van Leeuwen, J. Chem. Phys. **143**, 234101 (2015).
[72] N. Säkkinen, Y. Peng, H. Appel, and R. van Leeuwen, J. Chem. Phys. **143**, 234102 (2015).
[73] D. Karlsson and R. van Leeuwen, "Non-equilibrium Green's functions for coupled fermion-boson systems," in *Handbook of Materials Modeling: Methods: Theory and Modeling*, edited by W. Andreoni and S. Yip (Springer International Publishing, Cham, 2020), pp. 367–395.
[74] M. Schüler, J. Berakdar, and Y. Pavlyukh, Phys. Rev. B **93**, 054303 (2016).
[75] D. Karlsson, R. van Leeuwen, Y. Pavlyukh, E. Perfetto, and G. Stefanucci, Phys. Rev. Lett. **127**, 036402 (2021).
[76] Y. Pavlyukh, E. Perfetto, D. Karlsson, R. van Leeuwen, and G. Stefanucci, Phys. Rev. B **105**, 125135 (2022).
[77] Y. Pavlyukh, E. Perfetto, D. Karlsson, R. van Leeuwen, and G. Stefanucci, Phys. Rev. B **105**, 125134 (2022).
[78] N. M. Hoffmann, C. Schäfer, N. Säkkinen, A. Rubio, H. Appel, and A. Kelly, J. Chem. Phys. **151**, 244113 (2019).

[79]E. Boström, P. Helmer, P. Werner, and C. Verdozzi, Phys. Rev. Res. **1**, 013017 (2019).
[80]T. E. Reinhard, U. Mordovina, C. Hubig, J. S. Kretchmer, U. Schollwöck, H. Appel, M. A. Sentef, and A. Rubio, J. Chem. Theory Comput. **15**, 2221 (2019).
[81]M. Weber and J. K. Freericks, arXiv:2107.04096 [cond-mat, physics:quant-ph] (2021).
[82]M. Weber and J. K. Freericks, Phys. Rev. E **105**, 025301 (2022).
[83]I. Tavernelli, U. F. Röhrig, and U. Rothlisberger, Mol. Phys. **103**, 963 (2005).
[84]B. F. E. Curchod, U. Rothlisberger, and I. Tavernelli, ChemPhysChem **14**, 1314 (2013).
[85]R. R. Pela and C. Draxl, arXiv:2201.12146 [cond-mat] (2022).
[86]C. Brockt, F. Dorfner, L. Vidmar, F. Heidrich-Meisner, and E. Jeckelmann, Phys. Rev. B **92**, 241106 (2015).
[87]B. Kloss, D. R. Reichman, and R. Tempelaar, Phys. Rev. Lett. **123**, 126601 (2019).
[88]J. Stolpp, J. Herbrych, F. Dorfner, E. Dagotto, and F. Heidrich-Meisner, Phys. Rev. B **101**, 035134 (2020).
[89]S. R. White, Phys. Rev. Lett. **69**, 2863 (1992).
[90]U. Schollwöck, Rev. Mod. Phys. **77**, 259 (2005).
[91]U. Schollwöck, Ann. Phys. **326**, 96 (2011).
[92]M. L. Wall, A. Safavi-Naini, and A. M. Rey, Phys. Rev. A **94**, 053637 (2016).
[93]T. Köhler, J. Stolpp, and S. Paeckel, SciPost Phys. **10**, 058 (2021).
[94]J. Stolpp, T. Köhler, S. R. Manmana, E. Jeckelmann, F. Heidrich-Meisner, and S. Paeckel, Comput. Phys. Commun. **269**, 108106 (2021).
[95]E. Jeckelmann and S. R. White, Phys. Rev. B **57**, 6376 (1998).
[96]C. Zhang, E. Jeckelmann, and S. R. White, Phys. Rev. Lett. **80**, 2661 (1998).
[97]C. Zhang, E. Jeckelmann, and S. R. White, Phys. Rev. B **60**, 14092 (1999).
[98]C. Guo, A. Weichselbaum, J. von Delft, and M. Vojta, Phys. Rev. Lett. **108**, 160401 (2012).
[99]B. Friedman, Phys. Rev. B **61**, 6701 (2000).
[100]H. Wong and Z.-D. Chen, Phys. Rev. B **77**, 174305 (2008).
[101]D. Jansen, J. Bonča, and F. Heidrich-Meisner, Phys. Rev. B **102**, 165155 (2020).
[102]D. Jansen, C. Jooss, and F. Heidrich-Meisner, Phys. Rev. B **104**, 195116 (2021).
[103]A. P. Horsfield, D. R. Bowler, H. Ness, C. G. Sánchez, T. N. Todorov, and A. J. Fisher, Rep. Prog. Phys. **69**, 1195 (2006).
[104]L. Wang, A. Akimov, and O. V. Prezhdo, J. Phys. Chem. Lett. **7**, 2100 (2016).
[105]B. Smith and A. V. Akimov, J. Phys.: Condens. Matter **32**, 073001 (2019).
[106]S. Mardazad, Y. Xu, X. Yang, M. Grundner, U. Schollwöck, H. Ma, and S. Paeckel, J. Chem. Phys. **155**, 194101 (2021).
[107]G. Stock and M. Thoss, Adv. Chem. Phys. **131**, 243 (2005).
[108]V. M. Freixas, A. J. White, T. Nelson, H. Song, D. V. Makhov, D. Shalashilin, S. Fernandez-Alberti, and S. Tretiak, J. Phys. Chem. Lett. **12**, 2970 (2021).
[109]L. Wang, J. Qiu, X. Bai, and J. Xu, Wiley Interdiscip. Rev.: Comput. Mol. Sci. **10**, e1435 (2020).
[110]A. Krotz and R. Tempelaar, J. Chem. Phys. **156**, 024105 (2022).
[111]T. Holstein, Ann. Phys. **8**, 325 (1959).
[112]D. V. Shalashilin, J. Chem. Phys. **130**, 244101 (2009).
[113]D. V. Shalashilin, J. Chem. Phys. **132**, 244111 (2010).
[114]Y. Tanimura and R. Kubo, J. Phys. Soc. Jpn. **58**, 101 (1989).
[115]L. Chen, Y. Zhao, and Y. Tanimura, J. Phys. Chem. Lett. **6**, 3110 (2015).
[116]N. Zhou, Z. Huang, J. Zhu, V. Chernyak, and Y. Zhao, J. Chem. Phys. **143**, 014113 (2015).
[117]L. Chen, M. F. Gelin, and D. V. Shalashilin, J. Chem. Phys. **151**, 244116 (2019).
[118]S. I. Pekar, *Untersuchungen Über die Elektronentheorie der Kristalle* (Akademie-Verlag, Berlin, 1954).
[119]R. P. Feynman, Phys. Rev. **97**, 660 (1955).
[120]R. Peierls, *Quantum Theory of Solids* (Clarendon Press, Oxford, 1955), p. 108.
[121]J. E. Hirsch and E. Fradkin, Phys. Rev. B **27**, 4302 (1983).
[122]R. T. Scalettar, N. E. Bickers, and D. J. Scalapino, Phys. Rev. B **40**, 197 (1989).
[123]R. M. Noack, D. J. Scalapino, and R. T. Scalettar, Phys. Rev. Lett. **66**, 778 (1991).
[124]M. Vekić, R. M. Noack, and S. R. White, Phys. Rev. B **46**, 271 (1992).
[125]R. J. Bursill, R. H. McKenzie, and C. J. Hamer, Phys. Rev. Lett. **80**, 5607 (1998).
[126]C. E. Creffield, G. Sangiovanni, and M. Capone, Eur. Phys. J. B **44**, 175 (2005).
[127]O. Bradley, G. G. Batrouni, and R. T. Scalettar, Phys. Rev. B **103**, 235104 (2021).
[128]M. V. Araújo, J. P. de Lima, S. Sorella, and N. C. Costa, Phys. Rev. B **105**, 165103 (2022).
[129]J. Ranninger and U. Thibblin, Phys. Rev. B **45**, 7730 (1992).
[130]E. V. L. de Mello and J. Ranninger, Phys. Rev. B **55**, 14872 (1997).
[131]Y. A. Firsov and E. K. Kudinov, Phys. Solid State **39**, 1930 (1997).
[132]J. Chatterjee and A. N. Das, Phys. Rev. B **61**, 4592 (2000).
[133]T. Hakioğlu, V. A. Ivanov, and M. Y. Zhuravlev, Physica A **284**, 172 (2000).
[134]H. Rongsheng, L. Zijing, and W. Kelin, Phys. Rev. B **65**, 174303 (2002).
[135]R. Qing-Bao and C. Qing-Hu, Commun. Theor. Phys. **43**, 357 (2005).
[136]S. Paganelli and S. Ciuchi, Eur. Phys. J.: Spec. Top. **160**, 343 (2008).
[137]S. Paganelli and S. Ciuchi, J. Phys.: Condens. Matter **20**, 235203 (2008).
[138]Y. Y. Zhang, X. G. Wang, and Q. H. Chen, Solid State Commun. **149**, 2106 (2009).
[139]S. A. Sato, A. Kelly, and A. Rubio, Phys. Rev. B **97**, 134308 (2018).
[140]L. K. McKemmish, R. H. McKenzie, N. S. Hush, and J. R. Reimers, Phys. Chem. Chem. Phys. **17**, 24666 (2015).
[141]J. R. Reimers, L. K. McKemmish, R. H. McKenzie, and N. S. Hush, Phys. Chem. Chem. Phys. **17**, 24641 (2015).
[142]J. E. Subotnik, A. Jain, B. Landry, A. Petit, W. Ouyang, and N. Bellonzi, Annu. Rev. Phys. Chem. **67**, 387 (2016).
[143]M. Capone, W. Stephan, and M. Grilli, Phys. Rev. B **56**, 4484 (1997).
[144]L.-C. Ku and S. A. Trugman, Phys. Rev. B **75**, 014307 (2007).
[145]D. Golež, J. Bonča, L. Vidmar, and S. A. Trugman, Phys. Rev. Lett. **109**, 236402 (2012).
[146]D. Jansen, J. Stolpp, L. Vidmar, and F. Heidrich-Meisner, Phys. Rev. B **99**, 155130 (2019).
[147]J. Bonča, S. A. Trugman, and I. Batistić, Phys. Rev. B **60**, 1633 (1999).
[148]D. Golež, J. Bonča, and L. Vidmar, Phys. Rev. B **85**, 144304 (2012).
[149]F. Dorfner, L. Vidmar, C. Brockt, E. Jeckelmann, and F. Heidrich-Meisner, Phys. Rev. B **91**, 104302 (2015).
[150]R. K. Kessing, P.-Y. Yang, S. R. Manmana, and J. Cao, arXiv:2111.06137 [cond-mat, physics:physics, physics:quant-ph] (2021).
[151]G. Wellein, H. Röder, and H. Fehske, Phys. Rev. B **53**, 9666 (1996).
[152]G. Wellein and H. Fehske, Phys. Rev. B **58**, 6208 (1998).
[153]L. Vidmar, J. Bonča, T. Tohyama, and S. Maekawa, Phys. Rev. Lett. **107**, 246404 (2011).
[154]J. Bonča, S. A. Trugman, and M. Berciu, Phys. Rev. B **100**, 094307 (2019).
[155]F. A. Y. N. Schröder and A. W. Chin, Phys. Rev. B **93**, 075105 (2016).
[156]C. Brockt and E. Jeckelmann, Phys. Rev. B **95**, 064309 (2017).
[157]V. Janković and N. Vukmirović, Phys. Rev. B **105**, 054311 (2022).
[158]J. Sun, B. Luo, and Y. Zhao, Phys. Rev. B **82**, 014305 (2010).
[159]B. Luo, J. Ye, and Y. Zhao, Phys. Status Solidi C **8**, 70 (2011).
[160]M. Born and K. Huang, *Dynamical Theory of Crystal Lattices* (Clarendon Press, 1954).
[161]M. Born and R. Oppenheimer, Ann. Phys. **389**, 457 (1927).
[162]J. C. Tully, in *Theoretical Chemistry Accounts: New Century Issue*, edited by C. J. Cramer and D. G. Truhlar (Springer, Berlin, Heidelberg, 2000), pp. 173–176.
[163]G. A. Worth and L. S. Cederbaum, Annu. Rev. Phys. Chem. **55**, 127 (2004).
[164]W. Lichten, Phys. Rev. **131**, 229 (1963).
[165]F. T. Smith, Phys. Rev. **179**, 111 (1969).
[166]M. Baer, Chem. Phys. Lett. **35**, 112 (1975).
[167]C. A. Mead and D. G. Truhlar, J. Chem. Phys. **77**, 6090 (1982).
[168]T. Van Voorhis, T. Kowalczyk, B. Kaduk, L.-P. Wang, C.-L. Cheng, and Q. Wu, Annu. Rev. Phys. Chem. **61**, 149 (2010).
[169]H. Köppel, W. Domcke, and L. S. Cederbaum, Adv. Chem. Phys. **57**, 59 (1984).
[170]J. Spencer, L. Scalfi, A. Carof, and J. Blumberger, Faraday Discuss. **195**, 215 (2016).
[171]S. Giannini and J. Blumberger, Acc. Chem. Res. **55**, 819 (2022).
[172]B. R. Landry and J. E. Subotnik, J. Chem. Phys. **135**, 191101 (2011).
[173]B. R. Landry and J. E. Subotnik, J. Chem. Phys. **137**, 22A513 (2012).

[174]L. D. Landau, Phys. Z. Sowjet. **2**, 46 (1932).
[175]C. Zener, Proc. R. Soc. London, Ser. A **137**, 696 (1932).
[176]A. W. Sandvik, AIP Conf. Proc. **1297**, 135 (2010).
[177]R. Car and M. Parrinello, Phys. Rev. Lett. **55**, 2471 (1985).
[178]L. Verlet, Phys. Rev. **159**, 98 (1967).
[179]S. Paeckel, T. Köhler, A. Swoboda, S. R. Manmana, U. Schollwöck, and C. Hubig, Ann. Phys. **411**, 167998 (2019).
[180]G. Vidal, Phys. Rev. Lett. **93**, 040502 (2004).
[181] A. J. Daley, C. Kollath, U. Schollwöck, and G. Vidal, J. Stat. Mech.: Theory Exp. **2004**, P04005.
[182]S. R. White and A. E. Feiguin, Phys. Rev. Lett. **93**, 076401 (2004).
[183]J. Haegeman, J. I. Cirac, T. J. Osborne, I. Pižorn, H. Verschelde, and F. Verstraete, Phys. Rev. Lett. **107**, 070601 (2011).
[184]J. Haegeman, C. Lubich, I. Oseledets, B. Vandereycken, and F. Verstraete, Phys. Rev. B **94**, 165116 (2016).
[185]F. Verstraete, J. J. García-Ripoll, and J. I. Cirac, Phys. Rev. Lett. **93**, 207204 (2004).
[186]J. Sirker and A. Klümper, Phys. Rev. B **71**, 241101 (2005).
[187]A. E. Feiguin and S. R. White, Phys. Rev. B **72**, 220401 (2005).
[188]E. M. Stoudenmire and S. R. White, New J. Phys. **12**, 055026 (2010).
[189]C. Karrasch, J. H. Bardarson, and J. E. Moore, Phys. Rev. Lett. **108**, 227206 (2012).
[190]C. Karrasch, J. H. Bardarson, and J. E. Moore, New J. Phys. **15**, 083031 (2013).
[191] F. Verstraete and J. I. Cirac, arXiv:cond-mat/0407066 (2004).
[192]E. M. Stoudenmire and S. R. White, Annu. Rev. Condens. Matter Phys. **3**, 111 (2012).
[193]R. Orús, Ann. Phys. **349**, 117 (2014).
[194]B.-X. Zheng, C.-M. Chung, P. Corboz, G. Ehlers, M.-P. Qin, R. M. Noack, H. Shi, S. R. White, S. Zhang, and G. K.-L. Chan, Science **358**, 1155 (2017).
[195]B. Bruognolo, J.-W. Li, J. von Delft, and A. Weichselbaum, SciPost Phys. Lect. Notes **2021**, 25.
[196]J. Eisert, M. Cramer, and M. B. Plenio, Rev. Mod. Phys. **82**, 277 (2010).
[197]M. Fishman, S. R. White, and E. M. Stoudenmire, SciPost Physics Codebases (in press), e-print: arXiv:2007.14822 [cond-mat, physics:physics] (2021).
[198]P. Ehrenfest, Z. Phys. **45**, 455 (1927).
[199]A. Kirrander and M. Vacher, "Ehrenfest Methods for Electron and Nuclear Dynamics," in *Quantum Chemistry and Dynamics of Excited States*, edited by L. González and R. Lindh (John Wiley & Sons, Ltd., 2020), pp. 469–497.
[200]R. Kapral and G. Ciccotti, J. Chem. Phys. **110**, 8919 (1999).
[201] R. Grunwald, A. Kelly, and R. Kapral, in *Energy Transfer Dynamics in Biomaterial Systems*, Springer Series in Chemical Physics, edited by I. Burghardt, V. May, D. A. Micha, and E. R. Bittner (Springer, Berlin, Heidelberg, 2009), pp. 383–413.
[202]K. Ando, Chem. Phys. Lett. **360**, 240 (2002).
[203]E. Wigner, Phys. Rev. **40**, 749 (1932).
[204]H. Weyl, Z. Phys. **46**, 1 (1927).
[205]J. E. Moyal, Math. Proc. Cambridge Philos. Soc. **45**, 99 (1949).
[206]M. Hillery, R. F. O'Connell, M. O. Scully, and E. P. Wigner, Phys. Rep. **106**, 121 (1984).
[207]W. B. Case, Am. J. Phys. **76**, 937 (2008).
[208]I. Horenko, B. Schmidt, and C. Schütte, J. Chem. Phys. **115**, 5733 (2001).
[209]K. Ando and M. Santer, J. Chem. Phys. **118**, 10399 (2003).
[210]J. E. Subotnik, W. Ouyang, and B. R. Landry, J. Chem. Phys. **139**, 214107 (2013).
[211] I. G. Ryabinkin, C.-Y. Hsieh, R. Kapral, and A. F. Izmaylov, J. Chem. Phys. **140**, 084104 (2014).
[212]R. C. Brown and E. J. Heller, J. Chem. Phys. **75**, 186 (1981).
[213]M. Persico and G. Granucci, Theor. Chem. Acc. **133**, 1526 (2014).
[214]M. Barbatti and K. Sen, Int. J. Quantum Chem. **116**, 762 (2016).
[215]J. Suchan, D. Hollas, B. F. E. Curchod, and P. Slavíček, Faraday Discuss. **212**, 307 (2018).
[216]S. Mai, H. Gattuso, A. Monari, and L. González, Front. Chem. **6**, 495 (2018).
[217]A. Polkovnikov, Ann. Phys. **325**, 1790 (2010).
[218]A. García-Vela, R. B. Gerber, and D. G. Imre, J. Chem. Phys. **97**, 7242 (1992).
[219]M. S. Topaler, T. C. Allison, D. W. Schwenke, and D. G. Truhlar, J. Chem. Phys. **109**, 3321 (1998).
[220]D. Marx and J. Hutter, *Ab Initio Molecular Dynamics: Basic Theory and Advanced Methods* (Cambridge University Press, Cambridge, 2009).
[221] V. I. Gerasimenko, Theor. Math. Phys. **50**, 49 (1982).
[222]T. Yonehara, K. Hanasaki, and K. Takatsuka, Chem. Rev. **112**, 499 (2012).
[223]A. W. Jasper, S. Nangia, C. Zhu, and D. G. Truhlar, Acc. Chem. Res. **39**, 101 (2006).
[224]A. Bjerre and E. E. Nikitin, Chem. Phys. Lett. **1**, 179 (1967).
[225]J. C. Tully and R. K. Preston, J. Chem. Phys. **55**, 562 (1971).
[226]U. Müller and G. Stock, J. Chem. Phys. **107**, 6230 (1997).
[227]G. Granucci and M. Persico, J. Chem. Phys. **126**, 134114 (2007).
[228]B. R. Landry, M. J. Falk, and J. E. Subotnik, J. Chem. Phys. **139**, 211101 (2013).
[229]P. V. Parandekar and J. C. Tully, J. Chem. Phys. **122**, 094102 (2005).
[230]J. R. Schmidt, P. V. Parandekar, and J. C. Tully, J. Chem. Phys. **129**, 044104 (2008).
[231] A. Carof, S. Giannini, and J. Blumberger, Phys. Chem. Chem. Phys. **21**, 26368 (2019).
[232]R. Crespo-Otero and M. Barbatti, Chem. Rev. **118**, 7026 (2018).
[233]B. J. Schwartz, E. R. Bittner, O. V. Prezhdo, and P. J. Rossky, J. Chem. Phys. **104**, 5942 (1996).
[234]E. R. Bittner and P. J. Rossky, J. Chem. Phys. **103**, 8130 (1995).
[235]E. J. Heller, J. Chem. Phys. **62**, 1544 (1975).
[236]E. Neria and A. Nitzan, J. Chem. Phys. **99**, 1109 (1993).
[237]G. Granucci, M. Persico, and A. Toniolo, J. Chem. Phys. **114**, 10608 (2001).
[238]S. Fernandez-Alberti, A. E. Roitberg, T. Nelson, and S. Tretiak, J. Chem. Phys. **137**, 014512 (2012).
[239]L. Wang and O. V. Prezhdo, J. Phys. Chem. Lett. **5**, 713 (2014).
[240]S. Mai, P. Marquetand, and L. González, "Surface Hopping Molecular Dynamics," in *Quantum Chemistry and Dynamics of Excited States*, edited by L. González and R. Lindh (John, Wiley & Sons, Ltd., 2020), pp. 499–530.
[241] S. Mai, P. Marquetand, and L. González, Int. J. Quantum Chem. **115**, 1215 (2015).
[242]J. Qiu, X. Bai, and L. Wang, J. Phys. Chem. Lett. **9**, 4319 (2018).
[243]X. Bai, J. Qiu, and L. Wang, J. Chem. Phys. **148**, 104106 (2018).
[244]S. Giannini, A. Carof, and J. Blumberger, J. Phys. Chem. Lett. **9**, 3116 (2018).
[245]J. Qiu, X. Bai, and L. Wang, J. Phys. Chem. Lett. **10**, 637 (2019).
[246]L. Wang and D. Beljonne, J. Phys. Chem. Lett. **4**, 1888 (2013).
[247]J. Qiu, Y. Lu, and L. Wang, J. Chem. Theory Comput. **18**, 2803 (2022).
[248]I. Burghardt, H.-D. Meyer, and L. S. Cederbaum, J. Chem. Phys. **111**, 2927 (1999).
[249]I. Burghardt, M. Nest, and G. A. Worth, J. Chem. Phys. **119**, 5364 (2003).
[250]I. Burghardt, K. Giri, and G. A. Worth, J. Chem. Phys. **129**, 174104 (2008).
[251] G. A. Worth, M. A. Robb, and I. Burghardt, Faraday Discuss. **127**, 307 (2004).
[252]G. A. Worth and I. Burghardt, Chem. Phys. Lett. **368**, 502 (2003).
[253]G. W. Richings, I. Polyak, K. E. Spinlove, G. A. Worth, I. Burghardt, and B. Lasorne, Int. Rev. Phys. Chem. **34**, 269 (2015).
[254]A. S. Davydov, Sov. Phys. Usp. **25**, 898 (1982).
[255]L. Cruzeiro-Hansson, Phys. Rev. Lett. **73**, 2927 (1994).
[256]Y. Zhao, B. Luo, Y. Zhang, and J. Ye, J. Chem. Phys. **137**, 084113 (2012).
[257]T. Ma, M. Bonfanti, P. Eisenbrandt, R. Martinazzo, and I. Burghardt, J. Chem. Phys. **149**, 244107 (2018).
[258]C. Symonds, J. A. Kattirtzi, and D. V. Shalashilin, J. Chem. Phys. **148**, 184113 (2018).
[259]O. Bramley, C. Symonds, and D. V. Shalashilin, J. Chem. Phys. **151**, 064103 (2019).
[260]D. V. Shalashilin and M. S. Child, J. Chem. Phys. **128**, 054102 (2008).
[261] D. V. Makhov, C. Symonds, S. Fernandez-Alberti, and D. V. Shalashilin, Chem. Phys. **493**, 200 (2017).
[262]M. Ronto and D. V. Shalashilin, J. Phys. Chem. A **117**, 6948 (2013).
[263]C. Itzykson and J. Zuber, *Quantum Field Theory* (Courier Corporation, 2012).

[264]D. V. Makhov, W. J. Glover, T. J. Martinez, and D. V. Shalashilin, J. Chem. Phys. **141**, 054110 (2014).
[265]D. V. Makhov, T. J. Martinez, and D. V. Shalashilin, Faraday Discuss. **194**, 81 (2016).
[266]J. Zheng, X. Xu, R. Meana-Pañeda, and D. G. Truhlar, Chem. Sci. **5**, 2091 (2014).
[267]J. Zheng, R. Meana-Pañeda, and D. G. Truhlar, J. Phys. Chem. Lett. **5**, 2039 (2014).
[268]A. W. Jasper, M. D. Hack, and D. G. Truhlar, J. Chem. Phys. **115**, 1804 (2001).
[269]B. Bertini, F. Heidrich-Meisner, C. Karrasch, T. Prosen, R. Steinigeweg, and M. Źnidarič, Rev. Mod. Phys. **93**, 025003 (2021).
[270]C. Zhu, S. Nangia, A. W. Jasper, and D. G. Truhlar, J. Chem. Phys. **121**, 7658 (2004).
[271] H. Hashimoto and S. Ishihara, Phys. Rev. B **96**, 035154 (2017).
[272]C. Zhu, A. W. Jasper, and D. G. Truhlar, J. Chem. Phys. **120**, 5543 (2004).
[273]N. Shenvi, S. Roy, and J. C. Tully, J. Chem. Phys. **130**, 174107 (2009).
[274]D. V. Makhov, K. Saita, T. J. Martinez, and D. V. Shalashilin, Phys. Chem. Chem. Phys. **17**, 3316 (2015).
[275]T. J. Martinez, M. Ben-Nun, and R. D. Levine, J. Phys. Chem. **100**, 7884 (1996).
[276]M. Ben-Nun, J. Quenneville, and T. J. Martínez, J. Phys. Chem. A **104**, 5161 (2000).
[277]H. Wang, J. Phys. Chem. A **119**, 7951 (2015).

Chapter 8

Conclusion

In this thesis, there were two major goals. The first goal was to better understand the effects of electron-phonon interaction on quantities such as spectral functions, optical conductivity, and energy transport coefficients. The second goal was to study the transport through heterostructures and breakdown of charge density waves (CDWs). These goals were achieved using and further developing novel numerical methods and tailoring them specifically for electron-phonon models.

I started by introducing the Holstein model [43] in Ch. 2, which is a model consisting of propagating electrons interacting with local harmonic oscillators. It incorporates key features emerging from electron-phonon interaction, such as polaron and CDW formation, and can be extended to include a finite phonon bandwidth and electron-electron interaction. Numerically, the model poses a great challenge due to the large local Hilbert spaces needed to capture the correct phonon-induced physics. To tackle this, I used methods based on matrix-product states [111] and local basis optimization (LBO) [151].

In Ch. 3, I reviewed the key ideas of matrix-product-state algorithms, which is to find an efficient representation of a quantum state based on the reduced density matrices. I then explained one way the formalism can be used to do finite-temperature calculations efficiently (purification [138]), and I introduced the time-evolution algorithms tDMRG [132–134] and TDVP [135, 136]. In particular, I emphasized how these algorithms can be optimized for electron-phonon systems by using LBO. After that, I sketched some of the key ideas of a set of trajectory-based algorithms which provide efficient alternatives to a fully quantum-mechanical treatment of the phonons. Lastly, I discussed some of the new developments in the field.

I then shifted the focus to applications of the algorithms. In Ch. 4, I first presented a publication where we demonstrated that even though the infinite-temperature state used in purification is artificial for the Holstein model, we can still capture the correct low-temperature physics of the system. Building on this, we combined purification and the tDMRG algorithm with LBO (tDMRG-LBO) to calculate thermal expectation values.

We then proceeded to compute the polaron spectral function, the electron emission function, and the phonon spectral function. In general, spectral functions connect theoretical models, like the Holstein polaron, to experimental results, e.g., with ARPES [100, 101],

and being able to calculating them is important for a comprehensive understanding of both the measurements and the models. The goal of our work was to present an efficient method to compute these quantities, which can be used to study how they are effected by temperature. Another advantage is that the scheme is general enough to be combined with other time-evolution algorithms.

After that, I demonstrated that even though the tDMRG-LBO algorithm is sufficient to calculate spectral functions for the Hostein polaron model, it has difficulties reaching times long enough for good frequency resolution when the operators become more complicated. In particular for charge and energy currents, which are needed to extract transport coefficients. Therefore, I combined the TDVP algorithms (serial and parallel) with LBO, which we used to calculate the optical conductivity for the Holstein model with dispersive phonons at finite temperatures. The results were presented in our publication in Ch. 5.

Our work was motivated by the number of optical conductivity measurements in polaron systems, see, e.g., Refs. [25, 28, 31]. The goal of our research was to extend the scheme developed in Ch. 4 to now treat different versions of the Holstein model (with a finite phonon bandwidth and electron-electron interaction) efficiently. This numerical method helps us better understand the influence of electron-phonon coupling, bipolaron formation, phonon bandwidth, and temperature on optical conductivity spectra. We also demonstrated that the Born-Oppenheimer formalism can be used to interpret the polaron and bipolaron optical conductivity, even when accounting for electron-electron interaction. This holds, even when the interaction is strong enough to significantly change the spectra.

To conclude Ch. 5, I presented the first matrix-product-state-based study of the energy transport coefficient in the Holstein model at finite filling. These computations are a crucial step towards understanding the model's thermal conductivity. I demonstrated that for strong electron-phonon coupling and small phonon frequencies, the picture remains qualitatively the same for the optical conductivity and the energy transport coefficient. Both quantities display known small polaron features. For an intermediate coupling strength and frequency, the energy transport coefficient has a plateau at high frequencies, which remains even when the optical conductivity has decayed to zero. I also want to note that the results in Ch. 4 and Ch. 5 provide numerically exact benchmark data for other methods.

In Ch. 6, I presented a study of the Holstein model and the Holstein model coupled to two tight-binding leads (a Holstein heterostructure) in the ground state when a bias voltage is applied. Here, the aim was to investigate the breakdown of CDWs in both models in the CDW parameter regime. In the metallic phase, the goal was to compute a current-voltage diagram of the Holstein heterostructure for different electron-phonon interaction strengths. This was accomplished using tDMRG-LBO. We observed that the quasi-steady-state current flowing through the system visibly decrease when the electron-phonon coupling is increased. For the CDWs, bias voltages of the order of the polaron binding energy are needed for the electrons to leave the phonon induced potential and the CDW order parameter to decay. We further showed that the polaron structure of the first optimal mode remains stable during the initial tunneling process of the electrons.

Lastly, in Ch. 7, we pursued the question of whether a complete quantum-mechanical treatment of the phonons is necessary to tackle some typical solid-state physics problems.

We focused on the spread of an electron and on the decay of different CDWs. To do this, we compared the numerically exact tDMRG-LBO method to the trajectory-based methods: surface hopping [124–126], multitrajectory Ehrenfest [122, 123] (MTE), and multiconfigurational Ehrenfest [120, 121] (MCE). We found that all methods capture the spread of the electron density at initial times but that they later deviate from the tDMRG-LBO results. We also saw that MTE fails to accurately compute the time evolution of the phonon energy. We then compared MTE and tDMRG-LBO in a system with 13 sites at finite filling. Starting from different CDW initial states, we computed the time evolution of different electron and phonon observables. There, we found that MTE computes the electron order parameter very accurately for model parameters in the adiabatic-strong-coupling regime. For the dressed CDW, the initial dynamics of the kinetic energy are also well captured. In all cases, the MTE method gets different values for the phonon number, which indicates that it might not be well suited for studying energy transfer between electrons and phonons.

This thesis paves the way for addressing a series of other scientific questions. For example, recent results [38, 305] have shown that an electron-phonon model with a bond-Peierls coupling can lead to bipolaron-induced high-temperature superconductivity in a two-dimensional lattice. The numerical methods utilized here can be used to detect features distinguishing a bond-Peierls and a Holstein-type coupling (in a one-dimensional system) in experimentally accessible quantities like optical conductivity.

In the context of trajectory-based algorithms, it is a natural next step to combine MTE with large-scale DMRG simulations. This has already been explored with similar approaches for other methods in, e.g., Refs. [178, 239]. This might allow for longer time evolutions and one might be able to compute current-voltage diagrams in the CDW phase in the Holstein heterostructure. One could also try to treat more complicated systems, such as the Holstein-Kondo lattice model [277].

Furthermore, it would be interesting to compute spectral functions and conductivities using a trajectory-based approach. By comparing these to exact results, one could investigate which, if any, quasi-particle properties are captured. Since an extension of trajectory-based methods to finite temperatures already exists [304], one could also benchmark them to exact methods in setups where a single electron or CDW is coupled to a thermal phonon bath. Such a study might give new insight into the influence of temperature on the spread of electron density or CDW melting. Another challenging but exciting extension would be to compute out-of-equilibrium spectral functions and optical conductivities [260–262, 306].

Appendix A

Derivation of the spectral function

I am interested in what happens when a phononic system is cooled down to a temperature T, before inserting an electron and then letting the system time evolve. The derivation is textbook material, see, e.g., Ref. [184]. I start with $G_T^>(t,k) = -i\left\langle \hat{c}_k(t)\hat{c}_k^\dagger(0)\right\rangle_T$:

$$\begin{aligned} G_T^>(\omega,k) &= -i\int_{-\infty}^{\infty} dt e^{i\omega t}\left\langle e^{i\hat{H}t}\hat{c}_k e^{-i\hat{H}t}\hat{c}_k^\dagger\right\rangle_T \\ &= -i\Big(\int_0^{\infty} dt e^{i\omega t}\left\langle e^{i\hat{H}t}\hat{c}_k e^{-iHt}\hat{c}_k^\dagger\right\rangle_T + \int_{-\infty}^{0} dt e^{i\omega t}\left\langle e^{i\hat{H}t}\hat{c}_k e^{-i\hat{H}t}\hat{c}_k^\dagger\right\rangle_T\Big) \\ &= -i\int_0^{\infty} dt\Big(e^{i\omega t}\left\langle e^{i\hat{H}t}\hat{c}_k e^{-i\hat{H}t}\hat{c}_k^\dagger\right\rangle_T + e^{-i\omega t}\left\langle e^{-i\hat{H}t}\hat{c}_k e^{i\hat{H}t}\hat{c}_k^\dagger\right\rangle_T\Big). \end{aligned} \tag{A.1}$$

If I define $G_T(\omega,k) = \left\langle e^{iHt}c_k e^{-iHt}c_k^\dagger\right\rangle_T$, I get

$$G_T^>(\omega,k) = -i\int_0^{\infty} dt\Big(e^{i\omega t}G_T(t,k) + e^{-i\omega t}G_T^*(t,k)\Big). \tag{A.2}$$

I continue by inserting the identity operator $\mathbb{1} = \sum_n |n\rangle\langle n|$ and get $\left\langle e^{i\hat{H}t}\hat{c}_k e^{-i\hat{H}t}\hat{c}_k^\dagger\right\rangle = \frac{1}{Z}\sum_{n,m} e^{iE_nt}e^{-iE_mt}e^{-\beta E_n}\langle n|\hat{c}_k|m\rangle\langle m|\hat{c}_k^\dagger|n\rangle$ and after adding a regularization factor η to the exponent I obtain

$$\begin{aligned} \int_0^{\infty} dt e^{i\omega t-\eta t}\left\langle e^{i\hat{H}t}\hat{c}_k e^{-i\hat{H}t}\hat{c}_k^\dagger\right\rangle_T &= \frac{1}{Z}\int_0^{\infty} dt\sum_{n,m} e^{-\beta E_n}e^{it(\omega+E_n-E_m+i\eta)}\langle n|\hat{c}_k|m\rangle\langle m|\hat{c}_k^\dagger|n\rangle \\ &= \frac{1}{Z}\sum_{n,m} e^{-\beta E_n}\frac{\langle n|\hat{c}_k|m\rangle\langle m|\hat{c}_k^\dagger|n\rangle}{-i(\omega+E_n-E_m+i\eta)} = \frac{i}{Z}\sum_{n,m} e^{-\beta E_n}\frac{\langle n|\hat{c}_k|m\rangle\langle m|\hat{c}_k^\dagger|n\rangle}{(\omega+E_n-E_m+i\eta)}, \end{aligned} \tag{A.3}$$

and for the term with $G_T^*(t,k)$, I get

$$\begin{aligned} \int_0^{\infty} dt e^{-i\omega t-\eta t}\left\langle e^{-i\hat{H}t}\hat{c}_k e^{i\hat{H}t}\hat{c}_k^\dagger\right\rangle_T &= \frac{1}{Z}\int_0^{\infty} dt\sum_{n,m} e^{-\beta E_n}e^{-it(\omega+E_n-E_m-i\eta)}\langle n|\hat{c}_k|m\rangle\langle m|\hat{c}_k^\dagger|n\rangle \\ &= \frac{1}{Z}\sum_{n,m} e^{-\beta E_n}\frac{\langle n|\hat{c}_k|m\rangle\langle m|\hat{c}_k^\dagger|n\rangle}{i(\omega+E_n-E_m-i\eta)} = \frac{-i}{Z}\sum_{n,m} e^{-\beta E_n}\frac{\langle n|\hat{c}_k|m\rangle\langle m|\hat{c}_k^\dagger|n\rangle}{(\omega+E_n-E_m-i\eta)}. \end{aligned} \tag{A.4}$$

In total, I have

$$G_T^{>}(\omega,k) = -i\Big(\frac{i}{Z}\sum_{n,m} e^{-\beta E_n}\frac{\langle n|\,\hat{c}_k\,|m\rangle\,\langle m|\,\hat{c}_k^{\dagger}\,|n\rangle}{(\omega+E_n-E_m+i\eta)} + \frac{(-i)}{Z}\sum_{n,m} e^{-\beta E_n}\frac{\langle n|\,\hat{c}_k\,|m\rangle\,\langle m|\,\hat{c}_k^{\dagger}\,|n\rangle}{(\omega+E_n-E_m-i\eta)}\Big)$$
$$= \Big(\frac{1}{Z}\sum_{n,m} e^{-\beta E_n}\frac{\langle n|\,\hat{c}_k\,|m\rangle\,\langle m|\,\hat{c}_k^{\dagger}\,|n\rangle}{(\omega+E_n-E_m+i\eta)} - \frac{1}{Z}\sum_{n,m} e^{-\beta E_n}\frac{\langle n|\,\hat{c}_k\,|m\rangle\,\langle m|\,\hat{c}_k^{\dagger}\,|n\rangle}{(\omega+E_n-E_m-i\eta)}\Big)\,. \quad \text{(A.5)}$$

I now use that $\frac{1}{\omega-a+i\eta} - \frac{1}{\omega-a-i\eta} = \frac{-2i\eta}{(\omega-a)^2+(\eta)^2} = -2\pi i\delta(\omega-a)$ and get

$$G_T^{>}(k,\omega) = \frac{-2\pi i}{Z}\Big(\sum_{n,m} e^{-\beta E_n}\,\langle n|\,\hat{c}_k\,|m\rangle\,\langle m|\,\hat{c}_k^{\dagger}\,|n\rangle\,\delta(\omega+E_n-E_m)\Big)\,. \quad \text{(A.6)}$$

Finally, I get

$$A(k,\omega) = \frac{-1}{2\pi}\mathrm{Im}\{G_T^{>}(k,\omega)\}\,. \quad \text{(A.7)}$$

Appendix B

Single-site spectral functions

B.1 Single-site emission spectrum

I will here derive the single-site emission spectrum for the Holstein model. The formula is

$$A_s^+(\omega) = \sum_{n,m} \frac{e^{-\beta E_m}}{Z} |\langle n|\hat{c}|m\rangle|^2 \delta(\omega + E_n - E_m)\,, \tag{B.1}$$

where $|m\rangle$ and $|n\rangle$ are general eigenstates. For the derivation, I define $\tilde{g} = \gamma/\omega_0$ and start with one electron in the system. The eigenstates then become the coherent and excited states

$$|\tilde{m}\rangle = \frac{1}{\sqrt{\tilde{m}!}}(\hat{b}^\dagger + \tilde{g})^{\tilde{m}} |\tilde{0}\rangle\ , \tag{B.2}$$

with the eigenenergies $\epsilon_{\tilde{m}} = -\omega_0\tilde{g}^2 + \tilde{m}\omega_0$. The ground state is

$$|\tilde{0}\rangle = e^{-\tilde{g}^2/2} \sum_{m=0}^{\infty} \frac{(-\tilde{g})^m}{\sqrt{m!}} |m\rangle\ , \tag{B.3}$$

where $|m\rangle$ corresponds to the bare phonon states. Inserting this into Eq. (B.1), I get

$$A_s^+(\omega) = \sum_{n,\tilde{m}} \frac{e^{-\beta\epsilon_{\tilde{m}}}}{Z} |\langle n|\hat{c}|\tilde{m}\rangle|^2 \delta(\omega+\omega_0 n-\epsilon_{\tilde{m}}) = \sum_{n,\tilde{m}} \frac{e^{-\beta(-\omega_0\tilde{g}^2+\tilde{m}\omega_0)}}{Z} |\langle n|\hat{c}|\tilde{m}\rangle|^2 \delta(\omega+\omega_0 n-\epsilon_{\tilde{m}})\,, \tag{B.4}$$

where I used that $\langle n|$ are the bare phonon states. Since in $|\langle n|c_k|\tilde{m}\rangle|^2$, the electron states trivially overlap, I only focus on the phonon sector. There, following Ref. [65],

$$\langle n|\tilde{m}\rangle = e^{-\tilde{g}^2/2} \sum_{l=0}^{\min(\tilde{m},n)} (-1)^{n-l} \tilde{g}^{n+\tilde{m}-2l} \frac{\sqrt{\tilde{m}!n!}}{l!(\tilde{m}-l)!(n-l)!}\,. \tag{B.5}$$

Taking the limit $T \to 0$, only the sum over n will contribute and I have $\tilde{m} = 0$ and $l = 0$. This gives

$$\langle n|\tilde{m}\rangle = e^{-\tilde{g}^2/2}(-1)^0 \tilde{g}^{n+0-0} \frac{\sqrt{0!n!}}{0!(0)!(n-0)!} = e^{-\tilde{g}^2/2}\tilde{g}^n \frac{\sqrt{n!}}{n!}\,, \tag{B.6}$$

which for the emission function gives

$$\lim_{T\to 0} A_s^+ = \sum_n e^{-\tilde{g}^2}\tilde{g}^{2n}\frac{1}{n!}\delta(\omega+\omega_0 n+\tilde{g}^2\omega_0)\,. \tag{B.7}$$

This is just ω_0 spaced peaks. A_s^+ is shown for different temperatures in Ch. 4.

B.2 Single-site phonon spectral function

The single-site phonon spectral function is defined as

$$B_s(\omega) = \sum_{\tilde{n},\tilde{m}} e^{-\beta\epsilon_{\tilde{m}}} \left|\langle\tilde{n}|\hat{X}|\tilde{m}\rangle\right|^2 \delta(\omega-\tilde{n}\omega_0+\tilde{m}\omega_0) \tag{B.8}$$

To evauate Eq. (B.8), I first calculate

$$\langle\tilde{n}|\hat{X}|\tilde{m}\rangle = \langle\tilde{n}|\hat{b}^\dagger+\hat{b}|\tilde{m}\rangle\ . \tag{B.9}$$

I first evaluate $\hat{b}$ acting on the ground state $|\tilde{0}\rangle$ from Eq. (B.3) to verify that it is an eigenstate:

$$\begin{aligned}\hat{b}\,|\tilde{0}\rangle &= e^{-\tilde{g}^2/2}\sum_{m=0}^{\infty}\frac{(-\tilde{g})^m}{\sqrt{m!}}\hat{b}\,|m\rangle = e^{-\tilde{g}^2/2}\sum_{m=0}^{\infty}\frac{(-\tilde{g})^m}{\sqrt{m!}}\sqrt{m}\,|m-1\rangle \\ &= e^{-\tilde{g}^2/2}\sum_{m=0}^{\infty}\frac{(-\tilde{g})^m}{\sqrt{(m-1)!}}\,|m-1\rangle = -\tilde{g}e^{-\tilde{g}^2/2}\sum_{m=1}^{\infty}\frac{(-\tilde{g})^{m-1}}{\sqrt{(m-1)!}}\,|m-1\rangle = -\tilde{g}\,|\tilde{0}\rangle\end{aligned} \tag{B.10}$$

Next, I calculate

$$\hat{b}(\hat{b}^\dagger+\tilde{g}) = \hat{b}\hat{b}^\dagger+\tilde{g}\hat{b} = 1+\hat{b}^\dagger b+\tilde{g}\hat{b} = 1+(\hat{b}^\dagger+\tilde{g})\hat{b}\,, \tag{B.11}$$

and

$$\begin{aligned}\hat{b}(\hat{b}^\dagger+\tilde{g})^2 &= \hat{b}(\hat{b}^\dagger+\tilde{g})(\hat{b}^\dagger+\tilde{g}) = \Big(1+(\hat{b}^\dagger+\tilde{g})\hat{b}\Big)(\hat{b}^\dagger+\tilde{g}) = (\hat{b}^\dagger+\tilde{g})+(\hat{b}^\dagger+\tilde{g})\hat{b}(\hat{b}^\dagger+\tilde{g}) \\ &= (\hat{b}^\dagger+\tilde{g})+(\hat{b}^\dagger+\tilde{g})\Big(1+(\hat{b}^\dagger+\tilde{g})\hat{b}\Big) = 2(\hat{b}^\dagger+\tilde{g})+(\hat{b}^\dagger+\tilde{g})^2\hat{b}\,,\end{aligned} \tag{B.12}$$

and lastly

$$\begin{aligned}\hat{b}(\hat{b}^\dagger+\tilde{g})^3 &= \hat{b}(\hat{b}^\dagger+\tilde{g})(\hat{b}^\dagger+\tilde{g})(\hat{b}^\dagger+\tilde{g}) \\ &= \Big(2(\hat{b}^\dagger+\tilde{g})+(\hat{b}^\dagger+\tilde{g})^2\hat{b}\Big)(\hat{b}^\dagger+\tilde{g}) = 2(\hat{b}^\dagger+\tilde{g})^2+(\hat{b}^\dagger+\tilde{g})^2\hat{b}(\hat{b}^\dagger+\tilde{g}) \\ &= 2(\hat{b}^\dagger+\tilde{g})^2+(\hat{b}^\dagger+\tilde{g})^2\Big(1+(\hat{b}^\dagger+\tilde{g})\hat{b}\Big) = 2(\hat{b}^\dagger+\tilde{g})^2+(\hat{b}^\dagger+\tilde{g})^2+(\hat{b}^\dagger+\tilde{g})^3\hat{b} \\ &= 3(\hat{b}^\dagger+\tilde{g})^2+(\hat{b}^\dagger+\tilde{g})^3\hat{b}\,,\end{aligned} \tag{B.13}$$

which leads us to the assumption $\hat{b}(\hat{b}^\dagger+\tilde{g})^m = m(\hat{b}^\dagger+\tilde{g})^{m-1} + (\hat{b}^\dagger+\tilde{g})^m\hat{b}$. I prove by induction that for $m \to m+1$,

$$\begin{aligned}\hat{b}(\hat{b}^\dagger+\tilde{g})^{m+1} &= \hat{b}(\hat{b}^\dagger+\tilde{g})^m(\hat{b}^\dagger+\tilde{g}) = \Big(m(\hat{b}^\dagger+\tilde{g})^{m-1} + (\hat{b}^\dagger+\tilde{g})^m\hat{b}\Big)(\hat{b}^\dagger+\tilde{g}) \\ &= m(\hat{b}^\dagger+\tilde{g})^m + (\hat{b}^\dagger+\tilde{g}^m)\hat{b}(\hat{b}^\dagger+\tilde{g}) = m(\hat{b}^\dagger+\tilde{g})^m + (\hat{b}^\dagger+\tilde{g})^m\Big(1+(\hat{b}^\dagger+\tilde{g})\hat{b}\Big) \\ &= m(\hat{b}^\dagger+\tilde{g})^m + (\hat{b}^\dagger+\tilde{g})^m + (\hat{b}^\dagger+\tilde{g})^{m+1}\hat{b} = (m+1)(\hat{b}^\dagger+\tilde{g})^m + (\hat{b}^\dagger+\tilde{g})^{m+1}\hat{b}\,.\end{aligned} \tag{B.14}$$

Now, I evaluate

$$\begin{aligned}\hat{b}\,|\tilde{m}\rangle &= \frac{1}{\sqrt{\tilde{m}!}}\Big(\hat{b}(\hat{b}^\dagger+\tilde{g})^{\tilde{m}}\Big)\,|\tilde{0}\rangle = \frac{1}{\sqrt{\tilde{m}!}}(\tilde{m}(\hat{b}^\dagger+\tilde{g})^{\tilde{m}-1} + (\hat{b}^\dagger+\tilde{g})^{\tilde{m}}\hat{b})\,|\tilde{0}\rangle \\ &= \frac{\sqrt{\tilde{m}}}{\sqrt{(\tilde{m}-1)!}}(\hat{b}^\dagger+\tilde{g})^{\tilde{m}-1}\,|\tilde{0}\rangle + \frac{1}{\sqrt{\tilde{m}!}}(\hat{b}^\dagger+\tilde{g})^{\tilde{m}}(-\tilde{g})\,|\tilde{0}\rangle = \sqrt{\tilde{m}}\,|\widetilde{m-1}\rangle - \tilde{g}\,|\tilde{m}\rangle\ .\end{aligned} \tag{B.15}$$

This gives

$$\langle\tilde{n}|\hat{b}|\tilde{m}\rangle = \sqrt{\tilde{m}}\,\langle\tilde{n}|\widetilde{m-1}\rangle - \tilde{g}\,\langle\tilde{n}|\tilde{m}\rangle\ . \tag{B.16}$$

This means that

$$\begin{aligned}\langle\tilde{n}|\hat{X}|\tilde{m}\rangle &= \langle\tilde{n}|\hat{b}+\hat{b}^\dagger|\tilde{m}\rangle = \langle\tilde{n}|\hat{b}^\dagger|\tilde{m}\rangle + \langle\tilde{n}|\hat{b}|\tilde{m}\rangle \\ &= \sqrt{\tilde{n}}\,\langle\widetilde{n-1}|\tilde{m}\rangle - \tilde{g}\,\langle\tilde{n}|\tilde{m}\rangle + \sqrt{\tilde{m}}\,\langle\tilde{n}|\widetilde{m-1}\rangle - \tilde{g}\,\langle\tilde{n}|\tilde{m}\rangle \\ &= \sqrt{\tilde{n}}\,\langle\widetilde{n-1}|\tilde{m}\rangle + \sqrt{\tilde{m}}\,\langle\tilde{n}|\widetilde{m-1}\rangle - 2\tilde{g}\,\langle\tilde{n}|\tilde{m}\rangle\ ,\end{aligned} \tag{B.17}$$

where I applied $\hat{b}^\dagger$ to the left and $\hat{b}$ to the right. The total expression becomes

$$B_s(\omega) \;=\; \sum_{\tilde{n},\tilde{m}}\frac{e^{-\beta\epsilon_{\tilde{m}}}}{Z}\big|\sqrt{\tilde{n}}\,\langle\widetilde{n-1}|\widetilde{m}\rangle + \sqrt{\tilde{m}}\,\langle\tilde{n}|\widetilde{m-1}\rangle - 2\tilde{g}\,\langle\tilde{n}|\tilde{m}\rangle\big|^2\delta(\omega - \tilde{n}\omega_0 + \tilde{m}\omega_0)\,. \tag{B.18}$$

For the ground state,

$$\begin{aligned}\lim_{T\to 0}B_s(\omega) &= \sum_{\tilde{n}}\big|\sqrt{\tilde{n}}\,\langle\widetilde{n-1}|\tilde{0}\rangle - 2\tilde{g}\,\langle\tilde{n}|\tilde{0}\rangle\big|^2\delta(\omega-\tilde{n}\omega_0) \\ &= \big|-2\tilde{g}\,\langle\tilde{0}|\tilde{0}\rangle\big|^2\delta(\omega) + \big|\sqrt{1}\,\langle\tilde{0}|\tilde{0}\rangle\big|^2\delta(\omega-\omega_0) \\ &= \big|-2\tilde{g}\,\langle\tilde{0}|\tilde{0}\rangle\big|^2\delta(\omega) + \big|\sqrt{1}\,\langle\tilde{0}|\tilde{0}\rangle\big|^2\delta(\omega-\omega_0)\,,\end{aligned} \tag{B.19}$$

which is one peak at $\omega = 0$ and one at $\omega = \omega_0$. As temperature increases and additional peak at $\omega = -\omega_0$ should emerge.

Appendix C

Born-Oppenheimer surfaces and optical conductivity

C.1 Phonon fluctuations

I will first calculating the variance of the displacement operator for a harmonic oscillator:

$$\begin{aligned}\langle\hat{x}^2\rangle - \langle\hat{x}\rangle^2 &= \langle\hat{x}^2\rangle = \langle(\hat{b}^\dagger+\hat{b})^2\rangle = \langle(\hat{b}^\dagger+\hat{b})(\hat{b}^\dagger+\hat{b})\rangle = \langle\hat{b}^\dagger\hat{b}^\dagger+\hat{b}\hat{b}^\dagger+\hat{b}^\dagger\hat{b}+\hat{b}\hat{b}\rangle \\ &= \langle\hat{b}^\dagger\hat{b}^\dagger\rangle + \langle\hat{b}\hat{b}^\dagger\rangle + \langle\hat{b}^\dagger\hat{b}\rangle + \langle\hat{b}\hat{b}\rangle = \langle\hat{b}\hat{b}^\dagger\rangle + \langle\hat{b}^\dagger\hat{b}\rangle = \langle 1+\hat{n}\rangle + \langle\hat{n}\rangle \\ &= 1 + \langle 2\hat{n}\rangle = 1 + \frac{2}{e^{\beta\omega_0}-1} = \frac{e^{\beta\omega_0}-1+2}{e^{\beta\omega_0}-1} = \frac{e^{\beta\omega_0}+1}{e^{\beta\omega_0}-1} \\ &= \frac{e^{\beta\omega_0/2}}{e^{\beta\omega_0/2}}\frac{e^{\beta\omega_0/2}+1}{e^{\beta\omega_0/2}-1} = \frac{e^{\beta\omega_0/2}+e^{-\beta\omega_0/2}}{e^{\beta\omega_0/2}-e^{-\beta\omega_0/2}} = \coth(\beta\omega_0/2)\end{aligned} \tag{C.1}$$

C.2 Deriving the Born-Oppenheimer Hamiltonian for the Holstein dimer

To calculate the Born-Oppenheimer Hamiltonian, I first write $\hat{b}_i = \sqrt{\frac{m\omega_0}{2}}(\hat{x}_i + \frac{i}{m\omega_0}\hat{p}_i)$ and $\hat{b}_i^\dagger = \sqrt{\frac{m\omega_0}{2}}(\hat{x}_i - \frac{i}{m\omega_0}\hat{p}_i)$ with $\hbar = 1$. The phonon kinetic energy is $\sum_{i=1}^{L-1} t_{\mathrm{ph}}(\hat{b}_i^\dagger\hat{b}_{i+1} + \hat{b}_{i+1}^\dagger\hat{b}_i)$.

Rewritten in terms of $\hat{x}_i$ and $\hat{p}_i$, each term becomes

$$\begin{aligned}
&t_{\mathrm{ph}}(\hat{b}_i^\dagger \hat{b}_{i+1} + \hat{b}_{i+1}^\dagger \hat{b}_i) = t_{\mathrm{ph}} \frac{m\omega_0}{2} \Big((\hat{x}_i - \frac{i}{m\omega_0}\hat{p}_i)(\hat{x}_{i+1} + \frac{i}{m\omega_0}\hat{p}_{i+1}) \\
&+ (\hat{x}_{i+1} - \frac{i}{m\omega_0}\hat{p}_{i+1})(\hat{x}_i + \frac{i}{m\omega_0}\hat{p}_i) \Big) \\
&= t_{\mathrm{ph}} \frac{m\omega_0}{2} (\hat{x}_i\hat{x}_{i+1} + \hat{x}_{i+1}\hat{x}_i + \frac{1}{m^2\omega_0^2}\hat{p}_i\hat{p}_{i+1} + \frac{1}{m^2\omega_0^2}\hat{p}_{i+1}\hat{p}_i - \frac{i}{m\omega_0}\hat{p}_i\hat{x}_{i+1} \\
&+ x_i \frac{i}{m\omega_0}\hat{p}_{i+1} + \frac{i}{m\omega_0}\hat{x}_{i+1}\hat{p}_i - \frac{i}{m\omega_0}\hat{p}_{i+1}\hat{x}_i) \\
&= t_{\mathrm{ph}} m\omega_0 (\hat{x}_i\hat{x}_{i+1} + \frac{1}{m^2\omega_0^2}\hat{p}_i\hat{p}_{i+1}) \,.
\end{aligned} \tag{C.2}$$

The rest of the local terms in the Hamiltonian become

$$\begin{aligned}
\omega_0(\hat{b}_i^\dagger \hat{b}_i) &= \omega_0 \Big(\frac{m\omega_0}{2} (\hat{x}_i - \frac{i}{m\omega_0}\hat{p}_i)(\hat{x}_i + \frac{i}{m\omega_0}\hat{p}_i) \Big) \\
&= \frac{m\omega_0\omega_0}{2} (\hat{x}_i^2 + \frac{1}{m^2\omega_0^2}\hat{p}_i^2 + \hat{x}_i \frac{i}{m\omega_0}\hat{p}_i - \frac{i}{m\omega_0}\hat{p}_i\hat{x}_i) \\
&= \frac{m\omega_0\omega_0}{2} \Big(\hat{x}_i^2 + \frac{1}{m^2\omega_0^2}\hat{p}_i^2 + \frac{i}{m\omega_0}(\hat{x}_i\hat{p}_i - \hat{p}_i\hat{x}_i) \Big) \\
&= \frac{m\omega_0^2}{2} (\hat{x}_i^2 + \frac{1}{m^2\omega_0^2}\hat{p}_i^2 + \frac{i}{m\omega_0}[\hat{x}_i, \hat{p}_i]) \\
&= \frac{m\omega_0\omega_0}{2} (\hat{x}_i^2 + \frac{1}{m^2\omega_0^2}\hat{p}_i^2 - \frac{1}{m\omega_0}) \,,
\end{aligned} \tag{C.3}$$

and

$$\gamma \hat{n}_i (\hat{b}_i^\dagger + \hat{b}_i) = \gamma \hat{n}_i \sqrt{\frac{m\omega_0}{2}} (\hat{x}_i + \frac{i}{m\omega_0}\hat{p}_i + \hat{x}_i - \frac{i}{m\omega_0}\hat{p}_i) = \gamma \sqrt{\frac{m\omega_0}{2}} \hat{n}_i (2\hat{x}_i) \,, \tag{C.4}$$

The total Hamiltonian is now

$$\begin{aligned}
\hat{H} = \hat{H}_{\mathrm{ekin}} &+ \sum_{i=1}^{L} \Big(\gamma \sqrt{\frac{m\omega_0}{2}} \hat{n}_i (2\hat{x}_i) + \frac{m\omega_0^2}{2} (\hat{x}_i^2 + \frac{1}{m^2\omega_0^2}\hat{p}_i^2 - \frac{1}{m\omega_0}) \Big) \\
&+ t_{\mathrm{ph}} m\omega_0 \sum_{i=1}^{L-1} (\hat{x}_i\hat{x}_{i+1} + \frac{1}{m^2\omega_0^2}\hat{p}_i\hat{p}_{i+1}) \,,
\end{aligned} \tag{C.5}$$

where $\hat{H}_{\mathrm{ekin}}$ is electron kinetic energy operator (see Ch. 2). I now consider the dimer ($L = 2$), and write $\hat{q} = (\hat{x}_1 - \hat{x}_2)/\sqrt{2}$ and $\hat{Q} = (\hat{x}_1 + x_2)/\sqrt{2}$ which transforms to $\hat{x}_1 = \sqrt{2}\hat{q} + \hat{x}_2$ and $\hat{Q} = (\sqrt{2}\hat{q} + \hat{x}_2 + \hat{x}_2)/\sqrt{2} \to \hat{x}_2 = (1/\sqrt{2})(\hat{Q} - \hat{q})$ and $\hat{x}_1 = \sqrt{2}\hat{q} + (1/\sqrt{2})\hat{Q} - (1/\sqrt{2})\hat{q} = (1/\sqrt{2})(\hat{q} + \hat{Q})$. I further send $\hat{p}_i \to 0$ (slow phonons), $\hat{q}, \hat{Q} \to q, Q$, and ignore the constant

energy offset. Now,

$$\begin{aligned}\hat{H} =&\hat{H}_{\text{ekin}} + \gamma\sqrt{\frac{m\omega_0}{2}}\Big(\hat{n}_1 2\frac{1}{\sqrt{2}}(Q+q) + \hat{n}_2 2\frac{1}{\sqrt{2}}(Q-q)\Big)\\ &+ \frac{m\omega_0\omega_0}{2}\Big(\frac{1}{2}(q+Q)^2 + \frac{1}{2}(Q-q)^2\Big) + t_{\text{ph}} m\omega_0 \frac{1}{2}(q+Q)(q-Q)\\ &= \hat{H}_{\text{ekin}} + \gamma\sqrt{m\omega_0}\Big(Q(\hat{n}_1+\hat{n}_2) + q(\hat{n}_1-\hat{n}_2)\Big) + \frac{m\omega_0\omega_0}{2}\frac{1}{2}(2q^2+2Q^2+2qQ-2qQ)\\ &+ t_{\text{ph}} m\omega_0 \frac{1}{2}(Q^2-q^2)\,.\end{aligned} \tag{C.6}$$

For a constant electron density $\hat{n}_1+\hat{n}_2$, the Q's just correspond to an independent harmonic oscillator and can be neglected in the following calculations. I am then left with

$$\begin{aligned}\hat{H} &= \hat{H}_{\text{ekin}} + \gamma\sqrt{\frac{m\omega_0}{2}}\Big(q(\hat{n}_1-\hat{n}_2)\Big) + \frac{m\omega_0\omega_0}{2}q^2 + t_{\text{ph}} m\omega_0 \frac{1}{2}q^2\\ &= H_{\text{ekin}} + \gamma\sqrt{\frac{m\omega_0}{2}}\Big(q(\hat{n}_1-\hat{n}_2)\Big) + \frac{m\omega_0}{2}q^2(\omega_0 - t_{\text{ph}})\,.\end{aligned} \tag{C.7}$$

I now define $\bar{q} = q\sqrt{m\omega_0}$ and get

$$\begin{aligned}&H = H_{\text{ekin}} + \gamma\sqrt{m\omega_0}\Big(q(\hat{n}_1-\hat{n}_2)\Big) + \frac{m\omega_0}{2}q^2(\omega_0 - t_{\text{ph}}) \rightarrow\\ &\hat{H} = \hat{H}_{\text{ekin}} + \gamma\Big(\bar{q}(\hat{n}_1-\hat{n}_2)\Big) + \frac{1}{2}\bar{q}^2(\omega_0 - t_{\text{ph}}) = \hat{H}_{\text{ekin}} + \gamma\Big(\bar{q}(\hat{n}_1-\hat{n}_2)\Big) + \frac{1}{2}\bar{q}^2\tilde{\omega}_0\,,\end{aligned} \tag{C.8}$$

where I wrote $\tilde{\omega}_0 = \omega_0 - t_{\text{ph}}$. This is now $\hat{H}_{\text{BO}}$.

Written as a matrix,

$$\hat{H}_{\text{BO}} = \begin{pmatrix} \frac{\bar{q}^2}{2}\tilde{\omega}_0 + \gamma\bar{q} & -t_0 \\ -t_0 & \frac{\bar{q}^2}{2}\tilde{\omega}_0 - \gamma\bar{q}\end{pmatrix}, \tag{C.9}$$

with eigenvalues $E_\pm = \frac{1}{2}\Big(\bar{q}^2\tilde{\omega}_0 \pm 2\sqrt{(\gamma\bar{q})^2 + t_0^2}\Big)$. To find the $\bar{q}$ corresponding to the minima of E_-, take the derivative of E_- with respect to $\bar{q}$. This gives gives $\frac{dE_-}{dq} = \frac{1}{2}\Big(2\bar{q}\tilde{\omega}_0 -$

$\frac{2\gamma^2\bar{q}}{\sqrt{\gamma^2\bar{q}^2+t_0^2}}\Big) = \bar{q}\tilde{\omega}_0 - \frac{\gamma^2\bar{q}}{\sqrt{\gamma^2\bar{q}^2+t_0^2}}$. Finding extrema, $\frac{dE_-}{d\bar{q}} = 0$, gives $\bar{q} = 0$ and

$$\begin{aligned}
\frac{\gamma^2}{\sqrt{\gamma^2\bar{q}^2 + t_0^2}} &= \tilde{\omega}_0 \\
\gamma^4 &= \tilde{\omega}_0^2(\gamma^2\bar{q}^2 + t_0^2) \\
\gamma^4 - \tilde{\omega}_0^2 t_0^2 &= \tilde{\omega}_0^2(\gamma^2\bar{q}^2) \\
\frac{\gamma^4 - \tilde{\omega}_0^2 t_0^2}{\tilde{\omega}_0^2\gamma^2} &= \bar{q}^2 \\
\sqrt{\frac{\gamma^4 - \tilde{\omega}_0^2 t_0^2}{\tilde{\omega}_0^2\gamma^2}} &= \bar{q} \\
\rightarrow \pm\frac{\sqrt{\gamma^4 - \tilde{\omega}_0^2 t_0^2}}{\tilde{\omega}_0\gamma} &= \bar{q}_{min}\,.
\end{aligned} \tag{C.10}$$

Evaluating $E_\pm$ at $\bar{q}_{min}$ gives $E_\pm(\bar{q}_{min}) = \frac{1}{2}\Big(\frac{\gamma^4-\tilde{\omega}_0^2t_0^2}{\gamma^2\tilde{\omega}_0} \pm 2\sqrt{\gamma^2\frac{\gamma^4-\tilde{\omega}_0^2t_0^2}{\gamma^2\tilde{\omega}_0^2} + t_0^2}\Big) = \frac{1}{2}\Big(\frac{\gamma^4-\tilde{\omega}_0^2t_0^2}{\gamma^2\tilde{\omega}_0} \pm 2\sqrt{\frac{\gamma^4-\tilde{\omega}_0^2t_0^2}{\tilde{\omega}_0^2} + t_0^2}\Big)$ and $E_+ - E_- = 2\sqrt{\frac{\gamma^4-\tilde{\omega}_0^2t_0^2}{\tilde{\omega}_0^2} + t_0^2}$.

C.3 Deriving the optical conductivity

To derive the optical conductivity, I consider two harmonic potentials as a function of $\bar{q}$, separated at a distance d. I will consider transitions from the lower surface, noted with G, to the upper surface, noted with E. More details on the ansatz and derivation can be found in, e.g., Refs. [167, 307–309], whereas these notes mainly are based on calculations in Refs. [167, 309]. Note that a similar result was already derived in [58] (for a flat phonon band).

I first write the Hamiltonian $\hat{H}_0 = |G\rangle\,\hat{H}_G\,\langle G| + |E\rangle\,\hat{H}_E\,\langle E|$, where $|E\rangle$ is the excited and $|G\rangle$ is the lower Born-Oppenheimer state. Each term has a contribution from nuclear and electronic energy $\hat{H}_{G,E} = E_{g,e} + \hat{H}_{g,e}$. The oscillator Hamiltonians are $\hat{H}_e = \frac{\tilde{\omega}_0\hat{p}^2}{2} + \frac{1}{2}\tilde{\omega}_0\hat{\bar{q}}^2$ and $H_g = \frac{\tilde{\omega}_0\hat{p}^2}{2} + \frac{1}{2}\tilde{\omega}_0(\hat{\bar{q}} - d)^2$, and $E_{g,e}$ are the energies on the Born-Oppenheimer surface. I will also write $e^{i\hat{H}_0} = |G\rangle^{-i\hat{H}_G}\,\langle G| + |E\rangle\,e^{-i\hat{H}_E}\,\langle E|$, since the electron either can be on surface one (G) or surface two (E). I now make the approximation that the electron and phonon coordinates form a product state, $|G\rangle = |g, m\rangle$ and $|E\rangle = |e, m\rangle$. Here, $|e\rangle$ ($|g\rangle$) corresponds to the electron being on the upper (lower) Born-Oppenheimer surface, and m to all the configurations of the corresponding oscillator. The correlation function becomes

$$\begin{aligned}
C_T^C(t) &= \sum_{\tilde{n}=E,G} p_{\tilde{n}}\,\langle\tilde{n}|\,e^{i\hat{H}_0 t}\hat{J}e^{-i\hat{H}_0 t}\hat{J}\,|\tilde{n}\rangle \\
&= \sum_{\tilde{n}=E,G} p_{\tilde{n}}\,\langle\tilde{n}|\,(|G\rangle^{-i\hat{H}_G}\,\langle G| + |E\rangle\,e^{-i\hat{H}_E}\,\langle E|)\hat{J}(|G\rangle^{i\hat{H}_G}\,\langle G| + |E\rangle\,e^{i\hat{H}_E}\,\langle E|)\hat{J}\,|\tilde{n}\rangle\ ,
\end{aligned} \tag{C.11}$$

and $p_{\tilde{n}}$ is the corresponding thermal probability. To obtain the current operator in terms of $|e\rangle$ and $|g\rangle$, I use the notation $\hat{J} = it_0(|2\rangle\langle 1| - |1\rangle\langle 2|)$, where $|1\rangle\langle 2| = \hat{c}_1^\dagger \hat{c}_2$. I insert $\hat{\mathbb{1}} = |e\rangle\langle e| + |g\rangle\langle g|$ and get

$$\begin{aligned}\hat{J} = it_0(|2\rangle\langle 1| - |1\rangle\langle 2|) = it_0(&|e\rangle\langle e|2\rangle\langle 1|e\rangle\langle e| - |e\rangle\langle e|1\rangle\langle 2|e\rangle\langle e| \\ &+ |g\rangle\langle g|2\rangle\langle 1|g\rangle\langle g| - |g\rangle\langle g|1\rangle\langle 2|g\rangle\langle g| + |e\rangle\langle e|2\rangle\langle 1|g\rangle\langle g| - |e\rangle\langle e|1\rangle\langle 2|g\rangle\langle g| \\ &+ |g\rangle\langle g|2\rangle\langle 1|e\rangle\langle e| - |g\rangle\langle g|1\rangle\langle 2|e\rangle\langle e|)\,,\end{aligned} \tag{C.12}$$

since the diagonal terms cancel, I am left with

$$\begin{aligned}\hat{J} &= it_0(|e\rangle\langle e|2\rangle\langle 1|g\rangle\langle g| - |e\rangle\langle e|1\rangle\langle 2|g\rangle\langle g| + |g\rangle\langle g|2\rangle\langle 1|e\rangle\langle e| - |g\rangle\langle g|1\rangle\langle 2|e\rangle\langle e|) \\ &= it_0(\langle e|2\rangle\langle 1|g\rangle - \langle e|1\rangle\langle 2|g\rangle)|e\rangle\langle g| + (\langle g|2\rangle\langle 1|e\rangle - |g\rangle\langle g|1\rangle\langle 2|)|g\rangle\langle e|)\,.\end{aligned} \tag{C.13}$$

For the polaron, the eigenstates are known analytically and $it_0(\langle g|2\rangle\langle 1|e\rangle - \langle g|1\rangle\langle 2|e\rangle) = -it_0$. The total prefactor the becomes t_0^2. For the bipolaron, I verify numerically that the total prefactor is $2t_0^2$. Now, I make the assumption that the temperatures are so low that only the lower Born-Oppenheimer surface contributes to the partition function. I then get $Z = e^{-E_g\beta}\sum_n e^{-\hat{H}_{g,n}\beta}$, where $\hat{H}_{g,n}$ is the harmonic oscillator Hamiltonian (now written in the occupation basis n for convenience). Inserting the expression for the current $\hat{J}$ into Eq. (C.11), I get

$$C(t) = t_0^2 e^{-i(E_e - E_g)t}\langle e^{i\hat{H}_g t}e^{-i\hat{H}_e t}\rangle\,, \tag{C.14}$$

where $E_e - E_g$ is the difference in energy for the two harmonic oscillators and I define

$$F(t) = \langle e^{i\hat{H}_g t}e^{-i\hat{H}_e t}\rangle = \langle \hat{U}_g^\dagger \hat{U}_e\rangle\,. \tag{C.15}$$

I now use the Lang Firsov transformation, $e^{-\hat{S}}$ with $\hat{S} = d\sqrt{\frac{1}{2}}(\hat{a} - \hat{a}^\dagger)$ (now shifting $\bar{q}$ to $\bar{q} + d$), which gives $e^{-i\hat{H}_e t} = e^{\hat{S}}e^{-i\hat{H}_g t}e^{-S}$. I then define $\tilde{d} = d\sqrt{\frac{1}{2}}$ and insert this into Eq. (C.15):

$$\begin{aligned}F(t) = \langle e^{iH_g t}e^{-iH_e t}\rangle &= \langle e^{-\hat{S}}e^{\hat{S}}U_g^\dagger e^{-\hat{S}}e^{\hat{S}}\hat{U}_e e^{-\hat{S}}e^{S}\rangle = \langle e^{\hat{S}}\hat{U}_g^\dagger e^{-\hat{S}}e^{\hat{S}}\hat{U}_e e^{-\hat{S}}\rangle \\ &= \langle \hat{U}_e^\dagger e^{\hat{S}}\hat{U}_e e^{-\hat{S}}\rangle = \langle e^{\hat{S}(t)}e^{-\hat{S}}\rangle\end{aligned} \tag{C.16}$$

I now follow Ref. [167] and write

$$F(t) = \langle e^{-\tilde{d}(\hat{a}^\dagger e^{i\omega_0 t} - \hat{a}e^{-i\omega_0 t})}e^{\tilde{d}(\hat{a}^\dagger - \hat{a})}\rangle\,. \tag{C.17}$$

I will now write the phonon partition sum as Z and use that $e^{-\beta E_g}$ cancel. I will also use

that $[\hat{a}^\dagger, a] = -1$ and $e^{A+B} = e^A e^B e^{-1/2[A,B]}$ and follow Ref. [167] to get

$$\begin{aligned}
F(t) &= Z^{-1} Tr[e^{-\beta \hat{H}_{ph}} e^{-(\tilde{d}(\hat{a}^\dagger e^{i\tilde{\omega}_0 t} - \hat{a} e^{-i\tilde{\omega}_0 t}))} e^{\tilde{d}(\hat{a}^\dagger - \hat{a})}] \\
&= Z^{-1} \sum_n e^{-\beta\tilde{\omega}_0 n} \langle n| e^{-(\tilde{d}(a^\dagger e^{i\tilde{\omega}_0 t} - \hat{a} e^{-i\tilde{\omega}_0 t}))} e^{\tilde{d}(\hat{a}^\dagger - \hat{a})} |n\rangle \\
&= Z^{-1} \sum_n e^{-\beta\tilde{\omega}_0 n} \langle n| e^{-\tilde{d}\hat{a}^\dagger (e^{i\tilde{\omega}_0 t} - 1)} e^{\tilde{d}\hat{a}(e^{-i\tilde{\omega}_0 t} - 1)} e^{\tilde{d}^2 (e^{-i\tilde{\omega}_0 t} - 1)} |n\rangle \\
&= Z^{-1} \sum_n e^{-\beta\tilde{\omega}_0 n} L_n(|u|^2) e^{\tilde{d}^2 (e^{-i\tilde{\omega}_0 t} - 1)} \\
&= Z^{-1} \sum_n e^{-\beta\tilde{\omega}_0 n} L_n(|u|^2) e^{\tilde{d}^2 (e^{-i\tilde{\omega}_0 t} - 1)} \\
&= (1 - z) \sum_n z^n L_n(|u|^2) e^{\tilde{d}^2 (e^{-i\tilde{\omega}_0 t} - 1)}
\end{aligned} \tag{C.18}$$

where $z = e^{-\beta\tilde{\omega}_0}$, $u = -\tilde{d}(e^{-i\tilde{\omega}_0 t} - 1)$, $Z^{-1} = (1 - z)$, $\langle n| e^{u^* a^\dagger} e^{-ua} |n\rangle = L_n(|u|^2)$, and the L_n are the Laguerre polynomials. In the next step, I use the identity [167] $(1 - z) \sum_{n=0}^{\infty} L_n(|u|^2) z^n = e^{|u|^2 z/(z-1)}$ and that $z/(z-1) = -1/(e^{\beta\tilde{\omega}_0} - 1)$, $\bar{n} = 1/(e^{\beta\tilde{\omega}_0} - 1)$, and I get

$$\begin{aligned}
e^{|u|^2 z/(z-1)} e^{\tilde{d}^2 (e^{-i\tilde{\omega}_0 t} - 1)} &= e^{-|u|^2 \bar{n}} e^{-\tilde{d}^2 (e^{-i\tilde{\omega}_0 t} - 1)} \\
&= e^{|u|^2 z/(z-1)} e^{\tilde{d}^2 (e^{-i\tilde{\omega}_0 t} - 1)} \\
&= e^{-\tilde{d}^2 (1 - e^{i\tilde{\omega}_0 t})(1 - e^{-i\tilde{\omega}_0 t})\bar{n}} e^{\tilde{d}^2 (e^{-i\tilde{\omega}_0 t} - 1)} \\
&= e^{-\tilde{d}^2 (2 - e^{i\tilde{\omega}_0 t} - e^{-i\tilde{\omega}_0 t})\bar{n}} e^{\tilde{d}^2 (e^{-i\tilde{\omega}_0 t} - 1)} \\
&= e^{-\tilde{d}^2 (\bar{n} + \bar{n} - \bar{n} e^{i\tilde{\omega}_0 t} - \bar{n} e^{-i\tilde{\omega}_0 t})} e^{\tilde{d}^2 (e^{-i\tilde{\omega}_0 t} - 1)} \\
&= e^{\tilde{d}^2 (-\bar{n} - \bar{n} + \bar{n} e^{i\tilde{\omega}_0 t} + \bar{n} e^{-i\tilde{\omega}_0 t})} e^{\tilde{d}^2 (e^{-i\tilde{\omega}_0 t} - 1)} \\
&= e^{\tilde{d}^2 ((\bar{n}+1)(e^{-i\tilde{\omega}_0 t} - 1) + \bar{n}(e^{i\tilde{\omega}_0 t} - 1))}
\end{aligned} \tag{C.19}$$

I now start from the formula for the optical conductivity, see Eq. (2.31), and insert the correlation functions. I will further tailor $e^{i\omega_0 t}$ under the assumption that I have adiabatic phonons and correlation functions decay to zero while I still have $\omega_0 |t| \ll 1$. I then get

$$\begin{aligned}
\sigma(\omega) &= \frac{1 - e^{-\beta\omega}}{2\omega} \int_{-\infty}^{\infty} e^{i\omega t} \langle J(t) J \rangle \\
&= \frac{1 - e^{-\beta\omega}}{2\omega} t_0^2 \int_{-\infty}^{\infty} e^{i\omega t} dt e^{-i(E_e - E_g)t} e^{\tilde{d}^2 ((\bar{n}+1)(e^{-i\tilde{\omega}_0 t} - 1) + \bar{n}(e^{i\tilde{\omega}_0 t} - 1))} \\
&= \frac{1 - e^{-\beta\omega}}{2\omega} t_0^2 \int_{-\infty}^{\infty} e^{i\omega t} dt e^{-i(E_e - E_g)t} e^{\tilde{d}^2 ((\bar{n}+1)(1 - i\tilde{\omega}_0 t - \tilde{\omega}_0^2 t^2/2 - 1) + \bar{n}(1 + i\tilde{\omega}_0 t - \tilde{\omega}_0^2 t^2/2 - 1))} \\
&= \frac{1 - e^{-\beta\omega}}{2\omega} t_0^2 \int_{-\infty}^{\infty} e^{i\omega t} dt e^{-i(E_e - E_g)t} e^{\tilde{d}^2 ((\bar{n}+1)(-i\tilde{\omega}_0 t - \tilde{\omega}_0^2 t^2/2) + \bar{n}(i\tilde{\omega}_0 t - \tilde{\omega}_0^2 t^2/2))} \\
&= \frac{1 - e^{-\beta\omega}}{2\omega} t_0^2 \int_{-\infty}^{\infty} e^{i\omega t} dt e^{-i(E_e - E_g)t} e^{\tilde{d}^2 (-(2\bar{n}+1)\tilde{\omega}_0^2 t^2/2 - i\tilde{\omega}_0 t))} .
\end{aligned} \tag{C.20}$$

I now define $\tilde{x} = (2\bar{n}+1) = \coth(\beta\tilde{\omega}_0/2)$ and $\Delta_E = E_e - E_g$, this gives

$$\sigma(\omega) = \frac{1-e^{-\beta\omega}}{2\omega} t_0^2 \int_{-\infty}^{\infty} dt e^{-i(\Delta_E+\tilde{\omega}_0-\omega)t} e^{-\tilde{d}^2(\tilde{x}\tilde{\omega}_0^2 t^2/2)}\,, \tag{C.21}$$

which I solve by completing the square, $\int x e^{-ax^2+bx+c} = \int dx e^{-a(x-b/(2d))^2)} e^{b^2/(4a)} e^c = \sqrt{\pi/a} e^{b^2/(4a)} e^c$, which gives

$$\sigma(\omega) = \frac{1-e^{-\beta\omega}}{2\omega} \sqrt{\frac{2\pi}{\tilde{d}^2\tilde{x}\tilde{\omega}_0^2}} t_0^2 e^{-(\Delta_E+\tilde{d}^2\tilde{\omega}_0-\omega)^2/(2\tilde{d}^2\tilde{\omega}_0^2\tilde{x})} \tag{C.22}$$

In now insert $\tilde{d} = d\sqrt{\frac{1}{2}}$ and get

$$\sigma(\omega) = \frac{1-e^{-\beta\omega}}{2\omega} \sqrt{\frac{4\pi}{d^2\tilde{x}\tilde{\omega}_0^2}} t_0^2 e^{-(\Delta_E+\frac{d^2\tilde{\omega}_0}{2}-\omega)^2/(d^2\tilde{\omega}_0^2\tilde{x})}\,. \tag{C.23}$$

This formula is general and only d and Δ_E depends on whether we have a polaron or a bipolaron. Additionally, I rescale by a factor of 2 for systems ($L > 2$). This comes from the observation that when comparing the sum rules (kinetic energy) between 2 sites and systems with $L > 2$ (in the relevant parameter regime), a factor of two is missing. In total, this gives

$$\sigma(\omega) = \frac{1-e^{-\beta\omega}}{\omega} \sqrt{\frac{4\pi}{d^2\tilde{\omega}_0^2 \coth(\beta\tilde{\omega}_0/2)}} t_0^2 e^{-(\Delta_E+\frac{d^2\tilde{\omega}_0}{2}-\omega)^2/(d^2\tilde{\omega}_0^2\coth(\beta\tilde{\omega}_0/2))}\,. \tag{C.24}$$

For the polaron, I insert $d = 2\bar{q}_{\min}$ and $\Delta E = 0$, and get

$$\begin{aligned}\sigma(\omega) &= \frac{1-e^{-\beta\omega}}{\omega} \sqrt{\frac{4\pi}{\bar{q}_{\min}^2 4\coth(\beta\tilde{\omega}_0/2)\tilde{\omega}_0^2}} t_0^2 e^{-(2\bar{q}_{\min}^2\tilde{\omega}_0-\omega)^2/(4\bar{q}_{\min}^2\tilde{\omega}_0^2\coth(\beta\tilde{\omega}_0/2))} \\ &= \frac{1-e^{-\beta\omega}}{\omega} \sqrt{\frac{\pi}{\bar{q}_{\min}^2 \coth(\beta\tilde{\omega}_0/2)\tilde{\omega}_0^2}} t_0^2 e^{-(2\bar{q}_{\min}^2\tilde{\omega}_0-\omega)^2/(4\bar{q}_{\min}^2\tilde{\omega}_0^2\coth(\beta\tilde{\omega}_0/2))}\,.\end{aligned} \tag{C.25}$$

As a consistency check, I will first send $t_{\rm ph} \to 0$ ($\tilde{\omega}_0 \to \omega_0$), and get

$$\sigma(\omega) = \frac{1-e^{-\beta\omega}}{\omega} \sqrt{\frac{\pi}{\bar{q}_{\min}^2 \coth(\beta\omega_0/2)\omega_0^2}} t_0^2 e^{-(2\bar{q}_{\min}^2\omega_0-\omega)^2/(4\bar{q}_{\min}^2\omega_0^2\coth(\beta\omega_0/2))}\,. \tag{C.26}$$

I now send $t_0/\gamma \to 0$, so that $\bar{q}_{\min} = \frac{\gamma}{\omega_0}$. By defining $\gamma^2/\omega_0 = E_P$, I am left with

$$\begin{aligned}\lim_{\bar{q}_{\min}\to\frac{\gamma}{\omega_0}} \sigma(\omega) &= \frac{1-e^{-\beta\omega}}{\omega} \sqrt{\frac{\pi}{\frac{\gamma^2}{\omega_0^2}\omega_0^2 \coth(\beta\omega_0/2)}} t_0^2 e^{-(2\frac{\gamma^2}{\omega_0^2}\omega_0-\omega)^2/(4\frac{\gamma^2}{\omega_0^2}\omega_0^2\coth(\beta\omega_0/2))} \\ &= \frac{1-e^{-\beta\omega}}{\omega} \sqrt{\frac{\pi}{E_p\omega_0\coth(\beta\omega_0/2)}} t_0^2 e^{-(2E_p-\omega)^2/(4E_p\omega_0\coth(\beta\omega_0/2))}\,.\end{aligned} \tag{C.27}$$

Now taking $T \to 0$, I get

$$\lim_{\substack{T\to 0,\\ \bar{q}_{\min}\to\frac{\gamma}{\omega_0}}} \sigma(\omega) = \frac{t_0^2}{\omega}\sqrt{\frac{\pi}{E_p\omega_0}} e^{-(2E_p-\omega)^2/(4E_p\omega_0)}\,. \tag{C.28}$$

Appendix D

Convergence of the energy transport coefficients

I here demonstrate how I monitor the convergence for the single-site TDVP algorithm. There are two parameters to adjust, $\epsilon_{\text{bond},J}$, which as defined so that

$$\sum_{\text{discarded }\eta} s_\eta^2 / (\sum_{\text{all }\eta} s_\eta^2) < \epsilon_{\text{bond},J} \,, \tag{D.1}$$

and D_{min}, which is the minimum bond dimension. Both are set before applying the corresponding matrix-product operator to the thermal state. The reason for fixing D_{min} is that the initial state might be well described by a large bond dimension on a few sites, but that the small bond dimension on other sites will not suffice for convergence at later times. For most of the data shown here, a small $\epsilon_{\text{bond},J}$ was sufficient to converge the data, and fixing D_{min} only made a difference on the bonds close to the edges of the system. For this reason, setting $D_{\text{min}} \neq 0$ was only needed for very small systems, for example, when comparing to exact diagonalization data.

In Fig. D.1(a), I show the energy current-current correlation function for different values of $\epsilon_{\text{bond},J}$. I also show data calculated with p2TDVP-LBO, which dynamically updates the bond dimension on all bonds during the time evolution. One can see that all data are converged except for when $\epsilon_{\text{bond},J} = 10^{-3}$. Figure D.1(b) shows the bond dimension of the system after applying the matrix-product operator $\hat{J}^E$ to the thermal state. The figure verifies that changing $\epsilon_{\text{bond},J}$ increases the bond dimension on all sites in the bulk of the system. Furthermore, an interesting zig-zag pattern appears. This indicates that the bond dimension is dominated by the legs coupling the physical to the corresponding ancillary site. The black triangles show data calculated with p2TDVP-LBO at time $tt_0 = 12$. The bond dimensions seem to be updated more homogeneously in that algorithm, similar to what was observed in Ch. 5. However, a more systematic study is needed (in particular at $\epsilon_{\text{bond},J} = \epsilon_{\text{bond}}$). This is, however, consistent with the fact that the matrix-product operator only acts on the physical sites but that both the ancillary and physical states are time evolved in p2TDVP-LBO.

In Fig. D.2, I show the energy transport coefficients for different system sizes with

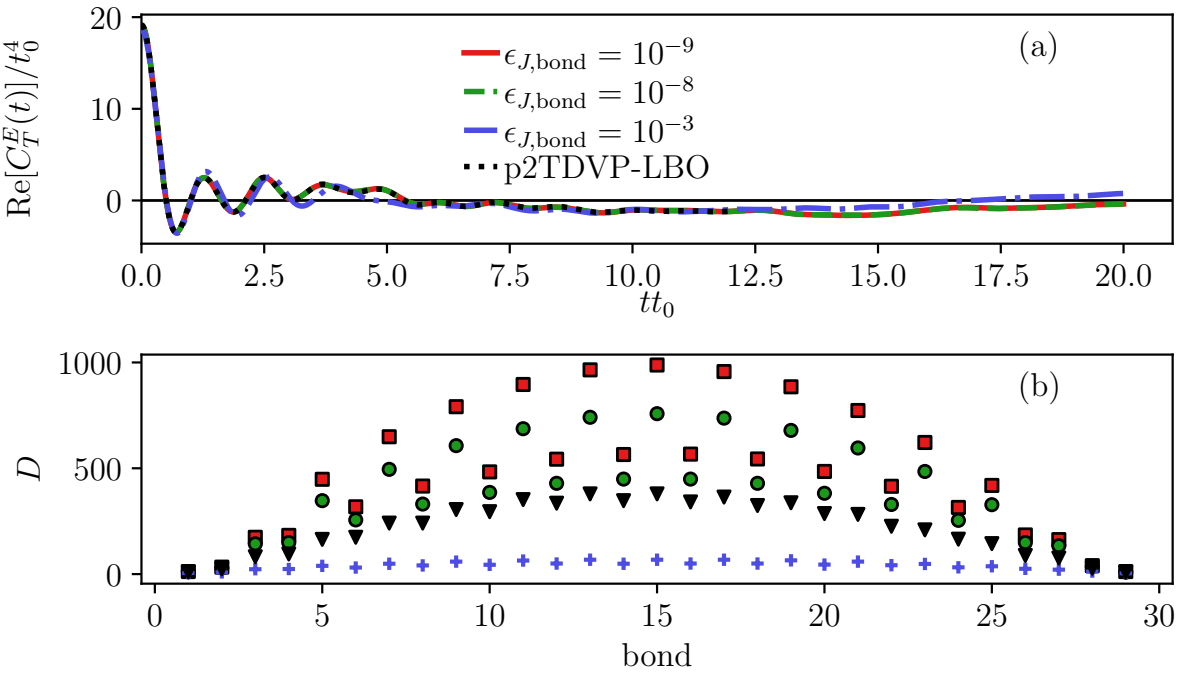

Figure D.1: (a) Real part of the energy current-current correlation function calculated with single-site TDVP for different $\epsilon_{\mathrm{bond},J}$. I also show p2TDVP-LBO data calculated with $\epsilon_{\mathrm{bond}} = 10^{-7}$ and $\epsilon_{\mathrm{LBO}} = 10^{-8}$. The calculations are done at $n = 1/3$ filling, and with $\gamma/t_0 = 1$, $\omega_0/t_0 = 1$, $M = 20$, $T/t_0 = 0.2$, and $L = 15$. (b) Bond dimensions after having applied the matrix-product operator $\hat{J}^E$ to the thermal state for the same parameters as in (a). The plus signs are calculated with $\epsilon_{\mathrm{bond},J} = 10^{-3}$, the circles with $\epsilon_{\mathrm{bond},J} = 10^{-8}$, the squares with $\epsilon_{\mathrm{bond},J} = 10^{-9}$, and the triangles with pTDVP-LBO. For the pTDVP-LBO data, I plot the bond dimension at time $tt_0 = 12$. Note that there are $2L - 1$ bonds since the thermal state has both physical and ancillary sites (see Ch. 3).

$n = 1/3$ filling. There are some finite size effects at low frequencies, but they disappear at high frequencies.

In Fig. D.3, I plot the energy transport coefficients with a finite phonon bandwidth [see Eq. (2.2)], which make the energy current more complicated [195] and the numerical simulations more difficult. The energy transport coefficients for $\gamma/t_0 = 1$, $\omega_0/t_0 = 1$, and $t_{\mathrm{ph}}/t_0 = 0.1$ can be seen in Fig. D.3(a). One sees that the difference in optical conductivity and the energy transport coefficient is similar to the difference in the data shown in Ch. 5, but larger oscillations in the amplitude of the plateau are present at high frequencies for $t_{\mathrm{ph}}/t_0 = 0.1$ compared to $t_{\mathrm{ph}}/t_0 = 0.0$ in Fig. D.2(a).

Figure D.3(b) shows the energy transport coefficient for $\gamma/t_0 = \sqrt{1.6}$, $\omega_0/t_0 = 0.4$, $T/t_0 = 0.1$, and two different values of t_{ph}/t_0. The interpretation based on the Born-Oppenheimer surfaces remains valid. As explained in Ch. 5, $t_{\mathrm{ph}}/t_0 > 0$ shifts the lower surface downwards, and thus the asymmetric Gaussian gets shifted to higher frequencies.

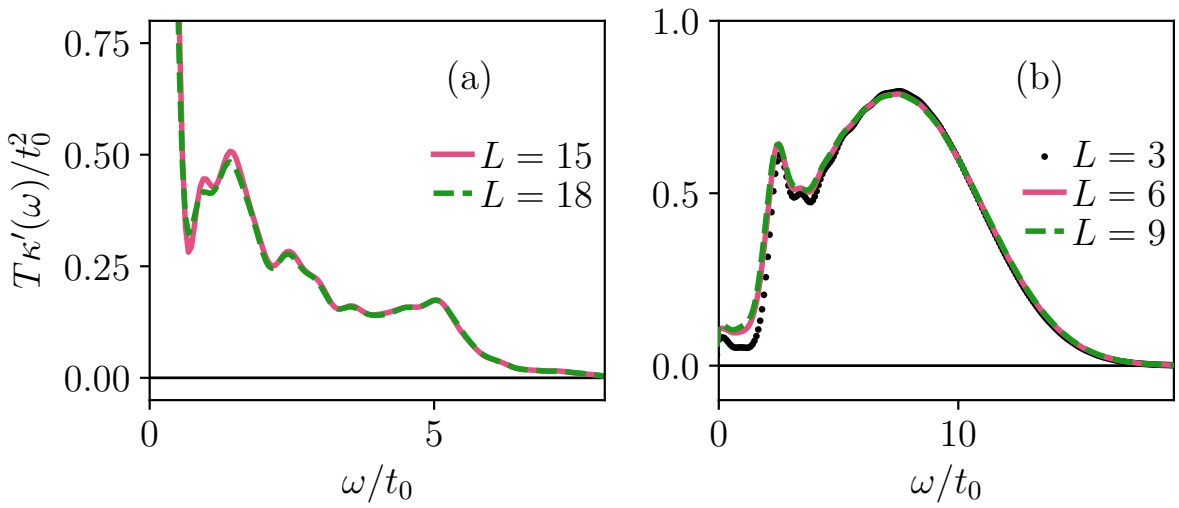

Figure D.2: (a) Energy transport coefficients for $\gamma/t_0 = 1$, $\omega_0/t_0 = 1$, $M = 20$, $T/t_0 = 0.2$, $n = 1/3$ filling and different L. I use $\epsilon_J = 10^{-9}$, $t_{\text{tot}}t_0 = 12$, $\eta = 0.05/(4\pi)$, and Gaussian broadening. (b) Energy transport coefficients for $\gamma/t_0 = \sqrt{1.6}$, $\omega_0/t_0 = 0.4$, $T/t_0 = 0.5$, $M = 40$, and different L. I use $\epsilon_{\text{bond},J} = 10^{-8}$, $t_{\text{tot}}t_0 = 14$, $\eta = 0.1/(4\pi)$, and Gaussian broadening. For $L = 3$ and $L = 6$, I also use $D_{\text{min}} = 100$.

Also in this case, the interpretation based on the Born-Oppenheimer-surfaces seems valid.

In Fig. D.4, the optical conductivity and energy transport coefficient at different temperatures close to half filling is shown. I use $L = 9$ sites, $N_e = 4$ electrons, and model parameters $\gamma/t_0 = 3$ and $\omega_0/t_0 = 1$, which are in the charge-density-wave regime. The numerically calculated optical conductivity is plotted in Fig. D.4(a) together with the rescaled analytic expression from Appendix C. The data is qualitatively described by the polaron curve. In Fig. D.4(b), I show the energy transport coefficient for the same parameters. In addition to being dominated by small polaron physics, one sees that the spectrum is almost completely reproduced using the reduced energy current $\hat{J}_R^E$ from Ch. 5.

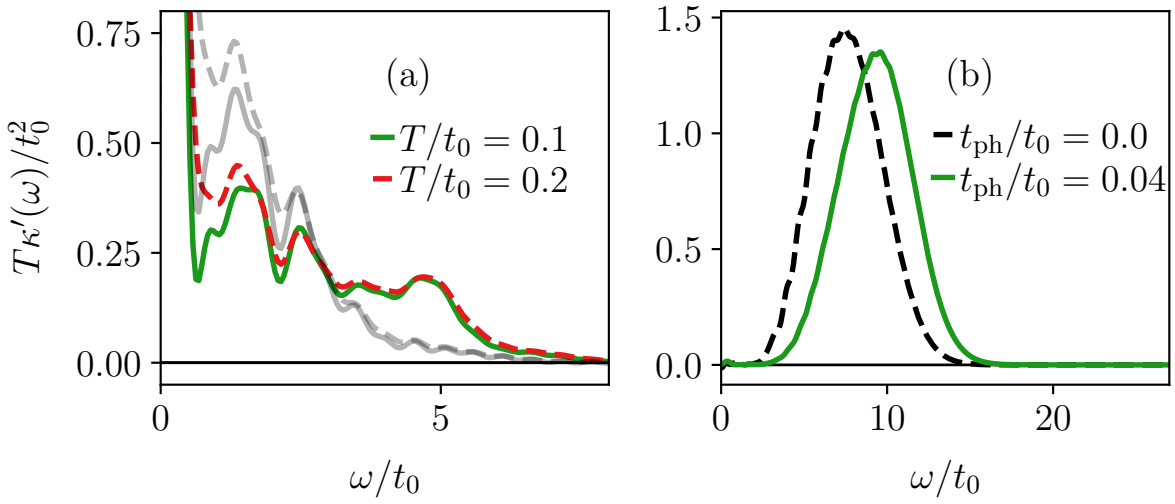

Figure D.3: (a) Energy transport coefficients for $\gamma/t_0 = 1$, $\omega_0/t_0 = 1$, $M = 20$, $L = 15$, $t_{\rm ph}/t_0 = 0.1$ and different T/t_0. I use $\epsilon_J = 10^{-9}$, $t_{\rm tot}t_0 = 12$, and $\eta = 0.05/(4\pi)$ and Gaussian broadening. The gray dashed lines are the optical conductivity rescaled by the factor $(2\gamma/\omega_0)^2$. (b) Energy transport coefficients for $\gamma/t_0 = \sqrt{1.6}$, $\omega_0/t_0 = 0.4$, $T/t_0 = 0.1$, $M = 40$, $t_{\rm ph}/t_0 = 0.04$ and $t_{\rm ph}/t_0 = 0.0$. I use $\epsilon_{{\rm bond},J} = 10^{-8}$ for $t_{\rm ph}/t_0 = 0.0$ and $\epsilon_{{\rm bond},J} = 10^{-7}$ for $t_{\rm ph}/t_0 = 0.04$. I also use $t_{\rm tot}t_0 = 14$, $\eta = 0.1/(4\pi)$, and Gaussian broadening.

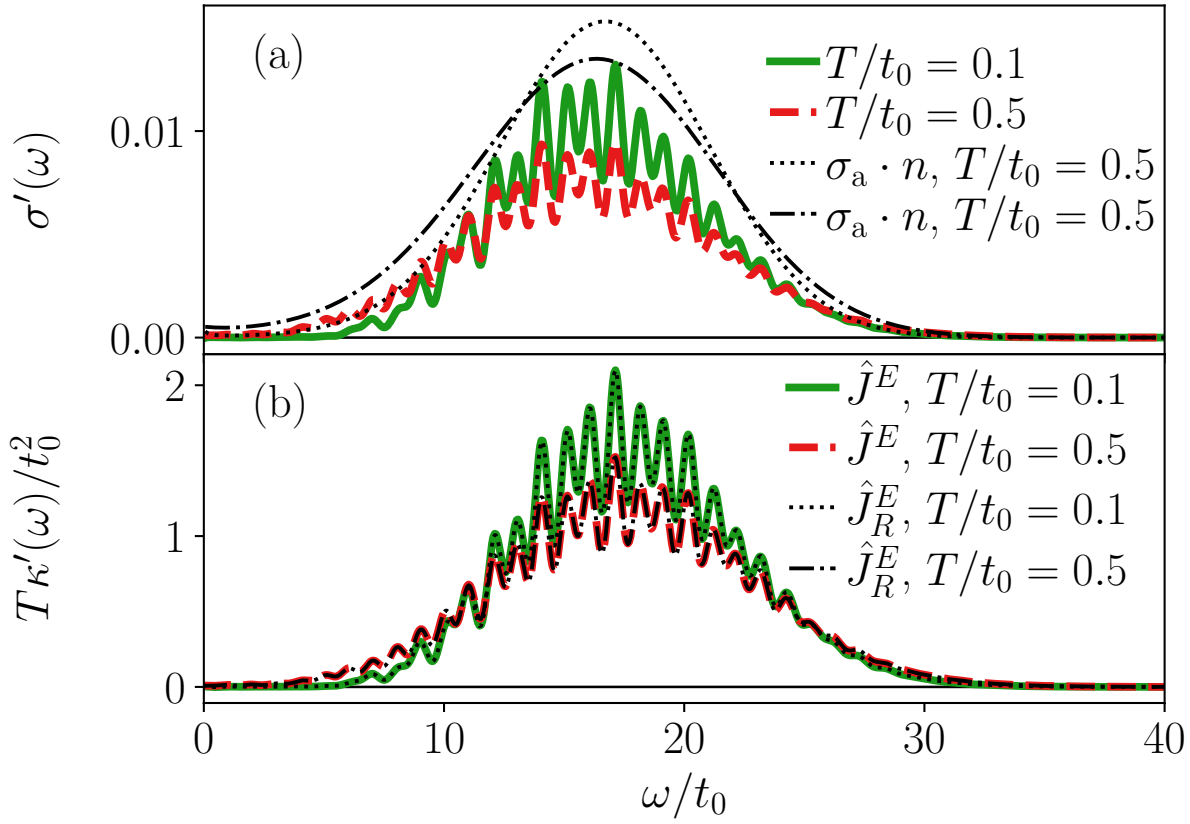

Figure D.4: (a) Optical conductivity for $\gamma/t_0 = 3$, $\omega_0/t_0 = 1$, $M = 40$, $L = 9$, at filling $n = (L-1)/(2L)$, and different T/t_0. I use $\epsilon_J = 10^{-8}$, $t_{\text{tot}}t_0 = 14$, $\eta = 0.5/(4\pi)$, and Gaussian broadening. The black lines are the analytical formula for the optical conductivity derived in Appendix C and rescaled by the filling n. (b) Energy transport coefficient for the same parameters as in (a). The black lines are the transport coefficient calculated with $\hat{J}^E_R$ from Ch. 5.

Bibliography

[1] P. Drude, Zur Elektronentheorie der Metalle, Ann. Phys. (Berl.) **306**, 566 (1900).

[2] P. Drude, Zur Elektronentheorie der Metalle; II. Teil. Galvanomagnetische und thermomagnetische Effecte, Ann. Phys. (Berl.) **308**, 369 (1900).

[3] N. W. Ashcroft and N. D. Mermin, *Solid State Physics* (Holt-Saunders, 1976).

[4] M. Born and R. Oppenheimer, Zur Quantentheorie der Molekeln, Ann. Phys. **389**, 457 (1927).

[5] M. Born and K. Huang, *Dynamical theory of crystal lattices* (Clarendon press, 1954).

[6] C. Franchini, M. Reticcioli, M. Setvin, and U. Diebold, Polarons in materials, Nat. Rev. Mater. **6**, 560 (2021).

[7] G. Grüner, The dynamics of charge-density waves, Rev. Mod. Phys. **60**, 1129 (1988).

[8] J. Bardeen, L. N. Cooper, and J. R. Schrieffer, Theory of superconductivity, Phys. Rev. **108**, 1175 (1957).

[9] A. J. Millis, P. B. Littlewood, and B. I. Shraiman, Double exchange alone does not explain the resistivity of $La_{1-x}Sr_xMnO_3$, Phys. Rev. Lett. **74**, 5144 (1995).

[10] H. Reik and D. Heese, Frequency dependence of the electrical conductivity of small polarons for high and low temperatures, J. Phys. Chem. Solids **28**, 581 (1967).

[11] S. Moser, L. Moreschini, J. Jaćimović, O. S. Barišić, H. Berger, A. Magrez, Y. J. Chang, K. S. Kim, A. Bostwick, E. Rotenberg, L. Forró, and M. Grioni, Tunable polaronic conduction in anatase TiO_2, Phys. Rev. Lett. **110**, 196403 (2013).

[12] P. Nagels, M. Denayer, and J. Devreese, Electrical properties of single crystals of uranium dioxide, Solid State Commun. **1**, 35 (1963).

[13] T. Nishio, J. Ahmad, and H. Uwe, Spectroscopic observation of bipolaronic point defects in $Ba_{1-x}K_xBiO_3$, Phys. Rev. Lett. **95**, 176403 (2005).

[14] C. Franchini, G. Kresse, and R. Podloucky, Polaronic hole trapping in doped $BaBiO_3$, Phys. Rev. Lett. **102**, 256402 (2009).

[15] Y. Yamada, O. Hino, S. Nohdo, R. Kanao, T. Inami, and S. Katano, Polaron ordering in low-doping $La_{1-x}Sr_xMnO_3$, Phys. Rev. Lett. **77**, 904 (1996).

[16] G.-m. Zhao, M. Hunt, H. Keller, and K. A. Müller, Evidence for polaronic supercarriers in the copper oxide superconductors $La_{2-x}Sr_xCuO_4$, Nature **385**, 236 (1997).

[17] J. M. D. Teresa, M. R. Ibarra, P. A. Algarabel, C. Ritter, C. Marquina, J. Blasco, J. García, A. del Moral, and Z. Arnold, Evidence for magnetic polarons in the magnetoresistive perovskites, Nature **386**, 256 (1997).

[18] H. Y. Huang, Z. Y. Chen, R.-P. Wang, F. M. F. de Groot, W. B. Wu, J. Okamoto, A. Chainani, A. Singh, Z.-Y. Li, J.-S. Zhou, H.-T. Jeng, G. Y. Guo, J.-G. Park, L. H. Tjeng, C. T. Chen, and D. J. Huang, Jahn-Teller distortion driven magnetic polarons in magnetite, Nat. Commun. **8**, 15929 (2017).

[19] J. Jaćimović, C. Vaju, A. Magrez, H. Berger, L. Forró, R. Gaál, V. Cerovski, and R. Žikić, Pressure dependence of the large-polaron transport in anatase TiO_2 single crystals, EPL **99**, 57005 (2012).

[20] M. Setvin, C. Franchini, X. Hao, M. Schmid, A. Janotti, M. Kaltak, C. G. Van de Walle, G. Kresse, and U. Diebold, Direct view at excess electrons in TiO_2 rutile and anatase, Phys. Rev. Lett. **113**, 086402 (2014).

[21] J. M. Frost, L. D. Whalley, and A. Walsh, Slow cooling of hot polarons in halide perovskite solar cells, ACS Energy Lett. **2**, 2647 (2017).

[22] D. Ghosh, E. Welch, A. J. Neukirch, A. Zakhidov, and S. Tretiak, Polarons in halide perovskites: A perspective, J. Phys. Chem. Lett. **11**, 3271 (2020).

[23] A. Machida, Y. Moritomo, and A. Nakamura, Spectroscopic evidence for formation of small polarons in doped manganites, Phys. Rev. B **58**, R4281 (1998).

[24] M. Quijada, J. Černe, J. R. Simpson, H. D. Drew, K. H. Ahn, A. J. Millis, R. Shreekala, R. Ramesh, M. Rajeswari, and T. Venkatesan, Optical conductivity of manganites: Crossover from Jahn-Teller small polaron to coherent transport in the ferromagnetic state, Phys. Rev. B **58**, 16093 (1998).

[25] S. Yoon, H. L. Liu, G. Schollerer, S. L. Cooper, P. D. Han, D. A. Payne, S.-W. Cheong, and Z. Fisk, Raman and optical spectroscopic studies of small-to-large polaron crossover in the perovskite manganese oxides, Phys. Rev. B **58**, 2795 (1998).

[26] A. S. Alexandrov and A. M. Bratkovsky, Carrier density collapse and colossal magnetoresistance in doped manganites, Phys. Rev. Lett. **82**, 141 (1999).

[27] N. N. Loshkareva, L. V. Nomerovannaya, E. V. Mostovshchikova, A. A. Makhnev, Y. P. Sukhorukov, N. I. Solin, T. I. Arbuzova, S. V. Naumov, N. V. Kostromitina, A. M. Balbashov, and L. N. Rybina, Electronic structure and polarons in $CaMnO_{3-\delta}$ single crystals: Optical data, Phys. Rev. B **70**, 224406 (2004).

[28] C. Hartinger, F. Mayr, A. Loidl, and T. Kopp, Polaronic excitations in colossal magnetoresistance manganite films, Phys. Rev. B **73**, 024408 (2006).

[29] C. Jooss, L. Wu, T. Beetz, R. F. Klie, M. Beleggia, M. A. Schofield, S. Schramm, J. Hoffmann, and Y. Zhu, Polaron melting and ordering as key mechanisms for colossal resistance effects in manganites, Proc. Natl. Acad. Sci. U.S.A. **104**, 13597 (2007).

[30] L. Wu, R. F. Klie, Y. Zhu, and C. Jooss, Experimental confirmation of Zener-polaron-type charge and orbital ordering in $Pr_{1-x}Ca_xMnO_3$, Phys. Rev. B **76**, 174210 (2007).

[31] S. Mildner, J. Hoffmann, P. E. Blöchl, S. Techert, and C. Jooss, Temperature- and doping-dependent optical absorption in the small-polaron system $Pr_{1-x}Ca_xMno_3$, Phys. Rev. B **92**, 035145 (2015).

[32] V. Coropceanu, J. Cornil, D. A. da Silva Filho, Y. Olivier, R. Silbey, and J.-L. Brédas, Charge transport in organic semiconductors, Chem. Rev. **107**, 926 (2007).

[33] A. Zhugayevych and S. Tretiak, Theoretical description of structural and electronic properties of organic photovoltaic materials, Annu. Rev. Phys. Chem. **66**, 305 (2015).

[34] G. Conibeer, S. Shrestha, S. Huang, R. Patterson, H. Xia, Y. Feng, P. Zhang, N. Gupta, M. Tayebjee, S. Smyth, Y. Liao, S. Lin, P. Wang, X. Dai, and S. Chung, Hot carrier solar cell absorber prerequisites and candidate material systems, Sol. Energy Mater. Sol. Cells **135**, 124 (2015).

[35] B. Kressdorf, T. Meyer, A. Belenchuk, O. Shapoval, M. ten Brink, S. Melles, U. Ross, J. Hoffmann, V. Moshnyaga, M. Seibt, P. Blöchl, and C. Jooss, Room-temperature hot-polaron photovoltaics in the charge-ordered state of a layered perovskite oxide heterojunction, Phys. Rev. Applied **14**, 054006 (2020).

[36] U. Diebold, The surface science of titanium dioxide, Surf. Sci. Rep. **48**, 53 (2003).

[37] C. Ahn, A. Cavalleri, A. Georges, S. Ismail-Beigi, A. J. Millis, and J.-M. Triscone, Designing and controlling the properties of transition metal oxide quantum materials, Nat. Mater. **20**, 1462 (2021).

[38] C. Zhang, J. Sous, D. R. Reichman, M. Berciu, A. J. Millis, N. V. Prokof'ev, and B. V. Svistunov, Bipolaronic high-temperature superconductivity, arXiv:2203.07380 (2022).

[39] F. Schmitt, P. S. Kirchmann, U. Bovensiepen, R. G. Moore, L. Rettig, M. Krenz, J.-H. Chu, N. Ru, L. Perfetti, D. H. Lu, M. Wolf, I. R. Fisher, and Z.-X. Shen, Transient electronic structure and melting of a charge density wave in $TbTe_3$, Science **321**, 1649 (2008).

[40] A. Tomeljak, H. Schäfer, D. Städter, M. Beyer, K. Biljakovic, and J. Demsar, Dynamics of photoinduced charge-density-wave to metal phase transition in $\mathbf{K}_{0.3}MoO_3$, Phys. Rev. Lett. **102**, 066404 (2009).

[41] N. Kida and M. Tonouchi, Spectroscopic evidence for a charge-density-wave condensate in a charge-ordered manganite: Observation of a collective excitation mode in $Pr_{0.7}Ca_{0.3}MnO_3$ by using THz time-domain spectroscopy, Phys. Rev. B **66**, 024401 (2002).

[42] S. Cox, J. Singleton, R. D. McDonald, A. Migliori, and P. B. Littlewood, Sliding charge-density wave in manganites, Nat. Mater. **7**, 25 (2008).

[43] T. Holstein, Studies of polaron motion: Part I. The molecular-crystal model, Ann. Phys. (N. Y.) **8**, 325 (1959).

[44] T. Holstein, Studies of polaron motion: Part II. The "small" polaron, Ann. Phys. **8**, 343 (1959).

[45] H. Fröhlich, H. Pelzer, and S. Zienau, XX. properties of slow electrons in polar materials, Lond. Edinb. Dublin philos. mag. j. sci. **41**, 221 (1950).

[46] T. D. Lee, F. E. Low, and D. Pines, The motion of slow electrons in a polar crystal, Phys. Rev. **90**, 297 (1953).

[47] R. J. Bursill, R. H. McKenzie, and C. J. Hamer, Phase Diagram of the One-Dimensional Holstein Model of Spinless Fermions, Phys. Rev. Lett. **80**, 5607 (1998).

[48] C. E. Creffield, G. Sangiovanni, and M. Capone, Phonon softening and dispersion in the 1D Holstein model of spinless fermions, Eur. Phys. J. B **44**, 175 (2005).

[49] D. Emin, Optical properties of large and small polarons and bipolarons, Phys. Rev. B **48**, 13691 (1993).

[50] A. S. Alexandrov, V. V. Kabanov, and D. K. Ray, From electron to small polaron: An exact cluster solution, Phys. Rev. B **49**, 9915 (1994).

[51] M. Capone, W. Stephan, and M. Grilli, Small-polaron formation and optical absorption in Su-Schrieffer-Heeger and Holstein models, Phys. Rev. B **56**, 4484 (1997).

[52] S. Fratini and S. Ciuchi, Dynamical mean-field theory of transport of small polarons, Phys. Rev. Lett. **91**, 256403 (2003).

[53] O. S. Barišić, Variational study of the Holstein polaron, Phys. Rev. B **65**, 144301 (2002).

[54] O. S. Barišić, Calculation of excited polaron states in the Holstein model, Phys. Rev. B **69**, 064302 (2004).

[55] O. S. Barišić, Holstein light quantum polarons on the one-dimensional lattice, Phys. Rev. B **73**, 214304 (2006).

[56] G. Schubert, G. Wellein, A. Weisse, A. Alvermann, and H. Fehske, Optical absorption and activated transport in polaronic systems, Phys. Rev. B **72**, 104304 (2005).

[57] J. Loos, M. Hohenadler, A. Alvermann, and H. Fehske, Phonon spectral function of the Holstein polaron, J. Phys. Condens. Matter **18**, 7299 (2006).

[58] S. Fratini and S. Ciuchi, Optical properties of small polarons from dynamical mean-field theory, Phys. Rev. B **74**, 075101 (2006).

[59] O. S. Barišić and S. Barišić, Phase diagram of the Holstein polaron in one dimension, Eur. Phys. J. B **64**, 1 (2008).

[60] L. Vidmar, J. Bonča, and S. A. Trugman, Emergence of states in the phonon spectral function of the Holstein polaron below and above the one-phonon continuum, Phys. Rev. B **82**, 104304 (2010).

[61] L. Vidmar, J. Bonča, M. Mierzejewski, P. Prelovšek, and S. A. Trugman, Nonequilibrium dynamics of the Holstein polaron driven by an external electric field, Phys. Rev. B **83**, 134301 (2011).

[62] F. Dorfner, L. Vidmar, C. Brockt, E. Jeckelmann, and F. Heidrich-Meisner, Real-time decay of a highly excited charge carrier in the one-dimensional Holstein model, Phys. Rev. B **91**, 104302 (2015).

[63] C. Brockt and E. Jeckelmann, Scattering of an electronic wave packet by a one-dimensional electron-phonon-coupled structure, Phys. Rev. B **95**, 064309 (2017).

[64] D. Jansen, J. Stolpp, L. Vidmar, and F. Heidrich-Meisner, Eigenstate thermalization and quantum chaos in the Holstein polaron model, Phys. Rev. B **99**, 155130 (2019).

[65] J. Bonča, S. A. Trugman, and M. Berciu, Spectral function of the Holstein polaron at finite temperature, Phys. Rev. B **100**, 094307 (2019).

[66] B. Kloss, D. R. Reichman, and R. Tempelaar, Multiset matrix product state calculations reveal mobile Franck-Condon excitations under strong Holstein-type coupling, Phys. Rev. Lett. **123**, 126601 (2019).

[67] J. Bonča and S. A. Trugman, Dynamic properties of a polaron coupled to dispersive optical phonons, Phys. Rev. B **103**, 054304 (2021).

[68] P. Mitrić, V. Janković, N. Vukmirović, and D. Tanasković, Spectral functions of the Holstein polaron: Exact and approximate solutions, Phys. Rev. Lett. **129**, 096401 (2022).

[69] P. J. Robinson, I. S. Dunn, and D. R. Reichman, Cumulant methods for electron-phonon problems. I. Perturbative expansions, Phys. Rev. B **105**, 224304 (2022).

[70] V. Janković and N. Vukmirović, Spectral and thermodynamic properties of the Holstein polaron: Hierarchical equations of motion approach, Phys. Rev. B **105**, 054311 (2022).

[71] E. Jeckelmann, C. Zhang, and S. R. White, Metal-insulator transition in the one-dimensional Holstein model at half filling, Phys. Rev. B **60**, 7950 (1999).

[72] C. Zhang, E. Jeckelmann, and S. R. White, Dynamical properties of the one-dimensional Holstein model, Phys. Rev. B **60**, 14092 (1999).

[73] H. Zhao, C. Q. Wu, and H. Q. Lin, Spectral function of the one-dimensional Holstein model at half filling, Phys. Rev. B **71**, 115201 (2005).

[74] J. Loos, M. Hohenadler, and H. Fehske, Spectral functions of the spinless Holstein model, J. Phys. Condens. Matter **18**, 2453 (2006).

[75] H. Hashimoto and S. Ishihara, Photoinduced charge-order melting dynamics in a one-dimensional interacting Holstein model, Phys. Rev. B **96**, 035154 (2017).

[76] J. Stolpp, J. Herbrych, F. Dorfner, E. Dagotto, and F. Heidrich-Meisner, Charge-density-wave melting in the one-dimensional Holstein model, Phys. Rev. B **101**, 035134 (2020).

[77] M. Weber and J. K. Freericks, Field tuning beyond the heat death of a charge-density-wave chain, arXiv:2107.04096 (2021).

[78] J. Stolpp, T. Köhler, S. R. Manmana, E. Jeckelmann, F. Heidrich-Meisner, and S. Paeckel, Comparative study of state-of-the-art matrix-product-state methods for lattice models with large local Hilbert spaces without U(1) symmetry, Comput. Phys. Commun. **269**, 108106 (2021).

[79] M. Capone, G. Sangiovanni, C. Castellani, C. Di Castro, and M. Grilli, Phase separation close to the density-driven Mott transition in the Hubbard-Holstein Model, Phys. Rev. Lett. **92**, 106401 (2004).

[80] W. Koller, D. Meyer, Y. Ōno, and A. C. Hewson, First- and second-order phase transitions in the Holstein-Hubbard model, EPL **66**, 559 (2004).

[81] P. Werner and A. J. Millis, Efficient dynamical mean field simulation of the Holstein-Hubbard model, Phys. Rev. Lett. **99**, 146404 (2007).

[82] H. Fehske, G. Hager, and E. Jeckelmann, Metallicity in the half-filled Holstein-Hubbard model, EPL **84**, 57001 (2008).

[83] H. Fehske, D. Ihle, J. Loos, U. Trapper, and H. Büttner, Polaron formation and hopping conductivity in the Holstein-Hubbard model, Z. Phys. B **94**, 91 (1994).

[84] D. Ihle, H. Fehske, J. Loos, and U. Trapper, Bi-/polaron formation and optical conductivity in the Holstein-Hubbard model, Phys. C: Supercond. Appl. **235-240**, 2363 (1994).

[85] G. Wellein, H. Röder, and H. Fehske, Polarons and bipolarons in strongly interacting electron-phonon systems, Phys. Rev. B **53**, 9666 (1996).

[86] J. Bonča, T. Katrašnik, and S. A. Trugman, Mobile bipolaron, Phys. Rev. Lett. **84**, 3153 (2000).

[87] J. Bonča and S. A. Trugman, Bipolarons in the extended Holstein Hubbard model, Phys. Rev. B **64**, 094507 (2001).

[88] D. Golež, J. Bonča, and L. Vidmar, Dissociation of a Hubbard-Holstein bipolaron driven away from equilibrium by a constant electric field, Phys. Rev. B **85**, 144304 (2012).

[89] P. Werner and M. Eckstein, Field-induced polaron formation in the Holstein-Hubbard model, EPL **109**, 37002 (2015).

[90] F. Marsiglio, Impact of retardation in the Holstein-Hubbard model: a two-site calculation, arXiv:2205.10352 (2022).

[91] D. J. J. Marchand and M. Berciu, Effect of dispersive optical phonons on the behavior of a Holstein polaron, Phys. Rev. B **88**, 060301 (2013).

[92] N. C. Costa, T. Blommel, W.-T. Chiu, G. Batrouni, and R. T. Scalettar, Phonon dispersion and the competition between pairing and charge order, Phys. Rev. Lett. **120**, 187003 (2018).

[93] J. Bonča and S. A. Trugman, Electron removal spectral function of a polaron coupled to dispersive optical phonons, Phys. Rev. B **106**, 174303 (2022).

[94] A. Damascelli, Z. Hussain, and Z.-X. Shen, Angle-resolved photoemission studies of the cuprate superconductors, Rev. Mod. Phys. **75**, 473 (2003).

[95] A. Damascelli, Probing the electronic structure of complex systems by ARPES, Phys. Scr. **T109**, 61 (2004).

[96] J. A. Sobota, Y. He, and Z.-X. Shen, Angle-resolved photoemission studies of quantum materials, Rev. Mod. Phys. **93**, 025006 (2021).

[97] D. G. Cahill and R. O. Pohl, Thermal conductivity of amorphous solids above the plateau, Phys. Rev. B **35**, 4067 (1987).

[98] C. A. Paddock and G. L. Eesley, Transient thermoreflectance from thin metal films, J. Appl. Phys. **60**, 285 (1986).

[99] A. J. Schmidt, R. Cheaito, and M. Chiesa, A frequency-domain thermoreflectance method for the characterization of thermal properties, Rev. Sci. Instrum. **80**, 094901 (2009).

[100] M. Kang, S. W. Jung, W. J. Shin, Y. Sohn, S. H. Ryu, T. K. Kim, M. Hoesch, and K. S. Kim, Holstein polaron in a valley-degenerate two-dimensional semiconductor, Nat. Mater. **17**, 676 (2018).

[101] L. Kang, X. Du, J. S. Zhou, X. Gu, Y. J. Chen, R. Z. Xu, Q. Q. Zhang, S. C. Sun, Z. X. Yin, Y. W. Li, D. Pei, J. Zhang, R. K. Gu, Z. G. Wang, Z. K. Liu, R. Xiong, J. Shi, Y. Zhang, Y. L. Chen, and L. X. Yang, Band-selective Holstein polaron in Luttinger liquid material $A_{0.3}MoO_3$ (A = K, Rb), Nat. Commun. **12**, 6183 (2021).

[102] K. Zhang, X. Liu, H. Zhang, K. Deng, M. Yan, W. Yao, M. Zheng, E. F. Schwier, K. Shimada, J. D. Denlinger, Y. Wu, W. Duan, and S. Zhou, Evidence for a quasi-one-dimensional charge density wave in CuTe by angle-resolved photoemission spectroscopy, Phys. Rev. Lett. **121**, 206402 (2018).

[103] J. L. M. van Mechelen, D. van der Marel, C. Grimaldi, A. B. Kuzmenko, N. P. Armitage, N. Reyren, H. Hagemann, and I. I. Mazin, Electron-phonon interaction and charge carrier mass enhancement in $SrTiO_3$, Phys. Rev. Lett. **100**, 226403 (2008).

[104] J. T. Devreese, S. N. Klimin, J. L. M. van Mechelen, and D. van der Marel, Many-body large polaron optical conductivity in $SrTi_{1-x}Nb_xO_3$, Phys. Rev. B **81**, 125119 (2010).

[105] R. S. Li, L. Yue, Q. Wu, S. X. Xu, Q. M. Liu, Z. X. Wang, T. C. Hu, X. Y. Zhou, L. Y. Shi, S. J. Zhang, D. Wu, T. Dong, and N. L. Wang, Optical spectroscopy and ultrafast pump-probe study of a quasi-one-dimensional charge density wave in CuTe, Phys. Rev. B **105**, 115102 (2022).

[106] P. Hohenberg and W. Kohn, Inhomogeneous electron gas, Phys. Rev. **136**, B864 (1964).

[107] W. Kohn and L. J. Sham, Self-consistent equations including exchange and correlation effects, Phys. Rev. **140**, A1133 (1965).

[108] S. R. White, Density matrix formulation for quantum renormalization groups, Phys. Rev. Lett. **69**, 2863 (1992).

[109] S. R. White, Density-matrix algorithms for quantum renormalization groups, Phys. Rev. B **48**, 10345 (1993).

[110] U. Schollwöck, The density-matrix renormalization group, Rev. Mod. Phys. **77**, 259 (2005).

[111] U. Schollwöck, The density-matrix renormalization group in the age of matrix product states, Ann. Phys. (N. Y.) **326**, 96 (2011).

[112] A. Georges, G. Kotliar, W. Krauth, and M. J. Rozenberg, Dynamical mean-field theory of strongly correlated fermion systems and the limit of infinite dimensions, Rev. Mod. Phys. **68**, 13 (1996).

[113] A. W. Sandvik and J. Kurkijärvi, Quantum Monte Carlo simulation method for spin systems, Phys. Rev. B **43**, 5950 (1991).

[114] N. V. Prokof'ev and B. V. Svistunov, Polaron problem by diagrammatic quantum Monte Carlo, Phys. Rev. Lett. **81**, 2514 (1998).

[115] A. S. Mishchenko, N. V. Prokof'ev, A. Sakamoto, and B. V. Svistunov, Diagrammatic quantum Monte Carlo study of the Fröhlich polaron, Phys. Rev. B **62**, 6317 (2000).

[116] A. N. Rubtsov, V. V. Savkin, and A. I. Lichtenstein, Continuous-time quantum Monte Carlo method for fermions, Phys. Rev. B **72**, 035122 (2005).

[117] C. Lanczos, An iteration method for the solution of the eigenvalue problem of linear differential and integral operators, Journal of research of the National Bureau of Standards **45**, 255 (1950).

[118] S. R. Manmana, A. Muramatsu, and R. M. Noack, Time evolution of one-dimensional quantum many body systems, AIP Conf. Proc. **789**, 269 (2005).

[119] P. Prelovšek and J. Bonča, *Ground State and Finite Temperature Lanczos Methods*, *Strongly Correlated Systems: Numerical Methods*, 1–30 (Springer Berlin Heidelberg, 2013).

[120] D. V. Shalashilin, Quantum mechanics with the basis set guided by Ehrenfest trajectories: Theory and application to spin-boson model, J. Chem. Phys. **130**, 244101 (2009).

[121] D. V. Shalashilin, Nonadiabatic dynamics with the help of multiconfigurational Ehrenfest method: Improved theory and fully quantum 24d simulation of pyrazine, J. Chem. Phys. **132**, 244111 (2010).

[122] P. Ehrenfest, Bemerkung über die angenäherte Gültigkeit der klassischen Mechanik innerhalb der Quantenmechanik, Z. Phys. **45**, 455 (1927).

[123] J. C. Tully, Mixed quantum–classical dynamics, Faraday Discuss. **110**, 407 (1998).

[124] A. Bjerre and E. Nikitin, Energy transfer in collisions of an excited sodium atom with a nitrogen molecule, Chem. Phys. Lett. **1**, 179 (1967).

[125] J. C. Tully and R. K. Preston, Trajectory surface hopping approach to nonadiabatic molecular collisions: The reaction of H+ with D2, J. Chem. Phys. **55**, 562 (1971).

[126] J. C. Tully, Molecular dynamics with electronic transitions, J. Chem. Phys. **93**, 1061 (1990).

[127] S. R. White, Spin gaps in a frustrated Heisenberg model for CaV_4O_9, Phys. Rev. Lett. **77**, 3633 (1996).

[128] F. Verstraete and J. I. Cirac, Renormalization algorithms for quantum-many body systems in two and higher dimensions, arXiv:cond-mat/0407066 (2004).

[129] R. Orús, A practical introduction to tensor networks: Matrix product states and projected entangled pair states, Ann. Phys. (N. Y.) **349**, 117 (2014).

[130] E. Stoudenmire and S. R. White, Studying two-dimensional systems with the density matrix renormalization group, Annu. Rev. Condens. Matter Phys. **3**, 111 (2012).

[131] B. Bruognolo, J.-W. Li, J. von Delft, and A. Weichselbaum, A beginner's guide to non-abelian iPEPS for correlated fermions, SciPost Phys. Lect. Notes 25 (2021).

[132] G. Vidal, Efficient simulation of one-dimensional quantum many-body systems, Phys. Rev. Lett. **93**, 040502 (2004).

[133] A. J. Daley, C. Kollath, U. Schollwöck, and G. Vidal, Time-dependent density-matrix renormalization-group using adaptive effective Hilbert spaces, J. Stat. Mech. **2004**, P04005 (2004).

[134] S. R. White and A. E. Feiguin, Real-time evolution using the density matrix renormalization group, Phys. Rev. Lett. **93**, 076401 (2004).

[135] J. Haegeman, J. I. Cirac, T. J. Osborne, I. Pižorn, H. Verschelde, and F. Verstraete, Time-dependent variational principle for quantum lattices, Phys. Rev. Lett. **107**, 070601 (2011).

[136] J. Haegeman, C. Lubich, I. Oseledets, B. Vandereycken, and F. Verstraete, Unifying time evolution and optimization with matrix product states, Phys. Rev. B **94**, 165116 (2016).

[137] S. Paeckel, T. Köhler, A. Swoboda, S. R. Manmana, U. Schollwöck, and C. Hubig, Time-evolution methods for matrix-product states, Ann. Phys. (N. Y.) **411**, 167998 (2019).

[138] F. Verstraete, J. J. García-Ripoll, and J. I. Cirac, Matrix product density operators: Simulation of finite-temperature and dissipative systems, Phys. Rev. Lett. **93**, 207204 (2004).

[139] A. E. Feiguin and S. R. White, Finite-temperature density matrix renormalization using an enlarged Hilbert space, Phys. Rev. B **72**, 220401 (2005).

[140] S. R. White, Minimally entangled typical quantum states at finite temperature, Phys. Rev. Lett. **102**, 190601 (2009).

[141] T. Barthel, U. Schollwöck, and S. R. White, Spectral functions in one-dimensional quantum systems at finite temperature using the density matrix renormalization group, Phys. Rev. B **79**, 245101 (2009).

[142] E. M. Stoudenmire and S. R. White, Minimally entangled typical thermal state algorithms, New J. Phys. **12**, 055026 (2010).

[143] A. E. Feiguin and G. A. Fiete, Spectral properties of a spin-incoherent Luttinger liquid, Phys. Rev. B **81**, 075108 (2010).

[144] M. Binder and T. Barthel, Minimally entangled typical thermal states versus matrix product purifications for the simulation of equilibrium states and time evolution, Phys. Rev. B **92**, 125119 (2015).

[145] D. Gobert, C. Kollath, U. Schollwöck, and G. Schütz, Real-time dynamics in spin-$\frac{1}{2}$ chains with adaptive time-dependent density matrix renormalization group, Phys. Rev. E **71**, 036102 (2005).

[146] K. Burke, Perspective on density functional theory, J. Chem. Phys. **136**, 150901 (2012).

[147] P. Barmettler, M. Punk, V. Gritsev, E. Demler, and E. Altman, Relaxation of antiferromagnetic order in spin-1/2 chains following a quantum quench, Phys. Rev. Lett. **102**, 130603 (2009).

[148] S. Trotzky, Y.-A. Chen, A. Flesch, I. P. McCulloch, U. Schollwöck, J. Eisert, and I. Bloch, Probing the relaxation towards equilibrium in an isolated strongly correlated 1D Bose gas, Nat. Phys. **8**, 325 (2012).

[149] E. Y. Loh, J. E. Gubernatis, R. T. Scalettar, S. R. White, D. J. Scalapino, and R. L. Sugar, Sign problem in the numerical simulation of many-electron systems, Phys. Rev. B **41**, 9301 (1990).

[150] E. Koch, *DMFT: From Infinite Dimensions to Real Materials, Ch.11: Analytic Continuation of Quantum Monte Carlo Data* (Verlag des Forschungszentrum, 2018).

[151] C. Zhang, E. Jeckelmann, and S. R. White, Density matrix approach to local Hilbert space reduction, Phys. Rev. Lett. **80**, 2661 (1998).

[152] E. Jeckelmann and S. R. White, Density-matrix renormalization-group study of the polaron problem in the Holstein model, Phys. Rev. B **57**, 6376 (1998).

[153] T. Köhler, J. Stolpp, and S. Paeckel, Efficient and Flexible Approach to Simulate Low-Dimensional Quantum Lattice Models with Large Local Hilbert Spaces, SciPost Phys. **10**, 58 (2021).

[154] S. Mardazad, Y. Xu, X. Yang, M. Grundner, U. Schollwöck, H. Ma, and S. Paeckel, Quantum dynamics simulation of intramolecular singlet fission in covalently linked tetracene dimer, J. Chem. Phys. **155**, 194101 (2021).

[155] M. Moroder, M. Grundner, F. Damanet, U. Schollwöck, S. Mardazad, S. Flannigan, T. Köhler, and S. Paeckel, Metallicity in the dissipative Hubbard-Holstein model: Markovian and Non-Markovian tensor-network methods for open quantum many-body systems, arXiv:2207.08243 (2022).

[156] C. Brockt, F. Dorfner, L. Vidmar, F. Heidrich-Meisner, and E. Jeckelmann, Matrix-product-state method with a dynamical local basis optimization for bosonic systems out of equilibrium, Phys. Rev. B **92**, 241106 (2015).

[157] C. Guo, A. Weichselbaum, J. von Delft, and M. Vojta, Critical and strong-coupling phases in one- and two-bath spin-boson models, Phys. Rev. Lett. **108**, 160401 (2012).

[158] D. Jansen, J. Bonča, and F. Heidrich-Meisner, Finite-temperature density-matrix renormalization group method for electron-phonon systems: Thermodynamics and Holstein-polaron spectral functions, Phys. Rev. B **102**, 165155 (2020).

[159] C. Karrasch, J. H. Bardarson, and J. E. Moore, Finite-temperature dynamical density matrix renormalization group and the Drude weight of spin-1/2 chains, Phys. Rev. Lett. **108**, 227206 (2012).

[160] T. Barthel, Precise evaluation of thermal response functions by optimized density matrix renormalization group schemes, New J. Phys. **15**, 073010 (2013).

[161] C. Karrasch, J. H. Bardarson, and J. E. Moore, Reducing the numerical effort of finite-temperature density matrix renormalization group calculations, New J. Phys. **15**, 083031 (2013).

[162] T. Barthel, Matrix product purifications for canonical ensembles and quantum number distributions, Phys. Rev. B **94**, 115157 (2016).

[163] D. Kennes and C. Karrasch, Extending the range of real time density matrix renormalization group simulations, Comput. Phys. Commun. **200**, 37 (2016).

[164] D. Jansen, J. Bonča, and F. Heidrich-Meisner, Finite-temperature optical conductivity with density-matrix renormalization group methods for the holstein polaron and bipolaron with dispersive phonons, Phys. Rev. B **106**, 155129 (2022).

[165] E. M. Stoudenmire and S. R. White, Real-space parallel density matrix renormalization group, Phys. Rev. B **87**, 155137 (2013).

[166] P. Secular, N. Gourianov, M. Lubasch, S. Dolgov, S. R. Clark, and D. Jaksch, Parallel time-dependent variational principle algorithm for matrix product states, Phys. Rev. B **101**, 235123 (2020).

[167] G. Mahan, *Many-Particle Physics* (Plenum Publishers, 2000).

[168] T. Koch, J. Loos, A. Alvermann, A. R. Bishop, and H. Fehske, Transport through a vibrating quantum dot: Polaronic effects, J. Phys. Conf. Ser. **220**, 012014 (2010).

[169] T. Koch, J. Loos, and H. Fehske, Thermoelectric effects in molecular quantum dots with contacts, Phys. Rev. B **89**, 155133 (2014).

[170] A. Jovchev and F. B. Anders, Influence of vibrational modes on quantum transport through a nanodevice, Phys. Rev. B **87**, 195112 (2013).

[171] D. Jansen, C. Jooss, and F. Heidrich-Meisner, Charge density wave breakdown in a heterostructure with electron-phonon coupling, Phys. Rev. B **104**, 195116 (2021).

[172] F. Heidrich-Meisner, I. González, K. A. Al-Hassanieh, A. E. Feiguin, M. J. Rozenberg, and E. Dagotto, Nonequilibrium electronic transport in a one-dimensional Mott insulator, Phys. Rev. B **82**, 205110 (2010).

[173] S. Kirino and K. Ueda, Nonequilibrium current in the one dimensional Hubbard model at half-filling, J. Phys. Soc. Jpn. **79**, 093710 (2010).

[174] A. Khedri, T. A. Costi, and V. Meden, Nonequilibrium thermoelectric transport through vibrating molecular quantum dots, Phys. Rev. B **98**, 195138 (2018).

[175] M. ten Brink, S. Gräber, M. Hopjan, D. Jansen, J. Stolpp, F. Heidrich-Meisner, and P. E. Blöchl, Real-time non-adiabatic dynamics in the one-dimensional holstein model: Trajectory-based vs exact methods, J. Chem. Phys. **156**, 234109 (2022).

[176] B. Bertini, F. Heidrich-Meisner, C. Karrasch, T. Prosen, R. Steinigeweg, and M. Žnidarič, Finite-temperature transport in one-dimensional quantum lattice models, Rev. Mod. Phys. **93**, 025003 (2021).

[177] M. Weber and J. K. Freericks, Real-time evolution of static electron-phonon models in time-dependent electric fields, Phys. Rev. E **105**, 025301 (2022).

[178] M. D. Petrović, M. Weber, and J. K. Freericks, Theoretical description of time-resolved photoemission in charge-density-wave materials out to long times, arXiv:2203.11880 (2022).

[179] L. Chen, Y. Zhao, and Y. Tanimura, Dynamics of a one-dimensional Holstein polaron with the hierarchical equations of motion approach, J. Phys. Chem. Lett. **6**, 3110 (2015).

[180] L. Chen, M. F. Gelin, and D. V. Shalashilin, Dynamics of a one-dimensional Holstein polaron: The multiconfigurational Ehrenfest method, J. Chem. Phys. **151**, 244116 (2019).

[181] J. E. Hirsch and E. Fradkin, Phase diagram of one-dimensional electron-phonon systems. II. The molecular-crystal model, Phys. Rev. B **27**, 4302 (1983).

[182] R. H. McKenzie, C. J. Hamer, and D. W. Murray, Quantum Monte Carlo study of the one-dimensional Holstein model of spinless fermions, Phys. Rev. B **53**, 9676 (1996).

[183] I. G. Lang and Y. A. Firsov, Kinetic theory of semiconductors with low mobility, Sov. Phys. JETP **16**, 1301 (1963).

[184] H. Bruus and K. Flensberg, *Many-Body Quantum Theory in Condensed Matter Physics: An Introduction* (OUP Oxford, 2004).

[185] N. Pottier, *Nonequilibrium Statistical Physics: Linear Irreversible Processes* (Oxford University Press, 2010).

[186] M. Stone and P. Goldbart, *Mathematics for Physics: A Guided Tour for Graduate Students* (Cambridge University Press, 2009).

[187] R. Kubo, Statistical-mechanical theory of irreversible processes. i. general theory and simple applications to magnetic and conduction problems, J. Phys. Soc. Jpn. **12**, 570 (1957).

[188] J. M. Luttinger, Theory of thermal transport coefficients, Phys. Rev. **135**, A1505 (1964).

[189] B. S. Shastry, Sum rule for thermal conductivity and dynamical thermal transport coefficients in condensed matter, Phys. Rev. B **73**, 085117 (2006).

[190] H. Bethe, Zur Theorie der Metalle, Z. Phys. 205–2626 (1931).

[191] D. Emin and C. F. Hart, Phonon-assisted hopping of an electron on a Wannier-Stark ladder in a strong electric field, Phys. Rev. B **36**, 2530 (1987).

[192] F. Heidrich-Meisner, A. Honecker, D. C. Cabra, and W. Brenig, Zero-frequency transport properties of one-dimensional spin-$\frac{1}{2}$ systems, Phys. Rev. B **68**, 134436 (2003).

[193] M. Rigol, V. Dunjko, and M. Olshanii, Thermalization and its mechanism for generic isolated quantum systems, Nature **452**, 854 (2008).

[194] A. W. Sandvik, Computational studies of quantum spin systems, AIP Conf. Proc. **1297**, 135 (2010).

[195] C. Schönle, D. Jansen, F. Heidrich-Meisner, and L. Vidmar, Eigenstate thermalization hypothesis through the lens of autocorrelation functions, Phys. Rev. B **103**, 235137 (2021).

[196] J. Jaklič and P. Prelovšek, Lanczos method for the calculation of finite-temperature quantities in correlated systems, Phys. Rev. B **49**, 5065 (1994).

[197] J. Jaklič and P. Prelovšek, Finite-temperature properties of doped antiferromagnets, Adv. Phys. **49**, 1 (2000).

[198] A. Kirrander and M. Vacher, Ehrenfest Methods for Electron and Nuclear Dynamics, *Quantum Chemistry and Dynamics of Excited States*, 469–497 (John Wiley & Sons, Ltd, 2020).

[199] S. Östlund and S. Rommer, Thermodynamic limit of density matrix renormalization, Phys. Rev. Lett. **75**, 3537 (1995).

[200] M. B. Hastings, An area law for one-dimensional quantum systems, J. Stat. Mech.: Theory Exp. **2007**, P08024 (2007).

[201] J. Eisert, M. Cramer, and M. B. Plenio, Colloquium: Area laws for the entanglement entropy, Rev. Mod. Phys. **82**, 277 (2010).

[202] G. Vidal, J. I. Latorre, E. Rico, and A. Kitaev, Entanglement in quantum critical phenomena, Phys. Rev. Lett. **90**, 227902 (2003).

[203] J. I. Latorre, E. Rico, and G. Vidal, Ground state entanglement in quantum spin chains, Quantum Info. Comput. **4**, 48–92 (2004).

[204] G. Vidal, Efficient classical simulation of slightly entangled quantum computations, Phys. Rev. Lett. **91**, 147902 (2003).

[205] M. Fishman, S. R. White, and E. M. Stoudenmire, The ITensor software library for tensor network calculations (2020).

[206] A. Nocera and G. Alvarez, Symmetry-conserving purification of quantum states within the density matrix renormalization group, Phys. Rev. B **93**, 045137 (2016).

[207] M. P. Zaletel, R. S. K. Mong, C. Karrasch, J. E. Moore, and F. Pollmann, Time-evolving a matrix product state with long-ranged interactions, Phys. Rev. B **91**, 165112 (2015).

[208] P. Calabrese and J. Cardy, Evolution of entanglement entropy in one-dimensional systems, J. Stat. Mech.: Theory Exp. **2005**, P04010 (2005).

[209] T. Barthel, U. Schollwöck, and S. Sachdev, Scaling of the thermal spectral function for quantum critical bosons in one dimension, arXiv:1212.3570 (2012).

[210] J. Hauschild, E. Leviatan, J. H. Bardarson, E. Altman, M. P. Zaletel, and F. Pollmann, Finding purifications with minimal entanglement, Phys. Rev. B **98**, 235163 (2018).

[211] M. Suzuki, Generalized Trotter's formula and systematic approximants of exponential operators and inner derivations with applications to many-body problems, Commun. Math. Phys. **51**, 183 (1976).

[212] B. Kloss, Y. B. Lev, and D. Reichman, Time-dependent variational principle in matrix-product state manifolds: Pitfalls and potential, Phys. Rev. B **97**, 024307 (2018).

[213] M. Yang and S. R. White, Time-dependent variational principle with ancillary Krylov subspace, Phys. Rev. B **102**, 094315 (2020).

[214] Y. Xu, Z. Xie, X. Xie, U. Schollwöck, and H. Ma, Stochastic adaptive single-site time-dependent variational principle, JACS Au **2**, 335 (2022).

[215] J.-W. Li, A. Gleis, and J. von Delft, Time-dependent variational principle with controlled bond expansion for matrix product states, arXiv:2208.10972 (2022).

[216] S. R. White and I. Affleck, Spectral function for the $S = 1$ Heisenberg antiferromagetic chain, Phys. Rev. B **77**, 134437 (2008).

[217] Y. Tian and S. R. White, Matrix product state recursion methods for computing spectral functions of strongly correlated quantum systems, Phys. Rev. B **103**, 125142 (2021).

[218] Z. Huang, E. Gull, and L. Lin, Robust analytic continuation of green's functions via projection, pole estimation, and semidefinite relaxation (2020).

[219] H. Weyl, Quantenmechanik und Gruppentheorie, Z. Physik **46**, 1 (1927).

[220] E. Wigner, On the Quantum Correction For Thermodynamic Equilibrium, Phys. Rev. **40**, 749 (1932).

[221] J. E. Moyal, Quantum mechanics as a statistical theory, Proc. Cambridge Phil. Soc. **45**, 99 (1949).

[222] M. Hillery, R. F. O'Connell, M. O. Scully, and E. P. Wigner, Distribution functions in physics: Fundamentals, Physics Reports **106**, 121 (1984).

[223] W. B. Case, Wigner functions and Weyl transforms for pedestrians, Am. J. of Phys. **76**, 937 (2008).

[224] K. Ando, Non-adiabatic couplings in Liouville description of mixed quantum-classical dynamics, Chem. Phys. Lett. **360**, 240 (2002).

[225] K. Ando and M. Santer, Mixed quantum-classical Liouville molecular dynamics without momentum jump, J. Chem. Phys. **118**, 10399 (2003).

[226] A. W. Jasper, S. Nangia, C. Zhu, and D. G. Truhlar, Non-Born-Oppenheimer Molecular Dynamics, Acc. Chem. Res. **39**, 101 (2006).

[227] T. Yonehara, K. Hanasaki, and K. Takatsuka, Fundamental approaches to nonadiabaticity: Toward a chemical theory beyond the Born–Oppenheimer paradigm, Chem. Rev. **112**, 499 (2012).

[228] S. A. Gräber, Simulating real-time dynamics in the Holstein model with Ehrenfest methods, master's thesis, Georg-August-Universität Göttingen, Institute for Theoretical Physics (2021).

[229] M. ten Brink, PhD thesis (to be published), Georg-August-Universität Göttingen, Institute for Theoretical Physics (2022).

[230] M. Hohenadler, Charge and spin correlations of a Peierls insulator after a quench, Phys. Rev. B **88**, 064303 (2013).

[231] M. Hohenadler and G. G. Batrouni, Dominant charge density wave correlations in the Holstein model on the half-filled square lattice, Phys. Rev. B **100**, 165114 (2019).

[232] M. Weber, F. F. Assaad, and M. Hohenadler, Thermal and quantum lattice fluctuations in Peierls chains, Phys. Rev. B **98**, 235117 (2018).

[233] M. Weber, F. F. Assaad, and M. Hohenadler, Directed-loop quantum Monte Carlo method for retarded interactions, Phys. Rev. Lett. **119**, 097401 (2017).

[234] F. Assaad, *DMFT at 25: Infinite Dimensions Modeling and Simulation, Ch.7: Continuous-Time QMC Solvers for Electronic Systems in Fermionic and Bosonic Baths* (Verlag des Forschungszentrum, 2014).

[235] P. J. Robinson, I. S. Dunn, and D. R. Reichman, Cumulant methods for electron-phonon problems. II. The self-consistent cumulant expansion, Phys. Rev. B **105**, 224305 (2022).

[236] J. Bonča, S. A. Trugman, and I. Batistić, Holstein polaron, Phys. Rev. B **60**, 1633 (1999).

[237] L.-C. Ku, S. A. Trugman, and J. Bonča, Dimensionality effects on the Holstein polaron, Phys. Rev. B **65**, 174306 (2002).

[238] J. Bonča, Spectral function of an electron coupled to hard-core bosons, Phys. Rev. B **102**, 035135 (2020).

[239] A. Picano, F. Grandi, P. Werner, and M. Eckstein, Stochastic semiclassical theory for non-equilibrium electron-phonon coupled systems, arXiv:2209.00428 (2022).

[240] N. V. Smith and M. M. Traum, Angular-resolved ultraviolet photoemission spectroscopy and its application to the layer compounds $TaSe_2$ and TaS_2, Phys. Rev. B **11**, 2087 (1975).

[241] F. J. Himpsel and D. E. Eastman, Experimental energy dispersions for valence and conduction bands of palladium, Phys. Rev. B **18**, 5236 (1978).

[242] W. Eberhardt and E. W. Plummer, Angle-resolved photoemission determination of the band structure and multielectron excitations in Ni, Phys. Rev. B **21**, 3245 (1980).

[243] C. Kirkegaard, T. K. Kim, and P. Hofmann, Self-energy determination and electron–phonon coupling on Bi(110), New J. Phys. **7**, 99 (2005).

[244] J. Ranninger and U. Thibblin, Two-site polaron problem: Electronic and vibrational properties, Phys. Rev. B **45**, 7730 (1992).

[245] F. Marsiglio, The spectral function of a one-dimensional holstein polaron, Physics Letters A **180**, 280 (1993).

[246] E. V. L. de Mello and J. Ranninger, Dynamical properties of small polarons, Phys. Rev. B **55**, 14872 (1997).

[247] J. M. Robin, Spectral properties of the small polaron, Phys. Rev. B **56**, 13634 (1997).

[248] H. Fehske, J. Loos, and G. Wellein, Lattice polaron formation: Effects of nonscreened electron-phonon interaction, Phys. Rev. B **61**, 8016 (2000).

[249] M. Hohenadler, M. Aichhorn, and W. von der Linden, Spectral function of electron-phonon models by cluster perturbation theory, Phys. Rev. B **68**, 184304 (2003).

[250] M. Hohenadler, D. Neuber, W. von der Linden, G. Wellein, J. Loos, and H. Fehske, Photoemission spectra of many-polaron systems, Phys. Rev. B **71**, 245111 (2005).

[251] G. L. Goodvin, M. Berciu, and G. A. Sawatzky, Green's function of the Holstein polaron, Phys. Rev. B **74**, 245104 (2006).

[252] B. Lau, M. Berciu, and G. A. Sawatzky, Single-polaron properties of the one-dimensional breathing-mode Hamiltonian, Phys. Rev. B **76**, 174305 (2007).

[253] M. Berciu and G. L. Goodvin, Systematic improvement of the momentum average approximation for the Green's function of a Holstein polaron, Phys. Rev. B **76**, 165109 (2007).

[254] T. Hotta and E. Dagotto, *Theory of Manganites* (Springer Dordrecht, 2004).

[255] K. H. Kim, J. Y. Gu, H. S. Choi, G. W. Park, and T. W. Noh, Frequency shifts of the internal phonon modes in $La_{0.7}Ca_{0.3}MnO_3$, Phys. Rev. Lett. **77**, 1877 (1996).

[256] G. Wellein and H. Fehske, Self-trapping problem of electrons or excitons in one dimension, Phys. Rev. B **58**, 6208 (1998).

[257] S. Fratini, F. de Pasquale, and S. Ciuchi, Optical absorption from a nondegenerate polaron gas, Phys. Rev. B **63**, 153101 (2001).

[258] G. L. Goodvin, A. S. Mishchenko, and M. Berciu, Optical conductivity of the Holstein polaron, Phys. Rev. Lett. **107**, 076403 (2011).

[259] J. Rincón, E. Dagotto, and A. E. Feiguin, Photoinduced hund excitons in the breakdown of a two-orbital Mott insulator, Phys. Rev. B **97**, 235104 (2018).

[260] S. Paeckel, B. Fauseweh, A. Osterkorn, T. Köhler, D. Manske, and S. R. Manmana, Detecting superconductivity out of equilibrium, Phys. Rev. B **101**, 180507 (2020).

[261] J. Rincón and A. E. Feiguin, Nonequilibrium optical response of a one-dimensional Mott insulator, Phys. Rev. B **104**, 085122 (2021).

[262] S. Ejima, F. Lange, and H. Fehske, Nonequilibrium dynamics in pumped Mott insulators, Phys. Rev. Research **4**, L012012 (2022).

[263] C. Hess, C. Baumann, U. Ammerahl, B. Büchner, F. Heidrich-Meisner, W. Brenig, and A. Revcolevschi, Magnon heat transport in $(Sr, Ca, La)_{14}Cu_{24}O_{41}$, Phys. Rev. B **64**, 184305 (2001).

[264] T. Kawamata, N. Takahashi, T. Adachi, T. Noji, K. Kudo, N. Kobayashi, and Y. Koike, Evidence for ballistic thermal conduction in the one-dimensional S=1/2 Heisenberg antiferromagnetic spin system Sr_2CuO_3, J. Phys. Soc. Jpn. **77**, 034607 (2008).

[265] N. Hlubek, P. Ribeiro, R. Saint-Martin, A. Revcolevschi, G. Roth, G. Behr, B. Büchner, and C. Hess, Ballistic heat transport of quantum spin excitations as seen in $SrCuO_2$, Phys. Rev. B **81**, 020405 (2010).

[266] N. Hlubek, X. Zotos, S. Singh, R. Saint-Martin, A. Revcolevschi, B. Büchner, and C. Hess, Spinon heat transport and spin–phonon interaction in the spin-1/2 Heisenberg chain cuprates Sr_2CuO_3 and $SrCuO_2$, J. Stat. Mech.: Theory Exp. **2012**, P03006 (2012).

[267] E. Shimshoni, N. Andrei, and A. Rosch, Thermal conductivity of spin-$\frac{1}{2}$ chains, Phys. Rev. B **68**, 104401 (2003).

[268] A. L. Chernyshev and A. V. Rozhkov, Thermal transport in antiferromagnetic spin-chain materials, Phys. Rev. B **72**, 104423 (2005).

[269] A. L. Chernyshev and W. Brenig, Thermal conductivity in large $-J$ two-dimensional antiferromagnets: Role of phonon scattering, Phys. Rev. B **92**, 054409 (2015).

[270] A. L. Chernyshev and A. V. Rozhkov, Heat transport in spin chains with weak spin-phonon coupling, Phys. Rev. Lett. **116**, 017204 (2016).

[271] M. Galperin, A. Nitzan, and M. A. Ratner, Heat conduction in molecular transport junctions, Phys. Rev. B **75**, 155312 (2007).

[272] M. Galperin, M. A. Ratner, and A. Nitzan, Molecular transport junctions: vibrational effects, J. Phys. Condens. Matter **19**, 103201 (2007).

[273] Y. Dubi and M. Di Ventra, Colloquium: Heat flow and thermoelectricity in atomic and molecular junctions, Rev. Mod. Phys. **83**, 131 (2011).

[274] X. Qian, J. Zhou, and G. Chen, Phonon-engineered extreme thermal conductivity materialsn, Nature Mater. **20**, 1188 (2021).

[275] H. Rezania and F. Taherkhani, Polaron effects on the thermal conductivity of zigzag carbon nanotubes, Solid State Commun. **152**, 1776 (2012).

[276] J.-M. Bischoff and E. Jeckelmann, Density-matrix renormalization group method for the conductance of one-dimensional correlated systems using the Kubo formula, Phys. Rev. B **96**, 195111 (2017).

[277] R. Nourafkan and N. Nafari, Phase diagram of the Holstein-Kondo lattice model at half filling, Phys. Rev. B **79**, 075122 (2009).

[278] M. A. Green and S. P. Bremner, Energy conversion approaches and materials for high-efficiency photovoltaics, Nat. Mater. **16**, 23 (2017).

[279] M. Chávez-Cervantes, G. E. Topp, S. Aeschlimann, R. Krause, S. A. Sato, M. A. Sentef, and I. Gierz, Charge density wave melting in one-dimensional wires with femtosecond subgap excitation, Phys. Rev. Lett. **123**, 036405 (2019).

[280] D. Polli, M. Rini, S. Wall, R. W. Schoenlein, Y. Tomioka, Y. Tokura, G. Cerullo, and A. Cavalleri, Coherent orbital waves in the photo-induced insulator–metal dynamics, Nat. Mater. **6**, 643 (2007).

[281] B. Ifland, P. Peretzki, B. Kressdorf, P. Saring, A. Kelling, M. Seibt, C. Jooss, and J. Beilstein, Current–voltage characteristics of manganite–titanite perovskite junctions, Nanotechnol. **6**, 1467–1484 (2015).

[282] B. Ifland, J. Hoffmann, B. Kressdorf, V. Roddatis, M. Seibt, and C. Jooss, Contribution of Jahn-Teller and charge transfer excitations to the photovoltaic effect of manganite/titanite heterojunctions, New J. Phys. **19**, 063046 (2017).

[283] S. Andergassen, V. Meden, H. Schoeller, J. Splettstoesser, and M. R. Wegewijs, Charge transport through single molecules, quantum dots and quantum wires, Nanotechnology **21**, 272001 (2010).

[284] A. Khedri, T. A. Costi, and V. Meden, Exponential and power-law renormalization in phonon-assisted tunneling, Phys. Rev. B **96**, 195155 (2017).

[285] A. Khedri, V. Meden, and T. A. Costi, Influence of phonon-assisted tunneling on the linear thermoelectric transport through molecular quantum dots, Phys. Rev. B **96**, 195156 (2017).

[286] T. Shi, J. I. Cirac, and E. Demler, Ultrafast molecular dynamics in terahertz-STM experiments: Theoretical analysis using the Anderson-Holstein model, Phys. Rev. Research **2**, 033379 (2020).

[287] P. Schmitteckert, Nonequilibrium electron transport using the density matrix renormalization group method, Phys. Rev. B **70**, 121302 (2004).

[288] K. A. Al-Hassanieh, A. E. Feiguin, J. A. Riera, C. A. Büsser, and E. Dagotto, Adaptive time-dependent density-matrix renormalization-group technique for calculating the conductance of strongly correlated nanostructures, Phys. Rev. B **73**, 195304 (2006).

[289] S. Kirino, T. Fujii, J. Zhao, and K. Ueda, Time-dependent DMRG study on quantum dot under a finite bias voltage, J. Phys. Soc. Jpn. **77**, 084704 (2008).

[290] F. Heidrich-Meisner, A. E. Feiguin, and E. Dagotto, Real-time simulations of nonequilibrium transport in the single-impurity anderson model, Phys. Rev. B **79**, 235336 (2009).

[291] C. Guo, A. Weichselbaum, S. Kehrein, T. Xiang, and J. von Delft, Density matrix renormalization group study of a quantum impurity model with Landau-Zener time-dependent Hamiltonian, Phys. Rev. B **79**, 115137 (2009).

[292] A. Branschädel, G. Schneider, and P. Schmitteckert, Conductance of inhomogeneous systems: Real-time dynamics, Ann. Phys. (Berl.) **522**, 657 (2010).

[293] M. Nuss, M. Ganahl, H. G. Evertz, E. Arrigoni, and W. von der Linden, Steady-state and quench-dependent relaxation of a quantum dot coupled to one-dimensional leads, Phys. Rev. B **88**, 045132 (2013).

[294] F. Schwarz, I. Weymann, J. von Delft, and A. Weichselbaum, Nonequilibrium steady-state transport in quantum impurity models: A thermofield and quantum quench approach using matrix product states, Phys. Rev. Lett. **121**, 137702 (2018).

[295] T. Oka, R. Arita, and H. Aoki, Breakdown of a Mott insulator: A nonadiabatic tunneling mechanism, Phys. Rev. Lett. **91**, 066406 (2003).

[296] T. Oka and H. Aoki, Ground-state decay rate for the Zener breakdown in band and Mott insulators, Phys. Rev. Lett. **95**, 137601 (2005).

[297] T. Oka and H. Aoki, Dielectric breakdown in a Mott insulator: Many-body Schwinger-Landau-Zener mechanism studied with a generalized Bethe ansatz, Phys. Rev. B **81**, 033103 (2010).

[298] M. Eckstein, T. Oka, and P. Werner, Dielectric breakdown of Mott insulators in dynamical mean-field theory, Phys. Rev. Lett. **105**, 146404 (2010).

[299] J.-M. Bischoff and E. Jeckelmann, Density-matrix renormalization group study of the linear conductance in quantum wires coupled to interacting leads or phonons, Phys. Rev. B **100**, 075151 (2019).

[300] L. Zhang, U. Bhattacharya, A. Bachtold, S. Forstner, M. Lewenstein, F. Pistolesi, and T. Grass, Steady-state peierls transition in nanotube quantum simulator, arXiv:2206.08020 (2022).

[301] U. Bhattacharya, T. Grass, A. Bachtold, M. Lewenstein, and F. Pistolesi, Phonon-induced pairing in quantum dot quantum simulator, Nano Lett. **21**, 9661 (2021).

[302] F. Agostini and B. F. E. Curchod, Different flavors of nonadiabatic molecular dynamics, WIREs Comput. Mol. Sci. **9**, e1417 (2019).

[303] G. Li, B. Movaghar, A. Nitzan, and M. A. Ratner, Polaron formation: Ehrenfest dynamics vs. exact results, J. Chem. Phys. **138**, 044112 (2013).

[304] J. L. Alonso, C. Bouthelier-Madre, A. Castro, J. Clemente-Gallardo, and J. A. Jover-Galtier, About the computation of finite temperature ensemble averages of hybrid quantum-classical systems with molecular dynamics, New J. Phys. **23**, 063011 (2021).

[305] J. Sous, M. Chakraborty, R. V. Krems, and M. Berciu, Light bipolarons stabilized by peierls electron-phonon coupling, Phys. Rev. Lett. **121**, 247001 (2018).

[306] K. Zawadzki, L. Yang, and A. E. Feiguin, Time-dependent approach to inelastic scattering spectroscopies in and away from equilibrium: Beyond perturbation theory, Phys. Rev. B **102**, 235141 (2020).

[307] G. C. Schatz and M. A. Ratner, *Quantum Mechanics in Chemestry* (Dover Publications, Mineola, New York, 2002).

[308] A. Nitzan, *Chemical Dynamics in Condensed Phases* (Oxford University Press, New York, 2006).

[309] A. Tokmakoff, Lecture notes on time-dependent quantum mechanics and spectroscopy (accessed October 2022).

Research data

Chapter 4:
The data and the git repository is stored in the 10-Year-archive of the Institut für Theoretische Physik, Georg-August-Universität Göttingen (ITP) ("/net/theorie/rocks/jansen32/10-Years-Archive") as "finiteTJansenBoncaHM.tar.bz2".
The data shown in the publication can be found at https://arxiv.org/abs/2007.11343.
The finite temperature states are stored at the Archivsystems HSM at the GWDG at "/usr/users/a/jansen32/FTstates_HolspecFunc.bz2".
Chapter 5:
Section 5.1:
The data and the git repository is stored at the 10 Year archive ("/net/theorie/rocks/jansen32/10-Years-Archive") of ITP as "finiteTOPCJansenBoncaHM.tar.bz2".
The finite temperature states and data are stored at the Archivsystems HSM at the GWDG at "/usr/users/a/jansen32/FTOPCstates_and_data.tar.gz".
The data shown in the publication can be found at https://arxiv.org/abs/2206.00985.
The code used to generate the data is be published at https://gitlab.gwdg.de/jansen32/optical_cond_paper.
Sections 5.3 and 5.4:
The data and the git repository is stored at the 10 Year archive ("/net/theorie/rocks/jansen32/10-Years-Archive") of the ITP as "phd_sec53_54_data_repos.tar.gz".
Chapter 6:
The data and the git repository is stored at the 10 Year archive ("/net/theorie/rocks/jansen32/10-Years-Archive") of the ITP as "cdwbreakdownJansenJoossHM.tar.gz".
The data shown in the publication can be found at https://arxiv.org/abs/2109.07197.
The initial states are stored at the Archivsystems HSM at the GWDG at "/usr/users/a/jansen32/cdwbreakdownststates.tar.gz".
Chapter 7:
The data shown in the publication can be found at https://data.goettingen-research-online.de/dataset.xhtml?persistentId=doi:10.25625/YDU1XT.

All codes used to generate the data are stored at the 10 Year archive ("/net/theorie/rocks/jansen32/10-Years-Archive") of the ITP as "codes.tar.gz".

Acknowledgments

There are many people whose contributions played a role in this thesis. First, I want to thank Prof. Fabian Heidrich-Meisner for trusting me with the opportunity and for his guidance and supervision during this Ph.D. I also want to thank him for his time commitment to all of our projects and his inspiring enthusiasm for our work. I also thank him for his support in non-science-related matters. I also want to thank Prof. Stefan Kehrein for being my second reviewer. Furthermore, I want to thank the examination board for their time and, in particular, my TAC members, Prof. Christian Jooss and Prof. Peter Sollich for coming to my talks and sharing their ideas and perspectives.

I also want to thank Prof. Janez Bonča, he taught me so much about the Holstein model, and I am thankful for his time, patience, and the discussions. I additionally want to thank Christoph Schönle and Jakob Lötfering, I enjoyed and learned a lot from our discussions. I also benefited from the discussions in the SFB electron-phonon meetings with Prof. Christian Jooss, Prof. Peter Blöchl, Prof. Heidrich-Meisner, Dr. Jörg Hoffmann, Michael ten Brink, Birte Kressdorf, and Annika Dehning. Furthermore, I want to thank all my collaborators, but in particular Michael ten Brink for teaching me about the Born-Oppenheimer surfaces, Dr. Lev Vidmar for two great projects, and Dr. Miroslav Hopjan for collaborating on and discussing many topics. I also acknowledge the funding and support from the SFB 1073.

I am also grateful to Michael ten Brink, Constantin Meyer, Miroslav Hopjan, and Karun Gadge for their comments on my thesis. There have been many great discussions in the SFB and ITP but I want to specifically mention the ones with Suman Mondal, Eric Bertok, Jan Stolpp, Constantin Meyer, Sebastian Paeckel, Nils Abeling, Alexander Osterkorn, Arturo Romero Perez, Salvatore Manmana, Anna Seiler, and Rudolf Haindl.

I am thankful to Daniel Sanchez for showing me that physics is awesome, which led me on this path. This would also not have been possible without the support and encouragement of my family. You are the best! I am also very grateful to our neighbors in Melkeveien, Eirik and Marit, for their encouragement and interest in my work. Lastly, I want to thank my wife, Nathalie, for her patience, support, and for listening to all my practice talks. I also want to thank her for taking care of Jan Santiago when I was working (too much sometimes). This would not have been possible without you! I also want to thank my son, Jan Santiago, for taking care of his mom while I was in the office or traveling. Finally, I need to thank Jan Santiago for making me read "Quantum Mechanics for Babies" to him at least ten times (so far). I am starting to know that book quite well.